Morphologie et fonction des canaux semi-circulaires de l'oreille interne des mammifères souterrains

Charlène Selva

▶ **To cite this version:**

Charlène Selva. Morphologie et fonction des canaux semi-circulaires de l'oreille interne des mammifères souterrains. Paléontologie. Museum national d'histoire naturelle - MNHN PARIS, 2017. Français. NNT : 2017MNHN0034 . tel-04768170

HAL Id: tel-04768170

https://theses.hal.science/tel-04768170v1

Submitted on 5 Nov 2024

HAL is a multi-disciplinary open access archive for the deposit and dissemination of scientific research documents, whether they are published or not. The documents may come from teaching and research institutions in France or abroad, or from public or private research centers.

L'archive ouverte pluridisciplinaire **HAL**, est destinée au dépôt et à la diffusion de documents scientifiques de niveau recherche, publiés ou non, émanant des établissements d'enseignement et de recherche français ou étrangers, des laboratoires publics ou privés.

MUSEUM NATIONAL D'HISTOIRE NATURELLE

Ecole Doctorale Sciences de la Nature et de l'Homme – ED 227

Année 2017 **N°attribué par la bibliothèque**

|_|_|_|_|_|_|_|_|_|_|_|_|

THESE

Pour obtenir le grade de

DOCTEUR DU MUSEUM NATIONAL D'HISTOIRE NATURELLE

Spécialité : Biologie de l'Evolution et Paléontologie

Présentée et soutenue publiquement par

Charlène Selva

Le 30 novembre 2017

Morphologie et fonction des canaux semi-circulaires de l'oreille interne des mammifères souterrains

---

Sous la direction de **: Docteur Ladevèze Sandrine, Chargé de recherche CNRS**

Docteur Germain Damien, Maître de conférences Muséum

Docteur Peigné Stéphane, Chargé de recherche CNRS

Réalisée au sein de l'UMR 7207 – Centre de Recherche sur la Paléobiodiversité et les Paléoenvironnements

JURY :

Dr. Ladevèze Sandrine	**Chargé de recherche, CNRS, Paris (075)**	**Directeur de Thèse**
Dr. Germain Damien	**Maître de conférences, Muséum national d'Histoire naturelle, Paris (075)**	**Directeur de Thèse**
Dr. Peigné Stéphane	**Chargé de recherché, CNRS, Paris (075)**	**Directeur de Thèse**
Prof. Begall, Sabine	**Associate Professor, University of Duisburg-Essen, Essen (Allemagne)**	**Rapporteur**
Dr. Loïc Costeur	**Curator for Vertebrate Paleontology, Naturhistorisches Museum, Basel (Suisse)**	**Rapporteur**
Prof. Radim Šumbera	**Associate Professor, University of South Bohemia, Branišovská (Czech Republic)**	**Examinateur**
Prof. Bardet, Nathalie	**Directeur de recherche, CNRS, Paris (075)**	**Examinateur**
Dr. David Romain	**Post-doctorant, Max Planck Institute, Leipzig (Allemagne)**	**Invité**

Morphologie et fonction des canaux semi-circulaires de l'oreille interne des mammifères souterrains

Le mode de vie souterrain impose des contraintes mécaniques et un environnement sensoriel restreint chez les taupes. L'oreille interne, organe sensoriel qui gère l'équilibre, les mouvements de la tête et l'orientation spatiale joue un rôle primordial dans ce milieu. Ma thèse a pour but de définir quelles caractéristiques anatomiques ou fonctionnelles du système des canaux semicirculaires de l'oreille interne sont typiques de ce mode de vie, apparu indépendamment chez plusieurs clades de mammifères (marsupiaux, xénarthres, eulipotyphles, afrothères, rongeurs). Les études statistiques de la morphologie du système des canaux semicirculaires osseux et membraneux montrent qu'il n'y a pas de caractéristique anatomique liée au mode de vie souterrain. Les paramètres fonctionnels de l'organe permettent finalement de différencier les systèmes des canaux semicirculaires des mammifères souterrains des non-souterrains et de conclure que des morphologies différentes peuvent fournir les mêmes fonctions. Ce travail met en lumière une nouvelle adaptation convergente et fonctionnelle du système des canaux semicirculaires au mode de vie souterrain : les taupes ont une plus grande sensibilité de détection des mouvements de la tête et donc une meilleure orientation spatiale, ce qui compense la perte de la vue.

Mots-clés

CT-scan - Synchrotron - Morphométrie géométrique - Statistiques Multivariées - Labyrinthes Osseux et Membraneux - Taupes

Morphology and function of the semicircular ducts of the inner ear of the subterranean mammals

The subterranean lifestyle requires mechanical constraints and a restricted sensorial environment in moles. The inner ear, the sense organ that handles balance, head motions and spatial awareness, plays an important role in this milieu. My thesis aims at characterizing which anatomical or functional features of the semicircular duct system of the inner ear are typical for this lifestyle, appeared independently in several clades of mammals (marsupials, xenarthrans, eulipotyphlans, afrotherians, rodents). Statistical analyses of the morphology of the osseous and membranous semicircular duct system show that there are no anatomical features linked to the subterranean lifestyle. The functional parameters of the organ allow ultimately to differentiate the semicircular duct system of the subterranean mammals from the non-subterranean species and to conclude that different morphologies can lead to the same function. This work highlights a clear and new functional convergent adaptation of the semicircular duct system to the subterranean lifestyle: the moles present a higher sensitivity to detect head motions and therefore a better spatial awareness, which compensates the sight loss.

Keywords

CT-scan - Synchrotron - Geometric Morphometrics - Multivariate Statistics - Osseous and Membranous Labyrinths - Moles

Remerciements

La recherche s'enrichit des rencontres et des relations sociales. Cette idée a montré sa pertinence pendant mon doctorat : que ces contacts soient strictement professionnels ou amicaux, ils ont été indispensables au bon déroulement de mes années de thèse.
Merci à vous tous pour ces moments d'échanges !

Mon premier MERCI nominatif est directement adressé à Sandrine Ladevèze : merci de m'avoir fait découvrir le monde de la recherche, merci d'avoir été une encadrante patiente et idéale, merci de m'avoir formée depuis 5 ans, merci de m'avoir proposé des sujets de recherche passionnants, merci pour ton soutien, ta disponibilité et ton investissement, merci aussi pour notre magnifique relation qui n'est plus seulement professionnelle, merci de m'avoir fait rentrer dans ta vie, merci pour toutes nos discussions passionnées, merci d'avoir partagé avec moi les événements de ta vie… Mille tendres mercis, cette thèse n'existerait pas sans toi.

Mes Mercis suivants sont adressés à mon deuxième encadrant, Damien Germain et à mon directeur de thèse, Stéphane Peigné. Damien, merci pour nos moments de rigolades avec ma petite hulotte, merci pour tes regards complices remplis de sentiments de bienveillance, merci pour ton amitié. J'ai vraiment adoré travaillé avec toi sur les statistiques. Stéphane, merci de m'avoir enseigné le rôle de la politique dans le fonctionnement de la science, merci d'avoir partagé un morceau de ton bureau (c'est le plus beau de tous), merci de m'avoir aidée à garder les pieds sur terre concernant la quantité de projets que j'avais imaginés, merci pour nos discussions sur les films et autres sujets culturels pour lesquels j'ai toujours besoin d'apprendre, merci pour ta bonne humeur et tes blagues qui font vivre notre étage. Je pense constamment fort à toi et à ton combat plus personnel. Reviens vite, tu nous manques ☺

Vous êtes tous les trois des personnes extraordinaires et totalement bienveillantes. J'ai eu beaucoup de chance de vous avoir comme superviseurs, MERCI !
(à quand notre prochain repas chez Desvouges ?)

My warmest thanks to the members of my jury for their patience, their understanding and their encouragements. Sabine Begall, Loïc Costeur, Radim Šumbera, Nathalie Bardet and Romain David, thank you for your investment, your advices and your coming for my oral thesis.

Ce travail de thèse n'aurait pas pu se réaliser sans les collaborateurs Romain David et Jérémie Bardin. Romain, merci pour ta collaboration et ton investissement dans ce projet, j'ai adoré travailler avec toi, tu es un pédagogue hors pair et un très grand scientifique, j'ai beaucoup appris à tes côtés et je suis ravie de voir la suite de nos collaborations. Merci à toi et ton responsable (Jean-Jacques Hublin) pour le super accueil à quatre reprises au Max Planck Institut de Leipzig. Merci à toi et ta famille pour votre accueil et vos partages. (Et sache que j'ai presque fini *the witness*, on se fera un débrief ?)
Jérémie, merci beaucoup pour les analyses statistiques que tu as réalisées, merci pour ta patience quand tu m'as expliqué les différents tests, et merci de m'avoir fait découvrir le libanais du marché place Monge.

Je remercie Sylvie Crasquin, directrice de l'UMR 7207 ainsi que Christian de Muizon et Gaël Clément, respectivement ancien et nouveau directeur du département 'Origines et Evolution' pour l'accueil au sein du laboratoire.

Un chaleureux merci à l'équipe administrative du laboratoire : Angelina Bastos, Suzy Colas, Éric Tourneur, Mélinée Deretz, merci beaucoup de nous épauler dans nos démarches administratives, merci de ne pas avoir peur de répéter les informations et merci beaucoup de nous rendre la vie plus simple !
Merci à Maria, Michel et Bruno pour leur gentillesse.

Merci à Marie-Astrid Angel pour son aide précieuse.
Une pensée à l'ensemble des collègues du CR2P.

Merci aux responsables et gestionnaires des collections du Muséum que j'ai cotoyés : Christine Argot, Géraldine Véron, Aurélie Verguin, Violaine Nicolas et Marc Herbin. Merci pour vos disponibilités, vos conseils et vos aides dans la manipulation et préparation des spécimens.
Merci également à Alexander Stoessel, responsable des collections de Jena.
Un grand merci à Jérôme Dormion de Taup'green, qui nous a permis d'obtenir (enfin !) un spécimen de taupe européenne. Merci beaucoup pour ta réponse positive aussi rapide et d'avoir été aussi accommodant !
Merci à Lilian Cazes, photographe du laboratoire, pour les magnifiques photos qu'il a pris des nombreux spécimens de mon échantillonnage.
Merci à Miguel Garcia-Sanz et Maïté Adam pour les nombreux scans effectués à la plateforme AST-RX du Muséum.
Merci à Vincent Fernandez pour les scans effectués à l'ESRF. (il faudra se refaire une partie d'*Exploding Kittens* !)
Merci à David Plotzki pour les scans effectués au Max Planck Institut de Leipzig.
Un gigantesque merci à Florent Goussard, responsable de la plateforme 3D, pour ses aides amicales et toujours efficaces concernant la segmentation et le traitement des objets 3D.
Un magnifique merci à Patricia Wils, responsable à la plateforme AST-RX, pour sa gentillesse et sa bonne humeur lors de toutes ses explications pour mieux appréhender AVIZO.
Merci à Renaud Lebrun pour sa formation à Morphotools.
Merci aux membres de mon comité de thèse d'avoir veillé au bon déroulement de ma thèse : Romain David, Raphaël Cornette, Guillaume Billet, Anick Abourachid, Véronique Barriel et Antoine Zazzo.
Merci à Nathalie Machon, directrice de l'Ecole Doctorale 227 et ses collaborateurs Anaïs Ranera, Mahjouba Fassa et Ouahida Aloui pour leurs disponibilités et leurs attentions afin que nos thèses se déroulent le mieux possible.

Merci à Emilie Detouillon, ma responsable pour mes activités annexes d'enseignements et de médiation scientifique.
Merci à mes collègues docteurs avec qui j'ai enseigné auprès d'élèves du secondaire : Nina Marchi, Laurianne Cacheux, Arnaud Schmitt, Thomas Arbez, Julien Azuara, Silvia De Cesare, Margot Michaud et Paul Zaharias.
J'ai adoré faire mes missions doctorales et c'est aussi grâce à vous !
Merci à Véronique Barriel et Gaël Clément de m'avoir permis d'intervenir dans leurs modules d'enseignement.

Véronique, je veux aussi te dire merci pour tous nos échanges magiques le matin autour d'un café pour parler de nos expériences de vie et de sciences. J'adore ces moments de voisines de bureau.
(Et une pensée à Sophie Sanchez qui nous a rejoints avec sa bonne humeur et sa fraîcheur dans ce coin d'étage.)

Merci aux institutions m'ayant attribué des bourses qui m'ont permis de mener à bien mes travaux de thèse (bourse courte durée du DAAD, bourse « Transhumance » de Sorbonne-Universités, bourse « ATM » du Muséum).

Merci aux précédentes institutions et formations qui m'ont accueillie et qui m'ont permis d'arriver jusqu'à cette thèse : le master SEP (Véronique Barriel, Régine Vignes, Pascal Tassy), Jardin des Sciences de Strasbourg (Sébastien Soubiran et Kévin Janneau), Musée Requien d'Avignon (Evelyne Cregut), le Muséum d'Histoire naturelle de Montauban (Aude Bergeret), Université Tor

Vergata de Rome (Michele Scardi) et l'Université Paul Sabatier de Toulouse (Régis Cereghino, Francis Auclair, Bernard Andreu, Loïc Ten-Hage et Stéphan Maumont).

Merci à l'ASMU de nous proposer de superbes activités à prix accessibles et sur le lieu de travail (je pense particulièrement à Sophie Guillon et Véronique Rousseau, collègues de la gym ; et Didier Geffard-Kuriyama pour le club jeu).

Merci aux équipes du Bureau des Doctorants et Etudiants du Muséum (BDEM) pour les événements organisés afin de resserrer la communauté de jeunes scientifiques du Muséum.
Merci aux équipes du Young Natural History Scientists' Meeting de continuer à faire vivre ce magnifique congrès international. J'ai adoré m'investir dans ce projet !

Merci aux étudiants que j'ai encadré, c'était très enrichissant de travailler avec vous : Marine Lambert, Rohan Mansuit, Rémi Lefebvre et Kévin Le Verger. Et pour les trois derniers, je suis vraiment ravie pour vous de voir que vous êtes maintenant tous en doctorat ! Amusez-vous bien !

J'ai beaucoup de souvenirs avec tous les amis que j'ai rencontrés lors de ces années de recherches. Je ne pourrai pas être explicite, il me faudrait des pages et des pages afin de raconter les histoires que j'ai vécues avec chacun d'entre vous et pour montrer à quel point nos relations m'ont été indispensables. Je vous aime très fort.
J'ai une pensée amicale pour mes amis Erasmus et mes amis de licence.
Je pense avec nostalgie aux années Master pendant lesquelles j'ai rencontré de superbes personnes (Thibaut, Alexandre, Maxime, Océane, Guillaume, Anne, Eduardo, Nicolas…) avec deux mentions spéciales pour Meggy et Baptiste (et Marc-Alexandre en associé).
Je pense aussi à mes collègues muséum doctorants et post-doctorants anciens, actuels, nouveaux avec qui j'ai une quantité incroyable de souvenirs…. Séverine, Thomas, Rémi, Constance, François, Jorge, Eli, Lucas, Bastien, Valentin, Lee, Malcolm, Lucie, Mathilde, Donald, David, Ninon, Maxime, Martial…
Je pense aussi à la superbe bande d'amis que nous formons en tant que FT. Ce groupe d'amis est extraordinaire et précieux. Je pense fort à vous (Laetitia, Nicolas, Aurélie, Marc, Michel, Charles, Jérémy, Houda, Morgane, Dimitri, Raphaël…).

Merci beaucoup à toute ma famille pour votre soutien, vos encouragements et vos marques d'intérêt pour mon travail. Merci de venir à ma soutenance de thèse, ça me touche beaucoup. Merci à mon papa d'avoir organisé ce voyage pour moi et pour toute la famille. Ce sera une magnifique et précieuse expérience tous ensemble. Merci aussi d'avoir organisé le pot de thèse !
Et merci à ma maman et à ma sœur d'avoir fait les testeurs professionnels (et une petite pensée pour mes chiens Saga, Gypsie et Miel).

Et enfin, Rémi, pour toi, un seul petit mot mais qui veut dire tellement : merci.

La jeunesse, oui, mais pas à n'importe quel prix.

Stupeur et tremblement devant ce rat taupe nu

A qui une soirée était dédiée hier pour aider à mieux l'étudier.

Pourquoi ? Parce qu'on partage avec lui 93% de nos gènes, figurez-vous,

Et qu'il a le génie de savoir rester jeune très longtemps.

Il réussit l'exploit de vivre en moyenne jusqu'à 30 ans,

L'équivalent pour nous de 600 printemps, ça fait rêver non ?

Regardez-le comme il est, béni des dieux,

Il est laid comme le péché, translucide et tout fripé avec ses deux grandes dents de devant

Et ses petits yeux tout flippants, il est rosé comme un bébé, le rat taupe nu

Trois poils sur le caillou mais la patte poilue.

Il arrive même qu'il soit dodu si c'est une femelle, une reine, et qu'elle a sous ses ordres toute une colonie.

Chez les rats taupes nus, les classes sociales sont très très rigides.

On est reine, ou reproducteur, soldat, nourrice ou ouvrière.

On fait aussi la guerre quand on tombe sur une autre colonie au hasard d'une galerie et quand on gagne ce genre de conflits on saccage le territoire de l'ennemi. On exécute les mâles et on condamne ceux qu'on épargne à l'esclavage.

Alors c'est vrai qu'on résiste aux maladies, qu'on est insensible à la douleur et qu'on ne vieillit pas mais encore une fois, rester jeune à ce prix-là, franchement ?

Le modèle du rat taupe nu, c'est un petit peu comme celui de Dorian Gray ou de Dracula, ça fait rêver sur le papier

Mais quand on s'y penche de plus près, très peu pour moi.

Par Augustin Trapenard – Emission Boomerang – France Inter le 15/03/2017

Rat-taupe nu (*Heterocephalus glaber*) au *Smithsonian's National Zoo* (Washington)
© Charlène Selva, juin 2016

Table of contents

Introduction générale

Introduction générale

Les mammifères souterrains

A l'inverse de la plupart de mes camarades de doctorat, mon sujet de thèse concerne un groupe d'animaux regroupés pour leur écologie semblable et non pas pour une raison phylogénétique. Au sein des mammifères, il y a environ 300 espèces qui présentent un mode de vie souterrain : celles-ci passent la plupart de leur vie dans des terriers qu'elles ont creusés et dans lesquels elles exécutent leurs activités quotidiennes (Nevo, 1999 ; Begall et al., 2007). Ces espèces souterraines sont communément appelées taupes. Le terme fouisseur est associé aux espèces de mammifères qui creusent et utilisent des terriers pour des activités restreintes (comme le repos), bien qu'elles passent la plupart de leur vie en dehors des terriers. Ces deux définitions étant énoncées, il faut avoir conscience qu'il existe un continuum entre les espèces strictement souterraines et les espèces légèrement fouisseuse ; et même au sein des mammifères considérés comme souterrains, des strictement souterrains (e.g. Spalacidae) à ceux qui vont juste à l'entrée de leur terrier pour la recherche de nourriture (e.g. Ctenomyidae). Certaines espèces peuvent même montrer un mode de vie double comme la taupe étoilée (*Condylura cristata*) qui est fouisseuse et semi-aquatique.

A travers le clade des mammifères, le mode de vie souterrain est présent par convergence dans des clades indépendants et phylogénétiquement éloignés : on retrouve des taupes chez les marsupiaux (la taupe marsupiale, *Notoryctes typhlops*), chez les xénarthres (le tatou nain d'Argentine, *Chlamyphorus truncatus*), chez les afrothères (taupes dorées, environ 20 espèces), chez les eulipotyphles (taupe commune, environ 42 espèces) et chez les rongeurs (environ 254 espèces) (Fig. 1). Au sein même des rongeurs, le mode de vie souterrain apparaît très convergent et se retrouve chez plusieurs familles (e.g. Bathyergidae, Spalacidae, Geomyidae).

Le mode de vie souterrain est donc une adaptation très convergente au sein des mammifères, et est par ailleurs retrouvé sur l'ensemble du globe à l'exception de l'Antarctique.

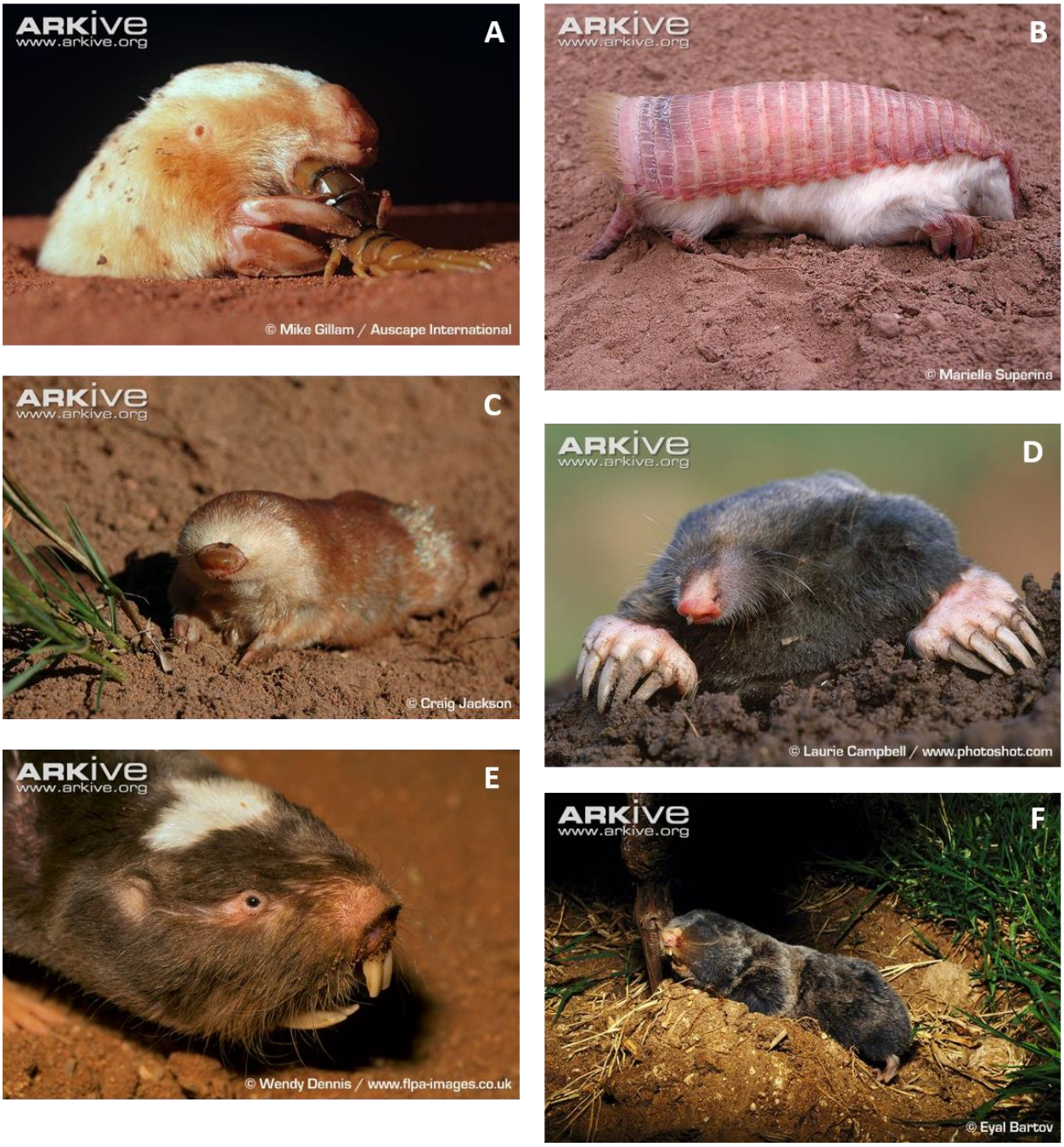

Figure 1: Diversity of subterranean mammals.

A- Marsupial mole, *Notoryctes typhlops* (Marsupialia)
B- Pink fairy armadillo, *Chlamyphorus truncates* (Xenarthra)
C- Juliana's golden-mole, *Neamblysomus julianae* (Afrotheria)
D- European mole, *Talpa europaea* (Eulipotyphla)
E- Damaraland mole rat, *Cryptomys damarensis* (Rodentia)
F- Egyptian blind mole rat, *Spalax aegyptiacus* (Rodentia)

Le terrier offre un refuge contre les prédateurs et les changements climatiques mais l'activité de fouissage demande beaucoup d'investissement énergétique. Les taupes présentent différentes stratégies pour creuser associées à des modifications anatomiques importantes qui assurent un fouissage efficace (Hildebrand et al., 1995) . On parle de « Humeral-rotation digging » pour les taupes communes chez lesquelles l'anatomie de la ceinture scapulaire et des membres antérieurs est drastiquement adaptée au fouissage. Le « head-lift digging » permet aux taupes dorées de nager dans le sable. Le comportement de « chisel-tooth digging » est particulièrement observé chez les rongeurs.

L'environnement sensoriel des terriers est simple, stable, sombre, monotone et dépourvu de nombreux stimuli que l'on retrouvent à la surface (Nevo, 1991; Burda et al., 1990, 1992; Credner et al., 1997). Les organes sensoriels qui ne sont pas stimulés présentent des régressions, alors que d'autres organes présentent des spécialisations pour contrebalancer les sens qui ne fonctionnent pas (Nevo, 1999). Les sens des mammifères souterrains font l'objet de nombreuses études pour comprendre les adaptations de ces animaux à cet environnement si particulier (Francescoli, 2000). La perte de la vue et la régression des yeux est un exemple classique dans l'étude des sens des mammifères souterrains (Nevo, 1999 ; Begall et al., 2007). Concernant l'oreille, l'audition a été très étudiée chez les mammifères souterrains mettant en avant les adaptations fonctionnelles et anatomiques de l'oreille externe, moyenne et interne au mode de vie souterrain, par exemple, pour être plus sensible aux basses fréquences. En revanche, l'oreille a très peu été étudiée pour sa fonction d'organe de l'équilibre et d'orientation (Lindenlaub et al., 1995 ; McVean, 1999 ; Crumpton, 2015).

Le système des canaux semicirculaires

Les éléments anatomiques et fonctionnels présentés ci-dessous, peuvent se retrouver dans les travaux de David et al. (2011), Ekdale (2015), Schultz et al. (2017) et Rabbitt et al. (2004). Je propose ici une présentation générale de l'organe étudié avec une mise en contexte anatomique et fonctionnelle. J'ai focalisé ma présentation sur les structures d'intérêt pour comprendre l'anatomie et la fonction du système des canaux semicirculaires (Fig. 2).

Le système des canaux semicirculaires est un organe composant le complexe de l'oreille. L'oreille est un système sensoriel ayant pour fonctions l'équilibre et l'audition. Il y a deux complexes de l'oreille, un de chaque côté du crâne. L'oreille chez les mammifères est divisée en trois zones appelées oreille externe, oreille moyenne et oreille interne. L'oreille externe est l'espace allant du pavillon de l'oreille à la membrane tympanique primaire (tympan) en passant par le conduit auditif externe. L'oreille moyenne est la cavité se trouvant entre le tympan et le crâne. Cet espace comprend la chaine des trois osselets : le malleus, l'incus et le stapes. La cavité tympanique de l'oreille moyenne est bordée dorso-latéralement par le crâne et ventralement par la bulle tympanique (si présente). L'oreille interne correspond à l'ensemble des structures de l'oreille se trouvant à l'intérieur de l'os pétrosal (ou pétreux), lui-même participant à la région postérolatérale du basicrâne. L'oreille moyenne et l'oreille interne sont en contact via deux ouvertures : la fenêtre vestibulaire, dans laquelle s'insère le stapes et la fenêtre cochléaire recouverte par une membrane tympanique secondaire. L'oreille interne est formée de plusieurs cavités interconnectées au sein du pétreux. Le volume de ces cavités correspond au labyrinthe osseux ('osseous inner ear' ou 'bony labyrinth' en anglais). On retrouve dans le labyrinthe osseux de nombreuses structures : la cochlée, le vestibule, la crus commune, les canaux semicirculaires antérieur, postérieur et latéral et leurs ampoules associées. Le labyrinthe osseux est souvent décrit en deux zones : la *pars canalicularis* et la *pars cochlearis* osseuses. On retrouve également l'emplacement des fenêtres cochléaire et vestibulaire. Le labyrinthe osseux est la seule structure de l'oreille interne que l'on peut observer chez les fossiles. A l'intérieur de cette cavité, se situent les tissus mous et les liquides. Le labyrinthe endolymphatique, entouré par une membrane épithéliale, contient de l'endolymphe et flotte dans le périlymphe, lui-même contenu dans la deuxième membrane épithéliale appelée labyrinthe périlymphatique. On associe souvent le

terme de labyrinthe membraneux au labyrinthe endolymphatique. Le labyrinthe endolymphatique (ou labyrinthe membraneux) est divisé en deux zones : la *pars inferior* et la *pars superior.* Le saccule et le canal cochléaire forment la *pars inferior*. La *pars superior* est composée de l'utricule et des trois canaux semicirculaires. En anglais, le terme « duct » sera associé aux canaux membraneux alors que le terme « canal » sera associé aux canaux osseux. L'utricule est sous-divisé en deux zones, l'utricule antérieur avec la *macula utriculi* et l'utricule postérieur avec la *macula neglecta.* Le set des trois canaux semicirculaires que l'on retrouve d'un côté se retrouve en miroir de l'autre côté du crâne pour donner un total de six canaux semicirculaires via le plan de symétrie bilatérale. Les canaux semicirculaires antérieur et postérieur sont considérés comme les canaux verticaux et le canal semicirculaire latéral est considéré comme le canal horizontal, qui est utilisé pour déterminer le plan de posture de la tête (Coutier et al., 2017). Les canaux semicirculaires d'un même côté (ipsilatéraux) peuvent être visualisés dans des plans globalement orthogonaux entre eux (Berlin et al., 2013). Le tour complet d'un canal semicirculaire est composé d'une partie fine, d'une partie utriculaire, d'une ampoule et pour les canaux verticaux, de la crus commune et pour le canal latéral, de la simple crus (*Crus membranaceum simplex*). Les ampoules sont des renflements ellipsoïdaux avec une déformation de forme caténoïdale sur la partie ventrale appelée *crista ampullaris.* Au-dessus de la *crista ampullaris* et remplissant toute la hauteur de l'ampoule, on retrouve une membrane gélatineuse appelée cupula. La cupula est une structure composée de deux couches de tissus conjonctifs fibreux entourant une couche gélatineuse. La *crista ampullaris* est recouverte d'un épithélium sensoriel composé de cellules ciliées (Rabbitt et al., 2004). Les cils de ces cellules se trouvent capturés dans la couche gélatineuse de la cupula. Les mouvements de rotation de la tête provoquent par inertie un mouvement du liquide endolymphatique dans le sens inverse du mouvement. Le déplacement du liquide au sein des canaux semicirculaire entraine une différence de pression de part et d'autre de la cupula provoquant un déplacement linéaire de celle-ci et entrainant les cils avec elle (Rabbitt et al., 2004).

a- Right and left bony labyrinth

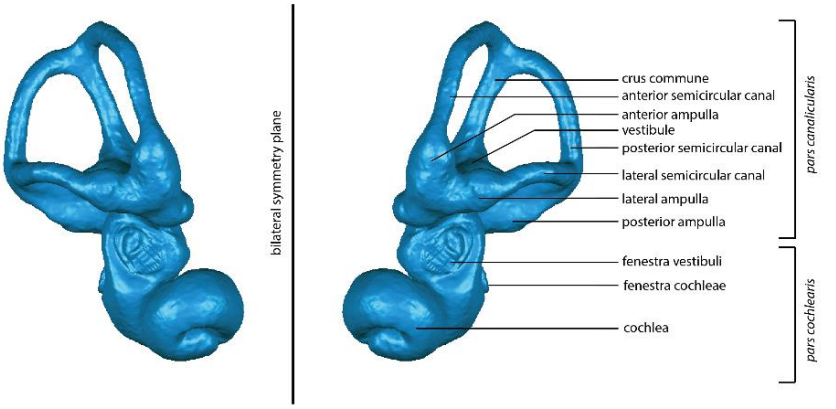

b- Membranous labyrinth in bony labyrinth

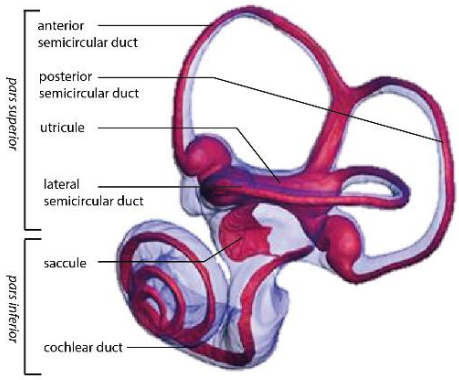

c- Soft tissues in osseous structure

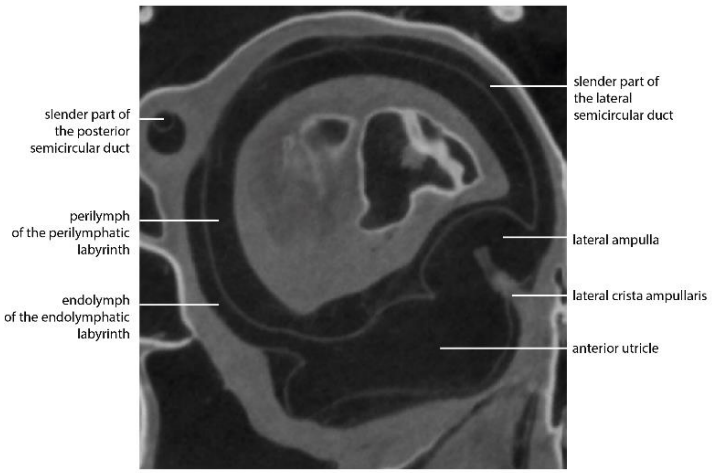

d- Anatomy of the membranous semicircular duct system

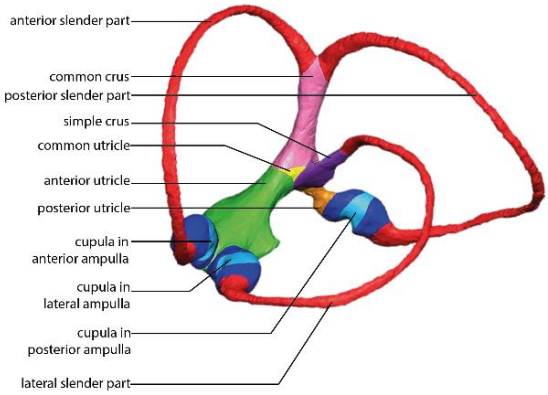

e- Axial section of an ampulla

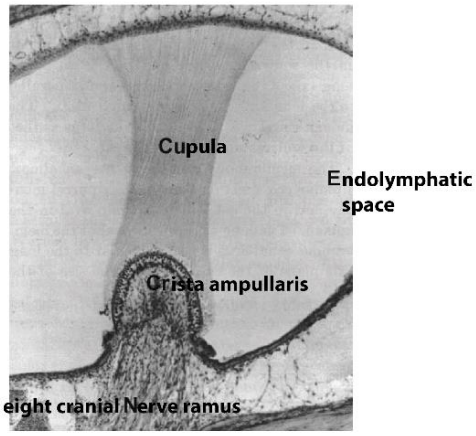

f- Schematic representation of the endolymphatic flow

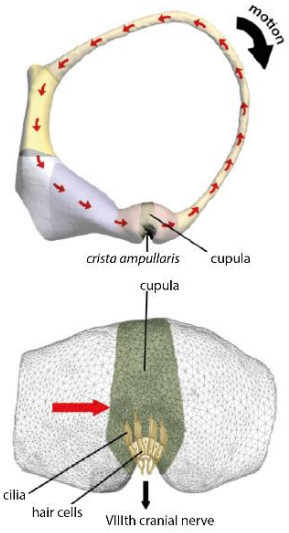

Figure 2: Anatomical structure of the inner ear.

a- Three-dimensional visualization in anterior view of the two bony labyrinths of the marsupial mole (*Notoryctes typhlops*) with bilateral symmetry plane.
b- Three-dimensional visualization in lateral view of the left membranous labyrinth (red) in the bony labyrinth (blue) of the macaque. Modified from David et al. (2016).
c- Raw visualization of stained membranous labyrinths through micro-CT scanning: soft tissues structures contained inside the bony labyrinth of the squirrel monkey. Modified from David et al. (2016).
d- Three-dimensional visualization of the semicircular duct system of the human. Modified from David et al. (2016).
e- Photomicrograph showing a cross-sectional view of the lateral ampulla of a squirrel monkey. Modified from Igarashi (1966).
f- Schematic representations of the endolymphatic flow (in red) in the anterior duct, with a focus on the ampulla. The size of the hair cells is exaggerated. Modified from Schmitt (2016).

L'implantation des différentes cellules ciliées n'est pas la même selon les canaux. Les cellules ciliées des canaux antérieur et postérieur seront activées par un mouvement de l'endolymphe de type ampullofugal (qui fuit l'ampoule), alors que ce flux sera inhibiteur pour le canal latéral. Les cellules ciliées du canal latéral seront elles activées par un flux ampullopétal (qui va vers l'ampoule). La déflection des cils entraine un potentiel d'action qui est transmis par le VIIIe nerf crânien jusqu'au cerveau. L'intégration des messages nerveux venant des six canaux semicirculaires permet au cerveau d'interpréter la direction, l'amplitude et la vitesse des mouvements de la tête. Il y a trois paires de canaux complémentaires : les deux canaux latéraux, un canal antérieur et le postérieur qui lui est opposé, et inversement. Grâce à l'orientation particulière des canaux semicirculaires, l'activation des cellules ciliées d'un canal semicirculaire est couplée à l'inhibition des cellules ciliées du canal du côté opposé qui lui est associé. Les informations sortant du système des canaux semicirculaires jouent un rôle dans l'activation de réflexes qui ont pour objectif principal de stabiliser le regard dans l'espace. Ainsi, ils entrainent des mouvements compensatoires de la tête par rapport au corps et des ajustements posturaux via le réflexe vestibulo-colique et des mouvements compensatoires des yeux par rapport à la tête via le réflexe vestibulo-cochléaire (Highstein et al. 2004). Le système des canaux semicirculaire joue un rôle primordial pour l'équilibre et fournit des informations nécessaires pour la navigation et la reconnaissance spatiale.

Le système des canaux semicirculaires peut également être considéré comme un objet de mécanique des fluides et ses paramètres fonctionnels permettent de traduire les évènements biomécaniques se produisant dans cet organe. En effet, les canaux

semicirculaires et la cupule agissent comme un objet appelé torsion pendulum, ce qui permet de traduire leurs comportements via des équations qui tâchent de décrire leur système (pour aller plus loin, voir les « Supplementary Information » de David et al., 2016). De ces équations sont issus des valeurs de « paramètres fontionnels » permettant de décrire et quantifier le fonctionnement du système des canaux semicirculaires.

De par la fonction de l'oreille interne, de nombreuses études antérieures fondées sur les mammifères ont régulièrement proposé une corrélation possible entre la morphologie de l'oreille interne et les types locomoteurs allant même jusqu'à proposer des inférences écologiques sur des fossiles (Spoor et al., 2002, 2007 ; Silcox et al., 2009 ; Macrini et al., 2010, 2013 ; Orliac et al., 2012 ; Billet et al., 2013 ; Pfaff et al., 2015, 2017). Parallèlement, un signal phylogénétique dans la morphologie des canaux semicirculaires a été mis en évidence chez certains groupes de mammifères (marsupiaux, Alloing-Séguier et al., 2013 ; artiodactyles, Mennecart et al., 2017).

Chez les mammifères souterrains, l'oreille interne a été de nombreuses fois étudiée afin de regarder les capacités auditives de ces espèces très adaptées à leur environnement particulier mais peu d'études concernent le système des canaux semicirculaires et leur rôle pour l'équilibre et la locomotion. Lindenlaub et al. (1995) et McVean (1999) se sont intéressés au labyrinthe membraneux de trois espèces de rongeurs souterrains. Et l'étude de Crumpton et al. (2015) s'est basée sur les labyrinthes osseux uniquement. Ces trois études proposent un lien entre la morphologie de l'organe étudié et le mode de vie, interprétant certaines structures comme des adaptations à la vie souterraine.

Problématiques de la thèse

1° Morphologie du labyrinthe osseux, proxy pour le mode de vie souterrain ?

Le premier objectif de ma thèse était de trouver une adaptation squelettique crânienne au mode de vie souterrain afin d'estimer la possibilité d'une vie sous terre chez certains fossiles, dont le squelette post-crânien n'est pas connu ou pas spécialisé. Replacés dans un contexte évolutif et temporel, ces résultats permettraient de préciser l'importance de ce mode de vie dans l'histoire des mammifères, en particulier au passage des grandes crises biologiques.

D'après les études précédentes, la morphologie du labyrinthe osseux semblait être fortement liée à la locomotion. De plus, l'os pétrosal (ou pétreux) entourant l'oreille interne osseuse est très dense et se retrouve en quantité et de bonne qualité dans le registre fossile. Ainsi, utiliser le labyrinthe osseux comme proxy pour déterminer la locomotion et le mode de vie des animaux semblait être une méthode pertinente. Pour mettre en marche cette idée, j'ai choisi d'échantillonner des fossiles connus pour leurs comportements fouisseurs ou souterrains (voir Chapitre 1 et Annexe 4) sur lesquels j'aurais tester le modèle d'inférence. Mais dans un premier temps, ma démarche était de tester la corrélation liant morphologie du labyrinthe osseux et le comportement fouisseur/souterrain chez les actuels. Pour cela j'ai échantillonné une grande quantité de crânes de mammifères souterrains (Annexe 1) et de leurs proches parents non-souterrains pour comparaison. Pensant le modèle de l'oreille interne osseuse comme proxy robuste, l'échantillonage avait pour but de représenter :

- l'ensemble de la diversité phylogénétique en échantillonant l'ensemble des familles comprenants des mammifères souterrains
- tous les types de fouissage des mammifères souterrains
- les activités de fouissage

En effet, je supposais que le modèle basé sur la morphologie du labyrinthe osseux permettrait de discriminer le mode de vie souterrain mais également l'activité de fouissage et même éventuellement les types de fouissage ne demandant pas tous le même investissement de la tête dans cette activité. A l'inverse de notre hypothèse de départ, et au contraire des études précédentes sur lesquelles nous fondions nos hypothèses, les premiers résultats (Chapitre 1 et études préliminaires en Annexe 2 et 3) obtenus pendant la thèse ne montrent pas un lien pertinent entre la morphologie de l'oreille interne osseuse et les

modes de vie. En conséquence, j'ai du revoir les objectifs de la thèse et j'ai décidé de ne pas traiter l'ensemble des crânes échantillonnés comme cela était prévu au départ (Fig. 3).

2° Trouver le lien entre mode de vie souterrain et système des canaux semicirculaire chez les mammifères actuels

Malgré le changement de cap en cours de thèse, l'objectif restait le même : trouver un éventuel proxy du mode de vie souterrain dans l'oreille interne (Fig. 3). La morphologie du labyrinthe osseux n'étant le modèle ni le plus pertinent ni le plus prometteur, j'ai décidé de tester si la morphologie du système des canaux semicirculaires membraneux pouvait porter un signal pour le mode de vie souterrain (Chapitre 2). Pour aller encore plus loin, j'ai testé les paramètres fonctionnels de cet organe (Chapitre 3).

Finalement, la démarche que j'ai adoptée était de trouver si il y a une adaptation de l'oreille interne au mode de vie souterrain chez les mammifères actuels, et le cas échéant si une inférence est possible chez les fossiles afin de déterminer leur mode de vie passé.

A- Objective at the beginning of the thesis: inference of subterranean behavior on extinct species

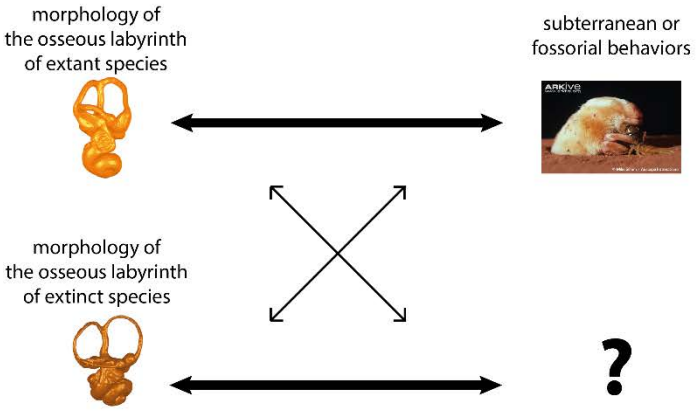

1° Characterize the osseous labyrinth morphology in extant species

2° Correlation between the osseous labyrinth morphology and subterranean or fossorial behaviors

3° Description of the osseous labyrinth morphology of extinct species

4° Inference of subterranean or fossorial behaviors for extinct species

BUT preliminary results show no correlations between the osseous labyrinth morphology and subterranean behavior in extant species.

B- Reformulation of the objective during the thesis: finding a correlation between the semicircular duct system and subterranean behavior

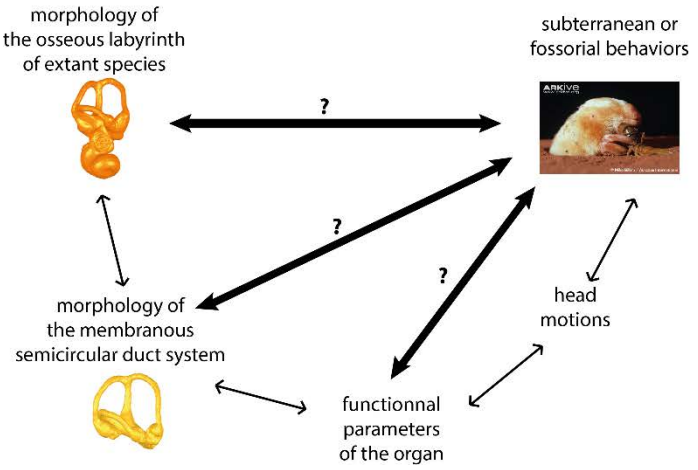

1° Correlation between the osseous labyrinth morphology and subterranean behavior?
--> Chapter 1 (and preliminary studies in appendices)

2° Correlation between the membranous labyrinth morphology and subterranean behavior?
--> Chapter 2

3° Correlation between the functionnal parameters and subterranean behavior?
--> Chapter 3

Figure 3: Schematic representation of the scientific approach during the thesis.

Méthodologies, Matériels et Financements

1° Accéder aux labyrinthes osseux : CT-scan

Le labyrinthe osseux étant une cavité à l'intérieur du crâne, j'ai dû recourir à la microtomographie à rayons X pour accéder à la structure sans détruire le crâne. Pendant ma thèse, j'ai acquis une grande quantité de scans qui n'ont malheureusement pas pu tous être exploités. La liste des crânes scannés durant ma thèse est disponible en Annexe 1. La quasi-totalité des spécimens font partie des collections du Muséum national d'Histoire naturelle et a été scannée à la plateforme AST-RX du MNHN. Ces scans ont pu être réalisés grâce à un financement Actions Thématiques du Muséum « Formes possibles, Formes réalisées 2015 » pour lequel j'étais porteuse de projet (Annexe 6).

2° Accéder aux labyrinthes membraneux : mise en contrastant + scans ou lumière Synchrotron

L'accès aux labyrinthes membraneux s'est fait via deux protocoles : des scans en contraste de phase à la lumière Synchrotron (ERSF) ou des scans classiques sur des spécimens ayant baigné dans du contrastant. La politique de gestion des spécimens en alcool du Muséum national d'Histoire naturelle n'autorise pas la mise en contrastant des spécimens. Dans un premier lieu, nous avons donc voulu accéder aux labyrinthes membraneux via la lumière Synchrotron qui ne détériore pas les spécimens de collection. Nous avons pu scanner plusieurs spécimens grâce à notre projet qui a été accepté (Annexe 7). Malheureusement, certains spécimens nécessaires à l'étude n'étaient pas exploitables et il a fallu trouver un système de remplacement. Après maintes péripéties, nous avons réussi à trouver des spécimens illustrant les taxons manquants qui pouvaient être placés en bain avec des contrastants (les scans classiques suivant le bain ont été réalisé au Max Planck Institut de Leipzig).

3° Exploitation des scans et modélisations des structures

L'exploitation des scans et la modélisation des structures du labyrinthe osseux et membraneux ont été réalisées via différents logiciels : ImageJ, Mimics, Avizo et Geomagic. J'ai pu travailler sur des postes dédiés à l'exploitation des images 3D à la plateforme 3D du

laboratoire CR2P (MNHN), à la plateforme de l'UMS 2700 (MNHN) et au laboratoire 3D du Max Planck Institut de Leipzig.

4° Appréhender la forme : morphométrie géométrique et statistiques

J'ai décidé de traiter la morphologie via des analyses de morphométrie géométrique. J'ai dû me former à cette méthode grâce au cours de l'école doctorale et via les échanges avec mes différents collaborateurs. Les logiciels auxquels je me suis formée sont les suivants : Avizo, Morphotools, Past et R.

5° Appréhender la fonction

La partie excitante de ma thèse était exploratoire : il s'agissait d'appréhender les paramètres fonctionnels de l'organe de l'équilibre et d'orientation grâce à une méthode nouvelle, issue des recherches de R. David. Pour cela, je me suis rendue à plusieurs reprises à l'Institut Max Planck de Leipzig, pour apprendre et travailler avec lui. J'ai réussi à obtenir deux financements pour mener à bien mes missions : DAAD et Transhumance pour lesquels j'étais porteuse de projet (Annexes 8 et 9).

Annexes disponibles à la fin du manuscrit de thèse

Appendixes available at the end of the thesis manuscript

Annexe 1. Liste des spécimens de mammifères actuels scannés au cours de cette thèse, avec financements associés
Appendix 1. List of extant mammal specimens scanned during the PhD, with associated grants

Annexe 2. Etude préliminaire de l'oreille interne des rongeurs fouisseurs
Appendix 2. Preliminary study of the inner ear of fossorial rodents

Annexe 3. Etude préliminaire de l'oreille interne des eulipotyphles
Appendix 3. Preliminary study of the inner ear of Eulipotyphla

Annexe 4. Etude préliminaire du labyrinthe osseux de thérapsides au comportement fouisseur
Appendix 4. Preliminary study of the bony labyrinth of therapsids with fossorial habits

Annexe 5. Article sur l'oreille de la Sarigue de Cuvier
Appendix 5. Paper on the ear of the opossum of Cuvier

Annexe 6. Projet pour 6 jours de CT-scans - Actions Thématiques du Muséum « Formes possibles, Formes réalisées 2015 » du Muséum national d'Histoire naturelle
Appendix 6. Proposal for 6 days of CT-scans - Actions Thématiques du Muséum « Formes possibles, Formes réalisées 2015 » from the Muséum national d'Histoire naturelle

Annexe 7. Projet pour 48h d'accès à la lumière synchrotron - *European Synchrotron Radiation Facility* (ESRF Grenoble)
Appendix 7. Proposal for 48h of access to the synchrotron light - *European Synchrotron Radiation Facility* (ESRF Grenoble)

Annexe 8. Projet pour une bourse de mission à destination du Max Planck Institut für Evolutionäre Anthropologie à Leipzig (Allemagne) - 1 200€ du DAAD (Office allemand d'échanges universitaires)
Appendix 8. Proposal for a work trip grant to the Max Planck Institut für Evolutionäre Anthropologie in Leipzig (Germany) - 1 200€ from DAAD (German Academic Exchange Service)

Annexe 9. Projet pour une bourse de mission à destination du Max Planck Institut für Evolutionäre Anthropologie à Leipzig (Allemagne) - 600€ de « Transhumance » (Bourse de mobilité internationale Sorbonne-Universités)
Appendix 9. Proposal for a work trip grant to the Max Planck Institut für Evolutionäre Anthropologie in Leipzig (Germany) – 600€ from "Transhumance" (Sorbonne-University Grant for international exchange)

References

Alloing-Séguier, L., Sánchez-Villagra, M. R., Lee, M. S., & Lebrun, R. (2013). The bony labyrinth in diprotodontian marsupial mammals: diversity in extant and extinct forms and relationships with size and phylogeny. *Journal of Mammalian Evolution*, *20*(3), 191-198.

Begall, S., Burda, H., & Schleich, C. (eds) (2007). *Subterranean rodents: news from underground*. Springer-Verlag, Berlin. xviii+398 p.

Berlin, J. C., Kirk, E. C., & Rowe, T. B. (2013). Functional implications of ubiquitous semicircular canal non-orthogonality in mammals. *PLoS One*, *8*(11), e79585.

Billet, G., Germain, D., Ruf, I., Muizon, C. D., & Hautier, L. (2013). The inner ear of *Megatherium* and the evolution of the vestibular system in sloths. *Journal of Anatomy*, *223*(6), 557-567.

Burda, H., Bruns, V., & Müller, M. (1990). Sensory adaptations in subterranean mammals. *Progress in Clinical and Biological Research*,*335*, 269.

Burda, H., Bruns, V., & Hickman, G. C. (1992). The ear in subterranean Insectivora and Rodentia in comparison with ground-dwelling representatives. I. Sound conducting system of the middle ear. *Journal of Morphology*, *214*(1), 49-61.

Coutier, F., Hautier, L., Cornette, R., Amson, E., & Billet, G. (2017). Orientation of the lateral semicircular canal in Xenarthra and its links with head posture and phylogeny. *Journal of Morphology*, *278*(5), 704-717.

Credner, S., Burda, H., & Ludescher, F. (1997). Acoustic communication underground: vocalization characteristics in subterranean social mole-rats (*Cryptomys sp*., Bathyergidae). *Journal of Comparative Physiology A: Neuroethology, Sensory, Neural, and Behavioral Physiology*, *180*(3), 245-255.

Crumpton, N., Kardjilov, N., & Asher, R. J. (2015). Convergence vs. specialization in the ear region of moles (Mammalia). *Journal of Morphology, 276*(8), 900-914.

David R. (2011). *Le système des canaux semi-circulaires des archosaures : anatomie, morphometrie, morphologie fonctionnelle, évolution*. Unpublished PhD thesis. Muséum national d'Histoire naturelle, Paris. 343p.

David, R., Stoessel, A., Berthoz, A., Spoor, F., & Bennequin, D. (2016). Assessing morphology and function of the semicircular duct system: introducing new in-situ visualization and software toolbox. *Scientific reports*, *6*, 32772.

Ekdale, E. G. (2016). Form and function of the mammalian inner ear. *Journal of Anatomy*, *228*(2), 324-337.

Francescoli, G. (2000). Sensory capabilities and communication in subterranean rodents; pp. 111-144, in Lacey, E. A., Patton, J. L., & Cameron, G. N. (eds), *Life underground: the biology of subterranean rodents.* University of Chicago Press, Illinois.

Hildebrand, M., Goslow, G. E., & Hildebrand, V. (1995). *Analysis of vertebrate structure*. John Wiley & Sons, New York. 657 p.

Highstein, S. M., Fay, R. R., & Popper, A. N. (eds). (2004). *The Vestibular System*. Springer handbook of auditory research, v. 19, New York. 560 p.

Igarashi, M. (1966). Dimensional study of the vestibular end organ apparatus. *Second Symposium on the Role of the Vestibular Organs in Space Exploration, NASA Ames Research Center, Moffett Field, CA*, 47-54.

Lindenlaub, T., Burda, H., & Nevo, E. (1995). Convergent evolution of the vestibular organ in the subterranean mole-rats, *Cryptomys* and *Spalax*, as compared with the aboveground rat, *Rattus*. *Journal of Morphology, 224*(3), 303-311.

Macrini, T. E., Flynn, J. J., Croft, D. A., & Wyss, A. R. (2010). Inner ear of a notoungulate placental mammal: anatomical description and examination of potentially phylogenetically informative characters. *Journal of Anatomy*, *216*(5), 600-610.

Macrini, T. E., Flynn, J. J., Ni, X., Croft, D. A., & Wyss, A. R. (2013). Comparative study of notoungulate (Placentalia, Mammalia) bony labyrinths and new phylogenetically informative inner ear characters. *Journal of Anatomy*, *223*(5), 442-461.

McVean, A. (1999). Are the semicircular canals of the European mole, *Talpa europaea*, adapted to a subterranean habitat? *Comparative Biochemistry and Physiology Part A: Molecular & Integrative Physiology, 123*(2), 173-178.

Mennecart, B., DeMiguel, D., Bibi, F., Rössner, G. E., Métais, G., Neenan, J. M., Wang, S., Schulz, G., Müller, B., & Costeur, L. (2017). Bony labyrinth morphology clarifies the origin and evolution of deer. *Scientific Reports, 7*(1), 13176.

Nevo, E. (1991). Evolutionary theory and processes of active speciation and adaptive radiation in subterranean mole rats, *Spalax ehrenbergi* superspecies, in Israel. *Evolutionary biology*, *25*, 1-125.

Nevo, E. (1999). *Mosaic evolution of subterranean mammals: regression, progression, and global convergence*. Oxford University Press, Oxford, 413 p.

Orliac, M. J., Benoit, J., & O'Leary, M. A. (2012). The inner ear of *Diacodexis*, the oldest artiodactyl mammal. *Journal of Anatomy*, *221*(5), 417-426.

Pfaff, C., Martin, T., & Ruf, I. (2015). Bony labyrinth morphometry indicates locomotor adaptations in the squirrel-related clade (Rodentia, Mammalia). *Proceedings of the Royal Society of London B: Biological Sciences, 282*(1809), 20150744.

Pfaff, C., Czerny, S., Nagel, D., & Kriwet, J. (2017). Functional morphological adaptations of the bony labyrinth in marsupials (Mammalia, Theria). *Journal of Morphology*, *278*(6), 742-749.

Rabbitt, R. D., Damiano, E. R., & Grant, J. W. (2004). Biomechanics of the semicircular canals and otolith organs.; pp. 153-201, in Highstein, S. M., Fay, R. R., & Popper, A. N. (eds), *The Vestibular System*. Springer handbook of auditory research, v. 19, New York.

Schmitt, A. (2016). *La région de l'oreille osseuse chez les Proboscidea (Afrotheria, Mammalia) : anatomie, fonction, évolution*. Unpublished PhD Thesis. Muséum national d'Histoire naturelle, Paris. 498p.

Schultz, J. A., Zeller, U., & Luo, Z. X. (2017). Inner ear labyrinth anatomy of monotremes and implications for mammalian inner ear evolution. *Journal of Morphology*, *278*(2), 236-263.

Silcox, M. T., Bloch, J. I., Boyer, D. M., Godinot, M., Ryan, T. M., Spoor, F., & Walker, A. (2009). Semicircular canal system in early primates. *Journal of Human Evolution*, *56*(3), 315-327.

Spoor, F., Bajpai, S., Hussain, S. T., Kumar, K., & Thewissen, J. G. (2002). Vestibular evidence for the evolution of aquatic behaviour in early cetaceans. *Nature*, *417*(6885), 163-166.

Spoor, F., Garland, T., Krovitz, G., Ryan, T. M., Silcox, M. T., & Walker, A. (2007). The primate semicircular canal system and locomotion. *Proceedings of the National Academy of Sciences*, *104*(26), 10808-10812.

Chapter 1

The morphology of the osseous inner ear cannot be a Proxy for locomotion in marsupial mammals

The morphology of the osseous inner ear cannot be a Proxy for locomotion in marsupial mammals

Charlène Selva[1], Jérémie Bardin[1], Damien Germain[1], Stéphane Peigné[1], Véra Weisbecker[2], Christian de Muizon[1] & Sandrine Ladevèze[1*]

[1] Centre de Recherches sur la Paléobiodiversité et les Paléoenvironnements (CR2P, UMR 7207), Sorbonne Universités-MNHN, CNRS, UPMC-Paris 6, Muséum national d'Histoire naturelle, CP38, 57 rue Cuvier F-75005, Paris, France.

[2] The University of Queensland, School of Biological Sciences, St. Lucia, 4072 QLD Australia.

Correspondence and requests for materials should be addressed to C.S. (email: charlene.selva@edu.mnhn.fr) or S.L. (email: sandrine.ladeveze@mnhn.fr).

Introduction

Marsupial mammals show a wide diversity in their traits of life, particularly in their feeding and locomotor habits, from the nectarivore pigmy possum to the scavenger Tasmanian devil, and from subterraneous or fossorial forms to gliding arboreal forms (Tyndale-Biscoe, 1973; Nowak, 2005). Marsupials exhibit such diversified ecologies that they represent an appropriate biological model to study adaptive convergences, particularly in their locomotions. The Marsupialia clade is less specious than the Placentalia clade, and is consequently easier to sample and more relevant to consider the phylogenetic aspect.

One interesting anatomical structure to investigate is the bony labyrinth of the inner ear, which contains the organs of balance and audition and is therefore likely to be linked to the locomotor patterns of vertebrates (e.g., Spoor et al., 2007; Walsh et al., 2009; Maddin & Sherratt, 2014). Since Jones & Spells (1963) and Mayne (1965), a strong theoretical background exists to support a causal relation between inner ear function and animal behaviours. However, technological constraints prevented to fully quantify the shape of the inner ear organs; consequently, the veracity of such causal relation failed to be tested. Consecutively to the development of state-of-the-art technology of X-ray microtomography, researchers tried to establish correlations between the limited (but easier to access) parameters provided by the bony labyrinth of the inner ear and locomotion behaviours (e.g., Spoor et al. 2007; Malinzak et al. 2012). Nonetheless, these studies mostly focused on placental mammals: marsupials are under-represented, diprotodontians (kangaroos and

relatives) being only included in analyses scrutinizing the relationship between shape and phylogeny (e.g., Alloing-Séguier et al., 2013). Moreover, most recent studies do not provide a comprehensive enough sampling among the entire clade Marsupialia, or even Metatheria if including fossils (e.g., Schmelzle et al. 2007; Alloing-Séguier, et al. 2013; Pfaff et al., 2016).

Here we propose a 3D landmarks-based procedure focused on the semicircular canals of the bony labyrinth. If we want to answer the question of the link between the shape of the inner ear and the head movements, itself linked to the locomotion, we do not need to consider the cochlea morphology. Moreover, the shape in three dimensions is better approximated by the landmark coordinates that characterize the conformation than by linear measurements and it has been shown that landmark data have certain advantages over other measurable components (e.g., Bookstein, 1997; Fabre et al., 2014; Lele & Richtsmeier, 1991; Zelditch, 2004). However, it is noteworthy that, even if the shape of the osseous inner ear will be better approximated through its landmarks coordinates, each part of the shape is not necessarily implied in the function. As a matter of fact, it has been suggested by different studies in mammals (e.g., Spoor et al., 2007; Cox & Jeffery, 2010; Billet et al., 2013; Pfaff et al., 2017) that only a few morphological features have an influence on the function of the inner ear, and thus a link with function/locomotion: the enclosed area of each semicircular canal, the length of the thin section of the canals, and the angle between each canal plan.

Therefore, our aim is to answer the following question: which part of the morphological variance is explained by the function, by the phylogeny, and by the mass (=allometry)? It is obvious that each of the three parameters is of crucial importance in our dataset, composed of a large clade with an important phylogenetic and ecological diversity. Our goal is here to understand the morphological diversity of the osseous inner ear of marsupials and to find out if a part of the morphological diversity is linked to the function and thereby the locomotion of the animal. In other words, does a gathering of similarly shaped osseous inner ears corresponds to a peculiar ecology or locomotion? If it is the case, can we infer with certainty the locomotion mode of extinct taxa?

Material and Methods

Material

The sample is composed of 41 extant marsupials for which the bony labyrinth of the inner ear was virtually extracted. It covers all of the 19 families of the clade Marsupialia (Wilson & Reeder, 2005), each of which being represented by at least one species (Supplementary Information SI-1). For each clade, we tried to sample at least two different locomotions. For example, the clade Petauridae is represented here by two gliders (*Petaurus norfolcensis* and *Petaurus breviceps*) and one arboreal species (*Dactylopsila trivirgata*). The clade Macropodidae is represented here by four hoppers (*Bettongia lesueur*, *Macropus rufus*, *Setonix brachyurus*, and *Potorous tridactylus*) and one arboreal species (*Dendrolagus ursinus*). Moreover, we tried to document as possible cases of convergencies as possible. For example, hoppers are found in macropodids but also in dasyurids (*Antechinomys laniger*) and thylacomyids (*Macrotis lagotis*) (see below).

The sample of extant species is completed with 13 fossils of Metatheria, among which one microbiotheriid (*Microbiotherium tehuelchum*, new data), four herpetotheriids (*Herpetotherium fugax*, Sánchez-Villagra et al., 2007; *Amphiperatherium minutum*, new data, Ladevèze et al., in prep.; *Peratherium elegans*, new data, Ladevèze et al., in prep.; *Peratherium cuvieri*, Selva & Ladevèze, 2016 –available in the Appendix 5 of the PhD manuscript), one peradectid (*Mimoperadectes houdei*, Horovitz et al., 2009), two pucadelphyids (*Andinodelphys cochabambensis* and *Pucadelphys andinus*, new data), and four sparassodonts (*Allqokirus australis*, Muizon et al., submitted; *Borhyaena tuberata*, *Prothylacinus patagonensis*, and *Sipalocyon gracilis*, new data). Moreover, as the subterranean locomotor mode is only represented by one extant species and no fossil taxa with petrosal remains among Metatheria, we also add a fossil known for its postcranial subterranean adaptations, which was also compared to the marsupial mole (Ladevèze et al., 2008), the meridiolestidan *Necrolestes patagonensis* (Rougier et al., 2012). The phylogenetic tree used in this work results from various sources and is available in Supplementary Information SI-2. The Marsupialia tree is based and calibrated according to Bininda-Edmonds et al. (2007), Benton et al. (2015), and Westerman et al. (2016) for *Antechinomus/Sminthopsis*. The extinct metatherians were branched according to Muizon et al. (in prep.), and Ladevèze et al. (in prep.). This is the largest sample of osseous inner ear of Marsupialia ever produced, which covers all the families and

locomotor modes, and allows to explore the entire clade with an exhaustive sample and not only a sample adapted for the diprotodont, as in previous studies (Alloing-Séguier et al., 2013; Pfaff et al., 2017).

To complete the morphological diversity within Metatheria, we included some fossils, with the final goal to test if a locomotion can be inferred to extinct taxa. The chosen fossils are well preserved specimens, for which skeletal remains are known and is likely to suggest a locomotor mode (see the Discussion part).

The ecological assignment for the extant species is based on different sources (see references in SI-1) and defined by two parameters:

- the locomotion mode according to six classes: arboreal, terrestrial-arboreal, terrestrial, hopper, glider and subterranean.
- the practice or non-practice of a fossorial behaviour (burrow vs non-burrow).

The choice to divide the locomotion into two parameters was the solution to respond the most pertinently to the various behaviours observed in marsupials. Some species can be defined as having the ability to dig burrows as well as a peculiar locomotion. Moreover, the species that dig burrows (= fossorial) can exhibit various locomotor modes (some can be terrestrial, other hoppers, and the mole is subterranean). Contrary to the previous studies on marsupials cited above, we separate here these two behaviours to describe more precisely the lifestyle of marsupials.

Some species sometimes exhibit various locomotion modes, and it has been difficult to choose which of these were the most relevant or the most descriptive. We chose the locomotor mode that was most commonly used by the animal and that implied the most constraints onto the head movements. For example, hoppers can be defined by their ability to perform bipedal (kangaroos are obvious hoppers) or quadrupedal ricochet (less obvious). *Antechinomys laniger* is considered as a hopper species because it performs quadrupedal ricochet during fast locomotion like the bilby *Macrotis lagotis*, and also hops like the hopping mouse *Notomys*, but it is also a terrestrial and fossorial animal that has been observed digging shallow burrows in captivity. *Chironectes minimus* is the only semi-aquatic species of marsupials; it is mainly terrestrial and has semi-aquatic but not extreme aquatic adaptations. It is therefore more relevant to consider it as terrestrial for statistics analyses. However, the only subterranean species of marsupials *Notoryctes typhlops*, cannot be considered as terrestrial because it

locomotion is way too extreme. A species is here considered as fossorial when it has been shown that it is able to dig burrows or forage underground or under the snow for food (e.g., *Lestodelphys halli*).

Locomotor habits have been suggested in anterior study and based on post-cranial anatomy for some of the fossil species of the present study, and will be compared to the results of the discriminant analysis.

CT-scanning and Segmentation

CT scanning was conducted at the X-ray Tomography Imagery Platform AST-RX of MNHN, using a GE Sensing and Inspection Technologies phoenix|x-ray v|tome|x L240-180 CT scanner. The CT-scan resolution for each species is given in the Supplementary Information SI-1. The data were reconstructed using phoenix datos|x© 2.0 reconstruction software, and then exported into 16- bit TIFF image stacks.

Post-processing was carried out at the Palaeontology Imaging Unit of the CR2P, MNHN. Mimics© 17.0 and Mimics© 18.0 (Materialise) were used for the 3D modelling (segmentation and 3D object rendering). For better rendering, 3D objects have undergone smoothing on Geomagic Studio© 12 (Raindrop Geomagic Inc) (see the precise procedure in Supplementary information SI-3) before being used for the landmarks editing procedure on AVIZO© 7.1 (Visualization Science Group) (see below and SI-4). When fossil specimens were not enough preserved, we had to improve the 3D rendering and sometimes to repair the 3D models thanks to the Geomagic software (SI-3). For example, the petrosal bone of *Microbiotherium* was broken and the bony labyrinth lacked the anterior semicircular canal. The latter was reconstructed based on the bony labyrinth of its extant relative, *Dromiciops gliroides* (Fig. 1).

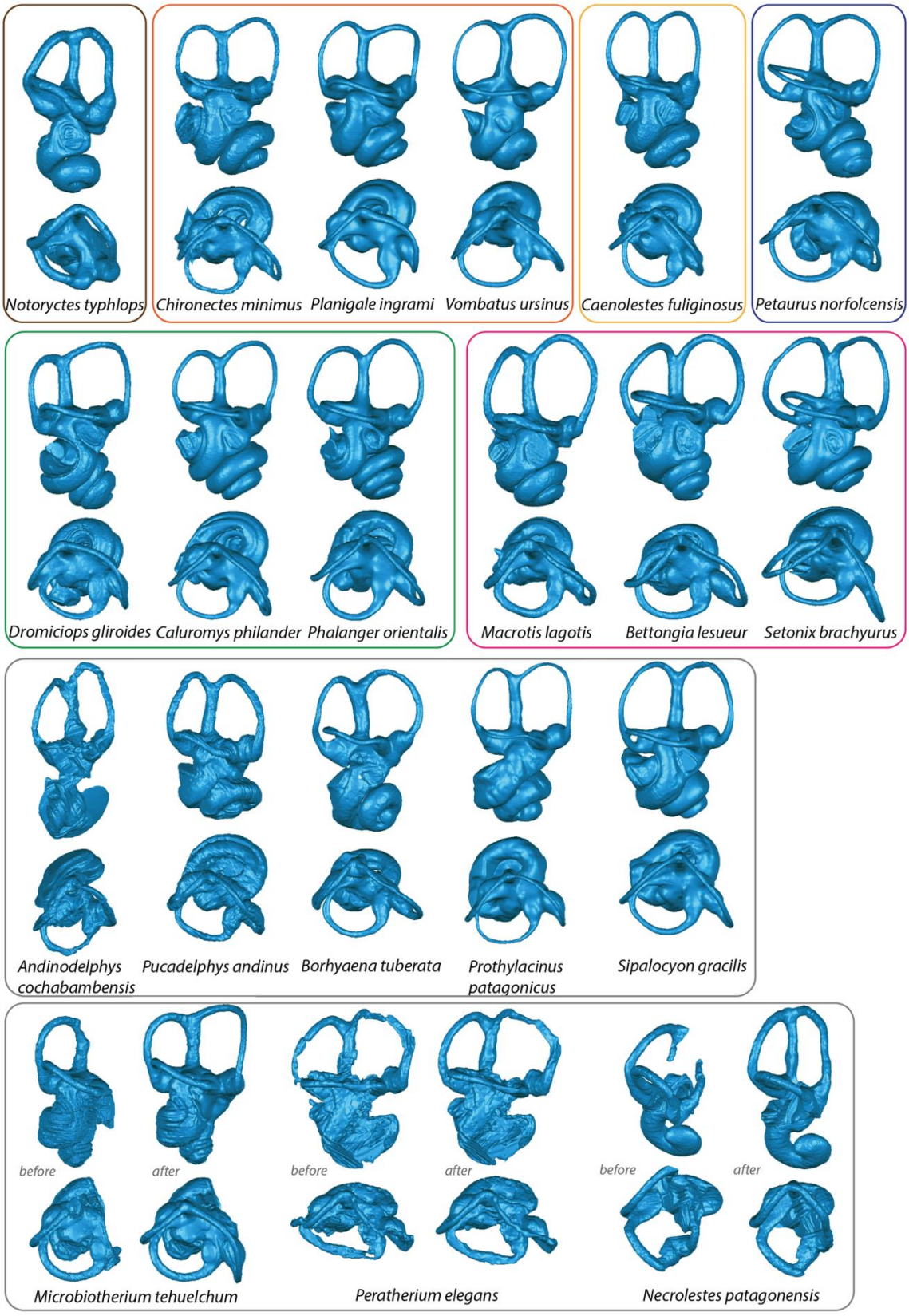

Figure 1: Morphological diversity of the bony labyrinth of metatherians, illustrated by a sample of 3D models. The selected extant species represent the ecological diversity encountered in today's marsupials (green=arboreal, yellow=terrestrial to arboreal, orange=terrestrial, brown=subterranean, blue=glider, pink=hopper). The first five inner ears of fossil metatherians (grey=unknown locomotion) are new data, and the three last are damaged specimens, which went through a reconstruction.

Geometric morphometrics

The landmarks are positioned on the 3D STL model of the semicircular canal of the bony labyrinth thanks to a new method inspired by the work of David et al. (2016) on the membranous labyrinth. This new method allows to better understand the shape than any other methods proposed so far, being based either on internal points but with no sliding (Alloing-Séguier et al., 2013) or on linear measurements (Schmelzle et al., 2007; Gunz et al., 2012; Pfaff et al., 2017).

A preliminary preparation of the dataset is necessary (SI-4) and consists in cutting the bony labyrinth into 6 anatomical areas with the Geomagic software, and to create a skeleton inside our object with the Avizo software, in order to position the most correctly as possible the internal landmarks.

Seven independent curves were defined on the semicircular canals (Fig. SI-2), each of which starting with a homologous landmark (Type I). The seven Type I (fixed) landmarks are positioned at the beginning of each curve and the sliding landmarks are on internal and external surfaces (Fig. SI-2).

Our definition of the homologous landmarks allows to access the angles, lengths, thickness, and twists of the semicircular canals, as well as the length of the crus commune.

The data analyses were performed with the R software (R Core Team, 2014), with the main packages Geomorph (Adams & Otarola-Castillo, 2013), Phylobase (Hackathon et al., 2013) and Hotelling (Curran, 2013). The complete R script is available in the Supplementary Information SI-5.

We performed a generalized Procrustes Analysis (GPA: Gower 1975; Rohlf & Slice 1990) on the fixed and sliding three-dimensional landmark coordinates using the library 'Geomorph'. The semilandmarks slides were based on minimizing bending energy (Bookstein 1997).

Next, a Principal Component Analysis (PCA) was performed on the mean of the Procrustes coordinates for each species in order to visualize the distribution of the 54 species in the morphospace and more particularly to discriminate our defined locomotor types. For each Principal Component, we were able to visualise the minimal and maximal conformations of the Procrustes coordinates (plotTangentSpace function).

The 'phylo4D' function is used to help reading the PCA and to better understand how the phylogeny impacts the morphospace.

To assess the degree of phylogenetic signal in the morphological data on each PC axis, we used Pagel's lambda (Pagel, 1999). This procedure calculates the value of lambda that best explains the tips values of traits under a brownian model. The higher the lambda, the stronger is the phylogenetic signal. As the lambda decreases and tends to zero, the closer the phylogeny is to a star tree.

The main goal of our study is to find out if there is a morphology of the inner ear specific to a locomotion type. For that purpose, we removed parameters likely to play a role in the morphology of the inner ear such as the phylogeny and the allometry. The allometry was checked with a regression between the body mass and the shape with the function 'procD.allometry'. And because of the presence of allometry, a Procrustes ANOVA was used to correct the shapes and remove the size effect. Allometry-corrected conformations were assessed as the residuals of inner ear shape data from the common allometric component. A second PCA on allometry-corrected shapes was performed. Two-sample Hotelling's T-squared tests were performed on the specimens' scores resulting from this new PCA. These tests have two main goals: to determine if the shape distribution of the semicircular canal of a defined group is (a) significantly different from the shape distribution for Metatheria and (b) significantly different from the shape distribution for the specimens outside the defined group.

The second PCA with the allometry-corrected conformations was performed in order to produce Principal Components for a phylogenetic flexible discriminant analysis (PFDA). Investigation on relationships between variables on taxa have been renewed in the 90's by the introduction of phylogenetic comparative methods which aim at removing phylogenetic signals from those variables to obtain independent and identically distributed variables (Felsenstein, 1985). The establishment of the relationship between a discrete variable and several continuous variables can be performed with discriminant analyses. Motani & Schmitz (2011) proposed a phylogeny-free version of the Flexible Discriminant Analysis (Hastie et al, 1994). The method allows one to find the linear combination of continuous variables that best separates groups of the discrete variable. Then, prediction on new samples (i.e. extinct taxa) can be done. We used this method to best discriminate the groups of locomotion types with the shape of the inner ear and to predict locomotion types of extinct taxa. The method can be

summarized in five steps. The Flexible Discriminant Analysis is an alternative to LDA that transform the discriminant problem in a general least square regression problem. Motani & Schmitz (2011) took advantage of this by introducing phylogenetic signal through PGLS calculations. Thus, the first step is to transform, for the extant taxa, the locomotion types (i.e. y: the explained discrete variable) in as many dummy variables (i.e. only 0 and 1). Second, the strength of the phylogenetic bias on the relationships between shape and function is assessed by a series of regression of y (locomotion/fossorial) against x (shape) when Pagel (1994)'s lambda (λ) varies from 0 to 1. Pagel's λ statistics is one of the two most widely used indices to measure and test phylogenetic signal, with Blomberg et al. (2003)'s K for univariate data or Adams (2014)'s K-mult for multivariate data. Under the assumption of a pure Brownian model of evolution, the optimal value of lambda for a given tree topology can be found by identifying the value that minimizes the residual sum of squares of the linear fit between the rescaled phylogenies containing the continuous and categorical data for each species. In other words, we try to maximize the correlation between form and function. A lambda value of zero indicates that phylogeny has no importance in the model, equivalent to a non-phylogenetic analysis. If lambda equals one, phylogeny is an important component of the model, with the residuals following a Brownian motion model of evolution. In this case, phylogenetic correction is necessary to ensure that the resulting projections into discriminant space are evolutionarily orthogonal. Third, both shapes variables and locomotion types are transformed to remove phylogenetic signal. Fourth, discriminant axes are obtained by the combination of PGLS and LDA calculations only on extant taxa. A cross validation procedure is used to evaluate the goodness of the classification. Fifth, predictions of locomotion type on extinct taxa can be done. They correspond to the minimum distance between each extinct taxon and gravity centres of each locomotion type on extant taxa in the discriminant space.

The entire procedure of the PDFA can be resumed as follows:

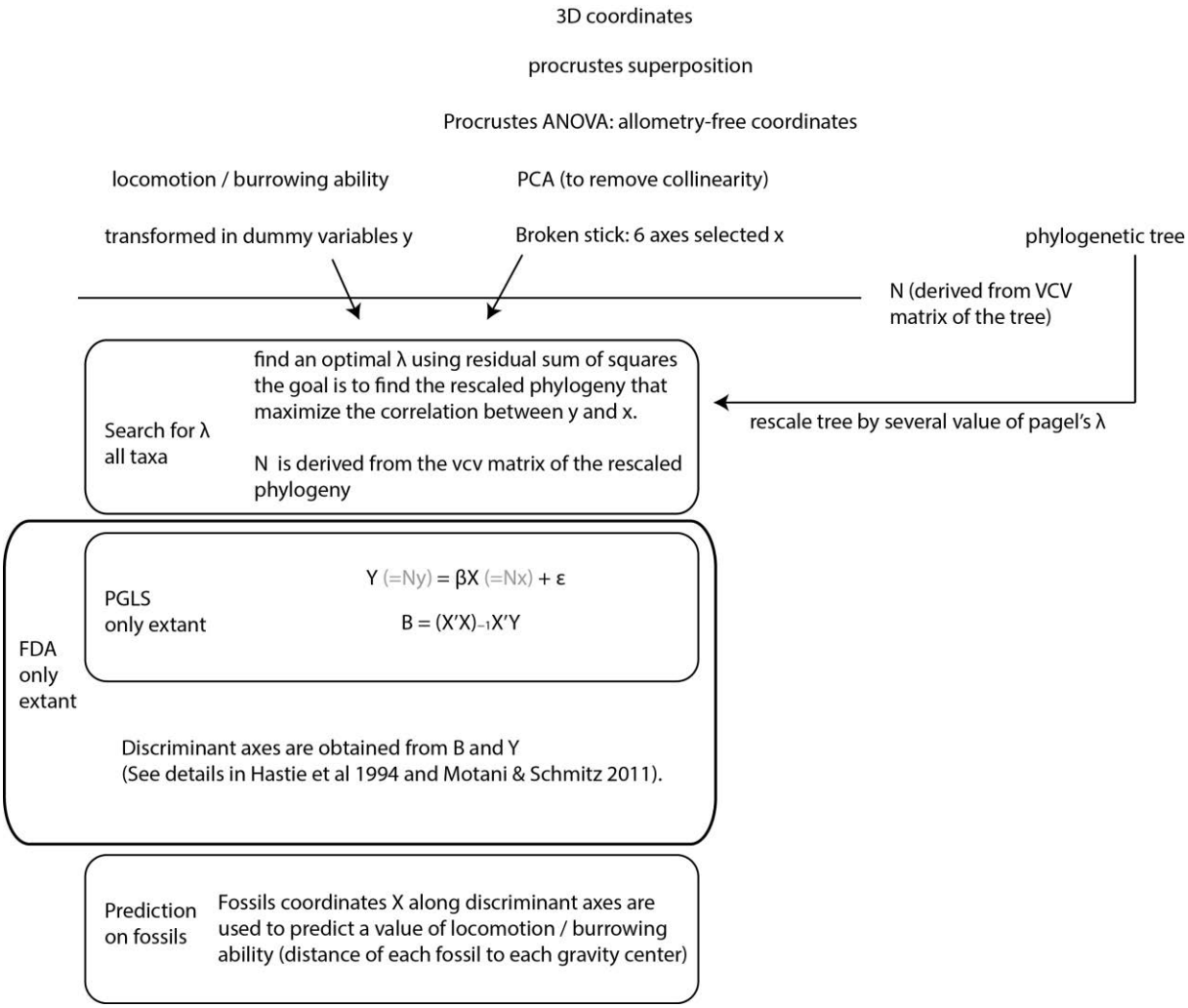

Institutional Abbreviations

AF, Analia Forasiepi, private collection, CCT Mendoza, Argentina; IEEUACH, Universidad Austral de Chile, Instituto de Ecología y Evolución, Valdivia, Chile; J/JM: Queensland Museum, Mammal collection; MACN, Museo Argentino de Ciencias Naturales Bernadino Rivadavia, Argentina; MNHN, Muséum national d'Histoire naturelle; NMV C, Museum of Victoria, Australia, Mammal Collection; PAR, Musée Crozatier, le Puy-en-Velay; RH, Robert Hoffstetter, private collection; USNM, United States National Museum of Natural History, Washington DC; YPM, Yale Peabody Museum, New Haven; ZMB, Museum für Naturkunde, Berlin.

Results

1- Shape variation and phylogenetic signal

The first PC explains 35% of the total variance, the PC2 14%, and the PC3 10%. The four first PCs account for 66.295% of the overall variance in the semicircular canals shape. The eighteen first PCs explain together more than 95% of the total variance (SI-6).

Visualized with the PCA, our dataset does not permit to discriminate the ecological groups among marsupials (see Figure 3, and the pairs in SI-7).

It is nonetheless interesting that on the PC1, the subterranean *Notoryctes typhlops* is at the most negative pole, while the hoppers and the gliders are at the most positive pole. However, the latter are included in a more inclusive cluster, which corresponds to a phylogenetic gathering of hoppers into macropodids and gliders into petauroids. As a matter of fact, the calculated lambdas indicate that the PCs 1, 3, 4, and 5 have a significant phylogenetic signal (Fig. 4, Table 1). The figure 4 shows the values on the four first PCs onto the phylogenetic tree. It is obvious that the most positive values of PC1 correspond to macropodids and petauroids, as previously interpreted from the figure 3. On the PC2, the interpretation is more delicate, but it seems that the most positive values are found in Macropodinae. The most negative values are found in very small species, such *as Tarsipes rostratus*, *Lestodelphys halli*, *Dromiciops gliroides*, *Planigale ingrami* (all below 80g), but also quite small species such as *Petaurus breviceps* and *Phascogale tapoatafa* (below 210g), and some very small fossils such as herpetotheriids, and *Microbiotherium* (below 200g). However, it is noteworthy that all the minute species do not exhibit negative values of PC2, and some larger species may exhibit negative values of PC2.

The PC3 is also difficult to interpret but the most negative values are found in extreme lifestyles: gliders and subterraneans (*Notoryctes* and *Necrolestes*).

Table 1: Lambdas of the eight first PC axes

PCs	PC1	PC2	PC3	PC4	PC5
Lambda	0.9999339	8.084579e-05	0.9999339	0.9146494	0.523006
P value	2.904817e-08	1	0.0001870681	0.02959529	0.02381202
PCs	PC6	PC7	PC8		
Lambda	6.610696e-05	6.610696e-05	6.610696e-05		
P value	1	1	1		

It is noteworthy that two fossils are isolated from the global dataset: *Andinodelphys* at the most positive pole of the PC2 and negative pole of the PC1, and *Necrolestes* (which is not a metatherian) at the most negative pole of the PC1. We may suspect a bizarre morphology of the bony labyrinth of *Andinodelphys*, probably resulting from the fossilization. The isolated petrosal of this species is indeed slightly and transversally crushed (Ladevèze & Muizon, 2007). *Necrolestes* falls outside the metatherian dataset, which is not surprising, and is found in the negative pole of the PC1, as the marsupial mole.

The extreme morphologies of the semicircular canals of the bony labyrinth on the two first PCs are the following. At the most positive pole of the PC1, the crus commune is short, the semicircular canals are thin, both the anterior semicircular (ASC) and posterior (PSC) canals have a strong curvature and are rounded, the ASC and PSC join at the crus commune drawing a V (apical insertion), the posterior part of the lateral semicircular canal (LSC) goes above the posterior ampulla. This conformation is typical of the Petauroidea (without *Dactylopsila*) and Macropodiformes. At the most negative pole of the PC1, the morphology is at the extreme opposite: the crus commune is long, the semicircular canals are thick, the ASC is the longest, the ASC and PSC are not strongly curved and are verticaly elongated, the joint ASC/PSC/crus commune has a T shape (lateral insertion), the posterior arm of the LSC enters the vestibule at the level with the posterior ampulla. This conformation is characteristic of the marsupial mole.

At the most positive pole of the PC2, the canals are thick, the crus commune is short, the ASC is the longest, the angle between the ASC and PSC is obtuse. This conformation is characteristic of the fossil pucadelphyid *Andinodelphys*, which is unique among the sample being at such a high positive value of PC2. At the most negative pole of the PC2, the canals are thin, the crus commune is long, the joint ASC/PSC/crus commune has a V shape, the angle between the ASC and PSC is right-angled. This morphology is typical of *Tarsipes rostratus*, and also the two herpetotheriids *Amphiperatherium minutum* and *Peratherium elegans*.

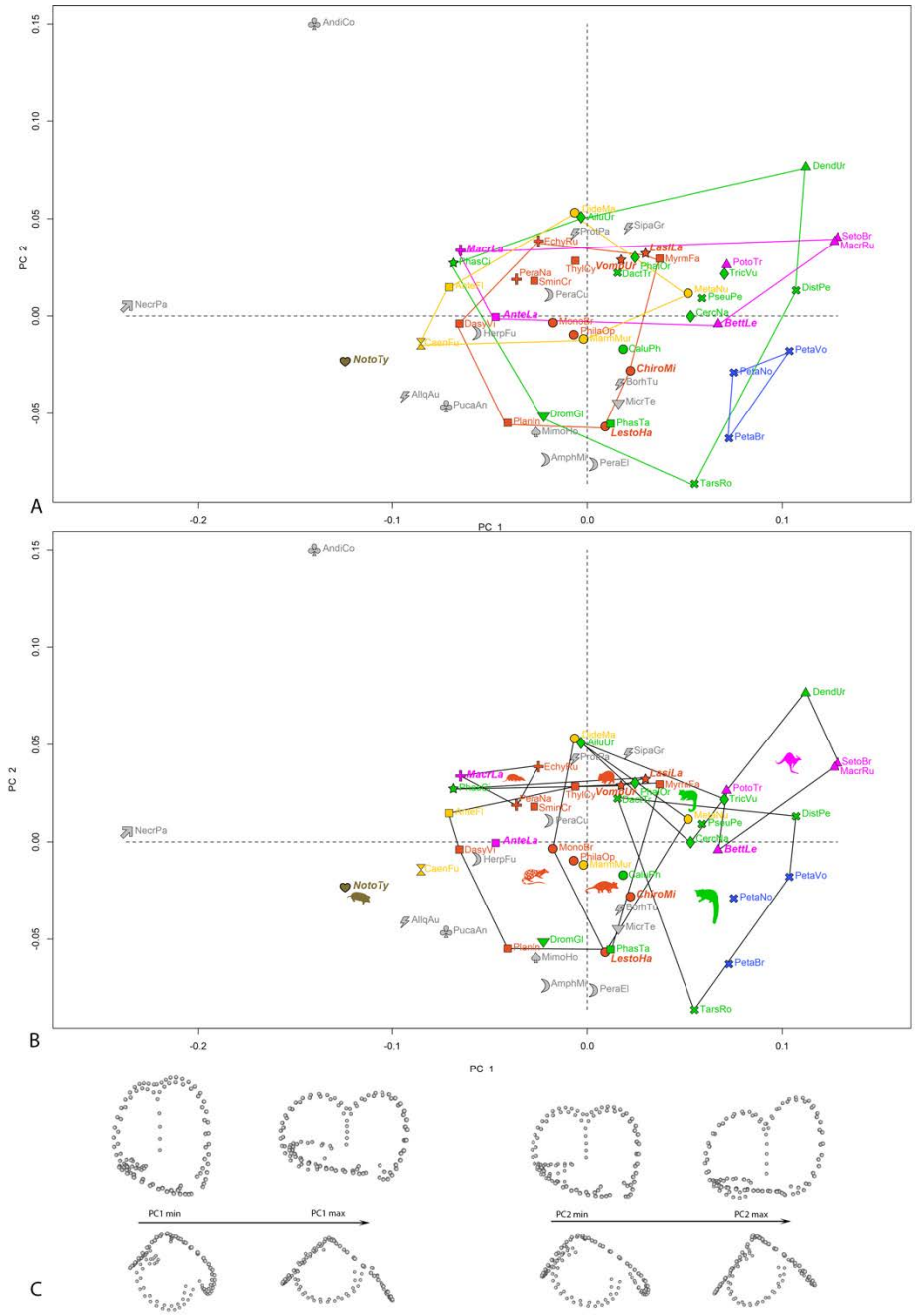

Figure 3: Results of the principal components analyses performed on the morphometric data of the semicircular canals of the bony labyrinth of metatherians. A. A first clustering is highlighted with coloured envelopes gathering locomotor modes. B. A second clustering shows black envelopes gathering clades. Each clade is indicated with a symbolic silhouette, the colour of which represents the reconstructed locomotor ancestral state (SI-8). C. The most extreme conformations of the landmark coordinates of the semicircular canals of the bony labyrinth are shown at the most negative (min) and most positive (max) poles of the PC1 and PC2. Abbreviations: symbols for the clades as follows: circle=Didelphimorphia, square=Dasyuromorphia, triangle=Macropodiformes, cross (x)=Petauroidea, losange=Phalangeroidea, star=Vombatiformes, cross (+)=Peramelemorphia, reversed triangle=Microbiotheriia, hourglass=Paucituberculata, heart=Notoryctemorphia, moon=Herpetotheriidae, spade=Peradectidae, clover=Pucadelphyidae, bolt=Sparassodonta, arrow=Meridiolestida. Colors for the locomotions as follows: green=arboreal, yellow=terrestrial to arboreal, orange=terrestrial, brown=subterranean, blue=glider, pink=hopper, unknown (fossils)=grey. The fossorial extant species are in bold italics.

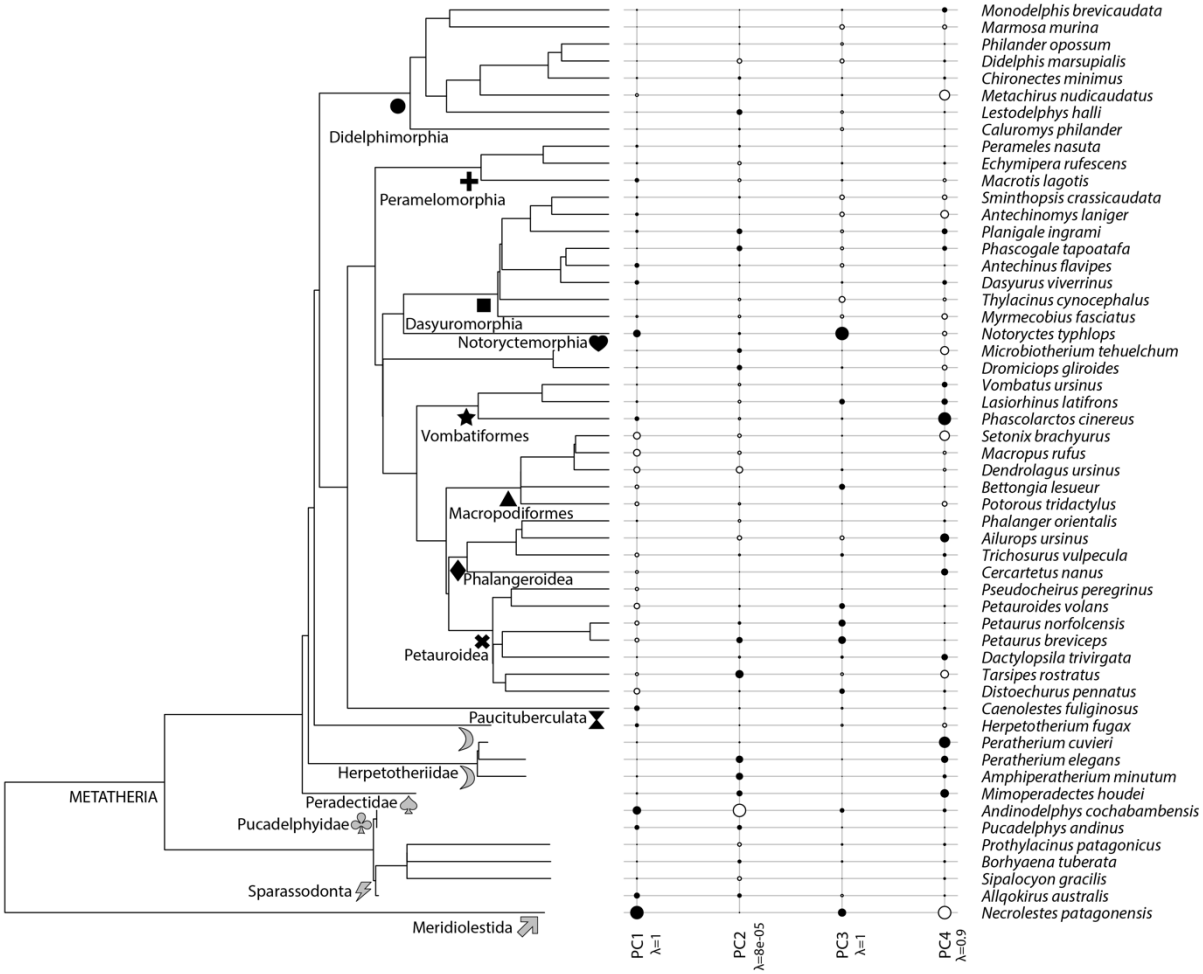

Figure 4: Phylogeny of Metatheria associated with the CP values for each species. Each clade is indicated by the same symbol than in figure 3. The lambdas are given for the four first PC axes.

2- Allometry

As noted before, most of the minute species are found at the most negative pole of the PC2, which made us suspect an allometry effect. As a matter of fact, there is a significant effect of the allometry (p-value=0.001) and a bivariate plotting of the log of the body size and the shape shows that the observed and quantified changes of shape are size-related (SI-9).

As previously observed by Alloing-Séguier et al. (2013) in diprotodontans, bony labyrinths of larger specimens possess ASC and PSC proportionally longer and LSC proportionally smaller (SI-9). The PSC of smaller specimens is positioned in a low position so that the joint ASP/PSC/crus commune has a T-shape. Such a pattern of morphological variation related to allometry is also found among primates (Lebrun et al. 2010).

3- Two-sample Hotelling's T-squared test

In order to verify if the morphologies associated with the most extreme locomotions (i.e., subterranean and gliding) and the burrow ability were significantly different from the morphologies found in the complete sample or in other taxa, we performed a two-sample hotelling's T square test onto the PCA scores based on the allometry-corrected data.

The morphological differences between burrowers and the complete sample (burrowers + non burrowers + unknown) are not significatively different (p-value=0.9096), and nor are the differences between burrowers and non-burrowers (p-value=0.2368).

Hoppers do not have a significantly different morphology of their bony labyrinth as compared to either the complete sample (hoppers + non hoppers + unknown) are not significantly different (p-value =0.3073) or non-hoppers (p-value =0.1386).

Gliders do have a significantly different morphology as compared to non-gliders (p-value =0.0154) but not as compared to the complete sample (gliders + non gliders + unknown) (p-value =0.718).

Subterraneans (here the marsupial mole *Notoryctes typhlops* and the meridiolestidan *Necrolestes patagonensis*) exhibit a significantly different morphology as compared to non subterraneans (p-value =0) and to the complete sample (subterraneans + non subterraneans + unknown) (p-value =0.0038).

4- Phylogenetic signal and phylogenetic discriminant analyses

Optimal lambda values for locomotor mode and burrowing ability were close to 0 (0.01 and 0 respectively). Considering the predicted classes and the class means in discriminant space, the percentages of good attributions were higher as regard burrowing ability than locomotor mode (85% against 78%). With 85% of good attributions, the confusion matrix shows that all the non-burrower species (33) were identified as such, whereas only 2 out of 8 burrowers were correctly identified. The confusion matrix of locomotor modes shows that 100% of the glider and subterranean species were well attributed (Table 2). As a matter of fact, in the morphospace only these two extreme locomotor modes are well discriminated from the global sample (Fig. 5). The most positive pole of the DA1 clusters the marsupial mole with *Necrolestes patagonensis* and *Andinodelphys cochabambensis*. The most negative pole of the DA2 gathers the gliders.

Table 2: Confusion matrix of locomotor modes. 78% of the species were correctly assigned to their locomotions.

	true					
predicted	arboreal	glider	hopper	subterranean	terrestrial	terrestrial - arboreal
arboreal	10	0	0	0	2	0
glider	0	3	1	0	0	0
hopper	1	0	5	0	0	0
subterranean	0	0	0	1	0	0
terrestrial	2	0	0	0	10	2
terrestrial - arboreal	0	0	0	0	1	3

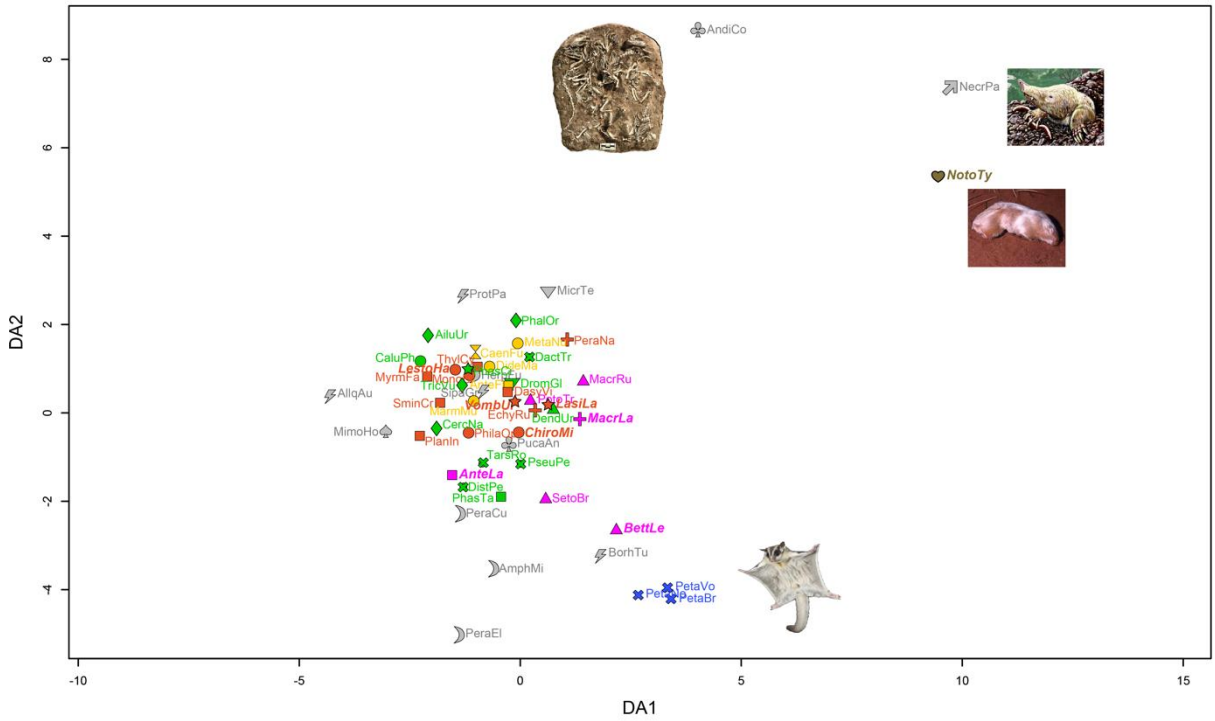

Figure 5: Result of the two first axes of the PFDA. The colours and symbols are the same than those used in the figure 3.

Discussion

1- Shape variation and phylogenetic signal

In mammals, it has been repeatedly stated that the radius of curvature and the size of the canals were the features of the semicircular canals that had the strongest correlation with locomotor agility (e.g., Cox & Jeffery, 2010; Spoor et al., 2007). Moreover, other studies highlighted that the main functional morphological signal of the bony labyrinth is found in the diameter of the semicircular canals (Billet et al., 2013 in xenarthrans; Pfaff et al., 2017 in marsupials). The present study confirms these findings but with a non-negligible restriction: only the bizarre morphologies of the semicircular canals of subterranean and glider marsupials is correlated with the locomotion. None of the other locomotor types can be discriminated with the morphology of the bony labyrinth. If we compare gliders versus subterranean versus

others, we indeed find that the marsupial mole is characterized by thicker canals, not strongly curved ASC and PSC, a longer crus commune, and the posterior arm of the LSC that enters the vestibule at the level with the posterior ampulla (negative values of PC1). On the contrary, gliders exhibit thinner canals, strongly curved and rounded ASC and PSC, a shorter crus commune, and the posterior part of the LSC that goes above the posterior ampulla (positive values PC1 and negative values PC2). The diameter of the semicircular canals, together with their relative size, have been considered to be linked to locomotor habits, and more particularly, the small and thick semicircular canals of sloths are likely to be linked to their low agility and slow locomotion (Spoor et al. 2007; Billet et al., 2013).

There is a strong phylogenetic signal in the PC1 and PC3, on which several clades are distinguished from the global dataset (Table 1, Figs 3, 4). At the most positive pole of the PC1 are the Macropodiformes, among which the Macropodidae (which are all hoppers) have the most positive values. At the most negative pole of the PC3 are the Dasyuromorphia, among which the Sminthopsinae have the most negative values. On the contrary, the PC2 allows to distinguish the most extreme locomotions, being the gliders and the marsupial moles, which are also very small specimens. As noted before, minute species are found at the negative pole of the PC2, which indicates that modifications in the shape of the bony labyrinth are linked with the bodymass of the animal. Previous studies in other mammals however concluded that there was a weak allometric effect on the bony labyrinth shape (e.g., Billet et al., 2013, 2015; Mennecart et al., 2017).

Alloing-Séguier (2013) showed that there was an obvious phylogenetic signal in the bony labyrinth shape, and in their PCA, high-level diprotodontian taxonomic groups were well separated in PC1-PC2 space: Macropodiformes, Phalangeroidea, Petauroidea, and Vombatiformes. In the present analysis, diprotodonts are well separated from other Marsupialia in PC1-PC2 space. Most, but not all, high-level Marsupialia clades are also well separated in PC1-PC2 space: Macropodiformes, Petauroidea (except Dactylopsila), Phalangeroidea, and Peramelomorphia.

Modifications of the bony labyrinth shape in marsupials are therefore driven by both body mass and phylogeny. In order to be able to decipher any ecological signal in the shape of the semicircular canals of the bony labyrinth, we corrected the landmarks coordinates relatively

to the body mass, and we performed two different analyses: a two-sample hotelling's T square test and a phylogenetic flexible discriminant analysis.

2- The morphology of the bony labyrinth allows to discriminate extreme locomotions only

Assuming that, in one hand, lesser agile animals (such as fossorial or subterranean species) have smaller canals relatively to body mass and, in the other hand, more agile animals (such as arboreal and gliding species, in which the stabilization of vision is especially important) have larger canals relatively to body mass, we should be able to discriminate these locomotions, linked to relative agility, thanks to the morphology of the semicircular canals. We conducted a two-sample hotelling's T square test onto the PCA scores based on allometry-corrected data, which statistically confirms that the morphology of the bony labyrinth of subterranean taxa is different from that of non-subterranean taxa, and that the morphology of the bony labyrinth of gliders is different from that of non-gliders. However, arboreal marsupials or even hopper marsupials cannot be distinguished from the other species with different locomotions.

It is striking that this statistic test has never been used in any of the previous studies dealing with the same question that our present study. And yet, that previous study highlighted an ecological signal, based only on the visualization of the shape variation on a classic PCA. Taking a brighter look at Pfaff et al. (2017)'s results, it appears that: i) the clustering of hoppers can also be interpreted as the clade Macropodiformes; ii) the PC axes presented in their study do not discriminate the gliders; iii) the marsupial mole is close to the Tasmanian devil, which may result from a phylogenetic effect (see the phylogenies of Asher et al., 2004; Cardillo et al., 2004; Beck, 2008). It would therefore be very enlightening to conduct a two-sample hotelling's T square test onto this dataset to verify the conclusion of the authors.

3- Is the morphology of the bony labyrinth a relevant proxy to infer locomotor modes in fossils?

In the DA1-DA2 space of the PFDA, three taxa fall far out from the marsupial morphospace (Fig. 5): the marsupial mole, the pucadelphyid *Andinodelphys cochabambensis*, the meridiolestidan *Necrolestes patagonensis*. The latter was considered with confidence as a subterranean mammal, based on postcranial remains typical of an animal living underground (Asher et al., 2007). This "subterranean cluster" is not surprising given that the morphology of the bony labyrinth of these two subterranean mammals is significantly different from that of

non-subterranean marsupials. *Andinodelphys* is known by a dozen skeletons and skulls, six of which were found intermingled, indicating that they probably were gregarious and lived in burrows (Muizon et al., in press). *Andinodelphys* is supposed to have been more arboreal than its contemporary *Pucadelphys andinus* (Muizon & Argot, 2003). None of the available data relative to its way of life suggest subterranean habits, and we suspect that its bizarre bony labyrinth morphology is due to a fossilisation bias. For future studies, the bony labyrinth of a petrosal enclosed in a skull should be preferentially used.

The phylogenetic discriminant analysis erroneously predicted locomotion classes for seven out of 41 extant marsupials (SI-11). For example, the hopper *Bettongia lesueur* (P=0.47) was predicted glider (P=0.52). The arboreal kangaroo *Dendrolagus ursinus* (P=0.31) was predicted hopper (P=0.62), which makes sense since it does perform quadrupedal ricochet, but contrary to other hopper macropodids it can move its hind legs independently from one another (Jones & Parish, 2005; Richardson, 2012). The other wrong attributions concerned terrestrial to arboreal marsupials, which is not surprising given that these classes are mixed up in the central morphospace (Fig. 5).

Concerning the fossil taxa (SI-11), the pucadelphyid *Andinodelphys cochabambensis* and the meridiolestidan *Necrolestes patagonensis* were both predicted as subterraneans (P=1), because they share the same morphospace than the marsupial mole. As explained before, it makes senses for *Necrolestes* but it seems that that the sampled specimen of *Andinodelphys* is weird enough to be considered as deformed.

It is noteworthy that some predicted classes of locomotor modes for fossils were in accordance with their inferred locomotion from previous works (SI-1, and SI-12). *Pucadelphys andinus* was described as terrestrial (P=0.85) (Muizon & Argot, 2003), *Prothylacinus patagonicus* as terrestrial-arboreal (P=0.83) (Argot, 2004), *Herpetotherium fugax* as primarily terrestrial (P=0.9) (Sánchez-Villagra et al., 2007). Three terrestrial-arboreal fossils are here predicted slightly differently: *Sipalocyon gracilis* as terrestrial (P=0.73), *Mimoperadectes houdei* as terrestrial (P=0.85), and *Amphiperatherium minutum* as arboreal (P=0.7); but we have to keep in mind that these locomotor classes were not differentiated in extant taxa. *Microbiotherium tehuelchum* is predicted arboreal (P=0.57), just like its living representative *Dromiciops gliroides.*

One very bizarre prediction concerns the terrestrial *Borhyaena tuberata*, which was a predator with hyaena-like features (Argot, 2004), which is here predicted glider (P≈1). Other weird fossils are the two herpetotheriids *Peratherium elegans* and *P. cuvieri* which are predicted hoppers (P=0.77 and P=0.7 respectively). One might be open to fantasist hypotheses, but such predictions are obviously false.

As regard burrowing abilities, only two out of the eight burrower marsupials were correctly predicted (SI-12): the marsupial mole and the bilby *Macrotis lagotis* (P=0.98 and 0.5 respectively). The others were predicted as non-burrowers, which can be understandable for *Antechinomys laniger*, which digs in rare and particular cases, and *Lestodelphys halli*, which sometimes forages under the snow for food. However, wombats, the burrowing bettong, and the aquatic opossum clearly dig burrow but are not predicted as such.

Five out of 13 fossil species were classified as burrowers (SI-12). *Necrolestes patagonensis* (P=0.96) is a subterranean mammal and would have certainly demonstrated burrowing abilities. *Pucadelphys andinus* (P=0.69) was a small terrestrial metatherian, which lived in group in burrows –which it may have dug then- along the banks of a river (Ladevèze et al., 2011). *Allqokirus australis* (P=0.81) is only known by cranial and dental remains (Muizon et al., in prep.). It is here predicted as terrestrial and burrower. One improbable prediction concerns again *Borhyaena tuberata* (P=0.79), which is expected to be a burrowing glider of 36kgs. *Peratherium elegans* could have been a burrower in a lacustrine environment (P=0.52), occupying burrows in the same way as that reconstructed for the pucadelphyids of Tiupampa.

Conclusion

The most recent and updated study of the correlation between the bony labyrinth shape and locomotion in marsupials stated that there was a functional signal in the shape of the semicircular canals and that the locomotion mode of extinct metatherians could be inferred in future studies independent of any evidence of postcranial material (Pfaff et al., 2017). However, our study, based on a larger dataset of extant marsupials and completed by fossil metatherians, shows that it is not possible. The locomotor classes defined in extant taxa do not fit with observed morphology of the semicircular canals of the bony labyrinth. Moreover, burrowing marsupials are not discriminated among our sample. Nevertheless, we found that

extreme lifestyles, such as in the air and underground, were correlated with a peculiar morphology. Nonetheless, only two subterranean taxa are included in our study, and it is obvious that future studies would benefit from including various subterranean species.
A study of the head rotations during multiple behaviours in various mammal species shown that the colugo, a gliding scandentian, has a high angular velocity magnitude, while slow sloth has a low angular velocity magnitude (Malinzak et al., 2012). We can therefore make the hypothesis that the semicircular canals of gliding marsupials responds to high speed locomotion and high angular velocity magnitude in their head movements. On the contrary subterranean mammals are expected to display lesser amplified head movements. This should be tested in future studies.

The marsupial clade may not represent such a good model to study ecological convergences, mainly because locomotor modes are strongly linked to the phylogeny (SI-8). Moreover, the two most extreme behaviours did not occur in different clades: there is only one subterranean marsupial and the gliding forms are all petauroids. It would be an exciting future direction to study the convergences of the subterranean lifestyle in placental mammals, and more particularly in rodents, which exhibit a large amount of adaptive convergences to this life underground.

The relevancy of using the morphology of the bony labyrinth instead of the morphology of the membranous labyrinth, or even the functional membranous parameters has never been proven, and was recently questioned by David et al. (2016). Our results suggest that bony labyrinth based methodologies are in fact unreliable to determine ecology and that a bony-to-membranous labyrinth based methodology, such as that proposed by Romain David (in prep.), taking phylogenetically specific correlations between bones and soft tissues, is needed if one wants to infer anything from fossil bony labyrinths with satisfactory precision. Soft tissues investigation is crucial to compute functionnal parameters of the inner ear, which are directly correlated to head movements and are the most likely to determine the lifestyle of animals.

Supplementary Information

SI-1. Presentation of the database of the metatherian species selected for the study.

SI2. Phylogenetic calibrated tree of Metatheria.

SI-3. Improvement of the 3D model rendering: Smoothing and repairs of some specimens with Geomagic.

SI-4. 3D data preparation and protocol of fixing landmarks with AVIZO.

SI-5. R script of the geometric morphometrics procedure.

SI-6. PCA summary.

SI-7. Pairs of the ten first Principal Components.

SI-8. Optimisation of the character locomotion onto the phylogenetic tree of Metatheria.

SI-9. Regression shape vs bodymass and PCA with allometry-corrected data.

SI-10. Pairs of the ten first Principal Components, resulting from the analysis with allometry-corrected data.

SI-11. Phylogenetic Discriminant Analysis of the locomotor classes.

SI-12. Phylogenetic Discriminant Analysis of the burrowing ability.

SI-13. SI References.

Online Material

OM-1. Phylogenetic calibrated tree of Metatheria.

OM-2. Matrix of landmark coordinates.

OM-3. Text file of sliding landmarks.

OM-4. R script of the geometric morphometrics procedure.

OM-5. R script to source the main PFDA functions.

Acknowledgements

This work was financially supported by three MNHN grants: ‘PPF Biodiversité 2008’, the ‘ATM Formes 2014’ and ‘ATM Form and Function 2015’ which especially helped for the scans of the specimens. Tim Ryan (University Center for Quantitative X-ray Imaging, Penn State) for the scans of *Pucadelphys andinus*, *Borhyaena tuberata*, *Prothylacinus patagonicus*, and *Sipalocyon gracilis*. We are indebted to many colleagues from the MNHN: Miguel Garcia Sanz and Maïté Adam, operators of the AST-RX platform for the many scans performed (UMS 2700); Florent

Goussard, in charge of the 3D platform of the CR2P (UMR 7207) for technical advices; Patricia Wils, in charge of the 3D platform at the UMS 2700 for her precious help on the AVIZO software; Christine Argot, for access to the palaeontological collection; Géraldine Véron, for access to the comparative collections of mammals. We warmly thank Analia Forasiepi (CONICET Mendoza) for the loan of *Chironectes* and *Lestodelphys*, Emmanuel Magne (Musée Crozatier) for the loan of *Peratherium elegans*, Marcelo Sánchez-Villagra for the free scans *Herpetotherium fugax* and *Mimoperadectes houdei*.

References

Adams, D. C. (2014). A generalized K statistic for estimating phylogenetic signal from shape and other high-dimensional multivariate data. *Systematic Biology, 63*(5), 685-697.

Adams, D. C., & Otárola-Castillo, E. (2013). geomorph: an R package for the collection and analysis of geometric morphometric shape data. *Methods in Ecology and Evolution*, *4*(4), 393-399.

Alloing-Séguier, L., Sánchez-Villagra, M. R., Lee, M. S., & Lebrun, R. (2013). The bony labyrinth in diprotodontian marsupial mammals: diversity in extant and extinct forms and relationships with size and phylogeny. *Journal of Mammalian Evolution*, *20*(3), 191-198.

Asher, R. J., Horovitz, I., Martin, T., & Sánchez-Villagra, M. R. (2007). Neither a rodent nor a platypus: a reexamination of *Necrolestes patagonensis* Ameghino. *American Museum Novitates, 3546*, 1-40.

Asher, R. J., Horovitz, I., & Sánchez-Villagra, M. R. (2004). First combined cladistic analysis of marsupial mammal interrelationships. *Molecular phylogenetics and evolution*, *33*(1), 240-250.

Beck, R. M. (2008). A dated phylogeny of marsupials using a molecular supermatrix and multiple fossil constraints. *Journal of Mammalogy*, *89*(1), 175-189.

Benton, M. J., Donoghue, P. C., Asher, R. J., Friedman, M., Near, T. J., & Vinther, J. (2015). Constraints on the timescale of animal evolutionary history. *Palaeontologia Electronica*, *18*(1), 1-106.

Billet, G., Germain, D., Ruf, I., de Muizon, C., & Hautier, L. (2013). The inner ear of *Megatherium* and the evolution of the vestibular system in sloths. *Journal of Anatomy 223*, 557–567.

Billet, G., Hautier, L. & Lebrun, R. (2015). Morphological diversity of the bony labyrinth (inner ear) in extant Xenarthrans and its relation to phylogeny. *Journal of Mammalogy, 96*(4), 658–672.

Bininda-Emonds, O. R., Cardillo, M., Jones, K. E., MacPhee, R. D., Beck, R. M., Grenyer, R., Price, S. A., Vos, R. A., Gittleman, J. L., & Purvis, A. (2007). The delayed rise of present-day mammals. *Nature*, *446*(7135), 507.

Blomberg, S. P., Garland, T., & Ives, A. R. (2003). Testing for phylogenetic signal in comparative data: behavioral traits are more labile. *Evolution*, *57*, 717–745.

Bookstein, F. L. (1997). *Morphometric tools for landmark data: geometry and biology*. Cambridge University Press.

Cardillo, M., Bininda-Emonds, O. R., Boakes, E., & Purvis, A. (2004). A species-level phylogenetic supertree of marsupials. *Journal of Zoology*, *264*(1), 11-31.

Cox, P. G., & Jeffery, N. (2010). Semicircular canals and agility: the influence of size and shape measures. *Journal of Anatomy*, *216*(1), 37-47.

Curran, J. M. (2013). Hotelling: Hotelling's t-squared test and variants. R package version 1.0–2.

David, R., Stoessel, A., Berthoz, A., Spoor, F., & Bennequin, D. (2016). Assessing morphology and function of the semicircular duct system: introducing new in-situ visualization and software toolbox. *Scientific reports*, *6*, 32772.

Fabre, A. C., Cornette, R., Huyghe, K., Andrade, D. V., & Herrel, A. (2014). Linear versus geometric morphometric approaches for the analysis of head shape dimorphism in lizards. *Journal of Morphology, 275*(9), 1016-1026.

Felsenstein, J. (1985). Phylogenies and the comparative method. *The American Naturalist*, *125*(1), 1-15.

Gower, J. C. (1975). Generalized procrustes analysis. *Psychometrika*, *40*(1), 33-51.

Hackathon, R., Bolker, B., Butler, M., Cowan, P., de Vienne, D., Eddelbuettel, D., Holder, M., Jombart, T., Kembel, S., Michonneau, F., Orme, D., O'Meara, B.n Paradis, E., Regetz, J., & Zwickl, D.. (2013). phylobase: Base package for phylogenetic structures and comparative data. https://cran.r-project.org/web/packages/phylobase/.

Hastie, T., Tibshirani, R., & Buja, A. (1994). Flexible discriminant analysis by optimal scoring. *Journal of the American statistical association*, *89*(428), 1255-1270.

Horovitz, I., Martin, T., Bloch, J., Ladevèze, S., Kurz, C., & Sánchez-Villagra, M. R. (2009). Cranial anatomy of the earliest marsupials and the origin of opossums. *PLoS One*, *4*(12), e8278.

Jones, C., & Parish, S. (2005). *Field Guide to Australian Mammals*. Steve Parrish Publishing group, Archerfield, Queensland. 215 p.

Jones, G. M., & Spells, K. E. (1963). A theoretical and comparative study of the functional dependence of the semicircular canal upon its physical dimensions. *Proceedings of the Royal Society of London B: Biological Sciences*, *157*(968), 403-419.

Ladevèze, S., Asher, R. J., & Sánchez-Villagra, M. R. (2008). Petrosal anatomy in the fossil mammal Necrolestes: evidence for metatherian affinities and comparisons with the extant marsupial mole. *Journal of Anatomy*, *213*(6), 686-697.

Ladevèze, S, de Muizon, C., & Selva, C. (in prep.). What are "opossum-like" fossils? The phylogeny of herpetotheriid and peradectid metatherians, based on new features from the petrosal anatomy. *Journal of Systematic Palaeontology*.

Ladevèze, S., & de Muizon, C. (2007). The auditory region of early Paleocene Pucadelphydae (Mammalia, Metatheria) from Tiupampa, Bolivia, with phylogenetic implications. *Palaeontology*, *50*(5), 1123-1153.

Lebrun, R., De León, M. P., Tafforeau, P., & Zollikofer, C. (2010). Deep evolutionary roots of strepsirrhine primate labyrinthine morphology. *Journal of Anatomy*, *216*(3), 368-380.

Lele, S., & Richtsmeier, J. T. (1991). Euclidean distance matrix analysis: A coordinate-free approach for comparing biological shapes using landmark data. *American Journal of Physical Anthropology, 86*(3), 415-427.

Maddin, H. C., & Sherratt, E. (2014). Influence of fossoriality on inner ear morphology: insights from caecilian amphibians. Journal *of Anatomy*, *225*(1), 83-93.

Malinzak, M. D., Kay, R. F., & Hullar, T. E. (2012). Locomotor head movements and semicircular canal morphology in primates. *Proceedings of the National Academy of Sciences*, *109*(44), 17914-17919.

Mayne, R. (1965). The "match" of the semicircular canals to the dynamic requirements of various species. *The Role of the Vestibular Organs in the Exploration of Space, NASA SP-77*, 57-67.

Mennecart, B., DeMiguel, D., Bibi, F., Rössner, G. E., Métais, G., Neenan, J. M., Wang, S., Schulz, G., Müller, B., & Costeur, L. (2017). Bony labyrinth morphology clarifies the origin and evolution of deer. *Scientific Reports, 7*(1), 13176.

de Muizon, C., & Argot, C. (2003). Comparative anatomy of the Tiupampa didelphimorphs: an approach to locomotory habits of early marsupials; pp. 43–62 in M Jones, C Dickman, & M Archer (eds), *Predators with Pouches: The Biology of Carnivorous Marsupials*. CSIRO Publishing, Collingwood, Victoria.

de Muizon, C., Ladevèze, S. & Céspedes, R. (in press). The beginning of the age of therian mammals in South America: Tiupampa, a transition between Northern and Southern worlds in the basal Paleocene.; in E. Delson & E. Sargis (eds), *Vertebrate Paleobiology and Paleoanthropology*, Book Series. Springer Science & Business Media Publishers.

de Muizon, C., Ladevèze, S., Goussard, F., Vignaud, R., & Selva, C. (in prep.). The cranial anatomy of *Allqokirus australis* (Sparassodonta, Metatheria) from the early Palaeocene of Tiupampa (Bolivia) and a reassessment of the affinities of the Tiupampa carnivorous metatherians. *Geodiversitas*.

Nowak, R. M. (2005). Walker's marsupials of the world. JHU Press.

Pagel, M. (1999). Inferring the historical patterns of biological evolution. *Nature*, *401*, 877-884.

Pfaff, C., Czerny, S., Nagel, D., & Kriwet, J. (2017). Functional morphological adaptations of the bony labyrinth in marsupials (Mammalia, Theria). *Journal of Morphology*, *278*(6), 742-749.

R Core Team. (2014). R: A language and environment for statistical computing [Internet]. Vienna, Austria.

Richardson, K. (2012). *Australia's amazing kangaroos*. CSIRO Publishing, Collingwood, Victoria. 234 p.

Rohlf, F. J., & Slice, D. (1990). Extensions of the Procrustes method for the optimal superimposition of landmarks. *Systematic Biology*, *39*(1), 40-59.

Rougier, G. W., Wible, J. R., Beck, R. M., & Apesteguía, S. (2012). The Miocene mammal *Necrolestes* demonstrates the survival of a Mesozoic nontherian lineage into the late Cenozoic of South America. *Proceedings of the National Academy of Sciences*, *109*(49), 20053-20058.

Sánchez-Villagra, M., Ladevèze, S., Horovitz, I., Argot, C., Hooker, J. J., Macrini, T. E., Martin, T., Moore-Fay, S., de Muizon, C, Schmelzle, T., & Asher, R. J. (2007). Exceptionally preserved North American Paleogene metatherians: adaptations and discovery of a major gap in the opossum fossil record. *Biology Letters*, *3*(3), 318-322.

Schmelzle, T., Sánchez-Villagra, M. R., & Maier, W. (2007). Vestibular labyrinth diversity in diprotodontian marsupial mammals. *Mammal Study*, *32*(2), 83-97.

Schmitz, L., & Motani, R. (2011). Nocturnality in dinosaurs inferred from scleral ring and orbit morphology. *Science*, *332*(6030), 705-708.

Selva, C., & Ladevèze, S. (2017). Computed microtomography investigation of the skull of Cuvier's famous 'opossum' (Marsupialiformes, Herpetotheriidae) from the Eocene of Montmartre. *Zoological Journal of the Linnean Society*, *180*(3), 672-693.

Spoor, F., Garland, T., Krovitz, G., Ryan, T. M., Silcox, M. T., & Walker, A. (2007). The primate semicircular canal system and locomotion. *Proceedings of the National Academy of Sciences*, *104*(26), 10808-10812.

Tyndale-Biscoe, H. (1973) [2005]. *Life of marsupials*. CSIRO Publishing, Collingwood, Victoria. 442 p.

Walsh, S. A., Barrett, P. M., Milner, A. C., Manley, G., & Witmer, L. M. (2009). Inner ear anatomy is a proxy for deducing auditory capability and behaviour in reptiles and birds. *Proceedings of the Royal Society of London B: Biological Sciences*, *276*(1660), 1355-1360.

Westerman, M., Krajewski, C., Kear, B. P., Meehan, L., Meredith, R. W., Emerling, C. A., & Springer, M. S. (2016). Phylogenetic relationships of dasyuromorphian marsupials revisited. *Zoological Journal of the Linnean Society*, *176*(3), 686-701.

Wilson, D. E., & Reeder, D. A. M. (eds). (2005). *Mammal Species of the World: A Taxonomic and Geographic Reference*. Volume 1. Third Edition. Baltimore (Maryland): Johns Hopkins University Press. xxxvii + 743 p.

Zelditch, M. (2004). *Geometric Morphometrics for Biologists: A Primer*. Amsterdam: Elsevier, Academic Press.

SUPPLEMENTARY INFORMATION

Supplementary Information 1. Presentation of the database of the metatherian species selected for the study. Each species is described by its systematics, its specimen reference, its ecology (locomotion, diet, and weight), and the scan resolution of its 3D model of the bony labyrinth.

Table SI-1: Database of the metatherian species selected for the study. Fossil taxa are in ligth blue.

Supra-familial	Family	Species	# specimen	Status	Weight (g)	Reference bodymass	Locomotion	Locomotion -additionnal data	Reference locomotion	Diet	Reference diet	Burrow (1) vs. non burrow (0)	CT-scan Resolution (µm)
Australidelphia, Diprotodontia, Phalangeroidea	Phalangeridae	Ailurops ursinus	MNHN.ZM.AC.A2597	extant	10000	Armati et al., 2006	arboreal		Armati et al., 2006 ; Tyndale-Biscoe, 1973	entirely folivorous	Armati et al., 2006	0	18.63
Pucadelphyda, Sparassodonta	Mayulestidae	Allqokirus australis	MHNC 8267	extinct	132	Myers (2001)' equation [log y = – 3.465 + 3.436(log TSL)]	unknown					unknown	9.15
	Herpetotheriidae	Amphiperatherium minutum	MNHN.Pal.GY.682	extinct	5.8	Myers (2001)' equation [log y = – 3.465 + 3.436(log TSL)]	unknown	terrestrial - arboreal	Crochet, 1980			unknown	16.5
Pucadelphyda	Pucadelphyidae	Andinodelphys cochabambensis	MHNC 8370	extinct	235	Myers (2001)' equation [log y = – 3.465 + 3.436(log TSL)]	unknown	terrestrial - arboreal	Muizon & Argot, 2003			unknown	9.15
Australidelphia, Dasyuromorphia	Dasyuridae	Antechinomys laniger	MNHN.ZM.MO.1897.1495	extant	25	Jackson, 2003	hopper	terrestrial AND quadrupedal ricochet during fast locomotion like the bandicoot (Armati et al., 2006) ; hopping like *Notomys* (Tyndale-Biscoe, 1973) ; squats burrows made by other species to perform torpor (IUCN); digs shallow burrows in captivity (IUCN)	Armati et al., 2006 ; Tyndale-Biscoe, 1973	arthropods, small vertebrates	Jackson, 2003	1	6.23
Australidelphia, Dasyuromorphia	Dasyuridae	Antechinus flavipes	MNHN.ZM.AC.12.797	extant	50	Jackson, 2003	terrestrial - arboreal		Jones & Parish, 2005	arthropods, small vertebrates	Jackson, 2003	0	21.58
Australidelphia, Diprotodontia, Macropodifromes	Potoroidae	Bettongia lesueur	MNHN.ZM.MO.1998.177	extant	1500	Jackson, 2003	hopper	terrestrial/fossorial AND bipedal (Menkhorst & Knight, 2013) + quadrupedal hopping (Claridge et al. (eds), 2007) ; terrestrial but digs burrows (the only macropodid that build burrows) (Jones & Parrish, 2005) ; analog of the rabbit: jumper and burrower	Jones & Parish, 2005	omnivorous ,roots, tubers, fungi undergroun d, leaf, fruit, seeds	Menkhorst & Knight, 2013 ; Jones & Parish, 2005	1	28.91

Pucadelphyda, Sparassodonta	Borhyaenidae	Borhyaena tuberata	YPM 15120	extinct	36400	Ercoli et al., 2011	unknown	terrestrial, cursorial	Argot, 2004			unknown	28
Paucituberculata	Caenolestidae	Caenolestes fuliginosus	MNHN.ZM.MO.1982-2587	extant	37	Animal Diversity Web	terrestrial - arboreal		Kirsch & Waller, 1979	arthropods, fruits, small vertebrates	Gardner, 2007	0	18.63
Didelphimorphia	Didelphidae	Caluromys philander	MNHN.ZM.MO.1987.234	extant	235	Armati et al., 2006	arboreal		Armati et al., 2006 ; Tyndale-Biscoe, 1973	frugivore, nectarivore	Armati et al., 2006	0	27.66
Australidelphia, Diprotodontia, Phalangeroidea	Burramyidae	Cercartetus nanus	MNHN.ZM.MO.1992.343	extant	25	Armati et al., 2006	arboreal		Jones & Parish, 2005	nectar, pollen, fruits, insects	Armati et al., 2006	0	6.23
Didelphimorphia	Didelphidae	Chironectes minimus	MACN 13053	extant	665	Armati et al., 2006	terrestrial	semi-aquatic	Armati et al., 2006	small fish, frogs, insects and other invertebrates (crabs)	Armati et al., 2006	1	36.15
Australidelphia, Diprotodontia, Petauroidea	Petauridae	Dactylopsila trivirgata	J6202	extant	387	Jackson, 2003	arboreal		Jones & Parish, 2005	insects, invertebrates, fruits, nectar, exudates	Armati et al., 2006	0	53
Australidelphia, Dasyuromorphia	Dasyuridae	Dasyurus viverrinus	MNHN.ZM.AC.A2627	extant	1090	Armati et al., 2006	terrestrial		Jones & Parish, 2005	insects, small birds in nests, small mammals , carrion, grass, fruits	Jones & Parish, 2005	0	28.91
Australidelphia, Diprotodontia, Macropodifromes	Macropodidae	Dendrolagus ursinus	MNHN.ZM.MO.1880.1465	extant	8000	De Magalhaes & Costa, 2009	arboreal	hopper quadrupedal ricochet AND hind legs can move independently of one anotehr	Jones & Parish, 2005; Richardson, 2012	leaf, fruits (browser)	Jackson, 2003	0	52.27
Didelphimorphia	Didelphidae	Didelphis marsupialis	RH161	extant	1120	Armati et al., 2006	terrestrial - arboreal	lives predominantly on the ground	Tyndale-Biscoe, 1973	opportunistic: carrion, insects, fallen fruits or large earthworms	Tyndale-Biscoe, 1973	0	18.63

Australidelphia, Diprotodontia, Petauroidea	Acrobatidae	Distoechurus pennatus	JM9611	extant	45	Tyndale-Biscoe, 1973	arboreal	highly arboreal	animaldiversity.org	nectar, pollen and plant exudates in addition to invertebrates.	Armati et al., 2006	0	27.9
Australidelphia, Microbiotheria	Microbiotheriidae	Dromiciops gliroides	IEEUACH 2162	extant	35	Gardner, 2007	arboreal	semi-arboreal	Armati et al., 2006	insects and larvae	Armati et al., 2006	0	12.74
Australidelphia, Peramelemorphia	Peramelidae	Echymipera rufescens	MNHN.ZM.MO.1962.2147	extant	1250	Jackson, 2003; Jones & Parish, 2005	terrestrial		Jones & Parish, 2005	invertebrates, fruits, plant matter	Jackson, 2003; Jones & Parish, 2005	0	29.26
	Herpetotheriidae	Herpetotherium fugax	ZMB 50672	extinct	32.2	Myers (2001)' equation [log y = – 3.465 + 3.436(log TSL)]	unknown	terrestrial - arboreal (primilarly terrestrial + scansorial)	Sanchez-Villagra et al., 2007			unknown	20
Australidelphia, Diprotodontia, Vombatiformes	Vombatidae	Lasiorhinus latifrons	MNHN.ZM.MO.1869.761	extant	27000	Jackson, 2003; Jones & Parish, 2005	terrestrial	fossorial: share burrows	Jones & Parish, 2005	young shoots of native grasses	Jones & Parish, 2005	1	40
Didelphimorphia	Didelphidae	Lestodelphys halli	unnumbered specimen, AF	extant	76	Armati et al., 2006	terrestrial	like the north temperate weasels, may forage under the snow for small vertebrates and arthropods or, alternatively, enters periods of torpor during winter (Redford and Eisenberg 1992)	Jones et al. (eds), 2003	arthropods, small vertebrates (and fat storage in the tail)	Jones et al. (eds), 2003	1	16.39
Australidelphia, Diprotodontia, Macropodifromes	Macropodidae	Macropus rufus	NMV C23045 *(http://digimorph.org/specimens/Macropus_rufus/skull/)*	extant	51000	(up to 85 kg) Jones & Parrish, 2005; Armati et al., 2006	hopper	bipedal ricochet	Richardson, 2012	likewise grass specialists but tend to switch to forbs in a wet winter or spring	Armati et al., 2006	0	208.98
Australidelphia, Peramelemorphia	Thylacomyidae	Macrotis lagotis	MNHN.ZM.MO.1872-172	extant	1650	Jones & Parish, 2005	hopper	fossorial: only bandicoot that burrows underground, digging tunnels three meters long and up to two meters deep AND quadrupedal ricochet	Tyndale-Biscoe, 1973; Jones & Parris, 2005	insects, fungi, seeds, bulbs, fruits	Jones & Parish, 2005	1	29.26
Didelphimorphia	Didelphidae	Marmosa murina	MNHN.ZM.MO.2001-2239	extant	50	Tyndale-Biscoe, 1973	terrestrial - arboreal		Gardner, 2007	insects, fruits	Tyndale-Biscoe, 1973	0	18.63

Didelphimorphia	Didelphidae	Metachirus nudicaudatus	MNHN.ZM.MO.2175	extant	470	Jones et al. (eds), 2003	terrestrial - arboreal	more cursorial and less arboreal than Micoureus, Caluromys, Didelphis and Philander	Armati et al., 2006	fruits, invertebrates, small vertebrates	Tyndale-Biscoe, 1973	0	18.63
Australidelphia, Microbiotheria	Microbiotheriidae	Microbiotherium tehuelchum	YPM 15038	extinct	61	Abello et al., 2012	unknown					unknown	21
	Peradectidae	Mimoperadectes houdei	USNM 482355	extinct	736.7	Myers (2001)' equation [log y = – 3.465 + 3.436(log TSL)]	unknown	terrestrial - arboreal	Horovitz et al., 2009			unknown	30
Didelphimorphia	Didelphidae	Monodelphis brevicaudata	MNHN.ZM.MO.2004-317	extant	85	Tyndale-Biscoe, 1973; Jones et al. (eds), 2003	terrestrial	mainly terrestrial but short prehensile tail	Armati et al., 2006; Jones et al. (eds), 2003	insects, fruits	Tyndale-Biscoe, 1973	0	23.48
Australidelphia, Dasyuromorphia	Myrmecobiidae	Myrmecobius fasciatus	J10732	extant	507.5	Jackson, 2003; Jones & Parish, 2005	terrestrial	mainly terrestrial, scratches for food	Jones & Parish, 2005	myrmecophagous (ants, termites)	Armati et al., 2006	0	44.5
Meridiolestida		Necrolestes patagonensis	YPM 15384	extinct	14	Myers (2001)' equation [log y = – 3.465 + 3.436(log TSL)]	unknown	subterranean	Asher et al. 2007			unknown	13.55
Australidelphia, Notoryctemorphia	Notoryctidae	Notoryctes typhlops	MNHN.ZM.MO.1892-1243	extant	55	Jackson, 2003; Jones & Parish, 2005	subterranean	constructs burrows and forages beneath the surface; digging and sand-swimming	Armati et al., 2006	insects (Ants, ant pupae, chrysomelid beetles, sawfly larvae, beetle larvae, small lizards)	Jackson, 2003; Jones & Parish, 2005	1	17.63
Australidelphia, Peramelemorphia	Peramelidae	Perameles nasuta	MNHN.ZM.AC.A12417	extant	975	Jones & Parish, 2005	terrestrial		Jones & Parish, 2005	insects, larvae, plant roots and tubers	Jones & Parish, 2005	0	18.63
	Herpetotheriidae	Peratherium cuvieri	MNHN.Pal.GY.679b	extinct	190.7	Myers (2001)' equation [log y = – 3.465 + 3.436(log TSL)]	unknown	terrestrial - arboreal	Crochet, 1980			unknown	35.46
	Herpetotheriidae	Peratherium elegans	PAR.39.22	extinct	140.5	Myers (2001)' equation [log y = – 3.465 + 3.436(log TSL)]	unknown	terrestrial - arboreal	Crochet, 1980			unknown	23.42
Australidelphia, Diprotodontia, Petauroidea	Pseudocheiridae	Petauroides volans	JM2633	extant	1300	Armati et al., 2006; Jones & Parrish, 2005	glider		Armati et al., 2006; Jones & Parrish, 2005	leaves, flowers, fruits	Jones & Parish, 2005	0	44.5

Australidelphia, Diprotodontia, Petauroidea	Petauridae	Petaurus breviceps	MNHN.ZM.MO.1996-2287	extant	127.5	Armati et al., 2006; Jones & Parrish, 2005	glider		Armati et al., 2006; Jones & Parrish, 2005	wattle gum, eucalyptus sap, pollen, nectar, insects	Jones & Parish, 2005	0	23.48
Australidelphia, Diprotodontia, Petauroidea	Petauridae	Petaurus norfolcensis	MNHN.ZM.MO.2007.68	extant	245	[P. sciurus synonym P. norfolcensis] Jones & Parrish, 2005	glider		Jones & Parish, 2005	insects, wattle gum and seeds, eucalyptus sap, nectar, pollen	Jones & Parish, 2005	0	27.66
Australidelphia, Diprotodontia, Phalangeroidea	Phalangeridae	Phalanger orientalis	MNHN.ZM.MO.1998.993	extant	3000	animal Diversity Web	arboreal		Armati et al., 2006	fruits, leaves	Armati et al., 2006	0	9.49
Australidelphia, Dasyuromorphia	Dasyuridae	Phascogale tapoatafa	MNHN.ZM.MO 2007.18	extant	210	Jackson, 2003	arboreal	highly arboreal	Armati et al., 2006	insects, spiders, small vertebrates, nectar	Jones & Parish, 2005	0	32.88
Australidelphia, Diprotodontia, Vombatiformes	Phascolarctidae	Phascolarctos cinereus	MNHN.ZM.AC.A2553	extant	8000	Armati et al., 2006; Jones & Parrish, 2005	arboreal		Armati et al., 2006; Jones & Parrish, 2005	eucalyptus leaves	Jones & Parish, 2005	0	32.03
Didelphimorphia	Didelphidae	Philander opossum	MNHN.ZM.MO.2003.153	extant	425	Jones et al. (eds), 2003	terrestrial		Gardner, 2007	omnivorous: fruits, nectar, leaves and bark, invertebrates, vertebrates	Gardner, 2007	0	18.63
Australidelphia, Dasyuromorphia	Dasyuridae	Planigale ingrami	JM4943	extant	4.2	Armati et al., 2006; Jackson, 2003	terrestrial	terricolous, forage constantly	Animaldiversity.org	small vertebrates, invertebrates	Animaldiversity.org	0	27.9
Australidelphia, Diprotodontia, Macropodifromes	Potoroidae	Potorous tridactylus	J6475	extant	1150	Armati et al., 2006; Jones & Parrish, 2005	hopper		Jones & Parish, 2005	fungi, plant roots and tubers, invertebrates	Jones & Parish, 2005	0	53
Pucadelphyda, Sparassodonta	Prothylacinidae	Prothylacinus patagonicus	YPM 15700	extinct	31790	Ercoli et al., 2011	unknown	terrestrial - arboreal	Argot, 2004			unknown	40

Australidelphia, Diprotodontia, Petauroidea	Pseudocheiridae	Pseudocheirus peregrinus	MNHN.ZM.MO.1844-229	extant	900	Armati et al., 2006; Jones & Parrish, 2005	arboreal		Armati et al., 2006; Jones & Parrish, 2005	leaves, flowers, fruits	Jones & Parish, 2005	0	28.91
Pucadelphyda	Pucadelphyidae	Pucadelphys andinus	MHNC 8266	extinct	19.82	Ladevèze et al., 2011	unknown	terrestrial	Muizon & Argot, 2003			unknown	16.5
Australidelphia, Diprotodontia, Macropodifromes	Macropodidae	Setonix brachyurus	MNHN.ZM.MO.1998.118	extant	3300	Armati et al., 2006; Jones & Parrish, 2005	hopper	bipedal ricochet	Richardson, 2012	grass, leaves and succulent plants	Jones & Parish, 2005	0	29.22
Pucadelphyda, Sparassodonta	Hathliacynidae	Sipalocyon gracilis	AMNH 9264	extinct	2110	Ercoli et al., 2011	unknown	terrestrial - arboreal	Argot, 2004			unknown	40
Australidelphia, Dasyuromorphia	Dasyuridae	Sminthopsis crassicaudata	MNHN.ZM.MO.1919-30	extant	15	Armati et al., 2006; Jones & Parrish, 2005	terrestrial		Jones & Parish, 2005	terrestrial and arboreal insects (and fat storage in the tail)	Jones et al. (eds), 2003	0	17.63
Australidelphia, Diprotodontia, Petauroidea	Tarsipedidae	Tarsipes rostratus	MNHN.ZM.MO.1895.473	extant	9.5	Armati et al., 2006; Jones & Parrish, 2005	arboreal		Jones & Parish, 2005	pollen, nectar	Armati et al., 2006; Jones & Parrish, 2005	0	6.23
Australidelphia, Dasyuromorphia	Thylacinidae	Thylacinus cynocephalus	MNHN.ZM.AC.1883.352	extant	22500	Jones et al. (eds), 2003	terrestrial		Jones et al. (eds), 2003	generalist predators of prey between <1 kg and 30 kg	Jones et al. (eds), 2003	0	18.70
Australidelphia, Diprotodontia, Phalangeroidea	Phalangeridae	Trichosurus vulpecula	MNHN.ZM.MO.1889-115	extant	2850	Armati et al., 2006; Jones & Parrish, 2005	arboreal		Jones & Parish, 2005	leaves, flowers, fruits, seeds, insects, occasionally small birds, eggs	Jones & Parish, 2005	0	28.91
Australidelphia, Diprotodontia, Vombatiformes	Vombatidae	Vombatus ursinus	MNHN.ZM.AC.A3289	extant	30500	Jones & Parish, 2005	terrestrial	fossorial	Jones & Parish, 2005	native grasses, sedges, rushes, shrub and tree roots	Jones & Parish, 2005	1	81.79

Supplementary Information 2. Phylogenetic calibrated tree of Metatheria.

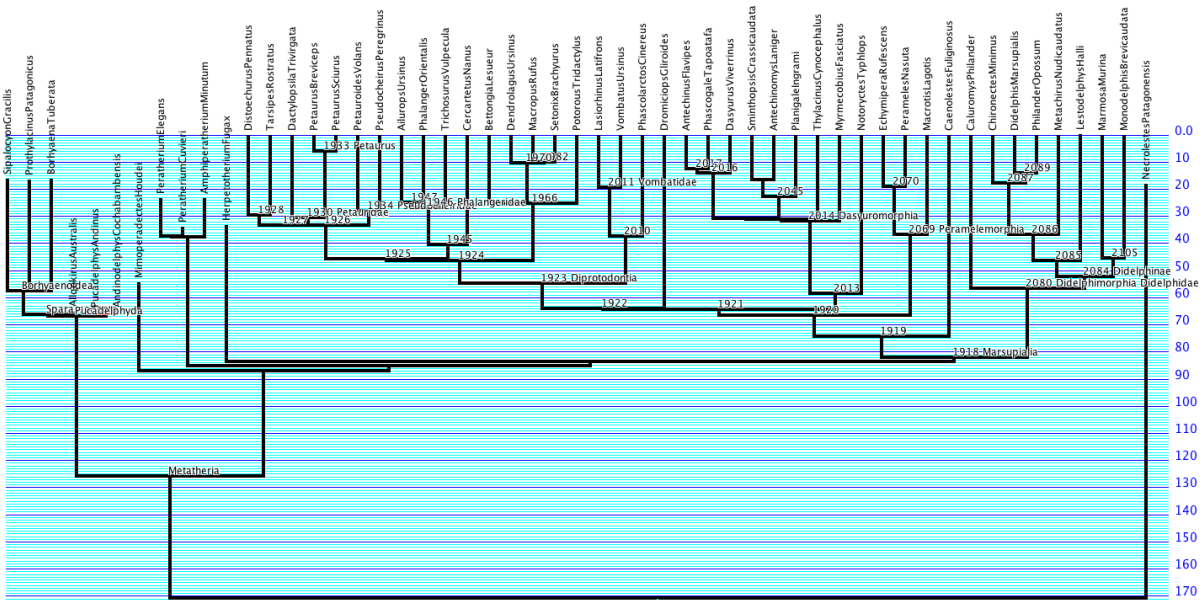

Figure SI-1: Phylogenetic calibrated tree of Metatheria, built with Mesquite (Maddison & Maddison, 2017) and modified from Bininda-edmonds (2007).

METATHERIA

Maximum range based only on fossils: base of the Barremian to the top of the Holocene or **130.000** to 0.000 Ma

Minimum age of oldest fossil (stem group age): 125.45 Ma (*Sinodelphys szalayi*)

Divergence with Eutheria : 170 Ma

NOTOMETATHERIA

ealiest fossil: Early/Lower Paleocene or **65.500** - 61.700 Ma

Pucadelphyidae

ealiest fossil: Early/Lower Paleocene or **65.500** - 61.700 Ma

Pucadelphyidae sister-group to Sparassodonta according to Muizon et al. (submitted)

Borhyaenoidea

earliest fossil: Casamayoran **55.8** - 48.0

--Borhyaenidae

earliest fossil: Casamayoran **55.8** - 48.0

--Hathliacynidae

earliest fossil: Casamayoran **55.8** - 48.0

Peradectidae

--Mimoperadectes houdei

in Horovitz et al. (2009): Type and only known specimen prepared from the lower part of the Willwood Formation; Early Wasatchian (uppermost Arfia shoshoniensis interval zone, early Eocene, between 54.7–54.4 Mya [Gingerich, 2001]).

Herpetotheriidae

--Herpetotherium fugax

in Sánchez-Villagra et al. (2007): Two fairly complete skulls and associated postcranial bones from the White River Formation, ca 33 Myr old (Evanoff et al. 1992) were identified as *Herpetotherium fugax* based on dental features

--***Peratherium elegans***

Age range: 28.4 to 23.03 Ma (data from fossilworks.org)

--***Peratherium cuvieri***

Age range: 37.2 to 33.9 Ma (data from fossilworks.org)

--***Amphiperatherium minutum***

Age range: 37.2 to 23.03 Ma (data from fossilworks.org)

MARSUPIALIA

Marsupialia calibrated tree according to Bininda-Edmonds (2007), and Westerman et al. (2016) for *Antechinomys*/*Sminthopsis*.

Calibration from http://fossilcalibrations.org/
recommended citations: Benton et al. (2015)
http://palaeo-electronica.org/content/fc-1
node minimum age: 47.6 Ma
The early Eocene locality of Murgon, source of Djarthia, correlate with the Ypresian marine stage (Beck, 2012), the top of which is 47.8 Ma ± 0.2 Myr = 47.6 Ma (Gradstein et al., 2012), which we use as the paleontological minimum constraint for Marsupialia.

--Dasyuridae, Sminthopsinae : age of divergence of *Antechinomys* (+ *S. longicaudata*) from other *Sminthopsis* species from Westerman et al. (2016).

Supplementary Information 3. Improvement of the 3D model rendering: Smoothing and repairs of some specimens with Geomagic.

The fossils may have sustained damages resulting from the fossilization and the corresponding 3D osseous inner ear can present missing and ruined parts. The protocole followed in this study is only possible on net and clean 3D models especially for the skeleton computation and for the landmarks editing.

Geomagic software allows to edit 3D objects to improve the 3D rendering and to obtain clean 3D models. Helped by the effective functions of Geomagic, improvement of 3D models stays a subjective work of reconstruction. The interpretations and modifications have to be cautious and parsimonious. Aware of this warning, this work allows us to work with incredible and rare fossil species.

Here are presented some functions used in Geomagic to improve 3D rendering:

- The functions “Select” and “Delete” can be used to clean the 3D model deleting the damaged or unnecessary material.
- The function group “Fill Holes” and especially the parameter “Bridge” allows us to reconstruct step by step a missing part. This functions can be used to group two 3D structures.
- The “Offset” group of functions is used to modify a structure. With a selected structure, it is possible to deform it (“Deform region”) and to thin or thicken it (“Shell”>”Thicken”).

Peratherium elegans was really damaged and the 3D model couldn’t be used to compute the skeleton. The work for this specimen was to clean and fill the holes.

Microbiotherium tehuelchum had all the anterior semicircular canal and ampulla missing. I used its closest relative *Dromiciops gliroides* to reconstruct the missing parts.

A part of anterior canal and of the common crus was completely gone for *Necrolestes patagonensis*. I used the inner ear of *Notoryctes typhlops* to help me for the reconstruction of the missing parts (I choosed this species because it has a very similar morphology of the inner ear, although being a marsupial and *Necrolestes* being outside therian mammals). The interpretation of the missing parts was guided by the conformation of the remaining structures, which indicate the beginning/end and the rough shape of the missing parts.

Supplementary Information 4. 3D data preparation and protocol of fixing and sliding landmarks with AVIZO®.

The protocol we used in this work stem from the methodology of David et al. (2016) on the membranous labyrinth, which is here adapted to the bony labyrinth with the collaboration of Romain David. The protocol set up in this study allows to formalize the data between different researchers and to improve the comparisons between the studies.

Organisation des dossiers de travail :

Data

- SpeciesName1
- SpeciesName2
- SpeciesName3

> Matrix

> ScanRef

> LandmarksBony

> MaxAxesBony

> Other

> SurfacesBony

> VolumesBony

1- Modéliser le labyrinthe osseux du spécimen d'intérêt

Avec MIMICS 18.0 :

- Modéliser l'aqueduc vestibulaire dans un calque séparé
- Ne pas laisser de trou dans la segmentation
- Sélectionner seulement le départ des fenêtres
- Bien enlever le nerf cochléaire (=modiolus vide)
- Noter l'unité de l'environnement de travail
- Noter la résolution
- Modéliser le calque en custom, sans lissage avec Matrix reduction 1x1x1
- Exporter en STL ASCII et sauvegarder dans Data-SpeciesName-ScanRef-VolumesBony
  Avec le nom rv_SpeciesName_Control_Bony

Avec AVIZO 7.1 :

- Mêmes conseils que pour MIMICS
- Ne pas utiliser la baguette magique, plutôt pinceau ou lasso

- Sauvegarder le Projet en Avizo Pack and Go

2- Préparation du modèle 3D osseux : smoothing et découpe

Avec GEOMAGIC 2012 :

- Importer le STL ASCII rv_SpeciesName_Control_Bony
- Référer l'unité de travail et dire "non" à Mesh Doctor
- Si nombre de triangle de l'objet > 400 000, Décimer (Polygons > Decimate) :
  Triangle count à 400 000 ; Fix boundaries uncheck ; Advanced tout cocher au max ; Max aspect ratio coché au min ; APPLY ; Ok.

- Select (Selection Mode > Visible Only) : clic gauche sur une partie visible de l'objet ; Select>Manifold Component ; Reverse ; Delete. (suppression des triangles isolés)

- Relax (Polygons>Smooth>Relax) : Max Min Max ; uncheck Fix doundary ; deviation tolerance au max ; APPLY ; OK

- Smooth>Remove SPikes : laisser à 50% et APPLY ; si trop fort annuler et baisser la valeur ; OK

- Repair>Mesh Doctor : cocher Non Manifold , Self intersection , Highly Creased Edges et Small Holes , Apply jusqu'à que tout soit = 0
  Si Mesh Doctor ne fonctionne pas (les valeurs montent ou ne descendent plus) appuyer sur Delete à la fin du Mesh Doctor (surfaces rouges supprimées, et normalement tout est à 0 dans mesh doctor). Puis Fill Hall (Polygons) en tangent et complete ; APPLY et OK.

- Sauvegarde : Clic droit sur l'objet dans la colonne de gauche et sauvegarder en STL ASCII dans ScanRef>Other sous le nom r_SpeciesName_Bony

- The 3D model needs beforehand to be cut into 6 anatomical parts.

The torus of each semicircular canal is composed of a slender tubular part that generally accounts at least for half the total length of the torus. The torus is also composed of a utricular part, an ampulla part and, for the vertical ducts, of a common crus part. Anterior semicircular canals (ASC) are composed of an anterior slender duct (Sa), a common crus (CC), an anterior utricle (Ua--> only available through the membranous) and an anterior ampulla (Aa). Posterior semicircular canals (PSC) are composed of a posterior slender duct (Sp), a common crus, a posterior utricle (Up -->

membranous) and a posterior ampulla (Ap). Lateral semicircular canals (LSC) are composed of a lateral slender duct (Sl), an anterior utricle and a lateral ampulla (Al). ASC and LSC are connected through the anterior utricle, whereas ASC and PSC are connected through the common crus.

- Polygons>Boundaries>Create>Boundary from spline

Creation of anatomical boundaries:

Ampoule antérieure/Slender ASC

Ampoule postérieure/Slender PSC (quand crus commune secundaria, arrêter la découpe au contact LSC et PSC)

Ampoule latérale/Slender LSC

Slender ASC/CC

Slender PSC/CC

CC/Vestibule

Slender LSC/Vestibule (quand crus commune secundaria, arrêter la découpe au contact entre le LSC et PSC)

Cochlée/Vestibule (commencer au-dessus de la fenêtre vestibulaire, longer la fenêtre et passer sous le saccule, suivre les limites du saccule jusqu'à la fenêtre cochléaire, bien mettre la fenêtre côté cochlée et rejoindre le point de départ)

Si la cochlée et le vestibule se touchent ailleurs, séparer les deux grâce aux boundaries ou avec Select>Delete>Fill All>Tangent.

- Séparation des différentes parties
- Clic droit sur les objets dans la colonne de gauche, dupliquer 5x (on a donc 6 objets)
- On sélectionne le futur ASC dans la colonne de gauche, on clique gauche ((en Visible only) sur le modèle dans la zone d'intérêt, on fait Select components (Bounded components) > Reverse > Delete.
- Le faire pour tous les autres objets (PSC, LSC, CC, Vest, Cochlée)
- Sauvegarder les 3 SC en STL ASCII dans ScanRef>SurfacesBony sous le nom rs_SpeciesName_Sa_Bony, rs_SpeciesName_Sp_Bony et rs_SpeciesName_Sl_Bony.
- Sélectionner les 3 CSC dans la colonne de gauche, et cliquer sur Polygons>Fill Holes>Fill All>Flat et complete, APPLY et OK.
- Les sauvegarder en STL ASCII dans ScanRef>VolumesBony sous le nom rv_SpeciesNames_Sa_Bony, rv_SpeciesNames_Sp_Bony et rv_SpeciesNames_Sl_Bony.
- Sélectionner vestibule et cochlée dans la colonne de gauche, et cliquer sur Polygons>Fill Holes>Fill All>Flat et complete, APPLY et OK.

- Les sauvegarder en STL ASCII dans ScanRef>VolumesBony sous le nom rv_SpeciesNames_Vest_Bony et rv_SpeciesNames_Coch_Bony.
- Dupliquer la CC, sur la première copie, remplir la zone de contact avec le slender CSP avec Polygons>Fill Holes>Fill single>Flat et complete en cliquant sur la zone et en recliquant sur Fill single.
- Sauvegarder l'objet sous le nom rs_SpeciesName_Cca_Bony dans ScanRef>SurfacesBony en STL ASCII.
- Faire l'inverse sur l'autre et la sauvegarder avec le nom Ccp.
- Sélectionner la Ccp, faire Polygons>Fill Holes>Fill all en flat et complete, APPLY, OK.
- Sauvegarder l'objet sous le nom rv_SpeciesName_CC_Bony dans ScanRef>VolumesBony en STL ASCII.

3- Pose des Landmarks

Avec AVIZO 7.1 :

- OpenData : r_SpeciesName_Bony (dans Other)
- Clic sur l'objet dans la fenetre de droite , Convert>Scan Surface To volume avec dimensions 250x250x250 ; APPLY
- Clic droit sur le nouvel objet>Image Processing>Skeletonization>Auto Skeleton > APPLY
- Supprimer tous les objets sauf le squelette
- Open Data>VolumesBony, ouvrir tous les fichiers volume sauf le Control_Bony
- Ouvrir des Surface View pour chacun des objets et dans Surface View, dans Colors, roll en constant, cliquer double sur damier coloré et modifier les couleurs (CC rose , CSC rouges, Vest vert, Coch jaune) [facultatif]

- Créer les jeux de landmarks : clic droit sur la zone avec objet > Create>Points and Lines>Landmarks

- F2 pour renommer en rcs_SpeciesName_Sa_Bony

- Dupliquer (CTRL+D) et renommer en
  rcs_SpeciesName_Sa/_Sp/_Sl/_CC/_Aa/_Sap/_Al/_Sul_Bony
  et
  res_SpeciesName_Sa/_Sp/_Sl_Bony

- Placer un landmark : cliquer sur le set de landmark, cliquer sur Landmark Editor (icône en bas à gauche) et utiliser l'outil Add pour ajouter un L, l'outil remove pour supprimer, l'outil move pour déplacer et l'outil transform pour translater

! Toujours landmarker de l'ampoule vers l'utricule ! Commencer par poser les landmarks en interne (rcs = central) puis en externe (res=externe). Pour les slenders (Sa, Sp, Sl=slender des ASC, PSC, et LSC), positionner le canal perpendiculaire au plan de l'écran pour bien placer les points sur le canal.

- Rcs_Sa

Cacher tous les objets 3D sauf la CC et le Sa. Placer le premier Landmark au centre de la surface de contact avec l'ampoule ant. sur le Sa. Cacher le Sa, faire apparaitre le squelette et placer les Landmarks (au moins 25) sur le squelette jusqu'à la surface de contact avec la CC. Placer le dernier Landmark au centre de cette surface.

- Rcs_Sp

Idem

- Rcs_Sl

Idem et placer le premier et le dernier Landmarks sur les sections du vestibule (sur Vest_Bony et pas sur Sl_Bony)

- Rcs_CC

Afficher Vest et poser le premier L au croisement théorique des deux CSC, continuer jusqu'à la surface du vestibule et placer le dernier au centre de la section (au moins 5 Landmarks)

- Res_Sa

Placer le premier Landmark sur la surface du modèle 3D (afficher les modèles Vest et Sa). Le placer au centre de l'ampoule, sur la surface ventrale, en dessous de l'ampoule, au niveau de la crista, s'aider de la forme de l'ampoule et de l'arrivée du nerf. Continuer en suivant la ligne de crête du canal (souvent la zone réfléchissante) jusqu'au rebord de l'objet.

- Res_Sp

Idem

- Res_Sl

Idem mais position du premier Landmark sur la surface antérieure. Suivre la ligne de crête jusqu'à la zone de connexion avec le vestibule

Attention, si vous avez une seconde crus commune, continuer de poser des Landmarks au-dessus de la SCC puis créer un set de Landmarks temporaires où les Landmarks sont placés sur la crête réfléchissante interne. Ce set de Landmarks nous aidera à repositionner les Landmarks posés sur la SCC. Positionné l'objet en profils et translater (outil Transform) les Landmarks sur la même trajectoire en vous aidant des Landmarks internes.

(pour l'outil transform, attention, il faut mettre la boule dans le plan avant de la bouger, c'est à dire jouer avec les épingles vertes jusqu'à obtenir une croix)

- Rcs_Aa

Afficher l'ampoule antérieure en transparent (aller dans le 'Surface View' du vestibule) et afficher le squelette. Positionner le premier Landmark sur le squelette au-dessus du premier Landmark de rcs_Sa. La position correspond à la crista (à l'intérieur de l'ampoule). Rajouter 2-3 Landmarks dans l'ampoule pour rejoindre le Sa.

- Rcs_SAp

Idem. Continuer à positionner les Landmarks vers le Sp. ! Si SCC, positionner les L à l'intérieur de la SCC pour rejoindre le Sp qui s'est arrêté au contact des PSC et LSC).

- Rcs_Al

Idem

- Rcs_Sul

Ces Landmarks lient le slender lat au vestibule. Sans SCC rajouter juste un Landmark sur squelette à l'endroit où le slender latéral rentre dans le vestibule. Le point est alors positionné dans le vestibule latéral.

Si SCC, il faut poser des Landmarks en interne du Sl au vestibule afin de landmarker le sl qui se trouve dans la SCC. Poser les Landmarks sur le squelette s'il passe bien au centre du Sl. Sinon (le plus courant), positionner les points au-dessus de Sl et les repositionner à la bonne hauteur avec l'outil transform en s'aidant du set de Landmarks rcs_sp et des Landmarks temporaires placés en interne.

- Enregistrer les landmarks : Clic droit sur les objets, enregistrer sous Landmarks (Data>SpeciesName>ScanRef>LandmarksBony)

4- Pré-analyse

Vérifier la présence de tous les dossiers.

Vérifier le nom des fichiers et leur organisation.

Data

- SpeciesName1
- SpeciesName2
- AiluropsUrsinusA2597
  - > Matrix
  - > ScanRef
    - > LandmarksBony
    - > MaxAxesBony
    - > Other
    - > SurfacesBony
    - > VolumesBony

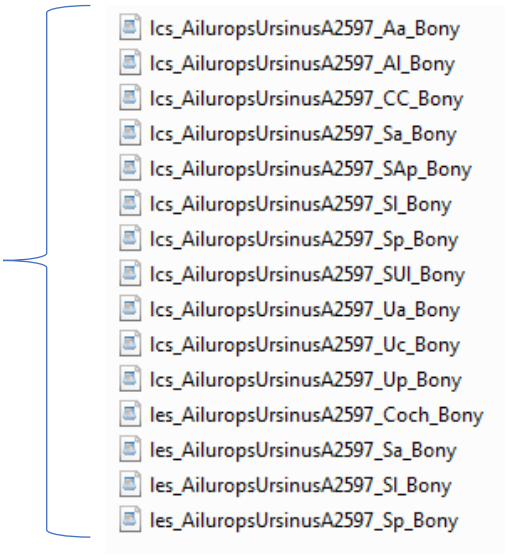

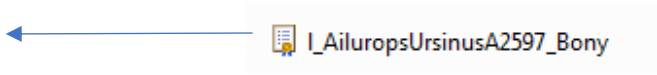

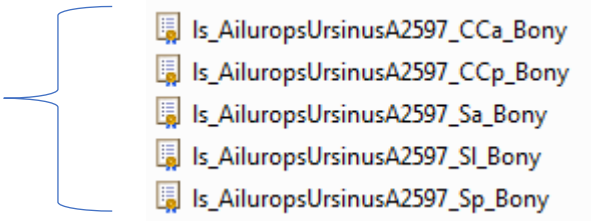

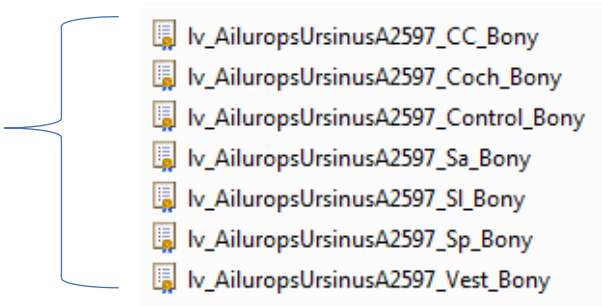

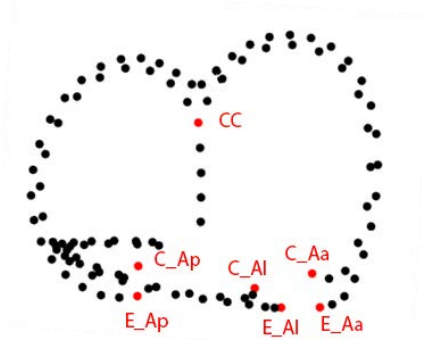

C_Aa	Center of the anterior ampulla
C_Al	Center of the lateral ampulla
C_Ap	Center of the posterior ampulla
CC	Bifurcation point of the crus commune
E_Aa	Pointing of the anterior crista on the external surface of the ampulla
E_Ap	Pointing of the posterior crista on the external surface of the ampulla
E_Al	Pointing of the lateral crista on the external surface of the ampulla

	#1 C_Aa	14 sliding	#15 C_Ap	14 sliding	#30 C_Al	14 sliding	#45 CC	4 sliding	#50 E_Aa	19 sliding	#70 E_Ap	19 sliding	#90 E_Al	19 sliding
species 1	x1 y1 z1	...	x15 y15 z15	...	x30 y30 z30	...	x45 y45 Z45	...	x50 y50 z50	...	x70 y70 z70	...	x90 y90 z90	... x110 y110 z110
species 2	x1 y1 z1	...	x15 y15 z15	...	x30 y30 z30	...	x45 y45 Z45	...	x50 y50 z50	...	x70 y70 z70	...	x90 y90 z90	... x110 y110 z110
species 3	x1 y1 z1	...	x15 y15 z15	...	x30 y30 z30	...	x45 y45 Z45	...	x50 y50 z50	...	x70 y70 z70	...	x90 y90 z90	... x110 y110 z110
...														
species 54	x1 y1 z1	...	x15 y15 z15	...	x30 y30 z30	...	x45 y45 Z45	...	x50 y50 z50	...	x70 y70 z70	...	x90 y90 z90	... x110 y110 z110

Figure SI-2: Organisation of the 103 sliding landmarks and 7 fixed landmarks (in red) presented on the consensus shape.

The matrix of the landmark coordinates for each species is organized as shown in the table and the species order is the same as that in the Table SI-1.

Supplementary Information 5. R script of the geometric morphometrics procedure.

Three files are available as Online Material and are loaded for the analyses: the matrix of landmark coordinates ('landmarks_marsup.csv'), the identification of fixed and sliding landmarks ('slide_marsup'), and the phylogenetic tree ('phylogeny_marsup').

The written scripts are also available as Online Material.

```
#### to save 3D representations in PLY (openable on 3D manage software), the function
writePLY("file_name.ply") is available. It is saving the 3D representations opened in a window
(be careful, you should have only one 3D representation in one window to save it. If there are
more than one representation, it doesn't work).
#### to save graphical datas, possibility to right click on the graphical window and choose
copy as vectorial and past on Illustrator software (on illustrator, delete the clipping mask
in "object")
#### Be careful to the 3D representations of graphical and conformation, you should save data
without perspective. To do this, press and hold the Scroll Wheel and move the mouse forward to
delete the perpective rendering.
#### to save table, 'write.table(object, file = "file_name.txt")' or capture.output(object,
file = "adjusted_shape.txt")


################### Initialisation ####################

rm(list=ls(all=TRUE))

################# install packages for the first use #######

install.packages("ape", dependencies = TRUE);library(ape)
install.packages("FactoMineR", dependencies = TRUE);library(FactoMineR)
install.packages("shapes", dependencies = TRUE);library(shapes)
install.packages("phytools", dependencies = TRUE);library(phytools)
install.packages("geomorph", dependencies = TRUE);library(geomorph)
install.packages("class", dependencies = TRUE);library(class)
install.packages("geiger", dependencies = TRUE);library(geiger)
install.packages("lattice", dependencies = TRUE);library(lattice)
install.packages("mda", dependencies = TRUE);library(mda)
install.packages("phangorn", dependencies = TRUE);library(phangorn)
install.packages("phylobase", dependencies = TRUE);library(phylobase)
install.packages("Hotelling", dependencies = TRUE);library(Hotelling)
install.packages("vegan", dependencies = TRUE);library(vegan)
library(MASS)


################### Loading libraries ####################

library(ape)
library(FactoMineR)
```

```
library(shapes)
library(phytools)
library(geomorph) ### éventuellement recharger package geiger si problème
library(class)
library(geiger)
library(lattice)
library(mda)
library(phangorn)
library (phylobase)
library(MASS)
library(Hotelling)
library (tibble)
library(vegan)


#################### Loading raw datasets ####################

### tree # phylogeny_marsup.nex
arbre<-read.nexus(file.choose())
arbre<-multi2di(arbre)

### Landmarks Matrix  ## landmarks_marsup.csv
dat<-read.csv(file.choose(),header=F,sep=";")
colnames(dat)<-c("taxon","fossilornot","bodyM","loco",rep(paste(c("x","y","z"),sep=""),110),
"burrow")

# reorder everything with the order of the tip labels of the tree
       dat <- dat[match(arbre$tip.label,dat$taxon),]

coord<-dat[,5:334]
datlist<-list()
for(i in 1:54) {
       datlist[[i]]<-t(matrix(coord[i,],3,110))
}
ldmarks<-array(unlist(datlist),dim=c(110,3,54))
dimnames(ldmarks)[[3]]<-dat[,1]


### landmarks slide ##slide_marsup.txt
SLIDERS = as.matrix(read.table(file.choose(), header = TRUE))

#################### Coloring Landmarks and Species ############
landmarks_color=
factor(c("1","0","0","0","0","0","0","0","0","0","0","0","0","0","0","1","0","0","0","0","0","
0","0","0","0","0","0","0","0","0","1","0","0","0","0","0","0","0","0","0","0","0","0","0","0"
,"1","0","0","0","0","1","0","0","0","0","0","0","0","0","0","0","0","0","0","0","0","0","0","
0","0","1","0","0","0","0","0","0","0","0","0","0","0","0","0","0","0","0","0","0","0","1","0"
,"0","0","0","0","0","0","0","0","0","0","0","0","0","0","0","0","0","0","0"))
```

```
################### Performing the Generalized Procrustes Analysis ####################

GPA_MARSUP = gpagen(ldmarks, curves = SLIDERS, surfaces = NULL, PrinAxes = TRUE, max.iter =
NULL, ProcD = FALSE, Proj = TRUE)
plotAllSpecimens(GPA_MARSUP$ coords, mean = TRUE, links = NULL)
summary(GPA_MARSUP)


################### Plot consensus shape ####################

plot3d(GPA_MARSUP$consensus, aspect = FALSE, col=as.numeric(landmarks_color), size = 8,
box=FALSE, axes=FALSE)


################### PCA analysis of procrustes residuals ####################

PCA = plotTangentSpace(GPA_MARSUP$coords, axis1 = 1, axis2 = 2, warpgrids = TRUE, mesh = NULL,
label = dat$taxon, groups = dat$loco, verbose = TRUE, out.col = 1)

pairs(PCA$pc.scores[,1:10], col=as.numeric(dat$loco)) #### dat$loco corresponds to the 7
levels of locomotion (including unknown for the extinct species)
pairs(PCA$pc.scores[,1:10], col=as.numeric(dat$burrow)) ### dat$burrow corresponds to the 3
levels of burrowing (including unknown for the extinct species)


Ancestor = plotGMPhyloMorphoSpace(arbre, GPA_MARSUP$coords, tip.labels = TRUE, node.labels =
TRUE, ancStates = TRUE, xaxis = 1, yaxis = 2, zaxis = "time")
Ancestor <- arrayspecs(Ancestor,110,3)

# plot avec env convexe
#first, create the function plotg with the following
plotg <- function(mat,cols=c(1,2),groupe, pchull=TRUE,llocate=TRUE,lcex=1.2, titre = ' ', aspr
= 1) {
        groupe <- as.factor(groupe)
        groupn <- unique(groupe)
        groupc <- as.numeric(groupn)
        col1 <- cols[1]
        col2 <- cols[2]
        matc <- mat[,c(col1, col2)]
        xlbl <- paste("Axis",col1,sep = " ")
        ylbl <- paste("Axis",col2,sep = " ")
        lim1 <- range(matc[,1])
        lim2 <- range(matc[,2])
        plot(matc[,1],matc[,2],xlim=lim1,ylim=lim2,
col=as.numeric(groupe),pch=20,xlab=xlbl,ylab=ylbl,cex=1.5, asp=aspr, main = titre)
        if (pchull == TRUE) {
                for(i in 1:length(groupn)) {
                        gp <- matc[which(groupe == groupn[i]),]
                        if(ncol(as.matrix(gp)) > 1) {
                                gpc <- gp[chull(gp),]
                                gpc <- rbind(gpc, gpc[1,])
```

```
                        lines(gpc[,1],gpc[,2],col=groupc[i],lty=1,lwd=1.5)
                    }
                }
            }
             if (llocate == TRUE) {
                    print("positionner la souris à l\'emplacement du coin supérieur gauche
de la boite légende")
                    print(" ... puis cliquer 1 seule fois avec le BOUTON GAUCHE")
                    lloc <- locator(1)
                    legend(lloc$x,lloc$y,as.vector(groupn),col=groupc,bty="n",pch=20,
cex=lcex)
             }
 }

#plot with convex contours
plotg(PCA$pc.scores # matrice avec données
,c(1,2)# colonnes concernées
,dat$loco      # facteur de regroupement
)
text(PCA$pc.scores [,1],PCA$pc.scores [,2],substr(dat$taxon,1,5))

#Compare the shape of the first taxon with the reconstructed ancestral morphotype
plotRefToTarget(Ancestor[,,1], GPA_MARSUP$coords[,,1], method = "points", mag = 1)

#to obtain nice 3D representation, this function of comparaison is better. Possible to save in
.ply format
plotRefToTarget(PCA$pc.shapes$PC1min, PCA$pc.shapes$PC1min, method = "points", mag = 1)
plotRefToTarget(PCA$pc.shapes$PC1max, PCA$pc.shapes$PC1max, method = "points", mag = 1)

# graphical visualization of the PCA axes ~ phylogeny
treePlot(phylo4d(arbre, data.frame(PCA$pc.scores[,1:4])))


################### Allometry ####################

DATA_Allo = geomorph.data.frame(GPA_MARSUP, bodyM=dat$bodyM)

Allometry = procD.allometry(coords~bodyM, data=DATA_Allo)


plot(Allometry, method = "RegScore", label = dimnames(Allometry$A)[[3]]) ## more informations
on ?procD.allometry
plot(Allometry, method = "PredLine", label = dimnames(Allometry$A)[[3]]) ## more informations
on ?procD.allometry


plotRefToTarget(Allometry$Ahat.at.min, Allometry$Ahat.at.min, method = "points", mag = 1)
plotRefToTarget(Allometry$Ahat.at.max, Allometry$Ahat.at.max, method = "points", mag = 1)
```

```
################### Allometry corrected shapes ####################

Anova = procD.lm(Allometry$formula, data = Allometry$data, RRPP=TRUE)
shape.resid = arrayspecs(Anova$residuals, p=dim(GPA_MARSUP$coords)[1],
k=dim(GPA_MARSUP$coords)[2])
adj.shape = shape.resid + array(GPA_MARSUP$consensus, dim(shape.resid))

###capture.output(adj.shape, file = "adjusted_shape.txt")


############# PCA analysis of procrustes residuals (corrected for allometry) #############

PCA.adj = plotTangentSpace(adj.shape, axis1 = 1, axis2 = 2, warpgrids = TRUE, mesh = NULL,
label = dat$taxon, groups = dat$loco, verbose = TRUE, out.col = 1)

PCA.adj = plotTangentSpace(adj.shape, axis1 = 1, axis2 = 2, warpgrids = TRUE, mesh = NULL,
label = dat$taxon, groups = dat$burrow, verbose = TRUE, out.col = 1)

pairs(PCA.adj$pc.scores[,1:10], col=as.numeric(dat$loco)) #### dat$loco corresponds to the 7
levels of locomotion (including unknown for the extinct species)
pairs(PCA.adj$pc.scores[,1:10], col=as.numeric(dat$burrow))

# broken stick : how many axes ?
       barplot(PCA.adj $ pc.summary$ importance[2,])
       library(vegan)
       lines(bstick(53)) #-> donc 6 axes

#################################################################################################
                            Locomotions ????
#################################################################################################

###    Beforehand, upload the pfda functions with 'script_phyloFDA.R'    ####


# Ordering data to match tip labels.
       ddA <- PCA.adj $pc.scores

# Defining groups and taxa
       gA <- dat$loco;names(gA)<- dat$taxon # contains data on ecology/behavior
       taxaA <- dat$taxon # species names

# Selection data shape, training and test taxa
       XA <- ddA[,1:15] # we are selecting 6 variables
       testtaxa <- dat$taxon[dat$fossilornot=="extinct"] # specifying taxa that are extinct
       trainingtaxa <- setdiff(dat$taxon,testtaxa)
       testtaxan <- which(dat$fossilornot=="extinct") # same but row nufBMmbers
       X <- XA[-testtaxan,]
       dd <- ddA[-testtaxan,]
       g <- gA[-testtaxan]
       arbreAct <- drop.tip(arbre, as.character(testtaxa))
```

```
# Identifying optimal lambda: where is the strongest correlation between form and ecology
among living taxa?

       filename_stem <- "ecology" # A plot will appear in separate window; a pdf is saved in
your working directory.
       ol1 <- optLambda(X,g,arbreAct,idc=filename_stem)
       optl <-ol1$optlambda
       pfda <- phylo.fda.pred(XA,gA,taxaA,arbre,testtaxan,val=optl)

       # cross validation
       pfda$confusion # Misclassified poroportion listed as "error"
       sum(diag(pfda$confusion))/sum(pfda$confusion) # ratio good attribution
       setwd(choose.dir())
       write.csv(pfda$confusion,file="confusion_locomotion.csv",sep =";")

# Now, let's extract predictions for the fossils.

       test.class <- as.character(predict(pfda, pfda$DATAtest, type="class"))

# Discriminant scores scores for the fossils are retreived this way.

       test.variates <- predict(pfda, pfda$DATAtest, type="variates")

# Posterior probabilities of group affiliations are available, too.

       test.prob <- predict(pfda, pfda$DATAtest, type="posterior")

# And now let's put everything together (here shown for the fossils):

       test.results <- cbind(test.class, test.prob, test.variates)
       colnames(test.results) <- c("predicted class", "P(arboreal)", "P(glider)", "P(hopper)",
"P(subterranean)","P(terrestrial)","P(terrestrial - arboreal)", "DA1", "DA2", "DA3", "DA4",
"DA5")
       rownames(test.results) <- testtaxa

       test.results # Let's take a look what we got.
       setwd(choose.dir())
       write.table(test.results ,"LocoPredictFossiProba.csv",sep =";")
       write.table(pfda$fit$fitted.values ,"newcoords.csv",sep =";")
       write.table(pfda$fit$coefficients ,"coeff_pc_fd.csv",sep =";")

# same for extants
       training.class <- as.character(predict(pfda, pfda$DATA, type="class"))
       training.variates <- predict(pfda, pfda$DATA, type="variates")
       training.prob <- predict(pfda, pfda$DATA, type="posterior")
       training.results <- cbind(as.character(g), training.class, training.prob,
training.variates)
       colnames(training.results) <- c("true class","predicted class", "P(arboreal)",
"P(glider)", "P(hopper)", "P(subterranean)","P(terrestrial)","P(terrestrial - arboreal)",
"DA1", "DA2", "DA3", "DA4", "DA5")
       rownames(training.results) <- trainingtaxa
```

```
        write.table(training.results ,"LocomotionPredictExtantProba.csv",sep =";")

# organizing a bit the data for the plot
        # extant
        training <- as.data.frame(cbind(training.variates, as.character(dat$loco[-testtaxan])))
        colnames(training) <- c("DA1", "DA2", "DA3", "DA4", "DA5", "locomotion")
        rownames(training) <- dat$taxon[-testtaxan]
        #extinct
        unknown <- as.character(rep("unknown", times=length(testtaxan)))
        test <- as.data.frame(cbind(test.variates, unknown))
        colnames(test) <- c("DA1", "DA2", "DA3", "DA4", "DA5", "locomotion")
        rownames(test) <- testtaxa
        # all put together
        scatter <- rbind(training, test)
        scatter[, 1:5] <- lapply(scatter[,1:5], as.character)
        scatter[, 1:5] <- lapply(scatter[,1:5], as.numeric)
        # each locomotion in its own group
        ar <- scatter[scatter$locomotion=="arboreal",];ar[, 1:5] <- lapply(ar[,1:5],
as.character);ar[, 1:5] <- lapply(ar[,1:5], as.numeric)
        gl <- scatter[scatter$locomotion=="glider",] ;gl[, 1:5] <- lapply(gl[,1:5],
as.character);gl[, 1:5] <- lapply(gl[,1:5], as.numeric)
        h <- scatter[scatter$locomotion=="hopper",] ;h[, 1:5] <- lapply(h[,1:5],
as.character);h[, 1:5] <- lapply(h[,1:5], as.numeric)
        s <- scatter[scatter$locomotion=="subterranean",];s[, 1:5] <- lapply(s[,1:5],
as.character);s[, 1:5] <- lapply(s[,1:5], as.numeric)
        t <- scatter[scatter$locomotion=="terrestrial",] ;t[, 1:5] <- lapply(t[,1:5],
as.character);t[, 1:5] <- lapply(t[,1:5], as.numeric)
        tear <- scatter[scatter$locomotion=="terrestrial - arboreal",] ;tear [, 1:5] <-
lapply(tear [,1:5], as.character);tear [, 1:5] <- lapply(tear [,1:5], as.numeric)
        u <- scatter[scatter$locomotion=="unknown",];u [, 1:5] <- lapply(u [,1:5],
as.character);u [, 1:5] <- lapply(u [,1:5], as.numeric)

# plot / pdf
        A<-"DA1"
        B<-"DA2"
        #pdf(file=paste(A,"_",B,".pdf",sep=''),useDingbats=FALSE) # set pdf ready to write
        plot(eval(parse(text=paste("ar$",A))), eval(parse(text=paste("ar$",B))),
          asp=1,
          xlim=range(eval(parse(text=paste("scatter$",A)))),
          ylim=range(eval(parse(text=paste("scatter$",B)))),
          pch=21, col="black", bg="gray",
          cex=1.25, cex.lab=1.5,
          xlab=parse(text=A), ylab=parse(text=B));
        points(eval(parse(text=paste("gl$",A))), eval(parse(text=paste("gl$",B))), pch=21,
cex=1.25, col="black", bg="green");
        points(eval(parse(text=paste("h$",A))), eval(parse(text=paste("h$",B))), pch=21,
cex=1.25, col="black", bg="red");
        points(eval(parse(text=paste("s$",A))), eval(parse(text=paste("s$",B))), pch=21,
cex=1.25, col="black", bg="cyan");
        points(eval(parse(text=paste("t$",A))), eval(parse(text=paste("t$",B))), pch=21,
cex=1.25, col="black", bg="blue");
```

```
       points(eval(parse(text=paste("tear$",A))), eval(parse(text=paste("tear$",B))), pch=21,
cex=1.25, col="black", bg="orange");
       points(eval(parse(text=paste("u$",A))), eval(parse(text=paste("u$",B))), pch=24,
cex=1.25, col="black", bg="white");
       box(lwd=2); axis(1, lwd=2, lwd.ticks=2); axis(2, lwd=2, lwd.ticks=2)
       text(eval(parse(text=paste("scatter$",A))),eval(parse(text=paste("scatter$",B))),substr
(rownames(scatter),1,5),adj=1)
       legend(locator(1),c("arboreal","glider","hopper","subterranean","terrestrial","terrestr
ial -
arboreal","unknown"),pch=c(21,21,21,21,21,21,24),col=rep("black",9),pt.bg=c("gray","green","re
d","cyan","blue","orange","white"))
       #dev.off()

##############################################################################################
                              Burrow or not ????
##############################################################################################

# Ordering data to match tip labels.
       ddA <- PCA.adj $pc.scores

# Defining groups and taxa
       gA <- dat$burrow;names(gA)<- dat$taxon # contains data on ecology/behavior
       taxaA <- dat$taxon # species names

# Selection data shape, training and test taxa
       XA <- ddA[,1:6] # we are selecting 6 variables
       testtaxa <- dat$taxon[dat$fossilornot=="extinct"] # specifying taxa that are extinct
       testtaxan <- which(dat$fossilornot=="extinct") # same but row numbers
       X <- XA[-testtaxan,]
       dd <- ddA[-testtaxan,]
       g <- gA[-testtaxan]
       arbreAct <- drop.tip(arbre, as.character(testtaxa))

# Identifying optimal lambda: where is the strongest correlation between form and ecology
among living taxa?

       filename_stem <- "burrow" # A plot will appear in separate window; a pdf is saved in
your working directory.
       ol1 <- optLambda(X,g,arbreAct,idc=filename_stem)
       optl <-ol1$optlambda
       pfda <- phylo.fda.pred(XA,gA,taxaA,arbre,testtaxan,val=optl )

       # cross validation
       pfda$confusion # Misclassified poroportion listed as "error"
       sum(diag(pfda$confusion))/sum(pfda$confusion) # ratio good attribution
       setwd(choose.dir())
       write.csv(pfda$confusion,file="confusion_burrow.csv",sep =";")

# Now, let's extract predictions for the fossils.

       test.class <- as.character(predict(pfda, pfda$DATAtest, type="class"))
```

```
# Discriminant scores scores for the fossils are retreived this way.

        test.variates <- predict(pfda, pfda$DATAtest, type="variates")

# Posterior probabilities of group affiliations are available, too.

        test.prob <- predict(pfda, pfda$DATAtest, type="posterior")

# And now let's put everything together (here shown for the fossils):

        test.results <- cbind(test.class, test.prob, test.variates)
        colnames(test.results) <- c("predicted class", "P(non burrow)", "P(burrow)","DA1")
        rownames(test.results) <- testtaxa

        test.results # Let's take a look what we got.
        setwd(choose.dir())
        write.table(test.results ,"BurrowPredictFossiProba.csv",sep =";")
        write.table(pfda$fit$fitted.values ,"newcoords.csv",sep =";")
        write.table(pfda$fit$coefficients ,"coeff_pc_fd.csv",sep =";")

# same for extants
        training.class <- as.character(predict(pfda, pfda$DATA, type="class"))
        training.variates <- predict(pfda, pfda$DATA, type="variates")
        training.prob <- predict(pfda, pfda$DATA, type="posterior")
        training.results <- cbind(as.character(g), training.class, training.prob,
training.variates)
        colnames(training.results) <- c("true class","predicted class", "P(non burrow)",
"P(burrow)","DA1")
        rownames(training.results) <- trainingtaxa
        write.table(training.results ,"BurrowPredictExtantProba.csv",sep =";")

# organizing a bit the data for the plot
        # extant
        training <- as.data.frame(cbind(training.variates, as.character(dat$burrow[-
testtaxan])))
        colnames(training) <- c("DA1", "burrow")
        rownames(training) <- dat$taxon[-testtaxan]
        #extinct
        unknown <- as.character(rep("unknown", times=length(testtaxan)))
        test <- as.data.frame(cbind(test.variates, unknown))
        colnames(test) <- c("DA1", "burrow")
        rownames(test) <- testtaxa

# plot / pdf
        par(mfrow=c(2,1))
        hist(training.variates[training.results==0],xlim=c(-1,6))
        hist(training.variates[training.results==1],xlim=c(-1,6))
        #test
        plot(training.variates[training.results==0],rep(0,length(training.variates[training.res
ults==0])),pch=20,main="not burrow",xlim=c(-1,6))
```

```
       points(test.results[test.results[,1]=="0",4],rep(0,length(test.results[test.results[,1]
=="0",4])),pch=24)
       plot(training.variates[training.results==1],rep(0,length(training.variates[training.res
ults==1])),pch=20,main="burrow",xlim=c(-1,6))
       points(test.variates[test.results==1],rep(0,length(test.variates[test.results==1])),pch
=24)


### H test between burrowers and complete sample (burrowers + non burrowers + unknwon)
library(Hotelling)
res.test<-hotelling.test(ddA[,1:6],
ddA[dat$fossilornot=="extant"&dat$burrow=="1",1:6],perm=T,B=10000,progBar=T)
res.test$pval

### H test between burrowers and non burrowers
res.test<-hotelling.test(ddA[dat$fossilornot=="extant"&dat$burrow=="0",1:6],
ddA[dat$fossilornot=="extant"&dat$burrow=="1",1:6],perm=T,B=10000,progBar=T)
res.test$pval

### H test between gliders and complete sample (gliders + non gliders + unknown)
res.test<-hotelling.test(ddA[,1:6],
ddA[dat$fossilornot=="extant"&dat$loco=="glider",1:6],perm=T,B=10000,progBar=T)
res.test$pval

### H test between gliders and non gliders
res.test<-hotelling.test(ddA[c(39,40, 41),1:6], ddA[-c(39,40,
41),1:6],perm=T,B=10000,progBar=T)
res.test$pval

# H test between subterraneans (Notoryctes + Necrolestes) and complete sample (subterraneans +
non subterraneans + unknwon)
res.test<-hotelling.test(ddA[,1:6], ddA[c(1,37),1:6],perm=T,B=10000,progBar=T)
res.test$pval

# H test between subterraneans (Notoryctes + Necrolestes) and non subterraneans
res.test<-hotelling.test(ddA[c(1,37),1:6], ddA[-c(1,37),1:6],perm=T,B=10000,progBar=T)
res.test$pval

### H test between hoppers and complete sample (hoppers + non hoppers + unknown)
res.test<-hotelling.test(ddA[,1:6],
ddA[dat$fossilornot=="extant"&dat$loco=="hopper",1:6],perm=T,B=10000,progBar=T)
res.test$pval

### H test between hoppers and non hoppers
res.test<-hotelling.test(ddA[c(15, 17, 31, 32, 47, 49),1:6], ddA[-c(15, 17, 31, 32, 47,
49),1:6],perm=T,B=10000,progBar=T)
res.test$pval
```

R script to source the main PFDA functions:

```
## phylo.FDA.v0.2

require(nnet)
require(mda)
require(ape)
require(geiger)
require(lattice)

###-------------------------------------------------------------------------
### Internal function from the package mda
###-------------------------------------------------------------------------
"contr.fda" <-
function (p = rep(1, d[1]), contrast.default = contr.helmert(length(p)))
{
d <- dim(contrast.default)
sqp <- sqrt(p/sum(p))
x <- cbind(1, contrast.default) * outer(sqp, rep(1, d[2] +
1))
qx <- qr(x)
J <- qx$rank
qr.qy(qx, diag(d[1])[, seq(2, J)])/outer(sqp, rep(1, J -
1))
}

###-------------------------------------------------------------------------
### Associated functions modified from the package mda
###-------------------------------------------------------------------------
"predict.phylo.fda" <-
function (object, newdata, type = c("class", "variates", "posterior",
"hierarchical", "distances"), prior, dimension = J - 1, ...)
{
dist <- function(x, mean, m = ncol(mean)) (scale(x, mean,
FALSE)^2) %*% rep(1, m)
type <- match.arg(type)
means <- object$means
Jk <- dim(means)
J <- Jk[1]
k <- Jk[2]
if (type == "hierarchical") {
if (missing(dimension))
dimension.set <- seq(k)
else {
dimension.set <- dimension[dimension <= k]
if (!length(dimension.set))
dimension.set <- k
dimension <- max(dimension.set)
}
}
```

```
else dimension <- min(max(dimension), k)
if (missing(newdata))
y <- predict(object$fit)
else {
if (inherits(newdata, "data.frame") || is.list(newdata)) {
Terms <- delete.response(terms(object))
attr(Terms, "intercept") <- 0
newdata <- model.matrix(Terms, newdata)
}
y <- predict(object$fit, newdata)
}
y <- y %*% object$theta[, seq(dimension), drop = FALSE]
lambda <- object$values
alpha <- sqrt(lambda[seq(dimension)])
sqima <- sqrt(1 - lambda[seq(dimension)])
newdata <- scale(y, FALSE, sqima * alpha)
if (missing(prior))
prior <- object$prior
else {
if (any(prior < 0) | round(sum(prior), 5) != 1)
stop("innappropriate prior")
}
means <- means[, seq(dimension), drop = FALSE]
switch(type, variates = return(newdata), class = {
n <- nrow(newdata)
prior <- 2 * log(prior)
mindist <- dist(newdata, means[1, ], dimension) - prior[1]
pclass <- rep(1, n)
for (i in seq(2, J)) {
ndist <- dist(newdata, means[i, ], dimension) - prior[i]
l <- ndist < mindist
pclass[l] <- i
mindist[l] <- ndist[l]
}
## 2001-10-27: Need to provide levels or else if we get an error
## if the predicted classes do no contain all possible classes.
## Reported by Greg Jefferis <jefferis@stanford.edu>, fix by
## Bj/orn-Helge Mevik <bjorn-helge.mevik@matforsk.no>.
return(factor(pclass, levels = seq(J),
labels = dimnames(means)[[1]]))
}, posterior = {
pclass <- matrix(0, nrow(newdata), J)
for (i in seq(J)) pclass[, i] <- exp(-0.5 * dist(newdata, means[i,
], dimension)) * prior[i]
dimnames(pclass) <- list(dimnames(newdata)[[1]], dimnames(means)[[1]])
return(pclass/drop(pclass %*% rep(1, J)))
}, hierarchical = {
prior <- 2 * log(prior)
Pclass <- vector("list", length(dimension.set))
names(Pclass) <- paste("D", dimension.set, sep = "")
for (ad in seq(along = dimension.set)) {
```

```
d <- dimension.set[ad]
dd <- seq(d)

mindist <- dist(newdata[, dd, drop = FALSE], means[1, dd, drop = FALSE],
d) - prior[1]
pclass <- rep(1, nrow(newdata))
for (i in seq(2, J)) {
ndist <- dist(newdata[, dd, drop = FALSE], means[i, dd,
drop = FALSE], d) - prior[i]
l <- ndist < mindist
pclass[l] <- i
mindist[l] <- ndist[l]
}
levels(pclass) <- dimnames(means)[[1]]
Pclass[[ad]] <- pclass
}
rownames <- dimnames(newdata)[[1]]
if (is.null(rownames))
rownames <- paste(seq(nrow(newdata)))
return(structure(Pclass, class = "data.frame", row.names = rownames,
dimensions = dimension.set))
}, distances = {
dclass <- matrix(0, nrow(newdata), J)
for (i in seq(J)) dclass[, i] <- dist(newdata, means[i, ],
dimension)
dimnames(dclass) <- list(dimnames(newdata)[[1]], dimnames(means)[[1]])
return(dclass)
})
}
"predict.polyreg.modified" <-
function (object, newdata, ...)
{
if (missing(newdata)) {
z <- fitted(object)
if (is.null(z))
stop("need to supply newdata")
else return(z)
}
degree <- object$degree
monomial <- object$monomial
newdata %*% object$coef
}
"polyreg.modified" <-
function (x, y, w, degree = 1, monomial = FALSE, ...)
{
#x <- polybasis(x, degree, monomial)
y <- as.matrix(y) # just making sure ...
if (iswt <- !missing(w)) {
if (any(w <= 0))
stop("only positive weights")
w <- sqrt(w)
```

```
y <- y * w
x <- x * w
}
qrx <- qr(x)
coef <- as.matrix(qr.coef(qrx, y))

fitted <- qr.fitted(qrx, y)
if ((df <- qrx$rank) < ncol(x))
coef[qrx$pivot, ] <- coef
if (iswt)
fitted <- fitted/w
structure(list(fitted.values = fitted, coefficients = coef,
degree = degree, monomial = monomial, df = df), class = "polyreg.modified")
}
"print.phylo.fda" <-
function (x, ...)
{
if (!is.null(cl <- x$call)) {
cat("Call:\n")
dput(cl)
}
cat("\nDimension:", format(x$dimension), "\n")
cat("\nPercent Between-Group Variance Explained:\n")
print(round(x$percent, 2))
error <- x$confusion
df <- x$fit
if (!is.null(df))
df <- df$df
if (!is.null(df)) {
cat("\nDegrees of Freedom (per dimension):", format(sum(df)),
"\n")
}
if (!is.null(error)) {
n <- as.integer(sum(error))
error <- format(round(attr(error, "error"), 5))
cat("\nTraining Misclassification Error:", error, "( N =",
n, ")\n")
}
invisible(x)
}
"plot.phylo.fda" <- function(pfdamodel,gfactor=pfdamodel$g,prdfactor=pfdamodel$prd)
{
pfdavar <- predict(pfdamodel, type="variate")
lim1x <- c(min(pfdavar[,1]),max(pfdavar[,1]))
lim1y <- c(min(pfdavar[,2]),max(pfdavar[,2]))
m1 <- 4;m2 <- 1
oldpar<-
par(no.readonly=FALSE);on.exit(par(oldpar));x11(height=8,width=14);par(mfrow=c(1,2),mar=c(m1,m
1,m1,m2),oma=c(m2,m2,m2,m2));
matplot(pfdavar[gfactor==levels(gfactor)[1],1], pfdavar[gfactor==levels(gfactor)[1],2],
xlab="pFDA1",ylab="pFDA2", xlim=lim1x, ylim=lim1y, pch=1, col=1, main="True
```

```
Classes",sub=paste("lambda = ",pfdamodel$val," intrcpt=",pfdamodel$intercept,"
eqprior=",pfdamodel$eqprior,sep=""))
for (i in 2:nlevels(gfactor)) matplot(pfdavar[gfactor==levels(gfactor)[i],1],
pfdavar[gfactor==levels(gfactor)[i],2], add=TRUE, pch=i, col=i)
legend(min(lim1x),max(lim1y),levels(gfactor), pch=1:nlevels(gfactor), col=1:nlevels(gfactor))

legend(min(lim1x),min(lim1y)+(max(lim1y)-min(lim1y))*0.1,paste("lambda = ",pfdamodel$val,"
intrcpt=",pfdamodel$intercept," eqprior=",pfdamodel$eqprior," ",sep=""))
addEllipseGrp(pfdavar[,1],pfdavar[,2],gfactor, pval=0.95, num=30)
matplot(pfdavar[prdfactor==levels(prdfactor)[1],1],
pfdavar[prdfactor==levels(prdfactor)[1],2], xlab="pFDA1",ylab="pFDA2", xlim=lim1x, ylim=lim1y,
pch=1, col=1, main="Predicted Classes",sub=paste("lambda = ",pfdamodel$val,"
intercept=",pfdamodel$intercept," eqprior=",pfdamodel$eqprior,sep=""))
for (i in 2:nlevels(prdfactor)) matplot(pfdavar[prdfactor==levels(prdfactor)[i],1],
pfdavar[prdfactor==levels(prdfactor)[i],2], add=TRUE, pch=i, col=i)
legend(min(lim1x),max(lim1y),levels(prdfactor), pch=1:nlevels(prdfactor),
col=1:nlevels(prdfactor))
legend(min(lim1x),min(lim1y)+(max(lim1y)-
min(lim1y))*0.1,paste(levels(prdfactor),"=",pfdamodel$prior," ",sep=""))
legend(max(lim1x)-(max(lim1x)-
min(lim1x))*0.2,max(lim1y),signif(attr(pfdamodel$confusion,"error"),4))
invisible()
}

###-------------------------------------------------------------------------
### Main pFDA function with training data only
###-------------------------------------------------------------------------
"phylo.fda" <-function (data,grp,tretre,val=1,treetrans=rescale,
dimension = J - 1, eps = .Machine$double.eps,
keep.fitted = (n * dimension < 1000),
method=polyreg.modified,intercept=TRUE,eqprior=FALSE,priin=1)
{
this.call <- match.call()
if(intercept) data <- cbind(Intercept=rep(1,nrow(data)),data)
data <- as.matrix(data)
tretre <- treetrans(tretre,"lambda", val)
g <- as.factor(grp)
ng <- nlevels(g)
W <- vcv.phylo(tretre)
invW<-solve(W)
invW.eig <- eigen(invW)
N <- invW.eig$vectors %*% diag(sqrt(invW.eig$values)) %*% solve(invW.eig$vectors)
divnum <-det(N)^(1/nrow(N))
N <- N/divnum
DATA <- N%*%data #Rao (4,57); transforming the data to linear
n <- nrow(DATA)
y <- matrix(0,nrow(data),ng)
for (i in 1:nrow(data)){y[i,g[i]] <- 1}
Y <- N%*%y #Dummy matrix with phylo bias removed
x <- DATA
fg <- factor(g)
```

```
prior <- colSums(Y)/sum(colSums(Y))
if(eqprior) prior <- c(rep(1/ng,ng))
if(priin != 1) prior<-priin
cnames <- levels(fg)
g <- as.numeric(fg)
J <- length(cnames)
weights <- rep(1, n)
dp <- tapply(weights, g, sum)/n
theta <- contr.helmert(J)
theta <- contr.fda(dp, theta)

Theta <- Y%*%theta #fda p.7, above eq2
fit <- method(x, Theta, weights)
rss <- t(Theta-fit$fitted) %*% (Theta-fit$fitted)
ssm <- t(Theta) %*% fitted(fit)/n
ed <- svd(ssm, nu = 0)
thetan <- ed$v
lambda <- ed$d
lambda[lambda > 1 - eps] <- 1 - eps
discr.eigen <- lambda/(1 - lambda)
pe <- (100 * cumsum(discr.eigen))/sum(discr.eigen)
dimension <- min(dimension, sum(lambda > eps))
if (dimension == 0) {
warning("degenerate problem; no discrimination")
return(structure(list(dimension = 0, fit = fit, call = this.call),
class = "phylo.fda"))
}
thetan <- thetan[, seq(dimension), drop = FALSE]
pe <- pe[seq(dimension)]
alpha <- sqrt(lambda[seq(dimension)])
sqima <- sqrt(1 - lambda[seq(dimension)])
vnames <- paste("v", seq(dimension), sep = "")
means <- scale(theta %*% thetan, FALSE, sqima/alpha)
dimnames(means) <- list(cnames, vnames)
names(lambda) <- c(vnames, rep("", length(lambda) - dimension))
names(pe) <- vnames
frml <- "grp~"
nc <- ncol(data)
varnam <- colnames(data)
for(i in 1:(nc-1)) frml <- paste(frml,varnam[i],"+", sep="")
frml <- paste(frml,varnam[nc], sep="")
frml <- as.formula(frml)
dset <- as.data.frame(cbind(grp,DATA))
Terms <- as.call(fda(formula = frml, data = dset, weights = weights))
obj <- structure(list(percent.explained = pe, values = lambda,
means = means, theta.mod = thetan, dimension = dimension,
prior = prior, fit = fit, call = this.call, terms = Terms),
class = "phylo.fda")
obj$confusion <- confusion(predict(obj), fg)
obj$prd <- predict(obj)
obj$g <- as.factor(grp)
```

```
obj$val <- val
obj$rss <- sum(diag(rss))
obj$intercept <- intercept
obj$eqprior <- eqprior
if (!keep.fitted)
obj$fit$fitted.values <- NULL
obj
}

###-------------------------------------------------------------------------
### Main pFDA function with training and test data
###-------------------------------------------------------------------------

"phylo.fda.pred" <-function (dataA,grpA,taxtaxA,tretreA,testlistn,val=1,treetrans=rescale,
method=polyreg.modified,sbcls=floor(table(grp)/4),
dimension = J - 1, eps = .Machine$double.eps, keep.fitted = (n * dimension <
1000),intercept=TRUE,eqprior=FALSE,priin=1)
{
## Preparing data
this.call <- match.call()
if(intercept) dataA <- cbind(Intercept=rep(1,nrow(dataA)),dataA)
dataA <- as.data.frame(dataA)
nA <- nrow(dataA)
testlist <- taxtaxA[testlistn]
trainінglist <- taxtaxA[-testlistn]
rownames(dataA) <- taxtaxA
tretre <- drop.tip(tretreA,testlistn)
grp <- grpA[-testlistn]
grp <- grp[grp %in% names(table(grp))[table(grp) > 0], drop=TRUE]
g <- as.factor(grp)
ng <- nlevels(g)
grpA <- as.factor(grpA)
ntest <- length(testlist)
dataA <- as.matrix(dataA)
tretreA <- treetrans(tretreA,"lambda", val)
W <- vcv.phylo(tretreA)
invW<-solve(W)
invW.eig <- eigen(invW)
N <- invW.eig$vectors %*% diag(sqrt(invW.eig$values)) %*% solve(invW.eig$vectors)
divnum <-det(N)^(1/nrow(N))
N <- N/divnum
invN <- solve(N)
y <- matrix(0,nA,nlevels(grpA))
for (i in 1:nA){y[i,grpA[i]] <- 1}
Y <- N%*%y #Dummy matrix with phylo bias removed
Y <- Y[-testlistn,1:ng]
DATAA <- N%*%as.matrix(dataA) #Rao (4,57); transforming the data to linear
DATA <- DATAA[-testlistn,]
DATAtest <- DATAA[testlistn,]
n<-nrow(DATA)
m<-nrow(DATAtest)
```

```
x <- DATA
fg <- factor(g)
prior <- colSums(Y)/sum(colSums(Y))
if(eqprior) prior <- c(rep(1/ng,ng))
if(priin != 1) prior<-priin
cnames <- levels(fg)
g <- as.numeric(fg)
J <- length(cnames)
weights <- rep(1, n)
dp <- tapply(weights, g, sum)/n
theta <- contr.helmert(J)
theta <- contr.fda(dp, theta)
Theta <- Y%*%theta #fda p.7, above eq2

fit <- method(x, Theta, weights)
rss <- t(Theta-fit$fitted) %*% (Theta-fit$fitted)
ssm <- t(Theta) %*% fitted(fit)/n
ed <- svd(ssm, nu = 0)
thetan <- ed$v
lambda <- ed$d
lambda[lambda > 1 - eps] <- 1 - eps
discr.eigen <- lambda/(1 - lambda)
pe <- (100 * cumsum(discr.eigen))/sum(discr.eigen)
dimension <- min(dimension, sum(lambda > eps))
if (dimension == 0) {
warning("degenerate problem; no discrimination")
return(structure(list(dimension = 0, fit = fit, call = this.call),
class = "fda"))
}
thetan <- thetan[, seq(dimension), drop = FALSE]
pe <- pe[seq(dimension)]
alpha <- sqrt(lambda[seq(dimension)])
sqima <- sqrt(1 - lambda[seq(dimension)])
vnames <- paste("v", seq(dimension), sep = "")
means <- scale(theta %*% thetan, FALSE, sqima/alpha)
dimnames(means) <- list(cnames, vnames)
names(lambda) <- c(vnames, rep("", length(lambda) - dimension))
names(pe) <- vnames
frml <- "grp~"
nc <- ncol(dataA)
varnam <- colnames(dataA)
for(i in 1:(nc-1)) frml <- paste(frml,varnam[i],"+", sep="")
frml <- paste(frml,varnam[nc], sep="")
frml <- as.formula(frml)
dset <- as.data.frame(cbind(grp,DATA))
Terms <- as.call(fda(formula = frml, data = dset, weights = weights))
obj <- structure(list(percent.explained = pe, values = lambda,
means = means, theta.mod = thetan, dimension = dimension,
prior = prior, fit = fit, call = this.call, terms = Terms),
class = "phylo.fda")
obj$confusion <- confusion(predict(obj), fg)
```

```
obj$prd <- predict(obj)
obj$x<-x
obj$g <- as.factor(grp)
obj$val <- val
obj$rss <- sum(diag(rss))
obj$intercept <- intercept
obj$eqprior <- eqprior
obj$DATAtest <- DATAtest
obj$DATA <- DATA
tpred <- predict(obj,DATAtest)
tpredn <- as.numeric(tpred)
tpred <- as.matrix(tpred)
rownames(tpred) <- testlist
obj$testprediction <- tpred
obj$testprediction_numeral <- tpredn
if (!keep.fitted)

obj$fit$fitted.values <- NULL
obj
}


###------------------------------------------------------------------------
### Function for optimal lambda value search
###------------------------------------------------------------------------

"phylo.RSS"<-function (datain,grp,tretre,val=1,treetrans=rescale)
{
  dataInO <- as.matrix(datain)
  dataInI <- cbind(Intercept=rep(1,nrow(dataInO)),dataInO)
  tretre <- treetrans(tretre,"lambda", val)
  n <- nrow(datain)
  g <- as.factor(grp)
  ng <- nlevels(g)
  W <- vcv.phylo(tretre)
  invW<-solve(W)
  y <- matrix(0,n,ng) #Dummy matrix without phylo bias
  for (i in 1:n){y[i,g[i]] <- 1}
  invW.eig <- eigen(invW)
  N <- invW.eig$vectors %*% diag(sqrt(invW.eig$values)) %*% solve(invW.eig$vectors)
  Y <- N %*% y # Pretending that there is no phylogenetic bias in y; otherwise Y <- N%*%y
  DATAI <- N%*%dataInI
  bhatI <- solve(t(dataInI)%*%invW%*%dataInI)%*%t(dataInI)%*%invW%*%y #Rohlf (9) -- data
biased still Rao (4,64)
  yhatI <- dataInI%*%bhatI #Rohlf (11)
  RSSyI <- t(y-yhatI) %*% invW %*% (y-yhatI) #Martins and Hansen 1997 (9)
  l0I<- lm(Y~DATAI-1)
  list(RSS=sum(diag(RSSyI)))
}

##dataA=XA;grpA=gA;taxtaxA=taxaA;tretreA=treA;testlistn=testtaxan;val=0;treetrans=lambdaTree
```

```
"phylo.RSS.pred" <-function (dataA,grpA,taxtaxA,tretreA,testlistn,val=1,treetrans=rescale)
{
  dataA <- as.data.frame(dataA)
  nA <- nrow(dataA)
  testlist <- taxtaxA[testlistn]
  trainlist <- taxtaxA[-testlistn]
  rownames(dataA) <- taxtaxA
  tretre <- drop.tip(tretreA,testlistn)
  grp <- grpA[-testlistn]
  grp <- grp[grp %in% names(table(grp))[table(grp) > 0], drop=TRUE]
  g <- as.factor(grp)
  ng <- nlevels(g)
  grpA <- as.factor(grpA)
  icptA <- rep(1,nA)
  dataA <- cbind(icptA,dataA)
  ntest <- length(testlist)
  tretreA <- treetrans(tretreA,"lambda", val)

  W <- vcv.phylo(tretreA)
  invW<-solve(W)
  invW.eig <- eigen(invW)
  N <- invW.eig$vectors %*% diag(sqrt(invW.eig$values)) %*% solve(invW.eig$vectors)
  invN <- solve(N)
  y <- matrix(0,nA,nlevels(grpA))
  for (i in 1:nA){y[i,grpA[i]] <- 1}
  Y <- N%*%y #Dummy matrix with phylo bias removed
  Y <- Y[-testlistn,1:ng]
  DATAA <- N%*%as.matrix(dataA) #Rao (4,57); transforming the data to linear
  DATA <- DATAA[-testlistn,]
  BHAT <- solve(t(DATA)%*%DATA)%*%t(DATA)%*%Y
  YHAT <- DATA%*%BHAT
  l0<- lm(Y~DATA-1)
  RSSY <- t(Y-YHAT) %*% (Y-YHAT)
  list(RSS=sum(diag(RSSY)))
}

##measurements=X;grps=g;mytree=tre;idc=filename_stem

"optLambda" <-
function(measurements,grps,mytree,idc="default",sstep=0.01,srange=c(0,1),fldr="./")
{
  lambdalist <- seq(min(srange),max(srange),sstep)
  segnum <- length(lambdalist)
  rslt<-matrix(,segnum,2)
  colnames(rslt) <- c("Lambda","RSS")

  for(i in 1:segnum){
    lambdaval <- lambdalist[i]
    rss <- phylo.RSS(X,grps,mytree,val=lambdaval)
    rslt[i,] <- c(lambdaval,rss$RSS)
```

```
  }

  optlambda <- matrix(,1,1);colnames(optlambda)<- "RSS"
  optlambda[1,1]<-max(rslt[which(rslt[,2]==min(rslt[,2])),1])


matplot(rslt[,1],rslt[,2],type="l",xlab=expression(lambda),ylab="RSS",main="RSS",lty=1,col=1)
  abline(v=optlambda[1,1],col=2,lty=2);mtext(paste("Optimal Lambda = ",optlambda[1,1],sep=""))


pdf(height=11,width=6,file=paste(fldr,idc,".optLambda.pdf",sep=''));layout(matrix(c(1,2),2,1))

matplot(rslt[,1],rslt[,2],type="l",xlab=expression(lambda),ylab="RSS",main="RSS",lty=1,col=1)
  abline(v=optlambda[1,1],col=2,lty=2);mtext(paste("Optimal Lambda = ",optlambda[1,1],sep=""))
  dev.off()

  list(optlambda=optlambda,rslt=rslt)
}

"optLambda.pred" <-
function(measurementsA,grpsA,taxaA,mytreeA,testn,idc="default",sstep=0.01,srange=c(0,1),fldr="
./")

{
  lambdalist <- seq(min(srange),max(srange),sstep)
  segnum <- length(lambdalist)
  rslt<-matrix(,segnum,2)
  colnames(rslt) <- c("Lambda","RSS")

  for(i in 1:segnum){
    lambdaval <- lambdalist[i]
    rss <- phylo.RSS.pred(measurementsA,grpsA,taxaA,mytreeA,testn,val=lambdaval)
    rslt[i,] <- c(lambdaval,rss$RSS,rss$AICY) #replaced lLy with AICY
  }

  optlambda <- matrix(,1,1);colnames(optlambda)<- "RSS"
  optlambda[1,1]<-max(rslt[which(rslt[,2]==min(rslt[,2])),1])

matplot(rslt[,1],rslt[,2],type="l",xlab=expression(lambda),ylab="RSS",main="RSS",lty=1,col=1)
  abline(v=optlambda[1,1],col=2,lty=2);mtext(paste("Optimal Lambda = ",optlambda[1,1],sep=""))


pdf(height=11,width=6,file=paste(fldr,idc,".optLambda.pred.pdf",sep=''));layout(matrix(c(1,2),
2,1))

matplot(rslt[,1],rslt[,2],type="l",xlab=expression(lambda),ylab="RSS",main="RSS",lty=1,col=1)
  abline(v=optlambda[1,1],col=2,lty=2);mtext(paste("Optimal Lambda = ",optlambda[1,1],sep=""))
  dev.off()

  list(optlambda=optlambda,rslt=rslt)
)
```

Supplementary Information 6. PCA summary.

```
PC Summary

Importance of first k=53 (out of 54) components:
                          PC1    PC2     PC3     PC4     PC5     PC6     PC7
Standard deviation     0.06913 0.0435 0.03731 0.03159 0.02615 0.02321 0.02238
Proportion of Variance 0.34966 0.1384 0.10184 0.07299 0.05004 0.03942 0.03663
Cumulative Proportion  0.34966 0.4881 0.58996 0.66295 0.71299 0.75241 0.78904
                          PC8     PC9    PC10    PC11    PC12    PC13    PC14
Standard deviation     0.02003 0.01856 0.01749 0.01500 0.01422 0.01373 0.01216
Proportion of Variance 0.02935 0.02522 0.02238 0.01645 0.01480 0.01380 0.01082
Cumulative Proportion  0.81839 0.84361 0.86599 0.88244 0.89725 0.91104 0.92187
                         PC15    PC16     PC17     PC18     PC19     PC20
Standard deviation     0.01100 0.01050 0.009724 0.009322 0.008603 0.007984
Proportion of Variance 0.00886 0.00806 0.006920 0.006360 0.005420 0.004660
Cumulative Proportion  0.93072 0.93879 0.945700 0.952060 0.957480 0.962140
                          PC21     PC22    PC23     PC24    PC25     PC26
Standard deviation     0.007315 0.006968 0.00669 0.006059 0.00599 0.005486
Proportion of Variance 0.003920 0.003550 0.00327 0.002690 0.00263 0.002200
Cumulative Proportion  0.966060 0.969610 0.97288 0.975570 0.97819 0.980400
                          PC27     PC28     PC29     PC30    PC31     PC32
Standard deviation     0.005332 0.005173 0.004888 0.004433 0.00419 0.003932
Proportion of Variance 0.002080 0.001960 0.001750 0.001440 0.00128 0.001130
Cumulative Proportion  0.982480 0.984430 0.986180 0.987620 0.98890 0.990040
                          PC33     PC34     PC35     PC36    PC37     PC38
Standard deviation     0.003751 0.003693 0.003449 0.003373 0.00319 0.002889
Proportion of Variance 0.001030 0.001000 0.000870 0.000830 0.00074 0.000610
Cumulative Proportion  0.991060 0.992060 0.992930 0.993770 0.99451 0.995120
                          PC39     PC40     PC41     PC42     PC43     PC44
Standard deviation     0.002875 0.002779 0.002637 0.002415 0.002332 0.002264
Proportion of Variance 0.000600 0.000570 0.000510 0.000430 0.000400 0.000380
Cumulative Proportion  0.995730 0.996290 0.996800 0.997230 0.997620 0.998000
                          PC45     PC46     PC47     PC48     PC49     PC50
Standard deviation     0.002084 0.002029 0.001937 0.001895 0.001717 0.001652
Proportion of Variance 0.000320 0.000300 0.000270 0.000260 0.000220 0.000200
Cumulative Proportion  0.998320 0.998620 0.998890 0.999160 0.999370 0.999570
                          PC51     PC52     PC53
Standard deviation     0.001524 0.001376 0.001285
Proportion of Variance 0.000170 0.000140 0.000120
Cumulative Proportion  0.999740 0.999880 1.000000
```

Supplementary Information 7. Pairs of the ten first Principal Components.

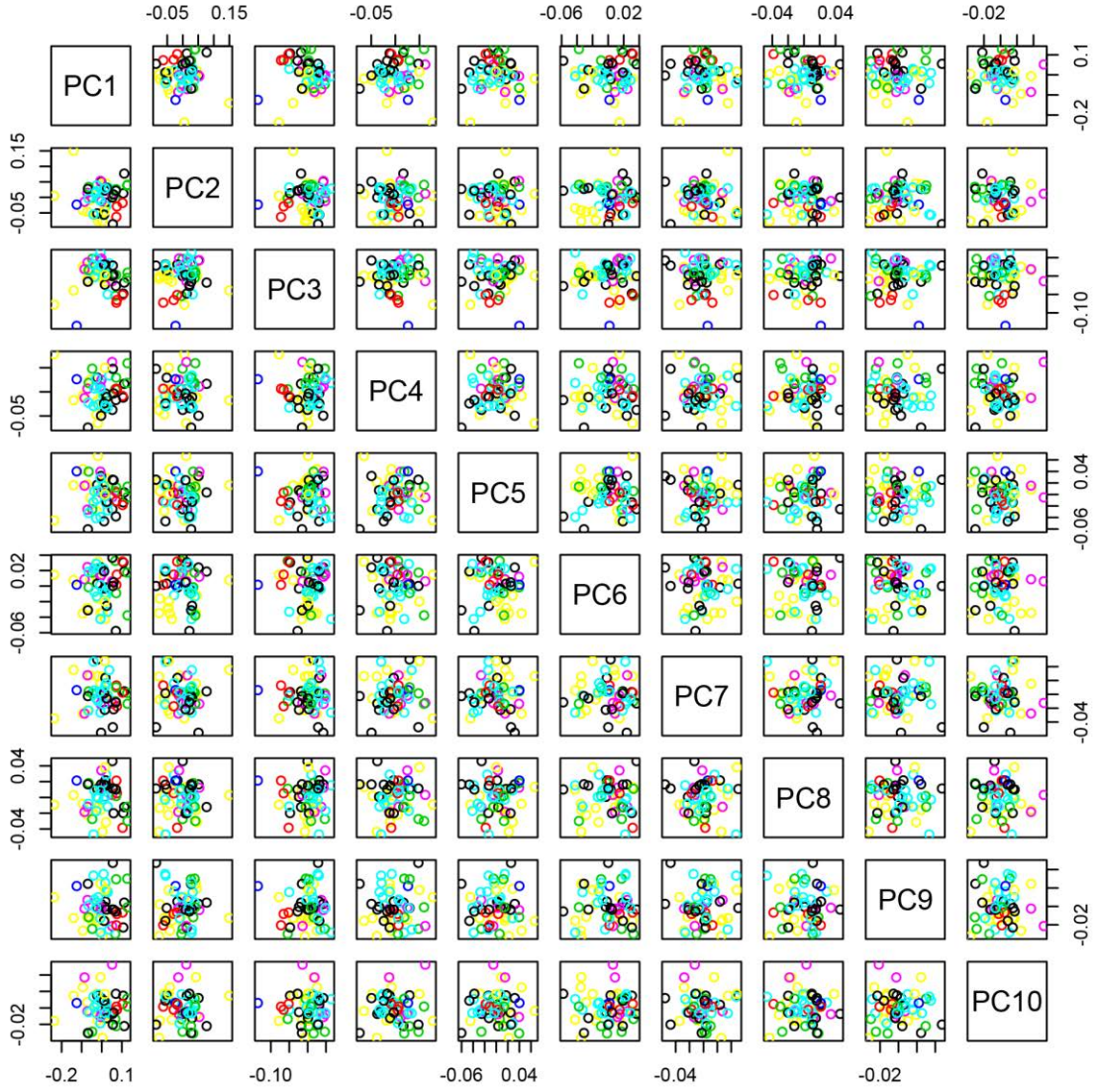

Figure SI-3: Pairs of the ten first Principal Components. Colors correspond to locomotor modes: yellow=fossils, blue=subterranean, red=glider, green=hopper, black=arboreal, pink=terrestrial-arboreal, light blue=terrestrial.

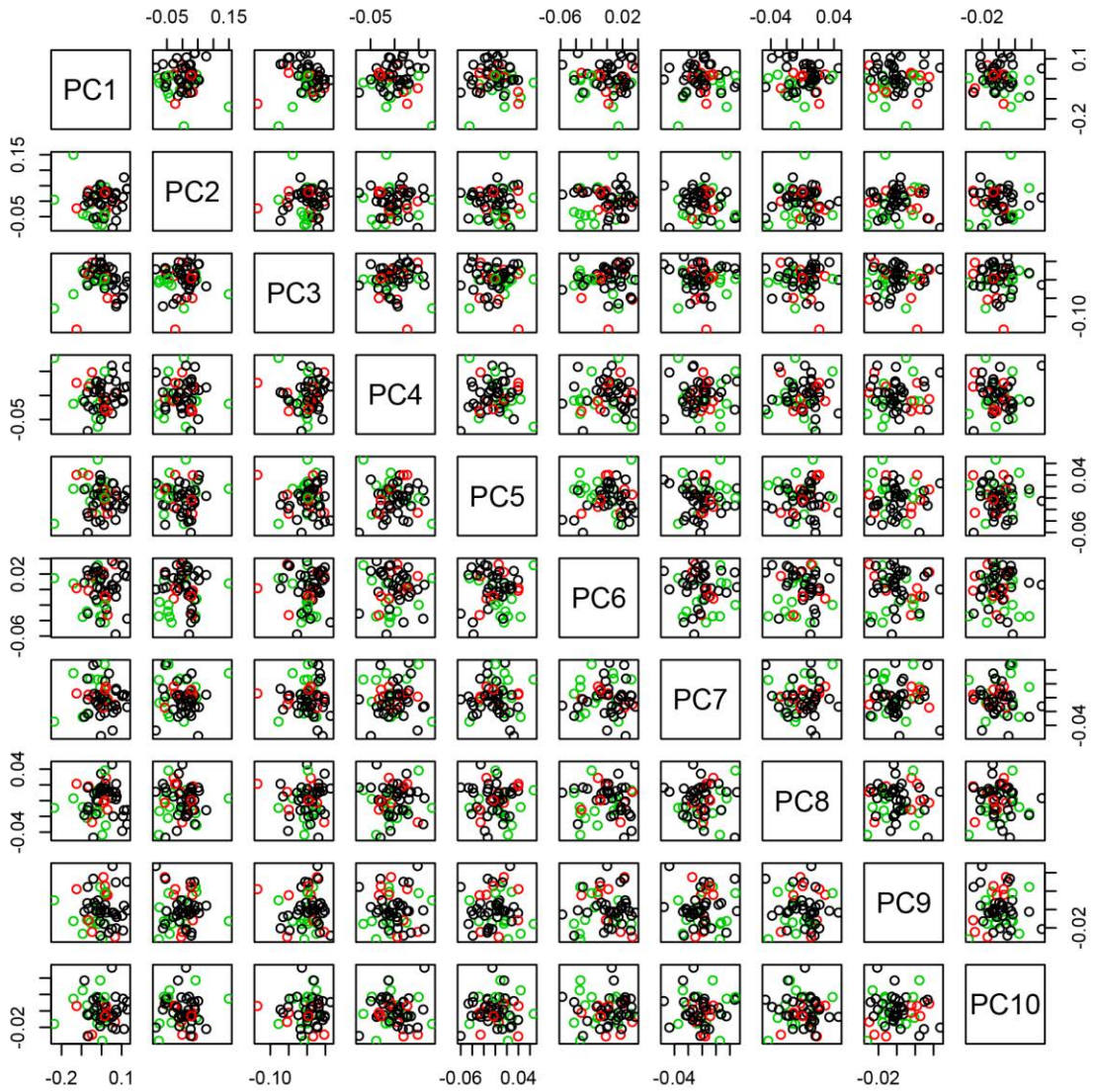

Figure SI-4: Pairs of the ten first Principal Components. Colors correspond to burrower (green) and non-burrower (red).

Supplementary Information 8. Optimisation of the character locomotion onto the phylogenetic tree of Metatheria.

To visualize the optimisations of the character dealing with the locomotor mode, we used the 'phylo4d' function of R from the 'phylobase' library, with the function 'make.simmap' referring to 'ace' (Ancestral Character Estimation) for the parameters.

The 'phylo4d' function perfoms a Maximum Likelyhood analysis with an equal rates model (ER) for discrete data, and with 100 simulations, as indicating in the script below:

```
        install.packages('tibble');library(phylobase)
        pA<-phylo4d(treA,data.frame(dat$loco,ddA[,1:7]))
        p<-phylo4d(tre,data.frame(g,X[,1:7]))
        treePlot(p,type="phylogram",tip.plot.fun ="bubbles",tip.color
=as.numeric(p@data$dat.loco))
        phenogram(tre,X[,1],as.numeric(g))
        trees <- make.simmap(tre, g, model = "ER", nsim = 100)
        plot(describe.simmap(trees, plot = FALSE))
        obj<-
phylomorphospace3d(tre,X[,c(2,6,7)],color=as.numeric(g),method="dynamic",control=list(ftype="o
ff"))# control=list(cex.col=as.numeric(g)))
        obj$points3d(X[,c(1,3,4)],cex=1.4,pch=21,bg=as.numeric(g))
```

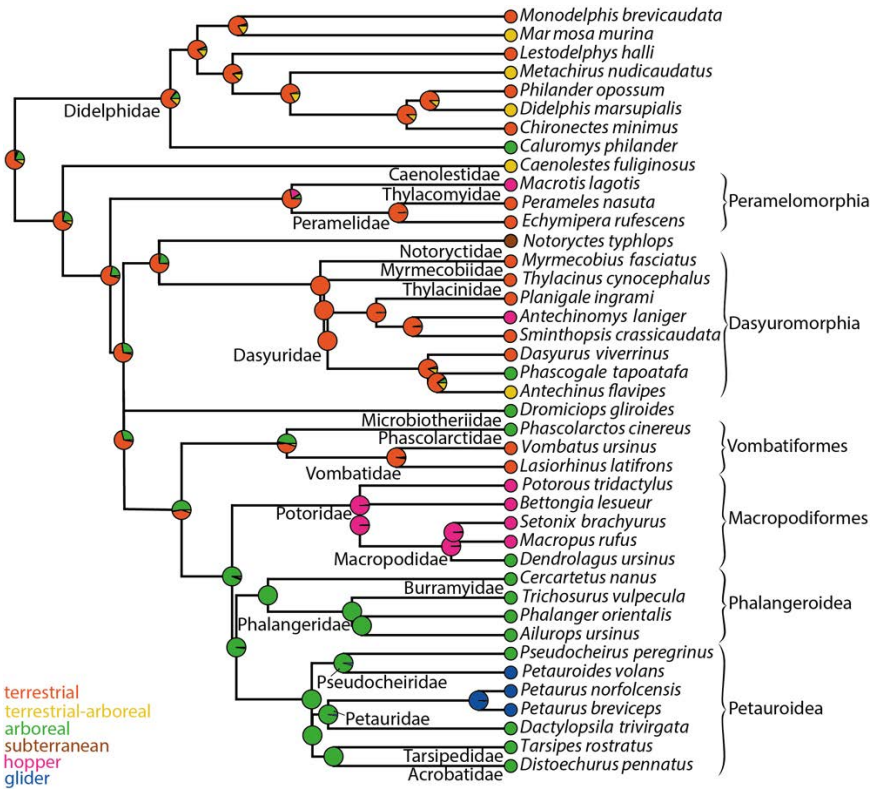

Figure SI-5: Phylogenetic tree of Metatheria showing the reconstruction of the ancestral character states of locomotion.

Supplementary Information 9. Regression shape vs bodymass and PCA with allometry-corrected data.

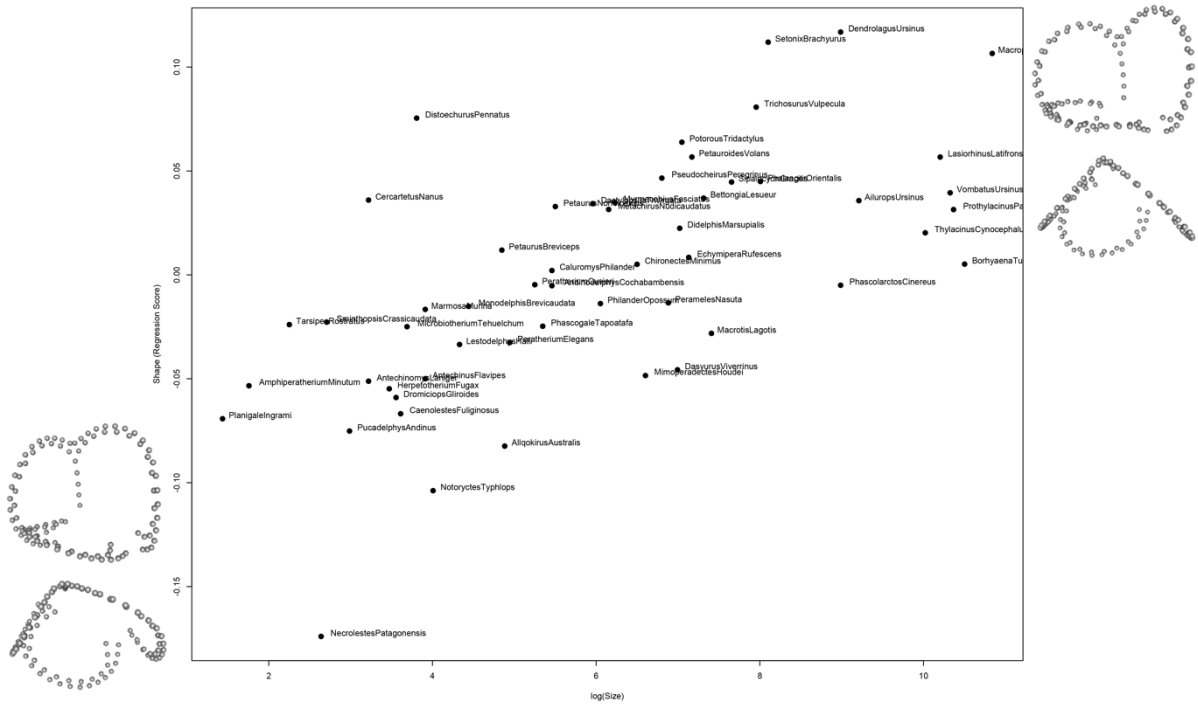

Figure SI-6: Regression shape vs bodymass. The extreme shapes of vestibular systems are shown for the smallest and largest species.

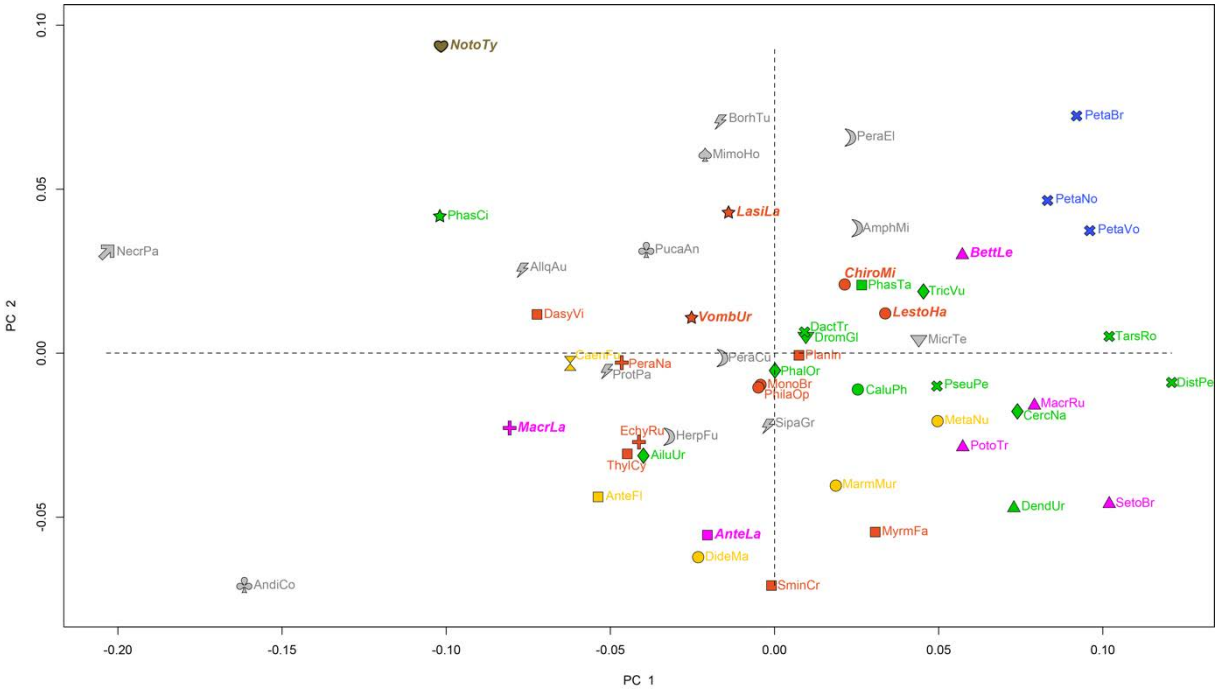

Figure SI-7: Results of the PCA performed on the allometry-corrected data of the vestibular system of the bony labyrinth of metatherians. Abbreviations: symbols for the clades as follows: circle=Didelphimorphia, square=Dasyuromorphia, triangle=Macropodiformes, cross (x)=Petauroidea, losange=Phalangeroidea, star=Vombatiformes, cross (+)=Peramelemorphia, reversed triangle=Microbiotheriia, hourglass=Paucituberculata, heart=Notoryctemorphia, moon=Herpetotheriidae,spade=Peradectidae, clover=Pucadelphyidae, bolt=Sparassodonta, arrow=Meridiolestida. Colors for the locomotions as follows: green=arboreal, yellow=terrestrial to arboreal, orange=terrestrial, brown=subterranean, blue=glider, pink=hopper, unknown (fossils)=grey. The fossorial extant species are in bold italics.

Supplementary Information 10. Pairs of the ten first Principal Components, resulting from the analysis with allometry-corrected data.

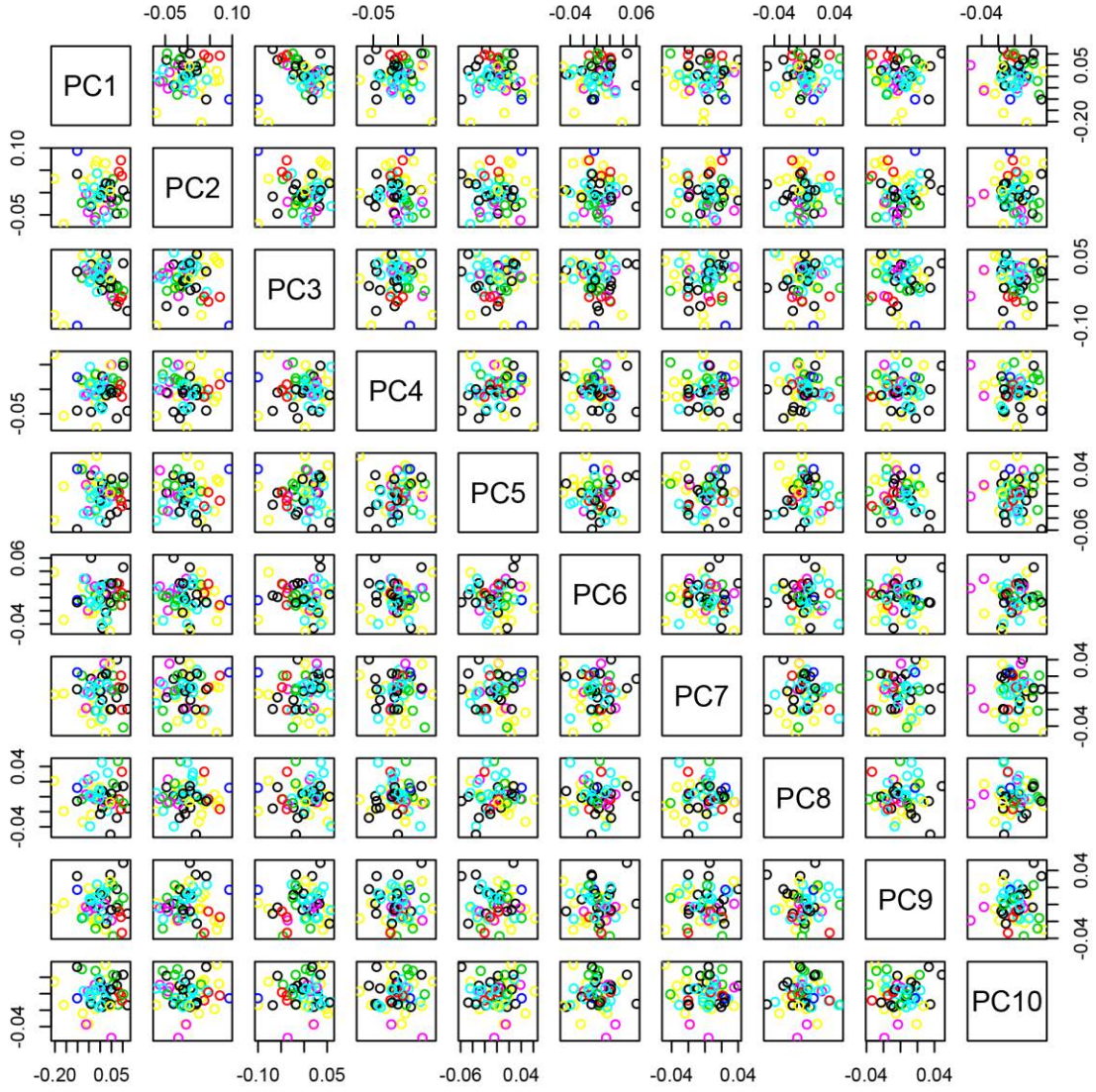

Figure SI-8: Pairs of the ten first Principal Components. Colors correspond to locomotor modes: yellow=fossils, blue=subterranean, red=glider, green=hopper, black=arboreal, pink=terrestrial-arboreal, light blue=terrestrial.

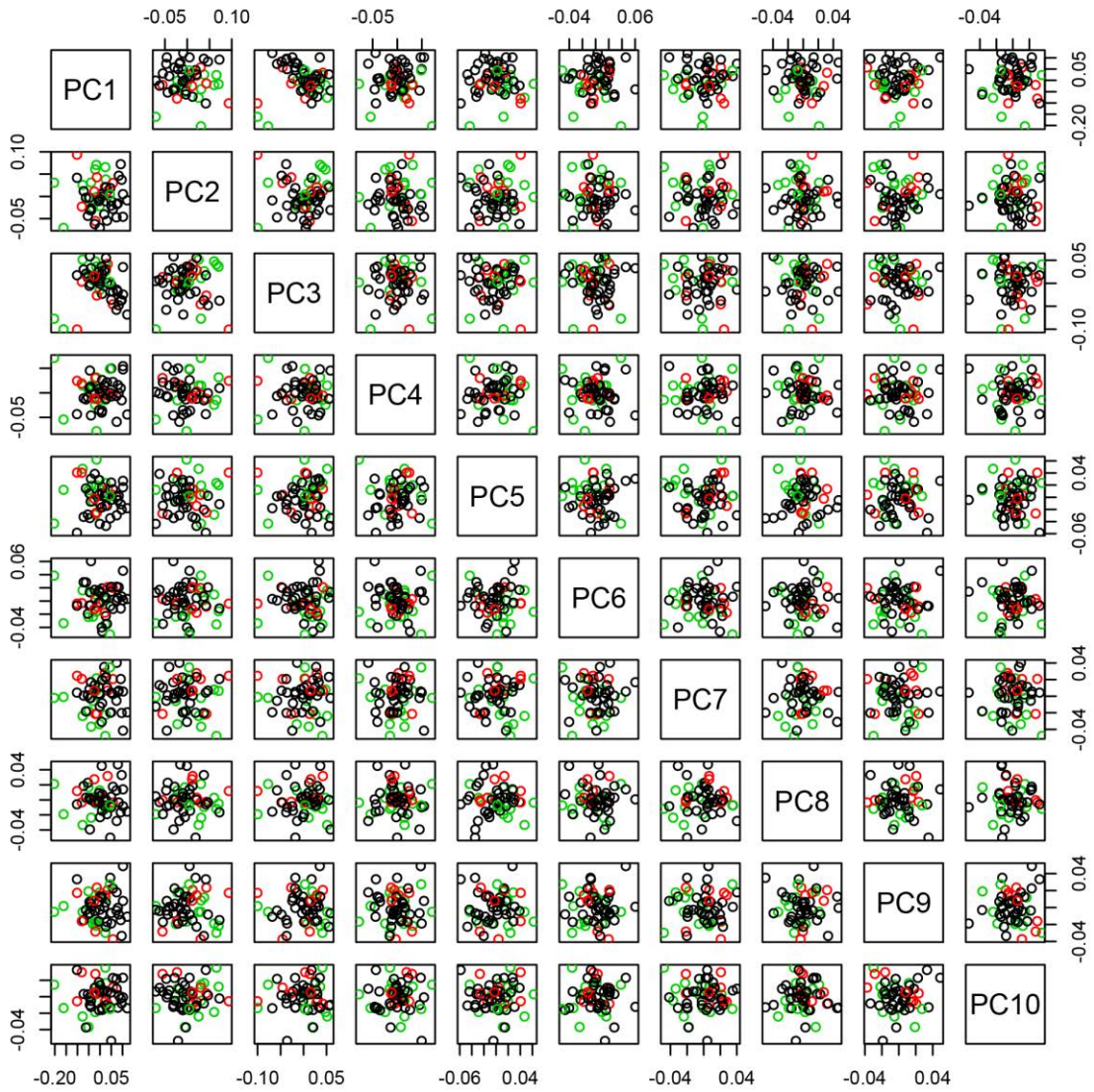

Figure SI-9: Pairs of the ten first Principal Components. Colors correspond to burrower (green) and non-burrower (red).

Supplementary Information 11. Phylogenetic Discriminant Analysis of the locomotor classes.

Table SI-2. Prediction of the locomotor classes for extant taxa.

	true class	predicted class	P(arboreal)	P(glider)	P(hopper)	P(subterranean)	P(terrestrial)	P(terrestrial arboreal)	DA1	DA2	DA3	DA4	DA5
AiluropsUrsinus	arboreal	arboreal	0.504417956766	3.979733504987	1.771042834734	1.075938591044	0.156965835285	0.338598497519	-2.088755	1.745856	-0.540537	-1.180623	0.684712
AntechinomysLaniger	hopper	hopper	0.002866742040	4.641183783380	0.873553568829	1.108727292673	0.117728192079	0.005851492409	-1.548013	1.411687	2.407520	1.428257	0.855406
AntechinusFlavipes	terrestrial arboreal	terrestrial	0.002353196752	2.180796976915	0.027886565556	1.956980237034	0.813524161185	0.156236074320	-0.251253	0.612475	2.215803	-0.194833	-1.242354
BettongiaLesueur	hopper	glider	0.005216969594	0.519692758244	0.471680863012	1.657747030797	0.003398889829	1.051931920414	2.169135	-2.652133	-0.259023	0.824366	0.495247
CaenolestesFuliginosus	terrestrial arboreal	terrestrial	0.005447361882	1.882125416805	0.000371933034	6.431795027533	0.629864824164	0.364315880898	-1.019997	1.377811	1.513239	-1.238333	-1.457446
CaluromysPhilander	arboreal	arboreal	0.740168295515	6.780098707581	5.266830973410	1.807228028891	0.256022655785	0.003756380380	-2.266573	1.150417	-1.093927	-0.112005	-0.162836
CercartetusNanus	arboreal	arboreal	0.998137967132	4.434957551190	1.577764896259	7.677035989403	0.001792596663	6.785799496995	-1.901181	0.370737	-2.932527	-1.254937	1.400447
ChironectesMinimus	terrestrial	terrestrial	0.215763321585	7.243743594035	0.007427423046	1.747398258581	0.750520082034	0.026281929590	-0.050713	0.429253	-0.142977	-0.952655	-1.018209
DactylopsilaTrivirgata	arboreal	arboreal	0.996515204361	9.216709798742	5.323067833896	4.907142691836	0.003430413305	4.905834395532	0.206678	1.262682	-3.260567	-0.620547	0.878105
DasyurusViverrinus	terrestrial	terrestrial	0.035866780815	7.329941037186	0.020059176272	6.746645209603	0.918591383140	0.025482652441	-0.274563	0.517824	0.851833	0.181283	-0.948248
DendrolagusUrsinus	arboreal	hopper	0.311509347318	2.616930098453	0.617339937721	3.396220354717	0.069427996829	0.001722456436	0.739564	0.097229	-0.280647	1.439038	1.953877
DidelphisMarsupialis	terrestrial arboreal	terrestrial arboreal	0.025002291108	6.955519778549	0.005844322032	2.375367253492	0.033597405248	0.935555981540	-0.694011	1.038284	1.220050	-1.133462	2.288099
DistoechurusPennatus	arboreal	arboreal	0.963906711814	1.304489941540	0.004371206388	1.477672044228	0.031388435363	0.000332341943	-1.285895	-1.166575	-1.364743	0.013266	1.234709
DromiciopsGliroides	arboreal	terrestrial	0.102607453588	2.433935188962	0.004614221422	3.144660243487	0.643522818684	0.249255481964	-0.239233	0.663410	0.490508	-1.127177	-0.389038
EchymiperaRufescens	terrestrial	terrestrial arboreal	0.000918854608	2.422272349351	0.040990283905	1.484871109600	0.291785888479	0.666304730778	0.340544	0.051928	2.579560	-1.195337	-0.781727
LasiorhinusLatifrons	terrestrial	terrestrial	0.364843284873	6.959227029504	0.019461193192	6.087252718694	0.615450270148	0.000244555862	0.622695	0.221153	-1.032307	1.118295	-1.239174
LestodelphysHalli	terrestrial	arboreal	0.537951375403	1.584323348565	0.000796713007	2.046454736306	0.459728866623	0.001523044950	-1.468473	0.951858	-0.835000	0.718426	-0.415973
MacropusRufus	hopper	hopper	0.005061706228	8.172271807926	0.836110659950	5.621641550702	0.150223945818	0.008603606279	1.422559	0.713467	1.483904	1.242442	0.332561
MacrotisLagotis	hopper	hopper	4.815426333337	3.324192539774	0.988062949325	6.719311944935	0.011318920044	0.000569943124	1.341498	-0.137572	2.724421	1.848018	0.321000
MarmosaMurina	terrestrial arboreal	terrestrial arboreal	0.149793966847	3.746278913176	0.001341572873	6.531518450932	0.066722715110	0.782141741421	-1.059344	0.288063	0.360391	-1.936207	1.622333
MetachirusNudicaudatus	terrestrial arboreal	terrestrial arboreal	1.242319510281	2.886248937931	5.296671411772	2.406190654942	0.000314370306	0.999667909824	-0.049131	1.573837	2.471785	-3.482501	1.308672
MonodelphisBrevicaudata	terrestrial	terrestrial	0.287661718187	4.853330955432	0.000723482719	1.736387287682	0.608449804246	0.103164994360	-1.149019	0.840042	-0.082705	-0.989195	-0.327217
MyrmecobiusFasciatus	terrestrial	terrestrial	0.056260270274	7.667920501433	0.091733671256	4.739968796575	0.851625536924	0.000380521544	-2.107364	0.806204	0.889962	3.201019	-0.011237
NotoryctesTyphlops	subterranean	subterranean	2.202055549848	1.983380377767	2.039079109460	1	9.144706821215	4.352505212885	9.457919	5.350383	-0.868757	0.154695	-0.117259
Perameles Nasuta	terrestrial	terrestrial	0.031373855244	8.071672081233	0.036404691727	1.223213175510	0.883276777033	0.048944667921	1.075602	1.652527	0.758668	0.260348	-0.824351
PetauroidesVolans	glider	glider	6.292386932723	0.999986608626	1.326452548009	3.420426126466	6.347898089400	4.455536632467	3.325814	-3.968163	-0.314291	-0.651224	-0.388027
PetaurusBreviceps	glider	glider	1.410287747064	0.999999910180	7.354115091713	2.859780615717	2.153349246933	2.251209745212	3.408774	-4.206427	-1.340861	-1.693551	-0.478406
PetaurusNorfolcensis	glider	glider	2.715290223797	0.999887425471	0.000111784170	1.194968835102	5.107555221459	8.072931446923	2.673985	-4.121630	0.237552	-0.698171	-0.184588
PhalangerOrientalis	arboreal	arboreal	0.982413898623	2.715341623802	5.664622596445	2.718012227036	0.017506863125	2.259202240287	-0.097615	2.089087	-2.707985	1.210547	0.648528
PhascogaleTapoatafa	arboreal	terrestrial	0.447881669315	0.000680208048	0.003006977360	4.412828033528	0.548187948132	0.000243197142	-0.434237	-1.906915	-1.245615	-0.402635	-2.047556
PhascolarctosCinereus	arboreal	arboreal	0.608091686025	7.685329727280	5.118857038393	4.845235775644	0.391633442332	0.000223682994	-1.179173	0.974782	-1.732423	0.298814	-1.646885
PhilanderOpossum	terrestrial	arboreal	0.586817703065	2.136330246167	0.041925694763	2.620530435701	0.363142352097	0.008114228705	-1.178737	-0.471541	-0.116623	0.494447	0.786509
PlanigaleIngrami	terrestrial	terrestrial	0.046579056720	5.772238213539	6.075131379810	1.369531227432	0.953080715929	0.000279475458	-2.269761	-0.516413	-0.369587	-0.020443	-3.160244
PotorousTridactylus	hopper	hopper	0.090862992018	1.606458010422	0.609704656263	4.149214999520	0.298082477094	0.001349585559	0.241787	0.256422	0.416645	1.952215	0.598871
PseudocheirusPeregrinus	arboreal	arboreal	0.795121779307	2.066896796044	0.111120634549	9.562351660572	0.092244056164	0.001492861010	0.007309	-1.153033	-0.792507	0.409072	1.255888
SetonixBrachyurus	hopper	hopper	0.003841100638	0.000191447856	0.975177609585	8.457475838831	0.018687968480	0.002101873438	0.583237	-1.952501	1.376361	0.440345	1.153511
SminthopsisCrassicaudata	terrestrial	terrestrial	0.030362301288	8.709022396174	0.015402240908	2.459569097046	0.494791751261	0.459443706454	-1.793394	0.232128	1.680348	-0.444085	0.517035
TarsipesRostratus	arboreal	arboreal	0.396588633681	1.179251452384	0.369113988153	1.814333781847	0.234212175355	8.508488352251	-0.856001	-1.145771	-0.406062	2.309750	0.571445
ThylacinusCynocephalus	terrestrial	terrestrial	0.115354491494	1.181338331120	0.001435700216	1.399436321304	0.871214863288	0.011994944882	-0.984384	1.001327	0.064824	0.091851	-1.067390
TrichosurusVulpecula	arboreal	arboreal	0.964924993982	8.664347736940	1.998261894227	1.263143959876	0.034940950994	0.000114072316	-1.310330	0.631112	-2.318911	-0.064182	-0.005391
VombatusUrsinus	terrestrial	terrestrial	0.047353223203	4.660320942466	0.017408095813	1.024017174278	0.923022663407	0.012215970972	-0.127630	0.260807	0.556429	0.153801	-1.208162

Table SI-3. Prediction of the locomotor classes for fossil taxa.

	predicted class	P(arboreal)	P(glider)	P(hopper)	P(subterranean)	P(terrestrial)	P(terrestrial or arboreal)	DA1	DA2	DA3	DA4	DA5
NecrolestesPatagonensis	subterranean	1.153229599948	2.559803808200	1.043846560349	1	9.904851216977	5.842738458876	9.7430	7.3804	2.5869	1.1575	1.0274
PucadelphysAndinus	terrestrial	0.054331252869	3.327500396699	0.096553367209	2.744317551809	0.849008187130	0.000106860041	-0.2509	-0.7346	0.0952	1.8650	-1.6614
AndinodelphysCochabambensis	subterranean	1.180796612981	1.207445423546	1.017396786654	0.999955257680	6.239514384679	4.474224537138	4.0087	8.6637	1.0144	-4.5185	1.9989
AllqokirusAustralis	terrestrial	0.029828224448	3.689166281220	1.200900226164	8.172238814193	0.967233968163	0.002925798385	-4.3267	0.3568	0.5183	0.0710	-2.1822
BorhyaenaTuberata	glider	0.000397980358	0.996297591193	0.002458109662	2.679737621708	0.000845173508	1.145277497478	1.7911	-3.2304	-0.5114	-0.3942	-1.3931
ProthylacinusPatagonicus	terrestrial or arboreal	0.001130390409	1.881267735494	3.415981628243	4.124664321273	0.173000848315	0.825865345293	-1.3192	2.6615	1.4927	-2.2400	-1.7155
SipalocyonGracilis	terrestrial	0.191184049681	3.086958736236	0.078061595439	4.989593977365	0.727614386965	0.003139967604	-0.8639	0.4983	0.2957	1.5851	0.1303
MimoperadectesHoudei	terrestrial	0.146665534232	5.492476389910	7.772134568117	2.440948569341	0.853248579473	8.164941998132	-3.0304	-0.4348	-1.0580	1.6661	-2.8654
AmphiperatheriumMinutum	arboreal	0.703978308286	0.137822600584	0.018241538108	2.710446819814	0.139940659036	1.689398399009	-0.5697	-3.5540	-1.6344	0.1413	-1.1852
PeratheriumElegans	hopper	0.188108101935	0.000839204009	0.767199810558	5.399983063096	0.043852883495	9.789267206620	-1.3277	-5.0131	-2.8093	6.8087	-2.4809
PeratheriumCuvieri	hopper	0.003366003238	7.383246621468	0.697373189561	4.556984138555	0.299259814913	9.184539049421	-1.3064	-2.2613	0.9901	3.8433	-1.9178
HerpetotheriumFugax	terrestrial	0.019009579322	1.396019064337	0.062151387167	1.727372868717	0.898106172716	0.020732860779	-1.0332	0.9334	1.5107	1.2825	-0.2703
MicrobiotheriumTehuelchum	arboreal	0.569981594567	1.855989825098	7.887321651814	1.088939939695	0.174834287830	0.255105244200	0.6216	2.7500	-1.1124	-1.7811	0.2380

Supplementary Information 12. Phylogenetic Discriminant Analysis of the burrowing ability.

Table SI-4. Prediction of the burrowing ability for extant taxa (burrow=1, non burrow=0).

	true class	predicted class	P(non burrow)	P(burrow)	DA1
AiluropsUrsinus	0	0	0.931378417415	0.068621582584	-0.601703
AntechinomysLaniger	1	0	0.934428014726	0.065571985273	-0.641567
AntechinusFlavipes	0	0	0.911998858312	0.088001141687	-0.381004
BettongiaLesueur	1	0	0.798015710959	0.201984289040	0.4079317
CaenolestesFuliginosus	0	0	0.730768839018	0.269231160981	0.7150562
CaluromysPhilander	0	0	0.899569336539	0.100430663460	-0.261692
CercartetusNanus	0	0	0.988329770105	0.011670229894	-2.099577
ChironectesMinimus	1	0	0.820289789952	0.179710210047	0.2898194
DactylopsilaTrivirgata	0	0	0.870886057464	0.129113942535	-0.029652
DasyurusViverrinus	0	0	0.771374619976	0.228625380023	0.5370681
DendrolagusUrsinus	0	0	0.968672179676	0.031327820323	-1.275295
DidelphisMarsupialis	0	0	0.911668617818	0.088331382181	-0.377643
DistoechurusPennatus	0	0	0.981824414630	0.018175585369	-1.731725
DromiciopsGliroides	0	0	0.657120390173	0.342879609826	0.9997872
EchymiperaRufescens	0	0	0.810701044129	0.189298955870	0.3419654
LasiorhinusLatifrons	1	0	0.630288936790	0.369711063209	1.0955306
LestodelphysHalli	1	0	0.879839699614	0.120160300385	-0.096815
MacropusRufus	0	0	0.941242752892	0.058757247107	-0.737285
MacrotisLagotis	1	1	0.497997458346	0.502002541653	1.5385051
MarmosaMurina	0	0	0.940215734740	0.059784265259	-0.722216
MetachirusNudicaudatus	0	0	0.868810012814	0.131189987185	-0.014649
MonodelphisBrevicaudata	0	0	0.911548655734	0.088451344265	-0.376425
MyrmecobiusFasciatus	0	0	0.950919371069	0.049080628930	-0.892870
NotoryctesTyphlops	1	1	0.016745582941	0.983254417058	4.8638588
PeramelesNasuta	0	0	0.634462798013	0.365537201986	1.0808424
PetauroidesVolans	0	0	0.907453786338	0.092546213661	-0.335718
PetaurusBreviceps	0	0	0.663634784140	0.336365215859	0.9760241
PetaurusNorfolcensis	0	0	0.788385860250	0.211614139749	0.4559667
PhalangerOrientalis	0	0	0.858588347339	0.141411652660	0.0564133
PhascogaleTapoatafa	0	0	0.935370827726	0.064629172273	-0.654240
PhascolarctosCinereus	0	0	0.642427882710	0.357572117289	1.0526123
PhilanderOpossum	0	0	0.783717624247	0.216282375752	0.4786765
PlanigaleIngrami	0	0	0.921401576135	0.078598423864	-0.481839
PotorousTridactylus	0	0	0.908101687604	0.091898312395	-0.342050
PseudocheirusPeregrinus	0	0	0.912421897361	0.087578102638	-0.385326
SetonixBrachyurus	0	0	0.946916647990	0.053083352009	-0.825281
SminthopsisCrassicaudata	0	0	0.982627121967	0.017372878032	-1.769346
TarsipesRostratus	0	0	0.905711390878	0.094288609121	-0.318887
ThylacinusCynocephalus	0	0	0.873825200676	0.126174799323	-0.051246
TrichosurusVulpecula	0	0	0.883545838834	0.116454161165	-0.125884
VombatusUrsinus	1	0	0.747915517180	0.252084482819	0.6422461

Table SI-5. Prediction of the burrowing ability for fossil taxa (burrow=1, non burrow=0).

	predicted class	P(non burrow)	P(burrow)	DA1
NecrolestesPatagonensis	1	0.038275882438	0.961724117561	4.16943
PucadelphysAndinus	1	0.309824919868	0.690175080131	2.18720
AndinodelphysCochabambensi	0	0.581504163426	0.418495836573	1.26283
AllqokirusAustralis	1	0.188392034331	0.811607965668	2.72678
BorhyaenaTuberata	1	0.206169979381	0.793830020618	2.63488
ProthylacinusPatagonicus	0	0.619588554712	0.380411445287	1.13288
SipalocyonGracilis	0	0.843056273773	0.156943726226	0.15660
MimoperadectesHoudei	0	0.658570122174	0.341429877825	0.99451
AmphiperatheriumMinutum	0	0.752846424139	0.247153575860	0.62070
PeratheriumElegans	1	0.481661922208	0.518338077791	1.59198
PeratheriumCuvieri	0	0.805015477964	0.194984522035	0.37193
HerpetotheriumFugax	0	0.802766055741	0.197233944258	0.38360
MicrobiotheriumTehuelchum	0	0.701350291584	0.298649708415	0.83350

Supplementary Information 13. SI References.

Abello MA, Ortiz-Jaureguizar E & Candela AM. 2012. Chapter 10- Paleoecology of the Paucituberculata and Microbiotheria (Mammalia, Marsupialia) from the late Early Miocene of Patagonia; pp.156-172 in Vizcaíno SF, Kay RF & Bargo S (eds), Early Miocene Paleobiology in Patagonia: High-Latitude Paleocommunities of the Santa Cruz Formation. Cambridge University Press, Cambridge.

Argot C. 2004. Evolution of South American mammalian predators (Borhyaenoidea): anatomical and palaeobiological implications. Zoological Journal of the Linnean Society 140(4): 487-521.

Armati P, Dickman C & Hume I (eds). 2006. Marsupials. Cambridge: Cambridge University Press. doi:10.1017/CBO9780511541889

Asher RJ, Horovitz I, Martin T, Sánchez-Villagra MR. 2007. Neither a rodent nor a platypus: a reexamination of Necrolestes patagonensis Ameghino. American Museum Novitates 3546: 1–40.

Benton, M. J., Donoghue, P. C., Asher, R. J., Friedman, M., Near, T. J., & Vinther, J. 2015. Constraints on the timescale of animal evolutionary history. Palaeontologia Electronica, 18(1), 1-106.

Crochet J-Y. 1980. Les Marsupiaux Du Tertiaire d'Europe. Paris: Editions de la Fondation Singer-Polignac, 279.

de Magalhaes JP & Costa J. 2009. A database of vertebrate longevity records and their relation to other life-history traits. Journal of Evolutionary Biology 22: 1770-1774.

Ercoli MD & Prevosti FJ. 2011. Estimación de masa de las especies de Sparassodonta (Metatheria, Mammalia) de la Edad Santacrucense (Mioceno Temprano) a partir de tamaños de centroide de elementos apendiculares: inferencias paleoecológicas. Ameghiniana 48: 462–479.

Gardner AL. (ed.). 2007. Mammals of South America . Volume 1: Marsupials, Xenarthrans, Shrews, and Bats. University of Chicago Press, Chicago, Illinois, and London, United Kingdom, 669 pp.

Horovitz I, Martin T, Bloch J, Ladevèze S, Kurz C & Sánchez-Villagra MR. 2009. Cranial anatomy of the earliest marsupials and the origin of opossums. PLoS ONE 4: e8278.

Jackson S. 2003. Australian Mammals: Biology and Captive Management. CSIRO Publishing, , Collingwood, Victoria. 524 p.

Jones C & Parish S. 2005. Field Guide to Australian Mammals. Steve Parrish Publishing group, Archerfield, Queensland. 215 p.

Jones M, Dickman CR & Archer M (eds). 2003. Predators with pouches: the biology of carnivorous marsupials. CSIRO Publishing, Collingwood, Victoria. 486 p.

Kirsch JAW & Waller PF. 1979. Notes on the trapping and behavior of the Caenolestidae (Marsupialia). Journal of Mammalogy 60: 390–437.

Ladevèze S, Muizon C de, Beck RM, Germain D & Cespedes-Paz R. 2011. Earliest evidence of mammalian social behaviour in the basal Tertiary of Bolivia. Nature 474: 83–86.

Maddison, W. P. & D.R. Maddison. 2017. Mesquite: a modular system for evolutionary analysis. Version 3.31 http://mesquiteproject.org

Menkhorst P & Knight F. 2013. A field guide to the mammals of Australia. 3rd edition. Oxford University Press, Oxford. 274 p.

Muizon C de & Argot C. 2003. Comparative anatomy of the Tiupampa didelphimorphs; An approach to locomotory habits of early marsupials; pp. 43–62 in M Jones, C Dickman, & M Archer (eds), Predators with Pouches: The Biology of Carnivorous Marsupials. CSIRO Publishing, Collingwood, Victoria.

Myers TJ. 2001. Prediction of marsupial body mass. Australian Journal of Zoology 49: 99-118.

Richardson K. 2012. Australia's amazing kangaroos. CSIRO Publishing, Collingwood, Victoria. 234 p.

Sánchez-Villagra MR, Ladevèze S, Horovitz I, Argot C, Hooker JJ, Macrini T, Martin T, Moore-Fay S, Muizon C de, Schmelzle T & Asher RJ. 2007. Exceptionally preserved North American Paleogene metatherians: adaptations and discovery of a major gap in the opossum fossil record. Proceedings of the Royal Society, Biology Letters 3: 318–322.

Tyndale-Biscoe H. 1973 [2005]. Life of marsupials. CSIRO Publishing, Collingwood, Victoria. 442 p.

Westerman, M., Krajewski, C., Kear, B. P., Meehan, L., Meredith, R. W., Emerling, C. A., & Springer, M. S. (2016). Phylogenetic relationships of dasyuromorphian marsupials revisited. Zoological Journal of the Linnean Society, 176(3), 686-701.

Chapter 2

Anatomy of the membranous semicircular ducts of the inner ear does not reflect the subterranean lifestyle in mammals

Anatomy of the membranous semicircular ducts of the inner ear does not reflect the subterranean lifestyle in mammals.

Charlène Selva[1], Romain David[2], Damien Germain[1], Alexander Stoessel[2,3], Stéphane Peigné[1] & Sandrine Ladevèze[1]

[1] Centre de Recherches sur la Paléobiodiversité et les Paléoenvironnements (CR2P, UMR 7207), Sorbonne Universités-MNHN, CNRS, UPMC-Paris 6, Muséum national d'Histoire naturelle, CP38, 57 rue Cuvier F-75005, Paris, France.

[2] Department of Human Evolution, Max Planck Institute for Evolutionary Anthropology, Deutscher Platz 6, 04103 Leipzig, Germany.

[3] Phyletisches Museum, Vor dem Neutor 1, 07743 Jena, Germany.

Correspondence and requests for materials should be addressed to C.S. (email: charlene.selva@edu.mnhn.fr) or R.D. (email: romain_david@eva.mpg.de).

Introduction

Across the mammalian clade, around 300 species present a subterranean ecology: they spend most of their lives in self-constructed burrows wherein they do all their activities (forage, breed, rest) (Nevo, 1999; Begall et al., 2007). The subterranean lifestyle is a convergent trait shared by various clades of mammals, among which marsupials (the marsupial mole), xenarthrans (the pink fairy armadillo), afrotherians (the golden moles), lipotyphlans (e.g. the European mole) and rodents (e.g. the pocket gophers and the mole rats). These subterranean mammals exhibit strong body adaptations to life underground such as a reduction of the eyes, tube-like body shape, loss of the outer ear, or hypertrophy of the forelimb (Nevo, 1999). Many comparative studies of the auditory region have focused on subterranean mammals, especially on the middle ear (e.g., Koyabu et al. 2017; Mason et al.,2001, 2016) or on the acoustic communication (e.g., Begall & Burda, 2006; Pleštilová et al., 2016; Gerhardt et al., 2017) in the objective to understand their adaptations to this particular environment. However, the inner ear (which contains the sensory organ of balance and spatial orientation) of subterranean mammals has not been investigated in many works. In the past, only Lindenlaub et al. (1995) and McVean (1999) studied the inner ear and especially the membranous vestibular system to characterize its adaptation to subterranean lifestyle (but their works were restricted to three subterranean mammals and one specimen of comparison). More recently, the advent of micro-computed tomography provides an easier

way to reach hidden anatomical structures in-situ and in three dimensions, which led to generalize studies on the osseous inner ear of mammals, including subterranean species in the sample for comparison (Pfaff et al., 2015; Billet et al., 2012) or even more specific work on the osseous inner ear of subterranean mammals (Crumpton et al., 2015). These last studies focused on the bony semicircular canals rather than the delicate membranous ducts they enclose, which however is likely to provide the essential and relevant information for functional analyses.

Previous studies on the mammalian inner ear morphology concluded that there was a link between the morphology of the semicircular canals and the locomotion (e.g. Spoor et al., 2007; Pfaff et al., 2015, 2017; Billet et al. 2012). Same assumptions were addressed on moles (Crumpton et al., 2015; Lindenlaub et al., 1995; McVean, 1999), assigning an ecological signal to certain anatomical structures interpreted as adaptations to the subterranean lifestyle.

The main goal of our study is to test if the anatomy of the membranous semicircular ducts reflects the subterranean lifestyle in mammals. To do so, we firstly investigate the detailed anatomy of the membranous semicircular duct system of five subterranean species belonging to five different clades. Thanks to tissue staining and X-ray micro tomography, the use of the new method described by David et al. (2016) allows us to obtain the complete membranous labyrinth in-situ and in 3D. Secondly, the 3D shapes of the membranous semicircular duct system of the five subterranean mammals are compared, through Geometric Morphometrics analyses, to 25 membranous semicircular ducts of non-subterranean mammals, in order to characterize an eventual particular shape as adaptation to the subterranean lifestyle.

Material and Methods

Five subterranean species and specimens of comparison

The present study focuses on five subterranean species of mammals from five distant clades: the Hottentot golden mole (*Amblysomus hottentotus*), the pink fairy armadillo (*Chlamyphorus truncatus*), the naked mole-rat (*Heterocephalus glaber*), the marsupial mole (*Notoryctes typhlops*), and the common European mole (*Talpa europaea*). These five species will be named as 'moles' in this work. Further information relative to systematics, collection numbers, scanning modes and voxel sizes are listed in the Table 1.

Table 1: Information concerning the five subterranean mammal species selected for this study.

Species Name	Common Name	Clade	N° specimen and institution	Scanning mode	Voxel size
Amblysomus hottentotus	Hottentot golden mole	Afrotheria	Phyletisches Museum (Jena) Mam.5550.42402	Stain CT-scan (MPI Leipzig)	6.03 um
Chlamyphorus truncatus	pink fairy armadillo	Xenarthra	Muséum national d'Histoire naturelle (Paris) CG.1903-82	Synchrotron light scan (ESRF Grenoble)	6.23 um
Heterocephalus glaber	naked mole-rat	Rodentia	Muséum national d'Histoire naturelle (Paris) CG.1884.1778	Synchrotron light scan (ESRF Grenoble)	6.23 um
Notoryctes typhlops	marsupial mole	Marsupialia	Muséum national d'Histoire naturelle (Paris) CG.1893.473	Synchrotron light scan (ESRF Grenoble)	6.23 um
Talpa europaea	common European mole	Eulipotyphla	Research collection of Romain David	Stain CT-scan (MPI Leipzig)	5.12 um

The sample of comparison is composed of 25 mammal species (Romain David, personal communication). The species list of the total sample is available in SI-2. The phylogenetic relationships and divergence time between the species are based on the 'timetree' project (Kumar et al., 2017) (the nexus file is available as Online Material). The total sample is composed of 16 Euarchontoglires, 9 Laurasiatheria, 1 Afrotheria, 1 Xenarthra, 2 Marsupialia and 1 Monotremata.

Accessing and describing the semicircular duct system of the membranous labyrinth

The methodology of David et al. (2016) is followed in this study because it is the only way to access and provide a formal description of the membranous inner ear. We present here a resume of the protocol used for the present study of the membranous inner ear of five subterranean mammals, further and more complete details being provided in the original publication and its supplementary information (David et al., 2016).

1-In-situ visualization of the membranous vestibular system

To access to the delicate membranous inner ear, we used two different ways of scanning. The pink fairy armadillo, the naked mole-rat and the marsupial mole specimens were scanned with the Synchrotron light with Propagation Phase Contrast imaging at high resolutions, at the European Synchrotron Radiation Facility based in Grenoble (ESRF). The Hottentot golden mole and the common European mole were scanned with classic X-ray micro-tomography at the Max Planck Institute for Evolutionary Anthropology based in Leipzig. These two specimens were previously immersed in a stain solution with phosphotungstic acid (PTA) that allowed an efficient visualization of the different parts of the membranous inner ear (Fig. 1). All details concerning the staining protocol and the CT-scan parameters are available in David. et al. (2016). The resolution with which each specimen was scanned is indicated in the table 1.

2-Segmenting the semicircular duct system

The segmentation of the semicircular duct system of each specimen was made with the AVIZO software (licence 7.1 at MPI, Leipzig and licence 9.1 at MNHN, Paris). This software allows exploiting heavy data and providing efficient tools for segmenting. The segmentation consists in isolating the membranous labyrinth from the surrounding tissues. As indicated in the method of David et al. (2016), the segmentation here corresponds to the careful selection of the endolymph volume all along the semicircular ducts without including surrounding membranes into the selection (Fig. 1). At the end of the segmentation, we obtain a STL file of the 3D object of the complete semicircular duct system.

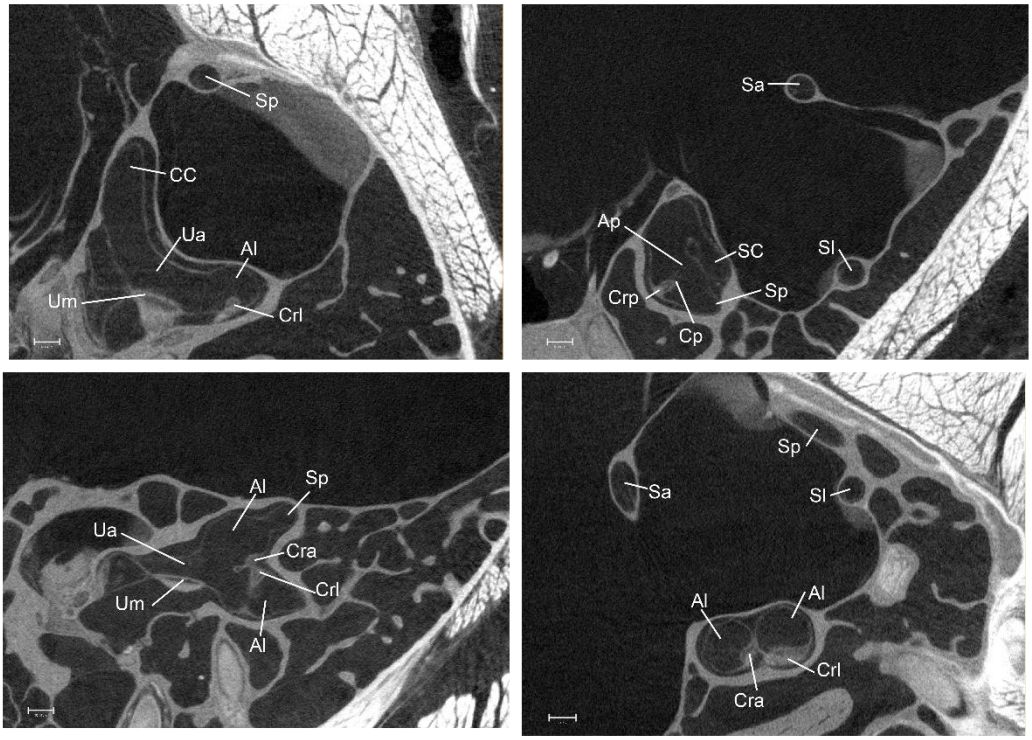

Figure 1: Raw visualizations of stained membranous labyrinths through micro-CT scanning.

Soft-tissues structures are visible inside the bony labyrinth of the Hottentot golden mole specimen. Aa, Ap, Al, anterior, posterior and lateral ampullae; Ca, Cp, Cl, anterior, posterior and lateral cupulae (artificially shrunk); CC, common crus; Cra, Crp, Crl, anterior, posterior and lateral cristae ampullares; Sa, Sp, Sl, slender parts of the anterior, posterior and lateral semicircular ducts; SC, simple crus; Ua, anterior utriculus; Um, macula utriculi.

3-Preparation of the input data required by the Ariadne Software

From the complete volume of the membranous inner ear, we split the semicircular duct system into anatomical parts, required as input data by the 'Morphometry Auto Batch' function of Ariadne© (David et al., 2016). Performed with Geomagic Studio 12 Software, this cutting consists in dividing the semicircular duct system into the 11 parts that will be used to create 12 surface files and 11 volume files saved in STL format. These parts, presented in figure 2, are the slender parts of the anterior, posterior and lateral ducts, the common crus, the simple crus (*Crus membranaceum simplex*), the common, anterior and posterior utricular parts, and the anterior, posterior and lateral ampullary parts.

The second type of input data required by the 'Morphometry Auto Batch' of Ariadne is the coordinates of the central streamlines. This step consists in registering the coordinates of the central streamlines passing through each semicircular duct thanks to 3D landmarks placed on

the 3D skeleton, which is calculated from the complete volume of the membranous vestibular system. The placement of the 3D landmarks is done with AVIZO and their set-up is presented in the figure 2.

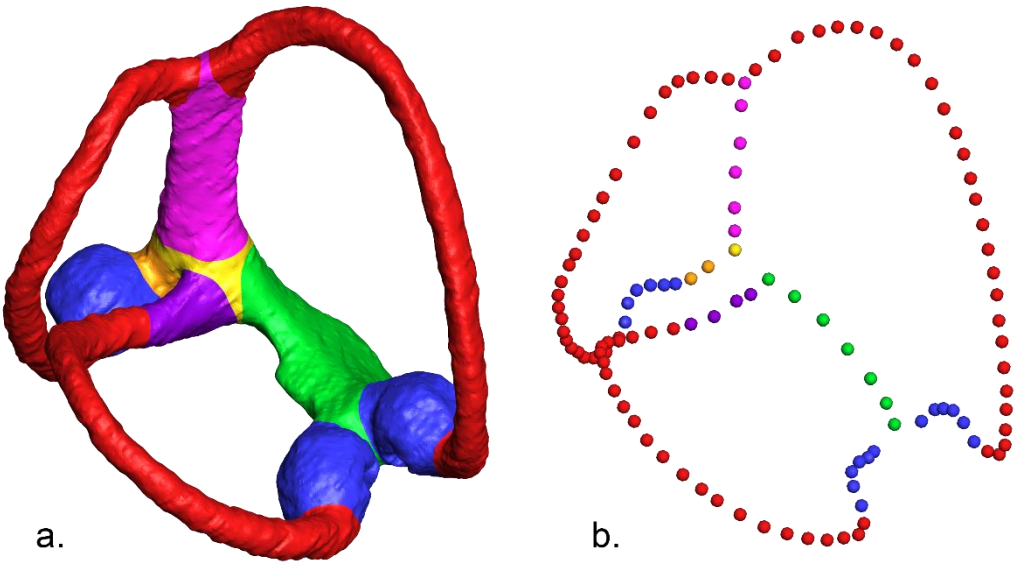

Figure 2: Input data required by the 'Morphometry Auto Batch' of Ariadne. (a) The right semicircular duct system of the Hottentot golden mole specimen is cut in 11 coloured anatomical parts, required as separate STL files. (b) The landmarks set registers the pathway of the central streamlines of the ducts. Colours: red, slender ducts; blue, ampullae; pink, common crus; purple, simple crus; green, anterior utricle; orange, posterior utricle; yellow, common utricle.

4-Obtaining formalized morphological parameters

The prepared data are analysed through the Ariadne Software and especially the 'Morphometry Auto Batch'. This batch provides formalized morphological parameters on the membranous semicircular duct system, such as:

- the volume of endolymph that is contained inside each relevant anatomical part of the semicircular duct system,
- the surface area of the inner walls of each anatomical part of the semicircular ducts,
- the maximal area enclosed by the central streamline of each semicircular duct,
- the length of the central streamlines running inside each part of the semicircular duct system,
- the mean cross-sectional radius of the endolymphatic volume contained inside the slender part of each semicircular duct,
- the mean cross-sectional areas of the cupulae.

All the results that will be presented here are the output data of the 'Morphometry Auto Batch' of the Software Ariadne. The other batches offered by Ariadne (such as those that provide functional parameters) are not used in this study.

We used the R software (R Core Team, 2014) to perform phylogenetic generalized linear models (PGLS) on the formalized morphological parameters of the 30 mammal species of the study to look for a potential influence of the allometry (centroid size) and/or the phylogeny (the R script is available in SI-9 and as Online Material). Morphological parameters were corrected and computed without the centroid size effect for the 30 species and for the reconstructed mammal morphotype, which can be compared to the morphology of the five subterranean mammals.

5-Quantifying shape with Geometric Morphometrics

The 3D landmarks placed on the 3D skeleton of each specimen can be compared, through Geometric Morphometrics Analyses, to understand the morphological diversity of the membraneous inner ear. Beforehand of any statistical comparison, prerequisite steps are needed: the set-up of landmarks was made with the AVIZO software, and the control and resampling of the number of sliding landmarks was made with the MORPHOTOOLS software (Specht 2007; Lebrun 2008). A total of 6 type-I landmarks are placed on each 3D model (Fig. 3): one at the common utricule (Uc), one at the end of the anterior utricule corresponding to the junction of the anterior and lateral semicircular streamline (Ua_e), one at the center of the anterior ampulla and above the anterior crista (Cr_a), one at the center of the posterior ampulla and above the posterior crista (Cr_p), one at the center of the lateral ampulla and above the lateral crista (Cr_l), and one at the beginning of the common crus corresponding to the junction of the anterior and posterior semicircular streamline (CC_b). The organization of the total 132 landmarks (126 sliding landmarks and 6 type-I landmarks) is presented in figure 3. The matrix of landmark coordinates for the 30 specimens of the study is explained in SI-1 and SI- 2, and is available as Online Material.

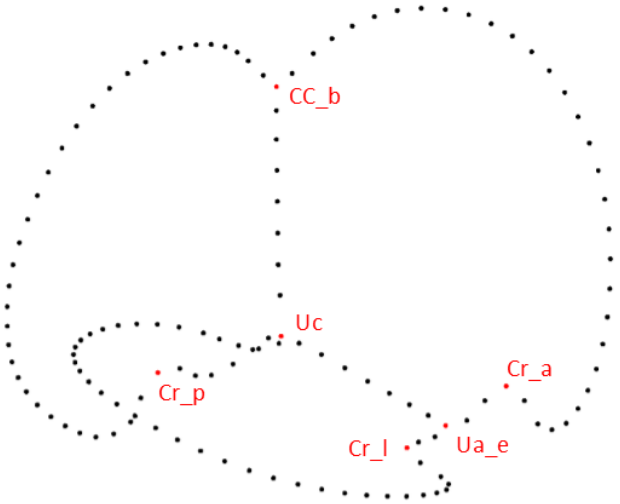

First landmark	Final landmark	Number of sliding Landmarks
Uc	Ua_e	7
Ua_e	Cr_a	2
Cr_a	CC_b	30
CC_b	Uc	7
Ua_e	Cr_l	2
Cr_l	Uc	38
Uc	Cr_p	6
Cr_p	CC_b	34

Figure 3: Organisation of the 126 sliding landmarks and 6 fixed landmarks presented on the consensus shape.
In red, the 6 fixed landmarks placed on homologous anatomical position. In black, the sliding landmarks between the fixed landmarks. The number of sliding landmarks between two fixed landmarks is indicated in the table. In total, each semicircular duct is defined with 50 landmarks.

The data analysis was performed with the R software (R Core Team, 2014) and the R script is available in SI-3 and as Online Material. A scheme of the entire protocol is provided in figure 4. A generalized Procrustes Analysis (GPA: Gower 1975; Rohlf & Slice 1990) was performed on the fixed and sliding landmarks using the library 'Geomorph' (Adams & Otarola-Castillo, 2013; Sherratt, 2014). The semilandmarks slides were based on the minimizing bending energy (Bookstein, 1997). Phylogenetical signal Kmult (multivariate K-statistic) was performed on the set of Procrustes-aligned specimens (Adams, 2014; Blomberg et al., 2003). This statistic test estimates the degree of phylogenetic signal present in the shape data for a given phylogeny. The higher the *K*-value is, the stronger the phylogenetic signal. Principal Component Analysis on the 'raw' shapes was performed in order to visualize the distribution of the 30 species in the morphospace and specifically spot the subterranean mammals compared to the other mammal species. The 'plotTangentSpace' function performs a PCA of shape variation. Associated to the PCA, the function 'phylo4d' combines the phylogenetic tree with the PCA axes. It improves the visualization of the phylogeny impact on the shape diversity. Using the tree with branch lengths (OM-4), the 'plotGMPhyloMorphoSpace' function of 'geomorph' displays the ancestral state for each node of the phylogenetic tree and more particularly to

visualize the mammal morphotype configuration corresponding to the first node of the tree. The mammal morphotype is plotted *a posteriori* on the graphical representations of PCA. The two-sample Hotelling's T-squared test (Curran, 2013) was performed to test for the difference in two multivariate means. In our study, the test was performed on the mean of the specimens' scores to answer two questions: does the shape distribution of the semicircular duct system of moles a) significantly differ from the shape distribution for mammals and b) significantly differ from the shape distribution for non-subterranean mammals.

At first, the question (a) could appear useless and not relevant, because, obviously, the shape variation of moles is confined within the total variation of mammals. But the Hotelling test compares multivariate means, here the mean of the specimens' projections, the comparison groups being moles versus mammals. Thereby, the question we ask is: does the mean shape distribution of moles differs from the mean shape distribution of mammals. Moles being mammals, they remain included in the total group because all mammalian species (of the study) contribute to obtain the mean of the mammals' projections. Hypothetically, if moles show slightly different shapes from the entire group of mammals, there will not be significantly different means of the two compared groups (although the mean of moles could be significantly different from the mean of non-moles). If moles show strong different shapes from the total group mammals, the resulting mean could be significantly different from mean of the total group (Fig. 5).

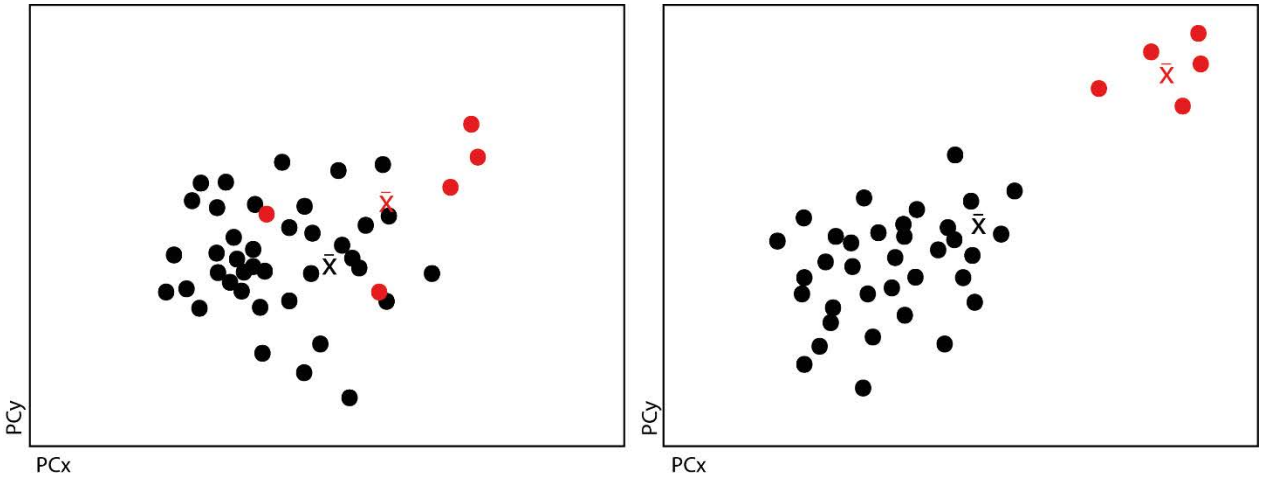

Figure 5: Theoretical example of the results of two PCAs showing alternative distributions of the specimen in the PC space. Left, the five moles (red) do not have a significantly different mean of their shape scores compared to the total group mammals (red+black). Right, the five moles (red) do have a significantly different mean of their shape scores compared to the total group mammals.

Because the main goal of the study is to find if there is a morphology of the inner ear specific of the subterranean lifestyle, we decided to remove parameters that can play a role in the morphology of the inner ear such as the phylogeny and the allometry. The visualization of size-shape pattern (allometry) was checked with the function 'procD.allometry' which quantifies the relative amount of shape variation attributable to covariation with size. For our study, the single independent continuous variable representing size is the centroid size calculated during the GPA. We are focusing on the size of the ear and not on the size of the species. Procrustres ANOVA was performed to quantify the relative amount of shape variation attributable to the centroid size and to calculate the corresponding residuals, which are used to compute the adjusted shapes. These new coordinates represent the shape without the size effect. Phylogenetical signal Kmult (multivariate K-statistic) was performed a second time on this new set of adjusted shapes. PCA and corresponding two-sample Hotelling's T-squared tests were performed on these new adjusted shapes. Using the tree calibrated with branch lengths (OM-7), the 'plotGMPhyloMorphoSpace' function of 'geomorph' displays the ancestral state for each node of the phylogenetic tree, which that allows us to compare the 30 specimens of the study to the mammal morphotype, corresponding to the first node. The mammal morphotype is plotted *a posteriori* on the graphical representations of the PCA. The 3D morphology of the membraneous inner ear of the mammal morphotype is also reconstructed thanks to the 3D landmarks. The mammal morphotype conformation thus obtained corresponds to an allometry-adjusted shape and is relevant to be compared with size-effect free 3D conformation of the five moles.

To take into consideration the role of the phylogeny in the shape, we performed a phylogenetic PCA on the new adjusted shapes with the function 'phyl.pca' from the package 'phytools' (Revell, 2012). The value of the argument lambda requested by the function was calculated with the prediction model of Revell (2012) with the parameter Kmult previously calculated. The function will aim to highlight the diversity within the clades. The two-sample Hotelling's T squared tests were not performed on the scores directly. To keep considering the phylogeny, we performed these tests on residuals between the terminal taxa and the nearest nodes (see specific explanations in the Results section).

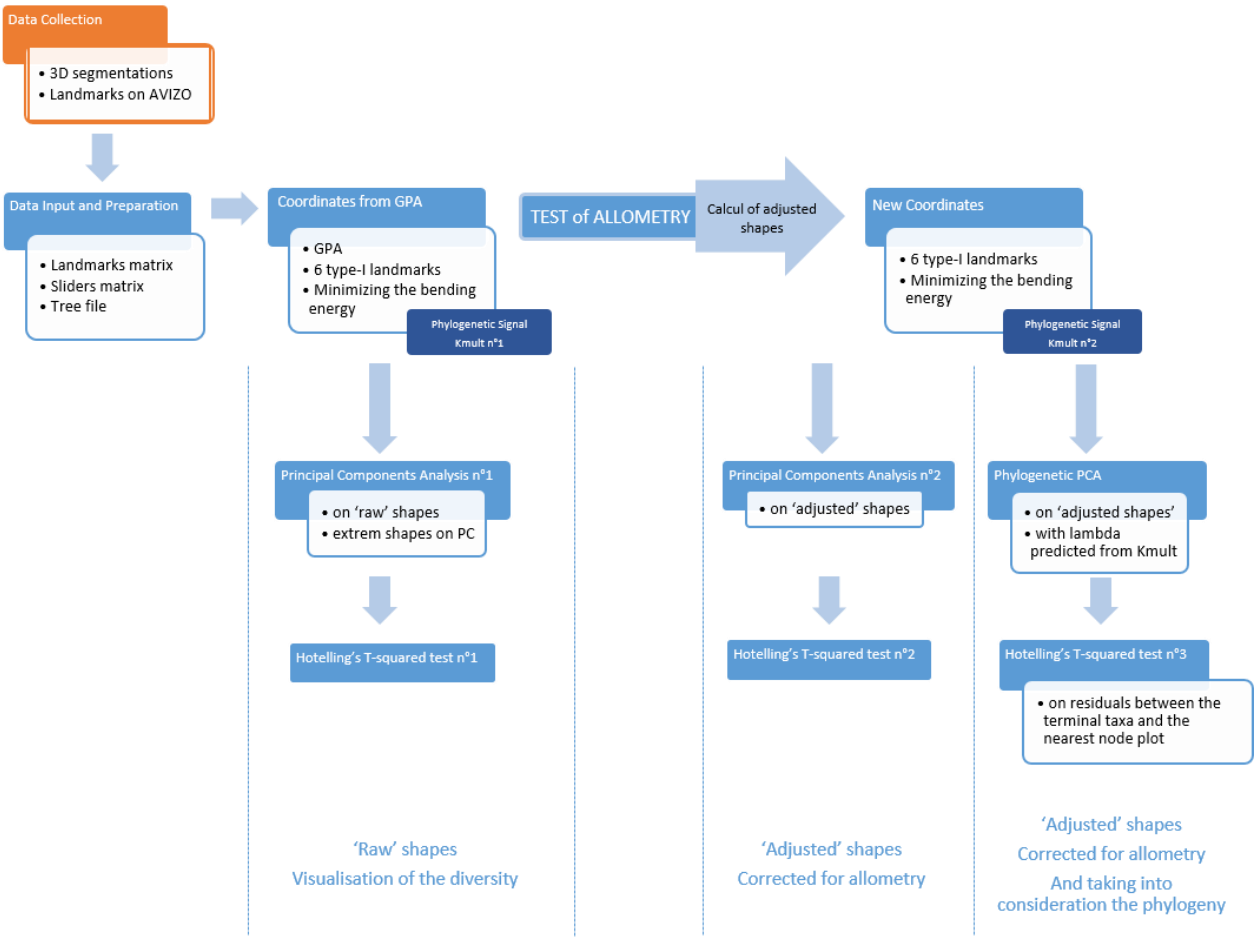

Figure 4: Simplified diagram of the Geometric Morphometrics analysis.

Results

1- Comparative Anatomical Description of the semicircular duct system

The nomenclature used here to describe and compare the semicircular duct system is based on previous anatomical (e.g., Ekdale, 2013, 2016; David, 2011) and methodological (David et al., 2016) studies of the mammalian inner ear.

Contained inside the bony labyrinth of the inner ear, itself contained inside the paired mammalian ear bone –the petrosal bone-, the semicircular duct system is part of the sensory organ of balance and essential for navigation. It is a component of the *pars inferior* of the endolymphatic labyrinth or membranous labyrinth. It is composed of three ducts: the anterior, the posterior and the lateral semicircular duct.

The anterior semicircular duct is composed of five structures: the anterior ampulla, the anterior slender part, the common crus, the common utricule and the anterior utricule. The posterior semicircular duct is composed of five structures: the posterior ampulla, the posterior slender part, the common crus, the common utricule and the posterior utricule. The lateral semicircular duct is composed of five structures: the lateral ampulla, the lateral slender part, the simple crus, the common utricule and the anterior utricule. Some structures are in common between the ducts themselves: the common utricule composes the three ducts; the common crus is in common between the anterior and posterior ducts; the anterior utricule is in common between the anterior and the lateral ducts.

The anterior and posterior semicircular duct connect though the common crus. The anterior and lateral semicircular duct connect though the anterior utricule. The anterior utricule is the common structure where the anterior and lateral ducts merge. The *macula utriculi* is situated anteriorly on the ventral side of this structure. It detects horizontal linear accelerations of the head. The posterior utricule contains the *macula neglecta*. The ampullae are ovoid structures with a catenoidal-shaped deformation on their floor called *crista ampullaris.* From this deformation, the gelatinous membrane -called cupula- fills the ampulla transversally above the crista. The *crista ampullaris* is covered by sensory epithelium that is mainly composed of mechanosensory hair cells captured in the cupula. As the head rotates, movement of the endolymph within the semicircular ducts will displace the cupula, thereby exciting the hair cells (Hillman & McLaren, 1979; Rabbitt et al., 2009).

Structure by structure, we provide here a comparative anatomical description of the semicircular duct system of the five subterranean mammals of the study (Fig. 6). The morphological parameters for the five species are available in Table 2.

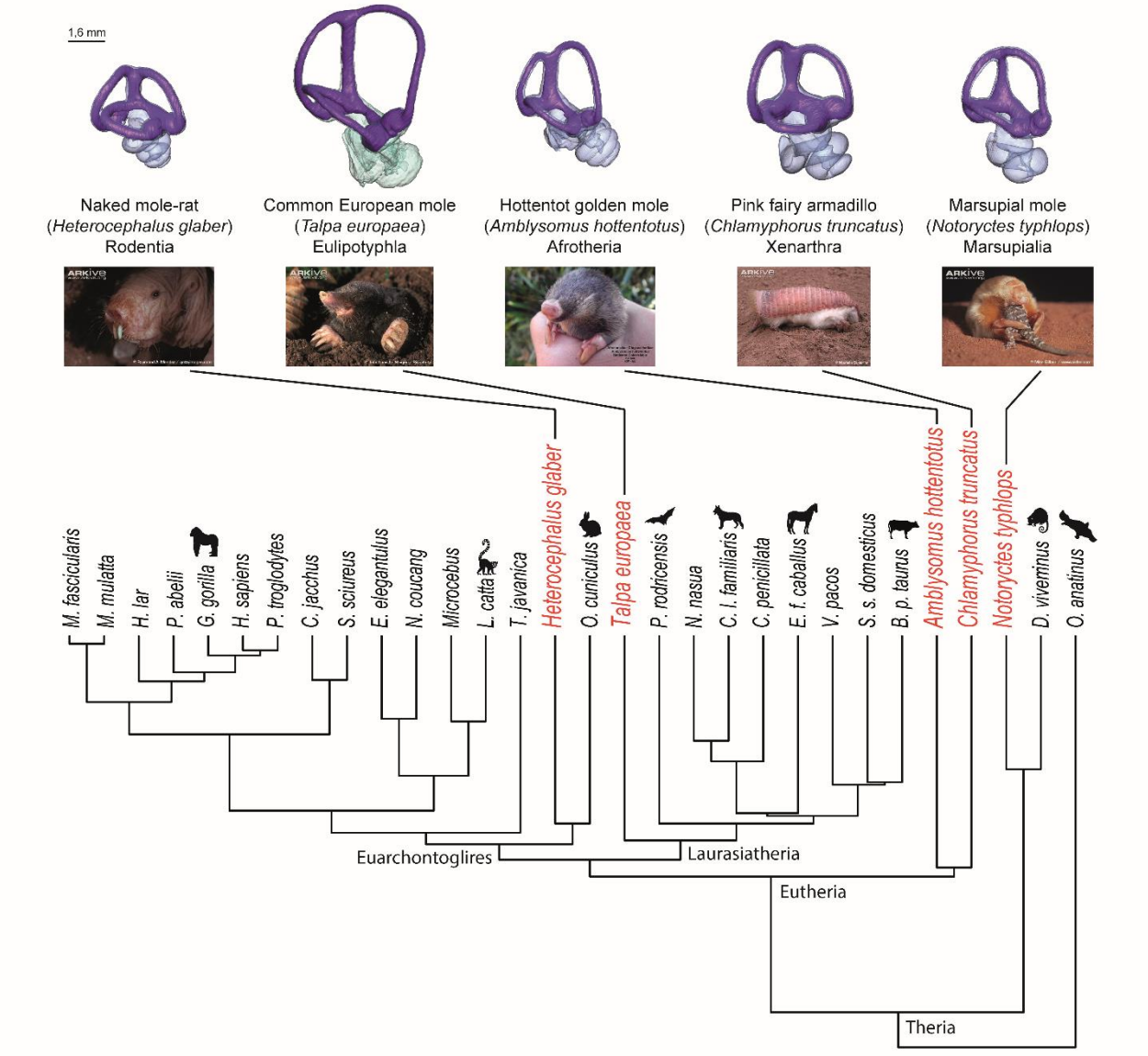

Figure 6: Three-dimensional visualization of the segmented vestibular system of the five subterranean species.

The membranous vestibular system in purple is here presented in the transparent osseous inner ear in blue for the five subterranean species. On the same scale. The phylogeny presents the 25 other mammal species used for comparison. Note the convergence of the subterranean lifestyle in mammals.

The general organization of the membranous inner ear is similar for the five subterranean mammals (Fig. 6). It is composed of three semicircular ducts: the anterior, the posterior and

the lateral semicircular duct presented in-plane views with details of their anatomy in the figure 7.

The total volume of the endolymph of the five species is comprised between 0.95 µl for the Hottentot golden mole and 1.90 µl for the pink fairy armadillo. The inner ear of the European mole is much finer than the inner ear of the marsupial mole, the pink fairy armadillo and the naked mole-rat. For these three species, their centroid size is smaller than for the European mole and the total volume is larger than for the European mole. Thereby these three inner ears look thicker (Fig. 7). Though the European mole presents the largest centroid size, its inner ear has a small total volume of 1.10 µl. The general endolymph distribution along the ducts is globally similar but presents some variability.

For all the five species, the anterior semicircular duct contains the largest volume of endolymph between 0.54 µl for the Hottentot golden mole and 0.98 µl for the pink fairy armadillo, which represents on average 52.6% of the total volume (variability between 46.58% and 57.02%). The lateral semicircular duct contains an intermediate volume of endolymph between 0.47 µl for the Hottentot golden mole and 0.90 µl for the pink fairy armadillo, which represents on average 46.45% of the total volume (variability between 42.84% and 49.54%). For all the five species, the posterior semicircular duct contains the smallest volume of endolymph between 0.36 µl for the Hottentot golden mole and 0.81 µl for the pink fairy armadillo, which represents on average 38.54% of the total volume (variability between 36.28% and 42.53%).

For the five species, the anterior semicircular duct is the longest with a minimum length of 5.76 mm for the naked mole rat and a maximum length of 8.65 mm for the European mole. These lengths are positively correlated to the centroid size: the larger the centroid size, the longer the length. For the Hottentot golden mole, the European mole and the naked mole-rat, the lateral semicircular duct is the second longest canal and the posterior semicircular duct is the smallest. On the contrary, for the pink fairy armadillo and the marsupial mole, the posterior semicircular duct is the second longest canal and the lateral semicircular duct is the smallest. The European mole presents the longest anterior and lateral semicircular ducts (respectively 8.65 mm and 6.95 mm) and the pink fairy armadillo has the longest posterior semicircular duct (6.98 mm). These lengths are linked to the enclosed area by the semicircular

ducts: the European mole presents the biggest anterior and lateral enclosed areas (respectively 5.16 mm² and 3.11 mm²) and the pink fairy armadillo the biggest posterior enclosed area (3.34 mm²). The naked mole rat exhibits the smallest length of anterior semicircular duct (5.76 mm), the Hottentot golden mole the smallest length of posterior semicircular duct (5.17 mm), and the marsupial mole the smallest length of lateral semicircular duct (5.40 mm). Except for the lateral semicircular duct, these lengths are linked to the enclosed area by the semicircular duct: the naked mole rat presents the smallest anterior enclosed area (2.23 mm²) and the Hottentot golden mole the smallest posterior enclosed area (1.81 mm²). For the lateral enclosed area, the naked mole rat has the smallest lateral enclosed area (1.84 mm²) but not the marsupial mole (1.93mm²). Because the marsupial mole exhibits a smaller lateral semicircular duct length and a larger enclosed area than that of the naked mole rat, the shape of the lateral enclosed area of the marsupial mole is more circular than that of the naked mole rat. The semicircular ducts are more or less rounded. For example, the lateral semicircular duct of the European mole is circular; on the contrary, the anterior semicircular duct of the naked mole rat is stretched and looks like an ellipse.

For the five species, the planes of the lateral and posterior semicircular ducts form an angle superior to 90 degrees: between 93.32° for the naked mole rat and 100.28° for the European mole. They are the most obtuse angles between the ducts planes except for the marsupial mole for which this is the angle between the anterior and the posterior semicircular duct planes. For all the species, the planes of the anterior and lateral semicircular ducts form the most acute angle, between 68.21° for the marsupial mole and 85.59° for the naked mole rat. The planes of the anterior and posterior semicircular ducts form an angle between 86.98° for the marsupial mole and 99.17° for the naked mole rat.

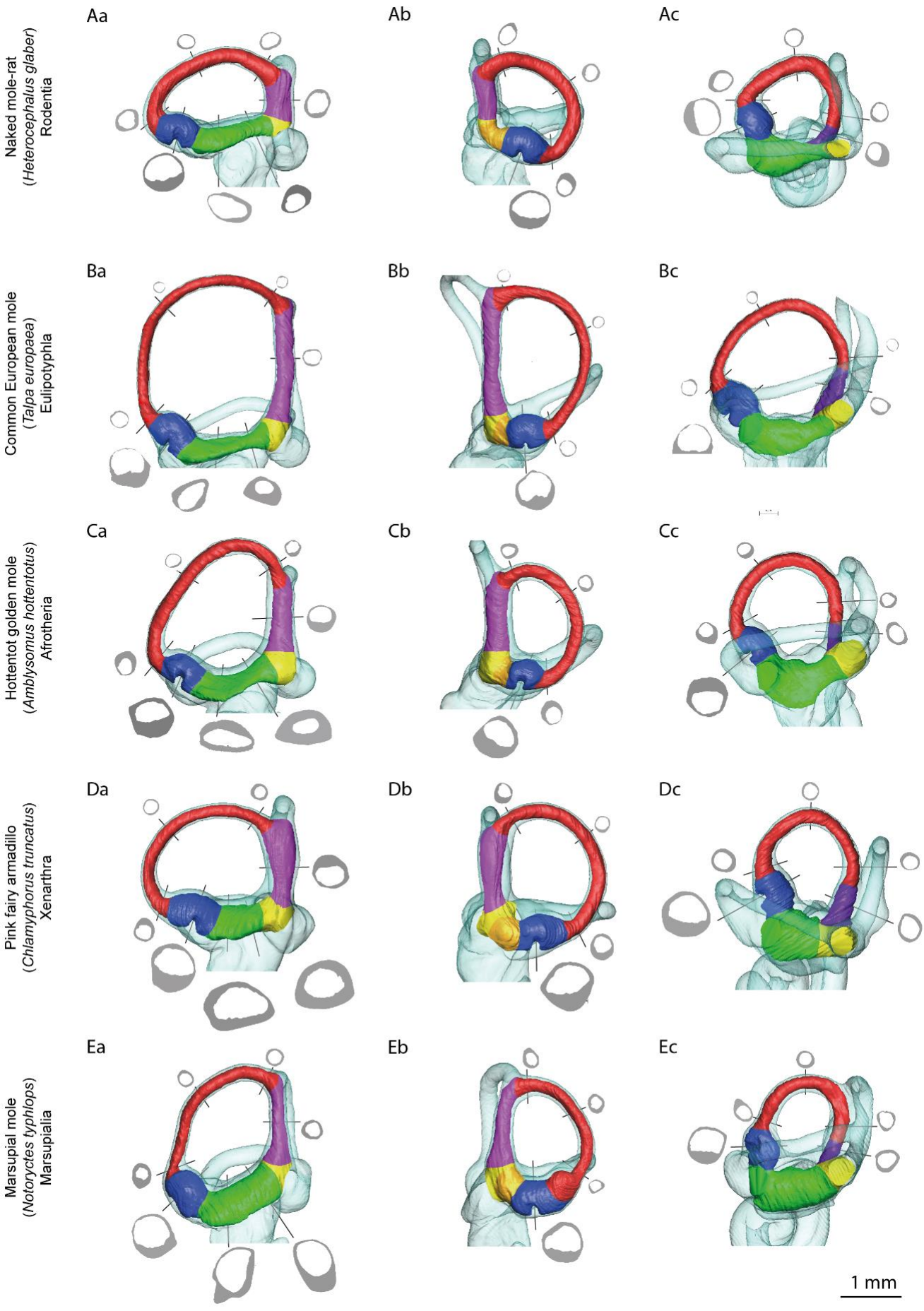
Naked mole-rat
(Heterocephalus glaber)
Rodentia
Common European mole
(Talpa europaea)
Eulipotyphla
Hottentot golden mole
(Amblysomus hottentotus)
Afrotheria
Pink fairy armadillo
(Chlamyphorus truncatus)
Xenarthra
Marsupial mole
(Notoryctes typhlops)
Marsupialia
Aa
Ab
Ac
Ba
Bb
Bc
Ca
Cb
Cc
Da
Db
Dc
Ea
Eb
Ec
1 mm

Figure 7: In-plane views of the semicircular ducts. From left to right, the anterior (a), posterior (b) and lateral (c) semicircular ducts of the naked mole-rat (A), the common European mole (B), the Hottentot golden mole (C), the pink fairy armadillo (D) and the marsupial mole (E). The semicircular ducts are presented here in-plane views by aligning the maximum response axis of each duct with the viewing direction (output of the 'Morphometry Auto Batch' of Ariadne Software). Slender ducts are shown in red, ampullae in blue, the common crus in pink, the simple crus in purple, the anterior utricle in green, the posterior utricle in orange and the common utricle in yellow. Sixteen cross-sections are presented with the endolymph in white and the perilymph in grey. At the same scale (1mm).

The common crus contains between 6% and 11 % of the total volume. The marsupial mole presents the thinnest common crus with 0.08 µl. For this species, the utricule side of the common crus is larger than the slender side. On the contrary, the Hottentot golden mole presents the common crus with the biggest volume of endolymph (0.17 µl) and the repartition along the common crus is particular: for this species, the slender part of the common crus is much larger than the utricule side. The three other species present a common crus with a uniform distribution of the volume along the structure; in other words, the circumference is constant. The mean cross-sectional area of the common crus is between 0.064 mm^2 for the European mole and 0.123 mm^2 for the pink fairy armadillo; the naked mole rat also exhibits an important cross-sectional area (0.110 mm^2). The membranous structure along the common crus fills almost the entire space in the osseous inner ear for the naked mole rat, the European mole and the marsupial mole. For the Hottentot golden mole and the pink fairy armadillo, the membranous structure of the common crus does not fill the entire space of the osseous inner ear. The longer the total length of the semicircular duct increases, the longer the common crus is; except for the marsupial mole that has a small length of the common crus compared to the total length of the anterior semicircular duct. The common crus represents about 20% of the length of the anterior semicircular duct. There is an essential exception for the naked mole rat for which the common crus represents only 13.20 % of the total anterior semicircular duct. For this specimen, the small length of the common crus drags down the slender part and gives an elliptical shape of the anterior semicircular duct.

The anterior utricule volume contains between 17.32% for the naked mole rat and 30.79% for the marsupial mole of the total volume. The marsupial mole and the pink fairy armadillo

present a large and thick anterior utricule. For this two species, the anterior utricule has a coarse shape of potato without distinct structures. Here the membraneous structure fills a good part of the osseous structure without major changes along the anterior utricule. For the other three species, the Hottentot golden mole, the European mole and the naked mole rat, the anterior utricule is thinner and longer. It is composed of two different parts: a narrow area closed to the crus commune and a spread area closed to the ampullae. The latter is the spot of the macula.
The posterior utricule contains between 0.06 µl (4.75%) to 0.22 µl (11.79%).

The ampullae contain between 0.08 µl for the posterior ampulla of the Hottentot golden mole and 0.23 µl for the posterior ampulla of the pink fairy armadillo. Generally, the ampullae represent about 10% of the total volume of endolymph with a variability between 8.27% and 13.64%. There is no pattern defining which one of the anterior, posterior or lateral ampullae is the largest or the smallest. For the three ampullae, the Hottentot golden mole exhibits the smallest ampullae: they contain between 0.08 µl and 0.09 µl, being the smallest percentage between 8.27% and 9.59% of the total volume. In absolute value, the pink fairy armadillo has the biggest ampullae: they contain between 0.18 µl for the lateral ampulla and 0.23 µl for the posterior ampulla. In percentage, the European mole has the biggest anterior and lateral ampullae with respectively 12.25% and 13.37% of the total volume; the marsupial mole has the biggest posterior ampulla with 13.64% of the total volume. The lateral ampulla of the marsupial mole shows a particular orientation: the crista is less ventrally oriented than the other species, its orientation is more lateral.

The slender parts show really diverse morphologies. They can be curved (e.g., the lateral of the pink fairy armadillo) or stretched (e.g., the anterior of the Hottentot golden mole). The volume in the slender parts represents around 10% of the total volume: 0.09 (9.06%) for the posterior slender part of the Hottentot golden mole to 0.15µ (12.37%) for the lateral slender part of the naked mole-rat. The slender parts represent around 50% of the total length of the duct: 2.96µ (44.33%) for the length of the anterior slender part of the marsupial mole to 3.04µ (58.31%) for the length of the posterior slender part of the naked mole-rat. The slender parts exhibit different kind of thickness: the thinnest is the anterior slender part of the European mole (0.026 mm^2) and the thickest is the lateral slender part of the naked mole-rat. Regarding

the cross section (Fig. 7), the membranous slender parts fill almost entirely the space offered by the osseous inner ear. This is really remarkable for the European mole for which there is no more space around the membranous semicircular duct. The insertions of the slender parts at the top of the common crus show different patterns: for the pink fairy armadillo and the naked mole-rat the insertion is lateral; the Hottentot golden mole, the insertion is really apical. The slender parts present a regular thickness all along the structure. The only exception is observed in the posterior slender part of the marsupial mole: close to the posterior ampulla, the slender part is consequently inflated.

The simple crus is more or less inflated depending on the species: it is long and thick for the pink fairy armadillo (length = 0.78 mm, cross section = 0.118 mm²); it is long and thin for the European mole (length = 0.84 mm, cross section = 0.048mm²); it is short and thick for the marsupial mole (length= 0.44 mm, cross section = 0.078 mm²).
It is noteworthy that there is no second crus commune in membranous structures. The second crus commune observed in some osseous inner ears are the consequences of bone development but do not translate the morphology of the membranous inner ear.

Table 2: Formalized Morphological Parameters of the five subterranean species of the study.

* Volumes are calculated from the anatomical volumes created with Geomagic.

* The structure lengths correspond to the streamline length of the structure (the streamline goes through the landmarks).

* The pitch plan corresponds to the bilateral symmetry plan. The yaw plan corresponds to the horizontal plan, perpendicular to the bilateral symmetry plan. The roll plan corresponds to the coronal, perpendicular to the two other plans. The roll plan is inevitably at a right angle to the lateral canal planes.

Species	***Amblysomus hottentotus***	***Chlamyphorus truncatus***	***Heterocephalus glaber***	***Notoryctes typhlops***	***Talpa europaea***
Average weight	70 gr	120 gr	37 gr	50 gr	100 gr
Centroid size	13.25	15.32	11.98	12.80	16.02
Distribution of the endolymph along the ducts (µl)					
V_{tot} - Total Volume of the membraneaous inner ear					
	0.95	1.90	1.24	1.44	1.10
V_{SDa} - Volume of the anterior semicircular duct and percent of the total volume					
	0.54 (57.02%)	0.98 (51.45%)	0.58 (46.58%)	0.81 (56.29%)	0.57 (51.66%)
V_{SDp} - Volume of the posterior semicircular duct and percent of the total volume					
	0.36 (38.10%)	0.81 (42.53%)	0.45 (36.28%)	0.54 (37.48%)	0.42 (38.30%)
V_{SDl} - Volume of the lateral semicircular duct and percent of the total volume					
	0.47 (48.80%)	0.90 (47.13%)	0.53 (42.84%)	0.71 (49.54%)	0.48 (43.91%)

V_{CC} - Volume of the common crus and percent of the total volume

0.10 (9.97%)	0.17 (9.20%)	0.08 (6.73%)	0.08 (5.79%)	0.12 (11.01%)

V_{UCa} - Volume of the anterior utricule and percent of the total volume

0.24 (25.50%)	0.45 (23.94%)	0.21 (17.32%)	0.44 (30.79%)	0.20 (18.33%)

V_{UCp} - Volume of the posterior utricule part and percent of the total volume

0.10 (10.79%)	0.22 (11.79%)	0.06 (4.75%)	0.13 (9.37%)	0.07 (6.74%)

V_{Aa} - Volume of the anterior ampulla and percent of the total volume

0.09 (9.59%)	0.20 (10.72%)	0.14 (11.05%)	0.18 (12.19%)	0.14 (12.25%)

V_{Ap} - Volume of the posterior ampulla and percent of the total volume

0.08 (8.27%)	0.23 (12.21%)	0.16 (12.80%)	0.20 (13.64%)	0.12 (11.14%)

V_{Al} - Volume of the lateral ampulla and percent of the total volume

0.09 (9.53%)	0.18 (9.64%)	0.13 (10.23%)	0.12 (8.32%)	0.15 (13.37%)

V_{Sa} - Volume of the anterior slender part and percent of the total volume

0.11 (11.96%)	0.14 (7.59%)	0.14 (11.49%)	0.11 (7.52%)	0.11 (10.07%)

V_{Sp} - Volume of the posterior slender part and percent of the total volume

0.09 (9.06%)	0.18 (9.33%)	0.15 (11.99%)	0.12 (8.67%)	0.10 (9.41%)

V_{Sl} - Volume of the lateral slender part and percent of the total volume

0.10 (10.51%)	0.17 (8.69%)	0.15 (12.37%)	0.12 (8.03%)	0.09 (8.56%)

V_{SC} - Volume of the simple crus and percent of the total volume

0.03 (3.27%)	0.09 (4.87%)	0.04 (2.92%)	0.03 (2.40%)	0.04 (3.64%)

Relative length of the different structures (mm)

L_{SDa} - Length of the anterior semicircular duct

7.12	7.33	5.76	6.68	8.65

L_{SDp} - Length of the posterior semicircular duct

5.17	6.98	5.21	5.71	6.55

L_{SDl} - Length of the lateral semicircular duct

6.15	6.15	5.79	5.40	6.95

L_{CC} - Length of the common crus and percent of the total length of the anterior semicircular duct

1.18 (16.58%)	1.42 (19.38%)	0.76 (13.20%)	1.34 (20.05%)	1.89 (21.85%)

L_{Sa} - Length of the anterior slender part and percent of the total length of the anterior semicircular duct

3.60 (50.57%)	3.62 (49.40%)	2.84 (49.38%)	2.96 (44.33%)	4.29 (49.65%)

L_{Sp} - Length of the posterior slender part and percent of the total length of the posterior semicircular duct

2.94 (56.73%)	3.78 (54.11%)	3.04 (58.31%)	2.74 (47.91%)	3.50% (53.39%)

L_{Sl} - Length of the lateral slender part and percent of the total length of the lateral semicircular duct

3.16 (51.40%)	3.17 (51.46%)	2.66 (46.03%)	2.66 (49.33%)	3.46 (49.87%)

L_{SC} - Length of the simple crus and percent of the total length of the lateral semicircular duct

0.51 (8.35%)	0.78 (12.72%)	0.54 (9.35%)	0.44 (8.19%)	0.84 (12.10%)

Area enclosed by the semicircular duct (mm^2)

A_{SDa} - Area enclosed by the anterior semicircular duct

3.41	3.77	2.23	3.08	5.16

A_{SDp} - Area enclosed by the posterior semicircular duct

1.81	3.34	1.83	2.17	2.84

A_{SDl} - Area enclosed by the lateral semicircular duct

2.33	2.49	1.84	1.93	3.11

Mean cross-sectional area of the different structures (mm^2)

a_{Sa} - Mean cross-sectional area of the anterior slender part

0.032	0.040	0.050	0.036	0.026

a_{Sp} - Mean cross-sectional area of the posterior slender part

0.029	0.047	0.049	0.046	0.030

a_{Sl} - Mean cross-sectional area of the lateral slender part

0.032	0.052	0.057	0.043	0.027

a_{CC} - Mean cross-sectional area of the common crus

0.081	0.123	0.110	0.062	0.064

a_{SC} - Mean cross-sectional area of the simple crus

	0.061	0.118	0.067	0.078	0.048
Ratio between cross-sectional radii					
gma_a - of the common crus and that of the anterior slender part					
	1.59	1.79	1.54	1.32	1.61
gma_p - of the common crus and that of the posterior slender part					
	1.68	1.69	1.59	1.17	1.47
bta_a - of the anterior utriculus and that of the anterior slender part					
	2.24	3.07	1.74	2.78	2.18
bta_p - of the posterior utriculus and that of the posterior slender part					
	2.67	2.44	1.49	2.07	2.30
bta_l - of the anterior utriculus and that of the lateral slender part					
	2.52	2.64	1.98	2.73	2.35
Thickness of the cristae (mm) and Surface area of the lumen cross section above the cristae (mm²)					
aCa_Md - Surface area of the lumen cross section above the anterior cristae					
	0.141	0.252	0.201	0.255	0.200
aCp_Md - Surface area of the lumen cross section above the posterior cristae					
	0.144	0.285	0.210	0.188	0.201
aCl_Md - Surface area of the lumen cross section above the lateral cristae					
	0.140	0.260	0.204	0.184	0.203
tCa-0.084 - Average Thickness of the anterior cristae					
	0.220	0.272	0.254	0.341	0.183
tCp-0.084 - Average Thickness of the posterior cristae					
	0.205	0.250	0.220	0.259	0.211
tCl-0.084 - Average Thickness of the lateral cristae					
	0.217	0.260	0.265	0.281	0.180
Angle between the duct plans and the anatomic plans (°)					
iSDaSDp_SD - Ipsilateral angle between the anterior semicircular duct and the posterior semicircular duct					
	89.87	87.77	86.98	99.17	95.90
iSDaSDl_SD - Ipsilateral angle between the anterior semicircular duct and the lateral semicircular duct					
	70.92	81.48	85.59	68.21	73.46
iSDlSDp_SD - Ipsilateral angle between the lateral semicircular duct and the posterior semicircular duct					
	100.08	92.22	93.32	96.76	100.28
sSDaSDp_SD - Synergistic angle between the anterior semicircular duct and the posterior semicircular duct					
	172.81	168.05	172.06	168.27	168.93
sSDlSDl_SD - Synergistic angle between the two lateral semicircular ducts					
	177.48	178.91	177.23	172.29	178.42
pSDa_SD - Angle between the pitch plan and the anterior semicircular duct					
	45.86	51.40	42.54	38.69	39.51
pSDp_SD - Angle between the pitch plan and the posterior semicircular duct					
	44.72	41.18	50.49	43.19	45.37
pSDl_SD - Angle between the pitch plan and the lateral semicircular duct					
	88.74	90.56	88.61	86.14	90.80
rSDa_SD - Angle between the roll and the anterior semicircular duct					
	49.74	40.00	47.66	57.51	55.72
rSDp_SD - Angle between the roll and the posterior semicircular duct					
	47.37	48.88	39.83	48.42	46.26
ySDp_SD - Angle between the yaw and the anterior semicircular duct					
	108.17	98.89	93.40	108.64	107.20
ySDp_SD - Angle between the yaw and the posterior semicircular duct					
	79.01	88.22	85.80	80.39	80.30
ySDp_SD - Angle between the yaw and the lateral semicircular duct					
	1.27	0.55	1.39	3.86	0.80

2- Comparaison with the mammal morphotype

The mammal morphotype allows us to compare the five subterranean to an objective specimen. In this way, we can light up anatomical structures which are really atypical. The formalized morphological parameters of the five subterranean species and the mammal morphotype (Table 3 and SI-10) are corrected to correspond to the same centroid size, which corresponds to the average centroid size of the sample. The 3D representations of the moles and the mammal morphotype (Fig. 8) are based on allometry-adjusted shapes. This allows us to compare the five subterranean mammals to the mammal morphotype at the same size and corrected from allometry. This specific reconstitution is more relevant for this comparison because the mammal morphotype reconstitution is not the simple mean of the other morphologies: it considers phylogeny and size.

Compared to the mammal morphotype (Fig. 8), the naked mole-rat presents the most different morphology of the semicircular duct system. The common crus of the naked mole-rat (1.98 mm) is highly smaller than the common crus of the mammal morphotype (3.35 mm). However, the total lengths of each duct are really similar, and the shapes of the semicircular ducts are really different: the mammal morphotype presents rounded semicircular ducts while they are really horizontally elongated for the naked mole-rat. The pink fairy armadillo is the second most different from the mammal morphotype. One principal difference concerns the anterior semicircular duct: it is high and at the same level of the posterior one for the mammal morphotype but it is less high (LSDa=16.42) and smaller than the posterior one for the pink fairy armadillo (LSDa=14.98). The shape of the lateral semicircular duct presents some differences: it is rounded for the mammal morphotype and elongated for the pink fairy armadillo. Finally, it is possible to notice differences with the European mole, mainly on the length of the anterior semicircular duct: 16.42 mm for the mammal morphotype against 16.96 mm.

Differences on the naked mole rat and the hottentot golden mole with the mammal morphotype are not clearly visible. The mean cross-sectional areas of the moles are not always thicker than the mean cross-sectional areas of the mammal morphotype.

These morphological differences can also be observed on the second PCA based on allometry-adjusted shape (SI-7).

Table 3: Corrected formalized morphological parameters for the five subterranean species and the mammal morphotype. Based on the phylogenetical relationships of the 30 species and the shape of their inner ear, the mammal morphotype is predicted for a centroid size equal to 32.65618167. The morphological parameters of the five subterranean mammals are corrected to correspond to the average centroid size (= 32.66).

	Mammal Morphotype	*Amblysomus hottentotus*	*Chlamyphorus truncatus*	*Heterocephalus glaber*	*Notoryctes typhlops*	*Talpa europaea*
Distribution of the endolymph along the ducts (µl)						
Vtot	6.80	6.03	8.92	9.59	9.74	4.72
Relative length of the different structures (mm)						
LSa	8.51	9.13	7.91	8.00	7.79	8.95
LSp	8.59	8.38	9.10	9.75	8.13	8.00
LSl	8.45	8.64	7.37	8.14	7.57	7.66
LCC	3.35	2.80	2.93	1.98	3.28	3.74
LSDa	16.42	16.69	14.98	14.86	16.19	16.96
LSDp	14.84	13.25	15.38	14.84	15.18	13.77
LSDl	14.09	14.71	12.78	15.27	13.36	13.84
Area enclosed by the semicircular duct (mm²)						
ASDa	17.82	18.96	15.91	15.04	18.31	20.01
ASDp	14.95	12.39	16.78	15.55	16.01	12.98
ASDl	13.16	14.33	11.43	13.87	12.74	13.05
Mean cross-sectional area of the different structures (mm²)						
aSa	0.058	0.067	0.075	0.114	0.078	0.047
aSp	0.060	0.058	0.084	0.105	0.094	0.052
aSl	0.053	0.059	0.087	0.114	0.082	0.044
aCC	0.220	0.303	0.372	0.477	0.244	0.181
Ratio between cross-sectional radii						
aCa_Md	0.568	0.402	0.607	0.644	0.757	0.457
aCp_Md	0.487	0.407	0.682	0.668	0.554	0.457
aCl_Md	0.485	0.399	0.626	0.654	0.547	0.464
tCa	0.288	0.250	0.309	0.324	0.475	0.158
tCp	0.272	0.230	0.276	0.288	0.334	0.217
tCl	0.305	0.247	0.309	0.368	0.390	0.166
Thickness of the cristae (mm) and Surface area of the lumen cross section above the cristae (mm²)						
iSDaSDp_SD	95.56	90.26	88.21	87.28	99.30	96.22
iSDaSDl_SD	78.33	72.76	82.68	88.38	69.75	74.43
iSDlSDp_SD	90.86	95.57	88.57	88.43	92.54	96.48
sSDaSDp_SD	170.27	169.96	165.52	168.64	164.93	166.65
sSDlSDl_SD	168.28	171.25	174.10	170.61	166.19	173.41
pSDa_SD	39.91	43.02	48.21	39.91	36.38	37.94
pSDp_SD	44.64	47.31	42.76	52.86	45.29	46.81
pSDl_SD	85.07	86.74	89.06	86.49	83.74	89.17
rSDa_SD	51.64	50.94	40.63	49.00	59.13	56.83
rSDp_SD	45.66	44.38	46.69	37.52	45.22	43.96
ySDa_SD	97.82	104.62	96.39	89.77	105.46	104.35
ySDp_SD	85.74	82.01	90.80	89.65	83.17	82.40
ySDl_SD	5.94	2.15	1.90	2.35	8.87	1.83

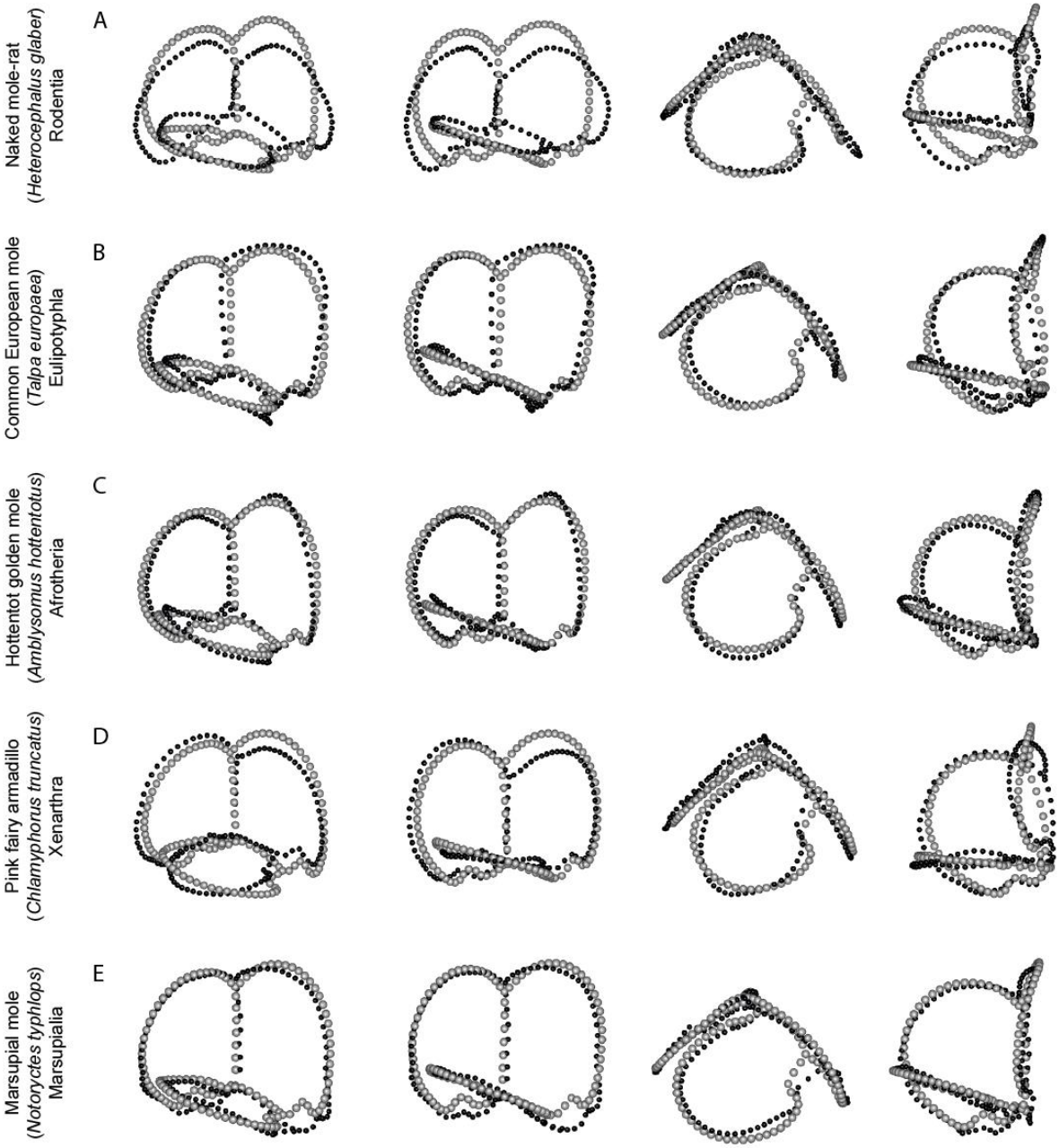

Figure 8: Comparison of the semicircular duct system of moles (in black) and the mammal morphotype (in grey).

The 3D representations are based on adjusted shapes (allometry-corrected), for the average centroid size (= 32.66).

3- Geometric Morphometrics

Morphological Diversity of the membranous semicircular duct system

The first objective here is to display the morphological disparity of the membranous semicircular duct system on 30 mammal species; the final goal being to understand the impact of phylogeny, ecology and/or allometry on shape.

Calculated on the 'raw' shape directly resulting from the GPA, the phylogenetic signal Kmult is equal to 0.571 with a p-value of 0.001 (the corresponding graphic of the function is in SI-4). The phylogeny explains significantly a part of the global disparity of the semicircular duct shape. The first PCA calculated on 'raw' data allows us to visualize the disparity of shapes (Fig. 9). The first axis (PC1) of the total 29 PCs represents 32% of the total variance, the second 15% (PC2) and the third 12% (PC3). 59% of the total variance is explained with the first three PCs and 10 PCs are needed to reach 90% of the total variance.

From the negative to positive scores, the shape changes observed along the PC1 are (Fig. 9):

- the common crus length increases. The insertion of the anterior and posterior semicircular duct at the top of the common crus is more apical for a small common crus (negative scores) and more lateral for long common crus (positive scores).
- the area enclosed by the lateral semicircular duct decreases. For negative scores, the plan of the lateral semicircular duct is clearly not perpendicular to the vertical axe of the common crus; it intersects the posterior semicircular duct plan, goes above the posterior ampulla and inserts itself highly in the common utricule. For positive scores, the lateral semicircular duct is well separated from the posterior semicircular duct and is more perpendicular to the vertical common crus axe. It is at the same level of the posterior ampulla and the insertion in the common crus is lower.
- the anterior and posterior enclosed areas are horizontally elongated to vertically stretched.
- the common utricule is straight to curved.
- the anterior semicircular duct plan is more curved in positive scores.

The conformation in high positive values of PC1 is characteristic of the platypus (*Ornithorhynchus anatinus*). The conformation in high negative values of PC1 is characteristic of the primate *Euoticus elegantulus*.

From the negative to positive scores, the shape changes observed along PC2 are (Fig. 9):

- the lateral enclosed area is ellipsoid to round. The lateral semicircular duct plan is almost perpendicular to the vertical axe of the common crus plan for the negative scores. For positive scores, the plan is strongly tilted with the posterior part more dorsally and the anterior part more ventrally.
- the plans of the anterior and posterior ducts are straight to wavy plans.

- the anterior and posterior semicircular ducts have a similar height for most negative scores, and the anterior semicircular duct is higher than the posterior one for most positive scores.

The conformation in high positive values of PC2 is characteristic of the European mole. The conformation in high negative values of PC2 is characteristic of the horse (*Equus ferus caballus*).

From the negative to positive scores, the shape changes observed along PC3 are (Fig. 9):

- the common utricule is long to short.
- the three ampullae are elongate to short.
- the anterior and lateral ampullae are distant to close.
- the anterior semicircular duct is ellipsoid to round.
- the posterior semicircular duct is angular to round.

The conformation in high positive value of PC3 is characteristic of the primate *Saimiri sciureus*. The conformation in high negative value of PC3 is characteristic of the naked mole rat.

The variation of the angle between the plans of the semicircular ducts does not appear to be the dominant feature to explain the total variability and we do not observe this parameter on the shape variation along the three first component. The European mole, the marsupial mole, the golden mole and the platypus plot on both positive high scores on PC1 and PC2. PC3 discriminates only the naked mole rat from all the other species (see Fig. 9 and pairs in SI-5). The phylogenetic signal is observable on the first three PCs. For example, the Euarchontoglires plot really closely in one cluster in the PC1-PC2 space (see Figs 9 and 10). Another example is the Scrotifera (Laurasiatheria minus *Talpa europaea*), which plots at the negative pole of the PC2 (see Fig. 9).

On the first third PCs, the five moles do not plot together but this considers only 59% of the total diversity. In order to consider a maximum of diversity information, the two-sample Hotelling's T squared test is performed twice. The shape of the inner ear of the five moles is not significantly different from that of the total 30 mammal species (p-value = 0.745), but the shape of the inner ear of the five moles is significantly different from that of the other 25 non-subterranean species (p-value = 0.0097).

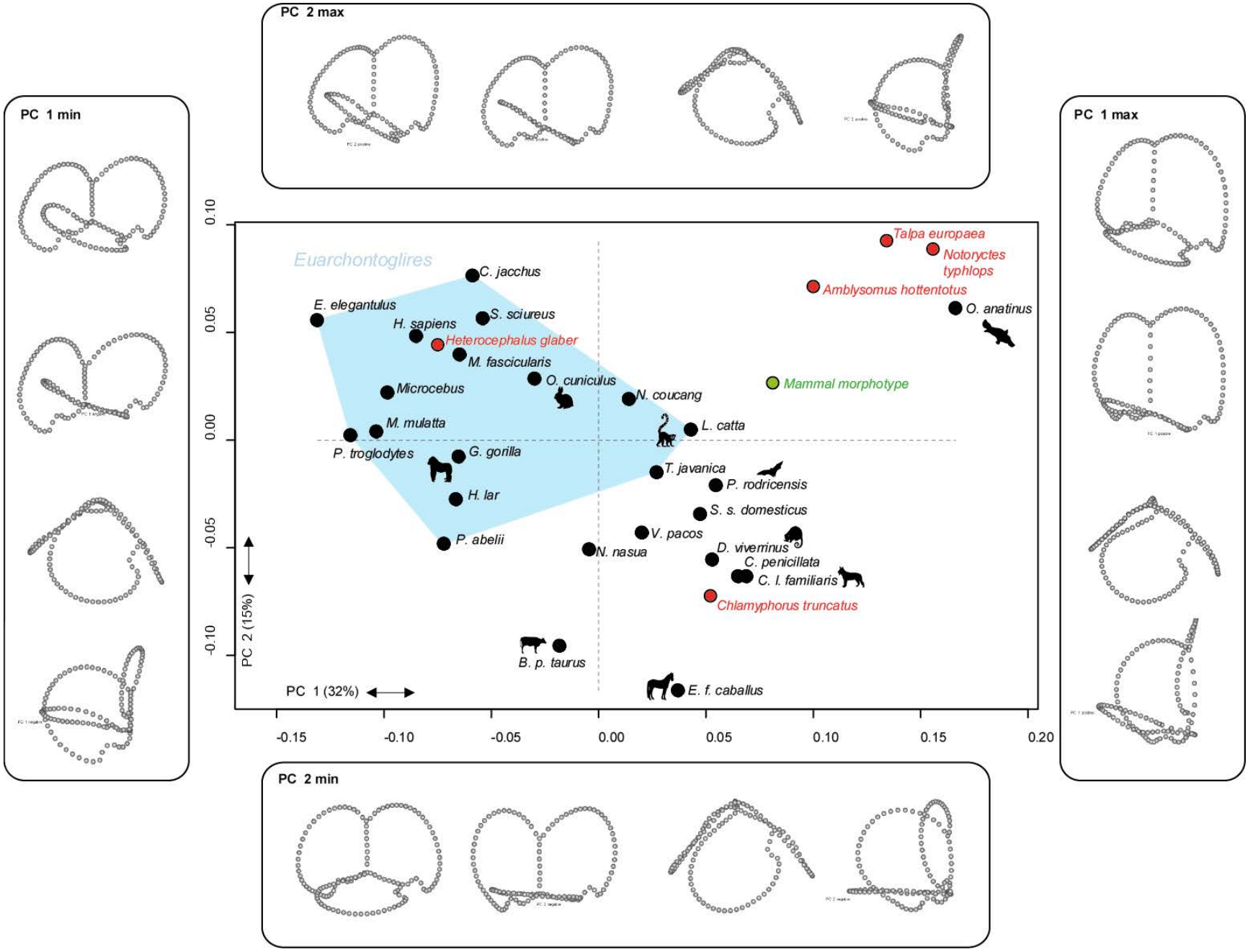
PC 2 max
PC 1 min
PC 1 max
PC 2 min
Euarchontoglires
C. jacchus
E. elegantulus
S. sciureus
H. sapiens
Heterocephalus glaber
M. fascicularis
O. cuniculus
Microcebus
N. coucang
M. mulatta
L. catta
P. troglodytes
G. gorilla
T. javanica
P. rodricensis
H. lar
S. s. domesticus
V. pacos
P. abelii
N. nasua
D. viverrinus
C. penicillata
C. l. familiaris
Chlamyphorus truncatus
B. p. taurus
E. f. caballus
Talpa europaea
Notoryctes typhlops
Amblysomus hottentotus
O. anatinus
Mammal morphotype
PC 2 (15%)
PC 1 (32%)
0.10
0.05
0.00
-0.05
-0.10
-0.15
-0.10
-0.05
0.00
0.05
0.10
0.15
0.20

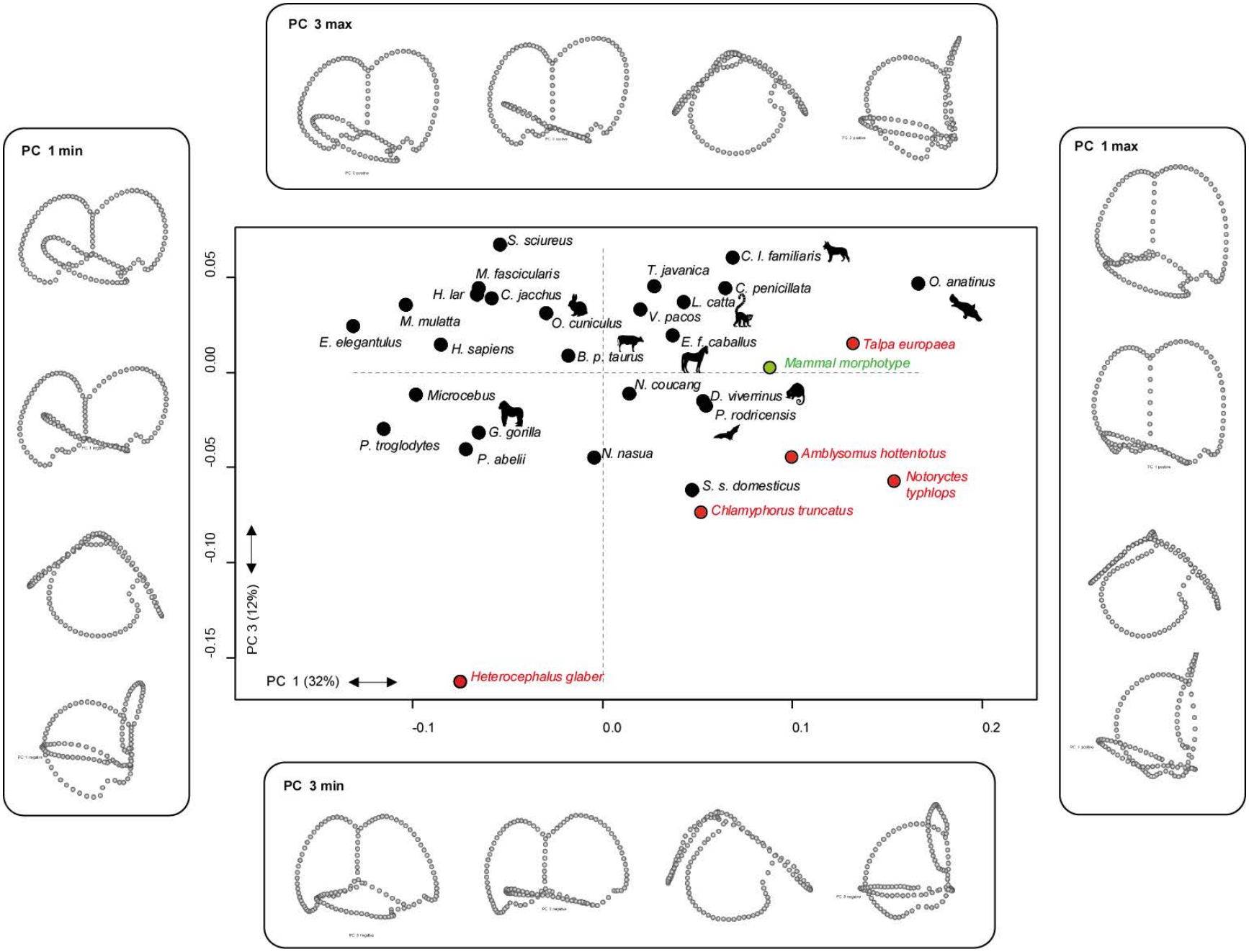
PC 3 max
PC 1 min
PC 1 max
PC 3 min
S. sciureus
C. l. familiaris
M. fascicularis
T. javanica
O. anatinus
H. lar
C. jacchus
C. penicillata
L. catta
M. mulatta
O. cuniculus
V. pacos
E. elegantulus
H. sapiens
E. f. caballus
Talpa europaea
B. p. taurus
Mammal morphotype
N. coucang
Microcebus
D. viverrinus
P. rodricensis
G. gorilla
P. troglodytes
P. abelii
N. nasua
Amblysomus hottentotus
Notoryctes typhlops
S. s. domesticus
Chlamyphorus truncatus
Heterocephalus glaber
PC 3 (12%)
PC 1 (32%)
0.05
0.00
-0.05
-0.10
-0.15
-0.1
0.0
0.1
0.2

Figure 9: Results of the Principal Components Analysis (PCA) based on the 3D coordinates of the membranous semicircular duct system of the 5 moles (in red) and the 25 non-subterranean species (in black) of the study.

The graphics presents the first three components of the shape space. PC shape variation is realized by the hypothetical vestibular system shapes at the extreme scores for PC1, PC2 and PC3. The mammal morphotype (in green) is spotted *a posteriori* on the graphics.

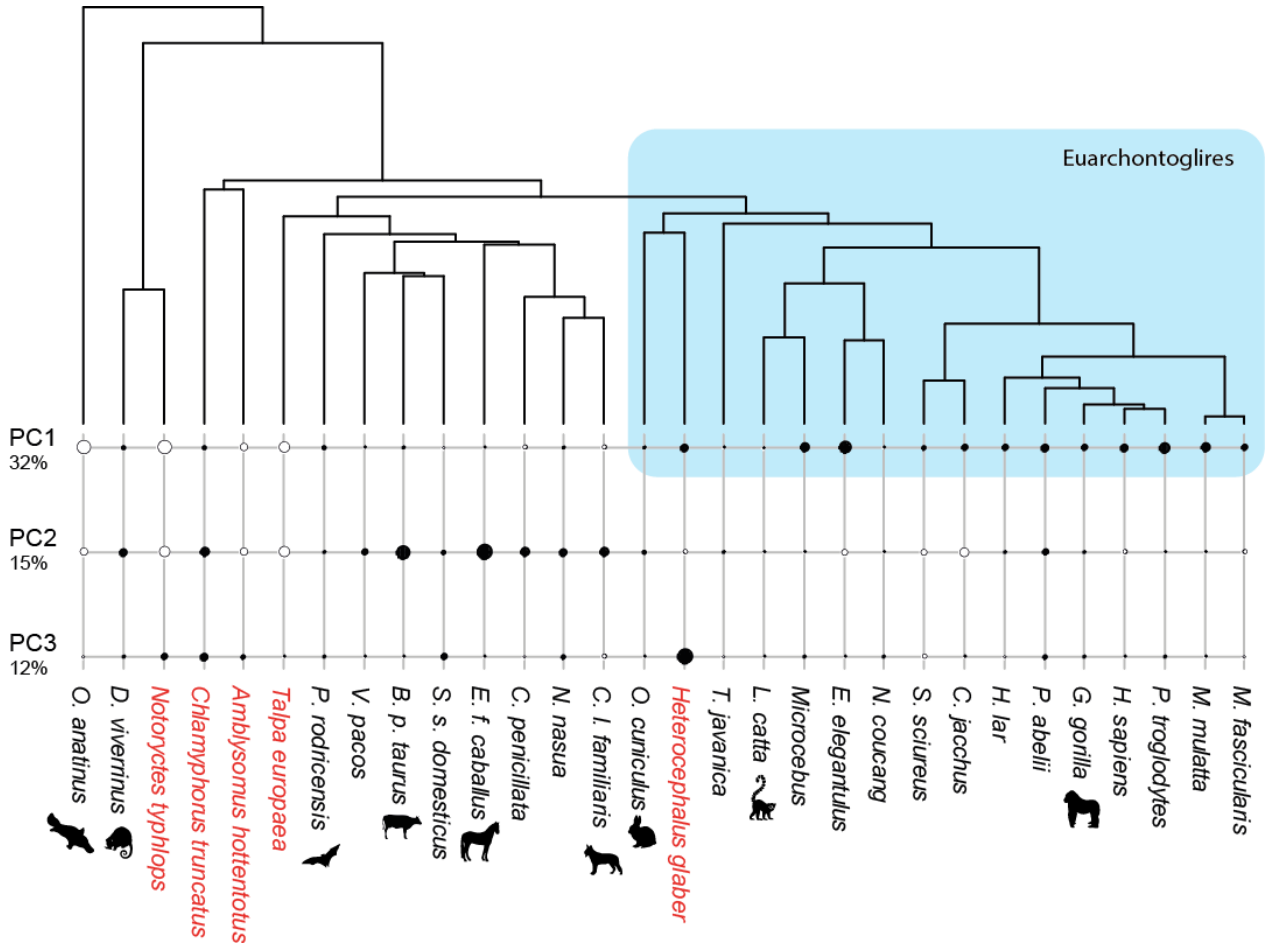

Figure 10: 'Phylo4d' representation with the first three PCs related to the phylogeny.

The five mole species are in red and the non-subterranean species in black. A large black circle represents a high negative score on the PC and a large white circle represents a high positive score on the PC. The Euarchontoglires are spotted in blue as an example to highlight the role of the phylogeny on the shape diversity.

Allometry

Our goal is to understand the morphological diversity of the membranous semicircular duct system in mammals and to understand how the ecological signal, the phylogenetical signal and/or the allometry play a role on the morphological variance. We now need to identify the parameters that potentially interfere with the ecological signal, and remove them. Concerning the allometry, the Procrustes ANOVA indicates that the 'raw' shapes are slightly but significantly correlated to the centroid size (p-value = 0.004). In other words, there is a slight but significant size effect on the shape of the membranous semicircular duct system (R^2 = 0.11). The figure 11 allows us to visualize the correlation between the centroid size and the shape.

From the minimum centroid size to the maximum centroid size, the shape changes observed along the centroid size increase are (Fig. 11):

- the common crus is longer to smaller.
- the anterior semicircular duct is higher than the posterior one for most minimum centroid sizes, and the anterior and posterior semicircular ducts have a similar height for most maximum centroid sizes.
- the three ampullae are elongate to short.
- the anterior and lateral ampullae are distant to close.
- the posterior and lateral semicircular ducts become relatively larger compared to the anterior semicircular duct.

The conformation at the minimum centroid size values is characteristic of the marsupial mole and the Hottentot golden mole. The conformation at the maximum centroid size values is characteristic of the horse (*E. f. caballus*) and the cow (*Bos taurus taurus*). Despite the fact that the sample exhibits a large range of centroid sizes (SI-6), it should be pointed out that the five moles present the five smallest centroid sizes.

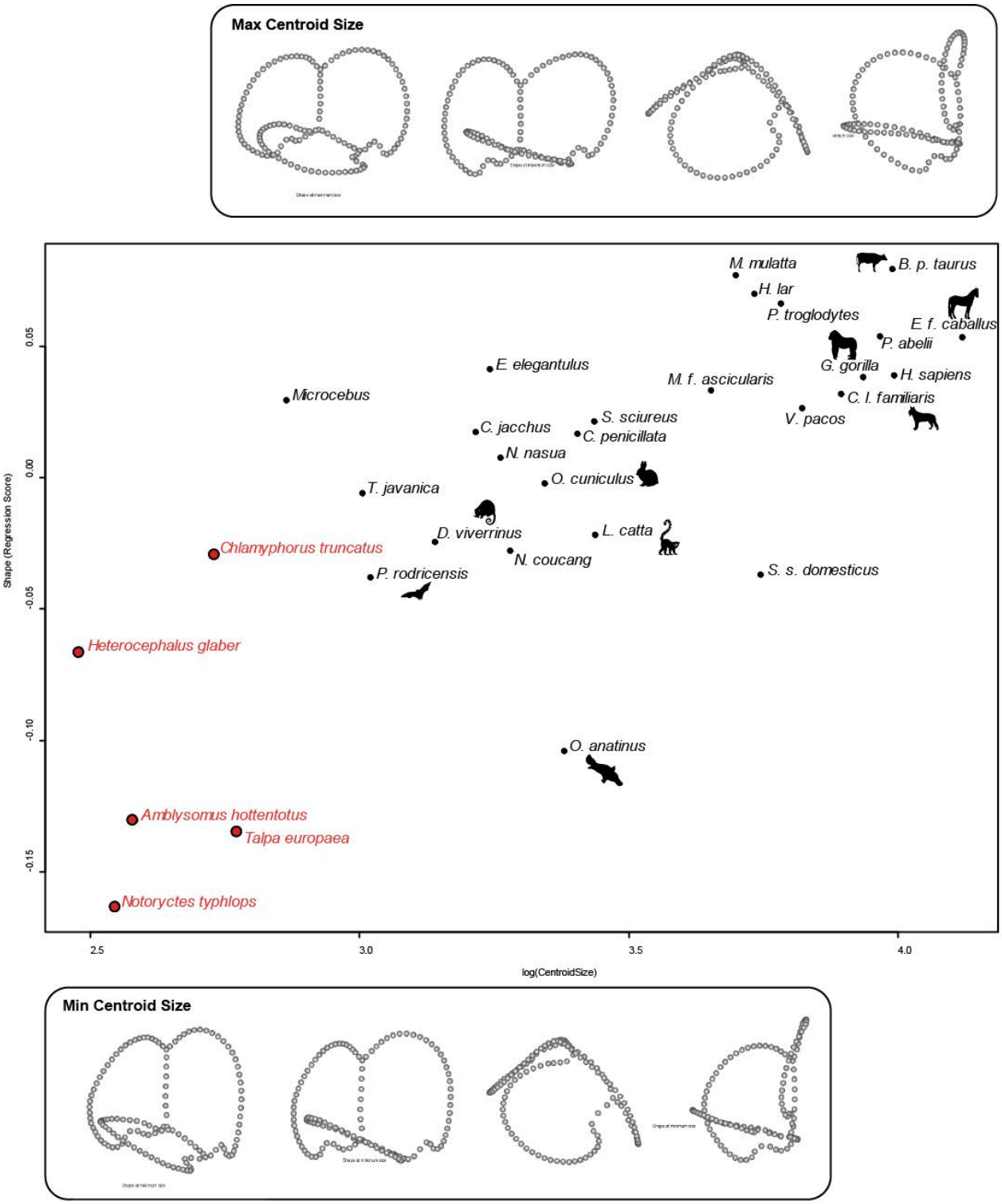

Figure 11: 'RegScore' plot method to visualize allometry.

Mole species in red and non-subterranean species in black. Representation of shapes for small and large centroid sizes.

Morphological Diversity of the adjusted shape

Calculated on the allometry-adjusted shape, the phylogenetic signal Kmult is now equal to 0.481 with a p-value of 0.001 (the corresponding graphic of the function is in SI-4). The phylogeny significantly explains a part of the global disparity of the corrected shape of the membranous semicircular duct. The second PCA computed on allometry-adjusted shape is available in SI-7. The PC1 of the total 28 PCs represents 33% of the total variance, the PC2 15% and the PC3 10%. 58% of the total variance is explained with the first three PCs and 11 PCs are needed to reach 90% of the total variance. The significant and observable shape changes along PC1, PC2 and PC3 are the same than those observed in the first PCA (but reversed on the scores). The European mole, the marsupial mole, the golden mole and the platypus do not plot anymore really closely. PC3 does not discriminate the naked mole-rat from all the other species (SI-7). The phylogenetic signal remains observable on the first three PCs (SI-8). On the new first third PCs, the five moles do not plot together but this considers only 58% of the total diversity. In order to consider a maximum of diversity information, the two-sample Hotelling's T squared test is performed twice. The shape of the semicircular duct system of the five moles is not significantly different from the shape distribution for mammals (p-value = 0.988) and the shape of the semicircular duct system of the five moles is not significantly different from the non-subterranean mammals (p-value = 0.886).

Consideration of the phylogenetical signal

Continuing the characterization of the morphological diversity, the phylogenetic PCA allows to take care of the phylogeny effects on the shape. This statistic test does not compute new corrected shapes but allows to consider the phylogenetic signal in order to highlight the morphological diversity within the clades.

The PC1 represents 26% of the total variance, PC2 15%, and PC3 11%. 52% of the total variance is explained by the first three PCs and 12 more PCs are needed to reach 90% of the total variance. In the PC1-PC2 space, the global organization of the specimens are similar to the results of the two first PCA (with PC1 and PC2 reversed compared to the first PCA) (Figs 9 and 12). For example, the Euarchontoglires still plot together at high positive values of PC1. Some exceptions must be noticed: in the previous PCA (Fig. 9), the naked mole rat plotted inside the Euarchontoglires cluster, here it plots more distant from the other Euarchontoglires. In the previous PCA (Fig. 9), the marsupial mole, the Hottentot golden mole and the European mole

plotted really distant from the other species; here they plot closer. In contrary, the pink fairy armadillo is here really well discriminated at high values of PC2.

The conformation at high positive values of PC1 is characteristic of the naked mole rat. The conformation at high negative values of PC1 is characteristic of the platypus. The conformation at high positive values of PC2 is characteristic of the pink fairy armadillo. The conformation at high negative values of PC2 is characteristic of the primate *S. sciureus*. The conformation at high positive values of PC3 is characteristic of the marsupial mole. The conformation at high negative values of PC3 is characteristic of the treeshrew *Tupaia javanica*. The five moles do not plot together neither in the PC1-PC2 space nor in the PC1-PC3 space.

With the phylogenetic PCA (Fig. 12), we are looking at the diversity within clades and thus at the moles' positions compared to their relatives: do each mole differ in the same way from their own clade? For example, the naked mole rat plots at higher values of PC1 compared to its relatives (e.g., the rabbit and other Euarchontoglires). If the other moles were also found at higher values of PC1, it could have been interpreted as an ecological signal: all the mole species of our study would have presented the same shape resulting from underground adaptation. However, it is not the case here, and apparently, no ecological adaptation has driven the evolution of the membranous inner ear of moles. It is noteworthy that only 26% of the diversity is considered by the PC1; for that reason, two-sample Hotelling's T squared tests were performed to consider all the diversity. They were conducted on residuals between the terminal taxa and the nearest nodes, and not on the scores directly.

The form variation between the five moles and their nearest nodes is not significantly different from the form variation for mammals (p-value = 0.9952) and the form variation between the five moles and their nearest nodes is not significantly different from the form variation of non-subterranean mammals (p-value = 0.9624). In other words, the mole species do not present the same morphological variability compared to their relatives, they do not exhibit any peculiar variation, compared to other mammals, which would be specific of their ecology.

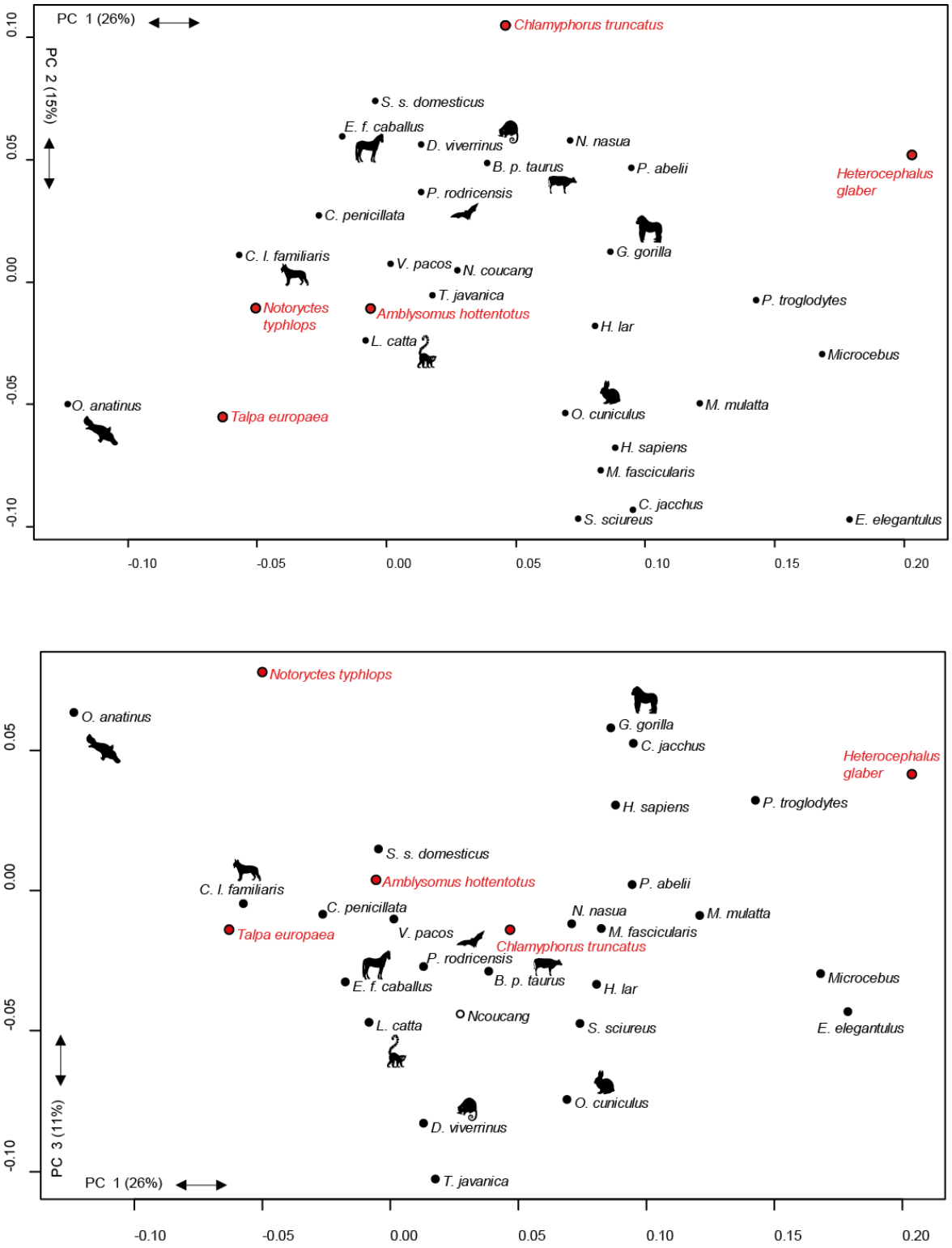

Figure 12: Results of the Phylogenetic Principal Components Analysis based on the allometry-adjusted shapes of the 5 moles (in red) and 25 non-subterranean species (in black) of the study.

The graphics present the first three PCs of the shape space.

Discussion

1-Do the new anatomical features of the membranous semicircular duct system of moles correspond to what was previously known?

The fragile membranous structures in the inner ear are hard to visualize undistorted and in full. The majority of previous studies focused on the easy-to-visualize bony semicircular canals rather than the delicate membranous ducts they enclose (e. g., Crumpton et al., 2015; Pfaff et al., 2015; Billet et al., 2012). Instead, undistorted and detailed three-dimensional (3D) visualization of the membranous semicircular duct system is something that has proven to be hard to achieve. Methods used most recently include dissections (Lindenlaub. Et al., 1995; McVean, 1999) and histological serial sectioning (Schultz et al., 2017). These techniques have particular limitations, mainly the destruction of the specimens which is not compatible with precious specimens (e. g., endangered species or collection specimens). In this study, the followed methodological approach of David et al. (2016) offers for the first time high-resolution 3D imagery and quantification of the complete membranous labyrinth in-situ inside the petrosal bone. This non-invasive visualization method based on X-ray micro tomography (micro-CT) provides high-quality information as presented in the Results section.

Concerning the moles, the comparison with previous studies of 3D data and formalized morphological parameters (as presented here) is not easy. Previous works mostly focused on the osseous inner ear and used different methods of measurements (Crumpton et al., 2015; Pfaff et al., 2015; Billet et al., 2012). Nonetheless, osseous inner ear measurements are, for example, available for the five moles of the present study: *Amblysomus hottentotus*, *Talpa europaea* and *Notoryctes typhlops* in Crumpton et al. (2015), *Talpa europaea* in Pfaff et al. (2015) and Billet at al. (2012), and *Notoryctes typhlops* in Pfaff et al. (2017). The most relevant study to which compare our results is that of McVean (1999), who took measurements on the membranous semicircular ducts of *Talpa europaea* (Table 4). The provided values are comparable with the ones that we obtained for the same species (Table 3), the majority of which fit in the confidence interval proposed in McVean (1999). However, some of the measurements from our study do not match with the interval confidence:

- The cross-sectional area of the anterior semicircular duct, and more generally, the mean cross-sectional areas of the semicircular ducts are in the minimum range of the compared confidence interval. This could be explained by the fact that the mean cross-sectional area calculated by McVean (1999) is based on the measured diameter then converted in cross-sectional area. Maybe the diameter measurement was not taken really perpendicular to the duct direction or maybe the ducts were ellipsoidal: in all cases, the diameter and therefore the cross-section would be overestimated.
- All the three streamline lengths from our study are smaller than those calculated by McVean (1999). It could be due to the different methods, but we would need the precise protocol and the original drawings of the projected inner ear to understand this particularity. It also can be explained by the natural variability.

Finally, the method we used in this study has been tested and approved in the original publication (David et al., 2016), and so far, there is no better way to investigate the anatomy of the membranous inner ear.

Table 4: Comparison of the morphological measurements of various features of the membranous semicircular duct of *Talpa europaea* with the previous study of McVean (1999).

Area enclosed by the semicircular duct (mm²)			
	anterior	posterior	lateral
McVean (1999)	5.36 ± 0.23	3.55 ± 0.76	3.12 ± 0.55
Present Study	5.16	2.84	3.11
Streamline length of the semicircular ducts (mm)			
	anterior	posterior	lateral
McVean (1999)	10.02 ± 0.42	7.97 ± 0.32	7.7 ± 0.66
Present Study	8.65	6.55	6.95
Mean cross-sectional area of the slender part (mm²)			
	anterior	posterior	lateral
McVean (1999)	0.036 ± 0.009	0.039 ± 0.011	0.042 ± 0.015
Present Study	0.026	0.03	0.027

2-Shape diversity of the semicircular duct system: which effects from the phylogeny and allometry?

The shape descriptions at minimum and maximum values of PCs correspond to the conformations highlighted in previous study, based on bony semicircular canals. For example, a longer crus commune is found at most positives values of PC (Fig. 9). This characteristic is also found in Mennecart & Costeur (2016) and associated with a thinner common crus. We find the same correlation of length and delicacy of the crus commune, when checking the linear measurements (the landmarks do not reflect the thickness of the structures). The European mole plots at high positive values of PC1 and shows a longer crus commune (= 3.74mm) than that of the mammal morphotype in average values of PC1 (=3.35mm), and than that of the naked mole-rat at negative values of PC1 (=1.98). Correlated with the elongation of the crus commune along the PC1 axis, the thickness decreases with a cross section area of 0.477 for the naked mole-rat, 0.220 for the mammal morphotype, and 0.181 for the European mole.

The role of the phylogeny to explain the shape diversity was already highlighted in previous studies (Spoor et al., 1995; Gunz et al. 2012; Ekdale, 2013; Macrini et al., 2013; Billet et al., 2015), some of which using the shape of the inner ear to add anatomical information in phylogenetic reconstructions (e. g., Mennecart et al., 2017). In our study, the phylogenetic signal plays evenly a role and can be seen for example with the cluster of the Euarchontoglires. The phylogenetic signal Kmult calculated on the 'raw' shape is significant and confirms that the phylogeny explains a part of the shape diversity of the semicircular duct system (Kmult=0.571 and p-value=0.001). The second Kmult calculated on the allometry-adjusted shape is smaller than the latter (Kmult = 0.481 and p-value = 0.001). The expected value of Kmult should be bigger on the allometry-adjusted shape because the removed size effect should highlight the other parameters such as phylogeny and ecology. That is not the case here and we have to consider that the size effect that has been removed was holding phylogenetical signal too. These two parameters appear closely linked, for example, when looking at the linear measurements (SI-11): the length of the common crus is an important anatomical feature to understand the allometry (Fig. 11) and we can noticed that the corresponding formalized morphological parameter 'Length of the Common Crus' (LCC) is

significantly correlated both to allometry (R^2 = 0.78, p-value = 5.656^{e}-11) and phylogeny (lambda = 0.851).

The size effect on the shape of semicircular ducts (allometry) was already shown in previous studies (e.g., Spoor et al. 2002; Alloing-Séguier et al. 2013). The configurations at minimum and maximum centroid sizes are similar to those described in previous studies.

In our sample, the shape diversity is explained firstly by the phylogeny and secondly by the allometry (as regard the p-values).

3-Does the morphology of the semicircular duct system allow us to determine an ecological signal?

Regarding the PCA on 'raw' data, the five moles do not plot together neither in the PC1-PC2 space nor in the PC1-PC3 space. Three of them nonetheless plot together at high positive values of PC1 and PC2: the European mole, the marsupial mole and the Hottentotus golden mole. This could emphasize a cluster of subterranean mammals but with non-negligible exception, the platypus being included in the cluster (or at least closer to it than to any other mammal of the sample). It is noteworthy that the platypus has fossorial habits; it digs burrows along riverbanks and lives in it (Serena et al., 1998). Living underwater, the environmental constraints are important too. This cluster could therefore be explained by ecological constraints linked to underground (including fossoriality) and underwater lifestyles. But this hypothesis can be questioned because the rabbit, another mammal digging burrows and living in it, plots really far from this cluster. Maybe this cluster can partially be explained by the allometry, because it explodes in the results of the second PCA based on allometry-adjusted data. The marsupial mole and the Hottentot golden mole plot more closely to their relatives. Only the platypus and the European mole keep showing really special shapes.

The position of the naked mole-rat and the pink fairy armadillo may be explained by the part of the phylogeny contained in the allometry. On the first PCA based on 'raw' data, these two species plot close to their relatives: in the cluster of the Euarchontoglires for the naked mole-rat and close to the Laurasiatheria+Euarchontoglires for the pink fairy armadillo. On the second PCA, this two species plot farther from their relatives. The removed allometry took away a part of the phylogenetic signal as well.

All these hypotheses concern only the first two axes, which correspond only to 44% of the total variability. The two-sample Hotelling's T-squared test allows to consider all the diversity for all the PCs and to step out from the subjective interpretation of graphical results of PCA. The first test on 'raw' data is significant: the shape of the membranous inner ear of the five moles is different from that of the other 25 non-subterranean species (p-value = 0.0097). This could be explained by the ecological signal. Due to their convergent lifestyle, the five moles could present anatomical features corresponding to ecological adaptations. The second test performed on allometry-adjusted shapes shows no more significant difference between the shape of the membranous inner ear of the five moles and that of the other 25 non-subterranean species (p-value = 0.886). This is very enlightening and suggests that the significantly different shape of the moles found by the first test is not due to an ecological signal, as proposed above, but is most likely due to the size-effect. The five moles indeed have the five smallest centroid sizes of the sample (Fig. 11). As a matter of fact, when correcting the shape from size effect, the shape distribution of the five moles is not anymore different from the shape distribution of the other species. To reassure this hypothesis, it is interesting to focus on the centroid size of the species. A Student's t-Test was performed on the centroid size of the moles compared to the centroid size of the others species: the centroid size of the moles is significantly different from the centroid size of the non-subterranean mammals (t = 8.5225, p-value = 3.615e-09).

Finally, we can conclude that the semicircular duct system of moles is not significantly different from the semicircular duct system of the non-subterranean species, and consequently, the anatomy of the semicircular duct system in moles is not modelled by the ecology.

Our method does not consider the thickness of the structures whereas it was assumed to be linked to their agility and ecological features (Spoor et al., 2007; Billet et al., 2013). The plot of the mean cross section of the semicircular ducts (SI-12) shows that the mean cross section of the moles is not different from the mean cross section of the other species.

Conclusion and Perspectives

Thanks to the new method of David et al. (2016), we are able to investigate the morphology of the membranous semicircular duct system, with exquisite rendering of the organ in-situ

and in 3D. For the first time, we provide a detailed comparative description of the membranous semicircular duct system of five moles, which can serve as a reference for future studies. This work enhances the knowledge of the semicircular duct system diversity and participates to the discussion on evolutionary morphology of the mammalian inner ear.
Contrary to previous works (Lindenlaub et al., 1995; McVean, 1999; Crumpton et al., 1995), our study leaves no doubt and proves that the anatomy of the membranous semicircular ducts of the inner ear does not reflect the subterranean lifestyle in mammals.

We have shown that the morphological diversity of the membranous semicircular duct system can be explained by the phylogenetical signal and the allometry. Controlling these parameters, the remaining observable morphological diversity of the semicircular duct system (Fig. 12) is not linked to the ecological signal and is better explained by the presence of natural interspecific variations and noises. The identification of highly variables structures of the semicircular duct system within the same species would greatly help in deciphering the part of variations within our dataset. We could set up a protocol to determine how much shape noise is attributable to the method, especially the landmarks editing and the model segmenting.
The present work could benefit from some improvements, such as the add of:
- non-subterranean species with small sizes to have small centroid sizes other than moles;
- other non-primates species to better visualize the mammal diversity, and particularly relatives of the five moles of the sample to better understand the morphology of their semicircular duct system.
If the assumption that extreme lifestyles cause extreme morphological specializations was true, subterranean mammals would have been discriminated from other less-constrained mammals, thanks to their inner ear morphology, which is the organ that detects the locomotor head movements. A previous study on the bony semicircular canal system (Chapter 1) suggested that only extreme locomotions among marsupials (gliders and the marsupial mole) were correlated with a peculiar morphology, even though there is only one species living underground in the clade Marsupialia.
Based on five subterranean mammals from five different clades, our study contradicts that finding. Taking into account that (1) the subterranean lifestyle is really restrictive on the head movements, the locomotion, and the environment perception, and (2) there is no ecological

signal in the morphology of the semicircular duct system of moles, we can hypothesize that there is no ecological signal in the morphology of the semicircular duct system of mammals, whatever the locomotion is (as suggested in the Chapter 1).

Finally, this work questions the relevancy of using the morphology of the membranous semicircular duct system to directly determine ecological features. A promising future work would be to use these new anatomical data to compute functional parameters of the semicircular duct system, which are directly correlated to the head movements and are the most likely to determine the lifestyle of animals (Chapter 3).

Supplementary Informations

SI-1. Organization of the 132 landmarks in the landmarks matrix.

SI-2. Order of the 30 species in the landmarks matrix.

SI-3. R script for Geometric Morphometrics.

SI-4. Kmult results.

SI-5. Pairs of the 10 first PCs resulting from the first PCA (on 'raw' shapes).

SI-6. Histogram of the centroid size of the 30 species.

SI-7. Result of the second PCA based on allometry-adjusted shapes.

SI-8. 'Phylo4d' representation with the first three PCs related to the second PCA.

SI-9. R script for Linear Morphometry.

SI-10. Morphological Parameters of the reconstructed mammal morphotype with a confidence interval of 95%.

SI-11. Phylogenetic signal and Allometry on Linear measurements.

SI-12. Plot of the cross-section area of the slender parts.

Online Material

OM-1. RScript_Geomorph.txt

OM-2. RData_FullLabyrinth.txt

OM-3. RData_FullLabyrinth_Slide.txt

OM-4. MammalTree.nex

OM-5. RScript_Ancestral_State_Morphometry.R

OM-6. RData_Morphometry_Mammals.txt

Acknowledgements

In order to carry out this work, CS had to be formed to the new method set up by RD. In this context, CS went three times to work with RD at the Max Planck Institute (Leipzig), and would like to thanks the Institute and particularly Jean-Jacques Hublin, director of Department of Human Evolution, for welcoming her and for the scans performed there. These travels and the resulting present study were financially supported by two major grants:

- "Short-Term Grant" from the Deutscher Akademischer Austauschdienst (DAAD), which encourages Franco-German collaborations.
- "Transhumance Grant" from the Doctoral School of the MNHN, which encourages young researcher to develop international collaborations.

We are grateful to Violaine Colin-Nicolas, Géraldine Véron, and Aurélie Verguin (MNHN) for the loan of the precious specimens from the Zoothèque of the MNHN, and Marc Herbin (MNHN), for the conditioning of the specimens and the staining protocol applied to some unfruitful specimens.

CS, DG, and SL warmly thank Vincent Fernandez (beam ED19, ESRF, Grenoble) for his expertise and precious help during their stay at the European Synchrotron Radiation Facility (Experiment LS-2427 ED19/2015) during which we performed major scans.

Finally, CS and SL would like to thank Jérôme Dormion of Taup'green who kindly helped them to provide a common European mole, which was, ironically, the most difficult species to obtain.

References

Adams, D.C. (2014). A generalized K statistic for estimating phylogenetic signal from shape and other high-dimensional multivariate data. *Systematic Biology, 63*, 685-697.

Adams, D. C., & Otárola-Castillo, E. (2013). geomorph: an R package for the collection and analysis of geometric morphometric shape data. *Methods in Ecology and Evolution*, *4*(4), 393-399.

Alloing-Séguier, L., Sánchez-Villagra, M. R., Lee, M. S., & Lebrun, R. (2013). The bony labyrinth in diprotodontian marsupial mammals: diversity in extant and extinct forms and relationships with size and phylogeny. *Journal of Mammalian Evolution*, *20*(3), 191-198.

Begall, S., & Burda, H. (2006). Acoustic communication and burrow acoustics are reflected in the ear morphology of the coruro (*Spalacopus cyanus*, Octodontidae), a social fossorial rodent. *Journal of Morphology*, *267*(3), 382-390.

Begall, S., Burda, H., & Schleich, C. (eds) (2007). *Subterranean rodents: news from underground*. Springer-Verlag, Berlin. xviii+398 p.

Billet, G., Hautier, L., Asher, R. J., Schwarz, C., Crumpton, N., Martin, T., & Ruf, I. (2012). High morphological variation of vestibular system accompanies slow and infrequent locomotion in three-toed sloths. *Proceedings of the Royal Society of London B: Biological Sciences*, rspb20121212.

Billet, G., Germain, D., Ruf, I., Muizon, C. D., & Hautier, L. (2013). The inner ear of *Megatherium* and the evolution of the vestibular system in sloths. *Journal of Anatomy*, *223*(6), 557-567.

Billet, G., Hautier, L., & Lebrun, R. (2015). Morphological diversity of the bony labyrinth (inner ear) in extant xenarthrans and its relation to phylogeny. *Journal of Mammalogy*, *96*(4), 658-672.

Blomberg SP, Garland T, Ives AR. (2003). Testing for phylogenetic signal in comparative data: behavioral traits are more labile. *Evolution, 57*, 717-745.

Bookstein, F. L. 1997. Landmark methods for forms without landmarks: morphometrics of group differences in outline shape. *Medical Image Analysis, 1*, 225-243.

Crumpton, N., Kardjilov, N., & Asher, R. J. (2015). Convergence vs. specialization in the ear region of moles (Mammalia). *Journal of Morphology, 276*(8), 900-914.

Curran, J. M. (2013). Hotelling: Hotelling's t-squared test and variants. R package version 1.0–2.

David R. (2011). *Le système des canaux semi-circulaires des archosaures : anatomie, morphometrie, morphologie fonctionnelle, évolution*. Unpublished PhD thesis. Muséum national d'Histoire naturelle, Paris. 343p.

David, R., Stoessel, A., Berthoz, A., Spoor, F., & Bennequin, D. (2016). Assessing morphology and function of the semicircular duct system: introducing new in-situ visualization and software toolbox. *Scientific reports*, *6*, 32772.

Ekdale, E. G. (2013). Comparative anatomy of the bony labyrinth (inner ear) of placental mammals. *PLoS One*, *8*(6), e66624.

Ekdale, E. G. (2016). Form and function of the mammalian inner ear. *Journal of Anatomy*, *228*(2), 324-337.

Gerhardt, P., Henning, Y., Begall, S., & Malkemper, E. P. (2017). Audiograms of three subterranean rodent species (gen. *Fukomys*) determined by auditory brainstem responses reveal extremely low high-frequency cut-offs. *Journal of Experimental Biology*, jeb-164426.

Gower, J. C. (1975). Generalized Procrustes analysis. *Psychometrika 40*, 33-51.

Gunz, P., Ramsier, M., Kuhrig, M., Hublin, J. J., & Spoor, F. (2012). The mammalian bony labyrinth reconsidered, introducing a comprehensive geometric morphometric approach. *Journal of Anatomy*, *220*(6), 529-543.

Hillman, D. E., & McLaren, J. W. (1979). Displacement configuration of semicircular canal cupulae. *Neuroscience*, *4*(12), 1989-2000.

Koyabu, D., Hosojima, M., & Endo, H. (2017). Into the dark: patterns of middle ear adaptations in subterranean eulipotyphlan mammals. *Royal Society Open Science*, *4*(9), 170608.

Kumar S, Stecher G, Suleski M, Hedges SB (2017) TimeTree: A Resource for Timelines, Timetrees, and Divergence Times. *Molecular Biology and Evolution, 34*(7), 1812-1819.

Lebrun R. (2008). *Evolution and development of the strepsirrhine primate skull*. Ph.D. Dissertation, University Montpellier II, University of Zürich, Montpellier, Zürich.

Lindenlaub, T., Burda, H., & Nevo, E. (1995). Convergent evolution of the vestibular organ in the subterranean mole-rats, *Cryptomys* and *Spalax*, as compared with the aboveground rat, *Rattus*. *Journal of Morphology, 224*(3), 303-311

Macrini, T. E., Flynn, J. J., Ni, X., Croft, D. A., & Wyss, A. R. (2013). Comparative study of notoungulate (Placentalia, Mammalia) bony labyrinths and new phylogenetically informative inner ear characters. *Journal of Anatomy*, *223*(5), 442-461.

Mason, M. J. (2001). Middle ear structures in fossorial mammals: a comparison with non-fossorial species. *Journal of Zoology*, *255*(4), 467-486.

Mason, M. J., Cornwall, H. L., & Smith, E. S. J. (2016). Ear structures of the naked Mole-Rat, *Heterocephalus glaber*, and its relatives (Rodentia: Bathyergidae). *PloS one*, *11*(12), e0167079.

McVean, A. (1999). Are the semicircular canals of the European mole, *Talpa europaea*, adapted to a subterranean habitat? *Comparative Biochemistry and Physiology Part A: Molecular & Integrative Physiology, 123*(2), 173-178.

Mennecart, B., & Costeur, L. (2016). Shape variation and ontogeny of the ruminant bony labyrinth, an example in Tragulidae. *Journal of anatomy*, *229*(3), 422-435.

Mennecart, B., DeMiguel, D., Bibi, F., Rössner, G. E., Métais, G., Neenan, J. M., Wang, S., Schulz, G. Müller, B., & Costeur, L. (2017). Bony labyrinth morphology clarifies the origin and evolution of deer. *Scientific Reports*, *7*, 13176.

Nevo, E. (1999). *Mosaic evolution of subterranean mammals: Regression, progression, and global convergence*. Oxford University Press, Oxford, 413 p.

Pfaff, C., Martin, T., & Ruf, I. (2015). Bony labyrinth morphometry indicates locomotor adaptations in the squirrel-related clade (Rodentia, Mammalia). *Proceedings of the Royal Society of London B: Biological Sciences, 282*(1809), 20150744.

Pfaff, C., Czerny, S., Nagel, D., & Kriwet, J. (2017). Functional morphological adaptations of the bony labyrinth in marsupials (Mammalia, Theria). *Journal of Morphology, 278*(6), 742-749.

Pleštilová, L., Hrouzková, E., Burda, H., & Šumbera, R. (2016). Does the morphology of the ear of the Chinese bamboo rat (*Rhizomys sinensis*) show "Subterranean" characteristics? *Journal of Morphology, 277*(5), 575-584.

Rabbitt, R. D., Breneman, K. D., King, C., Yamauchi, A. M., Boyle, R., & Highstein, S. M. (2009). Dynamic displacement of normal and detached semicircular canal cupula. *Journal of the Association for Research in Otolaryngology*, *10*(4), 497-509.

R Core Team (2014). R: A language and environment for statistical computing. Vienna, Austria: R Foundation for Statistical Computing; 2014.

Revell, L. J. (2012). phytools: an R package for phylogenetic comparative biology (and other things). *Methods in Ecology and Evolution*, *3*(2), 217-223.

Rohlf, F. J., and D. E. Slice. (1990). Extensions of the Procrustes method for the optimal superimposition of landmarks. *Systematic Zoology, 39*, 40-59.

Schultz, J. A., Zeller, U., & Luo, Z. X. (2017). Inner ear labyrinth anatomy of monotremes and implications for mammalian inner ear evolution. *Journal of Morphology, 278*(2), 236-263.

Serena, M., Thomas, J. L., Williams, G. A., & Officer, R. C. E. (1998). Use of stream and river habitats by the platypus, *Ornithorhynchus anatinus*, in an urban fringe environment. *Australian Journal of Zoology*, *46*(3), 267-282.

Sherratt, E. (2014). Quick guide to Geomorph v. 2.0. *Quick Guide to Geomorph.[Online][Accessed 5 July 2016] Available from: http://www. public. iastate. edu*.

Specht, M. (2007). *Spherical surface parameterization and its application to geometric morphometric analysis of the braincase*. Ph.D. Dissertation, University of Zürich Irchel, Zürich.

Spoor, F. R. E. D., & Zonneveld, F. R. A. N. S. (1995). Morphometry of the primate bony labyrinth: a new method based on high-resolution computed tomography. *Journal of Anatomy*, *186*(2), 271.

Spoor, F., Bajpai, S., Hussain, S. T., Kumar, K., & Thewissen, J. G. (2002). Vestibular evidence for the evolution of aquatic behaviour in early cetaceans. *Nature*, *417*(6885), 163-166.

Spoor, F., Garland, T., Krovitz, G., Ryan, T. M., Silcox, M. T., & Walker, A. (2007). The primate semicircular canal system and locomotion. *Proceedings of the National Academy of Sciences*, *104*(26), 10808-10812.

SUPPLEMENTARY INFORMATION

Supplementary Information 1. Organization of the 132 landmarks in the landmarks matrix.
The 6 type-I landmarks are identified in orange.

Landmarks Name	X	Y	Z
Uc	x1	y1	z1
	x2	y2	z2
	x3	y3	z3
	x4	y4	z4
	x5	y5	z5
	x6	y6	z6
	x7	y7	z7
	x8	y8	z8
Ua_e	x9	y9	z9
	x10	y10	z10
	x11	y11	z11
Cr_a	x12	y12	z12
	x13	y13	z13
Sa_b	x14	y14	z14
	x15	y15	z15
	x16	y16	z16
	x17	y17	z17
	x18	y18	z18
	x19	y19	z19
	x20	y20	z20
	x21	y21	z21
	x22	y22	z22
	x23	y23	z23
	x24	y24	z24
	x25	y25	z25
	x26	y26	z26
	x27	y27	z27
	x28	y28	z28
	x29	y29	z29
	x30	y30	z30
	x31	y31	z31
	x32	y32	z32
	x33	y33	z33
	x34	y34	z34
	x35	y35	z35
	x36	y36	z36
	x37	y37	z37
	x38	y38	z38
	x39	y39	z39
	x40	y40	z40
	x41	y41	z41
Sa_e	x42	y42	z42
CC_b	x43	y43	z43
	x44	y44	z44
	x45	y45	z45
	x46	y46	z46
	x47	y47	z47
	x48	y48	z48
	x49	y49	z49
UC-1	x50	y50	z50
	x51	y51	z51
	x52	y52	z52
	x53	y53	z53
	x54	y54	z54
	x55	y55	z55
	x56	y56	z56
Cr_p	x57	y57	z57
	x58	y58	z58
Sp_b	x59	y59	z59
	x60	y60	z60
	x61	y61	z61
	x62	y62	z62
	x63	y63	z63
	x64	y64	z64
	x65	y65	z65
	x66	y66	z66
	x67	y67	z67
	x68	y68	z68
	x69	y69	z69
	x70	y70	z70
	x71	y71	z71
	x72	y72	z72
	x73	y73	z73
	x74	y74	z74
	x75	y75	z75

	x76	y76	z76
	x77	y77	z77
	x78	y78	z78
	x79	y79	z79
	x80	y80	z80
	x81	y81	z81
	x82	y82	z82
	x83	y83	z83
	x84	y84	z84
	x85	y85	z85
	x86	y86	z86
	x87	y87	z87
	x88	y88	z88
	x89	y89	z89
	x90	y90	z90
Sp_e	x91	y91	z91
Ua_e-1	x92	y92	z92
	x93	y93	z93
Cr_l	x94	y94	z94
	x95	y95	z95
Sl_b	x96	y96	z96
	x97	y97	z97
	x98	y98	z98
	x99	y99	z99
	x100	y100	z100
	x101	y101	z101
	x102	y102	z102
	x103	y103	z103
	x104	y104	z104

	x105	y105	z105
	x106	y106	z106
	x107	y107	z107
	x108	y108	z108
	x109	y109	z109
	x110	y110	z110
	x111	y111	z111
	x112	y112	z112
	x113	y113	z113
	x114	y114	z114
	x115	y115	z115
	x116	y116	z116
	x117	y117	z117
	x118	y118	z118
	x119	y119	z119
	x120	y120	z120
	x121	y121	z121
	x122	y122	z122
	x123	y123	z123
	x124	y124	z124
	x125	y125	z125
	x126	y126	z126
	x127	y127	z127
Sl_e	x128	y128	z128
	x129	y129	z129
	x130	y130	z130
	x131	y131	z131
	x132	y132	z132

Supplementary Information 2. Order of the 30 species in the matrix of landmark coordinates (in red are the moles).

Order	Species
1	*B. p. taurus*
2	*C. jacchus*
3	*C. l. familiaris*
4	*C. penicillata*
5	*D. viverrinus*
6	*E. elegantulus*
7	*E. f. caballus*
8	*G. gorilla*
9	*H. lar*
10	*H. sapiens*
11	*L. catta*
12	*M. fascicularis*
13	*Microcebus*
14	*M. mulatta*
15	*N. coucang*
16	*N. nasua*
17	*O. anatinus*
18	*O. cuniculus*
19	*P. abelii*
20	*P. rodricensis*
21	*P. troglodytes*
22	*S. sciureus*
23	*S. s. domesticus*
24	*T. javanica*
25	*V. pacos*
26	*Amblysomus hottentotus*
27	*Chlamyphorus truncatus*
28	*Heterocephalus glaber*
29	*Notoryctes typhlops*
30	*Talpa europaea*

Supplementary Information 3. R script for geometric morphometric.

```
#### to save 3D representations in PLY (openable on 3D manage software), the
function writePLY("file_name.ply") is available. It is saving the 3D
representations opened in a window (be careful, you should have only one 3D
representation in one window to save it. If there are more than one representation,
it doesn't work).
#### to save graphical datas, possibility to right click on the graphical window
and choose copy as vectorial and past on Illustrator software (on illustrator,
delete the clipping mask in "object")
#### Be careful to the 3D representations of graphical and conformation, you should
save data without perspective. To do this, press and hold the Scroll Wheel and move
the mouse forward to delete the perpective rendering.
#### to save table, 'write.table(object, file = "file_name.txt")' or
capture.output(object, file = "adjusted_shape.txt")


#################### Initialisation ####################

rm(list=ls(all=TRUE))

################# install packages for the first use #######

install.packages("geomorph",dependencies=T)
install.packages("Hotelling",dependencies=T)
install.packages("tibble",dependencies=T)
install.packages("phylobase",dependencies=T)
install.packages("matrixcalc",dependencies=T)

#################### Loading libraries ####################

library(geomorph)
library(ape)
library(Hotelling)
library(tibble)
library(phylobase)
library(phytools)
library(phylosignal)
library(MASS)
library(geiger)
library(matrixcalc)


#################### Loading raw datasets ####################

DATA_FULL_raw = as.matrix(read.table(file.choose(), header = TRUE))
##RData_FullLabyrinth.txt
SLIDERS = as.matrix(read.table(file.choose(), header = TRUE))
##RData_FullLabyrinth_Slide.txt
TREE = read.nexus(file.choose()) ##MammalTree.nex



#################### Preparing datasets ####################

DATA_FULL = arrayspecs(DATA_FULL_raw,132,3)

dimnames(DATA_FULL)= list(NULL, NULL, c("Bptaurus", "Cjacchus", "Clfamiliaris",
"Cpenicillata", "Dviverrinus", "Eelegantulus",
"Efcaballus", "Ggorilla", "Hlar", "Hsapiens", "Lcatta", "Mfascicularis",
"Microcebus", "Mmulatta", "Ncoucang", "Nnasua", "Oanatinus",
"Ocuniculus", "Pabelii", "Prodricensis", "Ptroglodytes", "Ssciureus",
"Ssdomesticus", "Tjavanica", "Vpacos", "Amblysomus", "Chlamyphorus",
"Heterocephalus",
"Notoryctes", "Talpa"))
```

```
labels = c("Bptaurus", "Cjacchus", "Clfamiliaris", "Cpenicillata", "Dviverrinus",
"Eelegantulus",
"Efcaballus", "Ggorilla", "Hlar", "Hsapiens", "Lcatta", "Mfascicularis",
"Microcebus", "Mmulatta", "Ncoucang", "Nnasua", "Oanatinus",
"Ocuniculus", "Pabelii", "Prodricensis", "Ptroglodytes", "Ssciureus",
"Ssdomesticus", "Tjavanica", "Vpacos", "Amblysomus", "Chlamyphorus",
"Heterocephalus",
"Notoryctes", "Talpa")



################### Coloring Landmarks and Species ############

landmarks_color =
factor(c("1","0","0","0","0","0","0","0","1","0","0","1","0","0","0","0","0","0","0","0
","0","0","0","0","0","0","0","0","0","0","0","0","0","0","0","0","0","0","0","0","0","
0","0","0","1","0","0","0","0","0","0","0","0","0","0","0","0","0","1","0","0","0",
"0","0","0","0","0","0","0","0","0","0","0","0","0","0","0","0","0","0","0","0","0","0"
,"0","0","0","0","0","0","0","0","0","0","0","0","0","1","0","0","0","0","0","0","0","0
","0","0","0","0","0","0","0","0","0","0","0","0","0","0","0","0","0","0","0","0","0","
0","0","0","0","0","0","0","0","0","0"))
species_color =
factor(c("0","0","0","0","0","0","0","0","0","0","0","0","0","0","0","0","0","0","0","0
","0","0","0","0","0","0","0","1","1","1","1","1"))


################### Performing the Generalized Procrustes Analysis
####################

GPA_DATA_FULL = gpagen(DATA_FULL, curves = SLIDERS, surfaces = NULL, PrinAxes =
TRUE, max.iter = NULL, ProcD = FALSE, Proj = TRUE)
plotAllSpecimens(GPA_DATA_FULL$ coords, mean = TRUE, links = NULL)
summary(GPA_DATA_FULL)



################### Plot consensus shape ####################

plot3d(GPA_DATA_FULL$consensus, aspect = FALSE, col=as.numeric(landmarks_color),
size = 8, box=FALSE, axes=FALSE)


################### PCA analysis of procrustes residuals ####################

PCA_Brute = plotTangentSpace(GPA_DATA_FULL$coords, axis1 = 3, axis2 = 1, warpgrids
= TRUE, mesh = NULL, label = labels, groups = species_color, verbose = TRUE)

pairs(PCA_Brute$pc.scores[,1:10], col=as.numeric(species_color))


Ancestor = plotGMPhyloMorphoSpace(TREE, GPA_DATA_FULL$coords, tip.labels = TRUE,
node.labels = TRUE, ancStates = TRUE, xaxis = 1, yaxis = 3, zaxis = "time")
Ancestor = arrayspecs(Ancestor,132,3)  ## I changed the original sentence :
Ancestor_Allo = arrayspecs(Ancestor_Allo[1,],132,3)
dimnames(Ancestor)= list(NULL, NULL, "Ancestor") #doesn't work#


#Normally, this function is to compare two data, here the moles with mammal
morphotype (first arguments in grey and second argument in black)
open3d()
plotRefToTarget(Ancestor[,,1], GPA_DATA_FULL$coords[,,30], method = "points", mag =
1)
open3d()
plotRefToTarget(Ancestor[,,1], GPA_DATA_FULL$coords[,,29], method = "points", mag =
1)
open3d()
plotRefToTarget(Ancestor[,,1], GPA_DATA_FULL$coords[,,28], method = "points", mag =
1)
```

```
open3d()
plotRefToTarget(Ancestor[,,1], GPA_DATA_FULL$coords[,,27], method = "points", mag =
1)
open3d()
plotRefToTarget(Ancestor[,,1], GPA_DATA_FULL$coords[,,26], method = "points", mag =
1)


#to obtain nice 3D representations, this function of comparaison is nice.
Possibility to save in .ply format with the function writePLY("file_name.ply")
plotRefToTarget(PCA_Brute$pc.shapes$PC1min, PCA_Brute$pc.shapes$PC1max, method =
"points", mag = 1)
plotRefToTarget(PCA_Brute$pc.shapes$PC1max, PCA_Brute$pc.shapes$PC1max, method =
"points", mag = 1)


# graphical visualization of the PCA axes ~ phylogeny
treePlot(phylo4d(TREE, data.frame(PCA_Brute$pc.scores[,1:3])))


#################### Phylogenetic signal  ####################

## all shape ~ phylogeny = Kmult (Adams, 2014)
PS.shape.brut = physignal(GPA_DATA_FULL$coords, TREE, iter = 999, seed = NULL)
summary(PS.shape.brut)
plot(PS.shape.brut)


## PC axes from PCA_Brute ~ phylogeny ##### Should not be done on PC axes (see
Adams, 2014)
physignal(PCA_Brute$pc.scores[,2], TREE, iter = 999, seed = NULL)


#################### Hotelling T² ####################


A_Ho = PCA_Brute$pc.scores
B_Ho = A_Ho[26:30,]
C_Ho = A_Ho[1:25,]
### 15 PC > 95% of variance
Ho_Test = hotelling.test(A_Ho[,1:15], B_Ho[,1:15], shrinkage = FALSE, perm = TRUE,
B = 10000, progBar = TRUE)
Ho_Test_2 = hotelling.test(C_Ho[,1:15], B_Ho[,1:15], shrinkage = FALSE, perm =
TRUE, B = 10000, progBar = TRUE)



#################### Correction centroid sizes for the five subterranean species
####################


GPA_DATA_FULL$Csize[26] = GPA_DATA_FULL$Csize[26]/1000
GPA_DATA_FULL$Csize[27] = GPA_DATA_FULL$Csize[27]/1000
GPA_DATA_FULL$Csize[28] = GPA_DATA_FULL$Csize[28]/1000
GPA_DATA_FULL$Csize[29] = GPA_DATA_FULL$Csize[29]/1000
GPA_DATA_FULL$Csize[30] = GPA_DATA_FULL$Csize[30]/1000

hist(GPA_DATA_FULL$Csize)


###### Hotelling T² on centroid sizes ##########

t.test(GPA_DATA_FULL$Csize[1:25],GPA_DATA_FULL$Csize[26:30])

#################### Allometry ####################

DATA_Allo = geomorph.data.frame(GPA_DATA_FULL)
Allometry = procD.allometry(coords~Csize, data=DATA_Allo)
```

```
## 0.004 p value

plot(Allometry, method = "RegScore", label = labels)   ## more informations on
?procD.allometry
plot(Allometry, method = "PredLine", label = labels)   ## more informations on
?procD.allometry

plotRefToTarget(Allometry$Ahat.at.min, Allometry$Ahat.at.min, method = "points",
mag = 1)
plotRefToTarget(Allometry$Ahat.at.max, Allometry$Ahat.at.max, method = "points",
mag = 1)


################### Allometry corrected shapes ###################

Anova = procD.lm(Allometry$formula, data = Allometry$data, RRPP=TRUE)
shape.resid = arrayspecs(Anova$residuals, p=dim(GPA_DATA_FULL$coords)[1],
k=dim(GPA_DATA_FULL$coords)[2])
adj.shape = shape.resid + array(GPA_DATA_FULL$consensus, dim(shape.resid))



################### PCA analysis of procrustes residuals (corrected for allometry)
####################


GM_PCA = plotTangentSpace(adj.shape, axis1 = 1, axis2 = 3, warpgrids = TRUE, mesh =
NULL, label = labels, groups = species_color, verbose = TRUE)

Ancestor_Allo = plotGMPhyloMorphoSpace(TREE, adj.shape, tip.labels = TRUE,
node.labels = TRUE, ancStates = TRUE, xaxis = 1, yaxis = 2, zaxis = "time")
Ancestor_Allo = arrayspecs(Ancestor_Allo,132,3)
dimnames(Ancestor_Allo)= list(NULL, NULL, "Ancestor_Allo") ## doesn't work

plotGMPhyloMorphoSpace(TREE, adj.shape, tip.labels = TRUE, node.labels = TRUE,
ancStates = TRUE, xaxis = 1, yaxis = 2, zaxis = 3)

## Comparisons between the shape of the mammal morphotype and the adjusted shape of
the moles (shape corrected of allometry)
open3d()
plotRefToTarget(Ancestor_Allo[,,1], adj.shape[,,30], method = "points", mag = 1)
open3d()
plotRefToTarget(Ancestor_Allo[,,1], adj.shape[,,29], method = "points", mag = 1)
open3d()
plotRefToTarget(Ancestor_Allo[,,1], adj.shape[,,28], method = "points", mag = 1)
open3d()
plotRefToTarget(Ancestor_Allo[,,1], adj.shape[,,27], method = "points", mag = 1)
open3d()
plotRefToTarget(Ancestor_Allo[,,1], adj.shape[,,26], method = "points", mag = 1)

## Comparisons between the brute shape and the adjusted shape of the moles (shape
corrected of allometry)
open3d()
plotRefToTarget(GPA_DATA_FULL$coords[,,30], adj.shape[,,30], method = "points", mag
= 1)
open3d()
plotRefToTarget(GPA_DATA_FULL$coords[,,29], adj.shape[,,29], method = "points", mag
= 1)
open3d()
plotRefToTarget(GPA_DATA_FULL$coords[,,28], adj.shape[,,28], method = "points", mag
= 1)
open3d()
plotRefToTarget(GPA_DATA_FULL$coords[,,27], adj.shape[,,27], method = "points", mag
= 1)
open3d()
plotRefToTarget(GPA_DATA_FULL$coords[,,26], adj.shape[,,26], method = "points", mag
= 1)
```

```
# graphical visualization of the PCA axes ~ phylogeny
treePlot(phylo4d(TREE, data.frame(GM_PCA$pc.scores[,1:3])))


################### Phylogenetic signal (allometry corrected) ####################

## all shape (allometry corrected) ~ phylogeny
PS.shape = physignal(adj.shape, TREE, iter = 999, seed = NULL)
summary(PS.shape)
plot(PS.shape)

## PC axes from PCA 2 (allometry corrected) ~ phylogeny  ##### Should not be done
on PC axes (see ref from Romain David (ADAMS ?))
physignal(GM_PCA$pc.scores[,1], TREE, iter = 999, seed = NULL)



################### Hotelling T² (allometry corrected) ####################


A = GM_PCA$pc.scores
B = A[26:30,]
C = A[1:25,]
### 15 PC > 95% of variance
H_Test = hotelling.test(A[,1:15], B[,1:15], shrinkage = FALSE, perm = TRUE, B =
10000, progBar = TRUE)
H_Test_2 = hotelling.test(C[,1:15], B[,1:15], shrinkage = FALSE, perm = TRUE, B =
10000, progBar = TRUE)



#############################################################################
################## calculation of lambda needed for phylogenetic pca ############

#adj.shape.2darray = two.d.array(adj.shape)
#adj.shape.phylo4d = phylo4d(TREE, adj.shape.2darray)
#results = phyloSignal(adj.shape.phylo4d, methods = "K", reps = 999) ## not sure of
this lambda, maybe not specific for multivariate data
#summary(results$stat) ##### Maybe we can look at the mean of lambda = 0.3840 (
because we tried it for the K and Mean K of the phyloSignal function is egal to the
"real" K found with the physignal function)####################


## Model of Liam J. Revell to Predict Lambda with K = 0.4806

require(phytools); require(geiger)
nrep<-1000
P.K<-P.l<-l<-vector()

for(i in 1:nrep){
tree<-pbtree(n=50)
l[i]<-runif(n=1)
x<-fastBM(lambdaTree(tree,l[i]))
K<-phylosig(tree,x,test=T)
lambda<-phylosig(tree,x,method="lambda",test=T)
P.K[i]<-K$P
P.l[i]<-lambda$P
}

Model = lm(P.l~P.K)
x = 0.4806
x = as.data.frame(x)
colnames(x) = "P.K"
predict(Model,x, interval = "confidence")
#### fit = 0.51 / lwr = 0.48 / upr = 0.54
```

```
###### Tree transformation with the lambda = 0.51
TREE.lambda = rescale(TREE, "lambda", 0.51)
plot(TREE.lambda)
x11()  ## to open two windows and compare the graphics
plot(TREE)


#### TEST ### phylogenetic pca of adjusted shapes (allometry corrected)
###############
dataphylopca_allo = two.d.array(adj.shape)
phylopca_allo = phyl.pca(TREE.lambda, dataphylopca_allo, method = "BM")

summary(phylopca_allo)
pairs(phylopca_allo$S[,1:10], col = as.numeric(species_color))
plot(phylopca_allo$S[,c(1,3)], col =
as.numeric(species_color));text(phylopca_allo$S[,c(1,3)], col =
as.numeric(species_color), labels = labels)


### phylogenetic pca of adjusted shapes (allometry corrected) ###############
#dataphylopca_allo = two.d.array(adj.shape) ### transform a 3D matrix (= 3D array)
in 2D spcae (with the function two.d.array (contrary function of arrayspecs)
#phylopca_allo = phyl.pca(TREE, dataphylopca_allo, method = "BM") ## phylo PCA with
method on Brownien Mouvement
#phylopca_allo = phyl.pca(TREE, dataphylopca_allo, method = "lambda", opt =
"fixed", lambda = 0.1) #### does not seem to work with high lambda values#########


############### Calculation of residuals between the terminal taxa and nearest nodes
for Hotelling T² (allometry corrected) #######

TREE.lambda$edge ### terminal taxa (right column) associate to the nearest node
(left column)
TREE.lambda$tip.label ### terminal taxa order

pc1 = phylopca_allo$S[,1] ## on PC 1, taxons positions
node.pc1 = fastAnc(TREE.lambda,pc1) # state at the nodes for pc1
pc2 = phylopca_allo$S[,2]
node.pc2 = fastAnc(TREE.lambda,pc2)
pc3 = phylopca_allo$S[,3]
node.pc3 = fastAnc(TREE.lambda,pc3)
pc4 = phylopca_allo$S[,4]
node.pc4 = fastAnc(TREE.lambda,pc4)
pc5 = phylopca_allo$S[,5]
node.pc5 = fastAnc(TREE.lambda,pc5)
pc6 = phylopca_allo$S[,6]
node.pc6 = fastAnc(TREE.lambda,pc6)
pc7 = phylopca_allo$S[,7]
node.pc7 = fastAnc(TREE.lambda,pc7)
pc8 = phylopca_allo$S[,8]
node.pc8 = fastAnc(TREE.lambda,pc8)
pc9 = phylopca_allo$S[,9]
node.pc9 = fastAnc(TREE.lambda,pc9)
pc10 = phylopca_allo$S[,10]
node.pc10 = fastAnc(TREE.lambda,pc10)
pc11 = phylopca_allo$S[,11]
node.pc11 = fastAnc(TREE.lambda,pc11)
pc12 = phylopca_allo$S[,12]
node.pc12 = fastAnc(TREE.lambda,pc12)
pc13 = phylopca_allo$S[,13]
node.pc13 = fastAnc(TREE.lambda,pc13)
pc14 = phylopca_allo$S[,14]
node.pc14 = fastAnc(TREE.lambda,pc14)
pc15 = phylopca_allo$S[,15]
node.pc15 = fastAnc(TREE.lambda,pc15)
pc16 = phylopca_allo$S[,16]
node.pc16 = fastAnc(TREE.lambda,pc16)
pc17 = phylopca_allo$S[,17]
```

```
node.pc17 = fastAnc(TREE.lambda,pc17)
pc18 = phylopca_allo$S[,18]
node.pc18 = fastAnc(TREE.lambda,pc18)
pc19 = phylopca_allo$S[,19]
node.pc19 = fastAnc(TREE.lambda,pc19)
pc20 = phylopca_allo$S[,20]
node.pc20 = fastAnc(TREE.lambda,pc20)
pc21 = phylopca_allo$S[,21]
node.pc21 = fastAnc(TREE.lambda,pc21)
pc22 = phylopca_allo$S[,22]
node.pc22 = fastAnc(TREE.lambda,pc22)
pc23 = phylopca_allo$S[,23]
node.pc23 = fastAnc(TREE.lambda,pc23)
pc24 = phylopca_allo$S[,24]
node.pc24 = fastAnc(TREE.lambda,pc24)
pc25 = phylopca_allo$S[,25]
node.pc25 = fastAnc(TREE.lambda,pc25)
pc26 = phylopca_allo$S[,26]
node.pc26 = fastAnc(TREE.lambda,pc26)
pc27 = phylopca_allo$S[,27]
node.pc27 = fastAnc(TREE.lambda,pc27)
pc28 = phylopca_allo$S[,28]
node.pc28 = fastAnc(TREE.lambda,pc28)
pc29 = phylopca_allo$S[,29]
node.pc29 = fastAnc(TREE.lambda,pc29)


residual.pc1 = c(pc1[1]-node.pc1[11], pc1[2]-node.pc1[13], pc1[3]-node.pc1[3],
pc1[4]-node.pc1[12], pc1[5]-node.pc1[27], pc1[6]-node.pc1[25], pc1[7]-node.pc1[28],
pc1[8]-node.pc1[29], pc1[9]-node.pc1[14], pc1[10]-node.pc1[1], pc1[11]-
node.pc1[16], pc1[12]-node.pc1[26], pc1[13]-node.pc1[8], pc1[14]-node.pc1[28],
pc1[15]-node.pc1[23], pc1[16]-node.pc1[11], pc1[17]-node.pc1[17], pc1[18]-
node.pc1[10], pc1[19]-node.pc1[23], pc1[20]-node.pc1[21], pc1[21]-node.pc1[20],
pc1[22]-node.pc1[20], pc1[23]-node.pc1[29], pc1[24]-node.pc1[21], pc1[25]-
node.pc1[14], pc1[26]-node.pc1[5], pc1[27]-node.pc1[16], pc1[28]-node.pc1[3],
pc1[29]-node.pc1[5], pc1[30]-node.pc1[7])
residual.pc2 = c(pc2[1]-node.pc2[11], pc2[2]-node.pc2[13], pc2[3]-node.pc2[3],
pc2[4]-node.pc2[12], pc2[5]-node.pc2[27], pc2[6]-node.pc2[25], pc2[7]-node.pc2[28],
pc2[8]-node.pc2[29], pc2[9]-node.pc2[14], pc2[10]-node.pc2[1], pc2[11]-
node.pc2[16], pc2[12]-node.pc2[26], pc2[13]-node.pc2[8], pc2[14]-node.pc2[28],
pc2[15]-node.pc2[23], pc2[16]-node.pc2[11], pc2[17]-node.pc2[17], pc2[18]-
node.pc2[10], pc2[19]-node.pc2[23], pc2[20]-node.pc2[21], pc2[21]-node.pc2[20],
pc2[22]-node.pc2[20], pc2[23]-node.pc2[29], pc2[24]-node.pc2[21], pc2[25]-
node.pc2[14], pc2[26]-node.pc2[5], pc2[27]-node.pc2[16], pc2[28]-node.pc2[3],
pc2[29]-node.pc2[5], pc2[30]-node.pc2[7])
residual.pc3 = c(pc3[1]-node.pc3[11], pc3[2]-node.pc3[13], pc3[3]-node.pc3[3],
pc3[4]-node.pc3[12], pc3[5]-node.pc3[27], pc3[6]-node.pc3[25], pc3[7]-node.pc3[28],
pc3[8]-node.pc3[29], pc3[9]-node.pc3[14], pc3[10]-node.pc3[1], pc3[11]-
node.pc3[16], pc3[12]-node.pc3[26], pc3[13]-node.pc3[8], pc3[14]-node.pc3[28],
pc3[15]-node.pc3[23], pc3[16]-node.pc3[11], pc3[17]-node.pc3[17], pc3[18]-
node.pc3[10], pc3[19]-node.pc3[23], pc3[20]-node.pc3[21], pc3[21]-node.pc3[20],
pc3[22]-node.pc3[20], pc3[23]-node.pc3[29], pc3[24]-node.pc3[21], pc3[25]-
node.pc3[14], pc3[26]-node.pc3[5], pc3[27]-node.pc3[16], pc3[28]-node.pc3[3],
pc3[29]-node.pc3[5], pc3[30]-node.pc3[7])
residual.pc4 = c(pc4[1]-node.pc4[11], pc4[2]-node.pc4[13], pc4[3]-node.pc4[3],
pc4[4]-node.pc4[12], pc4[5]-node.pc4[27], pc4[6]-node.pc4[25], pc4[7]-node.pc4[28],
pc4[8]-node.pc4[29], pc4[9]-node.pc4[14], pc4[10]-node.pc4[1], pc4[11]-
node.pc4[16], pc4[12]-node.pc4[26], pc4[13]-node.pc4[8], pc4[14]-node.pc4[28],
pc4[15]-node.pc4[23], pc4[16]-node.pc4[11], pc4[17]-node.pc4[17], pc4[18]-
node.pc4[10], pc4[19]-node.pc4[23], pc4[20]-node.pc4[21], pc4[21]-node.pc4[20],
pc4[22]-node.pc4[20], pc4[23]-node.pc4[29], pc4[24]-node.pc4[21], pc4[25]-
node.pc4[14], pc4[26]-node.pc4[5], pc4[27]-node.pc4[16], pc4[28]-node.pc4[3],
pc4[29]-node.pc4[5], pc4[30]-node.pc4[7])
residual.pc5 = c(pc5[1]-node.pc5[11], pc5[2]-node.pc5[13], pc5[3]-node.pc5[3],
pc5[4]-node.pc5[12], pc5[5]-node.pc5[27], pc5[6]-node.pc5[25], pc5[7]-node.pc5[28],
pc5[8]-node.pc5[29], pc5[9]-node.pc5[14], pc5[10]-node.pc5[1], pc5[11]-
node.pc5[16], pc5[12]-node.pc5[26], pc5[13]-node.pc5[8], pc5[14]-node.pc5[28],
pc5[15]-node.pc5[23], pc5[16]-node.pc5[11], pc5[17]-node.pc5[17], pc5[18]-
```

```
node.pc5[10], pc5[19]-node.pc5[23], pc5[20]-node.pc5[21], pc5[21]-node.pc5[20],
pc5[22]-node.pc5[20], pc5[23]-node.pc5[29], pc5[24]-node.pc5[21], pc5[25]-
node.pc5[14], pc5[26]-node.pc5[5], pc5[27]-node.pc5[16], pc5[28]-node.pc5[3],
pc5[29]-node.pc5[5], pc5[30]-node.pc5[7])
residual.pc6 = c(pc6[1]-node.pc6[11], pc6[2]-node.pc6[13], pc6[3]-node.pc6[3],
pc6[4]-node.pc6[12], pc6[5]-node.pc6[27], pc6[6]-node.pc6[25], pc6[7]-node.pc6[28],
pc6[8]-node.pc6[29], pc6[9]-node.pc6[14], pc6[10]-node.pc6[1], pc6[11]-
node.pc6[16], pc6[12]-node.pc6[26], pc6[13]-node.pc6[8], pc6[14]-node.pc6[28],
pc6[15]-node.pc6[23], pc6[16]-node.pc6[11], pc6[17]-node.pc6[17], pc6[18]-
node.pc6[10], pc6[19]-node.pc6[23], pc6[20]-node.pc6[21], pc6[21]-node.pc6[20],
pc6[22]-node.pc6[20], pc6[23]-node.pc6[29], pc6[24]-node.pc6[21], pc6[25]-
node.pc6[14], pc6[26]-node.pc6[5], pc6[27]-node.pc6[16], pc6[28]-node.pc6[3],
pc6[29]-node.pc6[5], pc6[30]-node.pc6[7])
residual.pc7 = c(pc7[1]-node.pc7[11], pc7[2]-node.pc7[13], pc7[3]-node.pc7[3],
pc7[4]-node.pc7[12], pc7[5]-node.pc7[27], pc7[6]-node.pc7[25], pc7[7]-node.pc7[28],
pc7[8]-node.pc7[29], pc7[9]-node.pc7[14], pc7[10]-node.pc7[1], pc7[11]-
node.pc7[16], pc7[12]-node.pc7[26], pc7[13]-node.pc7[8], pc7[14]-node.pc7[28],
pc7[15]-node.pc7[23], pc7[16]-node.pc7[11], pc7[17]-node.pc7[17], pc7[18]-
node.pc7[10], pc7[19]-node.pc7[23], pc7[20]-node.pc7[21], pc7[21]-node.pc7[20],
pc7[22]-node.pc7[20], pc7[23]-node.pc7[29], pc7[24]-node.pc7[21], pc7[25]-
node.pc7[14], pc7[26]-node.pc7[5], pc7[27]-node.pc7[16], pc7[28]-node.pc7[3],
pc7[29]-node.pc7[5], pc7[30]-node.pc7[7])
residual.pc8 = c(pc8[1]-node.pc8[11], pc8[2]-node.pc8[13], pc8[3]-node.pc8[3],
pc8[4]-node.pc8[12], pc8[5]-node.pc8[27], pc8[6]-node.pc8[25], pc8[7]-node.pc8[28],
pc8[8]-node.pc8[29], pc8[9]-node.pc8[14], pc8[10]-node.pc8[1], pc8[11]-
node.pc8[16], pc8[12]-node.pc8[26], pc8[13]-node.pc8[8], pc8[14]-node.pc8[28],
pc8[15]-node.pc8[23], pc8[16]-node.pc8[11], pc8[17]-node.pc8[17], pc8[18]-
node.pc8[10], pc8[19]-node.pc8[23], pc8[20]-node.pc8[21], pc8[21]-node.pc8[20],
pc8[22]-node.pc8[20], pc8[23]-node.pc8[29], pc8[24]-node.pc8[21], pc8[25]-
node.pc8[14], pc8[26]-node.pc8[5], pc8[27]-node.pc8[16], pc8[28]-node.pc8[3],
pc8[29]-node.pc8[5], pc8[30]-node.pc8[7])
residual.pc9 = c(pc9[1]-node.pc9[11], pc9[2]-node.pc9[13], pc9[3]-node.pc9[3],
pc9[4]-node.pc9[12], pc9[5]-node.pc9[27], pc9[6]-node.pc9[25], pc9[7]-node.pc9[28],
pc9[8]-node.pc9[29], pc9[9]-node.pc9[14], pc9[10]-node.pc9[1], pc9[11]-
node.pc9[16], pc9[12]-node.pc9[26], pc9[13]-node.pc9[8], pc9[14]-node.pc9[28],
pc9[15]-node.pc9[23], pc9[16]-node.pc9[11], pc9[17]-node.pc9[17], pc9[18]-
node.pc9[10], pc9[19]-node.pc9[23], pc9[20]-node.pc9[21], pc9[21]-node.pc9[20],
pc9[22]-node.pc9[20], pc9[23]-node.pc9[29], pc9[24]-node.pc9[21], pc9[25]-
node.pc9[14], pc9[26]-node.pc9[5], pc9[27]-node.pc9[16], pc9[28]-node.pc9[3],
pc9[29]-node.pc9[5], pc9[30]-node.pc9[7])
residual.pc10 = c(pc10[1]-node.pc10[11], pc10[2]-node.pc10[13], pc10[3]-
node.pc10[3], pc10[4]-node.pc10[12], pc10[5]-node.pc10[27], pc10[6]-node.pc10[25],
pc10[7]-node.pc10[28], pc10[8]-node.pc10[29], pc10[9]-node.pc10[14], pc10[10]-
node.pc10[1], pc10[11]-node.pc10[16], pc10[12]-node.pc10[26], pc10[13]-
node.pc10[8], pc10[14]-node.pc10[28], pc10[15]-node.pc10[23], pc10[16]-
node.pc10[11], pc10[17]-node.pc10[17], pc10[18]-node.pc10[10], pc10[19]-
node.pc10[23], pc10[20]-node.pc10[21], pc10[21]-node.pc10[20], pc10[22]-
node.pc10[20], pc10[23]-node.pc10[29], pc10[24]-node.pc10[21], pc10[25]-
node.pc10[14], pc10[26]-node.pc10[5], pc10[27]-node.pc10[16], pc10[28]-
node.pc10[3], pc10[29]-node.pc10[5], pc10[30]-node.pc10[7])
residual.pc11 = c(pc11[1]-node.pc11[11], pc11[2]-node.pc11[13], pc11[3]-
node.pc11[3], pc11[4]-node.pc11[12], pc11[5]-node.pc11[27], pc11[6]-node.pc11[25],
pc11[7]-node.pc11[28], pc11[8]-node.pc11[29], pc11[9]-node.pc11[14], pc11[10]-
node.pc11[1], pc11[11]-node.pc11[16], pc11[12]-node.pc11[26], pc11[13]-
node.pc11[8], pc11[14]-node.pc11[28], pc11[15]-node.pc11[23], pc11[16]-
node.pc11[11], pc11[17]-node.pc11[17], pc11[18]-node.pc11[10], pc11[19]-
node.pc11[23], pc11[20]-node.pc11[21], pc11[21]-node.pc11[20], pc11[22]-
node.pc11[20], pc11[23]-node.pc11[29], pc11[24]-node.pc11[21], pc11[25]-
node.pc11[14], pc11[26]-node.pc11[5], pc11[27]-node.pc11[16], pc11[28]-
node.pc11[3], pc11[29]-node.pc11[5], pc11[30]-node.pc11[7])
residual.pc12 = c(pc12[1]-node.pc12[11], pc12[2]-node.pc12[13], pc12[3]-
node.pc12[3], pc12[4]-node.pc12[12], pc12[5]-node.pc12[27], pc12[6]-node.pc12[25],
pc12[7]-node.pc12[28], pc12[8]-node.pc12[29], pc12[9]-node.pc12[14], pc12[10]-
node.pc12[1], pc12[11]-node.pc12[16], pc12[12]-node.pc12[26], pc12[13]-
node.pc12[8], pc12[14]-node.pc12[28], pc12[15]-node.pc12[23], pc12[16]-
node.pc12[11], pc12[17]-node.pc12[17], pc12[18]-node.pc12[10], pc12[19]-
node.pc12[23], pc12[20]-node.pc12[21], pc12[21]-node.pc12[20], pc12[22]-
node.pc12[20], pc12[23]-node.pc12[29], pc12[24]-node.pc12[21], pc12[25]-
```

```
node.pc12[14], pc12[26]-node.pc12[5], pc12[27]-node.pc12[16], pc12[28]-
node.pc12[3], pc12[29]-node.pc12[5], pc12[30]-node.pc12[7])
residual.pc13 = c(pc13[1]-node.pc13[11], pc13[2]-node.pc13[13], pc13[3]-
node.pc13[3], pc13[4]-node.pc13[12], pc13[5]-node.pc13[27], pc13[6]-node.pc13[25],
pc13[7]-node.pc13[28], pc13[8]-node.pc13[29], pc13[9]-node.pc13[14], pc13[10]-
node.pc13[1], pc13[11]-node.pc13[16], pc13[12]-node.pc13[26], pc13[13]-
node.pc13[8], pc13[14]-node.pc13[28], pc13[15]-node.pc13[23], pc13[16]-
node.pc13[11], pc13[17]-node.pc13[17], pc13[18]-node.pc13[10], pc13[19]-
node.pc13[23], pc13[20]-node.pc13[21], pc13[21]-node.pc13[20], pc13[22]-
node.pc13[20], pc13[23]-node.pc13[29], pc13[24]-node.pc13[21], pc13[25]-
node.pc13[14], pc13[26]-node.pc13[5], pc13[27]-node.pc13[16], pc13[28]-
node.pc13[3], pc13[29]-node.pc13[5], pc13[30]-node.pc13[7])
residual.pc14 = c(pc14[1]-node.pc14[11], pc14[2]-node.pc14[13], pc14[3]-
node.pc14[3], pc14[4]-node.pc14[12], pc14[5]-node.pc14[27], pc14[6]-node.pc14[25],
pc14[7]-node.pc14[28], pc14[8]-node.pc14[29], pc14[9]-node.pc14[14], pc14[10]-
node.pc14[1], pc14[11]-node.pc14[16], pc14[12]-node.pc14[26], pc14[13]-
node.pc14[8], pc14[14]-node.pc14[28], pc14[15]-node.pc14[23], pc14[16]-
node.pc14[11], pc14[17]-node.pc14[17], pc14[18]-node.pc14[10], pc14[19]-
node.pc14[23], pc14[20]-node.pc14[21], pc14[21]-node.pc14[20], pc14[22]-
node.pc14[20], pc14[23]-node.pc14[29], pc14[24]-node.pc14[21], pc14[25]-
node.pc14[14], pc14[26]-node.pc14[5], pc14[27]-node.pc14[16], pc14[28]-
node.pc14[3], pc14[29]-node.pc14[5], pc14[30]-node.pc14[7])
residual.pc15 = c(pc15[1]-node.pc15[11], pc15[2]-node.pc15[13], pc15[3]-
node.pc15[3], pc15[4]-node.pc15[12], pc15[5]-node.pc15[27], pc15[6]-node.pc15[25],
pc15[7]-node.pc15[28], pc15[8]-node.pc15[29], pc15[9]-node.pc15[14], pc15[10]-
node.pc15[1], pc15[11]-node.pc15[16], pc15[12]-node.pc15[26], pc15[13]-
node.pc15[8], pc15[14]-node.pc15[28], pc15[15]-node.pc15[23], pc15[16]-
node.pc15[11], pc15[17]-node.pc15[17], pc15[18]-node.pc15[10], pc15[19]-
node.pc15[23], pc15[20]-node.pc15[21], pc15[21]-node.pc15[20], pc15[22]-
node.pc15[20], pc15[23]-node.pc15[29], pc15[24]-node.pc15[21], pc15[25]-
node.pc15[14], pc15[26]-node.pc15[5], pc15[27]-node.pc15[16], pc15[28]-
node.pc15[3], pc15[29]-node.pc15[5], pc15[30]-node.pc15[7])
residual.pc16 = c(pc16[1]-node.pc16[11], pc16[2]-node.pc16[13], pc16[3]-
node.pc16[3], pc16[4]-node.pc16[12], pc16[5]-node.pc16[27], pc16[6]-node.pc16[25],
pc16[7]-node.pc16[28], pc16[8]-node.pc16[29], pc16[9]-node.pc16[14], pc16[10]-
node.pc16[1], pc16[11]-node.pc16[16], pc16[12]-node.pc16[26], pc16[13]-
node.pc16[8], pc16[14]-node.pc16[28], pc16[15]-node.pc16[23], pc16[16]-
node.pc16[11], pc16[17]-node.pc16[17], pc16[18]-node.pc16[10], pc16[19]-
node.pc16[23], pc16[20]-node.pc16[21], pc16[21]-node.pc16[20], pc16[22]-
node.pc16[20], pc16[23]-node.pc16[29], pc16[24]-node.pc16[21], pc16[25]-
node.pc16[14], pc16[26]-node.pc16[5], pc16[27]-node.pc16[16], pc16[28]-
node.pc16[3], pc16[29]-node.pc16[5], pc16[30]-node.pc16[7])
residual.pc17 = c(pc17[1]-node.pc17[11], pc17[2]-node.pc17[13], pc17[3]-
node.pc17[3], pc17[4]-node.pc17[12], pc17[5]-node.pc17[27], pc17[6]-node.pc17[25],
pc17[7]-node.pc17[28], pc17[8]-node.pc17[29], pc17[9]-node.pc17[14], pc17[10]-
node.pc17[1], pc17[11]-node.pc17[16], pc17[12]-node.pc17[26], pc17[13]-
node.pc17[8], pc17[14]-node.pc17[28], pc17[15]-node.pc17[23], pc17[16]-
node.pc17[11], pc17[17]-node.pc17[17], pc17[18]-node.pc17[10], pc17[19]-
node.pc17[23], pc17[20]-node.pc17[21], pc17[21]-node.pc17[20], pc17[22]-
node.pc17[20], pc17[23]-node.pc17[29], pc17[24]-node.pc17[21], pc17[25]-
node.pc17[14], pc17[26]-node.pc17[5], pc17[27]-node.pc17[16], pc17[28]-
node.pc17[3], pc17[29]-node.pc17[5], pc17[30]-node.pc17[7])
residual.pc18 = c(pc18[1]-node.pc18[11], pc18[2]-node.pc18[13], pc18[3]-
node.pc18[3], pc18[4]-node.pc18[12], pc18[5]-node.pc18[27], pc18[6]-node.pc18[25],
pc18[7]-node.pc18[28], pc18[8]-node.pc18[29], pc18[9]-node.pc18[14], pc18[10]-
node.pc18[1], pc18[11]-node.pc18[16], pc18[12]-node.pc18[26], pc18[13]-
node.pc18[8], pc18[14]-node.pc18[28], pc18[15]-node.pc18[23], pc18[16]-
node.pc18[11], pc18[17]-node.pc18[17], pc18[18]-node.pc18[10], pc18[19]-
node.pc18[23], pc18[20]-node.pc18[21], pc18[21]-node.pc18[20], pc18[22]-
node.pc18[20], pc18[23]-node.pc18[29], pc18[24]-node.pc18[21], pc18[25]-
node.pc18[14], pc18[26]-node.pc18[5], pc18[27]-node.pc18[16], pc18[28]-
node.pc18[3], pc18[29]-node.pc18[5], pc18[30]-node.pc18[7])
residual.pc19 = c(pc19[1]-node.pc19[11], pc19[2]-node.pc19[13], pc19[3]-
node.pc19[3], pc19[4]-node.pc19[12], pc19[5]-node.pc19[27], pc19[6]-node.pc19[25],
pc19[7]-node.pc19[28], pc19[8]-node.pc19[29], pc19[9]-node.pc19[14], pc19[10]-
node.pc19[1], pc19[11]-node.pc19[16], pc19[12]-node.pc19[26], pc19[13]-
node.pc19[8], pc19[14]-node.pc19[28], pc19[15]-node.pc19[23], pc19[16]-
node.pc19[11], pc19[17]-node.pc19[17], pc19[18]-node.pc19[10], pc19[19]-
```

```
node.pc19[23], pc19[20]-node.pc19[21], pc19[21]-node.pc19[20], pc19[22]-
node.pc19[20], pc19[23]-node.pc19[29], pc19[24]-node.pc19[21], pc19[25]-
node.pc19[14], pc19[26]-node.pc19[5], pc19[27]-node.pc19[16], pc19[28]-
node.pc19[3], pc19[29]-node.pc19[5], pc19[30]-node.pc19[7])
residual.pc20 = c(pc20[1]-node.pc20[11], pc20[2]-node.pc20[13], pc20[3]-
node.pc20[3], pc20[4]-node.pc20[12], pc20[5]-node.pc20[27], pc20[6]-node.pc20[25],
pc20[7]-node.pc20[28], pc20[8]-node.pc20[29], pc20[9]-node.pc20[14], pc20[10]-
node.pc20[1], pc20[11]-node.pc20[16], pc20[12]-node.pc20[26], pc20[13]-
node.pc20[8], pc20[14]-node.pc20[28], pc20[15]-node.pc20[23], pc20[16]-
node.pc20[11], pc20[17]-node.pc20[17], pc20[18]-node.pc20[10], pc20[19]-
node.pc20[23], pc20[20]-node.pc20[21], pc20[21]-node.pc20[20], pc20[22]-
node.pc20[20], pc20[23]-node.pc20[29], pc20[24]-node.pc20[21], pc20[25]-
node.pc20[14], pc20[26]-node.pc20[5], pc20[27]-node.pc20[16], pc20[28]-
node.pc20[3], pc20[29]-node.pc20[5], pc20[30]-node.pc20[7])
residual.pc21 = c(pc21[1]-node.pc21[11], pc21[2]-node.pc21[13], pc21[3]-
node.pc21[3], pc21[4]-node.pc21[12], pc21[5]-node.pc21[27], pc21[6]-node.pc21[25],
pc21[7]-node.pc21[28], pc21[8]-node.pc21[29], pc21[9]-node.pc21[14], pc21[10]-
node.pc21[1], pc21[11]-node.pc21[16], pc21[12]-node.pc21[26], pc21[13]-
node.pc21[8], pc21[14]-node.pc21[28], pc21[15]-node.pc21[23], pc21[16]-
node.pc21[11], pc21[17]-node.pc21[17], pc21[18]-node.pc21[10], pc21[19]-
node.pc21[23], pc21[20]-node.pc21[21], pc21[21]-node.pc21[20], pc21[22]-
node.pc21[20], pc21[23]-node.pc21[29], pc21[24]-node.pc21[21], pc21[25]-
node.pc21[14], pc21[26]-node.pc21[5], pc21[27]-node.pc21[16], pc21[28]-
node.pc21[3], pc21[29]-node.pc21[5], pc21[30]-node.pc21[7])
residual.pc22 = c(pc22[1]-node.pc22[11], pc22[2]-node.pc22[13], pc22[3]-
node.pc22[3], pc22[4]-node.pc22[12], pc22[5]-node.pc22[27], pc22[6]-node.pc22[25],
pc22[7]-node.pc22[28], pc22[8]-node.pc22[29], pc22[9]-node.pc22[14], pc22[10]-
node.pc22[1], pc22[11]-node.pc22[16], pc22[12]-node.pc22[26], pc22[13]-
node.pc22[8], pc22[14]-node.pc22[28], pc22[15]-node.pc22[23], pc22[16]-
node.pc22[11], pc22[17]-node.pc22[17], pc22[18]-node.pc22[10], pc22[19]-
node.pc22[23], pc22[20]-node.pc22[21], pc22[21]-node.pc22[20], pc22[22]-
node.pc22[20], pc22[23]-node.pc22[29], pc22[24]-node.pc22[21], pc22[25]-
node.pc22[14], pc22[26]-node.pc22[5], pc22[27]-node.pc22[16], pc22[28]-
node.pc22[3], pc22[29]-node.pc22[5], pc22[30]-node.pc22[7])
residual.pc23 = c(pc23[1]-node.pc23[11], pc23[2]-node.pc23[13], pc23[3]-
node.pc23[3], pc23[4]-node.pc23[12], pc23[5]-node.pc23[27], pc23[6]-node.pc23[25],
pc23[7]-node.pc23[28], pc23[8]-node.pc23[29], pc23[9]-node.pc23[14], pc23[10]-
node.pc23[1], pc23[11]-node.pc23[16], pc23[12]-node.pc23[26], pc23[13]-
node.pc23[8], pc23[14]-node.pc23[28], pc23[15]-node.pc23[23], pc23[16]-
node.pc23[11], pc23[17]-node.pc23[17], pc23[18]-node.pc23[10], pc23[19]-
node.pc23[23], pc23[20]-node.pc23[21], pc23[21]-node.pc23[20], pc23[22]-
node.pc23[20], pc23[23]-node.pc23[29], pc23[24]-node.pc23[21], pc23[25]-
node.pc23[14], pc23[26]-node.pc23[5], pc23[27]-node.pc23[16], pc23[28]-
node.pc23[3], pc23[29]-node.pc23[5], pc23[30]-node.pc23[7])
residual.pc24 = c(pc24[1]-node.pc24[11], pc24[2]-node.pc24[13], pc24[3]-
node.pc24[3], pc24[4]-node.pc24[12], pc24[5]-node.pc24[27], pc24[6]-node.pc24[25],
pc24[7]-node.pc24[28], pc24[8]-node.pc24[29], pc24[9]-node.pc24[14], pc24[10]-
node.pc24[1], pc24[11]-node.pc24[16], pc24[12]-node.pc24[26], pc24[13]-
node.pc24[8], pc24[14]-node.pc24[28], pc24[15]-node.pc24[23], pc24[16]-
node.pc24[11], pc24[17]-node.pc24[17], pc24[18]-node.pc24[10], pc24[19]-
node.pc24[23], pc24[20]-node.pc24[21], pc24[21]-node.pc24[20], pc24[22]-
node.pc24[20], pc24[23]-node.pc24[29], pc24[24]-node.pc24[21], pc24[25]-
node.pc24[14], pc24[26]-node.pc24[5], pc24[27]-node.pc24[16], pc24[28]-
node.pc24[3], pc24[29]-node.pc24[5], pc24[30]-node.pc24[7])
residual.pc25 = c(pc25[1]-node.pc25[11], pc25[2]-node.pc25[13], pc25[3]-
node.pc25[3], pc25[4]-node.pc25[12], pc25[5]-node.pc25[27], pc25[6]-node.pc25[25],
pc25[7]-node.pc25[28], pc25[8]-node.pc25[29], pc25[9]-node.pc25[14], pc25[10]-
node.pc25[1], pc25[11]-node.pc25[16], pc25[12]-node.pc25[26], pc25[13]-
node.pc25[8], pc25[14]-node.pc25[28], pc25[15]-node.pc25[23], pc25[16]-
node.pc25[11], pc25[17]-node.pc25[17], pc25[18]-node.pc25[10], pc25[19]-
node.pc25[23], pc25[20]-node.pc25[21], pc25[21]-node.pc25[20], pc25[22]-
node.pc25[20], pc25[23]-node.pc25[29], pc25[24]-node.pc25[21], pc25[25]-
node.pc25[14], pc25[26]-node.pc25[5], pc25[27]-node.pc25[16], pc25[28]-
node.pc25[3], pc25[29]-node.pc25[5], pc25[30]-node.pc25[7])
residual.pc26 = c(pc26[1]-node.pc26[11], pc26[2]-node.pc26[13], pc26[3]-
node.pc26[3], pc26[4]-node.pc26[12], pc26[5]-node.pc26[27], pc26[6]-node.pc26[25],
pc26[7]-node.pc26[28], pc26[8]-node.pc26[29], pc26[9]-node.pc26[14], pc26[10]-
node.pc26[1], pc26[11]-node.pc26[16], pc26[12]-node.pc26[26], pc26[13]-
```

```
node.pc26[8], pc26[14]-node.pc26[28], pc26[15]-node.pc26[23], pc26[16]-
node.pc26[11], pc26[17]-node.pc26[17], pc26[18]-node.pc26[10], pc26[19]-
node.pc26[23], pc26[20]-node.pc26[21], pc26[21]-node.pc26[20], pc26[22]-
node.pc26[20], pc26[23]-node.pc26[29], pc26[24]-node.pc26[21], pc26[25]-
node.pc26[14], pc26[26]-node.pc26[5], pc26[27]-node.pc26[16], pc26[28]-
node.pc26[3], pc26[29]-node.pc26[5], pc26[30]-node.pc26[7])
residual.pc27 = c(pc27[1]-node.pc27[11], pc27[2]-node.pc27[13], pc27[3]-
node.pc27[3], pc27[4]-node.pc27[12], pc27[5]-node.pc27[27], pc27[6]-node.pc27[25],
pc27[7]-node.pc27[28], pc27[8]-node.pc27[29], pc27[9]-node.pc27[14], pc27[10]-
node.pc27[1], pc27[11]-node.pc27[16], pc27[12]-node.pc27[26], pc27[13]-
node.pc27[8], pc27[14]-node.pc27[28], pc27[15]-node.pc27[23], pc27[16]-
node.pc27[11], pc27[17]-node.pc27[17], pc27[18]-node.pc27[10], pc27[19]-
node.pc27[23], pc27[20]-node.pc27[21], pc27[21]-node.pc27[20], pc27[22]-
node.pc27[20], pc27[23]-node.pc27[29], pc27[24]-node.pc27[21], pc27[25]-
node.pc27[14], pc27[26]-node.pc27[5], pc27[27]-node.pc27[16], pc27[28]-
node.pc27[3], pc27[29]-node.pc27[5], pc27[30]-node.pc27[7])
residual.pc28 = c(pc28[1]-node.pc28[11], pc28[2]-node.pc28[13], pc28[3]-
node.pc28[3], pc28[4]-node.pc28[12], pc28[5]-node.pc28[27], pc28[6]-node.pc28[25],
pc28[7]-node.pc28[28], pc28[8]-node.pc28[29], pc28[9]-node.pc28[14], pc28[10]-
node.pc28[1], pc28[11]-node.pc28[16], pc28[12]-node.pc28[26], pc28[13]-
node.pc28[8], pc28[14]-node.pc28[28], pc28[15]-node.pc28[23], pc28[16]-
node.pc28[11], pc28[17]-node.pc28[17], pc28[18]-node.pc28[10], pc28[19]-
node.pc28[23], pc28[20]-node.pc28[21], pc28[21]-node.pc28[20], pc28[22]-
node.pc28[20], pc28[23]-node.pc28[29], pc28[24]-node.pc28[21], pc28[25]-
node.pc28[14], pc28[26]-node.pc28[5], pc28[27]-node.pc28[16], pc28[28]-
node.pc28[3], pc28[29]-node.pc28[5], pc28[30]-node.pc28[7])
residual.pc29 = c(pc29[1]-node.pc29[11], pc29[2]-node.pc29[13], pc29[3]-
node.pc29[3], pc29[4]-node.pc29[12], pc29[5]-node.pc29[27], pc29[6]-node.pc29[25],
pc29[7]-node.pc29[28], pc29[8]-node.pc29[29], pc29[9]-node.pc29[14], pc29[10]-
node.pc29[1], pc29[11]-node.pc29[16], pc29[12]-node.pc29[26], pc29[13]-
node.pc29[8], pc29[14]-node.pc29[28], pc29[15]-node.pc29[23], pc29[16]-
node.pc29[11], pc29[17]-node.pc29[17], pc29[18]-node.pc29[10], pc29[19]-
node.pc29[23], pc29[20]-node.pc29[21], pc29[21]-node.pc29[20], pc29[22]-
node.pc29[20], pc29[23]-node.pc29[29], pc29[24]-node.pc29[21], pc29[25]-
node.pc29[14], pc29[26]-node.pc29[5], pc29[27]-node.pc29[16], pc29[28]-
node.pc29[3], pc29[29]-node.pc29[5], pc29[30]-node.pc29[7])


residual.matrix = cbind(residual.pc1, residual.pc2, residual.pc3, residual.pc4,
residual.pc5, residual.pc6, residual.pc7, residual.pc8, residual.pc9,
residual.pc10, residual.pc11, residual.pc12, residual.pc13, residual.pc14,
residual.pc15, residual.pc16, residual.pc17, residual.pc18, residual.pc19,
residual.pc20, residual.pc21, residual.pc22, residual.pc23, residual.pc24,
residual.pc25, residual.pc26, residual.pc27, residual.pc28, residual.pc29)

###  ACP on residuals matrix (no a morpho geom PCA to check the data)
#pca.residuals = prcomp(residual.matrix)
#summary(pca.residuals)


################### Hotelling T² (allometry corrected + on residuals)
####################

AA = residual.matrix
BB = AA[26:30,]
CC = AA[1:25,]
HH_Test = hotelling.test(AA[,1:15], BB[,1:15], shrinkage = FALSE, perm = TRUE, B =
10000, progBar = TRUE, tol = 1e-12)
HH_Test_2 = hotelling.test(CC[,1:15], BB[,1:15], shrinkage = FALSE, perm = TRUE, B
= 10000, progBar = TRUE)

plot(HH_Test)
plot(HH_Test_2)
```

Supplementary Information 4. Kmult Results.

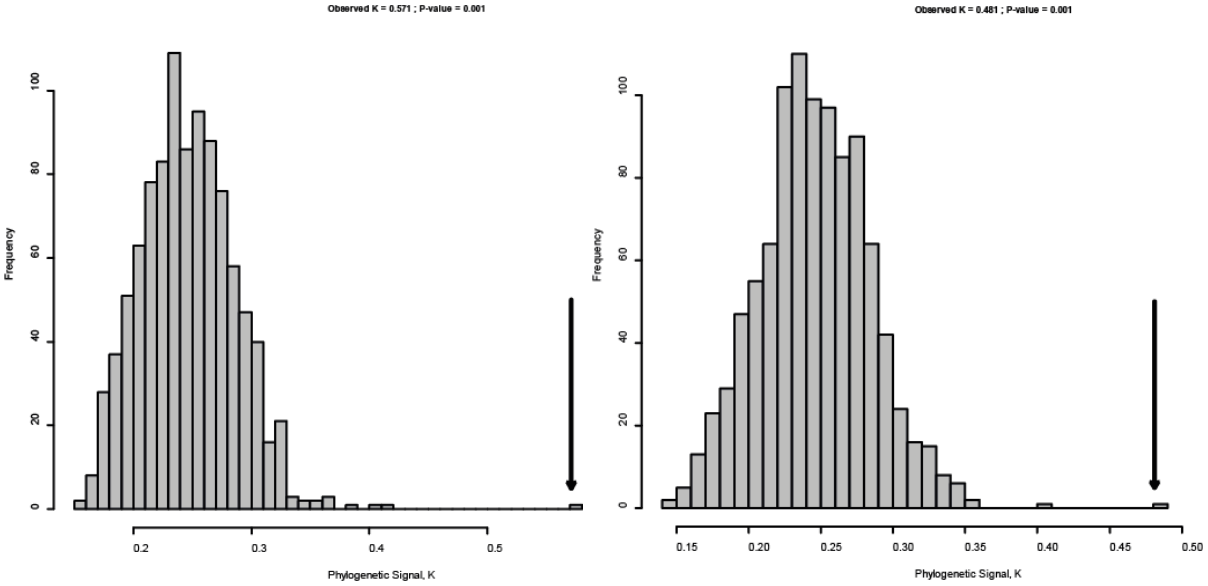

Supplementary Information 5. Pairs of the 10 first PCs resulting from the first PCA (on 'raw' shapes).

The five subterranean species are in red.

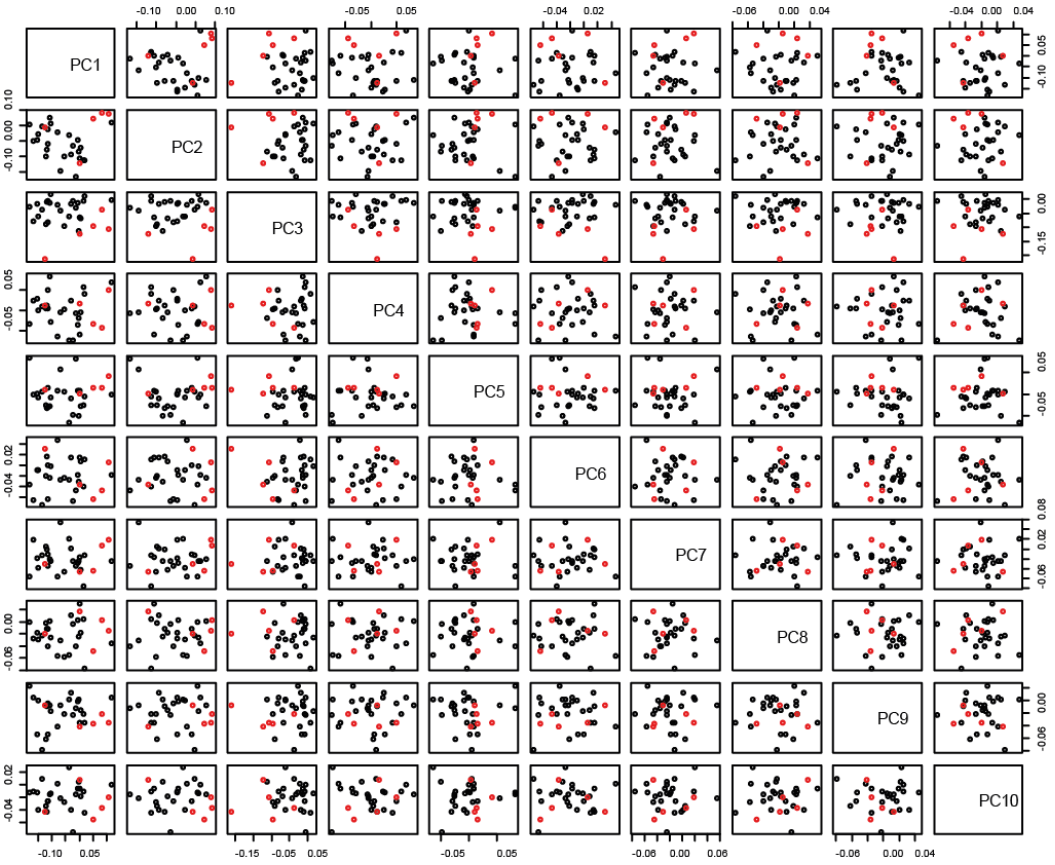

Supplementary Information 6. Histogram of the centroid size of the 30 species

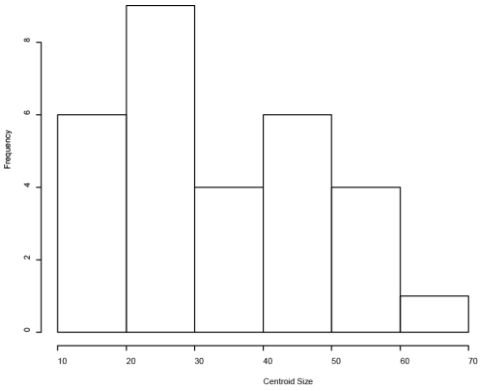

Supplementary Information 7. Result of the second PCA based on the allometry-adjusted shapes of the membranous semicircular ducts of the 5 moles (in red) and 25 non-subterranean species (in black).

The graphics present the first three PCs of the shape space. PC shape variation is realized by the hypothetical vestibular system shapes at the extreme scores for PC1, PC2 and PC3 (same scale). The mammal morphotype (in green) is spotted *a posteriori* in the graphics.

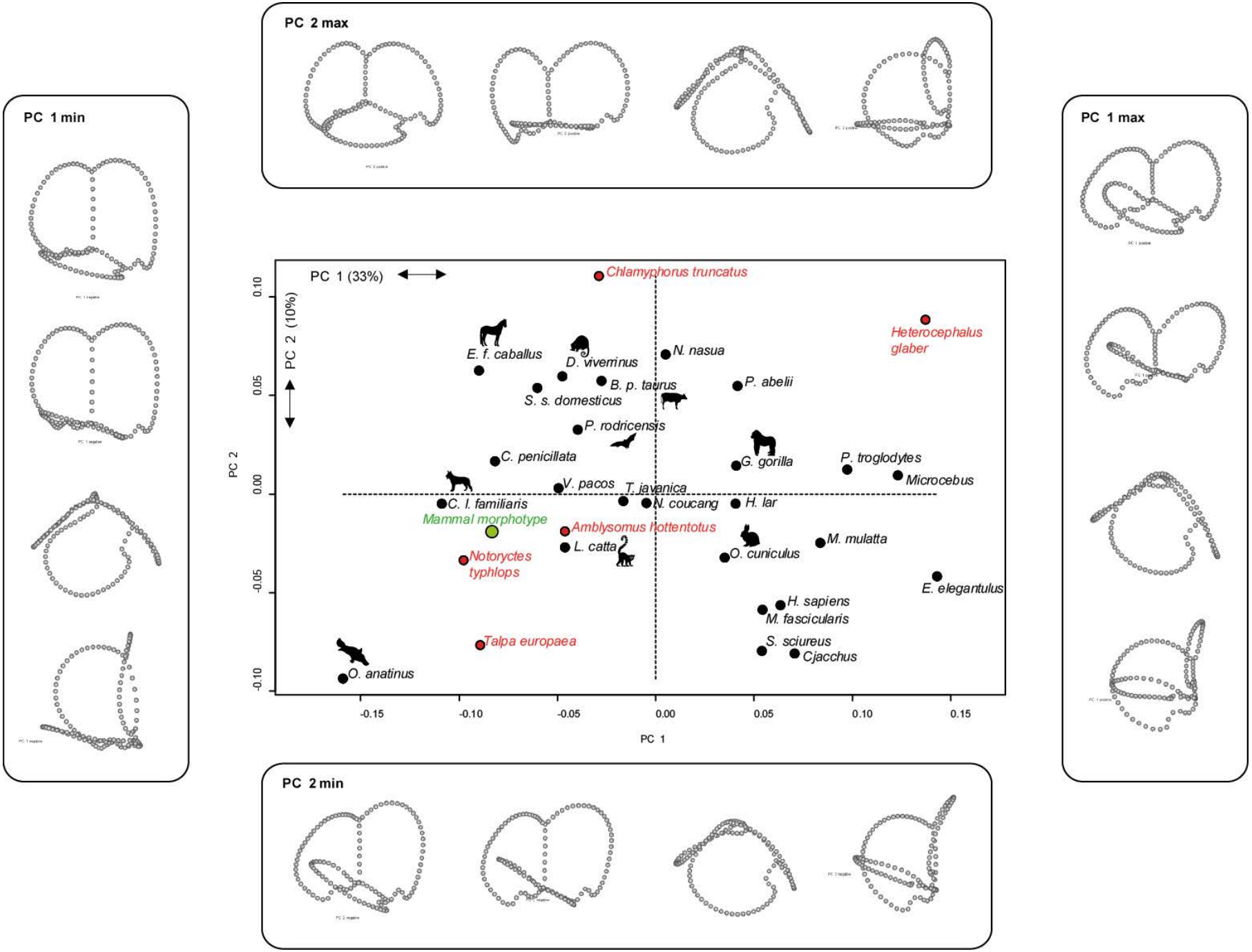
PC 2 max
PC 1 min
PC 1 max
PC 2 min
PC 1 (33%)
PC 2 (10%)
PC 1
PC 2
Chlamyphorus truncatus
Heterocephalus glaber
E. f. caballus
D. viverrinus
N. nasua
B. p. taurus
P. abelii
S. s. domesticus
P. rodricensis
C. penicillata
G. gorilla
P. troglodytes
Microcebus
V. pacos
T. javanica
C. l. familiaris
N. coucang
H. lar
Mammal morphotype
Amblysomus hottentotus
M. mulatta
L. catta
O. cuniculus
Notoryctes typhlops
E. elegantulus
H. sapiens
M. fascicularis
Talpa europaea
S. sciureus
Cjacchus
O. anatinus
0.10
0.05
0.00
-0.05
-0.10
-0.15
-0.10
-0.05
0.00
0.05
0.10
0.15

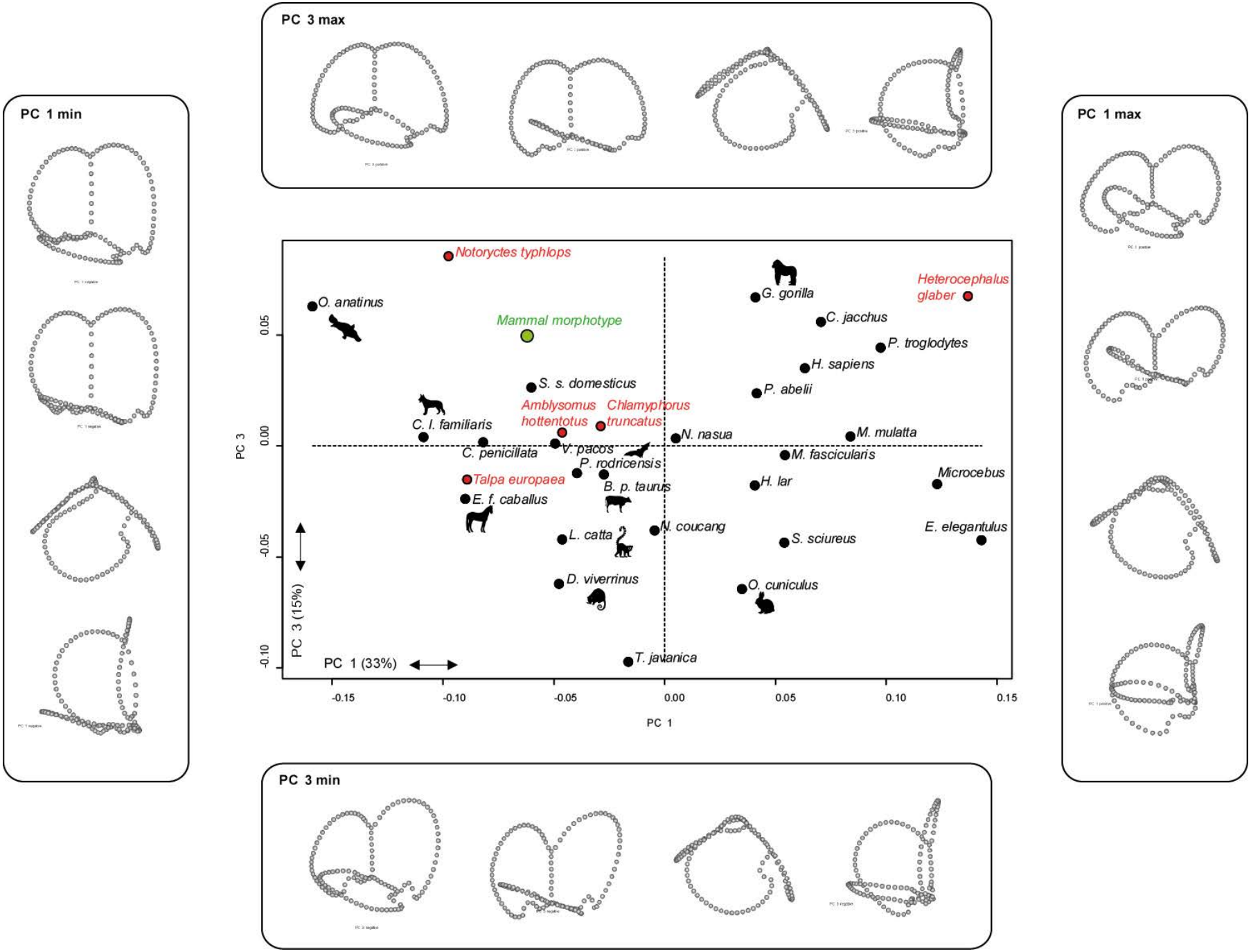
PC 3 max
PC 1 min
PC 1 max
PC 3 min
Notoryctes typhlops
O. anatinus
Mammal morphotype
S. s. domesticus
C. l. familiaris
Amblysomus hottentotus
Chlamyphorus truncatus
C. penicillata
V. pacos
P. rodricensis
Talpa europaea
B. p. taurus
E. f. caballus
L. catta
N. coucang
D. viverrinus
T. javanica
G. gorilla
Heterocephalus glaber
C. jacchus
P. troglodytes
H. sapiens
P. abelii
N. nasua
M. mulatta
M. fascicularis
H. lar
Microcebus
E. elegantulus
S. sciureus
O. cuniculus
PC 3
PC 3 (15%)
PC 1 (33%)
PC 1
0.05
0.00
-0.05
-0.10
-0.15
-0.10
-0.05
0.00
0.05
0.10
0.15

Supplementary Information 8. 'Phylo4d' representation with the first three PCs related to the second phylogeny (PCA on allometry-adjusted shapes).

The five mole species are in red and the non-subterranean species in black. A big black circle represents a high negative score on the PC and a big white circle represents a high positive score on the PC.

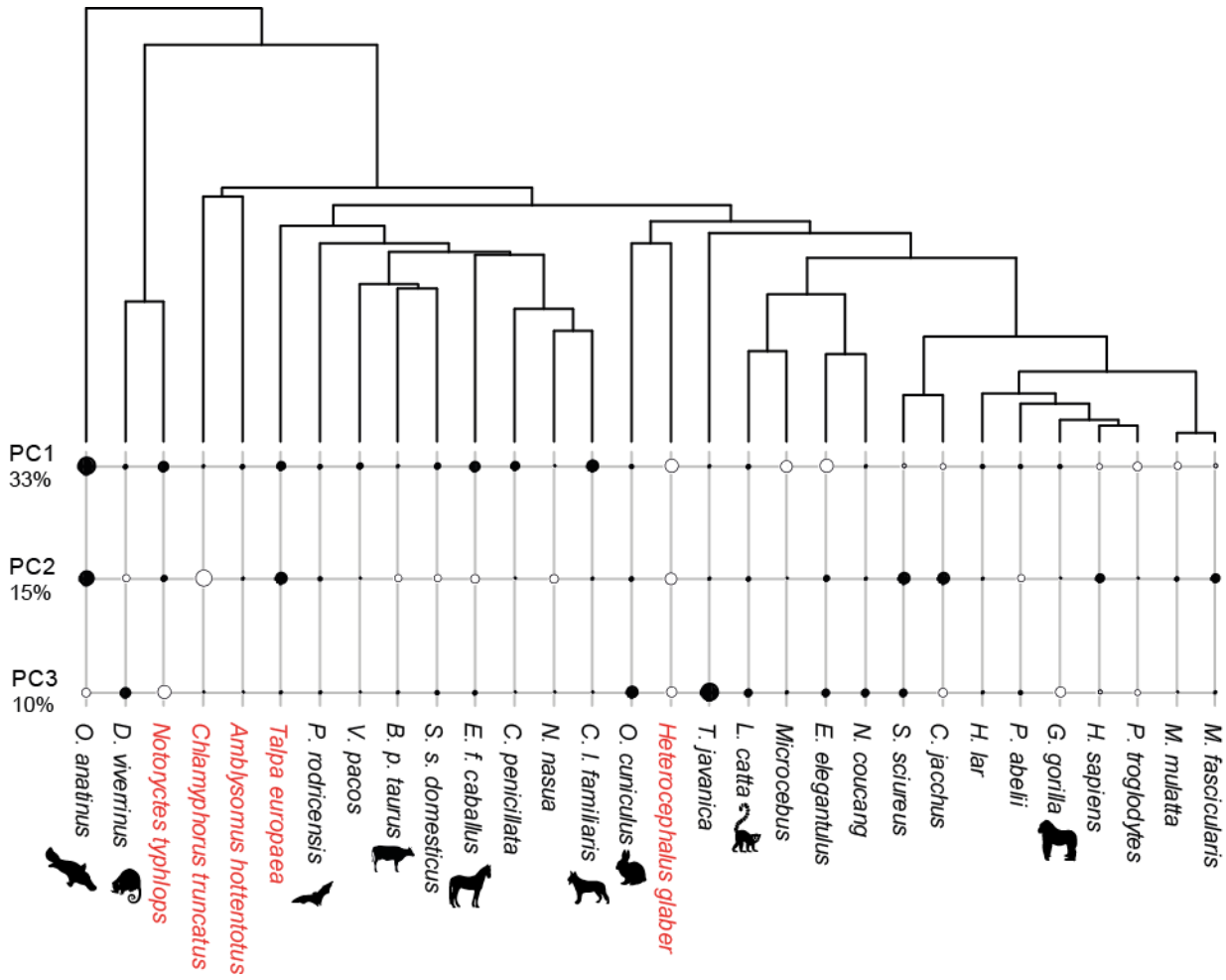

Supplementary Information 9. R script for linear morphometry.

```
#################### Initialisation ####################


rm(list=ls(all=TRUE))


################### Loading libraries ###################


library(phytools)
library(caper)
library(geiger)
library(MASS)


################### Loading functions ###################


joint.lambda<-function(tree,X){
  result<-optimize(f=likMlambda,X=X,C=vcv(tree),interval=c(0,1),     maximum=TRUE)
  return(list(lambda=result$maximum,logL=result$objective[1]))
}


################### Loading raw datasets ###################


DATA_AVERAGE = read.table(file.choose(), header = TRUE)    ###
RData_Morphometry_Mammals.txt" ###

TREE = read.nexus(file.choose())  ### MammalTree.nex

################### Check for missing specimens in tree/datasets
####################


TEST = name.check(TREE, data.names = DATA_AVERAGE[,1]) ### test pour savoir si les
noms sont identiques pour les deux docs
TREE = drop.tip(TREE, TEST$tree_not_data) ### fonction qui répare les eventuels
noms différents


################### Preparing sub datasets ###################


Names_AVERAGE = as.matrix(DATA_AVERAGE[,1, drop=FALSE]) #### garder la colone des
noms
Morpho_AVERAGE = data.matrix(DATA_AVERAGE[,3:36]) #### garder les valeurs sauf
centroid size
CS_AVERAGE = data.matrix(DATA_AVERAGE[,2, drop=FALSE]) #### la colonne centroide
size de côté

moles =
factor(c("1","1","1","1","1","0","0","0","0","0","0","0","0","0","0","0","0","0","0","0
","0","0","0","0","0","0","0","0","0","0","0","0"))
length(moles) ## pour vérifier le nombre de facteur

############ vizualisation ############################

plot(Morpho_AVERAGE[,12], Morpho_AVERAGE[,15], col = as.numeric(moles))
plot(Morpho_AVERAGE_LOG[,12], Morpho_AVERAGE_LOG[,15], col = as.numeric(moles))

plot((Morpho_AVERAGE_LOG[,12]/Morpho_AVERAGE_LOG[,15]), col = as.numeric(moles))
```

```
hist(Morpho_AVERAGE[,12]/Morpho_AVERAGE[,15])

################### Log transformation of some datasets ####################


Morpho_AVERAGE_LOG = log10(Morpho_AVERAGE)
CS_AVERAGE_LOG = log10(CS_AVERAGE)


################### Phylogenetic regression of morphological parameters onto
centroid size ####################


PGLS_SET_MorphoCS = data.frame(Names_AVERAGE, CS_AVERAGE_LOG, Morpho_AVERAGE_LOG,
stringsAsFactors=FALSE)


PGLS_Vtot = pgls(Vtot~Csize,comparative.data(TREE,PGLS_SET_MorphoCS,Taxa),lambda =
"ML")

PGLS_LSa = pgls(LSa~Csize,comparative.data(TREE,PGLS_SET_MorphoCS,Taxa),lambda =
"ML")
PGLS_LSp = pgls(LSp~Csize,comparative.data(TREE,PGLS_SET_MorphoCS,Taxa),lambda =
"ML")
PGLS_LSl = pgls(LSl~Csize,comparative.data(TREE,PGLS_SET_MorphoCS,Taxa),lambda =
"ML")
PGLS_LCC = pgls(LCC~Csize,comparative.data(TREE,PGLS_SET_MorphoCS,Taxa),lambda =
"ML")
PGLS_LSDa = pgls(LSDa~Csize,comparative.data(TREE,PGLS_SET_MorphoCS,Taxa),lambda =
"ML")
PGLS_LSDp = pgls(LSDp~Csize,comparative.data(TREE,PGLS_SET_MorphoCS,Taxa),lambda =
"ML")
PGLS_LSDl = pgls(LSDl~Csize,comparative.data(TREE,PGLS_SET_MorphoCS,Taxa),lambda =
"ML")

PGLS_ASDa = pgls(ASDa~Csize,comparative.data(TREE,PGLS_SET_MorphoCS,Taxa),lambda =
"ML")
PGLS_ASDp = pgls(ASDp~Csize,comparative.data(TREE,PGLS_SET_MorphoCS,Taxa),lambda =
"ML")
PGLS_ASDl = pgls(ASDl~Csize,comparative.data(TREE,PGLS_SET_MorphoCS,Taxa),lambda =
"ML")

PGLS_aSa = pgls(aSa~Csize,comparative.data(TREE,PGLS_SET_MorphoCS,Taxa),lambda =
"ML")
PGLS_aSp = pgls(aSp~Csize,comparative.data(TREE,PGLS_SET_MorphoCS,Taxa),lambda =
"ML")
PGLS_aSl = pgls(aSl~Csize,comparative.data(TREE,PGLS_SET_MorphoCS,Taxa),lambda =
"ML")
PGLS_aCC = pgls(aCC~Csize,comparative.data(TREE,PGLS_SET_MorphoCS,Taxa),lambda =
"ML")

PGLS_aCa_Md =
pgls(aCa_Md~Csize,comparative.data(TREE,PGLS_SET_MorphoCS,Taxa),lambda = "ML")
PGLS_aCp_Md =
pgls(aCp_Md~Csize,comparative.data(TREE,PGLS_SET_MorphoCS,Taxa),lambda = "ML")
PGLS_aCl_Md =
pgls(aCl_Md~Csize,comparative.data(TREE,PGLS_SET_MorphoCS,Taxa),lambda = "ML")

PGLS_tCa = pgls(tCa~Csize,comparative.data(TREE,PGLS_SET_MorphoCS,Taxa),lambda =
"ML")
PGLS_tCp = pgls(tCp~Csize,comparative.data(TREE,PGLS_SET_MorphoCS,Taxa),lambda =
"ML")
PGLS_tCl = pgls(tCl~Csize,comparative.data(TREE,PGLS_SET_MorphoCS,Taxa),lambda =
"ML")

PGLS_iSDaSDp_SD =
pgls(iSDaSDp_SD~Csize,comparative.data(TREE,PGLS_SET_MorphoCS,Taxa),lambda = "ML")
```

```
PGLS_iSDaSDl_SD =
pgls(iSDaSDl_SD~Csize,comparative.data(TREE,PGLS_SET_MorphoCS,Taxa),lambda =
0.000001)
PGLS_iSDlSDp_SD =
pgls(iSDlSDp_SD~Csize,comparative.data(TREE,PGLS_SET_MorphoCS,Taxa),lambda = "ML")
PGLS_sSDaSDp_SD =
pgls(sSDaSDp_SD~Csize,comparative.data(TREE,PGLS_SET_MorphoCS,Taxa),lambda = "ML")
PGLS_sSDlSDl_SD =
pgls(sSDlSDl_SD~Csize,comparative.data(TREE,PGLS_SET_MorphoCS,Taxa),lambda = "ML")

PGLS_pSDa_SD =
pgls(pSDa_SD~Csize,comparative.data(TREE,PGLS_SET_MorphoCS,Taxa),lambda = "ML")
PGLS_pSDp_SD =
pgls(pSDp_SD~Csize,comparative.data(TREE,PGLS_SET_MorphoCS,Taxa),lambda = "ML")
PGLS_pSDl_SD =
pgls(pSDl_SD~Csize,comparative.data(TREE,PGLS_SET_MorphoCS,Taxa),lambda = "ML")
PGLS_rSDa_SD =
pgls(rSDa_SD~Csize,comparative.data(TREE,PGLS_SET_MorphoCS,Taxa),lambda = "ML")
PGLS_rSDp_SD =
pgls(rSDp_SD~Csize,comparative.data(TREE,PGLS_SET_MorphoCS,Taxa),lambda = "ML")
PGLS_ySDa_SD =
pgls(ySDa_SD~Csize,comparative.data(TREE,PGLS_SET_MorphoCS,Taxa),lambda = "ML")
PGLS_ySDp_SD =
pgls(ySDp_SD~Csize,comparative.data(TREE,PGLS_SET_MorphoCS,Taxa),lambda = "ML")
PGLS_ySDl_SD =
pgls(ySDl_SD~Csize,comparative.data(TREE,PGLS_SET_MorphoCS,Taxa),lambda = "ML")


summary(PGLS_Vtot)
summary(PGLS_LSa)
summary(PGLS_LSp)
summary(PGLS_LSl)
summary(PGLS_LCC)
summary(PGLS_LSDa)
summary(PGLS_LSDp)
summary(PGLS_LSDl)
summary(PGLS_ASDa)
summary(PGLS_ASDp)
summary(PGLS_ASDl)
summary(PGLS_aSa)
summary(PGLS_aSp)
summary(PGLS_aSl)
summary(PGLS_aCC)
summary(PGLS_aCa_Md)
summary(PGLS_aCp_Md)
summary(PGLS_aCl_Md)
summary(PGLS_tCa)
summary(PGLS_tCp)
summary(PGLS_tCl)
summary(PGLS_iSDaSDp_SD)
summary(PGLS_iSDaSDl_SD)
summary(PGLS_iSDlSDp_SD)
summary(PGLS_sSDaSDp_SD)
summary(PGLS_sSDlSDl_SD)
summary(PGLS_pSDa_SD)
summary(PGLS_pSDp_SD)
summary(PGLS_pSDl_SD)
summary(PGLS_rSDa_SD)
summary(PGLS_rSDp_SD)
summary(PGLS_ySDa_SD)
summary(PGLS_ySDp_SD)
summary(PGLS_ySDl_SD)


################### Computation of morphological residuals without centroid size
####################
###### la PGLS permet de savoir si probleme d'allo et de phylogénie puis, ici, on
calcule les résidus grâce aux résultats de la PGLS et ensuite (section suivante)
```

```
grâce aux résidus on recalcule les nouvelles valeurs des paramètres standardiser
avec la centroid size moyenne

Morpho_Residuals_AVERAGE_LOG = Morpho_AVERAGE_LOG[,] - cbind(predict(PGLS_Vtot,
as.data.frame(CS_AVERAGE_LOG[,1, drop=FALSE])), predict(PGLS_LSa,
as.data.frame(CS_AVERAGE_LOG[,1, drop=FALSE])),
                                                        predict(PGLS_LSp,
as.data.frame(CS_AVERAGE_LOG[,1, drop=FALSE])), predict(PGLS_LSl,
as.data.frame(CS_AVERAGE_LOG[,1, drop=FALSE])),
                                                            predict(PGLS_LCC,
as.data.frame(CS_AVERAGE_LOG[,1, drop=FALSE])), predict(PGLS_LSDa,
as.data.frame(CS_AVERAGE_LOG[,1, drop=FALSE])),
                                                            predict(PGLS_LSDp,
as.data.frame(CS_AVERAGE_LOG[,1, drop=FALSE])),
                                                            predict(PGLS_LSDl,
as.data.frame(CS_AVERAGE_LOG[,1, drop=FALSE])), predict(PGLS_ASDa,
as.data.frame(CS_AVERAGE_LOG[,1, drop=FALSE])),
                                                            predict(PGLS_ASDp,
as.data.frame(CS_AVERAGE_LOG[,1, drop=FALSE])), predict(PGLS_ASDl,
as.data.frame(CS_AVERAGE_LOG[,1, drop=FALSE])),
                                                            predict(PGLS_aSa,
as.data.frame(CS_AVERAGE_LOG[,1, drop=FALSE])), predict(PGLS_aSp,
as.data.frame(CS_AVERAGE_LOG[,1, drop=FALSE])),
                                                            predict(PGLS_aSl,
as.data.frame(CS_AVERAGE_LOG[,1, drop=FALSE])), predict(PGLS_aCC,
as.data.frame(CS_AVERAGE_LOG[,1, drop=FALSE])),
                                                            predict(PGLS_aCa_Md,
as.data.frame(CS_AVERAGE_LOG[,1, drop=FALSE])), predict(PGLS_aCp_Md,
as.data.frame(CS_AVERAGE_LOG[,1, drop=FALSE])),
                                                            predict(PGLS_aCl_Md,
as.data.frame(CS_AVERAGE_LOG[,1, drop=FALSE])), predict(PGLS_tCa,
as.data.frame(CS_AVERAGE_LOG[,1, drop=FALSE])),
                                                            predict(PGLS_tCp,
as.data.frame(CS_AVERAGE_LOG[,1, drop=FALSE])), predict(PGLS_tCl,
as.data.frame(CS_AVERAGE_LOG[,1, drop=FALSE])), predict(PGLS_iSDaSDp_SD,
as.data.frame(CS_AVERAGE_LOG[,1, drop=FALSE])),

predict(PGLS_iSDaSDl_SD, as.data.frame(CS_AVERAGE_LOG[,1,
drop=FALSE])),predict(PGLS_iSDlSDp_SD, as.data.frame(CS_AVERAGE_LOG[,1,
drop=FALSE])),

predict(PGLS_sSDaSDp_SD, as.data.frame(CS_AVERAGE_LOG[,1,
drop=FALSE])),predict(PGLS_sSDlSDl_SD, as.data.frame(CS_AVERAGE_LOG[,1,
drop=FALSE])),
                                                            predict(PGLS_pSDa_SD,
as.data.frame(CS_AVERAGE_LOG[,1, drop=FALSE])),predict(PGLS_pSDp_SD,
as.data.frame(CS_AVERAGE_LOG[,1, drop=FALSE])),
                                                            predict(PGLS_pSDl_SD,
as.data.frame(CS_AVERAGE_LOG[,1, drop=FALSE])),predict(PGLS_rSDa_SD,
as.data.frame(CS_AVERAGE_LOG[,1, drop=FALSE])),
                                                            predict(PGLS_rSDp_SD,
as.data.frame(CS_AVERAGE_LOG[,1, drop=FALSE])),predict(PGLS_ySDa_SD,
as.data.frame(CS_AVERAGE_LOG[,1, drop=FALSE])),
                                                            predict(PGLS_ySDp_SD,
as.data.frame(CS_AVERAGE_LOG[,1, drop=FALSE])),predict(PGLS_ySDl_SD,
as.data.frame(CS_AVERAGE_LOG[,1, drop=FALSE])))


#################### Computing morphological parameters with CS of 32.65618167
####################


CScor_AVERAGE_LOG = as.data.frame(rep(log10(32.65618167),dim(CS_AVERAGE_LOG)[1]))
colnames(CScor_AVERAGE_LOG) = c("Csize")

CScor_Morpho_AVERAGE = 10^(Morpho_Residuals_AVERAGE_LOG + cbind(predict(PGLS_Vtot,
CScor_AVERAGE_LOG), predict(PGLS_LSa, CScor_AVERAGE_LOG),
```

```
                                                        predict(PGLS_LSp,
CScor_AVERAGE_LOG), predict(PGLS_LSl, CScor_AVERAGE_LOG),
                                                          predict(PGLS_LCC,
CScor_AVERAGE_LOG), predict(PGLS_LSDa, CScor_AVERAGE_LOG),
                                                          predict(PGLS_LSDp,
CScor_AVERAGE_LOG),
                                                          predict(PGLS_LSDl,
CScor_AVERAGE_LOG), predict(PGLS_ASDa, CScor_AVERAGE_LOG),
                                                          predict(PGLS_ASDp,
CScor_AVERAGE_LOG), predict(PGLS_ASDl, CScor_AVERAGE_LOG),
                                                          predict(PGLS_aSa,
CScor_AVERAGE_LOG), predict(PGLS_aSp, CScor_AVERAGE_LOG),
                                                          predict(PGLS_aSl,
CScor_AVERAGE_LOG), predict(PGLS_aCC, CScor_AVERAGE_LOG),
                                                          predict(PGLS_aCa_Md,
CScor_AVERAGE_LOG), predict(PGLS_aCp_Md, CScor_AVERAGE_LOG),
                                                          predict(PGLS_aCl_Md,
CScor_AVERAGE_LOG), predict(PGLS_tCa, CScor_AVERAGE_LOG),
                                                          predict(PGLS_tCp,
CScor_AVERAGE_LOG), predict(PGLS_tCl, CScor_AVERAGE_LOG), predict(PGLS_iSDaSDp_SD,
CScor_AVERAGE_LOG),

predict(PGLS_iSDaSDl_SD, CScor_AVERAGE_LOG),predict(PGLS_iSDlSDp_SD,
CScor_AVERAGE_LOG),

predict(PGLS_sSDaSDp_SD, CScor_AVERAGE_LOG),predict(PGLS_sSDlSDl_SD,
CScor_AVERAGE_LOG),
                                                          predict(PGLS_pSDa_SD,
CScor_AVERAGE_LOG),predict(PGLS_pSDp_SD, CScor_AVERAGE_LOG),
                                                          predict(PGLS_pSDl_SD,
CScor_AVERAGE_LOG),predict(PGLS_rSDa_SD, CScor_AVERAGE_LOG),
                                                          predict(PGLS_rSDp_SD,
CScor_AVERAGE_LOG),predict(PGLS_ySDa_SD, CScor_AVERAGE_LOG),
                                                          predict(PGLS_ySDp_SD,
CScor_AVERAGE_LOG),predict(PGLS_ySDl_SD, CScor_AVERAGE_LOG)))

##### Vizualisation on adjusted shapes
plot(CScor_Morpho_AVERAGE[,12], CScor_Morpho_AVERAGE[,15], col = as.numeric(moles))

#################### Prediction morphotype mammal ####################



x = CScor_Morpho_AVERAGE[,1]
names(x) = Names_AVERAGE
Vtot = c(fastAnc(TREE, x, CI = TRUE)$ace[1], fastAnc(TREE, x, CI = TRUE)$CI[1,])
x = CScor_Morpho_AVERAGE[,2]
names(x) = Names_AVERAGE
LSa = c(fastAnc(TREE, x, CI = TRUE)$ace[1], fastAnc(TREE, x, CI = TRUE)$CI[1,])
x = CScor_Morpho_AVERAGE[,3]
names(x) = Names_AVERAGE
LSp = c(fastAnc(TREE, x, CI = TRUE)$ace[1], fastAnc(TREE, x, CI = TRUE)$CI[1,])
x = CScor_Morpho_AVERAGE[,4]
names(x) = Names_AVERAGE
LSl = c(fastAnc(TREE, x, CI = TRUE)$ace[1], fastAnc(TREE, x, CI = TRUE)$CI[1,])
x = CScor_Morpho_AVERAGE[,5]
names(x) = Names_AVERAGE
LCC = c(fastAnc(TREE, x, CI = TRUE)$ace[1], fastAnc(TREE, x, CI = TRUE)$CI[1,])
x = CScor_Morpho_AVERAGE[,6]
names(x) = Names_AVERAGE
LSDa = c(fastAnc(TREE, x, CI = TRUE)$ace[1], fastAnc(TREE, x, CI = TRUE)$CI[1,])
x = CScor_Morpho_AVERAGE[,7]
names(x) = Names_AVERAGE
LSDp = c(fastAnc(TREE, x, CI = TRUE)$ace[1], fastAnc(TREE, x, CI = TRUE)$CI[1,])
x = CScor_Morpho_AVERAGE[,8]
names(x) = Names_AVERAGE
LSDl = c(fastAnc(TREE, x, CI = TRUE)$ace[1], fastAnc(TREE, x, CI = TRUE)$CI[1,])
x = CScor_Morpho_AVERAGE[,9]
```

```
names(x) = Names_AVERAGE
ASDa = c(fastAnc(TREE, x, CI = TRUE)$ace[1], fastAnc(TREE, x, CI = TRUE)$CI[1,])
x = CScor_Morpho_AVERAGE[,10]
names(x) = Names_AVERAGE
ASDp = c(fastAnc(TREE, x, CI = TRUE)$ace[1], fastAnc(TREE, x, CI = TRUE)$CI[1,])
x = CScor_Morpho_AVERAGE[,11]
names(x) = Names_AVERAGE
ASDl = c(fastAnc(TREE, x, CI = TRUE)$ace[1], fastAnc(TREE, x, CI = TRUE)$CI[1,])
x = CScor_Morpho_AVERAGE[,12]
names(x) = Names_AVERAGE
aSa = c(fastAnc(TREE, x, CI = TRUE)$ace[1], fastAnc(TREE, x, CI = TRUE)$CI[1,])
x = CScor_Morpho_AVERAGE[,13]
names(x) = Names_AVERAGE
aSp = c(fastAnc(TREE, x, CI = TRUE)$ace[1], fastAnc(TREE, x, CI = TRUE)$CI[1,])
x = CScor_Morpho_AVERAGE[,14]
names(x) = Names_AVERAGE
aSl = c(fastAnc(TREE, x, CI = TRUE)$ace[1], fastAnc(TREE, x, CI = TRUE)$CI[1,])
x = CScor_Morpho_AVERAGE[,15]
names(x) = Names_AVERAGE
aCC = c(fastAnc(TREE, x, CI = TRUE)$ace[1], fastAnc(TREE, x, CI = TRUE)$CI[1,])
x = CScor_Morpho_AVERAGE[,16]
names(x) = Names_AVERAGE
aCa_Md = c(fastAnc(TREE, x, CI = TRUE)$ace[1], fastAnc(TREE, x, CI = TRUE)$CI[1,])
x = CScor_Morpho_AVERAGE[,17]
names(x) = Names_AVERAGE
aCp_Md = c(fastAnc(TREE, x, CI = TRUE)$ace[1], fastAnc(TREE, x, CI = TRUE)$CI[1,])
x = CScor_Morpho_AVERAGE[,18]
names(x) = Names_AVERAGE
aCl_Md = c(fastAnc(TREE, x, CI = TRUE)$ace[1], fastAnc(TREE, x, CI = TRUE)$CI[1,])
x = CScor_Morpho_AVERAGE[,19]
names(x) = Names_AVERAGE
tCa = c(fastAnc(TREE, x, CI = TRUE)$ace[1], fastAnc(TREE, x, CI = TRUE)$CI[1,])
x = CScor_Morpho_AVERAGE[,20]
names(x) = Names_AVERAGE
tCp = c(fastAnc(TREE, x, CI = TRUE)$ace[1], fastAnc(TREE, x, CI = TRUE)$CI[1,])
x = CScor_Morpho_AVERAGE[,21]
names(x) = Names_AVERAGE
tCl = c(fastAnc(TREE, x, CI = TRUE)$ace[1], fastAnc(TREE, x, CI = TRUE)$CI[1,])
x = CScor_Morpho_AVERAGE[,22]
names(x) = Names_AVERAGE
iSDaSDp_SD = c(fastAnc(TREE, x, CI = TRUE)$ace[1], fastAnc(TREE, x, CI =
TRUE)$CI[1,])
x = CScor_Morpho_AVERAGE[,23]
names(x) = Names_AVERAGE
iSDaSDl_SD = c(fastAnc(TREE, x, CI = TRUE)$ace[1], fastAnc(TREE, x, CI =
TRUE)$CI[1,])
x = CScor_Morpho_AVERAGE[,24]
names(x) = Names_AVERAGE
iSDlSDp_SD = c(fastAnc(TREE, x, CI = TRUE)$ace[1], fastAnc(TREE, x, CI =
TRUE)$CI[1,])
x = CScor_Morpho_AVERAGE[,25]
names(x) = Names_AVERAGE
sSDaSDp_SD = c(fastAnc(TREE, x, CI = TRUE)$ace[1], fastAnc(TREE, x, CI =
TRUE)$CI[1,])
x = CScor_Morpho_AVERAGE[,26]
names(x) = Names_AVERAGE
sSDlSDl_SD = c(fastAnc(TREE, x, CI = TRUE)$ace[1], fastAnc(TREE, x, CI =
TRUE)$CI[1,])
x = CScor_Morpho_AVERAGE[,27]
names(x) = Names_AVERAGE
pSDa_SD = c(fastAnc(TREE, x, CI = TRUE)$ace[1], fastAnc(TREE, x, CI = TRUE)$CI[1,])
x = CScor_Morpho_AVERAGE[,28]
names(x) = Names_AVERAGE
pSDp_SD = c(fastAnc(TREE, x, CI = TRUE)$ace[1], fastAnc(TREE, x, CI = TRUE)$CI[1,])
x = CScor_Morpho_AVERAGE[,29]
names(x) = Names_AVERAGE
pSDl_SD = c(fastAnc(TREE, x, CI = TRUE)$ace[1], fastAnc(TREE, x, CI = TRUE)$CI[1,])
x = CScor_Morpho_AVERAGE[,30]
```

```
names(x) = Names_AVERAGE
rSDa_SD = c(fastAnc(TREE, x, CI = TRUE)$ace[1], fastAnc(TREE, x, CI = TRUE)$CI[1,])
x = CScor_Morpho_AVERAGE[,31]
names(x) = Names_AVERAGE
rSDp_SD = c(fastAnc(TREE, x, CI = TRUE)$ace[1], fastAnc(TREE, x, CI = TRUE)$CI[1,])
x = CScor_Morpho_AVERAGE[,32]
names(x) = Names_AVERAGE
ySDa_SD = c(fastAnc(TREE, x, CI = TRUE)$ace[1], fastAnc(TREE, x, CI = TRUE)$CI[1,])
x = CScor_Morpho_AVERAGE[,33]
names(x) = Names_AVERAGE
ySDp_SD = c(fastAnc(TREE, x, CI = TRUE)$ace[1], fastAnc(TREE, x, CI = TRUE)$CI[1,])
x = CScor_Morpho_AVERAGE[,34]
names(x) = Names_AVERAGE
ySDl_SD = c(fastAnc(TREE, x, CI = TRUE)$ace[1], fastAnc(TREE, x, CI = TRUE)$CI[1,])

Ancestor = rbind(Vtot, LSa, LSp, LSl, LCC, LSDa, LSDp, LSDl, ASDa, ASDp, ASDl, aSa,
aSp, aSl, aCC, aCa_Md, aCp_Md, aCl_Md, tCa, tCp, tCl, iSDaSDp_SD, iSDaSDl_SD,
iSDlSDp_SD, sSDaSDp_SD,
sSDlSDl_SD, pSDa_SD, pSDp_SD, pSDl_SD, rSDa_SD, rSDp_SD, ySDa_SD, ySDp_SD, ySDl_SD)


#### add mammal morphotype to the table CScor_Morpho#####

NAMESAnc = rbind(Names_AVERAGE, "Ancestor")
actuelancestor = rbind(CScor_Morpho_AVERAGE, t(Ancestor[,1]))
rownames(actuelancestor) = NAMESAnc
actuelancestor

molesAnc =
factor(c("1","1","1","1","1","0","0","0","0","0","0","0","0","0","0","0","0","0","0","0
","0","0","0","0","0","0","0","0","0","0","0","0","2"))
plot(actuelancestor [,12], actuelancestor [,15], col = as.numeric(molesAnc))


ACP = prcomp(actuelancestor)
biplot(ACP$x[,2:3],ACP$rotation[,2:3])
barplot(ACP$rotation[,1])

plot(ACP$x[,2], ACP$x[,3])
text(ACP$x[,2], ACP$x[,3], labels = NAMESAnc, col = as.numeric(molesAnc))
```

Supplementary Information 10. Morphological Parameters of the reconstructed mammal morphotype with a confidence interval of 95%.

Parameter	Predicted	CI - 95%	CI + 95%
Distribution of the endolymph along the ducts (µl)			
Vtot	6.80	4.15	9.46
Distribution of the endolymph along the ducts (µl)			
LSa	8.51	6.75	10.26
LSp	8.59	6.90	10.28
LSl	8.45	6.69	10.20
LCC	3.35	2.46	4.24
LSDa	16.42	14.81	18.04
LSDp	14.84	13.42	16.26
LSDl	14.09	12.08	16.11
Area enclosed by the semicircular duct (mm^2)			
ASDa	17.82	13.78	21.85
ASDp	14.95	12.14	17.77
ASDl	13.16	9.72	16.59
Mean cross-sectional area of the different structures (mm^2)			
aSa	0.058	0.028	0.088
aSp	0.060	0.028	0.091
aSl	0.053	0.020	0.085
aCC	0.220	0.034	0.405
Ratio between cross-sectional radii			
aCa_Md	0.568	0.405	0.731
aCp_Md	0.487	0.316	0.658
aCl_Md	0.485	0.336	0.634
tCa	0.288	0.181	0.395
tCp	0.272	0.189	0.354
tCl	0.305	0.216	0.395
Thickness of the cristae (mm) and Surface area of the lumen cross section above the cristae (mm^2)			
iSDaSDp_SD	95.56	84.70	106.42
iSDaSDl_SD	78.33	66.86	89.81
iSDlSDp_SD	90.86	81.58	100.13
sSDaSDp_SD	170.27	158.28	182.26
sSDlSDl_SD	168.28	152.68	183.88
pSDa_SD	39.91	29.14	50.68
pSDp_SD	44.64	37.45	51.83
pSDl_SD	85.07	72.96	97.18
rSDa_SD	51.64	41.06	62.22
rSDp_SD	45.66	38.62	52.70
ySDa_SD	97.82	89.09	106.56
ySDp_SD	85.74	76.07	95.41
ySDl_SD	5.94	-1.11	12.98

Supplementary Information 11. Influence of allometry and/or phylogeny in the shape of the membranous semicircular duct system of the inner ear of the 30 mammals of the study: results of the PGLS on the formalized-morphological parameters.

In the following table, the lambda for each formalized-morphological parameter indicates if there is an influence of phylogeny. The closest to 1 the lambda is (in red when >0.7 and in orange when about 0.5), the more important is the phylogeny in the definitive shape of the membranous labyrinth.

The p-value of R2 indicates if the shape of the membranous labyrinth is influenced by allometry (significance at p-value<0.05, in red).

Each type of allometry, as defined below, is underlined with a different colour.

Isometry: $R^2 = 0$: isometry. The trait 'y' increases in size as does the trait x (centroid size), with no changes in proportions.

Minorant allometry (yellow): $0<R^2<1$. The trait 'y' increases in size faster than the centroid size.

Majorant allometry: $R^2>1$. The trait 'y' increases in size slower than the centroid size.

Enantiometry: $R^2<0$ (blue). The trait 'y' decreases in size in absolute value when the centroid size decreases.

	Lambda	p-value of R^2	R^2
Distribution of the endolymph along the ducts (µl)			
Vtot	0.999	4.144e-16	0.9058
Relative length of the different structures (mm)			
LSa	0	<2.2e-16	0.959
LSp	0	<2.2e-16	0.977
LSl	0.720	<2.2e-16	0.9556
LCC	0.851	5.656e-11	0.7818
LSDa	0	<2.2e-16	0.9877
LSDp	0	<2.2e-16	0.9907
LSDl	0.555	<2.2e-16	0.9807
Area enclosed by the semicircular duct (mm^2)			
ASDa	0	<2.2e-16	0.9871
ASDp	0	<2.2e-16	0.992
ASDl	0.448	<2.2e-16	0.9871
Mean cross-sectional area of the different structures (mm^2)			
aSa	0	2.312e-07	0.6079
aSp	0	6.464e-07	0.5786
aSl	0	2.43e-05	0.4578
aCC	0	1.743e-10	0.7637
Ratio between cross-sectional radii			
aCa_Md	1	3.337e-13	0.8484
aCp_Md	1	1.953e-12	0.8281
aCl_Md	1	1.48e-13	0.8569
tCa	0	1.024e-07	0.6296
tCp	0	1.484e-10	0.7664
tCl	0.983	2.182e-07	0.6095
Thickness of the cristae (mm) and Surface area of the lumen cross section above the cristae (mm^2)			
iSDaSDp_SD	0	0.8936	-0.03504
iSDaSDl_SD	0	0.3332	-0.001043

iSDlSDp_SD	0	0.0227	0.1424
sSDaSDp_SD	0	0.1108	0.05575
sSDlSDl_SD	0	0.05355	0.0955
pSDa_SD	0	0.1484	0.04002
pSDp_SD	0	0.1281	0.0479
pSDl_SD	0	0.2713	0.008862
rSDa_SD	0	0.6147	-0.02622
rSDp_SD	0	0.06969	0.08104
ySDa_SD	0	0.06937	0.0813
ySDp_SD	0	0.01608	0.161
ySDl_SD	0	0.01112	0.1806

Supplementary Information 12. Plots of the cross section area of the anterior, posterior and lateral slender part with corresponding anterior, posterior and lateral area enclosed.

The five subterranean species are in red.

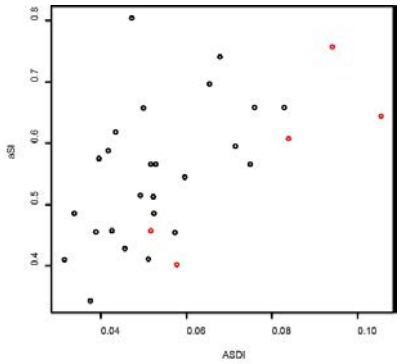

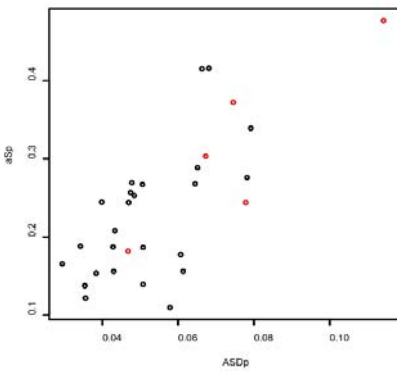

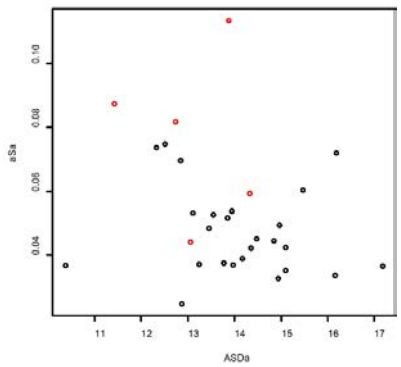

Chapter 3

Do functional parameters of the semicircular duct system of moles show an adaptation to the subterranean lifestyle?

Do functional parameters of the semicircular duct system of moles show an adaptation to the subterranean lifestyle?

Charlène Selva[1*], Romain David[2*], Damien Germain[1], Alexander Stoessel[2,3], Stéphane Peigné[1] & Sandrine Ladevèze[1]

* Co-first Authors

[1] Centre de Recherches sur la Paléobiodiversité et les Paléoenvironnements (CR2P, UMR 7207), Sorbonne Universités-MNHN, CNRS, UPMC-Paris 6, Muséum national d'Histoire naturelle, CP38, 57 rue Cuvier F-75005, Paris, France.

[2] Department of Human Evolution, Max Planck Institute for Evolutionary Anthropology, Deutscher Platz 6, 04103 Leipzig, Germany.

[3] Phyletisches Museum, Vor dem Neutor 1, 07743 Jena, Germany.

Correspondence and requests for materials should be addressed to C.S. (email: charlene.selva@edu.mnhn.fr) or R.D. (email: romain_david@eva.mpg.de).

Introduction

Many animals have colonized the subterranean habitat, for its shelter and unique sources of food (Nevo, 1979). In the mammalian clade, about 5% of the total extant species are found underground: around 300 species spend most of their lives in self-constructed burrows wherein they accomplish all their activities (forage, breed, rest) (Nevo, 1999; Begall et al., 2007). Subterranean lifestyle has been reported in several independent lineages, including marsupials (the marsupial mole), xenarthrans (the pink fairy armadillo), afrotherians (the golden moles), lipotyphlans (e.g. the European mole) and rodents (e.g. the pocket gophers and the mole-rats). These mammals from the underground, here referred as to moles, have evolved a number of morphological and physiological traits that are regarded as adaptations to the subterranean life, and, as such, moles represent a relevant model to study convergent adaptations.

The sensory environment of subterranean mammals is simple, stable, monotonous and deprived of complex stimuli present above (Nevo, 1991; Burda et al., 1990, 1992; Credner et al., 1997). The adjustments to this particular world may lead to structural or functional regressions of the sensory organs which are not stimulated, as well as a specialization of the sensory organs which compensate the useless sense(s).

For example, the auditory system shows both aspects (Pleštilová et al., 2016; Lindenlaub et al., 1995). On the one side, the hearing capacity of the moles has a vestigial aspect and tends to degenerate: the hearing sensitivity is reduced and the high-frequency hearing is restricted (e.g., Burda, 1992, 2006; Mason, 2001). And in the other side, the auditory system exhibits an adapted high sensitivity of low frequency hearing (e. g. West, 1985; Begall and Burda, 2006).

Another example concerns the famous reduction or loss of the vision in many subterranean mammals, often coupled with the degeneration of the eyes due to the dark environment (Walls, 1967). This loss of the vision could lead to a deficient orientation in space and could be compensated with a specialized semicircular duct system. The semicircular duct system is the sensory organ of balance, which provides needful information for navigation and spatial awareness. The semicircular duct, comprised within the inner ear, detects head rotations and, through the vestibulo-ocular and vestibulo-collic reflexes, provides a stable reference frame for the perception of body motion and spatial awareness. Previous studies have already tried to find out if the semicircular duct system shows structural or functional adaptations (and maybe compensation for the loss of sight) to the subterranean lifestyle, based on the morphology of the osseous inner ear (Crumpton et al, 2015; Pfaff et al., 2015) or of the membranous semicircular duct (Lindenlaub et al., 1995; McVean, 1999), and on the functional parameters based on the osseous inner ear (Pfaff et al., 2015) or the membranous structures (Lindenlaub et al., 1995).

Our study aims to highlight eventual functional adaptations of the semicircular duct system to the subterranean lifestyle, and more particularly the digging modes and the powerful spatial navigation of moles. To do so, we rely on the fine information contained in the organ (membranous inner ear). Thanks to tissue staining and X-ray micro tomography, the use of the new method described by David et al. (2016) allows us to obtain the complete membranous labyrinth in-situ and in 3D for five subterranean species and 25 non-subterranean species for comparison. Based on the membranous structures and thanks to the new software Ariadne, functional parameters are computed and compared between subterranean and non-subterranean species.

Material and Methods

The material and methods used for this work are the continuum of the previous chapter, which was focusing on the access to morphological data. Here, we are focusing on functional data that require some extra data preparation. The important steps are recalled here, further information being provided in the previous chapter. The present work is based on the exact same material as the Chapter 2 did, in order to facilitate the comparison of the results of both studies (membranous morphology versus functional parameters of the semicircular duct system of moles).

Five subterranean mammal species and specimens of comparison

The present study focuses on five subterranean species of mammals from five distant clades: the Hottentot golden mole (*Amblysomus hottentotus*), the pink fairy armadillo (*Chlamyphorus truncatus*), the naked mole-rat (*Heterocephalus glaber*), the marsupial mole (*Notoryctes typhlops*), and the common European mole (*Talpa europaea*). These five species will be named as 'moles' in this work. Further information relative to systematics, collection numbers, scanning modes and voxel sizes are listed in Table 1 (and see Chapter 2).

Table 1: Information concerning the five subterranean mammal species selected for this study.

Species Name	Common Name	Clade	N° specimen and institution	Scanning mode	Voxel size
Amblysomus hottentotus	Hottentot golden mole	Afrotheria	Phyletisches Museum (Jena) Mam.5550.42402	Stain CT-scan (MPI Leipzig)	6.03 um
Chlamyphorus truncatus	pink fairy armadillo	Xenarthra	Muséum national d'Histoire naturelle (Paris) CG.1903-82	Synchrotron light scan (ESRF Grenoble)	6.23 um
Heterocephalus glaber	naked mole-rat	Rodentia	Muséum national d'Histoire naturelle (Paris) CG.1884.1778	Synchrotron light scan (ESRF Grenoble)	6.23 um
Notoryctes typhlops	marsupial mole	Marsupialia	Muséum national d'Histoire naturelle (Paris) CG.1893.473	Synchrotron light scan (ESRF Grenoble)	6.23 um
Talpa europaea	common European mole	Eulipotyphla	Research collection of Romain David	Stain CT-scan (MPI Leipzig)	5.12 um

The sample of comparison is composed of 25 mammal species (R. D., personal communication). The species list of the total sample is available in SI-1. The phylogenetic relationships and divergence time between the species are based on the 'timetree' project (Kumar et al., 2017) (the nexus file is available as Online Material). An illustration of the phylogeny is available in the Chapter 2 (see Fig. 6 in chapter 2). The total sample is composed of 16 Euarchontoglires, 9 Laurasiatheria, 1 Afrotheria, 1 Xenarthra, 2 Marsupialia and 1 Monotremata.

Preparation of input data for Ariadne

Ariadne (David et al., 2016) is a software toolbox which provides comprehensive and improved morphological and functional analysis of the semicircular duct system. In Chapter 2, we used only a part of the total capacity of the software, the anatomical analysis. We present here the functional analysis.

The methodology of David et al. (2016) is followed in this study because it is currently the only reliable way to access and provide a formal description of the membranous inner ear. We present here a resume of the protocol used for the present study of the membranous inner ear of five subterranean mammals, more complete details being provided in the original publication and its supplementary information (David et al., 2016).

1-In-situ visualization of the membranous vestibular system

See Chapter 2

2-Segmenting the semicircular duct system

See Chapter 2

3-Cutting the 3D model and editing the streamline

See Chapter 2

4-Cupula modelling

3D models are needed to characterize the cupula of each semicircular duct. The cupula is thought to be secreted by the supporting cells of the *crista ampullaris*, hence the best way to approximate the cupula is to perform an extrusion of the shape of the *crista ampullaris* towards the ampulla roof. Performed with Geomagic 12 software, this cutting allows to obtain one volume and four surfaces STL files for each cupula (Fig. 1 a, b, c), which gives a total of 15 new STL files for each specimen.

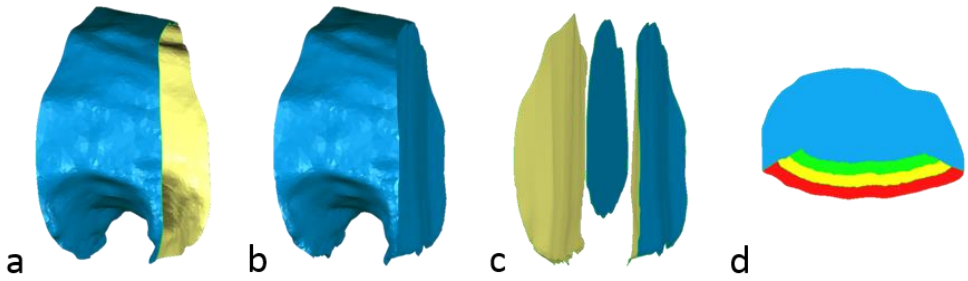

Figure 1: In-put data for the cupula. Example on the anterior ampulla of *Amblysomus hottentotus*.

a) Ampullary wall mesh. b) Volume mesh. c) Surfaces mesh of the slender duct face, of the middle cross-section and of the utricular face. d) Composition of 4 meshes (each color) to characterize the middle cross-section with the different stereocilia/kinocilia regions (in red: 0-30 µm, in yellow: 30-60 µm, in green: 60-90 µm).

Four additional STL files (Fig. 1 d) are needed to express the different models of stereocilia or kinocilia length, used to calculate the thickness of the cupula. These models are used to perform a finite element analysis (FEA) of cupula deflection.

5-Analysis through Ariadne software

Last input data asked by Ariadne before the analysis are:

- mid-sagittal plane of the vestibular frame of reference (frame of reference for both inner ears, based on a model of coupled ducts)
- internal temperature of the species (Table 2)
- hypothesis of sterocilia length (here we assume a medium length between 30 to 60 µm)
- shrinkage correction (here we assume no correction)

- assumption about the mode of deflection of the cupula (here we use the second proposition: “the cupula is considered to be clamped at the level of the *crista ampullaris* only and supported at the level of the walls of the ampulla”)
- choice of the segmentation error factor in voxel units (depends on the segmentation difficulty, here we assume the empirical value of 0.24 for the naked mole rat and the golden mole, 0.35 for the marsupial mole, 0.5 for the pink fairy armadillo and the European mole, based on the scan quality and difficulty of the segmentation process)

Table 2: Body mass and internal temperature used in this study for the five moles (and associated references).

Species Name	BM (g)	References for BM	Temperature (C°)	References for Temperature
Chlamyphorus truncatus	120	Billet et al., 2013	32	McBee & Baker, 1982
Heterocephalus glaber	37.9	Yosida et al., 2007	32	Johansen et al., 1976 Urison & Buffenstein, 1995
Notoryctes typhlops	51.25	Woinarski, 2014 Bennison et al., 2014 Withers et al., 2000	31	Withers et al., 2000
Amblysomus hottentotus	72.81	Kuyper, 1979 Scantlebury et al., 2008	33	Kuyper, 1979 Scantlebury et al., 2008
Talpa europaea	80	Southern, 1964	36.7	Poczopko & Chrzanowski, 1966

After loading the input files (3D volumes, surfaces, landmarks set), Ariadne performs various analyses. Our interest for this study concerns the complete biomechanical analysis of the semicircular duct system, including spatial mapping of the semicircular duct system mechanical sensitivity.

The results are given in different formats. The raw functional parameters are given in a text file format, but they can be visualized in a spatial mapping of the mechanical sensitivity and bode analysis thanks to the software Scilab 5.4.0 (www.scilab.org).

Statistical Analysis of the functional parameters

1-Functional parameters considered in this study

The semicircular ducts are governed by several functional parameters that Ariadne is able to compute. In this study, we are focusing on the parameters judged the most useful to define the vestibular capacities of the animals (Rabbitt et al. 2004; David et al., 2016), and the most relevant for our question because they are directly linked to head motion. The relations between semicircular duct function and head motion frequency is presented in figure 2.

The velocity bandwidth is the frequency range of head motion for which the deflection of the cupula is more in phase with angular velocity than with angular acceleration or angular displacement. The angular velocity of an object (here the head) is the rate of change of its angular displacement (the rotation of the head in a specified sense about a specified axis) with respect to time. The angular acceleration is the rate of change of angular velocity. Despite angular acceleration is the primary generator of endolymph flow, we are looking to work on the velocity bandwidth. For this frequency range, the semicircular ducts behave as angular velocity transducers and provide fundamental information for the vestibulo-ocular reflex (VOR) to stabilize the head motions and to have a stable reference frame for the perception.

The bandwidth of interest is surrounded by the lower corner frequency ‘w1’ and by the upper corner frequency ‘w2’. The natural frequency (w0) is in the middle of the bandwidth. The higher the natural frequency, the higher the tendency of the animal to experience frequent head motion overall. These parameters are particularly linked to the average cross-sectional area of the semicircular duct, highlighting the importance of using membranous structures instead of osseous structures which present very different measurements. It also implies high quality of segmented membranous labyrinths.

In this study, the bandwidth is more restricted and defined the range of frequency for which the deflection of the cupula is 90% or more in phase with angular velocity surrounded by the specific lower corner ‘w1_90’ and the specific upper corner ‘w2_90’ (Fig. 2).

The mechanical sensitivity, or mechanical gain, reflects the magnitude of the biomechanical response following a given head rotation and has been previously expressed, for example, in terms of cupula displacement (Oman et al., 1987; Lindenlaub et al., 1995; McVean, 1999). Here, the sensitivity is more accurate and expresses the amount of cupula deflection that

occurs in the areas where cilia can be found. In other words, the sensitivity (VG_s) here corresponds to the degree of deflection of the cilia per degree per second of head rotation. This new parameter cannot be compared to sensitivity values calculated in previous studies but Ariadne is also able to compute previous types of sensitivity that could be used for comparison ('VG_u_SDa', 'VG_u_SDp' and 'VG_u_SPl'). The higher the sensitivity, the more rotations are accurately detected, but the less the system can sustain high angular velocities without saturating (David, 2011). The higher the sensitivity, the more precise and sensitive is the semicircular duct system to detect head rotations. This parameter depends among others of the average cross-sectional area of the ducts and of the transfer factor for endolymph volume displacement to cilia deflection computed through FEA, using a 3D model of the cupula inferred from the membranous *crista ampullaris.* Obviously, studying the membranous semicircular ducts is more relevant and crucial to understand the sensitivity parameters across mammals.

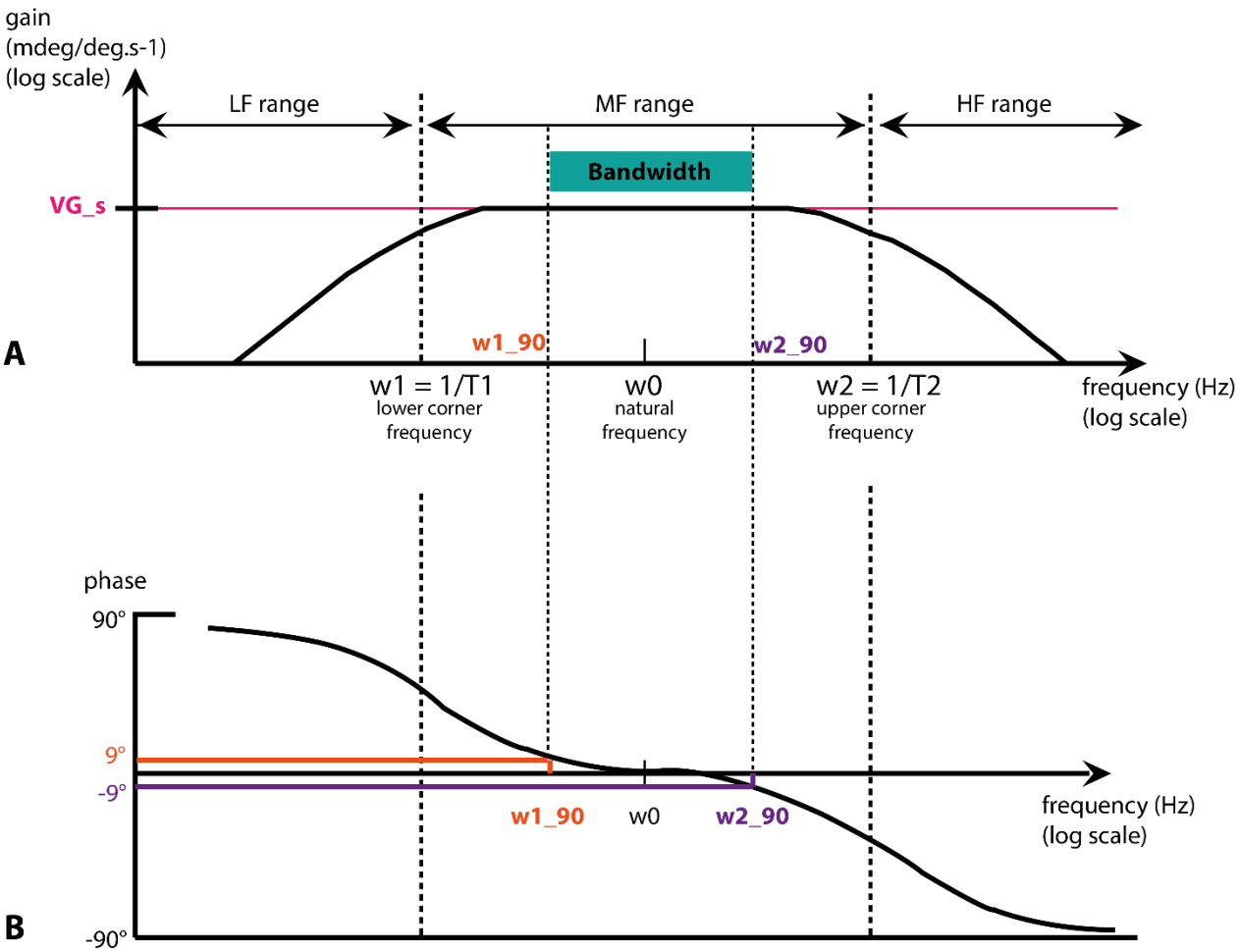

Figure 2: Theoretical bode plots illustrating how biomechanical gain (A) and phase (B) of the semicircular duct system are related to head motion frequency.

Here the metrics for semicircular duct gain corresponds to the average deflection of the cupulae where cilia are located. Modified from Jones & Milsum (1971) with data from David et al. (2016). Abbreviations: HF, high frequency; LF, low frequency; MF, middle frequency. In B, when the phase = +90°, the semicircular duct system is in phase with angular acceleration; when the phase = -90°, the semicircular duct system is in phase with angular displacement; and when the phase = 0°, the semicircular duct system is in phase with angular velocity.

In this work, we include both membranous inner ears of an individual to be able to deal with the integrated system of the semicircular duct system. We take into account that the anterior duct from on one side works in a push-pull fashion with the posterior duct from the other side. In that way, we can determine the most relevant sensitivity for each type of head rotation (in pitch 'VG_s_P', in roll 'VG_s_R' and in yaw 'VG_s_Y'; types of head rotation illustrated in Fig. 3) instead of considering only the sensibility for each semicircular duct. On the contrary, the previous type of sensitivity calculated by Oman et al. (1987) was given for each duct ('VG_u_SDa', 'VG_u_SDp' and 'VG_u_SPl') and not for each type of head rotation. As a matter of fact, previous studies did not have access to either both membranous inner ears or the semicircular duct system in the 3D reference; these parameters being crucial to take into account the plan of maximum response needed to compute the sensitivity for the type of head rotation.

Contrary to the sensitivity, the frequency bandwidth is not affected by the semicircular plan orientations that allowed us to present the 'w1_90' and 'w2_90' parameters depending of the vertical rotations together ('w1_90_PR', 'w2_90_PR') and the lateral rotations separately ('w1_90_Y', 'w2_90_Y').

To resume, in this study, we will present the following functional parameters for the five moles calculated by Ariadne:

- 'w1_90_PR', lower corner of the bandwidth in vertical rotations (pitch and roll)
- 'w1_90_Y', lower corner of the bandwidth in horizontal rotations (yaw)
- 'w2_90_PR', upper corner of the bandwidth in vertical rotations (pitch and roll)
- 'w2_90_Y', upper corner of the bandwidth in horizontal rotations (yaw)
- 'VG_s_P', "new" sensitivity of the semicircular duct system for pitch rotations

- ‘VG_s_R’, “new” sensitivity of the semicircular duct system for roll rotations
- ‘VG_s_Y’, “new” sensitivity of the semicircular duct system for yaw rotations
- ‘VG_u_SDa’, “previous” sensitivity of the anterior semicircular duct
- ‘VG_u_SDp’, “previous” sensitivity of the posterior semicircular duct
- ‘VG_u_SPl’, “previous” sensitivity of the lateral semicircular duct

2-Statistical analysis

Raw values of the functional parameters described above are effective values that define the semicircular duct capacities of an animals. The goal of this study is to compare these functional parameters of the five moles with 25 other mammals.

To do so, the data analysis was performed with the R software (R Core Team, 2014) and the R script is available in SI-2 and as Online Material (OM-1).

After loading the raw data (SI-1 and OM-2) and the nexus file (OM-3), the dataset are checked and formatted. Phylogenetic Generalized Least Squares regressions (PGLS) of the functional parameters onto body mass were performed with the 25 species of comparison (detailed list in SI-1). Then functional parameters were corrected and computed without the size effect for the 30 species, which can therefore be compared at equal body mass (72g).

We performed a first Principal Component Analysis (PCA) on the seven parameters. The results of the PCA are read in a graphical plot in three dimensions, but this rendering does not allow to consider all the diversity. Thus, a two-sample Hotelling’s T-squared test (Curran, 2013) was performed to test for the differences between two multivariate means. In our study, the test was performed on the mean of the specimens' scores to answer two questions: do the functional parameters of the semicircular duct system of moles a) significantly differ from the functional parameters for mammals and b) significantly differ from the functional parameters for non-subterranean mammals. To better understand the particularity of the functional parameters of the semicircular duct system of moles, we performed a second PCA only on the lower and upper corners, which aim to present the bandwidth evolution for our species. Finally, boxplots were performed on all the functional parameters comparing the moles to the other species.

Results

1- Raw functional parameters of the moles

The first results provided by Ariadne correspond to the raw functional parameters for each species, those of the moles being presented in table 3 and those for the other species in SI-1.

Table 3: Raw functional parameters for the five moles calculated by Ariadne.

With 'w1_90', 'w2_90' in Hz and 'VG_s' in mdeg/deg.s^{-1}. Abbreviations: BM, Body Mass, 'w1_90_PR', lower corner of the bandwidth in vertical rotations (pitch and roll), 'w1_90_Y', lower corner of the bandwidth in horizontal rotations (yaw), 'w2_90_PR', upper corner of the bandwidth in vertical rotations (pitch and roll), 'w2_90_Y', upper corner of the bandwidth in horizontal rotations (yaw), 'VG_s_P', "new" sensitivity of the semicircular duct system for pitch rotations, 'VG_s_R', "new" sensitivity of the semicircular duct system for roll rotations, 'VG_s_Y', "new" sensitivity of the semicircular duct system for yaw rotations.

Taxa	BM (g)	w1_90_PR	w1_90_Y	w2_90_PR	w2_90_Y	VG_s_P	VG_s_R	VG_s_Y
Chlamyphorus truncatus	120	1.55	2.3	15	13.3	4.1	3.8	6.8
Heterocephalus glaber	37.9	3.05	4.1	14.4	15.1	5.3	5.0	8.5
Notoryctes typhlops	51.25	2.35	3.7	16.8	17.1	5.0	2.8	7.2
Amblysomus hottentotus	72.81	2.3	2.6	20.9	19.4	4.1	3.5	5.7
Talpa europaea	80	0.97	0.83	19.8	18.8	2.7	1.9	2.8

The 'w2_90' functional parameter is slightly correlated with the phylogeny (see lambda in SI-3). The phylogeny effect can be evaluated based on the phylogenetic diversity of our sample, which contains five subterranean species from different clades. The 'w2_90' and 'VG_s' parameters are strongly correlated with the body mass (see R^2 and p-value in SI-3). That is why the comparison with other species is made on allometry-corrected data.

The second type of data provided by Ariadne are spatial sensitivity maps illustrating how various metrics of the sensitivity of the semicircular duct system vary relatively to the axis and directions of rotations. Such spatial map representations allow to visualize the different values of sensitivity corresponding to different head movements (Fig. 3).

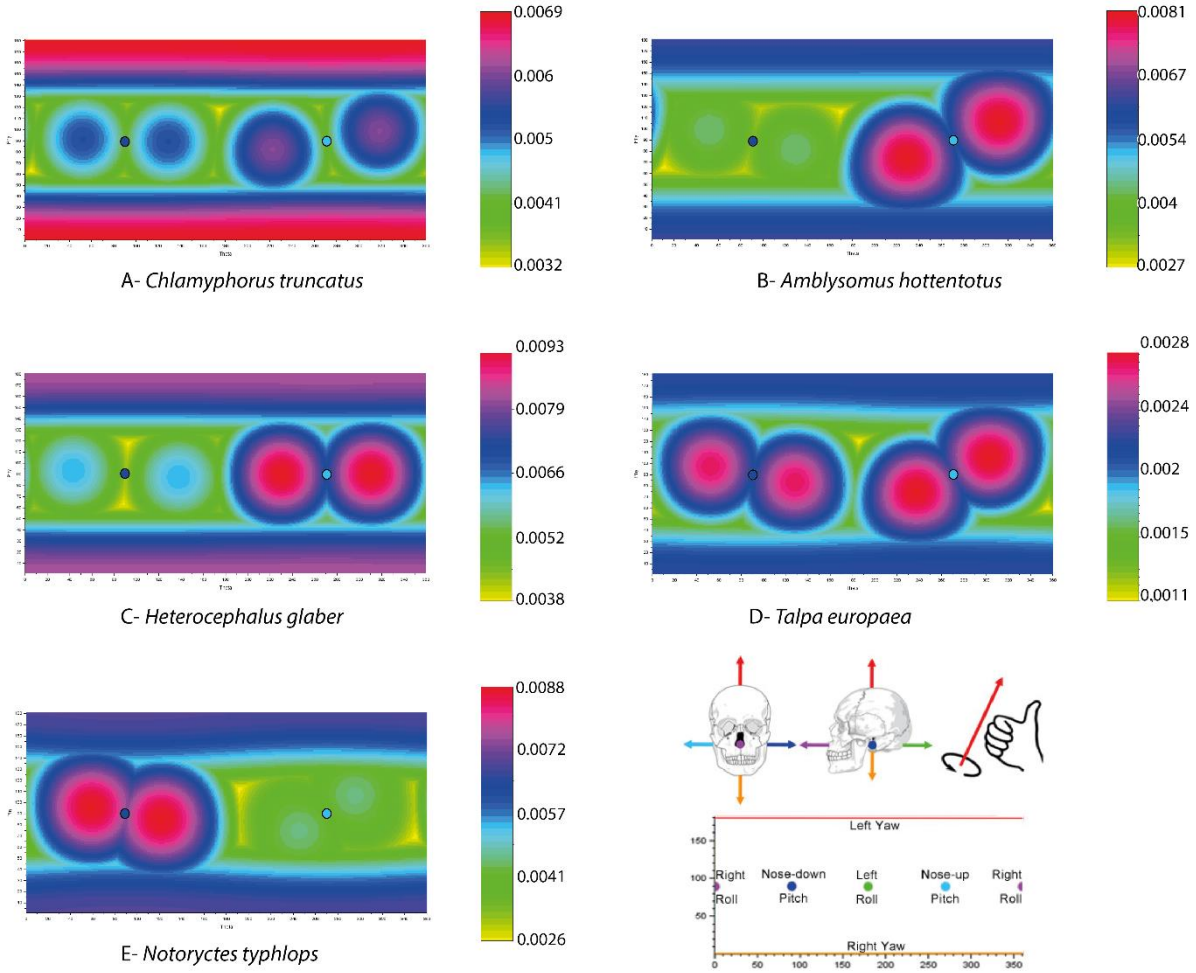

Figure 3: Spatial sensitivity maps illustrating how various metrics of the sensitivity of the semicircular duct system vary relatively to the axis and direction of rotations.

The sensitivity presented here considers the average deflection of areas of the cupulae where cilia can be found. The bottom right panel shows were to look on the spatial sensitivity maps for interpreting the sensitivity of the semicircular duct system to a particular head rotation (following the right hand rule: the thumb is the axis (arrow) and the others digits indicate the direction of rotation). To help the reading, the interesting spots for nose-down pitch (dark blue circle) and nose-up pitch (light blue circle) are marked directly on the maps.

2- Comparison with other non-subterranenan mammals based on size-effect corrected data

Here we compare the functional parameters corrected for allometry.

The first comparison is provided by the figure 4 which presents the average function of semicircular duct system of subterranean and non-subterranean species. The bode plots illustrate how biomechanical phase and gain of the semicircular duct system are related to head motion frequency for the subterranean and the non-subterranean species. Compared to

the non-subterranean species, the moles present the following differences: the average bandwidth is narrower, mostly reduced in the lower frequencies, and with a much higher sensitivity than non-subterranean species.

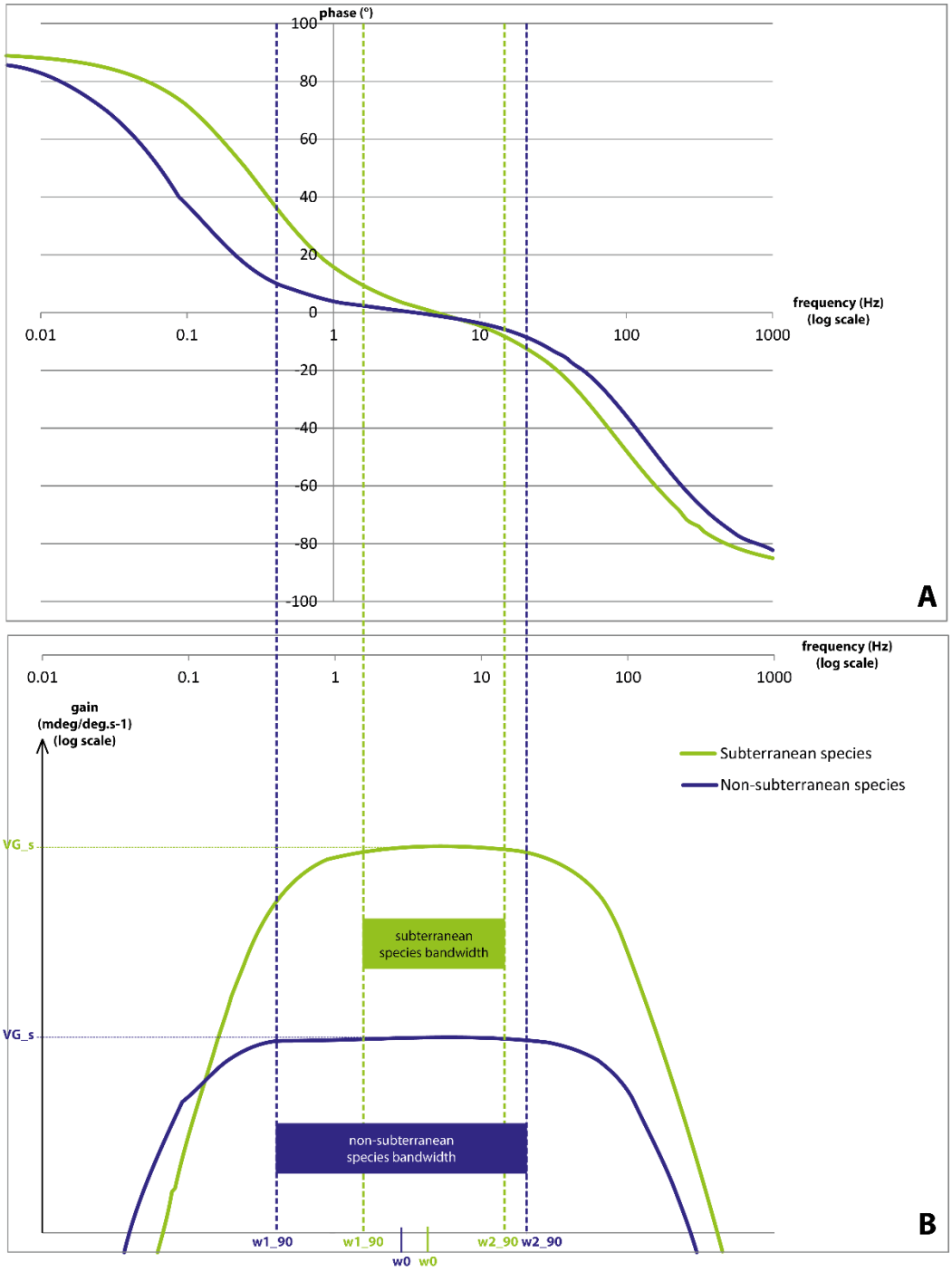

Figure 4: Bode plots illustrating how average biomechanical phase (A) and gain (B) of the semicircular duct system are related to head motion frequency for the subterranean and the non-subterranean species.

Here the metrics for semicircular duct gain corresponds to the average deflection of the cupulae where cilia are located.

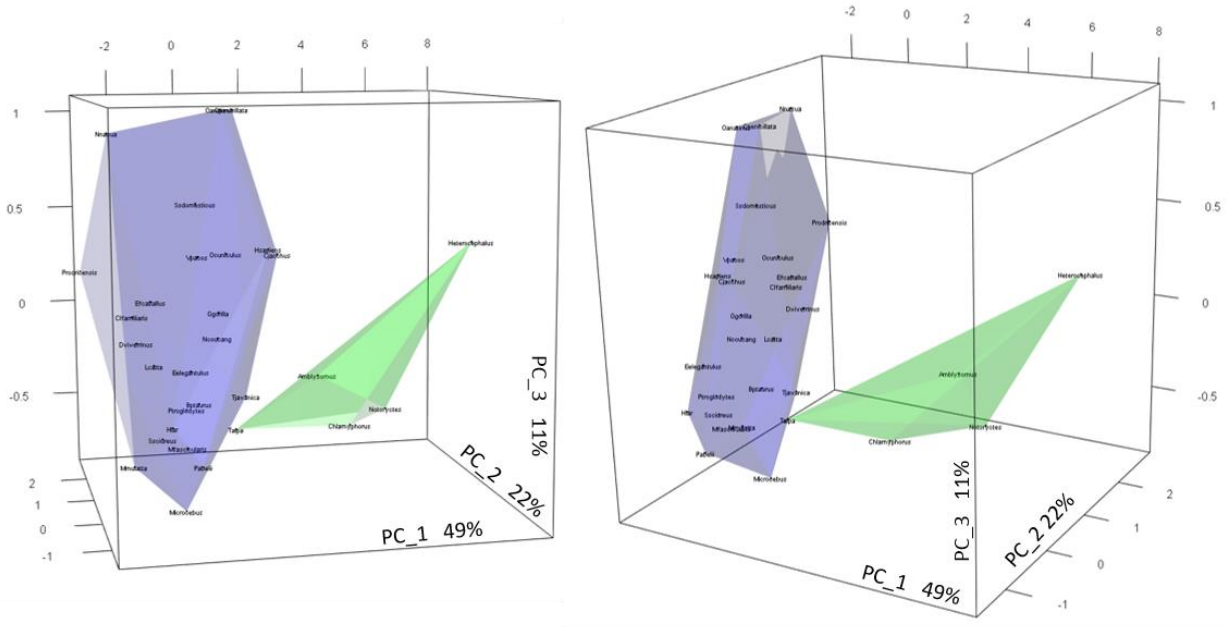

Figure 5: First Principal Component Analysis (PCA) based on the seven functional parameters corrected for size effect.
In blue, the 25 non-subterranean species and in green, the 5 subterranean species.

The first PCA is performed on the seven allometry-corrected parameters and is presented in figure 5. The PC1 represents 49% of the total variance, the PC2 22% and PC3 11%, thus the first three axes explain more than 82% of the total variance. The five moles do not spot really closely; nevertheless, they constitute a 3D cluster that does not overlap the cluster of the non-subterranean species. On the first third PCs, the five moles do plot together but this considers only 82% of the total diversity. In order to consider a maximum of diversity and verify the first observation, the two-sample Hotelling's T squared test is performed twice. The functional parameters of the semicircular duct system of the five moles is not significantly different from the functional parameters of mammals (p-value = 0.0836) but is significantly different from the functional parameters of non-subterranean mammals (p-value = 2e-04).

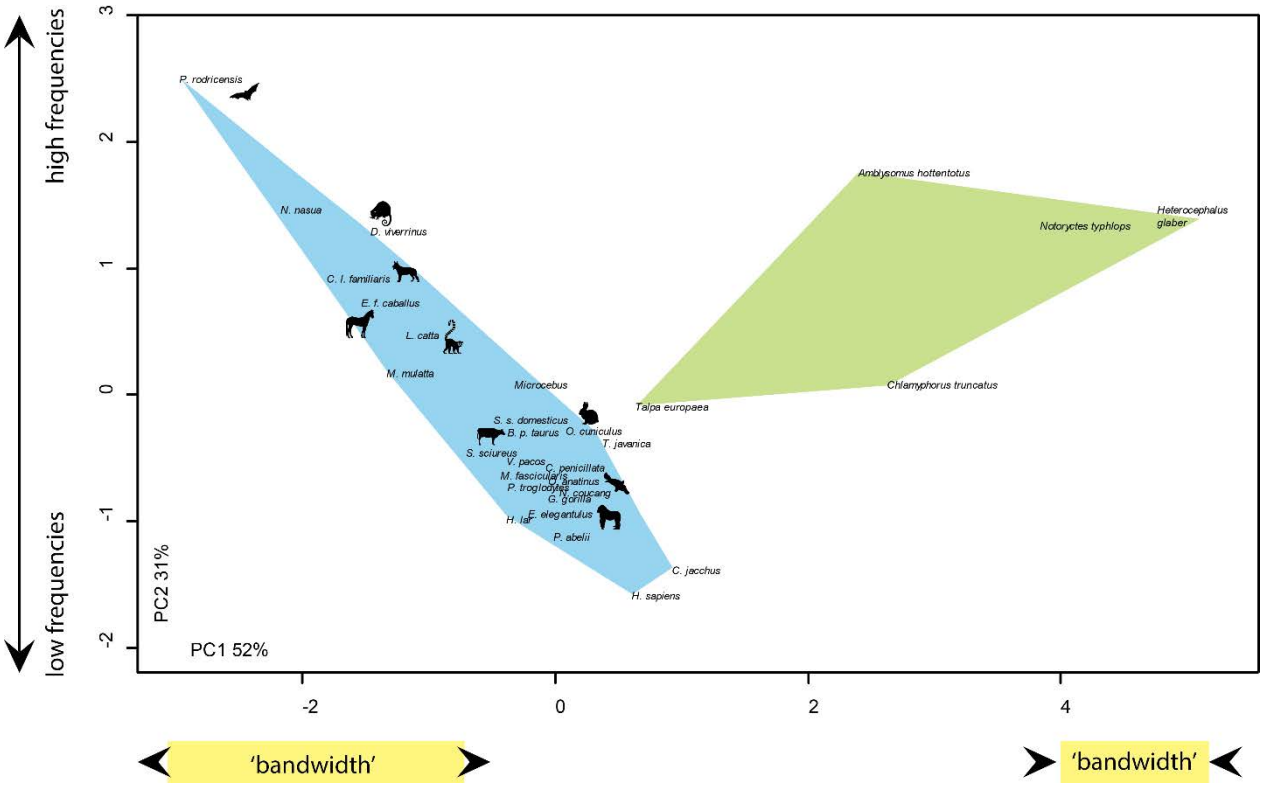

Figure 6: Second Principal Component Analysis (PCA) based on four functional parameters corrected for size effect.

In blue, the 25 non-subterranean species and in green, the 5 subterranean species. We are focusing on 'w1_90' and 'w2_90' parameters to understand the changes of the bandwidth.

The second PCA is performed on four allometry-corrected parameters to understand the changes of the bandwidth and is presented in figure 6. The PC1 represents 52% of the total variance, the PC2 31%, thus the first two axes explain more than 83% of the total variance. The five moles do not spot really closely but they cluster together and do not overlap with the cluster of the non-subterranean species. Subterranean and non-subterranean species are well-discriminated on the PC1. Looking at the loadings on the PC1 (Table 4), we observe an increase of the 'w1_90' parameters associated with a decrease of the 'w2_90' parameters along the PC1 going to positive values. In contrary, in negative values, the 'w1_90' parameters are decreasing and the 'w2_90' parameters are increasing. Remembering that the 'w1_90' and 'w2_90' parameters are the limits of the bandwidth, the PC1 thus separates species with a narrow bandwidth from species with a large bandwidth. Along the PC2, all the parameters increase with positive values. Thus, the bandwidth is translated in high frequency for positive values of PC2 and low frequency for negative values of PC2.

Table 4: Raw functional parameters for the five moles calculated by Ariadne.

	PC1	PC2
% of total variance	52%	31%
w1_90_PR	0.5187023	0.4809240
w1_90_Y	0.5217841	0.4723799
w2_90_PR	-0.4609693	0.5692827
w2_90_Y	-0.4961820	0.4706235

Finally, the box plots (Fig. 7) compare the distribution of the functional parameters between subterranean and non-subterranean species. The subterranean species present higher sensitivity than the non-subterranean species. The 'w1_90' parameters for subterranean species are greatly higher than those for non-subterranean species. The 'w2_90' parameters for subterranean species are slightly lower than those for non-subterranean species. These observations are in concordance with the information contained in the average bode plot (Fig. 4).

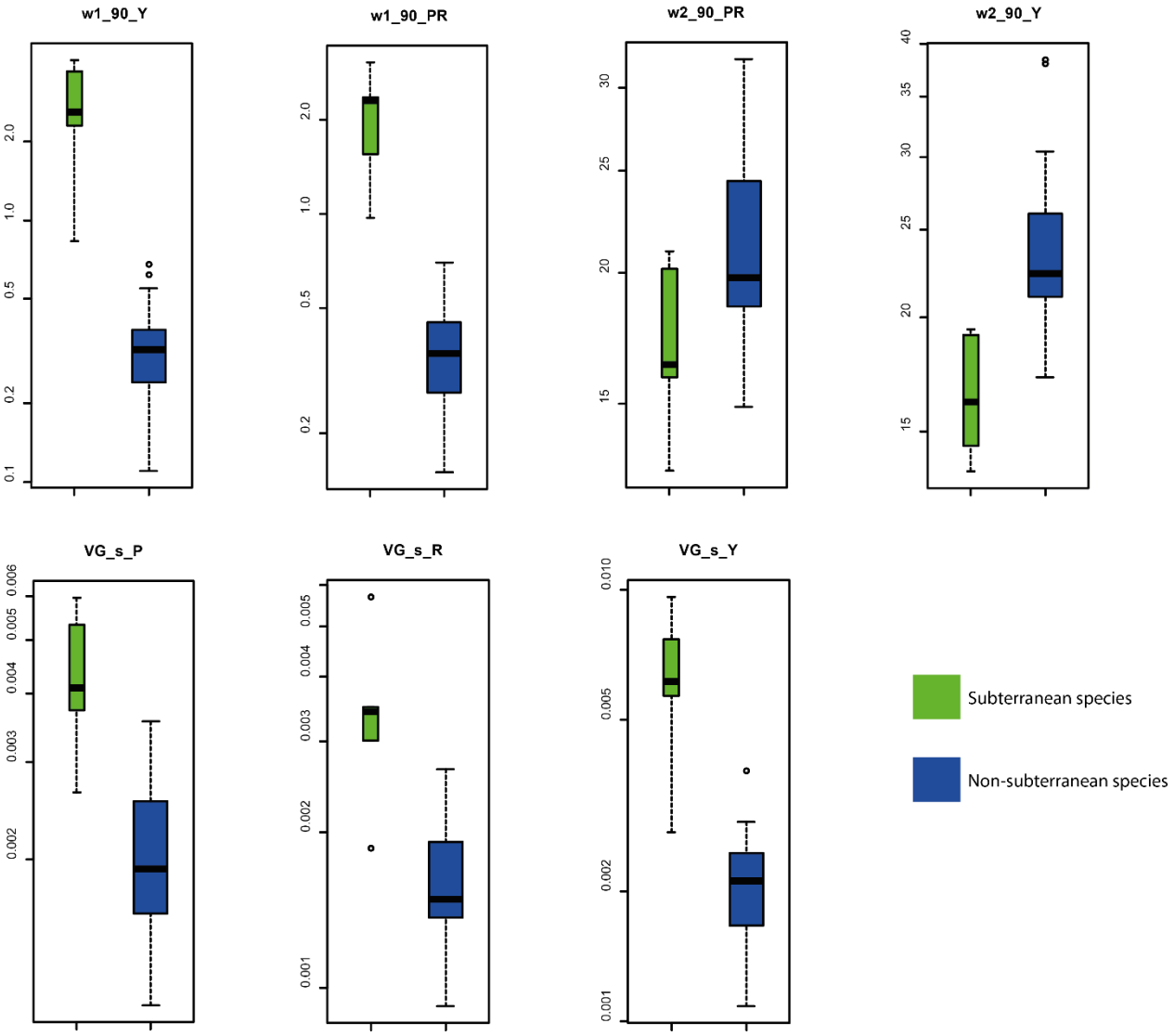

Figure 7: Box plots presenting the distribution of the functional parameters for subterranean and non-subterranean species.

In blue, the 25 non-subterranean species and in green, the 5 subterranean species.

Discussion

1-Are the functional parameters of the moles calculated in this study relevant compared to previous studies?

The improved definition of sensitivity used in this paper was already employed in a few previous studies (e. g. on primates by David et al., 2016).

To compare the values of sensitivity obtained here with those obtained in previous studies, we need to consider the sensitivity definition of Oman et al. (1987), which corresponds to the linear displacement of the cupula, and which was used to calculate the sensitivity of some subterranean mammals by Lindenlaub et al. (1995).

Ariadne, software used in this work, is able to compute values of sensitivity *sensu* Oman et al. (1987) and thus allows a comparison with the previous study of Lindenlaub et al. (1995) (table 5). We notice that the range of values of the sensitivity calculated through Ariadne and those calculated on previous studies is similar, comforting the reliability of the methodology we applied to study our specimens.

Table 5: Comparison of the results with the mechanical sensitivity of Oman et al. (1987).

Species Name and References of the data	Mechanical Sensitivity of Oman et al. (1987) **nm/degree/s**		
	Anterior semicircular duct VG_u_SDa	Posterior semicircular duct VG_u_SDp	Lateral semicircular duct VG_u_SDl
Rattus norvegicus Lindenlaub et al. 1995	7.38 ±0.71	5.04 ±0.59	5.11 ±0.57
Spalax ehrenbergi Lindenlaub et al. 1995	9.30 ±0.89	6.94 ±0.72	8.66 ±0.88
Cryptomys sp. Lindenlaub et al. 1995	8.52 ±0.80	6.75 ±0.69	8.05 ±0.76
Chlamyphorus truncatus	8.317	8.544	10.106
Heterocephalus glaber	11.189	8.956	10.737
Notoryctes typhlops	6.574	10.207	8.882
Amblysomus hottentotus	8.333	4.904	6.732
Talpa europaea	5.608	4.876	4.384

2-Sensitivity of the semicircular ducts and behaviors?

The raw values of the sensitivity (here defined as the degree of deflection of the cilia per degree per second of head rotation, as defined by David et al. (2016)) calculated for the five moles in yaw direction are always the highest compared to the sensitivity in pitch and roll rotations (this is not the case for non-subterranean species, SI-1). This indicates that the moles are more efficient to detect and feel the lateral head rotations than the vertical rotations, which allows a better navigation. Concurrently, lateral movements of the head might emphasize the contact of the muzzle's sensitive hairs with the lateral walls of the burrow, and therefore contribute to the powerful spatial navigation of moles (just in the same way as a blind person uses a stick to perceive its environment)?

Less sensitivity on vertical movements (pitch and roll) means that moles can experiment higher angular velocity without saturating the system, compared to the horizontal movement. In the same way, it might be linked to the digging behavior which could require vertical movements with higher angular velocity: for example when digging with the head (head-lift digging) or with the tooth (chisel-tooth digging) (Hildebrand et al., 1995; Nevo, 1999).

It is noteworthy that three species (Hottentot golden mole, marsupial mole, naked mole-rat) do not present the same range of sensitivity for nose-down pitch rotation and for nose-up pitch rotation: the sensitivity for nose-up pitch rotation is almost twice the sensitivity for nose-down pitch rotation. It means that these species detect with more delicacy the movements of head up and that they can experiment higher angular velocities for the head down without saturating the system. These moles (Hottentot golden mole, marsupial mole, naked mole-rat) are all known to have the head playing an important role during the digging behavior (Hildebrand et al., 1995; Nevo, 1999). The two first are swimming in the sand thanks to the head movements and the third digs with its incisors. Nose-down pitch movement might require higher velocity for these kinds of behavior.

To further test the assumptions exposed above and highlight an eventual link between sensitivity and digging behavior, it would be interesting to:

- Complete our sample with moles that exhibit different types of digging

- Observe head motion during the different types of digging thanks, for example, to cinefluorographical studies (Gambaryan et al., 2002) or X-ray reconstruction of moving morphology (XROMM) (Brainerd et al., 2010; Lin, 2017)
- Better characterize natural head motion in unconstrained subterranean species (Malinzak et al., 2012; Lin et al., 2017)

3-Does the semicircular duct system function differ between subterranean and non-subterranean mammals?

In the first PCA based on functional parameters corrected for allometry (Fig. 5), the 3D cluster of subterranean mammals does not overlap with the 3D cluster of the non-subterranean species. Confirmed by the Hotelling test, we can conclude that the semicircular duct system of subterranean mammals functions differently from that of non-subterranean mammals. However, the semicircular duct function in moles remains quite variable and occupies a large part of the 3D functional space.

If we scrutinize the functional parameters that differ between subterranean and non-subterranean mammals, we first observe that the sensitivity of the semicircular duct system of moles is higher than for the other species: in average gain (Fig. 4 B) and for each type of rotations (Fig. 7). The bandwidth of subterranean species is narrower than the bandwidth of non-subterranean species (Fig. 4 B and Fig. 6).

The lower corner (‘w1_90’) of the moles is clearly higher than the lower corner of the non-subterranean species which leads to a slightly increase of the natural frequency (‘w0’) compared to the non-subterranean species (Fig. 4).

Looking at the second PCA (Fig. 6), we can appreciate the relation between the width of the bandwidth (narrow or large) and the position of the bandwidth (in low frequencies or in high frequencies). Subterranean and non-subterranean species do not present the same pattern. For the non-subterranean mammals, the large bandwidths are coupled with high frequencies and less large bandwidths are coupled with low frequencies. For those species, large bandwidth associated with high frequencies is due to the increase of the upper corner. This pattern is optimized and adapted to experiment a large range of frequencies and can be particularly expected in acrobatic species with various gaits. On the contrary, for the moles,

narrower bandwidth are coupled with high frequencies and less narrow bandwidth with low frequencies. For those species, a narrow bandwidth associated with high frequencies is due to the shift of the lower corner towards high frequencies, whereas the upper corner frequency stays close to the one observed in other mammals. Thus, the moles are really sensitive but only for a narrow range of head motions, which is, *a priori*, not an advantage.

4-Adaptation to the subterranean lifestyle?

The extreme confinement to the underground dark environment has led to the loss of vision in many subterranean mammals and the acquisition of traits contributing to compensate the loss of this important sense (Nevo, 1999). Following this idea, we can assume that moles need a strong capacity of spatial navigation and detection of body motion and orientation. Indeed, numerous adaptive traits answering this problematic have already been observed in moles:

- Increase of sensitive skin, vibrissae and tactile hairs on the head and on the body which provide to the animal underground an easier perception of its environment and a unique tactile orienting behaviour (e. g. Crish et al., 2003, 2006; Partha et al., 2017; Begall et al., 2007; Catania & Remple, 2004)
- Perception of the Earth's magnetic field to perform their unique directional orientation (Nevo, 1999; Kimchi & Terkel, 2001a; Marhold et al., 1997).

Up to now, the successful spatial orientation has been observed for the blind mole-rats, as compared to other rodents thanks to ethological experimentations (Kimchi & Terkel, 2001b). For the semicircular duct system, a good efficiency to detect tiny changes of head motions and directions corresponds to a high value of the sensitivity and the moles effectively exhibit high values of sensitivity compared to non-subterranean mammals. This is a new functional convergent adaptation to the subterranean lifestyle, highlighted thanks to this study.

But we can wonder why the bandwidth of the moles presents an unusual pattern compared to the non-subterranean species. Indeed, to have a narrow bandwidth may not be interesting because moles have an efficient semicircular duct system only for this little range of frequencies. In fact, this unusual pattern is the consequence of the increase of the sensitivity. Increasing the sensitivity can be done in various ways:

- Increasing the radius of curvature of the semicircular ducts, which can be problematic for small mammals
- Increasing the cross sectional area of the semicircular duct, which leads to the decreasing of the upper corner frequency
- Modifying the morphology of the cupula, which lead to increasing the lower corner frequency

In the moles, the sensitivity has to be greatly increased while keeping a functional bandwidth. It is done by modifying cupula morphology, which leads to the observed increase of the lower corner frequency. To have a high lower corner frequency means that the semicircular duct system does not accurately detects low frequencies generally detected by most mammals.

In fact, this consequence is not a problem for the moles being blind (Nevo, 1999; Wetzel, 1985). Indeed, the only vestibular reflex that is active for low frequencies is the vestibulo-ocular reflex (VOR), which allows gaze stabilization (Highstein et al. 2004). Being blind, the moles do not drop an important ability. But for higher frequencies on the bandwidth, the semicircular duct system is giving information for the vestibulo-collic reflex (VCR) which aims to stabilize the head (Goldberg & Cullen, 2011). This ability needs to be maintained even in moles to allow correct balance, motor coordination and navigation.

Finally, the European mole seems to present a better vision as the other subterranean species of the sample (see Nevo, 1999: Appendices 1 and 2). This could explain why the European mole has a semicircular duct function pattern less particular than the other moles and this adds a supplementary clue to corroborate this hypothesis of functional convergent adaptation.

Conclusion and Perspectives

The new method used in this study (David et al, 2016) allows to access to the membranous inner ear, a crucial anatomical structure to compute the functional parameters of the semicircular duct system. This non-invasive method can be used on a large range of species and allows us to understand the adaptation to subterranean lifestyle, through the study of really rare and precious species.

It has been recently shown that both the morphology of osseous and membranous semicircular duct systems have failed to discriminate locomotor modes in mammals (Chapters 1 and 2 of the manuscript). However, the functional parameters derived from the membranous semicircular duct morphology are relevant to discriminate the subterranean behavior from other behaviors in mammals. The access to functional parameters is therefore crucial to test for eventual correlations between semicircular ducts and locomotion.

Here we highlight a clear and new functional convergent adaptation of the semicircular duct system to the subterranean lifestyle: the moles present a higher sensitivity than the non-subterranean species. This adaptation is linked with the regression of the eyes and participates to the compensation of the loss of vision to improve the detection of head motion, orientation, coordination and spatial awareness. This specialization of the semicircular duct system, in the same way as the increasing of sensitive skin, vibrissae and tactile hairs or the perception of the Earth's magnetic field, is a compensatory trait of the loss of an important sense, common for the moles.

Moles can perform vertical movements with higher angular velocity (lesser sensitivity on vertical head movements), and swimming and incisor-digging species perform nose-down pitch movements with higher velocity (higher sensitivity for nose-up pitch rotation). These results might be interpreted as eventual adaptations of the semicircular duct system to the digging behavior (especially the use or not of the head for digging). Future directions to deepen this question should include other subterranean species with different types of digging and should be based on characterized and formalized head motions while digging (versus other behaviors). Experimental works are thus needed to follow the animal journey across the ground and underground. Most data are available on the limbs movements (and sometimes the neck), thanks to X–ray cinematograph films (e.g., Gasc et al., 1985, 1986; Puttick et al., 1977), but with more recent 3D kinematics experiments, it would be very promising to scrutinize the head while the animal rests, digs, and navigates underground.

Supplementary Information

SI-1. List of the sample and raw data for the five moles and the 25 non-subterranean species of comparison.

SI-2. R script for the statistical analysis of the functional parameters.

SI-3. Influence of allometry and/or phylogeny on the functional parameters ('PGLS' on the 25 non-subterranean species).

Online Material

OM-1.RScript_Function.txt

OM-2.RData_Raw_Function.txt

OM-3.MammalTree.nex

Acknowledgements

In order to carry out this work, CS had to be formed to the new method set up by RD. In this context, CS went three times to work with RD at the Max Planck Institute (Leipzig), and would like to thanks the Institute and particularly Jean-Jacques Hublin, director of Department of Human Evolution, for welcoming her and David Plotzki for the scans he performed there. These travels and the resulting present study were financially supported by two major grants:

- "Short-Term Grant" from the Deutscher Akademischer Austauschdienst (DAAD), which encourages Franco-German collaborations.
- "Transhumance Grant" from the Doctoral School of the MNHN, which encourages young researcher to develop international collaborations.

We are grateful to Violaine Colin-Nicolas, Géraldine Véron, and Aurélie Verguin (MNHN) for the loan of the precious specimens from the Zoothèque of the MNHN, and Marc Herbin (MNHN), for the conditioning of the specimens and the staining protocol applied to some unfruitful specimens. CS, DG, and SL warmly thank Vincent Fernandez (beam ED19, ESRF, Grenoble) for his expertise and precious help during their stay at the European Synchrotron Radiation Facility (Experiment LS-2427 ED19/2015) during which we performed major scans.

Finally, CS and SL would like to thank Jérôme Dormion of Taup'green who kindly helped them to provide a common European mole, which was, ironically, the most difficult species to obtain.

References

Bennison, K., Clayton, J., Godfree, R., Pavey, C., & Wilson, M. (2014). Surfacing behaviour and ecology of the marsupial mole (*Notoryctes typhlops*) at Uluru-Kata Tjuta National Park. *Australian mammalogy*, *36*(2), 184-188.

Begall, S., & Burda, H. (2006). Acoustic communication and burrow acoustics are reflected in the ear morphology of the coruro (*Spalacopus cyanus*, Octodontidae), a social fossorial rodent. *Journal of Morphology*, *267*(3), 382-390.

Begall, S., Burda, H., & Schleich, C. (eds) (2007). *Subterranean rodents: news from underground*. Springer-Verlag, Berlin. xviii+398 p.

Billet, G., Germain, D., Ruf, I., Muizon, C. D., & Hautier, L. (2013). The inner ear of *Megatherium* and the evolution of the vestibular system in sloths. *Journal of Anatomy*, *223*(6), 557-567.

Brainerd, E. L., Baier, D. B., Gatesy, S. M., Hedrick, T. L., Metzger, K. A., Gilbert, S. L., & Crisco, J. J. (2010). X-ray reconstruction of moving morphology (XROMM): precision, accuracy and applications in comparative biomechanics research. *Journal of Experimental Zoology Part A: Ecological Genetics and Physiology*, *313*(5), 262-279.

Burda, H., Bruns, V., & Müller, M. (1990). Sensory adaptations in subterranean mammals. *Progress in clinical and biological research*,*335*, 269.

Burda, H., Bruns, V., & Hickman, G. C. (1992). The ear in subterranean Insectivora and Rodentia in comparison with ground-dwelling representatives. I. Sound conducting system of the middle ear. *Journal of Morphology*, *214*(1), 49-61.

Burda, H. (2006). Ear and eye in subterranean mole-rats, *Fukomys anselli* (Bathyergidae) and *Spalax ehrenbergi* (Spalacidae): progressive specialisation or regressive degeneration? *Animal Biology*, *56*(4), 475-486.

Catania, K. C., & Remple, F. E. (2004). Tactile foveation in the star-nosed mole. *Brain, behavior and evolution*, *63*(1), 1-12.

Credner, S., Burda, H., & Ludescher, F. (1997). Acoustic communication underground: vocalization characteristics in subterranean social mole-rats (*Cryptomys sp*., Bathyergidae). *Journal of Comparative Physiology A: Neuroethology, Sensory, Neural, and Behavioral Physiology*, *180*(3), 245-255.

Crish, S. D., Rice, F. L., Park, T. J., & Comer, C. M. (2003). Somatosensory organization and behavior in naked mole-rats I: vibrissa-like body hairs comprise a sensory array that mediates orientation to tactile stimuli. *Brain, behavior and evolution*, *62*(3), 141-151.

Crish, S. D., Dengler-Crish, C. M., & Catania, K. C. (2006). Central visual system of the naked mole-rat (*Heterocephalus glaber*). *The Anatomical Record*, *288*(2), 205-212.

Crumpton, N., Kardjilov, N., & Asher, R. J. (2015). Convergence vs. specialization in the ear region of moles (Mammalia). *Journal of Morphology, 276*(8), 900-914.

Curran, J. M. (2013). Hotelling: Hotelling's t-squared test and variants. R package version 1.0–2.

David R. (2011). *Le système des canaux semi-circulaires des archosaures : anatomie, morphometrie, morphologie fonctionnelle, évolution*. Unpublished PhD thesis. Muséum national d'Histoire naturelle, Paris. 343p.

David, R., Stoessel, A., Berthoz, A., Spoor, F., & Bennequin, D. (2016). Assessing morphology and function of the semicircular duct system: introducing new in-situ visualization and software toolbox. *Scientific reports*, *6*, 32772.

Dubost, G. (1968). Les mammifères souterrains. *Revue d'Ecologie et de Biologie du sol*, *5*(1), 99-133.

Gambaryan, P. P., Gasc, J. P., & Renous, S. (2002). Cinefluorographical study of the burrowing movements in the common mole, *Talpa europaea* (Lipotyphla, Talpidae). *Russian Journal of Theriology*, *1*(2), 91-109.

Gasc, J. P., Renous, S., Casinos, A., Laville, E., & Bou, J. (1985). Comparison of diverse digging patterns in some small mammals. *Fortschritte der Zoologie, 30*, 35-38.

Gasc, J. P., Jouffroy, F. K., Renous, S., & Blottnitz, F. V. (1986). Morphofunctional study of the digging system of the Namib Desert golden mole (*Eremitalpa granti namibensis*): cinefluorographical and anatomical analysis. *Journal of Zoology, 208*(1), 9-35.

Goldberg, J. M., & Cullen, K. E. (2011). Vestibular control of the head: possible functions of the vestibulocollic reflex. *Experimental brain research*, *210*(3-4), 331-345.

Highstein, S. M., Fay, R. R., & Popper, A. N. (eds). (2004). *The Vestibular System*. Springer handbook of auditory research, v. 19, New York. 560 p.

Hildebrand, M., Goslow, G. E., & Hildebrand, V. (1995). *Analysis of vertebrate structure*. New York: John Wiley & Sons. 657 p.

Johansen, K., Lykkeboe, G., Weber, R. E., & Maloiy, G. M. O. (1976). Blood respiratory properties in the naked mole-rat *Heterocephalus glaber*, a mammal of low body temperature. *Respiration physiology*, *28*(3), 303-314.

Jones, G. M., & Milsum, J. H. (1971). Frequency—response analysis of central vestibular unit activity resulting from rotational stimulation of the semicircular canals. *The Journal of Physiology*, *219*(1), 191-215.

Kimchi, T., & Terkel, J. (2001a). Magnetic compass orientation in the blind mole rat *Spalax ehrenbergi*. *Journal of Experimental Biology*, *204*(4), 751-758.

Kimchi, T., & Terkel, J. (2001b). Spatial learning and memory in the blind mole-rat in comparison with the laboratory rat and Levant vole. *Animal Behaviour*, *61*(1), 171-180.

Kumar S, Stecher G, Suleski M, Hedges SB (2017) TimeTree: A Resource for Timelines, Timetrees, and Divergence Times. *Molecular Biology and Evolution, 34* (7), 1812-1819.

Kuyper, M. A. (1979). *A biological study of the golden mole* Amblysomus hottentotus. MSc Dissertation, University of Natal, Durban.

Lehmann, W. H. (1963). The forelimb architecture of some fossorial rodents. *Journal of Morphology*, *113*(1), 59-76.

Lin, Y. F. (2017). *Burrowing and walking mechanisms of North American moles*. Doctoral Dissertations. University of Massachusetts Amherst. 921p.

Lin, Y. F., Chappuis, A., Rice, S., & Dumont, E. R. (2017). The effects of soil compactness on the burrowing performance of sympatric eastern and hairy-tailed moles. *Journal of Zoology*, *301*(4), 310-319.

Lindenlaub, T., Burda, H., & Nevo, E. (1995). Convergent evolution of the vestibular organ in the subterranean mole-rats, *Cryptomys* and *Spalax*, as compared with the aboveground rat, *Rattus*. *Journal of Morphology, 224*(3), 303-311.

Malinzak, M. D., Kay, R. F., & Hullar, T. E. (2012). Locomotor head movements and semicircular canal morphology in primates. *Proceedings of the National Academy of Sciences*, *109*(44), 17914-17919.

Marhold, S., Wiltschko, W., & Burda, H. (1997). A magnetic polarity compass for direction finding in a subterranean mammal. *Naturwissenschaften*, *84*(9), 421-423.

Mason, M. J. (2001). Middle ear structures in fossorial mammals: a comparison with non-fossorial species. *Journal of Zoology*, *255*(4), 467-486.

McBee, K., & Baker, R. J. (1982). *Dasypus novemcinctus*. *Mammalian Species, 162*, 1-9.

McVean, A. (1999). Are the semicircular canals of the European mole, *Talpa europaea*, adapted to a subterranean habitat? *Comparative Biochemistry and Physiology Part A: Molecular & Integrative Physiology, 123*(2), 173-178.

Nevo, E. (1979). Adaptive convergence and divergence of subterranean mammals. *Annual Review of Ecology and Systematics, 10*, 269–308.

Nevo, E. (1991). Evolutionary theory and processes of active speciation and adaptive radiation in subterranean mole rats, *Spalax ehrenbergi* superspecies, in Israel. *Evolutionary Biology*, *25*, 1-125.

Nevo, E. (1999). *Mosaic evolution of subterranean mammals: regression, progression, and global convergence*. Oxford University Press, Oxford, 413 p.

Oman, C. M., Marcus, E. N., & Curthoys, I. S. (1987). The influence of semicircular canal morphology on endolymph flow dynamics: An anatomically descriptive mathematical model. *Acta Oto-laryngologica*, *103*(1-2), 1-13.

Partha, R., Chauhan, B. K., Ferreira, Z., Robinson, J. D., Lathrop, K., Nischal, K. K., Chikina, M., & Clark, N. L. (2017). Subterranean mammals show convergent regression in ocular genes and enhancers, along with adaptation to tunneling. *eLife*, *6*.

Pfaff, C., Martin, T., & Ruf, I. (2015). Bony labyrinth morphometry indicates locomotor adaptations in the squirrel-related clade (Rodentia, Mammalia). *Proceedings of the Royal Society of London B: Biological Sciences, 282*(1809), 20150744.

Pleštilová, L., Hrouzková, E., Burda, H., & Šumbera, R. (2016). Does the morphology of the ear of the Chinese bamboo rat (*Rhizomys sinensis*) show “Subterranean” characteristics? *Journal of Morphology, 277*(5), 575-584.

Poczopko, P., & Chrzanowski, Z. (1966). Rectal and external body temperature in the mole (*Talpa europea* L.). *Bulletin de l'Académie Polonaise des Sciences. Série des Sciences Biologiques*, *14*(6), 443.

Puttick, J. U., & Gillian, M. (1977). The functional anatomy of the neck and forelimbs of the Cape golden mole, *Chrysochloris asiatica* (Lipotyphla: Chrysochloridae). *African Zoology, 12*(2), 445-458.

Rabbitt, R. D., Damiano, E. R., & Grant, J. W. (2004). Biomechanics of the semicircular canals and otolith organs.; pp. 153-201, in Highstein, S. M., Fay, R. R., & Popper, A. N. (eds), *The Vestibular System*. Springer handbook of auditory research, v. 19, New York.

R Core Team (2014). R: A language and environment for statistical computing. Vienna, Austria: R Foundation for Statistical Computing; 2014.

Scantlebury, M., Lovegrove, B. G., Jackson, C. R., Bennett, N. C., & Lutermann, H. (2008). Hibernation and non-shivering thermogenesis in the Hottentot golden mole (*Amblysomus hottentottus longiceps*). *Journal of Comparative Physiology B*, *178*(7), 887.

Southern, H. N. (ed.). (1964). *The handbook of British mammals* (Vol. 465). Mammal society (GB). Blackwell, Oxford.

Urison, N. T., & Buffenstein, R. B. (1995). Metabolic and body temperature changes during pregnancy and lactation in the naked mole rat (*Heterocephalus glaber*). *Physiological Zoology*, *68*(3), 402-420.

Walls, G. L. (1967). *The Vertebrate Eye and its Adaptative Radiation*. Hafner Pub. Co., New York.

West, C. D. (1985). The relationship of the spiral turns of the cochlea and the length of the basilar membrane to the range of audible frequencies in ground dwelling mammals. *The Journal of the Acoustical Society of America*, *77*(3), 1091-1101.

Wetzel, R. M. (1985). Taxonomy and distribution of armadillos, Dasypodidae; pp. 23-46, in Montgomery, G. G. (ed.), *The evolution and ecology of armadillos, sloths, and vermilinguas*. Sminthsonian Institution Press, Washington and London.

Withers, P. C., Thompson, G. G., & Seymour, R. S. (2000). Metabolic physiology of the north-western marsupial mole, *Notoryctes caurinus* (Marsupialia: Notoryctidae). *Australian Journal of Zoology*, *48*(3), 241-258.

Woinarski, J. C., Burbidge, A. A., & Harrison, P. L. (2014). The action plan for Australian mammals 2012. CSIRO Publishing, Melbourne.

Yosida, S., Kobayasi, K. I., Ikebuchi, M., Ozaki, R., & Okanoya, K. (2007). Antiphonal vocalization of a subterranean rodent, the naked mole-rat (*Heterocephalus glaber*). *Ethology, 113*(7), 703-710.

SUPPLEMENTARY INFORMATIONS

Supplementary Information 1. List of the sample and raw data for the five moles and the 25 non-subterranean species of comparison.

With w1_90, w2_90 in **Hz** and VG_s in **deg/deg.s^{-1}.**

Taxa	BM (g)	w1_90_PR	w1_90_Y	w2_90_PR	w2_90_Y	VG_s_P	VG_s_R	VG_s_Y
B. p. taurus	463409	0.34	0.48	5	5	0.0108	0.011	0.0151
C. penicillata	860	0.5	0.35	11.9	15.5	0.0052	0.0044	0.0036
D. viverrinus	982	0.53	0.62	17.1	19.7	0.0027	0.0024	0.003
E. f. caballus	376555	0.3	0.32	6.1	6.9	0.0095	0.0105	0.0134
G. gorilla	137433	0.39	0.32	5.3	6	0.0103	0.009	0.0112
H. lar	5900	0.15	0.11	8.9	10.5	0.0031	0.0024	0.0026
H. sapiens	67100	0.32	0.32	4.9	5.5	0.0111	0.01	0.0107
M. mulatta	7710	0.15	0.19	11.2	11.8	0.0026	0.0024	0.0038
N. nasua	3698	0.43	0.29	12.9	19.7	0.0032	0.0032	0.0026
O. anatinus	693	0.45	0.35	11.4	17	0.005	0.003	0.003
O. cuniculus	1950	0.6	0.52	11.4	12.9	0.0051	0.0049	0.0052
P. abelii	77900	0.2	0.27	5.7	6	0.006	0.0056	0.0085
P. rodricensis	255	0.41	0.36	25.9	31.1	0.0019	0.0014	0.0018
P. troglodytes	44289	0.27	0.24	6.6	7.5	0.0053	0.0051	0.0063
S. sciureus	680	0.2	0.19	14.4	16.1	0.0021	0.0016	0.0024
S. s. domesticus	55000	0.43	0.38	6.4	8.6	0.0087	0.0075	0.0079
T. javanica	54	0.7	0.68	21.6	19.6	0.0025	0.0024	0.0036
V. pacos	54325	0.35	0.23	6.4	7.7	0.0088	0.0068	0.0062
C. jacchus	321	0.61	0.45	11.6	13.5	0.0047	0.0028	0.0039
E. elegantulus	274	0.26	0.18	14.3	17.7	0.002	0.0019	0.0021
L. catta	2210	0.36	0.36	13.8	15.1	0.0034	0.0029	0.0038
Microcebus	54	0.56	0.55	24.5	22	0.0016	0.0014	0.0022
M. fascicularis	7550	0.23	0.28	9.6	9.7	0.0042	0.0036	0.0056
N. coucang	653	0.39	0.37	13.1	14.4	0.0036	0.003	0.0038
C. l. familiaris	62800	0.27	0.24	8.7	9.5	0.0075	0.0051	0.0067
Chlamyphorus truncatus	120	1.55	2.3	15	13.3	0.0041	0.0038	0.0068
Heterocephalus glaber	37.9	3.05	4.1	14.4	15.1	0.0053	0.005	0.0085
Notoryctes typhlops	51.25	2.35	3.7	16.8	17.1	0.005	0.0028	0.0072
Amblysomus hottentotus	72.81	2.3	2.6	20.9	19.4	0.0041	0.0035	0.0057
Talpa europaea	80	0.97	0.83	19.8	18.8	0.0027	0.0019	0.0028

Supplementary Information 2. R script for the statistical analysis of the functional parameters.

```
################### Initialisation ####################

rm(list=ls(all=TRUE))

################### Loading libraries ####################

library(phytools)
library(caper)
library(geiger)
library(MASS)
library(Hotelling)
library(rgl)
library(geometry)
library(scales)

################### Loading raw datasets ####################

DATA_AVERAGE = read.table(file.choose(), header = TRUE) ##
OM_2_RData_Raw_Function.txt
TREE = read.nexus(file.choose()) ## OM_3_MammalTree.nex

################### Check for missing specimens in tree/datasets
####################

TEST = name.check(TREE, data.names = DATA_AVERAGE[,1])
TREE = drop.tip(TREE, TEST$tree_not_data)

################### Preparing sub datasets ####################

Names_AVERAGE = as.matrix(DATA_AVERAGE[,1, drop=FALSE])
BM_AVERAGE = as.matrix(DATA_AVERAGE[,2, drop=FALSE])
Raw_Function_AVERAGE = data.matrix(DATA_AVERAGE[,3:9, drop=FALSE])

################### Log transformation of some datasets ####################

Raw_Function_AVERAGE_LOG = log10(Raw_Function_AVERAGE)
BM_AVERAGE_LOG = log10(BM_AVERAGE)

################### Phylogenetic regression of function parameters onto body mass
####################

PGLS_SET_BM = data.frame(Names_AVERAGE, BM_AVERAGE_LOG, Raw_Function_AVERAGE_LOG,
stringsAsFactors=FALSE)

PGLS_w1_90_PR = pgls(w1_90_PR~BM,comparative.data(TREE,PGLS_SET_BM,Taxa),lambda =
"ML")
PGLS_w1_90_Y = pgls(w1_90_Y~BM,comparative.data(TREE,PGLS_SET_BM,Taxa),lambda =
"ML")
```

```
PGLS_w2_90_PR = pgls(w2_90_PR~BM,comparative.data(TREE,PGLS_SET_BM,Taxa),lambda =
"ML")
PGLS_w2_90_Y = pgls(w2_90_Y~BM,comparative.data(TREE,PGLS_SET_BM,Taxa),lambda =
"ML")
PGLS_VG_s_P = pgls(VG_s_P~BM,comparative.data(TREE,PGLS_SET_BM,Taxa),lambda = "ML")
PGLS_VG_s_R = pgls(VG_s_R~BM,comparative.data(TREE,PGLS_SET_BM,Taxa),lambda = "ML")
PGLS_VG_s_Y = pgls(VG_s_Y~BM,comparative.data(TREE,PGLS_SET_BM,Taxa),lambda = "ML")

summary(PGLS_w1_90_PR)
summary(PGLS_w1_90_Y)
summary(PGLS_w2_90_PR)
summary(PGLS_w2_90_Y)
summary(PGLS_VG_s_P)
summary(PGLS_VG_s_R)
summary(PGLS_VG_s_Y)


################### Computation of function residuals without body mass
####################


Raw_Function_Residuals_AVERAGE_LOG = Raw_Function_AVERAGE_LOG -
cbind(predict(PGLS_w1_90_PR, as.data.frame(BM_AVERAGE_LOG[,1, drop=FALSE])),
predict(PGLS_w1_90_Y, as.data.frame(BM_AVERAGE_LOG[,1, drop=FALSE])),
                                                    predict(PGLS_w2_90_PR,
as.data.frame(BM_AVERAGE_LOG[,1, drop=FALSE])), predict(PGLS_w2_90_Y,
as.data.frame(BM_AVERAGE_LOG[,1, drop=FALSE])),
                                                      predict(PGLS_VG_s_P,
as.data.frame(BM_AVERAGE_LOG[,1, drop=FALSE])), predict(PGLS_VG_s_R,
as.data.frame(BM_AVERAGE_LOG[,1, drop=FALSE])),
                                                      predict(PGLS_VG_s_Y,
as.data.frame(BM_AVERAGE_LOG[,1, drop=FALSE])))


################### Computing functional parameters with BM of 72g
####################


BMcor_AVERAGE_LOG = as.data.frame(rep(log10(72),dim(BM_AVERAGE_LOG)[1]))
colnames(BMcor_AVERAGE_LOG) = c("BM")

BMcor_Raw_Function_AVERAGE = 10^(Raw_Function_Residuals_AVERAGE_LOG +
cbind(predict(PGLS_w1_90_PR, BMcor_AVERAGE_LOG), predict(PGLS_w1_90_Y,
BMcor_AVERAGE_LOG),
                                                      predict(PGLS_w2_90_PR,
BMcor_AVERAGE_LOG), predict(PGLS_w2_90_Y, BMcor_AVERAGE_LOG), predict(PGLS_VG_s_P,
BMcor_AVERAGE_LOG),
                                                      predict(PGLS_VG_s_R,
BMcor_AVERAGE_LOG), predict(PGLS_VG_s_Y, BMcor_AVERAGE_LOG)))

BMcor_Raw_Function_AVERAGE = data.frame(BMcor_Raw_Function_AVERAGE)
rownames(BMcor_Raw_Function_AVERAGE) = c(Names_AVERAGE)


################### Function PCA corrected for allometry ####################


PCA = prcomp(BMcor_Raw_Function_AVERAGE, scale = TRUE)
str(PCA)  ### read the values associated to the function
PCA$sdev/sum(PCA$sdev)  ### obtain the % of the parameters

################### Hotelling on function corrected for allometry
####################


A = PCA$x
B = A[26:30,]
C = A[1:25,]
```

```
H_Test = hotelling.test(A, B, shrinkage = FALSE, perm = TRUE, B = 10000, progBar =
TRUE)
H_Test_2 = hotelling.test(C, B, shrinkage = FALSE, perm = TRUE, B = 10000, progBar
= TRUE)


################### 3D visualisation of PCA ####################


plot3d(A[,1],A[,2],A[,3])

MammalHull = C[,1:3]
ts.surf = t(convhulln(MammalHull))
rgl.triangles(MammalHull[ts.surf,1],MammalHull[ts.surf,2],MammalHull[ts.surf,3],col
="blue",alpha=.2)

FossorialHull = B[,1:3]
ts.surf = t(convhulln(FossorialHull))
rgl.triangles(FossorialHull[ts.surf,1],FossorialHull[ts.surf,2],FossorialHull[ts.su
rf,3],col="green",alpha=.2)

text3d(A[,1],A[,2],A[,3], Names_AVERAGE, col="black", alpha=1, cex=0.6, adj =
c(0.5, 0.5))


################### 2D visualisation of bandwidth ####################


PCA = prcomp(BMcor_Raw_Function_AVERAGE[,1:4], scale = TRUE)
str(PCA)  ### read the values associated to the function
PCA$sdev/sum(PCA$sdev)  ### obtain the % of the parameters


A = PCA$x
B = A[26:30,]
C = A[1:25,]

MammalHull = chull(C[,1:2])
MammalHull = c(MammalHull, MammalHull[1])

FossorialHull = chull(B[,1:2])
FossorialHull = c(FossorialHull, FossorialHull[1])

plot(A[,1], A[,2], asp = 1, type = "n", xlab = "PC1", ylab = "PC2")

polygon(C[,1:2][MammalHull, ], lty = 0, lwd =1, col = alpha("blue",0.25))
polygon(B[,1:2][FossorialHull, ], lty = 0, lwd =1, col = alpha("green",0.25))

text(A[,1], A[,2], labels=rownames(A), cex= 0.5)


################### Boxplots ####################


Group = factor(c("Non-fossorial", "Non-fossorial", "Non-fossorial", "Non-
fossorial", "Non-fossorial", "Non-fossorial", "Non-fossorial", "Non-fossorial",
"Non-fossorial", "Non-fossorial","Non-fossorial", "Non-fossorial", "Non-fossorial",
"Non-fossorial", "Non-fossorial", "Non-fossorial", "Non-fossorial", "Non-
fossorial", "Non-fossorial", "Non-fossorial", "Non-fossorial", "Non-fossorial",
"Non-fossorial", "Non-fossorial", "Non-fossorial", "Fossorial", "Fossorial",
"Fossorial", "Fossorial", "Fossorial"))
boxplot(BMcor_Raw_Function_AVERAGE[,1]~Group, varwidth = TRUE, col = c("blue",
"green"), boxwex = 0.45, main ="w1_90_PR")
boxplot(BMcor_Raw_Function_AVERAGE[,2]~Group, varwidth = TRUE, col = c("blue",
"green"), boxwex = 0.45, main ="w1_90_Y")
boxplot(BMcor_Raw_Function_AVERAGE[,3]~Group, varwidth = TRUE, col = c("blue",
"green"), boxwex = 0.45, main ="w2_90_PR")
```

```
boxplot(BMcor_Raw_Function_AVERAGE[,4]~Group, varwidth = TRUE, col = c("blue",
"green"), boxwex = 0.45, main ="w2_90_Y")
boxplot(BMcor_Raw_Function_AVERAGE[,5]~Group, varwidth = TRUE, col = c("blue",
"green"), boxwex = 0.45, main ="VG_s_P")
boxplot(BMcor_Raw_Function_AVERAGE[,6]~Group, varwidth = TRUE, col = c("blue",
"green"), boxwex = 0.45, main ="VG_s_R")
boxplot(BMcor_Raw_Function_AVERAGE[,7]~Group, varwidth = TRUE, col = c("blue",
"green"), boxwex = 0.45, main ="VG_s_Y")




################################################################################
####
################### Excluding fossorials from the body mass regression
################################################################################
####

################### Check for missing specimens in tree/datasets
####################

TEST = name.check(TREE, data.names = DATA_AVERAGE[1:25,1])
TREE = drop.tip(TREE, TEST$tree_not_data)


################### Phylogenetic regression of function parameters onto body mass
####################

PGLS_SET_BM = data.frame(Names_AVERAGE, BM_AVERAGE_LOG, Raw_Function_AVERAGE_LOG,
stringsAsFactors=FALSE)
PGLS_SET_BM = PGLS_SET_BM[1:25,]

PGLS_w1_90_PR = pgls(w1_90_PR~BM,comparative.data(TREE,PGLS_SET_BM,Taxa),lambda =
"ML")
PGLS_w1_90_Y = pgls(w1_90_Y~BM,comparative.data(TREE,PGLS_SET_BM,Taxa),lambda =
"ML")
PGLS_w2_90_PR = pgls(w2_90_PR~BM,comparative.data(TREE,PGLS_SET_BM,Taxa),lambda =
"ML")
PGLS_w2_90_Y = pgls(w2_90_Y~BM,comparative.data(TREE,PGLS_SET_BM,Taxa),lambda =
"ML")
PGLS_VG_s_P = pgls(VG_s_P~BM,comparative.data(TREE,PGLS_SET_BM,Taxa),lambda = "ML")
PGLS_VG_s_R = pgls(VG_s_R~BM,comparative.data(TREE,PGLS_SET_BM,Taxa),lambda = "ML")
PGLS_VG_s_Y = pgls(VG_s_Y~BM,comparative.data(TREE,PGLS_SET_BM,Taxa),lambda = "ML")

summary(PGLS_w1_90_PR)
summary(PGLS_w1_90_Y)
summary(PGLS_w2_90_PR)
summary(PGLS_w2_90_Y)
summary(PGLS_VG_s_P)
summary(PGLS_VG_s_R)
summary(PGLS_VG_s_Y)

PGLS_w1_90_PR = pgls(w1_90_PR~1,comparative.data(TREE,PGLS_SET_BM,Taxa),lambda =
"ML")
PGLS_w1_90_Y = pgls(w1_90_Y~1,comparative.data(TREE,PGLS_SET_BM,Taxa),lambda =
"ML")


################### Computation of function residuals without body mass
####################


Raw_Function_Residuals_AVERAGE_LOG = Raw_Function_AVERAGE_LOG -
cbind(predict(PGLS_w1_90_PR, as.data.frame(BM_AVERAGE_LOG[,1, drop=FALSE])),
predict(PGLS_w1_90_Y, as.data.frame(BM_AVERAGE_LOG[,1, drop=FALSE])),
```

```
                                                                predict(PGLS_w2_90_PR,
as.data.frame(BM_AVERAGE_LOG[,1, drop=FALSE])), predict(PGLS_w2_90_Y,
as.data.frame(BM_AVERAGE_LOG[,1, drop=FALSE])),
                                                                  predict(PGLS_VG_s_P,
as.data.frame(BM_AVERAGE_LOG[,1, drop=FALSE])), predict(PGLS_VG_s_R,
as.data.frame(BM_AVERAGE_LOG[,1, drop=FALSE])),
                                                                  predict(PGLS_VG_s_Y,
as.data.frame(BM_AVERAGE_LOG[,1, drop=FALSE])))



################### Computing functional parameters with BM of 72g
####################


BMcor_Raw_Function_AVERAGE = 10^(Raw_Function_Residuals_AVERAGE_LOG +
cbind(predict(PGLS_w1_90_PR, BMcor_AVERAGE_LOG), predict(PGLS_w1_90_Y,
BMcor_AVERAGE_LOG),
                                                                  predict(PGLS_w2_90_PR,
BMcor_AVERAGE_LOG), predict(PGLS_w2_90_Y, BMcor_AVERAGE_LOG), predict(PGLS_VG_s_P,
BMcor_AVERAGE_LOG),
                                                                  predict(PGLS_VG_s_R,
BMcor_AVERAGE_LOG), predict(PGLS_VG_s_Y, BMcor_AVERAGE_LOG)))


BMcor_Raw_Function_AVERAGE = data.frame(BMcor_Raw_Function_AVERAGE)
rownames(BMcor_Raw_Function_AVERAGE) = c(Names_AVERAGE)



################### Function PCA corrected for allometry ####################


PCA = prcomp(BMcor_Raw_Function_AVERAGE, scale = TRUE)
str(PCA)  ### read the values associated to the function
PCA$sdev/sum(PCA$sdev)  ### obtain the % of the parameters

################### Hotelling on function corrected for allometry
####################

A = PCA$x
B = A[26:30,]
C = A[1:25,]

H_Test = hotelling.test(A, B, shrinkage = FALSE, perm = TRUE, B = 10000, progBar =
TRUE)
H_Test_2 = hotelling.test(C, B, shrinkage = FALSE, perm = TRUE, B = 10000, progBar
= TRUE)


################### 3D visualisation of PCA ####################

plot3d(A[,1],A[,2],A[,3])

MammalHull = C[,1:3]
ts.surf = t(convhulln(MammalHull))
rgl.triangles(MammalHull[ts.surf,1],MammalHull[ts.surf,2],MammalHull[ts.surf,3],col
="blue",alpha=.2)

FossorialHull = B[,1:3]
ts.surf = t(convhulln(FossorialHull))
rgl.triangles(FossorialHull[ts.surf,1],FossorialHull[ts.surf,2],FossorialHull[ts.su
rf,3],col="green",alpha=.2)

text3d(A[,1],A[,2],A[,3], Names_AVERAGE, col="black", alpha=1, cex=0.6, adj =
c(0.5, 0.5))
```

```
################### 2D visualisation of bandwidth ####################
####### without sensitivity

PCA = prcomp(BMcor_Raw_Function_AVERAGE[,1:4], scale = TRUE)
str(PCA)  ### read the values associated to the function
PCA$sdev/sum(PCA$sdev)  ### obtain the % of the parameters


A = PCA$x
B = A[26:30,]
C = A[1:25,]

MammalHull = chull(C[,1:2])
MammalHull = c(MammalHull, MammalHull[1])

FossorialHull = chull(B[,1:2])
FossorialHull = c(FossorialHull, FossorialHull[1])

plot(A[,1], A[,2], asp = 1, type = "n", xlab = "PC1", ylab = "PC2")

polygon(C[,1:2][MammalHull, ], lty = 0, lwd =1, col = alpha("blue",0.25))
polygon(B[,1:2][FossorialHull, ], lty = 0, lwd =1, col = alpha("green",0.25))

text(A[,1], A[,2], labels=rownames(A), cex= 0.5)


################### Boxplots ####################

Group = factor(c("Non-fossorial", "Non-fossorial", "Non-fossorial", "Non-
fossorial", "Non-fossorial", "Non-fossorial", "Non-fossorial", "Non-fossorial",
"Non-fossorial", "Non-fossorial","Non-fossorial", "Non-fossorial", "Non-fossorial",
"Non-fossorial", "Non-fossorial", "Non-fossorial", "Non-fossorial", "Non-
fossorial", "Non-fossorial", "Non-fossorial", "Non-fossorial", "Non-fossorial",
"Non-fossorial", "Non-fossorial", "Non-fossorial", "Fossorial", "Fossorial",
"Fossorial", "Fossorial", "Fossorial"))
boxplot(BMcor_Raw_Function_AVERAGE[,1]~Group, varwidth = TRUE, col = c("green",
"blue"), boxwex = 0.45, main ="w1_90_PR", log="y")
boxplot(BMcor_Raw_Function_AVERAGE[,2]~Group, varwidth = TRUE, col = c("green",
"blue"), boxwex = 0.45, main ="w1_90_Y", log="y")
boxplot(BMcor_Raw_Function_AVERAGE[,3]~Group, varwidth = TRUE, col = c("green",
"blue"), boxwex = 0.45, main ="w2_90_PR", log="y")
boxplot(BMcor_Raw_Function_AVERAGE[,4]~Group, varwidth = TRUE, col = c("green",
"blue"), boxwex = 0.45, main ="w2_90_Y", log="y")
boxplot(BMcor_Raw_Function_AVERAGE[,5]~Group, varwidth = TRUE, col = c("green",
"blue"), boxwex = 0.45, main ="VG_s_P", log="y")
boxplot(BMcor_Raw_Function_AVERAGE[,6]~Group, varwidth = TRUE, col = c("green",
"blue"), boxwex = 0.45, main ="VG_s_R", log="y")
boxplot(BMcor_Raw_Function_AVERAGE[,7]~Group, varwidth = TRUE, col = c("green",
"blue"), boxwex = 0.45, main ="VG_s_Y", log="y")
```

Supplementary Information 3. Influence of allometry and/or phylogeny on the functional parameters ('PGLS' on the 25 non-subterranean species).

In the following table, the lambda for each functional parameter indicates if there is an influence of phylogeny. The closest to 1 the lambda is, the more important is the phylogeny influencing the values of the functional parameter.

The p-value of R2 indicates if the functional parameters is influenced by allometry (significance at p-value<0.05).

	Lambda	p-value of R^2	R^2
w1_90_PR	0	0.03491	0.1437
w1_90_Y	0	0.1809	0.03629
w2_90_PR	0.615	1.006^{e-10}	0.8362
w2_90_Y	0.708	3.806^{e-10}	0.8163
VG_s_P	0	1.183^{e-07}	0.6991
VG_s_R	0	9.281^{e-09}	0.7581
VG_s_Y	0	9.844^{e-09}	0.7569

Conclusion Générale et Perspectives

Conclusion Générale et Perspectives

Conclusion (Fig. 1)

Dans le premier chapitre, les résultats exposés vont à l'encontre des études antérieures qui stipulaient une corrélation entre la morphologie du labyrinthe osseux et la locomotion. En effet, il semble que chez les marsupiaux, on ne peut prédire avec certitude la locomotion ou le mode de vie d'un animal à part de la morphologie de son système des canaux semicirculaires. Toutefois, les locomotions extrêmes (taupe marsupiale, marsupiaux planeurs) sont discriminées par la morphologie du système des canaux semicirculaires, mais les conclusions sont à modérer car seule une taupe existe chez ce clade de mammifères. Par ailleurs,les résultats des études préliminaires menées chez des taupes placentaires (chez les rongeurs et eulipotyphles, Annexes 2 et 3) laissent supposer qu'il n'est pas possible d'établir une corrélation entre la morphologie du labyrinthe osseux et le mode de vie souterrain.

Contrairement à ce que l'on pouvait attendre, la morphologie du labyrinthe membraneux n'est pas plus pertinente comme proxy pour le comportement souterrain. C'est ce que montrent les résultats du chapitre 2, chez cinq taupes mammaliennes de clades différents.

Alors, qu'en est-il des paramètres fonctionnels que l'on peut extraire de la morphologie du système des canaux semicirculaires membraneux ? Le troisième chapitre, fondé sur les mêmes taxons que le chapitre précédent, permet enfin de poser une corrélation entre le système des canaux semicirculaires et le mode de vie souterrain. L'étude met en évidence une nouvelle adaptation fonctionnelle des taupes à la vie souterraine : le système des canaux semicirculaires est plus sensible que celui des mammifères non-souterrains. Cette sensibilité accrue procure aux taupes une orientation plus sensible et une meilleure perception de leur environnement. Ce travail est un apport majeur pour comprendre l'écologie sensorielle des mammifères souterrains.

Mises en parallèle, les études que j'ai menées pendant ma thèse montrent que différentes formes de labyrinthe peuvent donner la même fonction. Pour cet organe un peu particulier, car régi par des règles de biomécanique des fluides, la relation forme/fonction n'est pas simple, et il apparaît crucial de faire preuve de beaucoup de précautions dans

l'interprétation des résultats, notamment issus d'études précédentes (références données en Introduction) qui concluaient sur l'existence d'un lien entre la morphologie de l'oreille interne et la locomotion.

Perspectives

1° L'inférence sur les fossiles est-elle alors possible ?

Le premier objectif de cette thèse était de mettre en place un modèle d'inférence fondé sur l'oreille interne. La corrélation démontrée chez les taxons actuels entre la morphologie de l'oreille interne (paramètres fonctionnels) et le mode de vie souterrain (Chapitre 3), permet alors d'imaginer utiliser ce lien pour faire des inférences sur les fossiles. Mais a priori, cela ne fonctionnerait pas. En effet, dans le chapitre 3, on explique l'adaptation fonctionnelle des taupes (= haute sensibilité) par une anatomie particulière de la cupule. A l'inverse des hypothèses posées par Crumpton et al. (2015), Lindenlaub et al. (1995) et McVean (1999), ce ne sont ni les rayons de courbures ni l'épaisseur des canaux qui montrent une adaptation à la vie souterraine, mais bien les paramètres de la cupule. Or cette structure n'est pas accessible sur le labyrinthe osseux. Il semble donc pour l'instant impossible d'observer sur un labyrinthe osseux une caractéristique morphologique dérivée de l'adaptation fonctionnelle de la cupule et donc d'inférer un mode de vie chez les fossiles. Cela montre les limites des inférences entre paramètres fonctionnels issus d'un tissu mou et structure osseuse. Une piste à suivre serait dans un premier temps d'élargir notre échantillonnage d'actuels pour avoir un nombre conséquent de modèles osseux/membraneux/paramètres fonctionnels, dans le but de pouvoir, dans un second temps inférer un labyrinthe membraneux duquel on extrait des paramètres fonctionnels aux taxons fossiles. Il serait pertinent de tester des inférences sur des taxons fossiles connus comme souterrains par l'étude de leur squelette post-crânien comportant des adaptations extrêmes ne laissant pas de doute sur leur mode de vie. Les fossiles devront également présenter une anatomie pas trop éloignée de celle des taxons actuels permettant la comparaison. En ce sens, *Necrolestes patagonensis* pourrait être un bon modèle (Rougier et al., 2012; Chapitre 1), bien que n'étant pas une mammifère thérien.

2° Trouve-t-on des adaptations fonctionnelles du système des canaux semicirculaires aux différents types de fouissage ?

Les différents types de fouissage observables chez les mammifères semblent impliquer la tête de manières différentes. Par exemple, entre le « head lifting » et le « humeral rotation digging », les mouvements de la tête sont foncièrement différents, la tête étant largement impliquée dans le premier. Dans un premier temps, il serait intéressant de quantifier / qualifier les différents types de mouvements de la tête en fonction des comportements (Malinzak et al., 2012). Ensuite, il s'agirait de rajouter des spécimens à l'échantillonnage du chapitre 3 pour observer d'éventuelles adaptations du système des canaux semicirculaires au type de fouissage.

3° Trouve-t-on la même adaptation fonctionnelle (=haute sensibilité) chez les autres espèces souterraines comme les caeciliens ?

Une poursuite intéressante de mes travaux serait d'appliquer la méthode utilisée (Chapitre 3) sur un autre clade pour tester s'il existe une même adaptation de l'oreille interne à la vie souterraine. Par exemple, il s'agirait de continuer les travaux de Maddin & Sherratt (2014), qui se sont intéressés à la morphologie mais pas aux paramètres fonctionnels d'amphibiens souterrains.

4° D'autres structures pouvant indiquer un mode de vie souterrain seraient-elles contenues dans les données acquises durant le doctorat ?

En effet, j'ai acquis un grand nombre de données pendant ma thèse, et je n'ai pas eu le temps de tout exploiter.

Par exemple, sur les données CT-scan des crânes, il serait intéressant de regarder la complexité des sutures qui semblent être liées à l'activité de fouissage, en conférant plus de force dans le crâne (c'est une hypothèse proposée par Christian Kammerer à l'ICVM au Symposium Life underground).

Sur les données Synchrotron, il pourrait être plus qu'instructif d'étudier les tissus mous in-situ et en 3D de la partie de l'oreille liée à l'audition (muscles, tendons, membranes de l'oreille moyenne mais aussi le canal cochléaire de l'oreille interne). Il s'agirait ici d'apporter de nouvelles données anatomiques pour l'étude de l'audition chez les mammifères souterrains

Conclusions of the thesis

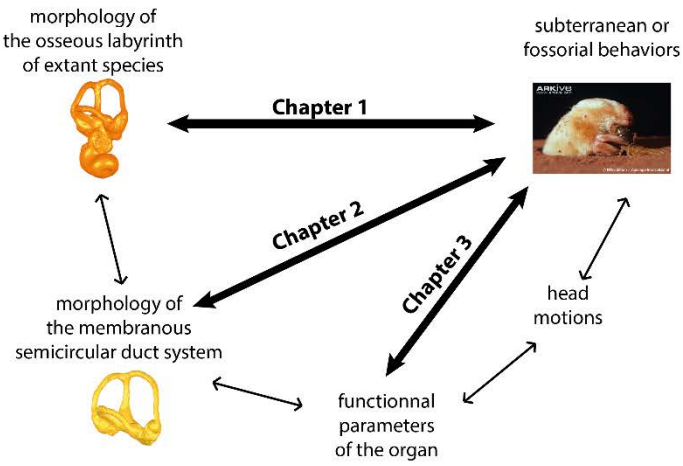

--> Chapter 1 (and preliminary studies in appendices)
No correlation between the osseous labyrinth morphology and locomotion
(*a priori* neither with subterranean behavior)

--> Chapter 2
No correlation between the membranous labyrinth morphology and subterranean behavior

--> Chapter 3
Correlation between the functionnal parameters and subterranean behavior

==> Different morphologies can lead to the same function
==> Highlighting of a clear and new functional convergent adaptation of the semicircular duct system to the subterranean lifestyle
==> Contribution to the study of sensory ecology of subterranean mammals

Perspectives

1° Possible inference on fossils?
2° Adaptations of the semicircular duct system for the different types of digging?
3° Same adaptation (high sensitivity) in other subterranean species as caecilians?
4° Other possible anatomical features adapted for subterranean lifestyle with data collected during the PhD ?

Figure 1: Schematic representation of the conclusions of my thesis.

References

Crumpton, N., Kardjilov, N., & Asher, R. J. (2015). Convergence vs. specialization in the ear region of moles (Mammalia). *Journal of morphology, 276*(8), 900-914.

Lindenlaub, T., Burda, H., & Nevo, E. (1995). Convergent evolution of the vestibular organ in the subterranean mole-rats, *Cryptomys* and *Spalax*, as compared with the aboveground rat, *Rattus*. *Journal of Morphology, 224*(3), 303-311.

Maddin, H. C., & Sherratt, E. (2014). Influence of fossoriality on inner ear morphology: insights from caecilian amphibians. Journal *of Anatomy*, *225*(1), 83-93.

Malinzak, M. D., Kay, R. F., & Hullar, T. E. (2012). Locomotor head movements and semicircular canal morphology in primates. *Proceedings of the National Academy of Sciences*, *109*(44), 17914-17919.

McVean, A. (1999). Are the semicircular canals of the European mole, *Talpa europaea*, adapted to a subterranean habitat? *Comparative Biochemistry and Physiology Part A: Molecular & Integrative Physiology, 123*(2), 173-178.

Rougier, G. W., Wible, J. R., Beck, R. M., & Apesteguía, S. (2012). The Miocene mammal *Necrolestes* demonstrates the survival of a Mesozoic nontherian lineage into the late Cenozoic of South America. *Proceedings of the National Academy of Sciences*, *109*(49), 20053-20058.

ANNEXES

APPENDIXES

Annexe 1. Liste des spécimens de mammifères actuels scannés au cours de cette thèse, avec financements associés
Appendix 1. List of extant mammal specimens scanned during the PhD, with associated grants

Annexe 2. Etude préliminaire de l'oreille interne des rongeurs fouisseurs
Appendix 2. Preliminary study of the inner ear of fossorial rodents

Annexe 3. Etude préliminaire de l'oreille interne des eulipotyphles
Appendix 3. Preliminary study of the inner ear of Eulipotyphla

Annexe 4. Etude préliminaire du labyrinthe osseux de thérapsides au comportement fouisseur
Appendix 4. Preliminary study of the bony labyrinth of therapsids with fossorial habits

Annexe 5. Article sur l'oreille de la Sarigue de Cuvier
Appendix 5. Paper on the ear of the opossum of Cuvier

Annexe 6. Projet pour 6 jours de CT-scans - Actions Thématiques du Muséum « Formes possibles, Formes réalisées 2015 » du Muséum national d'Histoire naturelle
Appendix 6. Proposal for 6 days of CT-scans - Actions Thématiques du Muséum « Formes possibles, Formes réalisées 2015 » from the Muséum national d'Histoire naturelle

Annexe 7. Projet pour 48h d'accès à la lumière synchrotron - *European Synchrotron Radiation Facility* (ESRF Grenoble)
Appendix 7. Proposal for 48h of access to the synchrotron light - *European Synchrotron Radiation Facility* (ESRF Grenoble)

Annexe 8. Projet pour une bourse de mission à destination du Max Planck Institut für Evolutionäre Anthropologie à Leipzig (Allemagne) - 1 200€ du DAAD (Office allemand d'échanges universitaires)
Appendix 8. Proposal for a work trip grant to the Max Planck Institut für Evolutionäre Anthropologie in Leipzig (Germany) - 1 200€ from DAAD (German Academic Exchange Service)

Annexe 9. Projet pour une bourse de mission à destination du Max Planck Institut für Evolutionäre Anthropologie à Leipzig (Allemagne) - 600€ de « Transhumance » (Bourse de mobilité internationale Sorbonne-Universités)
Appendix 9. Proposal for a work trip grant to the Max Planck Institut für Evolutionäre Anthropologie in Leipzig (Germany) – 600€ from "Transhumance" (Sorbonne-University Grant for international exchange)

ANNEXE 1. Liste des spécimens de mammifères actuels scannés au cours de cette thèse, avec financements associés
APPENDIX 1. List of extant mammal specimens scanned during the PhD, with associated grants

Table 1.1: List of all the specimens sampled and scanned during the PhD.

Species	Common name	Collection # (localisation ZTQ)	CT data	Modelisation / Landmarks	Ref. of loan	CT-Scan Projet	Grants
Monotremata							
Tachyglossus aculeatus	echidna	MNHN.ZM.MO.1995.707 (Zoo, Armoire 7)	phase-propagation Synchroton		Prêt 2015 / 103 ZTQ	Synchrotron 10/15	Synchrotron 10/15
Marsupialia							
Australidelphia, Diprotodontia, Phalangeroidea, Burramyidae							
Cercartetus nanus	eastern pygmy possum	MNHN.ZM.MO.1992.343 (Zoo, Armoire 7)	Phase-propagation Synchroton	3D model + landmarks	Prêt 2015 / 103 ZTQ	Synchrotron 10/15	Synchrotron 10/15
Australidelphia, Diprotodontia, Phalangeroidea, Phalangeridae							
Phalanger orientalis	grey cuscus	MNHN.ZM.MO.1998.993 (Zoo, Armoire 7)	Phase-propagation Synchroton	3D model + landmarks	Prêt 2015 / 103 ZTQ	Synchrotron 10/15	Synchrotron 10/15
Ailurops ursinus	Sulawesi bear cuscus	MNHN.ZM.AC.A2597	CT-scan	3D model + landmarks	Prêt 2014 / 12	AST-RX 2014-016	ATM 2014
Trichosurus vulpecula		ZM.MO.1889-115	CT-scan	3D model + landmarks	Prêt 2014 / 12	AST-RX 2014-016	ATM 2014
"Phalanger"		CG ZM.MO.1998.1253 (juvenile)	CT-scan	not used (juvenile)		AST-RX 2014-016	ATM 2014
Australidelphia, Diprotodontia, Petauroidea, Acrobatidae							
Acrobates pygmaeus	feathertail glider	CG ZM.MO.1996.2289	CT-scan	3D model, broken specimen		AST-RX 2014-016	ATM 2014
Distoechurus pennatus	feathertail possum	JM9611	CT-scan	3D model + landmarks	coll. V. Weisbecker		
Australidelphia, Diprotodontia, Petauroidea, Petauridae							
Petaurus breviceps	sugar glider	MNHN.ZM.MO.1996.2287	CT-scan	3D model + landmarks, broken cochlea	Prêt 2014 / 12	AST-RX 2014-016	ATM 2014

		MNHN.ZM.MO.1893.76	Phase-propagation Synchroton	3D model + landmarks	Prêt 2015 / 103 ZTQ	Synchrotron 10/15	Synchrotron 10/15
Petaurus norfolcensis	squirrel glider	MNHN.ZM.MO.2007.68	CT-scan	3D model + landmarks		AST-RX 2014-016	ATM 2014
Dactylopsila trivirgata	striped possum	J6202	CT-scan	3D model + landmarks	coll. V. Weisbecker		
Australidelphia, Diprotodontia, Petauroidea, Pseudocheiridae							
Petauroides volans	greater glider	MNHN.ZM.MO.1994-1278 JM2633	CT-scan CT-scan	3D model, broken specimen 3D model + landmarks	Prêt 2014 / 12 coll. V. Weisbecker	AST-RX 2014-016	ATM 2014
Pseudocheirus peregrinus	common ringtail possum	MNHN.ZM.MO.1844.229	CT-scan	3D model + landmarks	Prêt 2014 / 12	AST-RX 2014-016	ATM 2014
Australidelphia, Diprotodontia, Petauroidea, Tarsipedidae							
Tarsipes rostratus	honey possum	MNHN.ZM.MO.1895.473 (Zoo, Armoire 7)	Phase-propagation Synchroton	3D model + landmarks	Prêt 2015 / 103 ZTQ	Synchrotron 10/15	Synchrotron 10/15
Australidelphia, Diprotodontia, Macropodiformes, Potoroidae							
Bettongia lesueur	boodie, burrowing bettong	MNHN.ZM.MO.1998.177	CT-scan	3D model + landmarks		AST-RX 2014-016	ATM 2014
Potorous tridactylus	long-nosed potoroo	J6475	CT-scan	3D model + landmarks	coll. V. Weisbecker		
Australidelphia, Diprotodontia, Macropodiformes, Macropodidae							
Setonix brachyurus	quokka	MNHN.ZM.MO.1998.118	CT-scan	3D model + landmarks		AST-RX 2014-016	ATM 2014
Dendrolagus ursinus	tree kangaroo	MNHN.ZM.MO.1880.1465	CT-scan	3D model + landmarks		AST-RX 2014-016	ATM 2014
Australidelphia, Diprotodontia, Vombatiformes							
Vombatus ursinus	common wombat	MNHN.ZM.AC.A3289	CT-scan	3D model + landmarks	Prêt 2014 / 12	AST-RX 2014-016	ATM 2014
Lasiorhinus latifrons	southern hairy-nosed wombat	MNHN.ZM.MO.1869-761	CT-scan	3D model + landmarks	Prêt 2015 / 74	AST-RX 2015-040	ATM 2015
Phascolarctos cinereus	koala	MNHN.ZM.AC.A2553	CT-scan	3D model + landmarks	Prêt 2015 / 74	AST-RX 2015-040	ATM 2015
Australidelphia, Dasyuridae							

Antechinomys laniger	kultarr	MNHN.ZM.MO.1897.1495 (Zoo, Armoire 7)	Phase-propagation Synchroton	3D model + landmarks	Prêt 2015 / 103 ZTQ	Synchrotron 10/15	Synchrotron 10/15
Planigale ingrami	long-tailed planigale	JM4943	CT-scan	3D model + landmarks	coll. V. Weisbecker		
Antechinus flavipes	yellow-footed antechinus	MNHN.ZM.MO.A.12.797	CT-scan	3D model + landmarks	Prêt 2015 / 20	AST-RX 2015-009	ATM 2015
Phascogale tapoatafa	brush-tailed phascogale	MNHN.ZM.MO.2007.18	CT-scan	3D model + landmarks		AST-RX 2014-016	ATM 2014
Sminthopsis crassicaudata	fat-tailed dunnart	MNHN.ZM.MO.1919.30	CT-scan	3D model + landmarks		AST-RX 2014-016	ATM 2014
Dasyurus viverrinus	eastern quoll	MNHN.ZM.AC.A2627	CT-scan	3D model + landmarks	Prêt 2014/12	AST-RX 2014-016	ATM 2014
Australidelphia, Myrmecobiidae							
Myrmecobius fasciatus	numbat	MNHN.ZM.AC.A2564 J10732	CT-scan CT-scan	3D model, broken specimen 3D model + landmarks	Prêt 2014 / 12 coll. V. Weisbecker	AST-RX 2014-016	ATM 2014
Australidelphia, Peramelidae							
Perameles nasuta	long-nosed bandicoot	MNHN.ZM.AC.A12417	CT-scan	3D model + landmarks	Prêt 2014 / 12	AST-RX 2014-016	ATM 2014
Echymipera rufescens	long-nosed echymipera	MNHN.ZM.MO.1962.2147	CT-scan	3D model + landmarks	Prêt 65/00	AST-RX 2014-016	ATM 2014
Australidelphia, Thylacomyidae							
Macrotis lagotis	bilby	MNHN.ZM.MO.1872.172	CT-scan	3D model + landmarks		AST-RX 2014-016	ATM 2014
Australidelphia, Notoryctidae							
Notoryctes typhlops	marsupial mole	MNHN.ZM.MO.1893.473 (Zoo, Armoire 7) CG ZM.MO.1892.1243	phase-propagation Synchroton CT-scan	3D model + landmarks	Prêt 2015 / 103 ZTQ Prêt 2013 / 13	Synchrotron 10/15 AST-RX 2014-016	Synchrotron 10/15 ATM 2014
Australidelphia, Microbiotheriidae							
Dromiciops gliroides	Monito del monte	CG.1981.1075 (Zoo, Armoire 7) IEEUACH 2162	phase-propagation Synchroton CT-scan	3D model + landmarks	Prêt 2015 / 103 ZTQ	Synchrotron 10/15	Synchrotron 10/15

Caenolestidae							
Caenolestes fuliginosus	silky shrew opossum	MNHN.ZM.MO.1982-2587 MNHN.ZM.MO.1982.940 (Zoo, Armoire 7)	CT-scan phase-propagation Synchroton	3D model + landmarks	Prêt 2013 / 13 Prêt 2015 / 103 ZTQ	AST-RX 2014-016 Synchrotron 10/15	ATM 2014 Synchrotron 10/15
Didelphidae							
Chironectes minimus	water opossum	MACN 13053 MNHN.ZM.MO.1892.391	CT-scan phase-propagation Synchroton	3D model + landmarks	Prêt 2015 / 20 Prêt 2015 / 103 ZTQ	AST-RX 2014 / 060 (avec fossiles thérapsides) Synchrotron 10/15	crédits 2015 Synchrotron 10/15
Caluromys philander	bare-tailed woolly opossum	MNHN.ZM.MO.1987.234	CT-scan	3D model + landmarks		AST-RX 2014-016	ATM 2014
Didelphis marsupialis	common opossum	RH 161	CT-scan	3D model + landmarks		AST-RX 2014-016	ATM 2014
Marmosa murina	Linnaeus's mouse opossum	MNHN.ZM.MO.2001-2239	CT-scan	3D model + landmarks	Prêt 2014 / 12	AST-RX 2014-016	ATM 2014
Metachirus nudicaudatus	brown four-eyed opossum	MNHN.ZM.MO.2175	CT-scan	3D model + landmarks	Prêt 2014 / 12	AST-RX 2014-016	ATM 2014
Philander opossum	gray four-eyed opossum	MNHN.ZM.MO.2003.153	CT-scan	3D model + landmarks		AST-RX 2014-016	ATM 2014
Lestodelphys halli	Patagonian opossum	AF, private collection	CT-scan	3D model + landmarks			
Monodelphis brevicaudata	northern red-sided opossum	MNHN.ZM.MO.2004-317	CT-scan	3D model + landmarks	Prêt 2013 / 13	AST-RX 2014-016	ATM 2014
Placentaires							
Xenarthra, Dasypodidae							
Chlamyphorus truncatus	pink fairy armadillo	MNHN.ZM.MO.1903.82 (Zoo, Armoire 1) MNHN.ZM.MO.1962.56 MNHN.ZM.MO.1910.170 IRSNB 324B	phase-propagation Synchroton CT-scan CT-scan CT-scan	membranous 3D model + landmarks	Prêt 2015 / 103 ZTQ Prêt 2013/1 Prêt 2013/2	Synchrotron 10/15 AST-RX 2013-001 AST-RX 2013-001 AST-RX 2013-001	Synchrotron 10/15
Calyptophractus retusus	greater fairy armadillo	USNM 283134	CT-scan			scanned at the AMNH	

Cabassous unicinctus	southern naked-tailed armadillo	MNHN.ZM.MO.2007.374 MNHN.ZM.MO.1953.457	CT-scan CT-scan		Prêt 2013/2 Prêt 2013/2	AST-RX 2013-001 AST-RX 2013-001	
Zaedyus ciliatus	dwarf armadillo	MNHN.ZM.MO.2007.382 MNHN.ZM.MO.1917.135	CT-scan CT-scan		Prêt 2013/2 Prêt 2013/2	AST-RX 2013-001 AST-RX 2013-001	
Afrotheria, Chrysochloridae							
Calcochloris (Huetia) leucorhina	Congo golden mole	MNHN.ZM.MO.1984.499 MNHN-ZM-MO 1987-81 MNHN-ZM-MO 1953-460	phase-propagation Synchroton CT-scan CT-scan	membranous 3D model, not used (cristals inside, bizarre area of the vestibule)	Prêt 2015 / 103 ZTQ Prêt 2015 / 72 Prêt 2015 / 10	Synchrotron 10/15 AST-RX 2015-040 AST-RX 2015-009	Synchrotron 10/15 ATM 2015
Chrysochloris asiatica	Cape golden mole	MNHN.ZM.MO.1991.626	CT-scan		Prêt 2015 / 10	AST-RX 2015-009	ATM 2015
Eremitalpa granti	Grant's golden mole	MNHN-ZM-MO 1981-18	CT-scan		Prêt 2015 / 10	AST-RX 2015-009	ATM 2015
Afrotheria, Tenrecidae							
Hemicentetes semispinosus	lowland streaked tenrec	MNHN.ZM.MO.1962.2432 (1935-51 on the tag)	CT-scan		Prêt 2015 / 72	AST-RX 2015-040	
Potamogale velox	giant otter shrew	MNHN.ZM.MO.1970-319	CT-scan		Prêt 2015 / 72	AST-RX 2015-040	
Tenrec ecaudatus	common tenrec	MNHN.ZM.MO.1962-2459	CT-scan		Prêt 2015 / 72	AST-RX 2015-040	
Setifer setosus	greater hedgehog tenrec	MNHN.ZM.MO.1962-2420	CT-scan		Prêt 2015 / 72	AST-RX 2015-040	
Afrotheria, Tubulidentata, Orycteropodidae							
Orycteropus afer	aardvark	SMF 15605, 92288	CT-scan		courtesy of J. Benoit and T. Lehmann		
Laurasiatheria, Eulipotyphla, Talpidae							
Talpa europaea	European mole	MNHN.ZM.MO.1907.49 MNHN.ZM.MO.1953.829 MNHN.ZM.MO.1962.2033 MNHN.ZM.MO.1993.631 MNHN.ZM.MO.1993.633	phase-propagation Synchroton CT-scan CT-scan CT-scan CT-scan	not exploitable 3D model 3D model, broken 3D model 3D model, broken	Prêt 2015 / 103 ZTQ Prêt 2015 / 20 Prêt 2015 / 20 Prêt 2015 / 20 Prêt 2015 / 20	Synchrotron 10/15 AST-RX 2015-009 AST-RX 2015-009 AST-RX 2015-009 AST-RX 2015-009	Synchrotron 10/15 ATM 2015 ATM 2015 ATM 2015 ATM 2015

		MNHN.ZM.MO.1993.679 (=3852)	CT-scan	3D model, broken	Prêt 2015 / 20	AST-RX 2015-009	ATM 2015
		MNHN.ZM.MO.1995.3254	CT-scan	3D model	Prêt 2015 / 20	AST-RX 2015-009	ATM 2015
		MNHN.ZM.MO.2004.100	CT-scan	3D model, broken	Prêt 2015 / 20	AST-RX 2015-009	ATM 2015
		MNHN.ZM.MO.1932.3814	CT-scan		Prêt 2015 / 72	AST-RX 2015-039, -040	ATM Formes 2015
		MNHN.ZM.MO.1932.1659	CT-scan		Prêt 2015 / 72	AST-RX 2015-039, -040	ATM Formes 2015
		MNHN.ZM.MO.1932.3822	CT-scan		Prêt 2015 / 72	AST-RX 2015-039, -040	ATM Formes 2015
		MNHN.ZM.MO.1932.3862	CT-scan		Prêt 2015 / 72	AST-RX 2015-039, -040	ATM Formes 2015
		MNHN.ZM.MO.1940.86	CT-scan		Prêt 2015 / 72	AST-RX 2015-039, -040	ATM Formes 2015
		MNHN.ZM.MO.1929.473	CT-scan		Prêt 2015 / 72	AST-RX 2015-039, -040	ATM Formes 2015
		MNHN.ZM.AC.A1282	CT-scan		Prêt 2015 / 72	AST-RX 2015-039, -040	ATM Formes 2015
		MNHN.ZM.MO.1935.338	CT-scan		Prêt 2015 / 72	AST-RX 2015-039, -040	ATM Formes 2015
		MNHN.ZM.MO.2006.384	CT-scan		Prêt 2015 / 72	AST-RX 2015-039, -040	ATM Formes 2015
		MNHN.ZM.MO.1931.147	CT-scan		Prêt 2015 / 72	AST-RX 2015-039, -040	ATM Formes 2015
		MNHN.ZM.MO.1923.2386	CT-scan		Prêt 2015 / 72	AST-RX 2015-039, -040	ATM Formes 2015
		MNHN.ZM.MO.1923.657	CT-scan		Prêt 2015 / 72	AST-RX 2015-039, -040	ATM Formes 2015
		MNHN.ZM.MO.1923.17	CT-scan		Prêt 2015 / 72	AST-RX 2015-039, -040	ATM Formes 2015
		MNHN.ZM.MO.2014.854	CT-scan		Prêt 2015 / 72	AST-RX 2015-039, -040	ATM Formes 2015
		MNHN-ZM-MO 1923.22 or 1963-376 (both number on the tag)	CT-scan		Prêt 2015 / 72	AST-RX 2015-039, -040	ATM Formes 2015
Scalopus aquaticus (australis)	eastern mole	MNHN.ZM.MO.2006.377	CT-scan	3D model	Prêt 2015 / 10	AST-RX 2015-009	ATM 2015
Scapanus orarius	coast mole	MNHN.ZM.MO.2006.381	CT-scan	3D model	Prêt 2015 / 10	AST-RX 2015-009	ATM 2015
Euroscaptor micrura	Himalayan mole	MNHN.ZM.MO.1959.1795	CT-scan	3D model, broken	Prêt 2015 / 10	AST-RX 2015-009	ATM 2015
Galemys pyrenaicus	Pyrenean desman	MNHN.ZM.MO.1982.189	CT-scan	3D model	Prêt 2015 / 72	AST-RX 2015-039	ATM Formes 2015
Euroscaptor longirostris	long-nosed mole	MNHN.ZM.MO.1874.516	CT-scan	3D model, broken	Prêt 2015 / 72	AST-RX 2015-039	ATM Formes 2015
Mogera kobeae	Kobe mole	MNHN.ZM.MO.2000.197	CT-scan	3D model	Prêt 2015 / 72	AST-RX 2015-039	ATM Formes 2015
Condylura cristata	star-nosed mole	MNHN.ZM.MO.1984.507 (Zoo)	phase-propagation Synchroton		Prêt 2015 / 103 ZTQ	Synchrotron 10/15	Synchrotron 10/15

Laurasiatheria, Eulipotyphla, Erinaceidae							
Erinaceus europaeus	European hedgehog	MNHN.ZM.MO.1963.381	CT-scan	3D model	Prêt 2015 / 72	AST-RX 2015-039	ATM Formes 2015
Atelerix algirus	North African hedgehog	MNHN.ZM.MO.1955.650	CT-scan	3D model	Prêt 2015 / 91	AST-RX 2015-039	ATM Formes 2015
Laurasiatheria, Eulipotyphla, Soricidae							
Crocidura russula	White-toothed shrew	MNHN.ZM.MO.2008.116	CT-scan	3D model	Prêt 2015 / 91	AST-RX 2015-039	ATM Formes 2015
Sorex araneus	Eurasian shrew or Common shrew	MNHN.ZM.MO.1962.2010	CT-scan	3D model	Prêt 2015 / 91	AST-RX 2015-039	ATM Formes 2015
Laurasiatheria, Carnivora, Caniformia, Canidae							
Vulpes vulpes	red fox	MNHN.ZM.MO.1908.29	CT-scan		Prêt 2015 / 74	AST-RX 2015-039	ATM Formes 2015
Vulpes zerda	fennec	MNHN.ZM.M0.2001.2000	CT-scan		Prêt 2015 / 74	AST-RX 2015-039	ATM Formes 2015
Laurasiatheria, Carnivora, Caniformia, Mustelidae							
Arctonyx collaris	Hog badger	MNHN.ZM.AC.1877.704, 1961.186, MO.1962.1638	CT-scan	3D model	Project Peigné, Ladevèze	AST-RX 2013	ATM Formes 2013
Meles meles	European badger	21 specimens (cf Rozen-Rechels et al., 2016, BJLS)	CT-scan	3D model	Project Peigné, Ladevèze	AST-RX 2013	ATM Formes 2013
Lutra lutra	Common otter	MNHN.ZM.MO.1962.1738, 2005.597, 2005.598	CT-scan	3D model	Project Peigné, Ladevèze	AST-RX 2013	ATM Formes 2013
Gulo gulo	wolverine	MNHN.ZM.AC.1967.54, MO.2005.853	CT-scan	3D model	Project Peigné, Ladevèze	AST-RX 2013	ATM Formes 2013
Mustela putorius	European polecat	MNHN-ZM-MO 1990-77	CT-scan		Prêt 2015 / 74	AST-RX 2015-039	ATM Formes 2015
Laurasiatheria, Carnivora, Feliformia, Felidae							
Felis sylvestris	wildcat	MNHN.ZM.AC.1951.274, MO.1961.620, MO.1995.3151	CT-scan		Project Peigné, Ladevèze	AST-RX 2013	ATM Formes 2013
Laurasiatheria, Carnivora, Feliformia, Herpestidae							
Suricata suricatta	meerkat	MNHN.ZM.MO.1998.113	CT-scan		Prêt 2015 / 74	AST-RX 2015-039	ATM Formes 2015
Laurasiatheria, Pholidota							
Manis temmincki	ground pangolin	MNHN.ZM.MO.1917.235	CT-scan		Prêt 2015 / 74	AST-RX 2015-039	ATM Formes 2015
Manis pentadactyla	Chinese pangolin	MNHN.ZM.MO.1913.156	CT-scan		Prêt 2015 / 74	AST-RX 2015-039	ATM Formes 2015

Euarchontoglires, Rodentia, Myomorpha, Cricetidae (Arvicolinae)							
Arvicola amphibius	European water vole	MNHN.ZM.MO.1944.377	CT-scan	3D model	Prêt 2015 / 20	AST-RX 2015-009	ATM 2015
Arvicola sapidus	southern water vole	MNHN.ZM.MO.1993.1700	CT-scan		Prêt 2015 / 72	AST-RX 2015-040	
Lemmus lemmus	Norway lemming	MNHN.ZM.MO.1960.3839	CT-scan		Prêt 2015 / 72	AST-RX 2015-040	
Ellobius talpinus	northen mole vole	MNHN.ZM.MO.2001.1876	CT-scan		Prêt 2015 / 72	AST-RX 2015-040	
Euarchontoglires, Rodentia, Myomorpha, Muridae							
Rattus norvegicus	brown rat	MNHN.ZM.MO.1933.2110	CT-scan		Prêt 2015 / 72	AST-RX 2015-040	
Hydromys chryogaster	water rat	MNHN-ZM-AC A13434	CT-scan		Prêt 2015 / 72	AST-RX 2015-040	
Notomys alexis	spinifex hopping mouse	MNHN.ZM.MO.1993.3136 MNHN.ZM.MO.2001.472	phase-propagation Synchroton CT-scan		Prêt 2015 / 103 ZTQ Prêt 2015 / 91	Synchrotron 10/15 AST-RX 2015-040	Synchrotron 10/15
Gerbillus campestris	North African gerbil	MNHN.ZM.MO.1990.10	CT-scan	3D model	Prêt 2015 / 20	AST-RX 2015-009	ATM 2015
Meriones libycus	Lybian jird	MNHN.ZM.MO.1981.619	CT-scan	3D model	Prêt 2015 / 20	AST-RX 2015-009	ATM 2015
Euarchontoglires, Rodentia, Myomorpha, Spalacidae							
Myospalax psilurus	Transbaikal zokor	MNHN.ZM.MO.1961.922	CT-scan	3D model	Prêt 2015 / 10	AST-RX 2015-009	ATM 2015
Myospalax myospalax	zokor	MNHN.ZM.MO.1962.2361	CT-scan		Prêt 2015 / 72	AST-RX 2015-040	
Rhizomys pruinosus	hoary bamboo rat	MNHN.ZM.MO.1993.48	CT-scan	3D model	Prêt 2015 / 20	AST-RX 2015-009	ATM 2015
Spalax ehrenbergi	Middle East bling mole-rat	MNHN.ZM.MO.1879.1615 (Zoo, Armoire 4)	phase-propagation Synchroton		Prêt 2015 / 103 ZTQ	Synchrotron 10/15	Synchrotron 10/15
Nannospalax leucodon	lesser mole-rat	MNHN.ZM.MO.1961.1034	CT-scan		Prêt 2015 / 72	AST-RX 2015-040	
Tachyoryctes spendens	East African mole-rat	MNHN.ZM.MO.2015.384	CT-scan		Prêt 2015 / 72	AST-RX 2015-040	
Euarchontoglires, Rodentia, Castorimorpha, Heteromyidae							
Dipodomys elephantinus	big-eared kangaroo rat	MNHN.ZM.MO.1961.101	CT-scan	3D model	Prêt 2015 / 20	AST-RX 2015-009	ATM 2015
Euarchontoglires, Rodentia, Castorimorpha, Geomyidae							

Geomys bursaricus	plains pocket gopher	MNHN.ZM.MO.1962.952	CT-scan	3D model	Prêt 2015 / 10	AST-RX 2015-009	ATM 2015
Geomys susa		MNHN.ZM.MO.2007.287	CT-scan		Prêt 2015 / 72	AST-RX 2015-040	
Orthogeomys grandis	giant pocket gopher	MNHN.ZM.MO.1866.4	CT-scan		Prêt 2015 / 72	AST-RX 2015-040	
Cratogeomys fumosus	smocky pocket gopher	MNHN.ZM.MO.1962.2300	CT-scan		Prêt 2015 / 72	AST-RX 2015-040	
Thomomys bottae	Botta's pocket gopher	MNHN.ZM.MO.1898.1490 (Zoo, Armoire 6)	phase-propagation Synchroton		Prêt 2015 / 103 ZTQ	Synchrotron 10/15	Synchrotron 10/15
Thomomys bulbivorus	Camas pocket gopher	MNHN.ZM.MO.1962.950	CT-scan	3D model	Prêt 2015 / 10	AST-RX 2015-009	ATM 2015
Euarchontoglires, Rodentia, Castorimorpha, Castoridae							
Castor fiber	Eurasian beaver	MNHN.ZM.AC.A12552	CT-scan		Prêt 2015 / 72	AST-RX 2015-009	ATM 2015
Euarchontoglires, Rodentia, Hystricomorpha, Bathyergidae							
Bathyergus suillus	Cape dune mole-rat	MNHN.ZM.MO.1962.2299	CT-scan	3D model	Prêt 2015 / 10	AST-RX 2015-009	ATM 2015
Heliophobius argenteocinereus (cinereus)	Silvery mole-rat	MNHN.ZM.MO.1893.41	CT-scan	3D model	Prêt 2015 / 10	AST-RX 2015-009	ATM 2015
Cryptomys mechowi	Mechow's mole-rat	MNHN.ZM.MO.1911.666	CT-scan		Prêt 2015 / 72	AST-RX 2015-040	
Georychus capensis	Cape mole-rat	MNHN.ZM.MO.1988.111	CT-scan		Prêt 2015 / 72	AST-RX 2015-040	
Heterocephalus glaber	naked mole-rat	MNHN.ZM.MO.1884.1778 (Zoo, Armoire 3) MNHN.ZM.MO.1884.1578	phase-propagation Synchroton CT-scan	membranous 3D model + landmarks	Prêt 2015 / 103 ZTQ Prêt 2015 / 72	Synchrotron 10/15 AST-RX 2015-040	Synchrotron 10/15
Euarchontoglires, Rodentia, Hystricomorpha, Ctenomyidae							
Ctenomys brasiliensis	Brazilian tuco-tuco	MNHN.ZM.MO.1911.626 B (Zoo, Armoire 2)	phase-propagation Synchroton		Prêt 2015 / 103 ZTQ	Synchrotron 10/15	Synchrotron 10/15
Ctenomys opimus	Highland tuco-tuco	MNHN.ZM.MO.1961.672	CT-scan	3D model	Prêt 2015 / 10	AST-RX 2015-009	ATM 2015
Ctenomys porteous	Porteous's tuco-tuco	MNHN.ZM.MO.1919.1	CT-scan		Prêt 2015 / 72	AST-RX 2015-040	
Ctenomys sylvanus	Forest tuco-tuco	MNHN.ZM.MO.2007.136	CT-scan		Prêt 2015 / 72	AST-RX 2015-040	

Ctenomys tuconax	robust tuco-tuco	MNHN-ZM-MO 1903-598	CT-scan	3D model	Prêt 2015 / 10	AST-RX 2015-009	ATM 2015
Euarchontoglires, Rodentia, Hystricomorpha, Octodontidae							
Spalacopus cyanus	coruro	MNHN.ZM.MO.1971.1010	CT-scan		Prêt 2015 / 72	AST-RX 2015-040	
Octodon lunatus	moon-toothed degu	MNHN.ZM.MO.1993.346	CT-scan		Prêt 2015 / 72	AST-RX 2015-040	
Euarchontoglires, Rodentia, Hystricomorpha, Chinchillidae							
Lagostomus maximus	plains viscacha	MNHN.ZM.MO.1974.336	CT-scan		Prêt 2015 / 72	AST-RX 2015-040	
Euarchontoglires, Rodentia, Hystricomorpha, Caviidae							
Cavia aperera	Brazilian guinea pig	MNHN.ZM.MO.1986.470	CT-scan		Prêt 2015 / 72	AST-RX 2015-040	
Dolichotis patagonum	Patagonian mara	MNHN.ZM.MO.1976.393	CT-scan		Prêt 2015 / 72	AST-RX 2015-040	
Euarchontoglires, Rodentia, Hystricomorpha, Myocastoridae							
Myocastor coypus	coypu or nutria	MNHN.ZM.MO.2007.345	CT-scan		Prêt 2015 / 72	AST-RX 2015-040	
Euarchontoglires, Rodentia, Hystricomorpha, Cuniculidae							
Dasyprocta aguti	agouti	MNHN.ZM.MO.2001.1293	CT-scan		Prêt 2015 / 72	AST-RX 2015-040	
Euarchontoglires, Rodentia, Hystricomorpha, Abrocomidae							
Abrocoma cinerea	ashy chinchilla-rat	MNHN.ZM.MO.2007.139	CT-scan		Prêt 2015 / 91	AST-RX 2015-040	
Euarchontoglires, Rodentia, Sciuromorpha, Sciuridae							
Xerus erythropus	striped ground squirrel	MNHN.ZM.2013.2888	CT-scan	3D model	Prêt 2015 / 20	AST-RX 2015-009	ATM 2015
Cynomys ludovicianus	black-tailed prairie dog	MNHN.ZM.MO.1962.2179	CT-scan	3D model	Prêt 2015 / 20	AST-RX 2015-009	ATM 2015
Glaucomys volans	southern flying squirrel or assapan	MNHN.ZM.MO.1903.841 MNHN-ZM-MO 1939-707	phase-propagation Synchroton CT-scan		Prêt 2015 / 103 ZTQ Prêt 2015 / 72	Synchrotron 10/15 AST-RX 2015-040	Synchrotron 10/15
Marmota marmota	Alpine marmot	MNHN.ZM.MO.1934.1021	CT-scan		Prêt 2015 / 72	AST-RX 2015-040	

ANNEXE 2. Etude préliminaire de l'oreille interne des rongeurs fouisseurs
APPENDIX 2. Preliminary study of the inner ear of fossorial rodents

In the framework of a supervised internship of Licence 3: Marine Lambert, Licence BGST, Université de Cergy-Pontoise, Département de Biologie. Juin 2015.

Among mammals, rodents are probably the best example to illustrate repeated adaptations to underground lifestyle. This clade is known for occupying a wide range of ecological niches (amphibian, arboreal, gliding, terrestrial, fossorial). Burrowing subterreanean rodents spend their lives underground in extreme conditions (e.g., darkness, low ventilation, hypoxia,...) that are unsuitable for most other animals (Buffenstein, 2000). In response to these ecological constraints, they have evolved adapted morphological and physiological traits, such as digging forearms and teeth, modified vestibular organ, reduced vision (Lindenlaub et al., 1995; Partha et al., 2017). Rodents are therefore a choice model for our purpose: testing the correlation between the morphology of the bony vestibular system of the inner ear and the subterranean lifestyle (with various ways of digging).

In this preliminary study, which was made possible thanks to a MNHN (ATM) grant obtained in early-2015 (see Table 1.1), we sampled 14 rodent species. A second grant obtained in the late-2015, helped us to concretise our goal: for each family containing a subterranean species, sampling subterranean and fossorial species (8 fossorial here, indicated in red in the table 2.1), as well as their counter-parts (non-subterranean and non-fossorial). Non-fossorial rodents belonging to other families are also included in the final sample to represent the taxonomic and morphological diversity of the clade.

All the specimens (skull and skin) belong to the collection Zoology of Mammals, Mammifères & Oiseaux, MNHN.

Table 2.1: Measurements taken on the semicircular canal system of the inner ear of 14 rodent species. The measurements are derived from Spoor et al. (2007) for the radii, and Billet et al. (2013) for the others (see figure 2.1).

Species	Common name	# specimen	Measurements												
			IEH	H ASC	L ASC	D ASC	H PSC	L PSC	D PSC	H LSC	L LSC	D LSC	Angle ASC/PSC	Angle ASC/LSC	Angle PSC/LSC
Sciuromorpha, Sciuridae															
Xerus erythropus	striped ground squirrel	MNHN.ZM.MO.2013.2888	8,09	3,42	4,13	0,3	3,52	3,6	0,3	3,03	3,47	0,3	100,47	94,92	91,34
Cynomys ludovicianus	black-tailed prairie dog	MNHN.ZM.MO.1962.2179	6,87	2,36	3,44	0,34	2,38	2,9	0,39	2,93	2,63	0,43	85,3	99,55	93,89
Myomorpha, Muridae															
Gerbillus campestris	North African gerbil	MNHN.ZM.MO.1990.10	4,54	1,69	2,47	0,18	1,71	2,03	0,17	1,35	1,98	0,2	98,22	104,38	99,65
Meriones libycus	Lybian jird	MNHN.ZM.MO.1981.619	5,7	2,9	3,12	0,26	2,26	2,47	0,26	2,29	2,93	0,26	84,14	100,13	91,55
Castorimorpha, Heteromyidae															
Dipodomys elephantinus	big-eared kangaroo rat	MNHN.ZM.MO.1961.101	6,43	2,21	3,57	0,31	1,8	2,52	0,31	1,96	2,28	0,39	90,7	90,21	91,43
Myomorpha, Cricetidae (Arvicolinae)															
Arvicola amphibius	European water vole	MNHN.ZM.MO.1944.377	5,16	1,84	2,84	0,27	2,38	2,63	0,26	2,02	2,27	0,25	96,81	107,24	88,61
Castorimorpha, Geomyidae															
Thomomys bulbivorus	Camas pocket gopher	MNHN.ZM.MO.1962.950	5,42	1,58	3,14	0,36	1,57	2,35	0,36	2,22	1,68	0,39	89,52	85,13	84,63
Geomys bursarius	plains pocket gopher	MNHN.ZM.MO.1962.952	4,81	1,6	2,56	0,32	1,84	2,14	0,32	1,89	1,76	0,43	97,34	93,12	99,63
Hystricomorpha, Ctenomyidae															
Ctenomys tuconax	robust tuco-tuco	MNHN-ZM-MO 1903-598	6,65	1,97	2,54	0,39	1,14	1,46	0,44	1,55	1,66	0,54	102,66	105,29	92,27
Ctenomys opimus	Highland tuco-tuco	MNHN.ZM.MO.1961.672	6,34	1,6	2,71	0,46	0,85	1,25	0,59	1,29	1,85	0,56	88,19	92,85	105,34
Myomorpha, Spalacidae															
Rhizomys pruinosus	hoary bamboo rat	MNHN.ZM.MO.1993.48	6,55	2,53	3,45	0,43	1,87	2,2	0,43	1,78	1,76	0,51	95,21	93,11	82,31
Myospalax psilurus	Transbaikal zokor	MNHN.ZM.MO.1961.922	5,81	2,13	3,29	0,38	2,01	2,08	0,38	2,36	2,24	0,37	96,01	94,48	96,75
Hystricomorpha, Bathyergidae															
Heliophobius argenteocinereus	Silvery mole-rat	MNHN.ZM.MO.1893.41	4,83	1,19	2,01	0,45	0,65	1,23	0,44	1,2	1,33	0,45	100,94	87,23	87,08
Bathyergus suillus	Cape dune mole-rat	MNHN.ZM.MO.1962.2299	6,85	1,86	3,43	0,52	1,67	1,87	0,61	1,44	2,57	0,56	84,42	95,2	106,83

Species	Common name	# specimen	R ASC	R ASC/ IEH	R PSC	R PSC/ IEH	R LSC	R LSC/ IEH	MOYEN SC/IEH	H ASC/ H PSC	H ASC/ H LSC	H PSC/ H LSC	D ASC/ IEH	D PSC/ IEH	D LSC/ IEH	S Angle ASC/PS C	S Angle ASC/LSC	S Angle PSC/LSC
Sciuromorpha, Sciuridae																		
Xerus erythropus	striped ground squirrel	MNHN.ZM.MO .2013.2888	1,8875	0,2333 12732	1,78	0,2200 24722	1,62 5	0,2008 65266	0,21806 7573	0,97159 0909	1,12871 2871	1,16171 6172	0,0370 82818	0,0370 82818	0,0370 82818	0,88174 946	0,44278 607	0,36827 0799
Cynomys ludovicianus	black-tailed prairie dog	MNHN.ZM.MO .1962.2179	1,45	0,2110 62591	1,32	0,1921 39738	1,39	0,2023 28967	0,20184 3765	0,99159 6639	0,80546 0751	0,81228 6689	0,0494 90539	0,0567 68559	0,0625 90975	0,06263 4989	0,65219 3578	0,47226 7537
Myomorpha, Muridae																		
Gerbillus campestris	North African gerbil	MNHN.ZM.MO .1990.10	1,04	0,2290 7489	0,93 5	0,2059 47137	0,83 25	0,1833 70044	0,20613 069	0,98830 4094	1,25185 1852	1,26666 6667	0,0396 47577	0,0374 44934	0,0440 52863	0,76025 9179	0,87064 6766	0,70717 7814
Meriones libycus	Lybian jird	MNHN.ZM.MO .1981.619	1,505	0,2640 35088	1,18 25	0,2074 5614	1,30 5	0,2289 47368	0,23347 9532	1,28318 5841	1,26637 5546	0,98689 9563	0,0456 14035	0,0456 14035	0,0456 14035	0	0,67842 6052	0,37683 5237
Castorimorpha, Heteromyidae																		
Dipodomys elephantinus	big-eared kangaroo rat	MNHN.ZM.MO .1961.101	1,445	0,2247 27838	1,08	0,1679 62675	1,06	0,1648 52255	0,18584 7589	1,22777 7778	1,12755 102	0,91836 7347	0,0482 11509	0,0482 11509	0,0606 53188	0,35421 1663	0,22976 0289	0,37194 1272
Myomorpha, Cricetidae (Arvicolinae)																		
Arvicola amphibius	European water vole	MNHN.ZM.MO .1944.377	1,17	0,2267 44186	1,25 25	0,2427 32558	1,07 25	0,2078 48837	0,22577 5194	0,77310 9244	0,91089 1089	1,17821 7822	0,0523 25581	0,0503 87597	0,0484 49612	0,68412 527	1	0,25693 3116
Castorimorpha, Geomyidae																		
Thomomys bulbivorus	Camas pocket gopher	MNHN.ZM.MO .1962.950	1,18	0,2177 12177	0,98	0,1808 11808	0,97 5	0,1798 89299	0,19280 4428	1,00636 9427	0,71171 1712	0,70720 7207	0,0664 20664	0,0664 20664	0,0719 5572	0,29049 676	0	0,09461 6639
Geomys bursaricus	plains pocket gopher	MNHN.ZM.MO .1962.952	1,04	0,2162 16216	0,99 5	0,2068 60707	0,91 25	0,1897 0894	0,20426 1954	0,86956 5217	0,84656 0847	0,97354 4974	0,0665 28067	0,0665 28067	0,0893 97089	0,71274 2981	0,36137 4943	0,70636 2153
Hystricomorpha, Ctenomyidae																		
Ctenomys tuconax	robust tuco-tuco	MNHN-ZM-MO 1903-598	1,1275	0,1695 48872	0,65	0,0977 44361	0,80 25	0,1206 76692	0,12932 3308	1,72807 0175	1,27096 7742	0,73548 3871	0,0586 46617	0,0661 65414	0,0812 03008	1	0,91180 4613	0,40619 9021
Ctenomys opimus	Highland tuco-tuco	MNHN.ZM.MO .1961.672	1,0775	0,1699 52681	0,52 5	0,0828 07571	0,78 5	0,1238 17035	0,12552 5762	1,88235 2941	1,24031 0078	0,65891 4729	0,0725 55205	0,0930 59937	0,0883 28076	0,21868 2505	0,34916 3275	0,93923 3279
Myomorpha, Spalacidae																		
Rhizomys pruinosus	hoary bamboo rat	MNHN.ZM.MO .1993.48	1,495	0,2282 44275	1,01 75	0,1553 43511	0,88 5	0,1351 14504	0,17290 0763	1,35294 1176	1,42134 8315	1,05056 1798	0,0656 48855	0,0656 48855	0,0778 62595	0,59773 2181	0,36092 2659	0

Myospalax psilurus	Transbaikal zokor	MNHN.ZM.MO.1961.922	1,355	0,233218589	1,0225	0,175989673	1,15	0,197934596	0,202380952	1,059701493	0,902542373	0,851694915	0,065404475	0,065404475	0,063683305	0,640928726	0,422885572	0,588907015
Hystricomorpha, Bathyergidae																		
Heliophobus argenteocinereus	Silvery mole-rat	MNHN.ZM.MO.1893.41	0,8	0,165633147	0,47	0,097308489	0,6325	0,130952381	0,131297447	1,830769231	0,991666667	0,541666667	0,093167702	0,091097308	0,093167702	0,907120743	0,094979647	0,194535073
Bathyergus suillus	Cape dune mole-rat	MNHN.ZM.MO.1962.2299	1,3225	0,193065693	0,885	0,12919708	1,0025	0,146350365	0,156200438	1,113772455	1,291666667	1,159722222	0,075912409	0,089051095	0,081751825	0,015110879	0,455450023	1

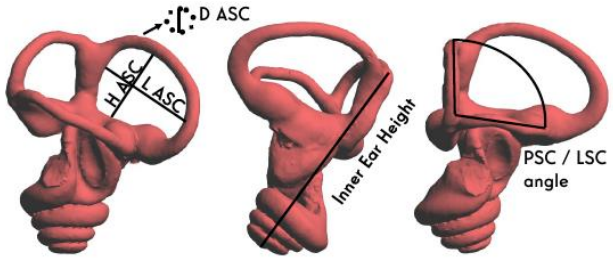

Quantifying shape with linear morphometrics

Twelve ratios calculated from measurements:

R ASC/IEH	H ASC/H PSC	D ASC/IEH	S Angle ASC/PSC
R PSC/IEH	H ASC/H LSC	D PSC/IEH	S Angle ASC/LSC
R LSC/IEH	H PSC/H LSC	D LSC/IEH	S Angle PSC/LSC

With R = 0.5*(H+L); S = observed value-smallest angle/widest angle-smallest angle;
IEH = Inner Ear Height

Figure 2.1: Measurements taken on the semicircular canal system of 14 rodents of the preliminary study.

We conducted a Principal Composant Analysis on the preliminar measurements, with the PAST software (Hammer et al., 2008), to have a first look at the morphological diversity of the bony inner ear of the selected 14 rodents (Fig. 2.2).

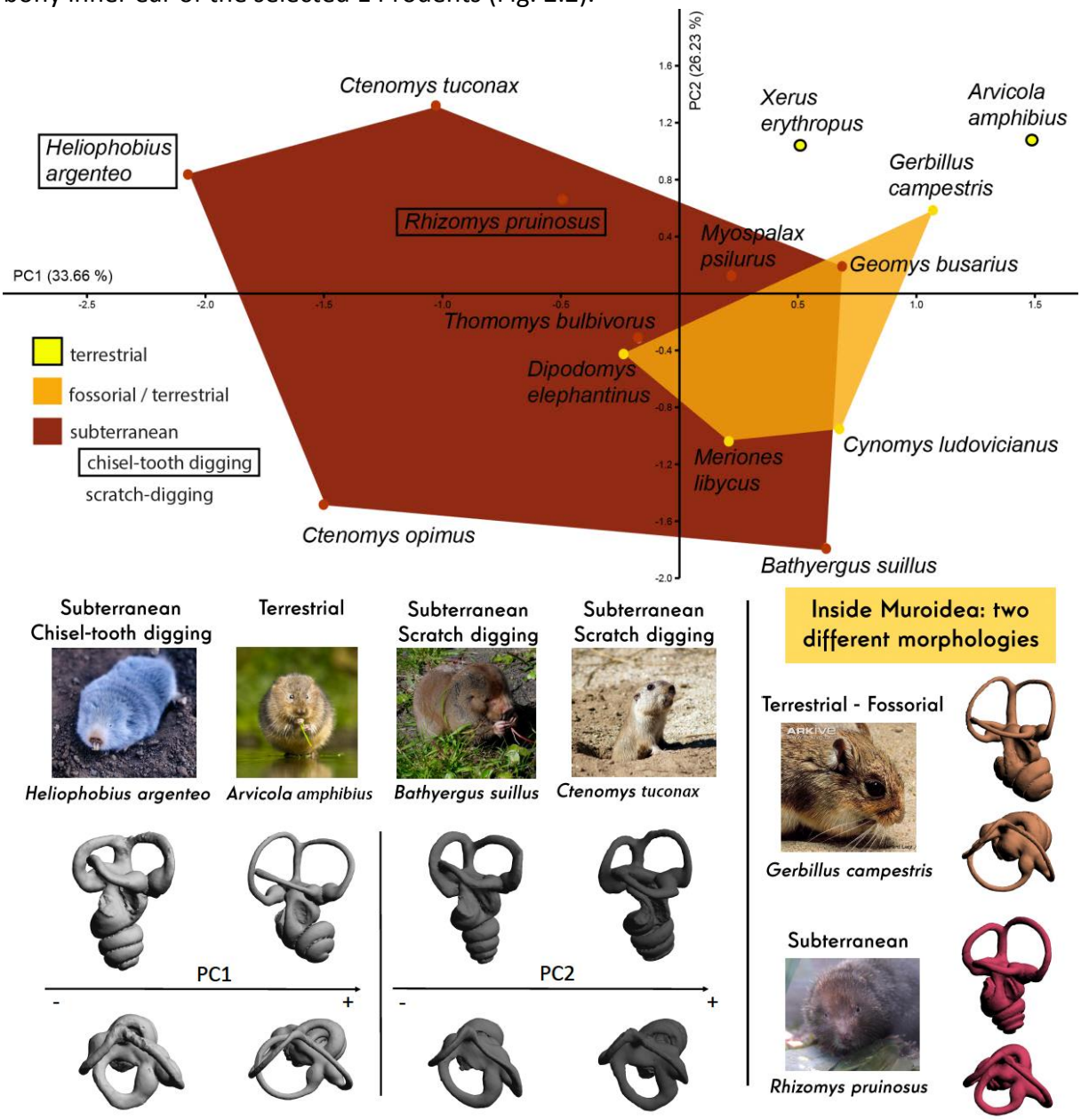

Figure 2.1: Result of the PCA of 12 linear measurements taken on the semicircular canal system of 14 rodents. 81.79% of the total variance is explained by the first three PCs.

In the PC1-PC2 space, the subterranean species are not discriminated from the other fossorial and terrestrial species, although there are clustered at lower and most negative values of the PC1. Our final goal will be to analyse landmarks coordinates on the final sample, for the reasons exposed in the Chapter 1, during next year.

References

Billet, G., Germain, D., Ruf, I., de Muizon, C., & Hautier, L. (2013) The inner ear of *Megatherium* and the evolution of the vestibular system in sloths. *J. Anat.* 223, 557–567.

Buffenstein, R. (2000). Ecophysiological responses of subterranean rodents to underground habitats. *Life underground: the biology of subterranean rodents (EA Lacey, JL Patton, and GN Cameron, eds.). University of Chicago Press, Illinois*, 62-110.

Hammer, Ø., Harper, D. A. T., & Ryan, P. D. (2008). PAST-palaeontological statistics, ver. 1.89. *Paleontological Museum, University of Oslo, Noruega.*

Lindenlaub, T., Burda, H., & Nevo, E. (1995). Convergent evolution of the vestibular organ in the subterranean mole-rats, *Cryptomys* and *Spalax*, as compared with the aboveground rat, *Rattus*. *Journal of Morphology*, 224(3), 303-311.

Partha, R., Chauhan, B. K., Ferreira, Z., Robinson, J. D., Lathrop, K., Nischal, K. K., ... & Clark, N. L. (2017). Subterranean mammals show convergent regression in ocular genes and enhancers, along with adaptation to tunneling. *eLife*, 6.

Spoor, F., Garland, T., Krovitz, G., Ryan, T. M., Silcox, M. T., & Walker, A. (2007). The primate semicircular canal system and locomotion. *Proceedings of the National Academy of Sciences*, *104*(26), 10808-10812.

ANNEXE 3. Etude préliminaire de l'oreille interne des eulipotyphles
APPENDIX 3. Preliminary study of the inner ear of Eulipotyphla

In the framework of a supervised internship (in between voluntary work M1/M2): Rémy Lefèvre, Master SEP MNHN, Juillet 2016.

Eulipotyphla (moles, shrews and hedgehogs) is a essential clade to study when the question of morphological adaptations to the underground life is addressed. In this preliminary study, we compared the semicircular canal system morphology of various eulipotyphlan species, a group that has radiated into diverse environments, such as terrestrial, aquatic and subterranean habitats. Furthermore, the abundance of intact skulls of the European mole in the mammal collections of the MNHN was the chance to provide the first study of intraspecific variations of the bony labyrinth in mammals.

Unfortunately, only 3 out of the 7 first inner ears of *Talpa europaea* were exploitable. Although the basicranium and petrosal seemed intact, the enclosed inner ears were sometimes partly broken. We now have 15 more scans of the European mole ears (Table 1.1), which will be prepared for a future study in the next years.

As for the preliminary study of rodents, we used the same linear measurements for a PCA, to have a first look at the morphological diversity of the bony inner ears of some selected eulipotyphlans (Table 3.1, Fig. 3.1).

Table 3.1: Measurements taken on the semicircular canal system of the inner ear of selected eulipotyphlan species.
N/A= non available, *= estimation

Species_	Specimen number (MNHN.ZM.	Lateralit y (L/R)	inversi on	Resolutio n (vox size µm)	Whole inner ear	Skull Volume (µm³)	Skull length (µm)	Skull width	Skull height	Theoric Volume	Inner Ear Volume	I.E.H.	ASCH	ASCW	ASCd	PSCH	PSCW	PSCd	LSCH	LSCW	LSCd	Angle ASC/PSC	Angle ASC/LSC	Angle PSC/LSC
Talpa_europaea	CG.1953.829	R	y	20,8263	y	5,40633E+11	28651,73	11457,5	9770,63	3,20748E+12	3362963349	4554,49	2423,67	2049,43	200,77	2003,75	1501,95	212,23	1784,11	1864,5	229,42	118,82	63,56	94,06
Talpa_europaea	CG.1953.829	L	y	20,8263	y	5,40633E+11	28651,73	11457,5	9770,63	3,20748E+12	3377244520	4481,33	2468,15	1956,57	197,33	2011,48	1481,76	215,23	1784,64	1919,81	225,99	114,66	68,31	90,35
Talpa_europaea	CG.1993.631	R	y	20,8263	n	6,54692E+11	29494,85	12313,79	10456,24	3,79764E+12	3388895111,23*	N/A	N/A	N/A	215,45*	N/A	N/A	209,9*	1814,71	1945,08	221,34	N/A	N/A	89,22
Talpa_europaea	CG.1993.631	L	y	20,8263	n	6,54692E+11	29494,85	12313,79	10456,24	3,79764E+12	3387110198,11*	N/A	N/A	N/A	N/A	N/A	N/A	209,05*	1823,1	1940,14	229,9	N/A	N/A	86,22
Talpa_europaea	CG.1995.3524	R	y	20,8263	y	N/A	27118,37	11149,1	9369,62	2,83286E+12	3345628092	4382,55	2314,07	1928,54	200,15	1938,74	1499,71	211,77	1779,89	1832,68	230,39	107,48	69,15	83,43
Talpa_europaea	CG.1995.3524	L	y	20,8263	y	N/A	27118,37	11149,1	9369,62	2,83286E+12	3330739075	4462,53	2420,14	1991,04	201,26	1913,29	1519,6	200,73	1777,2	1820,72	227,51	104,41	63,91	79,59
Talpa_europaea	CG.1993.633	R	y	20,8263	n	6,37578E+11	28946,44	12082,57	10188,05	3,56324E+12	3276490694,29*	4300,62*	N/A	N/A	188,82*	1745,65	1585,95	188,22	1885,56	1953,87	227,99	N/A	75,76	88,61
Talpa_europaea	CG.1993.633	L	y	20,8263	n	6,37578E+11	28946,44	12082,57	10188,05	3,56324E+12	3315032933,25*	4552,23	N/A	N/A	204,85*	1905,59	1551,44	207,57	1917,88	1890,66	233,46	N/A	67,54	87,71
Talpa_europaea	CG.2004.100	R	y	20,8263	n	5,60734E+11	28873,82	11982,14	9971,11	3,44971E+12	3326438885,71*	N/A	N/A	N/A	N/A	N/A	N/A	223,31	1888,54	1941,23	231,19	N/A	N/A	87,87
Talpa_europaea	CG.2004.100	L	y	20,8263	n	5,60734E+11	28873,82	11982,14	9971,11	3,44971E+12	3319030728,75*	N/A	N/A	N/A	N/A	N/A	N/A	215,73	1879,26	1923,11	235,46	N/A	N/A	78,67
Scalopus_aquaticus	CG.2006.377	R1	n	18,472	n	4,11471E+11	25473,74	13893,97	8171,4	2,89211E+12	3875924192,28*	4975,26*	2265,99*	1756,97*	243,9	1736,49	1305,76	258,82	1618,58	1800,65	255,21	N/A	71,99	92,93
Scalopus_aquaticus	CG.2006.377	L1	n	18,472	y	4,11471E+11	25473,74	13893,97	8171,4	2,89211E+12	4003774950	4989,48	2269,17	1678,61	252,95	1737,19	1314,5	237,09	1567,92	1793,34	266,07	102,84	67,96	97,77
Scalopus_aquaticus	CG.2006.377	R2	n	18,472	n	4,11471E+11	25719,69	13919,14	8137,13	2,91306E+12	3875924192,28*	4806,41*	2302,83*	1735,92*	239,58	1738,6	1342,43	252,55	1568,46	1808,26	248,45	N/A	72,92	80,75
Scalopus_aquaticus	CG.2006.377	L2	n	18,472	y	4,11471E+11	25719,69	13919,14	8137,13	2,91306E+12	4003774950	4961,01	2314,72	1673,52	253,04	1740,26	1372,07	248,08	1616,67	1792,48	260,63	108,03	75,66	93,95
Scalopus_aquaticus	CG.2006.377	R3	n	18,472	n	4,11471E+11	25112,36	13992,38	8175,79	2,87282E+12	3875924192,28*	4959,12*	2267,28*	1651,96*	240,71	1710,15	1296,79	265,8	1582,11	1766,89	251,04	N/A	80,36	81,25
Scalopus_aquaticus	CG.2006.377	L3	n	18,472	y	4,11471E+11	25112,36	13992,38	8175,79	2,87282E+12	4003774950	4971,69	2287,94	1696,88	253,09	1717,69	1384,98	261,55	1586,63	1788,63	256,69	100,42	67,23	85,29
Scapanus_orarius	CG.2006.381	R	n	21,5787	y	4,96238E+11	28704,5	13008,08	9408,96	3,51322E+12	2856230252	4972,3	2517,86	2033,82	194,39	2046,04	1555,14	196,93	1710,64	1967,37	203,4	114,44	71,72	104,67
Scapanus_orarius	CG.2006.381	L	n	21,5787	y	4,96238E+11	28704,5	13008,08	9408,96	3,51322E+12	2839646196	4995,2	2451,69	2056,3	205,53	2024,16	1489,64	212,99	1789,01	1949,97	205,03	117,5	73,89	101,8
Euroscaptor	CG.1959.1795	R	n	21,5787	n	4,65262E+11	27330,21	10188,68	8490,86	2,36435E+12	4489336756,11*	4880,13	N/A	N/A	N/A	1643,49	1433,96	220,27	1751,14	1438,53	241,06	N/A	N/A	103,97
Euroscaptor micrura	CG.1959.1795	L	n	21,5787	n	4,65262E+11	27330,21	10188,68	8490,86	2,36435E+12	4469374920,51*	4980,07	N/A	N/A	N/A	1724,48	1440,89	214,31	1664,65	1374,61	247,26	N/A	N/A	96,5
Talpa_europaea	CG.1962.2033	R	n	21,5787	y	5,02026E+11	29055,63	11724,16	10776,93	3,67119E+12	3196383978	4708,95	2486,06	1943,29	188,53	1887	1423,55	184,52	1817,92	1814,39	214,36	114,87	73,41	91,2
Talpa_europaea	CG.1962.2033	L	n	21,5787	n	5,02026E+11	29055,63	11724,16	10776,93	3,67119E+12	3260553876,84*	4742,51	2495,61	1935,32	191,32	2045,66	1341,06	181,56	1830,98	1906,31	221,99	112,14	66,96	99,93
Talpa_europaea	CG.1993.679	R	n	21,5787	n	5,86296E+11	28627,15	11653,44	9761,45	3,25647E+12	N/A	N/A	N/A	N/A	N/A	N/A	N/A	169,17*	1932,19	1865,34	209,08	N/A	N/A	N/A
Talpa_europaea	CG.1993.679	L	n	21,5787	n	5,86296E+11	28627,15	11653,44	9761,45	3,25647E+12	N/A	N/A	N/A	N/A	N/A	N/A	N/A	166,51*	1904,77	1992,09	205,77	N/A	N/A	N/A
Mogera_kobeae	CG.2000.197	R	y	23,5	y	7,96599E+11	33328,38	13658,36	12092,82	5,50478E+12	7526330203	5382,87	2474,26	2239,56	212,02	1914,52	1725,56	250,03	2175,73	2244,16	265,21	129,11	64,48	98,02
Mogera_kobeae	CG.2000.197	L	y	23,5	n	7,96599E+11	33328,38	13658,36	12092,82	5,50478E+12	7602436525,48*	5272,21	2385,33*	2207,95*	209,18	1842	1639,16	243,2	2148,27	2300,63	258,03	N/A	63,96	101,71
Euroscaptor_longirostris	CG.1874.516	R	y	23,5	n	2,89328E+11	23783,6	10283,61	8761,05	2,14279E+12	3965350268,45*	N/A	N/A	N/A	N/A	N/A	N/A	193,11	1481,55*	1542,85*	205,26	N/A	N/A	102,92*
Euroscaptor_longirostris	CG.1874.516	L	y	23,5	n	2,89328E+11	23783,6	10283,61	8761,05	2,14279E+12	4039495871,82*	4436,92*	N/A	N/A	197,8	1612,56	1377,69	180,56	1437,19	1517,21	187,6	N/A	65,82	103,59
Galemys_pyrenaicus	CG.1982.189	R	y	23,5	y	6,0383E+11	26411,21	13226,19	11476,05	4,00881E+12	4987549291	4607,22	2158,5	1855,98	228	2439,04	1912,29	214,16	1957,19	2063,67	246,05	106,63	80,51	97,33
Galemys_pyrenaicus	CG.1982.189	L	y	23,5	y	6,0383E+11	26411,21	13226,19	11476,05	4,00881E+12	4941963982	4863,25	2363,68	1735,5	228,58	2491,39	2140,05	218,83	1891,56	2009,78	244,18	101,49	76,56	97,23
Crocidura_russula	CG.2008.116	R	y	11,35	y	###########	16216,67	7571,07	4560,07	5,59874E+11	1432852485	2766,03	1342,65	1182,57	143,64	1165,74	923,51	144,46	746,68	961,48	162,62	97,46	74,47	82,87
Crocidura_russula	CG.2008.116	L	y	11,35	y	###########	16216,67	7571,07	4560,07	5,59874E+11	1435427774	2807,74	1381,16	1113,94	142,59	1155,88	869,58	152,82	783,11	943,52	166,53	102,2	76,27	89,05
Sorex_araneus	CG.1962.2010	R	y	11,35	y	###########	16228,29	5917,22	5283,33	5,07339E+11	1263291126	3037,17	1507,76	956,41	156,32	1321,35	1035,37	171,17	948,22	927,41	177,35	89,39	72,24	91,13
Sorex_araneus	CG.1962.2010	L	y	11,35	y	###########	16228,26	5917,22	5283,33	5,07338E+11	1249818882	2974,71	1465,48	924	147,5	1272,98	993,47	166,83	986,09	924,01	172,17	94,76	77,82	88,67
Atelerix algirus	CG.1955.650	R	n	32,7	y	4,73073E+12	50308,01	30584,96	14897,19	2,29218E+13	14382571563	5773,74	2556,33	2888,59	303,15	2315,56	2544,79	368,95	1959,06	1913,1	364,45	104,45	72,56	90,31
Atelerix algirus	CG.1955.650	L	n	32,7	y	4,73073E+12	50308,01	30584,96	14897,19	2,29218E+13	14233647265	5788,56	2249,11	2840,38	301,24	2304,33	2582,82	352,39	1919,77	1968,28	329,55	102,14	84,98	89,22
Erinaceus europaeus	CG.1963.381	R	n	32,7	y	5,04543E+12	50470,42	32733,74	13452,39	2,22245E+13	11173520968	5505,47	2404,14	2661,27	300,04	2251,84	2526,75	330,67	1903,17	2010,89	323,47	96,12	85,32	93,91
Erinaceus europaeus	CG.1963.381	L	n	32,7	y	5,04543E+12	50470,42	32733,74	13452,39	2,22245E+13	10892280137	5399,69	2328,32	2589,47	304,72	2214,27	2552,06	323,21	1927,89	1873,76	319,29	100,62	90,04	92,02

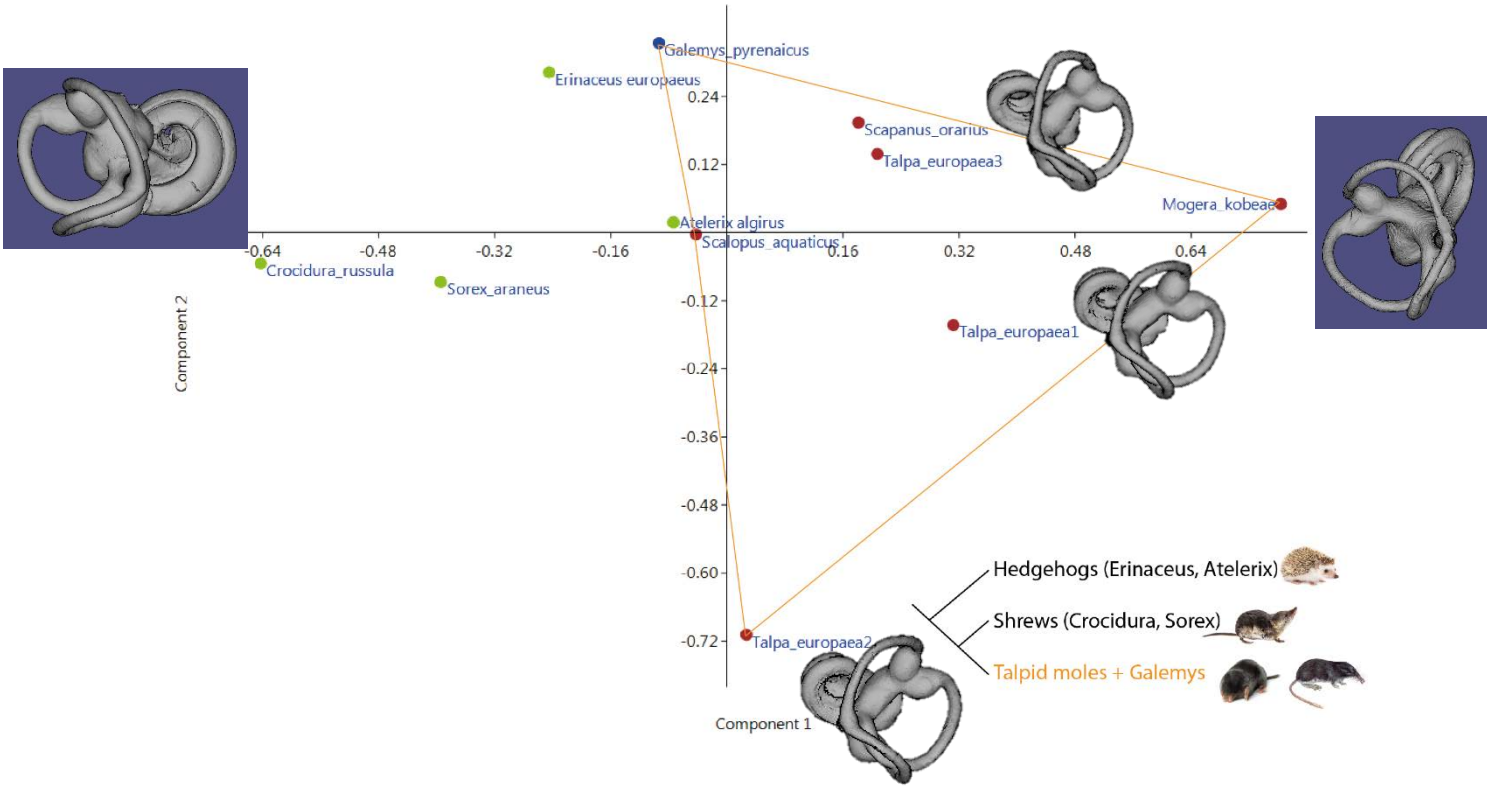

Figure 3.1: Result of the PCA of 12 linear measurements taken on the semicircular canal system of selected eulipotyphlans. 93% of the total variance is explained by the first three PCs.

The results of the PCA shows that :

1) there is an intraspecific variation of the morphology of the semicircular canal system of *Talpa*, mostly shown by the PC2. The four *Talpa* are clustered at positive values of PC1 but are scattered along the PC2.
2) the PC1 apparently discriminates the talpid moles (*Talpa*, *Scapanus*, *Mogera*) but it is most likely due to their phylogenetic affinities (clade Talpidae = talpid moles+*Galemys*)

This preliminary study highlights the need to increase our sample with more *Talpa* and more Eulipotyphla of various lifestyles (already scanned and pending to be treated, see Appendix 1), and to improve our data by using landmark coordinates rather than linear measurements.

ANNEXE 4. Etude préliminaire du labyrinthe osseux de thérapsides au comportement fouisseur

APPENDIX 4. Preliminary study of the bony labyrinth of therapsids with fossorial habits

In the framework of a supervised internship (in between voluntary work M1/M2): Rohan Mansuit, Master SEP MNHN, Juillet 2016: *Anatomical comparsion of the 3D models of the inner ears of tritylodontids*.

Therapsida is the most inclusive clade comprising mammals and their fossil relatives (Fig. 4.1). Throughout decades of discovery in the mesozoic fossil records, fossorial behaviour has been documented thanks to taphonomic evidence or even fossorial skeletal specializations (such as scratch digging) in many mammaliaform lineages (see Luo, 2007 for a review; Fig. 2).

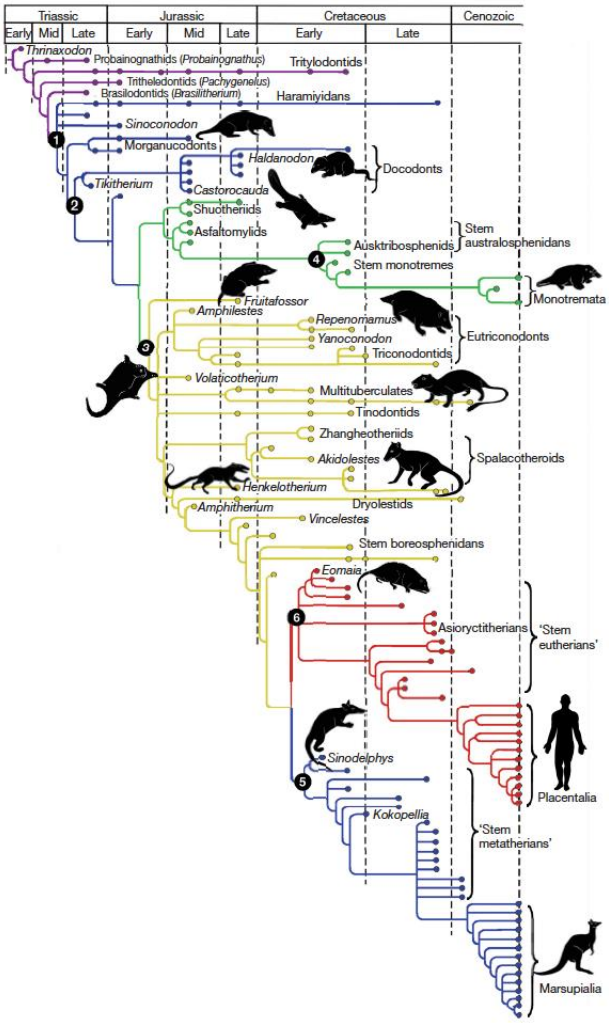

Figure 4.1: Phylogeny and diversification of Therapsida from Luo (2007).

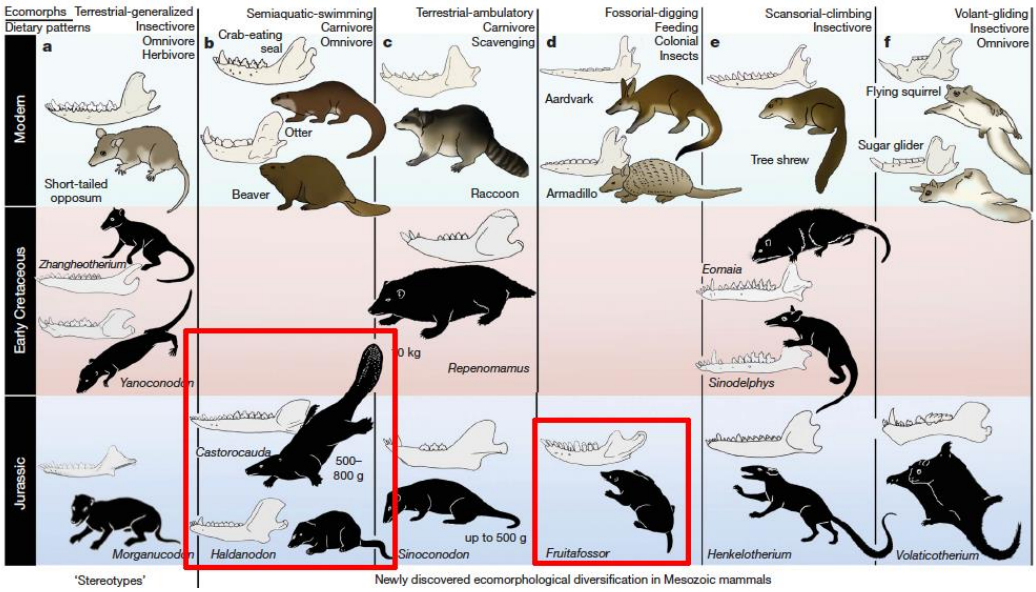

Figure 4.2: Ecological diversity of Mesozoic therapsids and convergences to modern mammal ecomorphotypes (from Luo, 2007).

Fossorial abilities are now shown to be widespread in multituberculates (Kielan-Jaworowska & Gambaryan, 1994). In docodonts, *Castorocauda* exhibits hypertrophied burrowing limbs and a broad, scaly and beaver-like tail for swimming (Ji et al, 2006), and *Haldanodon* presents morphological convergences to semi-aquatic moles (Martin, 2005, 2006). *Fruitafossor*, an early offshoot of mammal related to therians (Luo & Wible, 2005) has hypertrophied digging-limb features and a unique columnar and enamel-less teeth, which reminds the specializations for feeding on colonial insects, along with limbs built for scratch-digging, evolved convergently in armadillos and aardvarks.

Many fossilised burrow casts were found in the Early Triassic of southern Africa, the most famous being that comprising a unique mixed-species association: an injured temnospondyl amphibian (*Broomistega*) that sheltered in a burrow occupied by an aestivating therapsid (*Thrinaxodon*) (Fernandez et al., 2013).

Studies of the postcranial bone histology of nonmammaliaform therapsids have provided much information pertaining to their biology: for example, the thick bone walls of the limbs of *Tritylodon* (Botha, 2002) and *Trirachodon* (Botha & Chinsamy, 2004) suggest that they had a fossorial lifestyle.

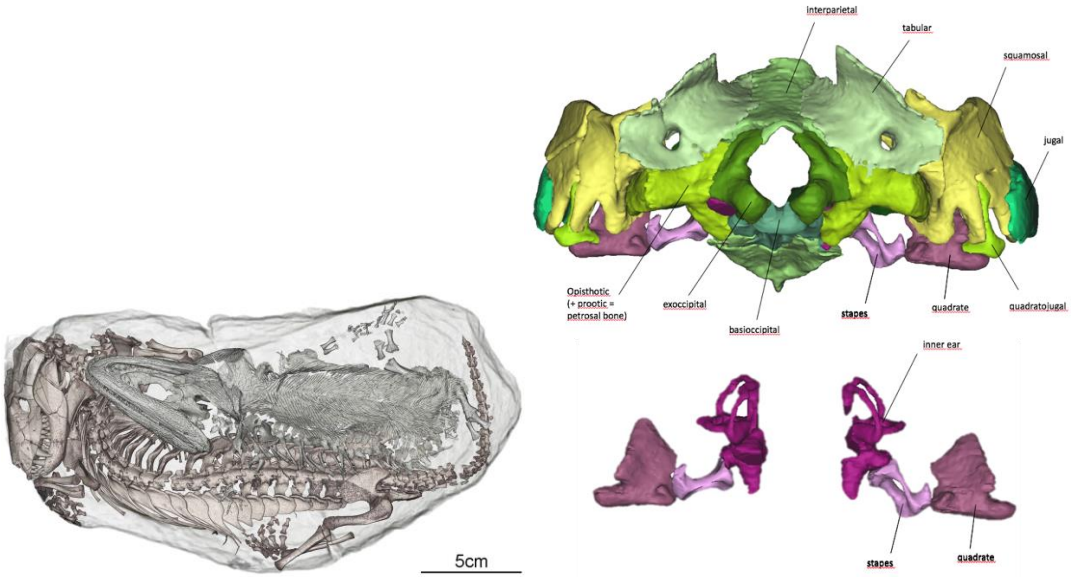

Figure 4.3: 3D rendering of the content inside the burrow cast containing the couple *Thrinaxodon*+temnospondyl (left) and 3D rendering of the skull end inner and middle ear of *Thrinaxodon liorhinus* (BP/1/7199).

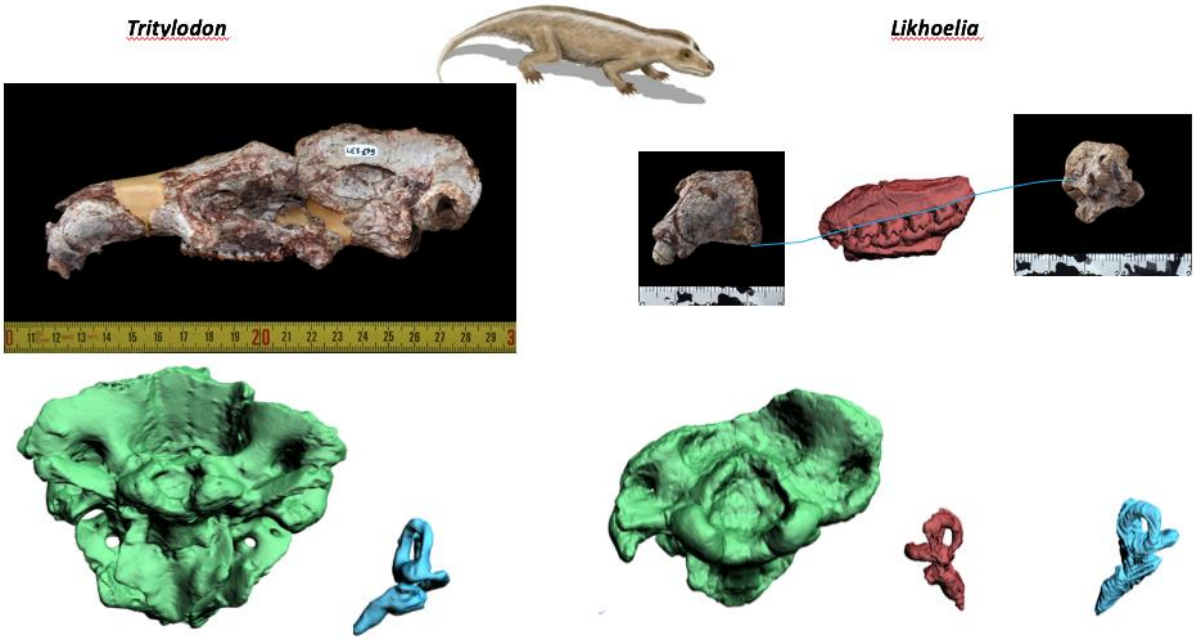

Figure 4.4: Skulls and 3D rendering of the basicranium (occiput facing) and inner ear of *Tritylodon longaevus* (MNHN.F.LES.179) and *Likhoelia ellenbergeri* (MNHN.F.LES.1, 2, 3).

The present study represents the first attempt to link the morphology of the bony labyrinth of selected therapsids to their fossorial lifestyle. Based on the Synchrotron images of *Thrinaxodon liorhinus* (BP/1/7199, Fig. 4.3) and the CT images of well-preserved skulls of two tritylodontids [*Tritylodon longaevus* MNHN.F.LES.179, and *Likhoelia ellenbergeri* MNHN.F.LES.1, which might be a junior synonym of the first] (Fig. 4.4).

The first steps of these studies (i.e., preparing and then exploiting the CT data) were very time-consuming (about 5 months dedicated to it) and kept me very busy at the beginning of my PhD. The segmentation of the entire skull of *Thrinaxodon* and the interpretation of its anatomy resulted in a pedagogic 3D anatomic atlas of an early therapsid skull. The revision of *Likhoelia ellenbergeri* from its first description by Ginsburg (1961, 1962) suggests a few

anatomical incoherencies (e.g., right maxillary instead of left) and that this specimen is more likely a juvenile form of *Tritylodon* (anatomy, dental eruption).

Two studies are foreseen:

- Comparative study of the cranial anatomy of *Tritylodon longaevus* and *Likhoelia ellenbergeri* from the basal Jurassic of Lesotho (Thabana Morena): do they pertain to the same species, *Likhoelia* being a juvenile form of *T. longaevus*?
- Does the inner ear morphology of Mesozoic therapsids correlate with their fossorial habits? The example of *Thrinaxodon* and *Tritylodon*.

References

Botha, J. (2002). *The palaeobiology of the non-mammalian cynodonts deduced from bone microstructure and stable isotopes* (Doctoral dissertation, University of Cape Town).

Botha, J., & Chinsamy, A. (2004). Growth and life habits of the Triassic cynodont Trirachodon, inferred from bone histology. *Acta Palaeontologica Polonica*, 49(4).

Fernandez, V., Abdala, F., Carlson, K. J., Rubidge, B. S., Yates, A., & Tafforeau, P. (2013). Synchrotron reveals Early Triassic odd couple: injured amphibian and aestivating therapsid share burrow. *PLoS One*, 8(6), e64978.

Ginsburg, L. (1961). Un nouveau tritylodonte du Trias supérieur du Basutoland (Afrique du Sud). *Comptes Rendus hebdomadaires des Séances de l'Académie des Sciences*, 252(24), 3853.

Ginsburg, L. (1962). Les tritylodontes. *Collogues Internationaux du Centre national de la Recherche Scientifique*, 104, 187-192.

Ji, Q., Luo, Z. X., Yuan, C. X., & Tabrum, A. R. (2006). A swimming mammaliaform from the Middle Jurassic and ecomorphological diversification of early mammals. *Science*, *311*(5764), 1123-1127.

Kielan-Jaworowska, Z., & Gambaryan, P. P. (1994). Postcranial anatomy and habits of Asian multituberculate mammals. *Fossils Strata*, 36, 1–92.

Luo, Z. X. (2007). Transformation and diversification in early mammal evolution. *Nature*, 450(7172), 1011-1019.

Luo, Z.-X., & Wible, J. R. (2005). A new Late Jurassic digging mammal and early mammalian diversification. *Science*, 308, 103–107.

Martin, T. (2005). Postcranial anatomy of *Haldanodon exspectatus* (Mammalia, Docodonta) from the Late Jurasssic (Kimmeridgian) of Portugal and its bearing for mammalian evolution. *Zool. J. Linn. Soc.*, 145, 219–248.

Martin, T. (2006). Paleontology: early mammalian evolutionary experiments. *Science*, 311, 1109–1110.

The Linnean Society of London ZOOLOGICAL Journal of the Linnean Society

Zoological Journal of the Linnean Society, 2016. With 7 figures

Computed microtomography investigation of the skull of Cuvier's famous 'opossum' (Marsupialiformes, Herpetotheriidae) from the Eocene of Montmartre

CHARLÈNE SELVA* and SANDRINE LADEVÈZE*

Centre de Recherche sur la Paléobiodiversité et les Paléoenvironnements (CR2P, UMR 7207), Sorbonne Universités MNHN CNRS UPMC–Paris 6, Muséum national d'Histoire naturelle, 57 rue Cuvier CP 38, F-75005 Paris, France

Received 8 March 2016; revised 8 July 2016; accepted for publication 13 August 2016

Two centuries ago, Georges Cuvier, the father of vertebrate palaeontology, described an almost complete skeleton of a small 'opossum' from the Montmartre Gypsum (late Eocene): *Peratherium cuvieri*. His description of the visible bones remains famous, as it was an unequivocal demonstration of his principle of correlation of parts. With the state-of-the-art technology of X-ray microtomography (computed tomography scanning), it is now possible to extend the investigation of the Cuvier's 'opossum', one of the most iconic specimens of the Muséum national d'Histoire naturelle (MNHN). Beneath the visible upper cheek teeth the skull is damaged and fragmented, but provides significant new data, with the most complete and informative structures being the paired petrosal bones. Comparisons with the didelphid *Marmosa murina* (Linnaeus, 1758) and three other fossil herpetotheriids [*Amphiperatherium minutum* Aymard, 1846, *Herpetotherium* cf. *fugax* Cope, 1873, and *Peratherium elegans* (Aymard, 1846)] suggest that dental features alone are not sufficient to discriminate between the different species, being based on highly variable, polymorphic features of the stylar shelf. The anatomy of the petrosal bone, which has yet to be described for *P. elegans* or *A. minutum*, reveals marked differences between *P. cuvieri* and *H.* cf. *fugax*, however, which brings into question the monophyly of Herpetotheriidae. Further investigation of petrosal characters for herpetotheriids would therefore shine new light on the phylogenetic affinities of Herpetotheriidae, in terms of both the relationships within the family and the position of Herpetotheriidae within Metatheria as a whole.

© 2016 The Linnean Society of London, *Zoological Journal of the Linnean Society*, 2016
doi: 10.1111/zoj.12495

ADDITIONAL KEYWORDS: CT scanning – Herpetotheriidae – Metatheria – *Peratherium cuvieri* petrosal anatomy.

INTRODUCTION

In 1804, the famous French palaeontologist Georges Cuvier described 'un squelette presque entier d'un petit quadrupède du genre des Sarigues, trouvé dans la pierre à plâtre des environs de Paris' (Cuvier, 1804: 277). This small fossil mammal from the late Eocene of the Montmartre Gypsum enabled Cuvier to demonstrate a fundamental law in palaeontology: the principle of correlation of parts, which allows one to infer the entire body of an organism from only part of its anatomy. Thus it became one of the most iconic historic specimens of the Muséum national d'Histoire naturelle (MNHN). In his memoirs, Cuvier (1804) described in detail the bones emerging from the gypsum matrix and how he compared them with the extant marsupial *Marmosa murina* (Linnaeus, 1758). Emphasising certain morphological characters, such as the elevation of the condyle, the width and height of the coronoid process, and the acute protrusion that forms the posterior angle of the jaw (observed on

*Corresponding authors.
E-mails: charlene.selva@edu.mnhn.fr; ladeveze@mnhn.fr

the right mandible), Cuvier identified the specimen as belonging to *Didelphes* (a marsupial group of imprecise definition, characterized by a generalized dental morphology, including 'opossum-like' molars). Through a detailed analysis of the morphology and arrangement of cusps on the visible molars, Cuvier confirmed his initial identification and was able to determine the nature of the specimen, which was assigned to *Peratherium cuvieri* (Fisher, 1829) a few years later. By extrapolation Cuvier predicted that hidden in the matrix were epipubic bones, a marsupial characteristic associated with 'opossum-like' teeth. Subsequently, these bones were extracted from their matrix in the presence of the foremost naturalists of the time, confirming Cuvier's theory; however, Cuvier did not attempt to access other bones enclosed in the matrix and his investigation on this specimen ended there. Nevertheless, more than two centuries later, it is clear that this fossil has not yet revealed all its secrets, because the visible upper jawbone suggests that the skull bones are probably present in the matrix. Using, state-of-the-art technology, X-ray computed microtomography (CT) scanning, it is now possible to extend Cuvier's investigation without damaging this historically significant specimen.

Peratherium cuvieri belongs to a key taxon in the evolutionary history of Metatheria (the clade of therian mammals that includes marsupials and all taxa that are more closely related to them than to placentals), and especially the origin of opossums (Didelphidae) (Sánchez-Villagra *et al.*, 2007; Horovitz *et al.*, 2008): the extinct family Herpetotheriidae. Herpetotheriids are marsupialiforms (*sensu* Vullo *et al.*, 2009), with teeth that are often described as 'opossum-like', and they are documented from Europe, Asia, Africa, and possibly South America, with an age range that spans from the Cretaceous to the Miocene (see Ladevèze, Smith & Smith, 2012 for references).

In this paper we continue Cuvier's investigation using CT-scanning technology to create three-dimensional (3D) reconstructions of the bones hidden in the matrix. These anatomical structures are observed here for the first time and compared, in the manner of Cuvier, to those of the extant mouse opossum *M. murina* and other members of Herpetotheriidae. After a general description of the skull and teeth, we focus on the well-preserved auditory region and particularly the ear bones (petrosals). This anatomical region is of particular interest as it has been shown to be phylogenetically informative (e.g. Sánchez-Villagra & Wible, 2002; Ladevèze, 2004), and it is likely to reveal species-specific features and to further clatify the taxonomic boundaries of the family Herpetotheriidae.

MATERIAL AND METHODS

Taxonomy and description of the specimen

The specimen is usually referred to as 'Cuvier's opossum', although it is not a didelphid, but rather a member of the 'opossum-like' fossil family Herpetotheriidae. It is the holotype for the species *P. cuvieri*, and it is currently stored in the palaeontological collections of the MNHN (Fig. 1). It currently comprises four parts: two gypsum slabs and two fragments of mandibles (see below). These last two fragments seem to correspond to two of the three fragments indicated in the register of Cuvier that were imprecisely numbered from 7906 to 7908 (Fig. S1, Supporting Information). Following the reorganization of the Montmartre Gypsum collection, new collection numbers starting with GY have been assigned to the material from this quarry. Consequently, the new numbers assigned to the holotype of *P. cuvieri* are: GY679a (formerly no. 7905 in Cuvier's collection), for the slab with the epipubic bones; GY679b (formerly no. 7904 in Cuvier's collection), for the slab with the cranial remains; GY679c (formerly nos 7906, 7907, or 7908 in Cuvier's collection), for the right mandible fragment with m2–m3; and GY679d (formerly nos 7906, 7907, or 7908 in Cuvier's collection), for the other right mandible fragment (teeth are not present on this last piece).

In his memoirs, Cuvier (1804) specified that he observed the following parts of the dental anatomy: the four right upper molars, the right upper canine, the right lower second, third, and fourth molars, one left anterior lower molar, and the left lower canine. Of these, the left anterior lower molar and the left lower canine are currently not observable. They are not listed in detail on the register of Cuvier, suggesting that they were not separate from the main slab, and yet they are not present on the slabs today. Finally, m4 is present neither as an individual element nor together with m2 and m3; it appears to have been lost. Despite the conservation efforts made on this specimen, parts of it are unfortunately missing and the specimen from the time of Cuvier differs from the 21st century specimen.

Locality and stratigraphic data

Cuvier's opossum was discovered in the upper bed of the gypsum quarries of Montmartre in Paris (Crochet, 1980; Fig. 2). This layer is dated Priabonian, from 37.8 to 33.9 Mya, which represents level MP17 (Gradstein *et al.*, 2012). The depositional environment corresponds to an arid lagoon system that was more connected to the rivers and lakes than were the lower beds (Dollot, Godbille & Ramond, 1905).

© 2016 The Linnean Society of London, *Zoological Journal of the Linnean Society*, 2016

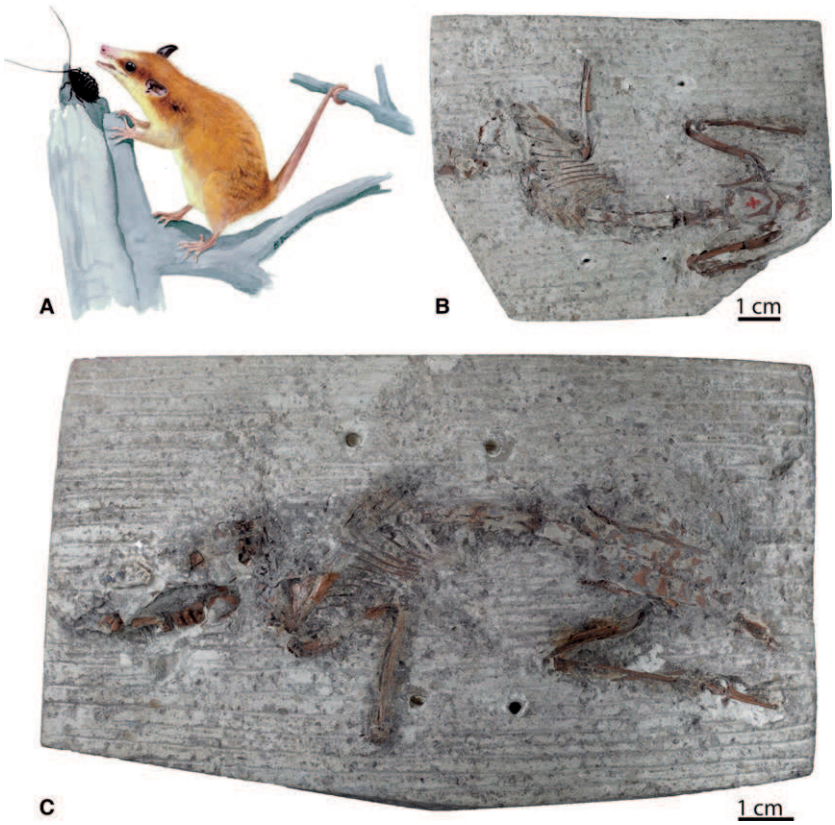

Figure 1. Artistic impression of 'Cuvier's opossum' *Peratherium cuvieri* (©B. Duhem, MNHN) (A), with photographs of the GY679a slab with the epipubic bones (B) and the GY679b slab with the cranial portion (C). Note the presence of the red cross indicating the location of epipubic bones on plate GY679a (B). Note the position of the emerged right jawbone, suggesting that the skull bones are probably present in the matrix.

This gypsum bed contains numerous bones belonging to the terrestrial fauna described by Cuvier, such as *Anoplotherium commune* Cuvier, 1804, *Palaeotherium magnum* Cuvier, 1804, and *Plagiolophus minor* (Cuvier, 1804). Another herpetotheriid marsupial was found in the same deposit: *Amphiperatherium minutum* Aymard, 1846.

CT-SCANNING METHODOLOGY

Micro-CT technology was used to extract information from specimen GY679b regarding the otherwise inaccessible bones hidden in the matrix. CT scanning was conducted at the X-ray Tomography Imagery Platform AST-RX of MNHN, using a GE Sensing and Inspection Technologies phoenix|x-ray v|tome|x L240-180 CT scanner. The scan was made with an isotropic voxel size of 0.02342520 μm under a voltage of 180 kV and a current of 0.2 mA. Three thousand projections over 360° with 333 ms of exposure time were used, with three averaged images per projection and one skipped image before each projection. The data were reconstructed using phoenix datos|x® 2.0 reconstruction software, and then exported into a 16-bit TIFF image stack of 1360 slices. Post-processing was carried out at the Palaeontology Imaging Unit of the MNHN Département Histoire de la Terre/CNRS UMR 7207. Mimics® 15.0 and Mimics® 17.0 (Materialise) were used for the 3D modelling (segmentation and 3D object rendering). For better rendering, 3D objects have undergone smoothing. Several parameters (iteration and smooth factor) were first tested on models of the teeth, to ensure that the models are as faithful to reality as possible. The same parameters were afterwards applied to the 3D models of the petrosal, bony labyrinth, and cranium. The 3D models of the bones are described and illustrated in the results section.

SPECIMENS OF COMPARISON

In order to complement Cuvier's original observations, we performed anatomical comparisons on the extant didelphid *M. murina* (MNHN-CG-2001-1966,

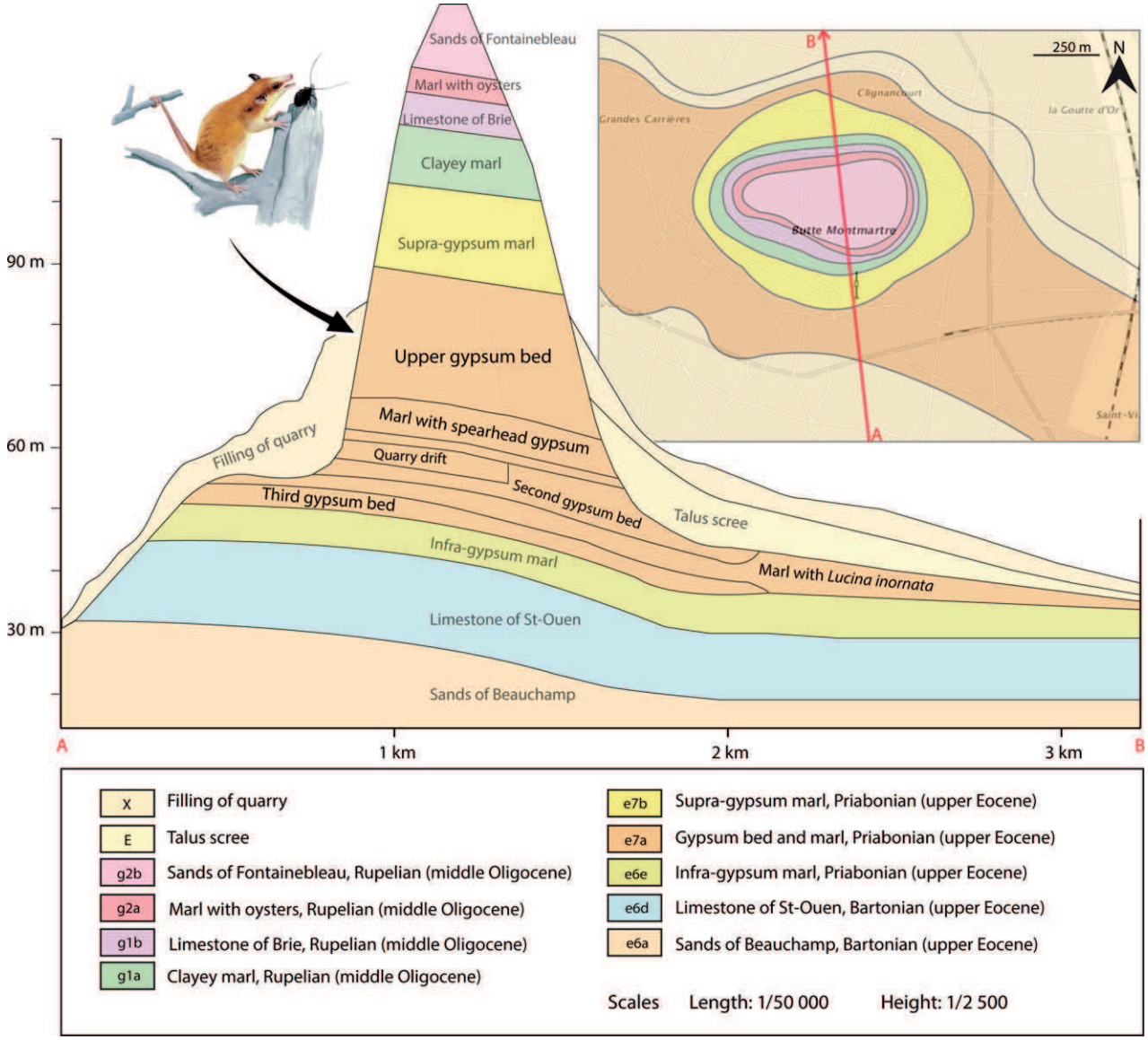

Figure 2. Location of the fossil remains of *Peratherium cuvieri* on the stratigraphic section of the 'butte de Montmartre' (modified from the geological map of Paris 1 : 50 000; Goguel & Soyer, 1973).

-2239), which Cuvier considered to be the extant species that most closely resembles the fossil specimen: 'Le *sarigue marmose* a presque les mêmes proportions que notre animal pour la largeur [apophyse coronoïde], mais la hauteur y est un peu moindre' (Cuvier, 1804: 281).

Three species of herpetotheriids for which the cranial anatomy is known were also used for comparative purposes. *Peratherium elegans* (Aymard, 1846) is the type species of the genus *Peratherium*. Specimen 2004-6-322-RON (PAR 39.22) was used for the cranial comparison, specimen MNHN-RZN-16 was used for comparison of the upper molars, and specimen MNHN-RZN-2 (holotype) was used for comparison of the lower molars (both are illustrated by Ladevèze *et al.*, 2012). At present, there is no petrosal available for description and comparison for this species (C.S. and S.L., unpubl. data).

Amphiperatherium minutum (Aymard, 1846) is a herpetotheriid that is contemporaneous with *P. cuvieri*. Specimen GY682 (formerly nos 7911 and 7912 of Cuvier's collection) also comes from the gypsum of Montmartre. The first piece is a skull and hemimandible preserved in occlusion. Using X-ray CT imaging and 3D modelling, the right P1, P2, DP3, M1, and M2 are visible in the upper jaw of this specimen, whereas in the lower jaw, the right p2, dp3, m1, m2, and m3 are observable. The second piece

© 2016 The Linnean Society of London, *Zoological Journal of the Linnean Society*, 2016

preserves the left P1, P2, DP3, M1, and M2. The teeth are very damaged, and hence the lingual part is absent. It is also noteworthy that this individual is a juvenile because the DP3 and dp3 are present. Currently, there is no petrosal available for description and comparison for this species (C.S. and S.L., unpubl. data).

Another herpetotheriid of interest is *Herpetotherium*, the skull of which was described by Gabbert (1998). More recently, *Herpetotherium* cf. *fugax* Cope, 1873 was described by Horovitz *et al.* (2008) and has been included in several phylogenetic analyses (e.g. Sánchez-Villagra *et al.*, 2007; Beck *et al.*, 2014; Williamson, Brusatte & Wilson, 2014). This is the only other herpetotheriid species for which the petrosal is known (ZMB 50672; see Horovitz *et al.*, 2008).

Nomenclature for descriptions

The following description of the skull of *P. cuvieri* is based on a comparison with extant didelphids, especially *M. murina* (Wible, 2003; Voss & Jansa, 2009).

The nomenclature for the tooth morphology is based on previous anatomical studies of the mammalian tribosphenic teeth (e.g. Van Valen, 1966; Reig, Kirsch & Marshall, 1987). The nomenclature used here to describe the petrosal is based on previous anatomical studies of the mammalian basicranium (e.g. Archer, 1976; MacPhee, 1981; Wible, 1990, 2003; Ladevèze, 2004).

INSIDE THE SKULL: ANATOMICAL DESCRIPTION OF PREVIOUSLY UNDESCRIBED FEATURES FOR *PERATHERIUM CUVIERI*

SYSTEMATIC PALAEONTOLOGY

Mammalia Linnaeus, 1758
Theria Parker and Haswell, 1897
Metatheria Huxley, 1880
Marsupialiformes Vullo *et al.*, 2009
Herpetotheriidae (Trouessart, 1829)
Peratherium Aymard, 1850
Peratherium cuvieri (Fisher, 1829)

Emended diagnosis of P. cuvieri (modified from Crochet, 1980): Small-sized species of *Peratherium*. Upper molars increase in size from M1 to M3; protofossa relatively large; stylar region moderately expanded and not constricted at the level of stylar cusp C (where this cusp is identifiable); conical stylar cusps, B being prominent, C not always identifiable, and when present isolated from B and D, ectoflexus variable (asymmetrical in the holotype, symmetrical in other specimens), and more pronounced on M3. Lower molars increase in size from m1 to m3, m4 subequal in length to the other molars (either slightly shorter or slightly longer, depending on the specimens being compared), posterior cingulid clearly distinct, except on m4, in which it is often absent.

Type locality: Gypsum from Montmartre, Paris, France.

Age: Priabonian (33.9–37.8 Mya), Late Eocene, MP17 (Gradstein *et al.*, 2012).

Holotype: MNHN GY679 in the Montmartre Gypsum collections, MNHN. The holotype is illustrated by Cuvier (1804: pl. 19; 1822: pl. 71).

Anatomical description of the skull

Crushing and fragmentation along almost the entire length of the skull of *P. cuvieri* (Fig. 3), and particularly in the cranial vault and orbitotemporal region, prevent the identification of some major bony relationships and some foramina and sulci, especially in the orbitotemporal and basicranial areas.

The rostrum of *P. cuvieri* is mostly composed of the maxillae. The premaxillae are missing; only a small piece of bone that might have been part of the right premaxilla is preserved, just anterior to the canine. Most of the lateral surface of the rostrum (Fig. 3B) is formed by the maxillae, as in didelphids. The well-preserved right maxilla contains the canine, alveoli for the double-rooted P2 and P3, and the four molars.

A very tiny foramen above the M1 might be an accessory foramen associated with the opening of the infraorbital canal (which is usually found above P2 or P3 in didelphids), or more probably a nutrient foramen.

The zygomatic arches are not preserved. There is no clear suture with the jugal visible, but the right maxilla projects a posterolateral process that protrudes as the anteriormost part of the zygomatic arch (which is usually formed by the jugal in didelphids).

The nasal bones are only partially preserved, and they are probably broken at their anterior ends (as is the anteriormost part of the rostrum). They are wider posteriorly than anteriorly, as in most didelphids, but they do not extend as far posteriorly as the tiny piece of bone that we interpret as the lacrimal (see below). Concurrent with the lack of nasolacrimal contact, the maxillae and frontals are in contact, as in didelphids.

© 2016 The Linnean Society of London, *Zoological Journal of the Linnean Society*, 2016

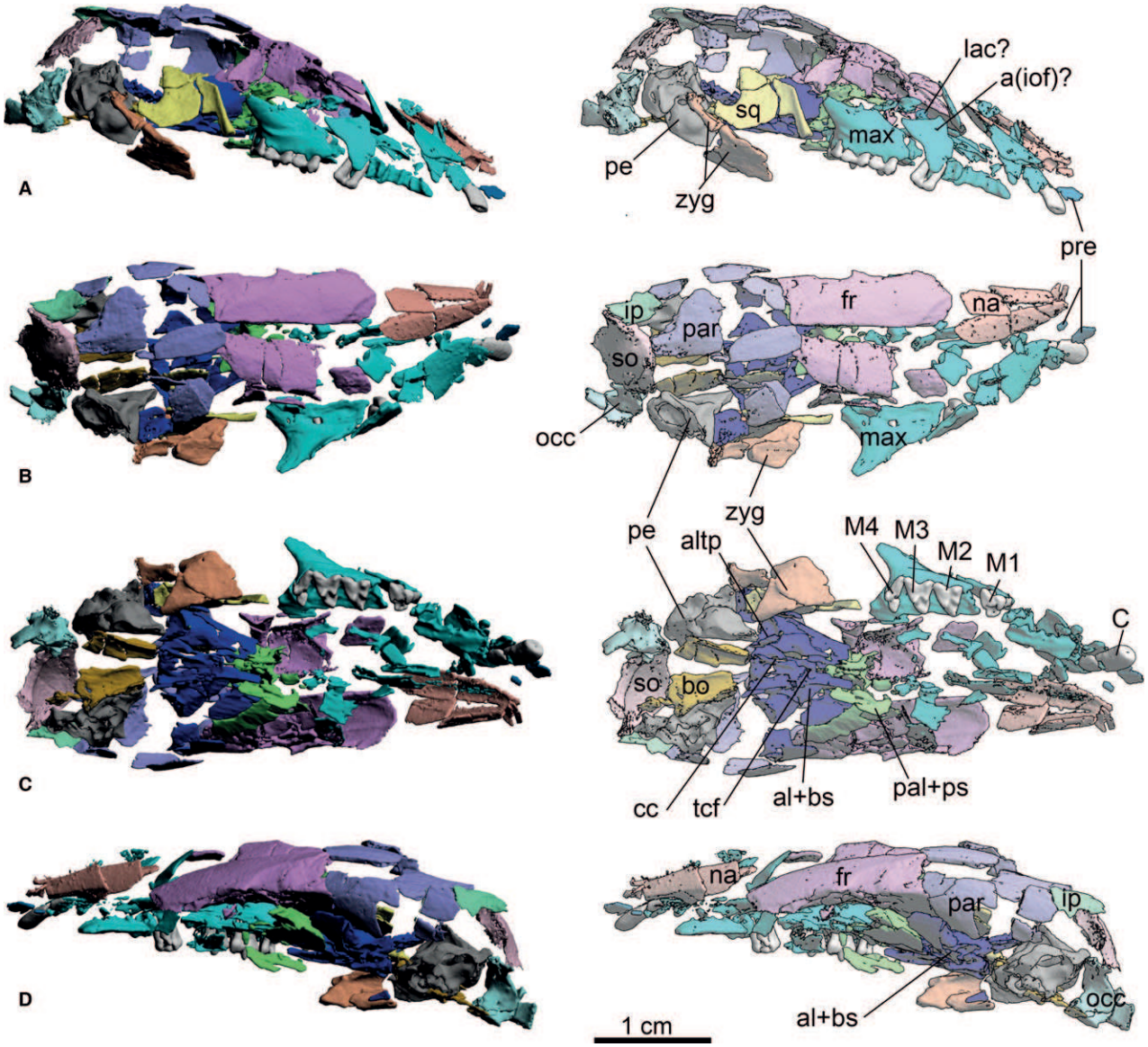

Figure 3. Three-dimensional (3D) reconstruction of the skull of *Peratherium cuvieri* (GY679b) in right-lateral (A), dorsal (B), ventral (C), and left-lateral (D) views. a(iof)?, possible accessory foramen of the infraorbital foramen; al+bs, alisphenoid and basisphenoid; altp, alisphenoid tympanic process; bo, basioccipital; C, upper right canine; cc, carotid canal; fr, frontal; ip, interparietal; lac?, possible lacrimal; max, maxillary; na, nasal; M1 to M4, upper right molars; occ, occipital; pal+ps, palatine and presphenoid; par, parietal; pe, petrosal; pre, premaxillary; so, supraoccipital; sq, squamosal; tcf, transverse canal foramen; zyg, zygomatic arch.

A tiny fragment of bone pierced by two small foramina lies in the anteriormost part of the orbit, between the right maxilla and frontal. This bone is likely to be a part of the right lacrimal with its two lacrimal foramina, as observed in most didelphids. No clear contact with any bone can be identified because of the state of preservation of the specimen. The identified right lacrimal is close to the palatine bone, as observed in didelphids, in which it is in posteroventral contact with the palatine bone.

The medial wall of the didelphid orbit is generally perforated by the sphenopalatine foramen in the palatine, the ethmoid foramen between the orbitosphenoid and frontal, the sphenorbital fissure between the palatine, orbitosphenoid, alisphenoid, presphenoid, and sometimes pterygoid, and the foramen rotundum in the alisphenoid. Unfortunately, the damaged and fragmented medial wall of the orbit of *P. cuvieri* does not preserve any identifiable foramina.

© 2016 The Linnean Society of London, *Zoological Journal of the Linnean Society*, 2016

The two frontal bones are the best-preserved cranial bones in *P. cuvieri*. The left frontal is almost complete. It produces, at its midpoint, a distinct postorbital process, which forms a flattened, triangular tubercle, as in most species of *Marmosa*, *Caluromys*, *Caluromysiops*, *Glironia*, and *Tlacuatzin* (Voss & Jansa, 2009).

The bones forming the lateral wall of the braincase (usually squamosal, parietal, and interparietal in didelphids) are only partially preserved. Three small pieces of bone on the lateral right side of the skull are considered here as part of the squamosal, bordered dorsally by the frontal and parietal. The posteriormost part of this region of the squamosal probably articulated with the jugal part of the zygomatic arch.

Only the anteriormost and dorsal parts of the parietal are preserved on both sides of the skull. There is no sagittal crest observed, as in most didelphids. A parietal–alisphenoid contact is exhibited by *P. cuvieri* (frontal–squamosal contact is absent), as in all didelphids except *Metachirus* (Voss & Jansa, 2009).

A fragment of bone on the left side of the skull lying dorsal to the parietal and contacting the supraoccipital at the level of the lambdoid crest is identified as part of the interparietal (as found in all didelphids). The degree of fusion of the interparietal and adjacent bones (parietal and supraoccipital) cannot be determined here because of the broken and deformed aspect of the skull. Among Marsupialia, Didelphidae are unique in having an interparietal fused to the supraoccipital but not to the parietals (Voss & Jansa, 2009).

The supraoccipital is almost completely preserved and medially borders the mastoid exposure of the petrosal, together with the exoccipital. The dorsal margin of the foramen magnum is formed by the exoccipitals and the supraoccipital, as in most didelphids (Voss & Jansa, 2009).

The exoccipital is only preserved in its right half-width. The paroccipital process of the exoccipital is inconspicuous, as in most didelphids. It is a low, rounded shelf of bone for the attachment of the sternocleidomastoideus muscle.

Only the posteriormost part of the ventral surface of the rostrum of *P. cuvieri*, formed by the palatine bone, is preserved. Only the ventral and posteriormost parts of the palatine are preserved relatively intact: the right lateral surface of the palatine is broken into multiple and displaced fragments. On the palate, we were only able to identify the palatine fenestrae, with the region of the palate anterior to these openings, including the vacuities between the maxilla and palatine bone (if present), being missing. Just posterior to the palatine remnant is the basisphenoid, which is the triangular bone in the centre of the skull ventral surface, bounded by the pterygoids, themselves bounded by the alisphenoid. The alisphenoid is sutured with the posteriormost part of the palatine on the right side of the skull, as in most didelphids in which the maxillary and alisphenoid bones are usually separated by the palatine on the orbital floor.

The alisphenoid exhibits two main openings in *P. cuvieri*. More anteriorly and adjacent to the basisphenoid, the transverse canal foramen, visible on the left side of the skull, transmits a vein communicating with the cavernous sinus (Sánchez-Villagra & Wible, 2002). Posteromedial to it is the carotid foramen, clearly visible on the right side, for the internal carotid artery. These foramina are found in most marsupials. The part of the alisphenoid that is usually perforated by ramifications of the trigeminal nerve (i.e. foramen ovale and foramen rotundum) is not preserved in this specimen. On the lateral side of the alisphenoid and anterior to the petrosal bones is a marked fossa, floored by a small process of the alisphenoid. This fossa is the hypotympanic sinus, which is covered ventrally by the alisphenoid tympanic process, as observed in didelphids. In opossums other than *Caluromys* and *Caluromysiops*, a distinct gap separates the alisphenoid tympanic process from the rostral tympanic process of the petrosal, which is also the case in *P. cuvieri*.

The basioccipital bone lies in between the two petrosal bones. It is a roughly hexagonal bone, broken in its mid-length. It forms the base of the skull between the petrosals and the anteroventral border of the foramen magnum.

The petrosal bones are described in a separate section. They are exposed on the occiput and on the ventral surface of the skull (between the exoccipital, basioccipital, and alisphenoid), as in most didelphids.

Because of the deformed and fragmentary aspect of the skull, a reconstruction of the endocranial cast is not possible. Two main features are visible inside the skull, however: the casts of the olfactory bulbs and the cribriform lamina. Covered by the frontal, the ethmoidal fossa contained the olfactory bulbs and is bounded anteriorly by the cribriform lamina, which separates the nasal cavity from the braincase. The olfactory bulbs were large and ovoid, as in *Monodelphis* (Macrini, Rowe & VandeBerg, 2007).

Anatomical description of the teeth

Here we provide a description of the preserved teeth of the holotype of *P. cuvieri* based on new techniques of observation. The teeth are visible outside the matrix, and thus are observable without microtomography techniques; however, 3D representations allow for better observation and easier interpretation, as

© 2016 The Linnean Society of London, *Zoological Journal of the Linnean Society*, 2016

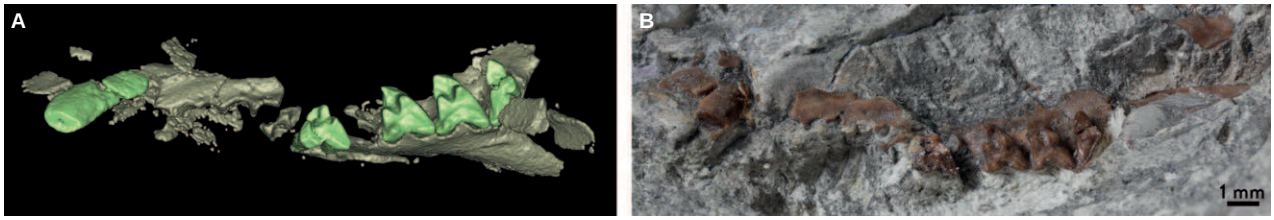

Figure 4. Upper dentition of *Peratherium cuvieri* (GY679b): 3D reconstruction (A), as compared with the photograph of the specimen (B). Note the detection of maxillary bones hidden in the matrix in (A).

shown in Figure 4. The diagnosis and the description of the species based on several specimens is available in Crochet (1980).

General observations

On slab GY679b, several pieces of bones and teeth are embedded in the gypsum matrix (Fig. 1). Thanks to the 3D modelling, we can interpret the various pieces of bone as belonging to the same upper right maxillary, owing to the relative disposition of the different pieces, which fit together.

From anterior to posterior, there are: a fragment with the upper right canine; a fragment with alveoli for the upper second and third premolars (P2 and P3); a fragment with the alveoli for the P3 on its anterior part, and of the first upper molar (M1) on its posterior part; a fragment with the right upper first molar (M1) and its roots; a fragment with the upper right molars 2, 3, and 4 (M2, M3, and M4); and finally two fragments of bone.

On the other slab, GY679a, no information concerning the dental anatomy is available. Specimen GY679c bears m2–m3 (Fig. 5Ac) in a piece of the right mandible, which also includes the alveoli for m4. GY679d is a fragment of the posterior region of the right mandible, on which the masseter pit is visible; the ramus of the dentary is broken, and mandibular foramen is observable on the lingual side (this specimen is not illustrated in this article because it is too fragmentary).

Upper teeth

The upper teeth are observed directly on slab GY679b (Fig. 1), and the 3D models reconstructed from CT data reveal additional details (Fig. 5A).

In cross section, the upper right canine is oval (elongate anteroposteriorly). The tip of the tooth is absent and thus the root canal is visible.

The right upper molars all have three roots and present a triangular outline in occlusal view. The cusps are tall and clearly marked. The teeth slightly increase in size from M1 to M3. The molars are clearly dilambdodont, that is to say the preparacrista, centrocrista, and postmetacrista form two reversed Vs when observed in occlusal view.

M1 is in poor condition. The talon is missing. The metaconule and paraconule are not preserved. The stylar shelf is also damaged, but the stylar cusps are still observable. The surfaces are heavily eroded. M1 is not in contact with the other molars: it has shifted to the anterior part of the maxillary as a result of breakage. This tooth is incomplete and too damaged to be described further.

M2 is well preserved. The stylar cusp A is located on a narrow spur projecting anteriorly. A paracingulum is present. Stylar cusp B is the highest stylar cusp. It is more massive than that on M3. The preparacrista connects to stylar cusp B. Stylar cusp C is not clearly distinguished. Stylar cusp D is the second highest stylar cusp. Stylar cusp E is located at the buccal apex of the postmetacrista. The ectoflexus of M2 is less pronounced than that of M3, but it is clearly marked and is asymmetrical. The stylar shelf is much wider than the talon. The paracone is clearly marked and narrow. The metacone is very high and very sharp. It is higher than the paracone in labial view. The centrocrista is V-shaped. The point of the V ends in the middle of the stylar shelf. The protofossa is deep. The lingual part of the talon is fractured: the protocone is observable, but on each side of it there are cracks at the level of the possible post- and precingula. Thus, the presence of a metaconule and paraconule is not determinable. Stylar cusp B, the paracone, and the protocone are aligned perpendicular to the anteroposterior axis. M2 and M3 are in contact: connected between stylar cusp E of M2 and the paracingulum and stylar cusp A of M3.

M3 is very well preserved. The paracingulum is better developed than that on the M2. The metastylar area is large. Stylar cusp A is located on a very narrow spur. Stylar cusps B and D are prominent, but cusp B is higher than cusp D. Stylar cusp C is not clearly distinguished and it does not form a proper cusp: it merely forms a slight bump on the stylar shelf. On the posterior edge of the stylar shelf, stylar cusp E is not well developed. The ectoflexus is

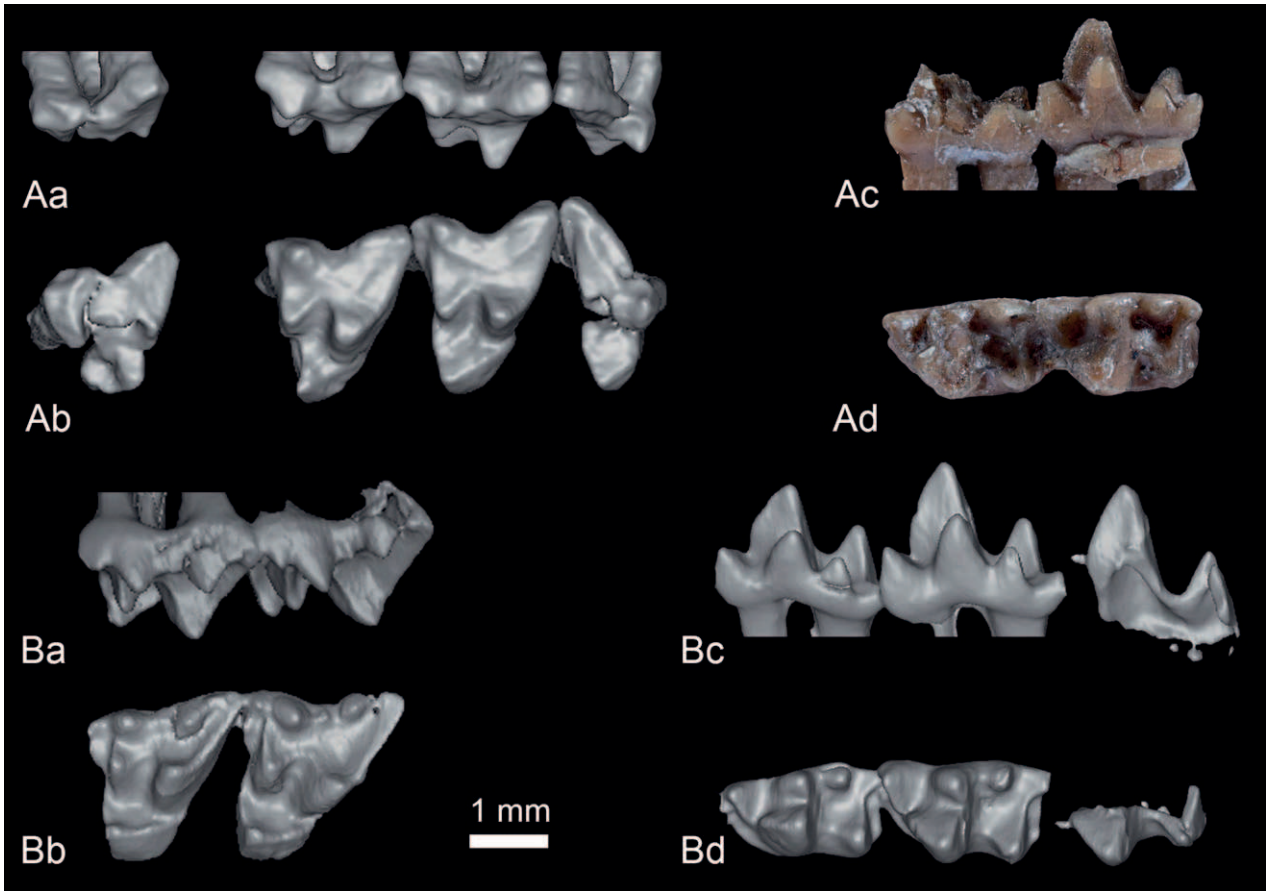

Figure 5. Upper and lower molars of *Peratherium cuvieri* (A): 3D model of right upper molars M1–M4 (GY679b) in labial (a) and occlusal (b) views (mirror effect) (a); photographs of right lower molars m2 and m3 (GY679c) in occlusal (mirror effect) (c) and lingual (d) views. Upper and lower molars of *Amphiperatherium minutum* (B): 3D model of right M1 and M2 (GY682) in labial (a) and occlusal (b) views (mirror effect); 3D model of right m1–m3 (GY682) in occlusal (mirror effect) (c) and lingual (d) views.

very pronounced, more so than on the M2, and is asymmetrical. The preparacrista connects to stylar cusp B and the postmetacrista connects to stylar cusp E. The paracone and metacone are very tall, with sharp crests. The metacone is the highest of the cusps, but in labial view the height difference between the metacone and paracone is smaller than on M2. The centrocrista forms a deep V that extends labially to the middle of the metastylar area. A paraconule and metaconule are present on the pre- and postprotocristae. The protocone is well defined and very tall. The protofossa is deep. An alignment of stylar cusp B, paracone, paraconule, and protocone perpendicular to the anteroposterior axis is observable. M3 and M4 are in contact: the connection is between stylar cusp E of M3 and the paracingulum and stylar cusp A of M4.

The talon of M4 is cracked, making description difficult. The stylar area is extremely reduced. The postmetacrista and stylar cusps C, D, and E are not observable on the stylar shelf. Stylar cusp A is located on a narrow spur. The paracingulum is strongly marked. Stylar cusp B is present but weakly developed. The metacone is very well developed and tall. It is located at the posterior edge of the tooth. Its base is narrow. A spur is formed along the posterior edge of the metacone. The paracone is broken by the crack, leaving only the base on the buccal side observable. A metaconule and paraconule are faintly identifiable on the pre- and postprotocristae. The protocone is clearly marked but much less so than on previous molars.

Lower molars

The lower molars in specimen GY679c (Fig. 5A) have two roots and have a rectangular outline in occlusal view. Lower molar m3 is slightly higher than m2. The roots of m2 and m3 are located on the lingual

© 2016 The Linnean Society of London, *Zoological Journal of the Linnean Society*, 2016

side of the mandible fragment. Lower molar m2 is poorly preserved. The posterior region of the trigonid containing the metaconid and protoconid is broken. The paraconid is well developed and tall, with a robust base. It is located very far forwards on the lingual side. The anterior cingulid is thin with a gutter shape. The breakage of the trigonid does not allow a more accurate description of the anterior region of the tooth. The trigonid is slightly longer than the talonid. The entoconid is clearly marked and tall. The rounded and sturdy base of the entoconid extends from the wall formed by the postentocristid, on the buccal side. It is noteworthy that the preentocristid is not distinct. The entoconid is higher than the hypoconulid and hypoconid, and also the paraconid. The cusp located furthest posteriorly is the hypoconulid. It is well developed but is not very high. It is strongly projected posteriorly. It is located on the same ridge as the entoconid, with the whole forming a wall, namely the postentocristid. The hypoconid is clearly marked and is buccally positioned. Its base is robust but is pinched so that the postcristid (= hypocristid) and the cristid obliqua are closer at the level of the postfossid. The postfossid is deep, with a rounded shape. The cristid obliqua is oriented lingually to the point of conact between the postmetacristid and postprotocristid. The hypoflexid is deep. The posterior cingulid is present and forms a gutter. Lower molar m2 contacts m3: the hypoconulid of m2 touches the paraconid of m3. There is a hypoconulid notch within the anterior cingulid of m3 that houses the hypoconulid of m2.

The m3 is well preserved. The trigonid is larger and higher than the talonid. The paraconid is clearly marked and high, with a robust base. It is located anteriorly on the lingual side. It is higher than the entoconid. The anterior cingulid is thin with a gutter shape. The metaconid is clearly marked and very tall. It lies on the lingual edge of the tooth. The protoconid is the highest of the cusps. Its base is very strong and dominates the tooth. The prefossid is deep with a triangular shape. The metacristid is perpendicular to the anteroposterior axis. The entoconid is clearly marked and tall. Its rounded and sturdy base arises from the wall on the buccal side. The entoconid is higher than the talonid and paraconid cusps. The hypoconulid projects strongly posteriorly. This cusp is marked but not very high, and is located on the postentocristid, which forms a wall. The paraconid, metaconid, entoconid, and hypoconulid are aligned parallel with the anteroposterior axis. Such a lingual position of the hypoconulid is characteristic of herpethoriids (Hooker *et al.*, 2008), in contrast to peradectids, in which it is located further buccally. The hypoconid is clearly marked and located very far buccally. Its base is sturdy but is pinched, as seen on m2. The postfossid is deep with a rounded shape. The cristid obliqua is lingually oriented to the point of contact between the postmetacristid and postprotocristid. The hypoflexid is deep. The posterior cingulid is present and forms a gutter.

Finally, it is noteworthy that the dental characteristics described here for *P. cuvieri* are not consistent with either the emended diagnosis of the genus (Hooker *et al.*, 2008) or with the diagnosis of the species (Crochet, 1980). Features of the lower molars listed in the emended diagnosis of the genus (Hooker *et al.*, 2008) do not fit with the morphology of *P. cuvieri* (in which the hypoconid is not taller than the entoconid). Moreover, the features concerning stylar cusps are not found in *P. cuvieri*, and it is noteworthy that variability in stylar cusp number within herpetotheriid species has been noted by several authors (e.g. Ladevèze *et al.*, 2012). For instance, although described as present in the diagnosis of *P. cuvieri* (Crochet, 1980), stylar cusp C of the holotype is not distinguishable on M2 and is very weak on M3. The ectoflexus, described as symmetrical in the diagnosis of the species (Crochet, 1980), is asymmetrical on the holotype. For these reasons, we offer an emended diagnosis for the species (page 6).

Anatomical description of the petrosal bone

The petrosal bone is located in the basicranial area, bounded by the alisphenoid, the basioccipital, the exoccipital, and the squamosal. This mammalian ear bone receives the tympanic membrane and the ossicular chain (middle ear), and houses the hearing (organ of Corti) and balance (vestibular system) organs. By convention, the petrosal bone is divided into two parts (Wible, 1990): the anteroventral pars cochlearis (or pars petrosa; MacIntyre, 1972), housing the cochlear duct and saccule of the inner ear; and the posterodorsal pars canalicularis (or pars mastoidea; MacIntyre, 1972), housing the utricule and semicircular canals (Wible, 2003).

The anatomical description is made in three views: tympanic, cerebellar, and lateral. A hypothetical reconstruction of the arteries, veins, and nerves is also presented (Fig. 6).

Tympanic view

This view shows the two main divisions of the petrosal (Fig. 6A). The pars cochlearis is represented by the large, teardrop-shaped, and inflated promontorium. The pars canalicularis is lateral and posterior to the promontorium.

The promontorium is broader posteriorly, and its ventral surface is strongly inflated because of the underlying turns of the cochlear duct. No sulcus runs on the smooth promontorium surface. Only the

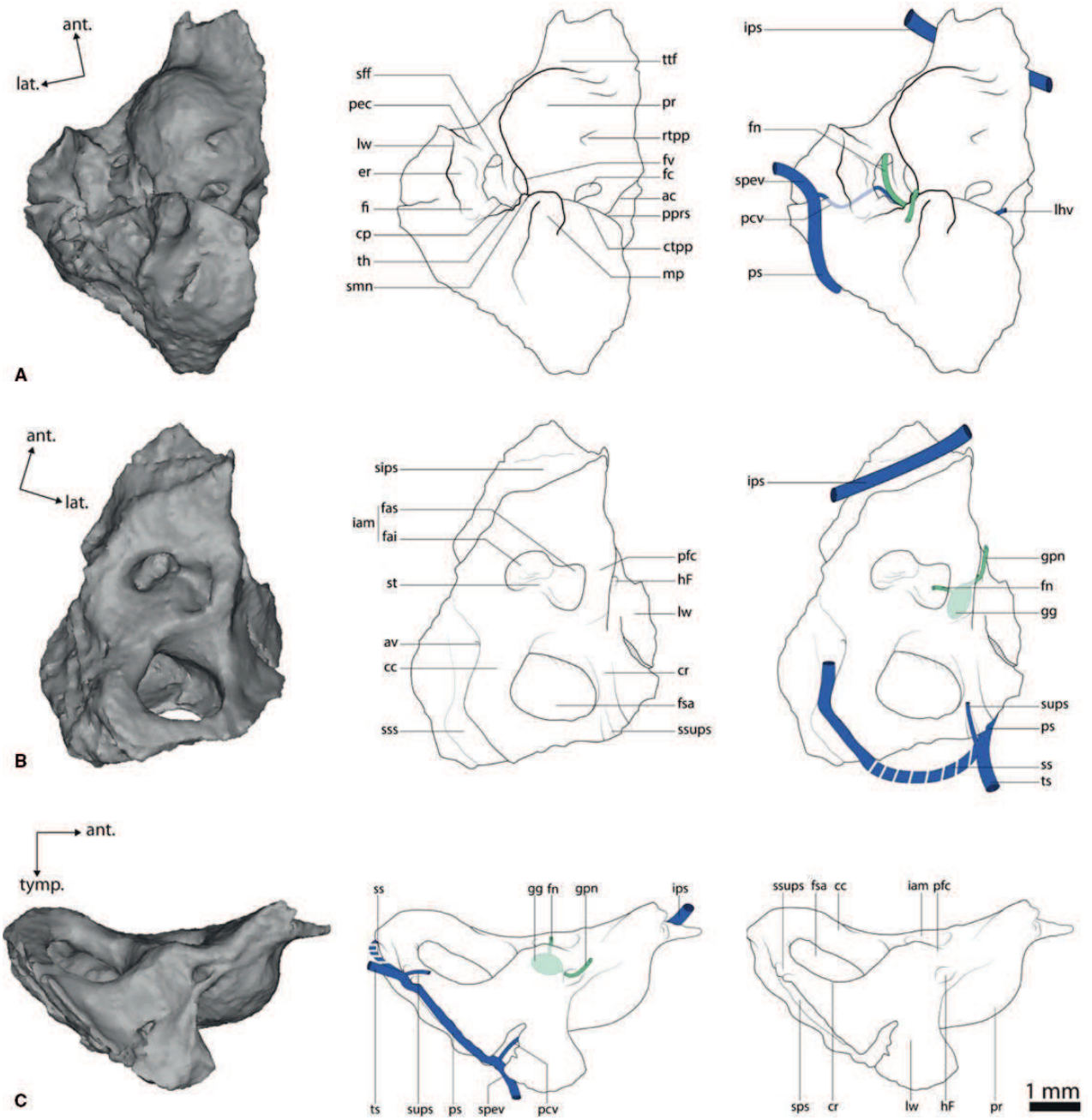

Figure 6. Three-dimensional (3D) model of the right petrosal of *Peratherium cuvieri* (GY679b) in tympanic (A), cerebellar (B), and lateral (C) views (reconstructed by computed tomography). ac, aquaeductus cochlearis; av, aquaeductus vestibularis; cc, crus commune; cp, crista parotica; cr, crista petrosa; ctpp, caudal tympanic process of petrosal; er, epitympanic recess; fai, foramen acousticum inferius; fas, foramen acousticum superius; fc, fenestra cochleae; fi, fossa incudis; fn, facial nerve; fsa, fossa subarcuata; fv, fenestra vestibuli; gg, geniculate ganglion; gpn, greater petrosal nerve; hF, hiatus fallopii; iam, internal auditory meatus; ips, inferior petrosal sinus; lhv, lateral head vein; lw, lateral wall of epitympanic recess; mp, mastoid process; pcv, prootic canal vein; pec, petrosal crest; pfc, prefacial commissure; pprs, postpromontorial sinus; pr, promontorium; ps, prootic sinus; rtpp, rostral tympanic process of petrosal; sff, secondary facial foramen; sips, sulcus for the inferior petrosal sinus; smn, stylomastoid notch; spev, sphenoparietal emissary vein; sps, sulcus for the prootic sinus; ss, sigmoid sinus; sss, sulcus for the sigmoid sinus; ssups, sulcus for the superior petrosal sinus; st, transverse septum; sups, superior petrosal sinus; th, tympanohyal; ttf, fossa for the tensor tympani muscle; ts, transverse sinus.

© 2016 The Linnean Society of London, *Zoological Journal of the Linnean Society*, 2016

rostral tympanic process of the petrosal (*sensu* MacPhee, 1981) forms a small prominence and rises above the fenestra cochleae. The inflated part of the promontorium is prolonged anteromedially by a thin wing of bone, broken anteriorly. As in extant marsupials, this structure, the anteromedial flange, would have been in contact with the basioccipital and basisphenoid on its medial side, and was most likely involved in the posteromedial border of the foramen ovale on its lateral side (Wible, 2003). On the lateral edge of the anteromedial flange, anteriorly to the promontorium, is a shallow fossa that probably accommodated the tensor tympani muscle.

There are two apertures in the posterior area of the promontorium. The medial opening, the fossula cochleae (*sensu* Wible *et al.*, 2009), is kidney-shaped. This aperture contains the fenestra cochleae and was in life occupied by the secondary tympanic membrane. The fossula cochleae is surmounted by a small edge that makes a medial separation between it and the aquaeductus cochlearis or cochlear canaliculus, which transmitted the perilymphatic duct into the petrosal. The aquaeductus cochlearis opens into a conical space near the jugular foramen. The lateral opening on the promontorium is the fenestra vestibuli, which in life lodged the footplate of the stapes. It is oval in shape, with a stapedial ratio of 1.76 (Segall, 1970).

Lateral to the fenestra vestibuli, a posteriorly directed aperture is here identified as the secondary facial foramen, which is not separated from the primary facial foramen. This opening transmits the main, or hyomandibular, branch of the facial nerve into the middle-ear space. The nerve pathway leaves a deep sulcus at the exit of the secondary facial foramen, the sulcus facialis. It lies posterior to the fenestra vestibuli and is surmounted posteroventrally by the crista parotica. The secondary facial foramen roof is narrow but prolonged anteriorly, forming the floor of the hiatus fallopii, through which exits the greater petrosal nerve (*sensu* Wible, 1990).

The lateral part of the pars canalicularis is fissured as a result of fossilization inside the gypsum. The sulcus for the prootic sinus runs on the lateral side of the pars canalicularis. The posterior sulcus is absent because of a crack. Posterolaterally to the promontorium and to the secondary facial foramen, there is an elongated depression that is separated from the latter by a crest. This depression is part of the middle ear and is formed by the epitympanic recess and the fossa incudis, which housed the ossicles in life. The manubrium of the malleus would have contacted the internal side of the tympanic membrane, and the head of malleus would have articulated with the incus inside the epitympanic recess (Van der Klaauw, 1931). The epitympanic recess is the broadest and lateralmost area of the depression. The deepest and most medial part of this depression is the fossa incudis, which housed in life the crus breve of the incus. The fossa incudis was probably bordered posterolaterally by the squamosal, as in all extant metatherians. The long crus of the incus would have articulated with the head of the stapes, the base of which occupies the fenestra vestibuli. The epitympanic recess is bounded laterally by a prominent triangular wall: the lateral wall of the epitympanic recess (*sensu* Ladevèze, 2004). Anteriorly, the epitympanic recess is bounded by a salient ridge: the petrosal crest (*sensu* Archer, 1976). This crest forms a boundary between the epitympanic recess and the foramen ovale, bounded posteromedially by the lateral edge of the anteromedial flange. The area containing the epitympanic recess and fossa incudis forms a roof covering the small tympanic foramen of the prootic canal, which lies in front of the secondary facial foramen.

The crista parotica bounds the fossa incudis medially, and it extends medially into a high, ventrally directed wall, towards the mastoid tympanic process (*sensu* Archer, 1976; Wible, 1990), to which was attached the sternocleidomastoideus muscle. On this wall, a small process is present just before the apex of the mastoid tympanic process. Based on comparisons with other herpetotheriid species (*P. elegans*, *A. minutum*, and *H.* cf. *fugax*; pers. obs.), this process is here considered to be the tympanohyal. It is poorly differentiated and has a ventral position. Between the tympanohyal and the apex of the mastoid tympanic process lies a narrow stylomastoid notch. Running posteromedially in the sulcus facialis, the facial nerve would have left the petrosal via the stylomastoid notch. The latter is bounded laterally by the tympanohyal and medially by the caudal tympanic process of the petrosal (*sensu* MacPhee, 1981). The prominent caudal tympanic process of the petrosal extends from the stylomastoid notch to the jugular foramen (posterior lacerate foramen of Archer, 1976), which lies between the basioccipital, the exoccipital, and the petrosal, and ventrally covers the posteriormost part of the promontorium and the depression posterodorsal to the promontorium. The deepest area of this depression is the stapedial fossa for the stapedius muscle. Medially to the stapedial fossa and to the fossula cochleae, a short furrow is bounded posteriorly by the caudal tympanic process and anteriorly by the promontorium. This is the postpromontorial tympanic sinus (*sensu* Wible, 1990), which runs to the jugular foramen ventrally to the aquaeductus cochlearis. The mastoid tympanic process is a massive process in contact posteroventrally with the caudal tympanic process. It extends

from the posteromedial side of the stylomastoid notch to the posterior half of the mastoid. The posterior area of the pars canalicularis is poorly preserved: the lateral part is missing. The medial, preserved part is the mastoid exposure, which is located between the squamosal, supraoccipital, and exoccipital in extant marsupials (Wible, 1990).

Cerebellar view

The cerebellar surface of the petrosal is teardrop-shaped, with a posterodorsally broad part and an anteroventrally narrow part. The surface shows two openings: the posterior fossa subarcuata on the broad part and the anterior internal acoustic meatus on the narrow part (Fig. 6B). These two openings are separated by a broad shelf of bone.

Posterodorsally, the fossa subarcuata is cylindrical, deep, and slightly wider than the internal acoustic meatus. The fossa subarcuata probably accommodated the paraflocculus of the cerebellum, as in extant marsupials (Sánchez-Villagra, 2002). The opening of the depression is wide: its diameter is equal to the maximum half width of the cerebellar surface.

The fossa subarcuata is bounded by three semicircular canals. The anterior semicircular canal (ASC) borders the opening of the fossa subarcuata posterolaterally, and the posterior semicircular canal (PSC) forms its medial wall. These two canals join at the crus commune on the medial wall of the fossa (Wible, 1990). The lateral semicircular canal (LSC) forms the internal wall of the fossa subarcuata on the tympanic side.

Anteriorly, the fossa subarcuata is delimited by a thick wall, the crista petrosa, which separates the fossa subarcuata from a ventrolaterally projecting bony expansion (Fig. 6B, C). This bony lamina may be regarded as a vestige of the anterior lamina of the petrosal (*sensu* Marshall & Muizon, 1995), as observed in *Herpetotherium* (Horovitz *et al.*, 2008) and some other fossil metatherians (e.g. Ladevèze & de Muizon, 2007, 2010; Horovitz *et al.*, 2009). In non-tribosphenic mammals and multituberculates, the anterior lamina is well developed and forms the lateral wall of the skull. In therians, this structure is generally missing or vestigial, and hence the petrosal is excluded from the lateral wall of the skull (see Discussion by Ladevèze, 2004; Rougier & Wible, 2006; Ladevèze & de Muizon, 2007).

The posteriormost part of the petrosal bone is missing; therefore, the sigmoid sinus pathway is missing on the posterior edge of the fossa. The fossa subarcuata is lacking its ventral covering, this part of the mastoid being absent. In lateral view, the transverse sinus bifurcation is visible on the posterolateral extremity (Fig. 6C). In extant marsupials, the transverse sinus divides into three branches: the superior petrosal sinus, the sigmoid sinus, and the prootic sinus (Wible, 1990; see below). The ramification for the superior petrosal sinus has left a trace on the posterolateral edge of the fossa subarcuata. This sulcus extends slightly onto the fossa subarcuata lateral wall. The sulcus for the sigmoid sinus is only present on the posteromedial edge of the fossa subarcuata, and extends up to the aqueductus vestibuli. The sulcus for the prootic sinus is broad and long; ventrolaterally, it borders the vestigial anterior lamina and emits a small vein into the prootic canal, via its cerebellar opening.

Anteromedial to the fossa subarcuata, the internal acoustic meatus forms a shallow depression for the facial (VII) and vestibulocochlear (VIII) nerves (Wible, 1990). The internal acoustic meatus is figure of eight-shaped and is divided into two size-equivalent openings, separated by a broad transverse septum. The medial aperture, the foramen acusticum inferius, transmitted two branches of the vestibulocochlear nerve to the internal substance of the petrosal: the cochlear branch ran through the anteriorly directed canal (tractus spiralis foraminosus of Meng & Fox, 1995), and the vestibular branch ran through the posteriorly directed canal (foramen singular of Meng & Fox, 1995). The lateral aperture, the foramen acusticum superius, received the facial nerve and one branch of the vestibulocochlear nerve that joined the internal substance (Wible, 1990). The cambered lateral wall of the internal acoustic meatus is formed by the prefacial commissure (which hides the facial nerve pathway dorsally) and the crista petrosa. Anteriorly to the internal acoustic meatus, a bony plate elongates and ends in a triangle shape. On this surface, a broad sulcus elongates anterolaterally to dorsomedially and received the inferior petrosal sinus.

The endolymphatic duct passed through the aqueductus vestibuli, which is a small slit located on the posteromedial area of the fossa subarcuata. The perilymphatic duct exited the petrosal via the aqueductus cochleae, which is a small circular foramen located in a conical depression posteromedial to the foramen acousticum inferius.

Lateral view

In this view, the cerebellar surface looks almost flat. The triangular vestigial anterior lamina dominates all the other stuctures, but is cracked transversely. It is delimited posteromedially by the crista petrosa, anteromedially by the prefacial commissure, and anteriorly by the hiatus Fallopii for passage of the greater petrosal nerve. At the anterior angle of the anterior lamina, the hiatus fallopii exhibits a roof and a floor that are at the same height in this view (= intermediate position from Sánchez-Villagra &

© 2016 The Linnean Society of London, *Zoological Journal of the Linnean Society*, 2016

Wible, 2002). On the external posterior edge of the anterior lamina, a large sulcus housed the prootic sinus. Some structures from the tympanic and cerebellar faces are observable. The fossa subarcuata entrance is visible on the posterior edge of the petrosal, and the promontorium is distinct anteriorly to the anterior lamina; however, the tympanic mastoid process is hidden behind the anterior lamina.

Soft tissue reconstruction

The complete reconstruction of the vascular and nervous systems in fossil petrosals depends on the impressions left on the bone by the cranial vessels (such as grooves, canals, and foramina), which makes it extremely difficult in some cases. Although damaged on the posterior part, the petrosal of *P. cuvieri* shows impressions that allow a reconstruction of the nerves and blood vessels, mostly inferred from didelphid anatomy (Wible, 1990, 2003).

Arteries and veins

The major veins of the metatherian petrosal are tributaries of the transverse sinus (e.g. Wible, 2003; Horovitz *et al.*, 2008). When the transverse sinus reaches the petrosal bone on the posterolateral angle of the fossa subarcuata, it divides into three branches: the superior petrosal sinus, the sigmoid sinus, and the prootic sinus. The marked depression on the posterolateral angle on the cerebellar surface of the petrosal bone indicates the path of the superior petrosal sinus and the prootic sinus. In *P. cuvieri*, the superior petrosal sinus pathway is slightly marked on the posterolateral edge of the fossa subarcuata, and extends anteriorly along the crista petrosa. The superior petrosal sinus then joins the cavernous sinus. The sigmoid sinus sulcus is visible only on the medial surface on the posteromedial angle of the fossa subarcuata, and extends up to the aqueductus vestibuli. This impression allows the hypothetical reconstruction of the sigmoid sinus pathway, which probably ran posteriorly to the fossa subarcuata and left the skull through the foramen magnum, as in extant marsupials (e.g. Archer, 1976).

Following the first two bifurcations, the transverse sinus transmits the prootic sinus, which would have run on the lateral surface of the petrosal, where a wide impression along the dorsoventral part of the anterior lamina is visible (Fig. 6C). The prootic sinus transmits the prootic canal vein at the mid-point of the anterior lamina. The prootic canal vein extends through the lateral wall thickness via the prootic canal and exits on the tympanic surface in front of the secondary facial foramen. The vein is then called the lateral head vein and runs along a sulcus confluent with the sulcus facialis (*sensu* MacIntyre, 1972). It reaches the postpromontorial sinus and leaves the petrosal with the inferior petrosal sinus, through the jugular foramen. In extant adult didelphids, after emitting the prootic canal vein, the prootic sinus anastomoses to the sphenoparietal emissary vein, which leaves the petrosal via the postglenoid foramen, which is located at the most lateral part of the anterior lamina (Wible, 2003).

Nerves

The facial nerve enters the petrosal via the foramen acousticum superius of the internal acoustic meatus (Wible, 1990), runs beneath the prefacial commissure, and enters into the cavum supracochleare (Voit, 1909), which encloses the geniculate ganglion. The cavum supracochleare is not entirely closed because the primary facial foramen is absent. As a matter of fact, the secondary facial foramen is directly visible in cerebellar view. The main branch of the facial nerve (or hyomandibular ramus) leaves the posterior aspect of the geniculate ganglion and enters the middle ear space via the secondary facial foramen. The posteroventral branch of the facial nerve runs in the deep sulcus facialis and exits the skull via the stylomastoid notch. The greater petrosal nerve leaves the anterior part of the geniculate ganglion and exits the cavum supracochleare via the hiatus fallopii.

Osseous inner ear

The osseous labyrinth is the cavity in the petrosal that in life contained the perilymph in which the membranous labyrinth was suspended. The osseous labyrinth consists of three parts: the semicircular canals, which contained the semicircular ducts; the vestibule, which contained the utricule and saccule; and the cochlea, which contained the cochlear duct (Starck, 1967).

The bony spiral laminae, which supported the spiral organ of hearing in life, are visible on the cochlear canal (Fig. 7), as in most therians (e.g. Meng & Fox, 1995; Luo *et al.*, 2011). The primary bony lamina projects from the inner wall of the cochlear canal and extends along most of the cochlear canal length. The secondary bony lamina projects from the outer wall of the cochlear canal and is distinct at the beginning of the first turn.

Among the three semicircular canals, the ASC has the most consistent diameter, followed by the PSC and then the lateral semicircular canal LSC (see Fig. 7; Table 1). The PSC plane is almost perpendicular to the ASC plane (105.72°). The ASC and the PSC meet medially at the crus commune. The LSC plane is almost perpendicular to the ASC and the PSC planes (see Table 1). The PSC and the LSC

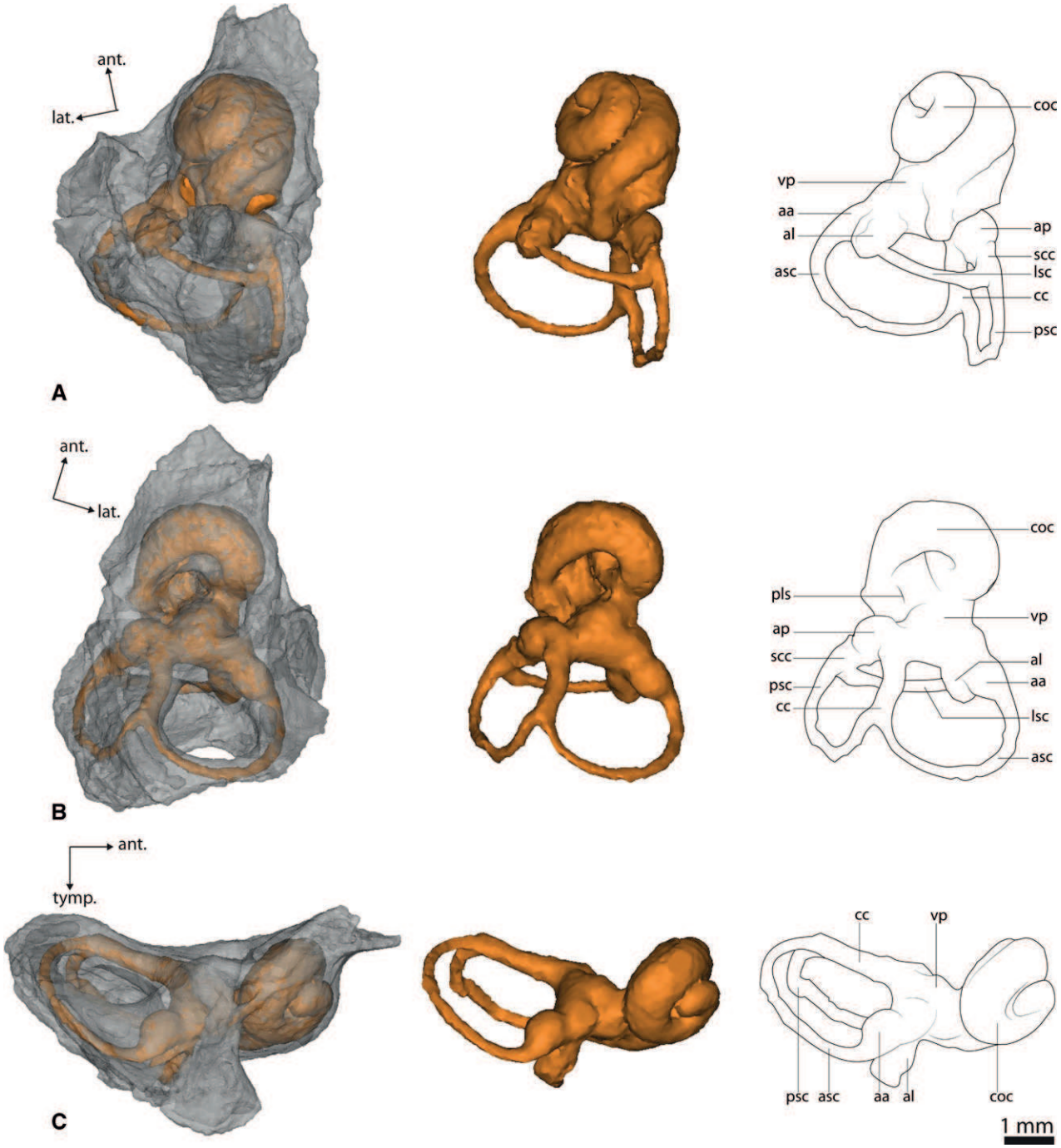

Figure 7. Right bony labyrinth of *Peratherium cuvieri* (GY679b) in tympanic (A), cerebellar (B), and lateral (C) views (reconstructed by computed tomography). aa, anterior ampulla; al, lateral ampulla; ap, posterior ampulla; asc, anterior semicircular canal; cc, crus commune; coc, cochlea; lsc, lateral semicircular canal; pls, primary bony lamina sulcus; psc, posterior semicircular canal; scc, second crus commune; vp, vestibule.

meet at the second common crus. The semicircular canals are housed in the fossa subarcuata walls. The ASC posteriorly surrounds the fossa subarcuata, whereas the PSC forms a medial wall to the latter. The LSC is part of the ventral wall of the fossa subarcuata. The vestibule is located between the cochlea (anteriorly) and the semicircular canals (posteriorly). The vestibule is the central area of the osseous labyrinth. With an irregular shape, the vestibule shows many bulges located at the junction

© 2016 The Linnean Society of London, *Zoological Journal of the Linnean Society*, 2016

Table 1. Measurements of various semicircular canals aspects, taken in *Peratherium cuvieri*, *Herpetotherium* cf. *fugax*, and *Marmosa murina*

	H ASC	W ASC	R ASC	H PSC	W PSC	R PSC	H LSC	W LSC	R LSC	IEH	Mean R SC/ IEH	H ASC/ H PSC	H ASC/ H LSC	H PSC/ H LSC	Angle ASC/ PSC	Angle ASC/ LSC	Angle PSC/ LSC	D ASC	D ASC/ IEH	D PSC	D PSC/ IEH	D LSC	D LSC/ IEH
P. cuvieri	2.18	2.31	1.12	1.75	1.90	0.91	1.23	1.57	0.70	4.07	0.22	1.25	1.77	1.42	105.72	109.07	98.94	0.10	0.02	0.22	0.05	0.11	0.03
H. cf. *fugax*	1.34	1.39	0.68	0.94	1.12	0.52	0.68	0.99	0.42	2.43	0.22	1.43	1.97	1.38	87.00	91.87	94.00	0.10	0.04	0.12	0.05	0.11	
M. murina	1.90	1.86	0.94	1.20	1.26	0.62	0.88	1.10	0.50	3.59	0.19	1.58	2.16	1.36	98.70	83.59	94.43	0.21	0.06	0.18	0.05	0.21	0.06

For each semicircular canal (anterior semicircular canal, ASC; posterior semicircular canal, PSC; lateral semicircular canal, LSC), the height (H), width (W), and diameter (D) were measured, as well as the angles between each other. The inner ear height (IEH) was measured after Billet *et al.* (2013). The radius of curvature for each semicircular canal was calculated following Spoor *et al.* (2007).

between the vestibule and the canals: the ampullae. The anterior ampulla lies dorsolateral to the vestibule, and is the link between the vestibule and the ASC. The lateral ampulla lies ventrolateral to the vestibule and is the link between the vestibule and the LSC. The posterior ampulla lies ventromedial to the vestibule and is the link between the vestibule and the crus commune. The cochlea is the largest part of the osseous labyrinth and occupies the most part of the pars cochlearis. This petrosal exhibits 1.6 turns of the cochlea (West, 1985). This number is low compared with the majority of extant marsupials: only the marsupial mole, *Notoryctes typhlops* (Stirling, 1889), and the wombat, *Vombatus ursinus* (Shaw, 1800), have such low values of cochlear coiling (see Horovitz *et al.*, 2008). *Herpetotherium* and the Montana metatherian described by Meng & Fox (1995) exhibit similar low numbers, namely 1.6 and 1.5 turns of the cochlea, respectively.

DISCUSSION

Anatomical comparison of the skull with other specimens

One skull of *P. elegans* from Ronzon has been described by Crochet (1980). It is crushed, especially in the basicranial area, and fragmentary, but less so than the skull of *P. cuvieri.* Anatomically, both appear very similar in many aspects; however, some features differ. The sagittal and nuchal crests are clearly marked in *P. elegans*, whereas they are not identifiable in *P. cuvieri*. The postorbital process of the frontal is more pronounced in *P. elegans* than in *P. cuvieri*. These differences might result from different individual ages or sexual dimorphism (for a discussion of sexual dimorphism in the marsupialiform *Pucadelphys*, see Ladevèze *et al.*, 2010).

One skull of a young individual from the gypsum of Montmartre was assigned to *Amphiperatherium minimum* and described by Crochet (1980). Again, it is a crushed and fragmentary specimen, especially in the basicranial area. Because of the young age of the individual, there is no postorbital process of the frontal and no sutural crests. The whole aspect of the skull is very similar to that of *P. cuvieri.* There is a distinct tympanic process of the alisphenoid.

The skull anatomy of *P. cuvieri* is also very similar to that known for *Herpetotherium* (Gabbert, 1998; Horovitz *et al.*, 2008). The nasals expand posteriorly along their contact with the frontals, and the frontals extend posteriorly to a position dorsal to the posteriormost limit of the orbitotemporal fossa. At the mid-length of the frontals, on the medial borders, are small postorbital processes, on the dorsal aspect of the jugal (not preserved in *P. cuvieri).* In

Herpetotherium, as in *P. cuvieri*, the orbital region is composed of fragments of the lacrimal, orbitosphenoid, palatine, and alisphenoid bones, but the topological relationships of each to one another cannot be determined with any certainty. Preserved in *Herpetotherium*, but not in *P. cuvieri*, are several features of the orbitotemporal region: from anterior to posterior, the sphenopalatine foramen, the posterior edge of the sphenorbital fissure, and the foramen rotundum.

In contrast to *Herpetotherium*, in which the sagittal suture and the parietal–supraoccipital contact form distinct crests, there are no such sutural crests visible in *P. cuvieri*.

The basicranium is better preserved in *Herpetotherium* than in *P. cuvieri*. In both, the most conspicuous parts of the alisphenoid are the entopterygoid processes and the tympanic processes. The alisphenoid and basisphenoid have no distinct suture: they form a 'sphenoid complex', with the posteriormost element being the auditory bulla and its posterior limit being the basioccipital contribution to the occipital. The carotid foramen is located at the posterolateral edge of the basisphenoid. As in *P. cuvieri*, *Herpetotherium* was likely to have had an internal carotid artery that ran medial to the auditory bulla, ventral to the basicapsular fissure, and entered the braincase directly through the anterior carotid foramen. The exits for the branches of the trigeminal nerve (nV1, nV2, and nV3) are identifiable in *Herpetotherium* but are not preserved in *P. cuvieri*. In *P. cuvieri*, as in *Herpetotherium*, the foramen ovale (for the mandibular nerve V3) may have been just lateral to the carotid foramen, in a common depression anteromedial to the apex of the promontory.

Anatomical comparison of the teeth with other specimens

Upper molars

Given the preservation of the selected specimens for comparison, M2 is chosen as the reference because it is the only tooth preserved in all taxa being compared. The upper and lower cheek teeth of *Amphiperatherium minutum* were modelled in the present study, and their 3D models are presented in Figure 5B.

Marmosa murina, the only extant taxon of the selection, shows a different morphology of the upper molars when compared with herpetotheriids. *Marmosa murina* is characterized by rather narrow cusps, conules, and cones that are shorter than those observed in other taxa, except for the metaconule, which is relatively high. The entire tooth has a very low topography, and the various cusps and crests are not well differentiated. The ectoflexus is very narrow, whereas it is clearly marked in herpetotheriids. The stylar shelves of *P. elegans*, *P. cuvieri*, and *A. minutum* are not alike at all points. In *P. elegans* and *P. cuvieri*, the stylar cusps are not very distinct nor very tall, except for stylar cusp B. Conversely, in *A. minutum* each cusp is distinct. In *P. cuvieri*, stylar cusp C is absent (or very weakly marked on M3). By contrast, this cusp is present and robust in *P. elegans* and *A. minutum*. In specimens of the genus *Peratherium*, the preparacristae and postmetacristae are not high and do not form a wall. Conversely, in *A. minutum*, the crests are very high and form walls. Thus, the stylar shelf of *P. cuvieri* and *P. elegans* have fairly low relief, whereas *A. minutum* has a stylar shelf with a strong topography: the stylar cusps are high, the crests form walls, and the stylar shelf is deep.

The morphology of the talon in *P. cuvieri*, *P. elegans*, and *A. minutum* is quite similar. The protoconule and metaconule are weakly developed but present. They are not taller than the protocristae. The protocones are distinct but only slightly taller than the protocristae.

Thus, the differences between the selected Herpetotheriidae mainly concern the stylar shelf. The main difference is the diversity of relief between specimens. It should be noted, however, that the specimen of *A. minutum*, which shows unworn molars with a high topography, is a juvenile; its young age may be one explanation for the sharp cusps and crests of the teeth.

Several authors have highlighted the significant variation of the morphology of the molars in generalist marsupials. These intra- and interspecific polymorphisms are mainly located on the stylar shelf, with this area not involved in the occlusion of the teeth (e.g. Martin, 2005; Ladevèze *et al.*, 2012). Furthermore, this variation in the morphology of the molars was demonstrated in herpetotheriids from the basal Eocene of Dormaal (*Peratherium constans* Teilhard de Jardin, 1927 and '*Amphiperatherium brabantense*' Crochet, 1979, with the latter being a junior synonym of the former species; see Ladevèze *et al.*, 2012).

Lower molars

The comparison is based on m3, the only tooth preserved in all specimens and showing some of the characters of interest. The lower molar m3 of *Amphiperatherium minutum* is present but broken, making the observation of any of these characters impossible.

Marmosa murina has different m3 morphology compared with the other taxa. As for M2, the topography of m3 is lower than that of the other taxa.

© 2016 The Linnean Society of London, *Zoological Journal of the Linnean Society*, 2016

Structures are less clearly marked: for example, the hypoconid is less pinched and the cristid obliqua is located less lingually. Finally, the absence of a posterior cingulid in this didelphid is a notable character (a distinct posterior cingulid is present in the three herpetotheriid species). This feature has already been highlighted by Voss & Jansa (2009).

The m3 of the three herpetotheriid species are very similar. Some features vary, but they are so slight that they do not seem to represent significant differences. It seems impossible to base a systematic determination on these molars alone.

Anatomical comparison of the petrosal bone

The petrosal bone of *P. cuvieri* is here compared with that of the extant opossum *M. murina* and with *H.* cf. *fugax*.

Tympanic view

The promontorium of *P. cuvieri* and *M. murina* is very rounded and forms the majority of the pars cochlearis. The promontorium of *H.* cf. *fugax* is rounded but comparatively smaller. On the medial area of the promontorium, the three species exhibit a rostral tympanic process of the petrosal. The rostral tympanic process of the petrosal forms an erected process, which is much higher and stronger in *M. murina* than in the two herpetotheriid species. The caudal tympanic process of the petrosal is present in all three species; it does not contact the rostral tympanic process of the petrosal; however in *P. cuvieri* and *M. murina*, it extends towards the promontorium and covers the deep stapedial fossa. The stapedial fossa of *H.* cf. *fugax* is much less covered by the caudal tympanic process of the petrosal, but is still very deep. On the lateral side, the fossa incudis and the epitympanic recess are continuous and closed anterolaterally by the petrosal crest in all three species. This area is very deep in *M. murina*, whereas the fossa incudis and the epitympanic recess are on the surface with low relief in *H.* cf. *fugax*; *P. cuvieri* has an intermediate topography for this area. *Peratherium cuvieri* and *M. murina* have a prootic canal. Based on the available data, this canal seems to be absent in *H.* cf. *fugax* (but the resolution of the 3D model might not be high enough to confirm the absence of the prootic canal). The secondary facial foramen is located more anteriorly relative to the fenestra vestibuli in *H.* cf. *fugax*. For *P. cuvieri* and *M. murina*, this foramen is located at the same level as the fenestra vestibuli. This also implies that the secondary facial foramen is close to the epitympanic recess, and a little crest separates these two structures in *P. cuvieri* and *M. murina*, unlike *H.* cf. *fugax*, in which these structures are well separated with no crest between them. The lateral wall of the epitympanic recess is well developed and high in *P. cuvieri* and *M. murina*, but it is not clearly marked in *H.* cf. *fugax*. In *P. cuvieri* and *M. murina*, the crista parotica leaving the epitympanic recess is salient and then extends medially to form a ventrally directed wall with a small prominence called the tympanohyal. In this case, the stylomastoid notch is not pronounced. Conversely, *H.* cf. *fugax* has a thick crista parotica, which extends medially to the tympanohyal, with the tympanohyal being very prominent and lateral to a pronounced stylomastoid notch. The three species have a large and high tympanic process of the mastoid. In *H.* cf. *fugax*, the fossula cochleae is long and narrow; it is smaller and more rounded in *M. murina.* The fenestra vestibuli is larger in *H.* cf. *fugax* than in *P. cuvieri* and *M. murina*.

Cerebellar view

The general appearance of the cerebellar surface is figure of eight-shaped in *M. murina* and *P. cuvieri*, and more elongate in *H.* cf. *fugax*. The internal acoustic meatus is shallow in all three species. The internal acoustic meatus of *H.* cf. *fugax* is relatively wider than in *P. cuvieri* and *M. murina*, as is its transverse septum. Inside the internal acoustic meatus, the primary facial foramen is present in *M. murina* but absent in *P. cuvieri* and *H.* cf. *fugax*. In *P. cuvieri* and *M. murina*, the prefacial commissure is wide and ventrally curved; it is directed towards the foramen acousticum superius, and covers the cavum supracochleare. In *H.* cf. *fugax*, the prefacial commissure is as wide as that of *P. cuvieri*, but forms a laterally directed 'handle'; the cavum supracochleare is thus less covered and the secondary facial foramen is directly observable in cerebellar view within the foramen acousticum superius. Indeed, the absence of a primary facial foramen is related to the absence of any closure of the cavum supracochleare; therefore, the secondary facial foramen is directly visible. This condition is very clear in *H.* cf. *fugax*, and is also found in *P. cuvieri*. In *P. cuvieri* and *M. murina*, the openings of the internal acoustic meatus and the fossa subarcuata are subequal; the two fossae are separated by a relatively thick wall. In *H.* cf. *fugax*, the opening of the internal acoustic meatus is narrower than the opening of the fossa subarcuata, and the two fossae are separated by a salient wall, which connects the prefacial commissure to the crus commune. In *P. cuvieri* and *H.* cf. *fugax*, the opening of the fossa subarcuata is larger than the fossa itself, which has a conical shape. Conversely, the entrance of the fossa subarcuata in *M. murina* is narrower than the inside, and the fossa is spherical. For the three

species, the expansion of the crista petrosa forms a thin lamina covering the anterolateral part of the fossa subarcuata. Behind the fossa subarcuata, *H.* cf. *fugax* has a thin plate of bone that extends posteriorly, whereas *P. cuvieri* and *M. murina* do not have this structure.

Lateral view

The hiatus fallopii position is clearly dorsal in *H.* cf. *fugax* and is intermediate in *P. cuvieri* and *M. murina*. Although the hiatus fallopii of *M. murina* is narrower than that of the other two species, a complete bony wall separates the cavum supracochleare (surrounding the geniculate ganglion) and the cavum epiptericum (surrounding the trigeminal ganglion). The same separation is present for the two herpetotheriids. As seen in the description, *P. cuvieri* retains a remnant of the anterior lamina of the petrosal. In contrast, *H.* cf. *fugax* and *M. murina* exhibit no lateral extension that might correspond to the anterior lamina. In lateral view, the cerebellar face of *H.* cf. *fugax* is not flat and is dominated by the bone plate located posteriorly to the fossa subarcuata. The cerebellar side of *H.* cf. *fugax* has a twisted shape: the opening of the fossa subarcuata is directed laterally, whereas the opening of the internal acoustic meatus is oriented dorsally. This twisted shape is less pronounced but present in *P. cuvieri* and *M. murina*.

Arteries and veins

The notch on the posterolateral corner of the fossa subarcuata, marking the bifurcation of the transverse sinus and the superior petrosal sinus and prootic sinus, is present in the three species. In *M. murina*, the superior petrosal sinus sulcus is less distinguished than in *P. cuvieri* and *H.* cf. *fugax*. For the three species, the sigmoid sinus emitted by the transverse sinus at the posterolateral corner of the fossa subarcuata runs along the fossa to reach its posteromedial angle. In *H.* cf. *fugax*, however, the sigmoid sinus runs dorsally to the thin posterior bone lamina and marks a notch on the posteromedial corner of the fossa subarcuata. In *P. cuvieri*, the prootic sinus runs along the posteroventral side of the anterior lamina. In *H.* cf. *fugax* and *M. murina*, which have no vestigial anterior lamina, the prootic sinus runs along the lateral surface of the petrosal, where it also leaves the impression of a wide groove. In all except *H.* cf. *fugax*, the prootic sinus emits a vein draining the lateral head vein via the prootic canal.

Nerves

The geniculate ganglion of *H.* cf. *fugax* is less covered than in *P. cuvieri* because the prefacial commissure of *H.* cf. *fugax* forms a 'handle' that is directed laterally. In *M. murina*, the geniculate ganglion is totally surrounded because of the presence of the primary facial foramen. The greater petrosal nerve exits through the hiatus fallopii, lateral to the foramen acousticum superius in *P. cuvieri* and *M. murina*, but more anteriorly in *H.* cf. *fugax*.

Osseous inner ear

In the three species, the ASC has the largest diameter, followed by the PSC, and finally the LSC (Table 1). Relative to the size of the osseous inner ear, the crus commune and the semicircular canals are higher and thinner in *P. cuvieri* and *H.* cf. *fugax* than in *M. murina* (Table 1). Indeed, the crus commune and the semicircular canals of the extant marsupial seem to be smaller and stockier. The three species all possess a second crus commune, which is probably a plesiomorphic feature in metatherians (Ladevèze, Asher & Sánchez-Villagra, 2008). *Peratherium cuvieri* and *H.* cf. *fugax* exhibit 1.6 turns of the cochlea and *M. murina* has 2.0 turns.

CONCLUSION

The increasing ease of access to advanced technology such as X-ray microtomography permits the historical specimens of natural history to be revisited. More than two centuries after its discovery, 'Cuvier's opossum' reveals new features that allow us to extend the investigation of Cuvier without damaging this iconic specimen. CT technology has allowed access to the skull bones hidden in the matrix, and a new and updated description of the skull, teeth, and petrosals of *P. cuvieri* is provided.

Concerning the teeth, the comparison between the extant opossum *M. murina* and the two extinct herpetotheriids *Peratherium elegans* and *Amphiperatherium minutum* reveals morphological overlap among the three herpetotheriid species. The specimen of *A. minutum* is from the same gypsum bed as *P. cuvieri*, and the two species cannot be clearly distinguished on the basis of molar characters only.

The description of the petrosal bone highlights characters found among extant Didelphidae that are likely to be plesiomorphic, such as the presence of a strong tympanic mastoid process, a well-developed promontorium surmounted by a small rostral process, and an intermediate position of the hiatus fallopii. The comparison of the petrosal anatomy of *P. cuvieri* and *H.* cf. *fugax* highlights interesting characters that could potentially define the family Herpetotheriidae, such as the absence of the primary facial foramen. *Herpetotherium* cf. *fugax* exhibits several characters not shared with *P. cuvieri*, however: for example, *P. cuvieri* and *M. murina* have a prominent rounded promontorium, whereas *H.* cf. *fugax*

© 2016 The Linnean Society of London, *Zoological Journal of the Linnean Society*, 2016

shows a much less prominent promontorium. *Peratherium cuvieri* has a relictual anterior lamina, whereas this feature is absent in *H.* cf. *fugax* and *M. murina*. A last example: the hiatus fallopii is intermediate in position in *M. marmosa* and *P. cuvieri*, but is entirely dorsal in *H.* cf. *fugax*. To continue the work of Horovitz *et al.* (2009), it would be relevant to integrate the new features of *P. cuvieri* in a phylogenetic framework. Moreover, the virtual extraction through CT scanning of the petrosal bones of *P. elegans* and *A. minutum* would represent a crucial step to delimit the species (additionally or instead of dental characters), and furthermore would help resolve the relationship of Herpetotheriidae to other metatherians, a critical phylogenetic issue to better understand the origin of Marsupialia and didelphids.

Besides the characters related to its external morphology, the petrosal houses the bony labyrinth (or osseous inner ear), which is the site of hearing and balance functions. The semicircular canals of the vertebrate labyrinth are known to help coordinate body movements, such as stabilization of the eye during locomotion (e.g., Spoor *et al.*, 2007; Billet *et al.*, 2013). Such features highlighted in *P. cuvieri* would therefore help in determining locomotor habits in fossil metatherians.

ACKNOWLEDGEMENTS

This work was financially supported by the 'ATM Formes 2014', especially for the scans of the comparison specimens and the financial support for a master's student. We are grateful to Robin Beck (University of Salford) and Thomas Macrini (St Mary's University San Antonio) for their comments that greatly improved our article. We are indebted to many colleagues from the MNHN: Gaël Clément, for the financial support for the scan of the *Sarigue de Cuvier*; Miguel Garcia Sanz, operator of the AST-RX platform; Florent Goussard, in charge of the 3D platform for technical advice and help during post-processing; Kevin Le Verger, for his invaluable help with segmentation of the skull; Christine Argot, for access to the palaeontological collection; Géraldine Véron, for access to the comparative collections of mammals; Lilian Cazes, for the great photographs of Cuvier's 'opossum', especially with the focus-stacking technique; Bernard Duhem, scientific designer at the UMS 2700, for the beautiful restoration of the *Sarigue de Cuvier*; Malcolm Sanders, for advice and technical help concerning PHOTOSHOP and ILLUSTRATOR that was very useful in the elaboration of the illustrations; and Sophie Fernandez, scientific graphic artist, for her help with the finalization of the figures.

REFERENCES

Archer M. 1976. The basicranial region of marsupicarnivores (Marsupialia), interrelationships of carnivorous mammals, and affinities of the insectivorous marsupial peramelids. *Zoological Journal of the Linnean Society* **59:** 217–322.

Beck R, Travouillon KJ, Aplin KP, Godthelp H, Archer M. 2014. The osteology and systematics of the enigmatic Australian Oligo-Miocene Metatherian *Yalkaparidon* (Yalkaparidontidae;Yalkaparidontia; ?Australidelphia; Marsupialia). *Journal of Mammalian Evolution* **21:** 127–172.

Billet G, Germain D, Ruf I, de Muizon C, Hautier L. 2013. The inner ear of *Megatherium* and the evolution of the vestibular system in sloths. *Journal of Anatomy* **223:** 557–567.

Crochet J-Y. 1980. *Les Marsupiaux Du Tertiaire d'Europe*. Paris: Editions de la Fondation Singer-Polignac, 279.

Cuvier G. 1804. Mémoire sur le squelette presque entier d'un petit quadrupède du genre des sarigues, trouvé dans la pierre à plâtre des environs de Paris. *Annales Du Muséum d'Histoire Naturelle* **V(XIII):**277–292.

Dollot A, Godbille P, Ramond G. 1905. Les grandes plâtrières d'Argenteuil (Seine-et-Oise), Historique, Genèse des formations gypseuses de la région parisienne. *Mémoires de la société géologique de France* **IV(I):**1–47.

Fisher JB. 1829. *Synopsis mammalium*. Sumtibus J.G. Cottae. Stuttgardtiae. 752.

Gabbert SL. 1998. Basicranial anatomy of *Herpetotherium* (Marsupialia: Didelphimorphia) from the Eocene of Wyoming. *American Museum Novitates* **3235:** 1–13.

Goguel J, Soyer R. 1973. *Carte géologique de la France à 1/50 000*: Paris, XXIII-14 (feuille 183). 3ème édition. Orléans: BRGM.

Gradstein FM, Ogg JG, Schmitz MD, Ogg GM. 2012. *The Geologic Time Scale 2012, Vol. 1 & 2*. First edition. Oxford: Elsevier BV.

Hooker JJ, Sánchez-Villagra MR, Goin FJ, Simons EL, Attia Y, Seiffert ER. 2008. The origin of Afro-Arabian 'didelphimorph' marsupials. *Palaeontology* **51:** 635–648.

Horovitz I, Ladevèze S, Argot C, Hooker JJ, Macrini TE, Martin T, Kurz C, de Muizon C, Sánchez-Villagra MR. 2008. The anatomy of *Herpetotherium fugax* Cope 1873, a metatherian from the Oligocene of North America. *Palaeontographica Abteilung A* **284:** 109–141.

Horovitz I, Martin T, Bloch J, Ladevèze S, Kurz C, Sánchez-Villagra MR. 2009. Cranial anatomy of the earliest marsupials and the origin of opossums. *PLoS ONE* **4:** e8278.

Ladevèze S. 2004. Metatherian petrosals from the Late Paleocene of Itaboraí (Brazil), and their phylogenetic implications. *Journal of Vertebrate Paleontology* **24:** 202–213.

Ladevèze S, de Muizon C. 2007. The auditory region of early Paleocene Pucadelphydae (Mammalia, Metatheria) from Tiupampa, Bolivia, with phylogenetic implications. *Palaeontology* **50:** 1123–1154.

Ladevèze S, de Muizon C. 2010. Evidence of early evolution of Australidelphia (Metatheria, Mammalia) in South

America: phylogenetic relationships of the metatherians from the Late Palaeocene of Itaboraí (Brazil) based on teeth and petrosal bones. *Zoological Journal of the Linnean Society* **159:** 746–784.

Ladevèze S, Asher RJ, Sánchez-Villagra MR. 2008. Petrosal anatomy in the fossil mammal *Necrolestes*: evidence for metatherian affinities and comparisons with the extant marsupial mole. *Journal of Anatomy* **213:** 686–697.

Ladevèze S, Smith R, Smith T. 2012. Reassessment of the morphology and taxonomic status of the earliest herpetotheriid marsupials of Europe. *Journal of Mammalian Evolution* **19:** 249–261.

Luo ZX, Ruf I, Schultz JA, Martin T. 2011. Fossil evidence on evolution of inner ear cochlea in Jurassic mammals. *Proceedings of the Royal Society of London B: Biological Sciences* **278:** 28–34.

MacIntyre GT. 1972. The trisulcate petrosal pattern of mammals. In: Dobzhansky T, Hecht MK, Steere WC, eds. *Evolutionary biology*. New-York: Plenum Press, 275–303.

MacPhee RDE. 1981. Auditory regions of primates and eutherian insectivores: morphology, ontogeny, and character analysis. *Contributions to Primatology* **18:** 1–282.

Macrini TE, Rowe T, VandeBerg JL. 2007. Cranial endocasts from a growth series of *Monodelphis domestica* (Didelphidae, Marsupialia): a study of individual and ontogenetic variation. *Journal of Morphology* **268:** 844–865.

Marshall LG, de Muizon C. 1995. Part II. The skull. In: de Muizon C, ed. *Pucadelphys andinus (Marsupialia, Mammalia) from the early Paleocene of Bolivia*, Vol. 165. Paris: Mémoires du Muséum national d'Histoire naturelle, 21–90.

Martin GM. 2005. Intraspecific variation in *Lestodelphys halli* (Marsupialia: Didelphimorphia). *Journal of Mammalogy* **86:** 793–802.

Meng J, Fox RC. 1995. Osseous inner ear structures and hearing in early marsupials and placentals. *Zoological Journal of the Linnean Society* **115:** 47–71.

Reig OA, Kirsch JAW, Marshall LG. 1987. Systematic relationships of the living and Neocenozoic American 'opossum-like' marsupials (suborder Didelphimorphia), with comments on the classification of these and of the Cretaceous and Paleogene New World and European metatherians. In: Archer M, ed. *Possums and opossums: studies in evolution*. Sydney: Surrey Beatty & Sons and the Royal Zoological Society of New South Wales, 1–89.

Rougier GW, Wible JR. 2006. Major changes in the ear region and basicranium of early mammals. In: Carrano M, Gaudin TJ, Blob R, Wible JR, eds. *Amniote paleobiology: phylogenetic and functional perspectives on the evolution of mammals, birds and reptiles*. Chicago, IL: University of Chicago Press, 269–311.

Sánchez-Villagra MR. 2002. The cerebellar paraflocculus and the subarcuate fossa in *Monodelphis domestica* and other marsupial mammals: the ontogeny and phylogeny of a brain-skull interaction. *Acta Theriologica* **47:** 1–14.

Sánchez-Villagra MR, Wible JR. 2002. Patterns of evolutionary transformation in the petrosal bone and some basicranial features in marsupial mammals, with special reference to didelphids. *Journal of Zoological Systematics and Evolutionary Research* **40:** 26–45.

Sánchez-Villagra MR, Ladevèze S, Horovitz I, Argot C, Hooker JJ, Macrini T, Martin T, Moore-Fay S, de Muizon C, Schmelzle T, Asher RJ. 2007. Exceptionally preserved North American Paleogene metatherians: adaptations and discovery of a major gap in the opossum fossil record. *Proceedings of the Royal Society, Biology Letters* **3:** 318–322.

Segall W. 1970. Morphological parallelisms of the bulla and auditory ossicles in some insectivores and marsupials. *Fieldiana: Zoology* **51:** 169–205.

Spoor F, Garland T, Krovitz G, Ryan TM, Silcox MT, Walker A. 2007. The primate semicircular canal system and locomotion. *Proceedings of the National Academy of Sciences of the United States of America* **104:** 10808–10812.

Starck D. 1967. Le Crâne Des Mammifères. In: Grassé PP, ed. *Traité de Zoologie. Anatomie, Systématique, Biologie*. Paris: Masson et Cie, Tome XVI, fascicule I, 405–549.

Van der Klaauw CJ. 1931. The auditory bulla in some fossil mammals, with a general introduction to this region of the skull. *Bulletin of the American Museum of Natural History* **LXII:**1–352.

Van Valen L. 1966. Deltatheridia, a new order of mammals. *Bulletin of the American Museum of Natural History* **132:** 1–126.

Voit M. 1909. Das Primordialcranium Des Kaninchens Unter Berücksichtigung Der Deckknochen. Ein Beitrag Zur Morphologie Des Säugetierschädels. *Anatomische Hefte* **38:** 425–616.

Voss RS, Jansa SA. 2009. Phylogenetic relationships and classification of didelphid marsupials, an extant radiation of New World metatherian mammals. *Bulletin of the American Museum of Natural History* **322:** 1–177.

Vullo R, Gheerbrant E, de Muizon C, Néraudeau D. 2009. The oldest modern therian mammal from Europe and its bearing on stem marsupial paleobiogeography. *Proceedings of the National Academy of Sciences of the United States of America* **106:** 19910–19915.

West CD. 1985. The relationship of the spiral turns of the cochlea and the length of the basilar membrane to the range of audible frequencies in ground dwelling mammals. *Journal of the Acoustical Society of America* **77:** 1091–1101.

Wible JR. 1990. Petrosals of Late Cretaceous marsupials from North America, and a cladistic analysis of the petrosal in therian mammals. *Journal of Vertebrate Paleontology* **10:** 183–205.

Wible JR. 2003. On the cranial osteology of the short-tailed opossum *Monodelphis brevicaudata* (Didelphidae, Marsupialia). *Annals of Carnegie Museum* **72:** 137–202.

Wible JR, Rougier GW, Novacek MJ, Asher RJ. 2009. The Eutherian mammal Maelestes gobiensis from the Late

© 2016 The Linnean Society of London, *Zoological Journal of the Linnean Society*, 2016

Cretaceous of Mongolia and the phylogeny of Cretaceous Eutheria. *Bulletin of the American Museum of Natural History* **327:** 1–123.

Williamson TE, Brusatte SL, Wilson GP. 2014. The origin and early evolution of metatherian mammals: the Cretaceous record. *ZooKeys* **465:** 1–76.

SUPPORTING INFORMATION

Additional supporting information may be found online in the supporting information tab for this article:

Figure S1. Photograph of the inventory of the Cuvier's 'opossum' in the catalogue of fossil bones of vertebrates (second volume, 1861).

© 2016 The Linnean Society of London, *Zoological Journal of the Linnean Society*, 2016

PROJET DETAILLE et ANNEXE :

ATM
« *Formes possibles, Formes réalisées*»
Demande de financement 2014- 2015

Porteur du projet : **SELVA Charlène**

Morphologie du système auditif et vestibulaire des mammifères et thérapsides creuseurs-fouisseurs

Résumé du projet :

Le mode de vie souterrain chez les vertébrés implique des modifications drastiques de tout le squelette de l'animal en réponse aux contraintes mécaniques dues à l'action de fouissage, ainsi qu'une modification des organes des sens pour une meilleure perception du milieu. L'appareil auditif et vestibulaire des mammifères permet d'analyser l'impact de ces deux contraintes environnementales ou fonctionnelles : (i) le système vestibulaire de l'oreille interne traduit les mouvements de la tête, qui joue un rôle fondamental dans le fouissage ; (ii) l'oreille moyenne et interne indique les capacités auditives de l'animal, notamment une meilleure réception des sons basses fréquences.

Le mode de vie creuseur-fouisseur est très répandu chez les mammifères actuellement, et aussi dans le passé, si l'on considère les mammifères éteints, les mammaliamorphes jusqu'à leurs lointains parents les thérapsides. Ce mode de vie a-t-il représenté un avantage adaptatif dans l'histoire évolutive des mammifères ?

Une étude comparative des oreilles d'amniotes fouisseurs actuels (mammifères/reptiles) obtenues par CT-Scan déterminera différents degrés de fouissage/creusage. Ces résultats seront ensuite appliqués aux fossiles afin d'estimer leur mode de vie. Replacés dans un contexte évolutif et temporel, ces résultats permettront de préciser l'importance de ce mode de vie dans l'histoire des mammifères, en particulier au passage des grandes crises biologiques.

Objectifs à atteindre grâce à la présente demande de financement :

i) Documenter l'anatomie des appareils vestibulaires et auditifs des mammifères fouisseurs actuels (grâce à la modélisation en 3D)

ii) Rechercher le signal fonctionnel avec l'étude de la morphologie de l'oreille interne (description anatomique, mesures de distance, morphométrie géométrique)

iii) Capacité vestibulaire, posture et locomotion : chercher la corrélation entre anatomie de l'oreille interne et mode de vie fouisseur grâce à la méthode développée par R. David.

iv) Inférence fonctionnelle chez les fossiles (spécimens fossiles déjà scannés)

v) Intégrer de nouvelles méthodes d'interprétation fonctionnelle grâce à la session de travail avec le post-doctorant R. David (Mission Allemagne)

Méthodes :
L'outil analytique privilégié est le microtomographe à rayons X de la plateforme AST-RX du MNHN ; cet outil permet d'accéder aux structures internes du crâne et de la région auditive de façon non destructive. La reconstruction de modèles virtuels en trois dimensions de l'oreille interne (labyrinthe osseux) sera réalisée sur la plateforme 3D de l'UMR7207. Grâce aux observations d'anatomie comparée, des mesures et des points-repère seront pris sur le labyrinthe osseux (cochlée, vestibule, canaux semi-circulaires) et des analyses multivariées seront conduites pour tenter d'établir une corrélation de type forme/fonction.

Échantillonnage pour les scans :

L'échantillonnage à constituer permettra de :

1) Représenter le mieux possible les différents clades présentant des taxons fouisseurs

Il s'agira d'essayer de représenter au maximum la diversité des fouisseurs :
- D'un point de vue phylogénétique, le choix des spécimens permet de représenter les différents clades présentant des taxons fouisseurs.
- D'un point de vue écologique, en plus des taxons strictement fouisseurs (généralement souterrains), des taxons écologiquement intermédiaires sont choisis pour documenter différents degrés de fouissage. Pour chacun des clades, en plus des taxons fouisseurs, des taxons généralistes terrestres sont choisis pour comparaison.

Pour appliquer la méthode de R. David (sous presse), l'idéal est d'avoir un spécimen conservé en fluide par clade afin d'étudier le labyrinthe membraneux. La morphologie du labyrinthe membraneux peut alors s'inférer sur les taxons phylogénétiquement proches où seul le labyrinthe osseux est disponible.

Ainsi, et dans un premier temps, il est indispensable d'échantillonner un spécimen en fluide par clade. Dans un second temps, il me semble pertinent d'échantillonner au moins deux taxons fouisseurs par famille, et ce pour chacun des clades plus inclusifs considérés (voir ci-après). Dans un troisième temps, des taxons creuseurs ou semi-fouisseurs et des taxons généralistes terrestres seront sélectionnés pour comparaison et pour chacun des clades.

2) Etudier la variabilité intraspécifique au sein de la taupe européenne *Talpa europaea*

Nous disposons de 13 CT-Scans (13 labyrinthes osseux modélisés en 3D) de la taupe européenne. Avec 20 individus au total, il serait possible d'avoir une meilleure idée de la variabilité intraspécifique de la morphologie de l'oreille interne chez cette espèce. Les collections ostéologiques du MNHN (ZMO, AC) possèdent un grand nombre de crâne de *Talpa europaea*.

Choix des spécimens : **TOTAL = 23 spécimens à scanner**
Les données des spécimens en vert sont déjà acquises.
Les données des spécimens en rouge doivent être acquises grâce à la présente demande.
Les données des spécimens en orange devront être acquises grâce à un projet synchrotron.

Monotrèmes : 1 *Ornithorhynchus anatinus* (ornithorynque) et 1 *Zaglossus bartoni* (échidné).

Marsupiaux
Fouisseur strict : 2 *Notoryctes typhlops* (taupes marsupiales) (1 spécimen ostéologique déjà scanné + 1 spécimen en fluide)
Fouisseur intermédiaire : **1 *Planigale maculata* (planigale)**, 1 *Vombatus ursinus* (wombat), 1 *Macrotis lagotis* (bilby), 1 *Dasyuroides byrnei* (Kowari), 1 Perameles nasuta (bandicoot en ostéo), 1 *Isoodon auratus (*bandicoot en fluide)
Généraliste terrestre : 1 *Dasyurus viverrinus* (chat marsupial).

Placentaires, de nombreux clades présentent des taxons fouisseurs :

Afrothériens
Fouisseurs stricts : au sein des taupes dorées (Chrysochloridae), qui ressemblent beaucoup à la taupe marsupiale, il existe 7 genres dont 3 sont échantillonnés (1 *Chlorotalpa sclateri*, 1 *Chrysochloris asiatica*, **1 *Eremitalpa granti*)**.
Fouisseurs intermédiaires : 1 *Orycteropus afer* (oryctérope), 1 *Potamogale velox* (Potamogale)
Généraliste terrestre : 1 *Tenrec ecaudatus* (tenrec)

Laurasiathériens
Fouisseurs stricts : il existe 13 genres de « Eu-taupes ». Seront échantillonnés: **1 *Condylura cristata*** (Am. Nord), **1 *Euroscaptor grandis*** (Asie), **1 *Scalopus aquaticus*** (Am. Nord), 13 *Talpa europaea* (Europe) **(+ 7 spécimens pour l'étude de variabilité intraspécifique).**
Fouisseurs intermédiaires : 1 *Galemys pyrenaicus* (desman des Pyrénées) ; 1 *Vulpes zerda* (fennec) ; 1 *Meles meles* (blaireau); **1 *Cynictis penicillata* (mangouste).**
Généralistes terrestres : 1 *Erinaceus europaeus* (hérisson), 1 *Atelerix frontalis* (hérisson) ; 1 *Pteronura brasiliensis* (loutre).

Euarchontoglires
Fouisseurs stricts : chez les rongeurs, 4 familles présentent des taxons fouisseurs :
- Ctenomyidae (Tuco-Tuco) : 2/3 genres ***Ctenomys*, *Actenomys*.**
- Bathyergidae (Rats-Taupes) : 2/5 genres, ***Bathyergus*, *Heliophobius*.**
- Spalacidae : 2/5 genres, ***Myospalax* (hamster-taupe),** *Spalax* (rat taupe)
- Geomyidae (rat à abajoues) : 2/6 genres, ***Geomys* (rat à abajoues creuseur), *Thomomys* (rat à abajoues des montagnes)**

Fouisseurs intermédiaires : 1 ***Arvicola sapidus***, 1 *Crocidura leucodon*, 1 *Xerus erythropus* (écureuil des terriers), 1 *Oryctolagus cuniculus* (lapin) ; **1 *Cynomys ludovicianus* (chien des prairies)**
Généralistes terrestres : 1 *Sciurus vulgaris* (écureuil), 1 *Sorex cinereus* (musaraigne)

Xénarthres
Fouisseurs stricts : 1 *Chlamyphorus truncatus* (tatou nain), 1 *Calyptophractus retusus* (tatou nain)
Fouisseurs intermédiaires : 1 *Chaetophractus villosus* (tatou)
Généralistes terrestres : 1 ***Dasypus pilosus* (tatou)**

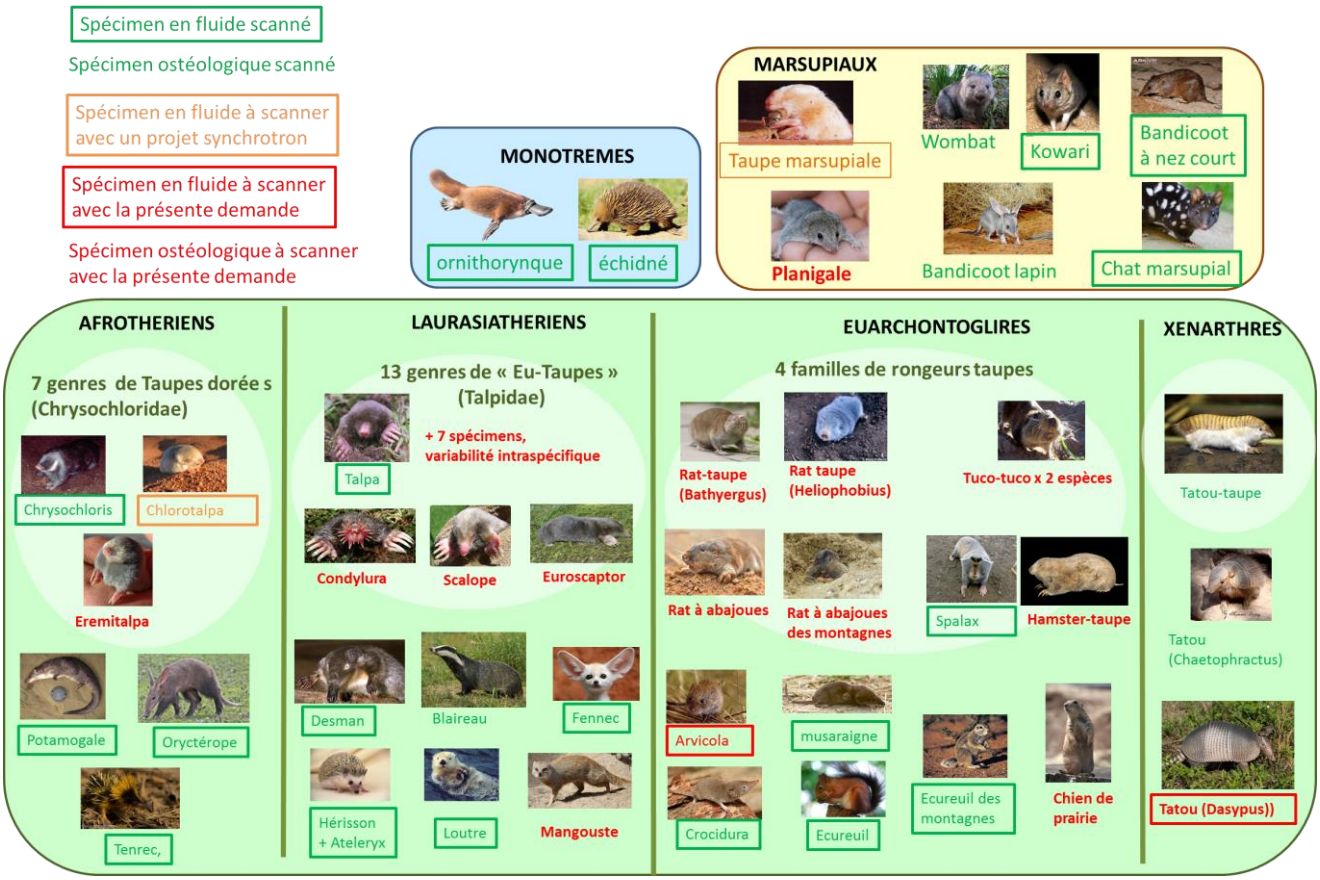

Session de travail - Mission d'étude méthodologique :
Durée : 2 semaines
Date : Juillet 2015
Lieu : Max Planck Institute for Evolutionary Anthropology, Deutscher Platz 6, 04103 Leipzig
Objectif : Intégrer les nouvelles méthodes d'interprétation fonctionnelle de l'oreille interne développées par R. David lors de sa thèse au MNHN et de ses études post-doctorales. Cette mission sous forme de session de travail me permettra également d'échanger avec R. David sur les différentes découvertes, recherches et méthodologies en rapport avec l'oreille interne. R. David, qui est membre de mon comité de thèse, approuve bien évidement ma venue.

Budget détaillé :

- **Mission : = 762€**
  Voyage : billet d'avion aller-retour / 200€
  Logement : logement dans un studio de l'institut, 14 nuits à 25€ par nuit / 350€
  Repas : environ 13€ par jour / 182€
  Transport : tickets de bus / 30€

- **Fonctionnement/Analyse : = 1500€**
  Frais d'analyses/acquisitions des données via la plateforme AST-RX (CT-Scan)
  Au total, 23 crânes de mammifères actuels (collections MNHN) :
  250€ la journée, 4 spécimens/jour, soit 1500€ pour les 23 spécimens.

TOTAL = 2262€

Liste des principales publications des participants, pertinentes pour ce projet :

Billet, G., Muizon, C. de, Schellhorn, R., Ruf, I., Ladevèze, S., & Bergqvist, L. 2014 (accepted). Petrosal and inner ear anatomy and allometry among specimens referred to Litopterna (Placentalia). Zoological Journal of the Linnean Society.

Billet G, Germain D, Ruf I, Muizon C de, Hautier L. 2013. The inner ear of *Megatherium* and the evolution of the vestibular system in sloths. *Journal of Anatomy* 223(6): 557-567.

Billet G, Hautier L, Asher R, Schwarz C, Crumpton N, Martin T, Ruf I. 2012. High morphological variation of vestibular system accompanies slow and infrequent locomotion in three-toed sloths. *Proceedings of the Royal Society B: Biology*. doi:10.1098/rspb.2012.1212.

David, R., Droulez, J., Allain, R., Berthoz, A., Janvier, P., & Bennequin, D. 2010. Motion from the past. A new method to infer vestibular capacities of extinct species. *Comptes Rendus Palevol*, 9(6), 397-410.

Germain, D., & Laurin, M. 2005. Microanatomy of the radius and lifestyle in amniotes (Vertebrata, Tetrapoda). *Zoologica Scripta*, 34(4), 335-350.

Joeckel RM, Peigné S, Skolnick RI & Hunt, RM, Jr. 2002. The auditory region and nasal cavity of Oligocene Nimravidae (Mammalia: Carnivora). *Journal of Vertebrate Paleontology* 22 : 830-847.

Ladevèze S, Muizon C de, Beck RM, Germain D & Cespedes-Paz R. 2011. Earliest evidence of mammalian social behaviour in the basal Tertiary of Bolivia. *Nature* 474: 83-86.

Ladevèze S, Asher RJ & Sánchez-Villagra MR. 2008. Petrosal anatomy in the fossil mammal *Necrolestes*: evidence for metatherian affinities and comparisons with the extant marsupial mole. *Journal of Anatomy* 213: 686-696.

Ladevèze S, Muizon C de, Colbert M & Smith T. 2010. 3D computational imaging of the petrosal of a new multituberculate mammal from the Late Cretaceous of China and its paleobiologic inferences. *CR Palevol* 9:319-330.

EUROPEAN SYNCHROTRON RADIATION FACILITY

ESRF User Office
CS 40220, F-38043 GRENOBLE Cedex 9, France
Delivery address: 71 avenue des Martyrs, 38000 GRENOBLE, France
Tel: +33 (0)4 7688 2552; fax: +33 (0)4 7688 2020; email: useroff@esrf.fr; web: http://www.esrf.fr

Application for beam time at ESRF – Experimental Method

This document should consist of a **maximum** of **two A4 pages** (including references) with a minimal font size of **12 pt**.

Correlation between the vestibular system of the inner ear and the lifestyle of mammals

Proposal Summary (should state the aims and scientific basis of the proposal) :
Marsupial mammals show a wide diversity in their traits of life, particularly in their feeding and locomotor habits, from the nectarivore pigmy possum to the scavenger Tasmanian devil, and from subterraneous or fossorial forms to gliding arboreal forms. The bony labyrinth of the inner ear contains the organs of balance and audition and may therefore be linked to the locomotor patterns of vertebrates.
Once demonstrated that the membranous labyrinth function and the animal behaviour are correlated, it is crucial to understand how the functional parameters are approximated by the bony labyrinth, and to evaluate the relevancy of the latter in ecological inferences.
The project will aim at finding correlations between the bony labyrinth morphology and the membranous labyrinth functioning in a wide sample of mammals. Furthermore, a large-scaled analysis based on marsupial and placental ecomorphological analogs will be launched to answer the following: do locomotor habits have a same structuration pattern of the inner ear?

Scientific background :
Since Jones & Spells (1963) and Mayne (1965), a strong theoretical background exists to support a causal relation between inner ear function and animal behaviours. However, technological constraints prevented to fully quantify the shape of the inner ear organs; consequently, the veracity of such causal relation failed to be tested. In the meantime, researchers tried to establish correlations between the limited (but easier to access) parameters provided by the bony labyrinth of the inner ear and locomotion behaviours (e.g., Spoor et al. 2007, Malinzak et al. 2012). Nonetheless, these studies suffer from two main biases. First, they mostly focus on placental mammals: marsupials are under represented, diprotondontians (kangaroos and relatives) being only included in analyses scrutinizing the relationship between shape and phylogeny (e.g., Alloing-Séguier et al., 2013). Second, and more importantly, the reliability of using non-functional bony labyrinth parameters instead of functional membranous ones to infer locomotor behaviours has implicitly never been addressed, except until recently by one of us (R.D.). Preliminary results strongly suggest that previous bony labyrinth based methodologies are in fact highly unreliable and that a new bony-to-membranous labyrinth based methodology, taking phylogenetically specific correlations between bones and soft tissues, is needed if one wants to infer anything from bony labyrinths with satisfactory precision (RD, in prep.).
We expect to overcome these biases through a comprehensive sampling of mammals, including all clades and various locomotions, and acquisition of inedite data on inner ear morphology thanks to phase contrast SR-μCT.

Experimental technique(s), required set-up(s), measurement strategy, sample details (quantity...etc):
When possible, we started to acquire conventional microCT data on beforehand stained specimens from the comparative anatomy collections of the MNHN. However, the marsupial specimens from the Zoothèque of the MNHN require an alternative non-invasive treatment. As such, the Synchrotron scan remains the only methodology possible. We selected 16 specimens (11 marsupials, 4 placentals and 1 monotreme for which data are still to be acquired), all preserved in alcohol. Their size (ear region only) is approximately from

5x5cm to 1x1cm (length x wide) (Fig. 1). We plan to scan them with voxel sizes ranging from 5 to 8 microns, a resolution which already gave satisfactory results (Fig. 2).
We will use propagation phase contrast imaging using high quality pink beams on the ID19, coupled with optimized sets of filters and scintillators. The energies will range from 26.5 to 70 keV depending on the specimen size. The data will be reconstructed using the single distance phase retrieval process of Paganin to ensure high quality data with high sensitivity for soft tissue imaging.

Figure 1. Two size-extreme specimens among marsupials sampled for this project: water opossum (left) one of the largest, pygmy gliding possum (right) one of the smallest.

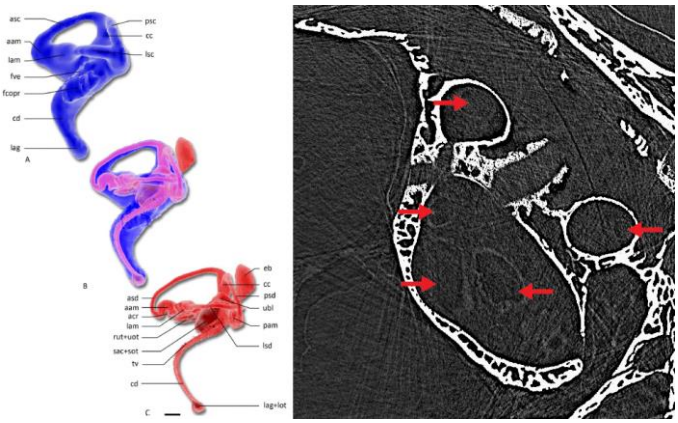

Figure 2. Synchrotron images of the osseous and membranous (red arrows) labyrinths of the inner ear of a crocodile (past project from RD). Left: the 3D reconstruction of the bony (blue) and membranous (red) labyrinths.

Beamline(s) and beam time requested with justification :

ID19 is well suited for this project. All the experiments will be performed in pink beam using low dose setup to ensure no risk for these invaluable specimens. Set up will be approximately 2 hours for each configuration. The detailed scan of the ear region will require 20 hours in total (including the centering time). Regarding to the complexity to mount the specimens, we are then requesting X Days (X shifts) of beamtime on ID19.

Results expected and their significance in the respective field of research :

With data on the membranous labyrinth of the inner sampled in one specimen per clade, coupled with data on the osseous labyrinth of the inner ear in the other relevant species among the sampled clades, we expect to have a solid dataset to highlight a correlation between the vestibular anatomy of the inner ear (reflecting head movements and balance) and the locomotion and lifestyle of the animal.
The ultimate goal of the project will be to infer lifestyle to fossils, from their intrapetrosal casts, if we succeed in highlighting, as expected, that the latters are relevant for reflecting the functions of their inner organs.

References

Alloing-Séguier T, Sánchez-Villagra MR, Lee MSY & Lebrun R. 2013. The bony labyrinth in diprotodontian marsupial mammals: diversity in extant and extinct forms and relationships with size and phylogeny. *J Mamm Evol* 20:191-198.
Jones MG & Spells KE. 1963. A theoretical and comparative study of the functional dependence of the semicircular canal upon its physical dimensions. *Proc R Soc B* 157, 403-419.
Mayne, R. 1965. The "match" of the semicircular canals to the dynamic requirements of various species. *The Role of the Vestibular Organs in the Exploration of Space. NASA SP-77*: 57-67.
Malinzak MD, Kay RF & Hullar TE. 2012. Locomotor head movements and semicircular canal morphology in primates. *Proc Natl Acad Sci USA* 109: 17914–17919.
Spoor F, Garland T, Krovitz G, Ryan TM, Silcox MT & Walker.A. 2007. The primate semicircular canal system and locomotion. *Proc Natl Acad Sci USA* 104: 10808-12.

Projet de candidature pour une bourse courte durée DAAD

L'oreille interne, un sujet à creuser

Étude de cas des mammifères souterrains

Candidate

Charlène Selva, doctorante au Muséum national d'Histoire naturelle, 2ème année
Centre de Recherche sur la Paléobiodiversité et les Paléoenvironnements – UMR 7207
8 rue Buffon – CP 38
75005 Paris
charlene_selva@msn.com – charlene.selva@edu.mnhn.fr
Tel : +33 6 85 40 07 94

Résumé du projet

Le projet a pour but de mettre en évidence la corrélation entre l'anatomie de l'oreille interne membraneuse et le mode de vie fouisseur grâce à la méthode développée par le collaborateur Romain David travaillant au Max Planck Institut für evolutionäre Anthropologie à Leipzig. Dans une perspective d'ouverture du projet de recherche, la corrélation établie pourrait permettre d'inférer un mode de vie aux fossiles. Replacés dans un contexte évolutif et temporel, ces résultats permettront de préciser l'importance de ce mode de vie dans l'histoire des mammifères, en particulier au passage des grandes crises biologiques.
L'oreille interne membraneuse, organe sensoriel, gère l'équilibre et les mouvements de la tête. Le mode de vie souterrain impose des mouvements de tête intenses et très fréquents. Ces contraintes mécaniques doivent se retranscrire dans la morphologie de cet organe. Afin de caractériser cette morphologie particulière de l'oreille interne membraneuse des mammifères fouisseurs, 10 spécimens sont étudiés : ils ont été scannés au synchrotron européen et les modélisations 3D de l'oreille ont commencé.

Le séjour d'un mois permettrait de finaliser le projet : vérifier les modélisations 3D, poser des landmarks, intégrer les données dans les programmes élaborés par l'hôte, lancer les analyses et émettre les premières interprétations. Les résultats nous permettront de caractériser la morphologie de l'oreille interne membraneuse (morphométrie classique et géométrique). Grâce aux logiciels, nous obtiendrons également les paramètres fonctionnels de l'oreille telle que la sensibilité.

Sommaire

Encadrants, Collaborateurs et Institutions

Directeur de thèse (HDR) :
Stéphane Peigné – Chargé de recherche CNRS – UMR 7207
peigne@mnhn.fr
Tel : +33 1 40 79 30 25

Co-encadrant :
Sandrine Ladevèze – Chargé de recherche CNRS – UMR 7207
ladeveze@mnhn.fr
Tel : +33 1 40 79 30 24

Co-encadrant :
Damien Germain – Maître de conférences MNHN – UMR 7207
germain@mnhn.fr
Tel : +33 1 40 79 30 96

Collaborateur :
Romain David – Post-doctorant au Max-Planck-Institut für evolutionäre Anthropologie (Leipzig)
romain_david@eva.mpg.de
Tel : +49 (0)341 / 3550-857

Taupe européenne creusant (magazine La Hulotte)

Contexte de la demande : mon sujet de thèse

Cette demande de financement me permettrait de finaliser un projet intégré à ma thèse intitulée « Morphologie du système vestibulaire et auditif des mammifères et thérapsides creuseurs-fouisseurs ». L'objectif de ma thèse est de caractériser le lien entre la morphologie de l'oreille interne et le style de vie souterrainne.

L'oreille interne (= labyrinthe membraneux) est un organe sensoriel composé de deux parties : le système vestibulaire qui permet de gérer l'équilibre et le système auditif qui contrôle l'ouïe (Fig. 1). Cet ensemble de tissus mous est contenu dans une cavité osseuse que l'on nomme labyrinthe osseux.

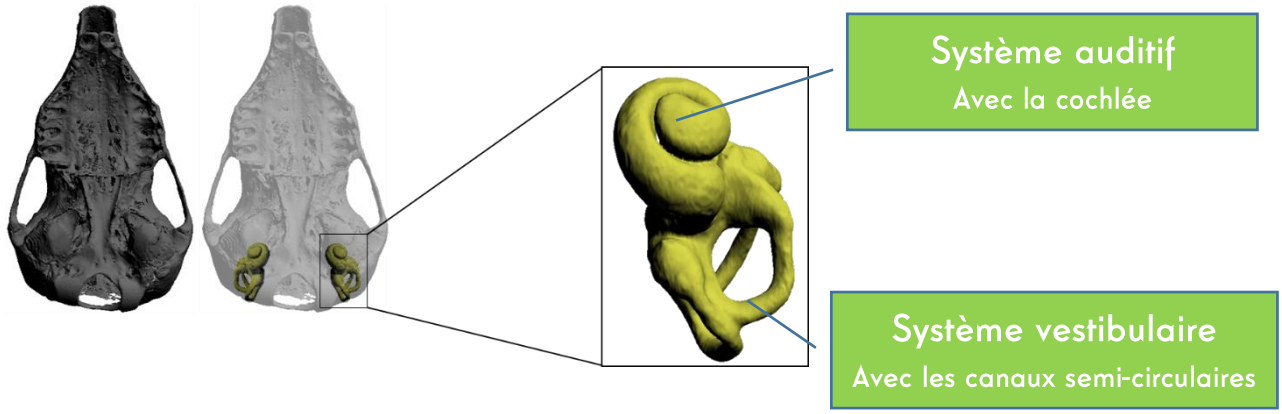

Figure 1 : Anatomie du labyrinthe. Ici, la modélisation correspond à un labyrinthe osseux de la taupe marsupiale, *Notoryctes typhlops*.

Le principal axe de mon sujet de thèse est de travailler sur la morphologie de cette cavité osseuse. Mais avec l'accord de mes encadrants, j'ai décidé de compléter ce premier axe en travaillant également sur la morphologie du labyrinthe membraneux (Fig. 2).

Ce projet de recherche s'est mis en place avec la collaboration de Romain David actuellement post-doctorant au Max Planck Institut für evolutionäre Anthropologie (Leipzig). Sa recherche consiste à mettre en place une méthodologie solide pour observer et caractériser la morphologie du labyrinthe membraneux.

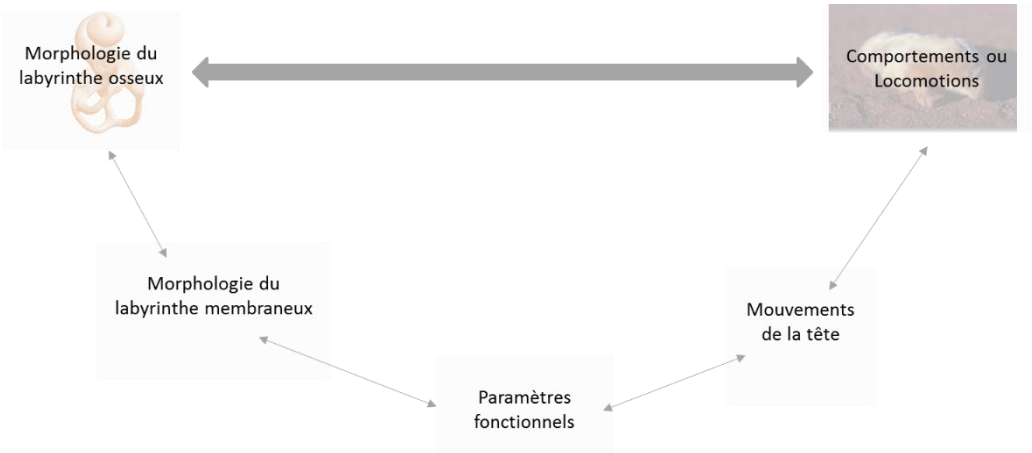

Figure 2 : Ce schéma représente les différents liens entre les objets d'étude. L'axe principal de ma thèse consiste à caractériser le lien entre morphologie du labyrinthe osseux et le comportement souterrain (flèche épaisse). En accord avec mes encadrants, une collaboration s'est ouverte avec Romain David pour travailler sur les liens entre morphologie du labyrinthe membraneux et locomotion (en passant par les paramètres fonctionnels et les mouvements de la tête). Ce projet fait partie intégrante de la thèse.

Contexte scientifique du projet

Bien que la structure générale de l'oreille interne membraneuse semble commune à l'ensemble des mammifères, la morphologie détaillée varie même entre groupe proche phylogénétiquement. Ceci implique que la forme du labyrinthe comporte des informations fonctionnelles et phylogénétiques. Les variations de dimensions, de formes et d'orientations, concernant principalement les canaux semi-circulaires (système vestibulaire) sont liées à la sensibilité aux mouvements de la tête et aux comportements locomoteurs.

Les mammifères souterrains sont alors un cas pratique parfait pour étudier la corrélation entre morphologie de l'oreille interne et type écologique. Effectivement, les mouvements de tête jouent un rôle incontournable chez les animaux au style de vie souterrain : tous les différents modes de fouissage sollicitent fortement la tête (Fig. 3). L'oreille interne doit permettre de gérer des mouvements de tête intenses et très fréquents, contraintes mécaniques qui doivent se retranscrire dans la morphologie de l'organe.

Figure 3 : Les différentes façons de creuser impliquent, dans tous les cas, des mouvements de la tête intenses et fréquents. Ces contraintes mécaniques doivent se retranscrire dans la morphologie du labyrinthe membraneux, organe gérant les mouvements de la tête.

Problématiques du projet

Le projet a donc pour objectifs :

i) Documenter l'anatomie des appareils vestibulaires et auditifs des mammifères fouisseurs actuels

ii) Rechercher le signal fonctionnel avec l'étude de la morphologie de l'oreille interne membraneuse

iii) Mettre en évidence la corrélation entre anatomie de l'oreille interne et mode de vie fouisseur grâce à la méthode développée par Romain David

Echantillonnages théorique et pratique

Au moins une espèce a été choisie par grand clade de taxon strictement souterrain. Le contrôle des signaux phylogénétique et fonctionnel se fait grâce aux données de Romain David : il a déjà implémenté suffisamment de taxons dans la méthodologie pour avoir un contrôle conséquent. L'échantillonnage permet de couvrir les trois grands clades de mammifères : les monotrèmes, les marsupiaux et les placentaires (Fig. 4). Pour chacun des clades, l'échantillonnage prend en compte la proportion de fouisseur. Enfin, l'échantillonnage permet de couvrir les différentes techniques utilisées par les animaux pour creuser.

En pratique, il a fallu choisir les spécimens adéquats conservés en alcool au sein des collections du muséum. Voici les 10 taxons choisis :

Chez les placentaires

- *Talpa* (taupe européenne)
- *Condylura* (taupe étoilée)
- *Ctenomys* (tuco-tuco)
- *Spalax* (rat-taupe)
- *Heterocephalus* (rat-taupe nu)
- *Thomomys* (gaufre à poche)
- *Chlamyphorus* (tatou nain taupe)
- *Chlorotalpa* (taupe dorée)

Chez les marsupiaux

- *Notoryctes* (taupe marsupiale)

Chez les monotrèmes

- *Zaglossus* (echidné)

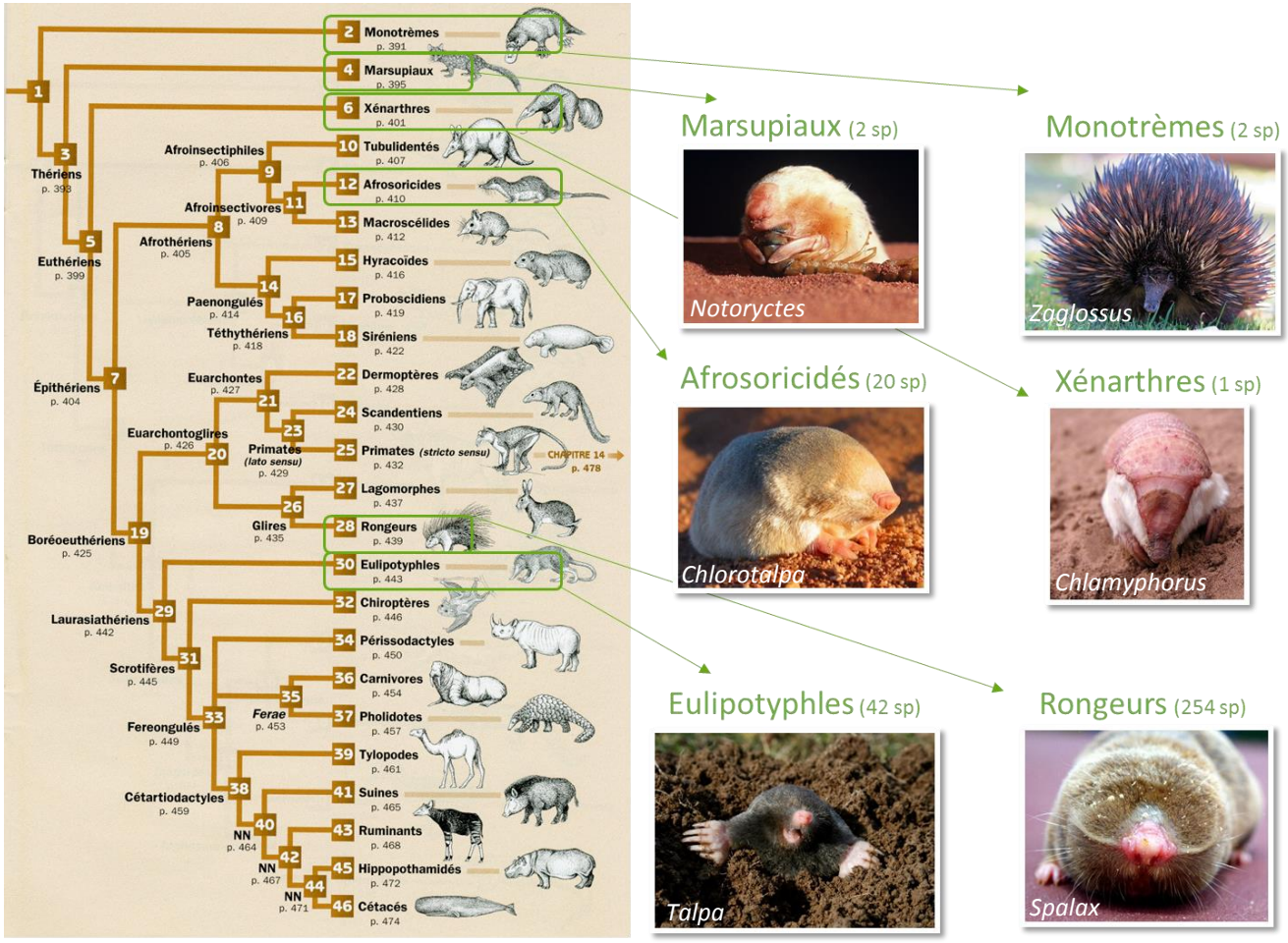

Figure 4 : Arbre phylogénétique consensuel des mammifères (Arbre Phylogénétique du Vivant – Lecointre) montrant les clades échantillonnés. Le nombre d'espèces souterraines comprises dans le clade est indiqué entre parenthèses.

Acquisition des données 1° : projet synchrotron (octobre 2015)

La plupart des spécimens choisis sont des pièces d'exception et les traitements invasifs sont donc interdits (Fig. 5). De ce fait, il était impossible d'utiliser la méthode classique pour accéder au labyrinthe membraneux qui consiste à baigner le spécimen dans du contrastant puis de le scanner grâce à un microtomographe (CT-scan). Ainsi, nous avons choisi une solution alternative : scanner nos spécimens avec la lumière synchrotron qui permet d'augmenter les contrastes et d'obtenir une excellente résolution sans abîmer les spécimens.

Figure 5 : Les spécimens exceptionnels conservés en alcool à la zoothèque du Muséum national d'Histoire naturelle à Paris. (De gauche à droite : *Spalax*, *Heterocephalus* et *Notoryctes*)

Le projet synchrotron a été déposé au début de l'année 2015 auprès de l'ESRF (synchrotron européen localisé à Grenoble). Il a été accepté et nous avons ainsi bénéficié de 48 heures de temps d'acquisition pour scanner les spécimens conservés en fluide. Pendant ce court séjour début octobre 2015, nous avons scanné les 10 spécimens du projet (Fig. 6). Les données traitées sont disponibles depuis fin novembre.

Figure 6 : Les 10 spécimens ont été scannés au synchrotron européen afin d'avoir un contraste suffisant sans abîmer les spécimens (octobre 2015).

Acquisition des données 2° : modélisation 3D
(décembre 2015 – juillet 2016)

A partir des coupes issues des scans synchrotron, le labyrinthe membraneux est reconstruit en 3 dimensions (Fig. 7), à l'aide des logiciels AVIZO et MIMICS en utilisant des écrans tactiles pour plus de précision. Cette étape a commencé en décembre 2015 et s'achèvera en juillet 2016 juste avant le séjour à Leipzig.

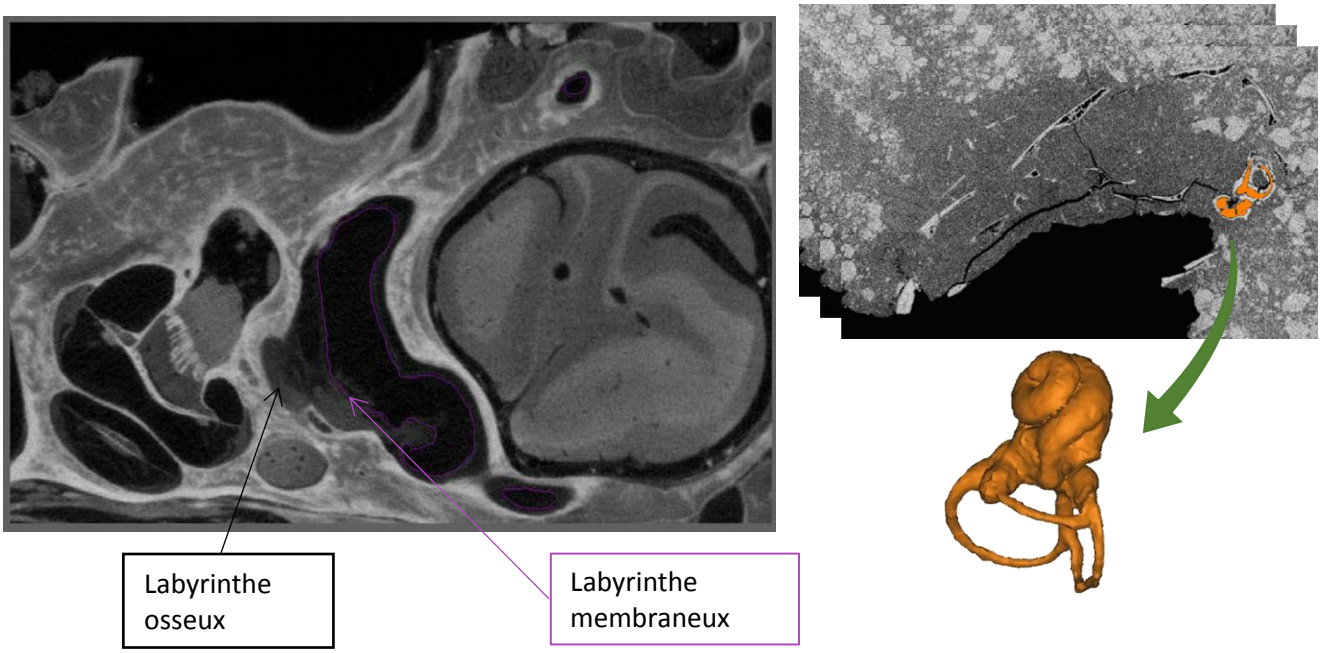

Figure 7 : L'illustration de gauche met en avant la présence du labyrinthe membraneux (= structure d'intérêt à modéliser) à l'intérieur de la cavité osseuse appelée labyrinthe osseux. L'illustration de droite schématise la modélisation : sur chacune des coupes issues du scan, il faut sélectionner les zones d'intérêt afin de modéliser en 3D l'objet dans son ensemble.

Traitement des modèles 3D et pose des landmarks (août 2016)

Le rendu des modèles 3D est ensuite optimisé (lissage de la surface, nettoyage et correction des imperfections). Les landmarks 3D sont positionnés sur la surface et le centre des labyrinthes membraneux via le logiciel AVIZO (Fig. 8).
Le traitement des modèles 3D et la position des landmarks suivent la méthodologie mise en place par Romain David.

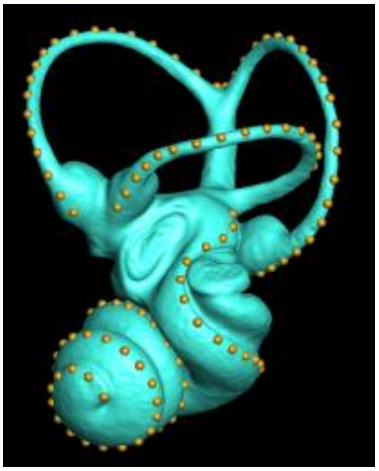

Figure 8 : La pose des landmarks se fera en suivant la méthodologie mise en place par Romain David qui supervisera le bon déroulement pendant le séjour en Allemagne (août 2016).

Analyse des données - Résultats attendus (août 2016)

Les données seront traitées par les différents programmes élaborés par Romain David. Ces programmes fournissent des données standardisées sur la morphologie de l'oreille interne (données de morphométrie classique et géométrique). En plus de ces données morphologiques, ces programmes donnent des indices chiffrés sur les paramètres fonctionnels du labyrinthe membraneux tel que la sensibilité. Ces données chiffrées seront interprétées grâce au référentiel existant dans le programme (mammifères généralistes terrestres). Cette comparaison permettra de caractériser les paramètres fonctionnels de l'oreille interne spécifiques à la vie souterraine.

Les résultats préliminaires suggèrent une morphologie particulière des labyrinthes membraneux des mammifères fouisseurs : ils sont plus épais que chez les mammifères terrestres généralistes. En ce qui concerne les paramètres fonctionnels, deux hypothèses non exclusives sont attendues :

- La morphologie de l'oreille interne traduit une sensibilité accrue aux mouvements horizontaux pour se repérer dans les galeries
- La morphologie de l'oreille interne ne traduit pas une sensibilité accrue aux mouvements verticaux afin de tolérer les mouvements de tête intenses réalisés pendant le fouissage

Faisabilité et Pertinence du projet

Le financement demandé me permettrait de finaliser ce projet clé de mon doctorat et de concrétiser le fruit de la collaboration entre nos deux institutions par l'écriture d'un article scientifique. Les données primaires sont déjà toutes acquises (scans synchrotron). Les données secondaires (modélisation 3D) sont en cour d'acquisition et tous les modèles 3D seront finis en juillet 2016. Le projet étant bien avancé, le financement d'un séjour d'un mois est adéquat et pertinent au vue des activités programmées : vérification des modèles 3D (quelques jours), pose des landmarks (1,5 semaine), intégration des données dans les programmes spécifiques (2 jours), analyses (1 jour) et interprétations (1 semaine). Le travail demandé par ces différentes étapes sera grandement facilité par le poste informatique présentant l'ensemble des logiciels nécessaires mis à ma disposition par l'institution hôte. L'ensemble du projet nécessite l'expertise du chercheur hôte, Romain David, imminent spécialiste de l'anatomie et physiologie de l'oreille interne et de l'analyse de données. Aussi, le traitement de données suivra la méthodologie élaborée par lui-même. Dans une perspective plus lointaine, ce séjour me permettrait aussi de consolider des liens pour un projet postdoctoral.

Planning du projet de recherche dans sa totalité

août 2015 → septembre 2015 → octobre 2015

1er séjour à Leipzig (15 jours) : formation sur la mécanique des fluides, les paramètres fonctionnels et l'anatomie du labvrinthe membraneux

Projet Synchrotron : Scan des 10 spécimens à ESRF

novembre 2015 → décembre 2015

Projet Synchrotron : Réception des données au laboratoire à Paris

2eme séjour à Leipzig (15 jours) : vérification des données issues du synchrotron et initiation à la segmentation du labvrinthe membraneux

janv. 2016 → fev. 2016 → mars 2016 → avril 2016 → mai 2016 → juin 2016 → juill. 2016

Modélisation 3D des labyrinthes membraneux

août 2016 : Séjour financé par votre bourse et conclusion du projet

Voir le planning détaillé

Publications des collaborateurs pertinentes avec le projet

David, R., Droulez, J., Allain, R., Berthoz, A., Janvier, P., & Bennequin, D. 2010. Motion from the past. A new method to infer vestibular capacities of extinct species. *Comptes Rendus Palevol*, 9(6), 397-410.

Germain, D., & Laurin, M. 2005. Microanatomy of the radius and lifestyle in amniotes (Vertebrata, Tetrapoda). *Zoologica Scripta*, 34(4), 335-350.

Joeckel RM, Peigné S, Skolnick RI & Hunt, RM, Jr. 2002. The auditory region and nasal cavity of Oligocene Nimravidae (Mammalia: Carnivora). *Journal of Vertebrate Paleontology* 22 : 830-847.

Ladevèze S, Muizon C de, Beck RM, Germain D & Cespedes-Paz R. 2011. Earliest evidence of mammalian social behaviour in the basal Tertiary of Bolivia. *Nature* 474: 83-86.

Ladevèze S, Asher RJ & Sánchez-Villagra MR. 2008. Petrosal anatomy in the fossil mammal *Necrolestes*: evidence for metatherian affinities and comparisons with the extant marsupial mole. *Journal of Anatomy* 213: 686-696.

Ladevèze S, Muizon C de, Colbert M & Smith T. 2010. 3D computational imaging of the petrosal of a new multituberculate mammal from the Late Cretaceous of China and its paleobiologic inferences. *CR Palevol* 9:319-330.

Selva C, Ladevèze S. 2016. Following Cuvier's investigation inside his famous opossum of Montmartre through microCT technologies. Soumis au Zoological Journal of Linnean Society.

Candidature au Projet Transhumance

L'oreille interne, un sujet à creuser

Étude de cas des mammifères souterrains

Candidate : Charlène Selva

Doctorante au Muséum national d'Histoire naturelle,
3ème année (1ère inscription le 1er octobre 2014)
Centre de Recherche sur la Paléobiodiversité et les Paléoenvironnements – UMR 7207
8 rue Buffon – CP 38
75005 Paris
charlene_selva@msn.com – charlene.selva@edu.mnhn.fr
Tel : +33 6 85 40 07 94

Encadrants, Collaborateurs et Institutions

Directeur de thèse (HDR) : (actuellement en congés de longue maladie)
Stéphane Peigné – Chargé de recherche CNRS – UMR 7207
stephane.peigne@mnhn.fr
Tel : +33 1 40 79 30 25
Co-encadrante :
Sandrine Ladevèze – Chargé de recherche CNRS – UMR 7207
sandrine.ladeveze@mnhn.fr
Tel : +33 1 40 79 30 24
Co-encadrant :
Damien Germain – Maître de conférences MNHN – UMR 7207
damien.germain@mnhn.fr
Tel : +33 1 40 79 30 96
Collaborateur :
Romain David – Post-doctorant au Max-Planck-Institut für evolutionäre Anthropologie (Leipzig)
romain_david@eva.mpg.de
Tel : +49 (0)341 / 3550-857

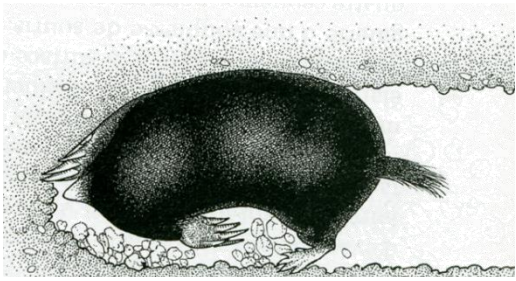

Taupe européenne creusant (magazine La Hulotte)

Contexte de la demande : mon sujet de thèse

Cette demande de financement me permettrait de finaliser une étude majeure de ma thèse, intitulée **« Morphologie du système vestibulaire et auditif des mammifères et thérapsides creuseurs-fouisseurs »**. L'objectif de ma thèse est de caractériser le lien entre la morphologie de l'oreille interne et le mode de vie souterrain chez les mammifères.
L'oreille interne (= labyrinthe membraneux) est un organe sensoriel composé de deux parties : le système vestibulaire qui permet de gérer l'équilibre et le système auditif qui contrôle l'ouïe (Fig. 1). Cet ensemble de tissus mous est contenu dans une cavité osseuse, le labyrinthe osseux.

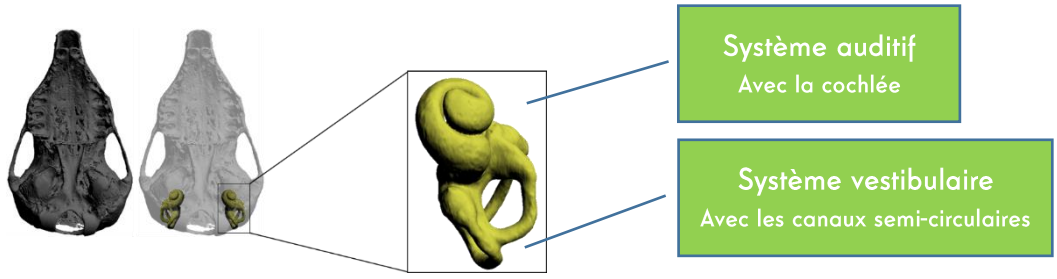

Figure 1 : Anatomie du labyrinthe osseux de l'oreille interne.
Ici, le modèle 3D est celui du labyrinthe osseux de la taupe marsupiale, *Notoryctes typhlops*.

Le principal axe de mon sujet de thèse concerne la morphologie de cette cavité osseuse. Toutefois, avec l'accord de mes encadrants, j'ai décidé de compléter ce premier axe en travaillant également sur la morphologie du labyrinthe membraneux (Fig. 2), élément crucial car directement lié aux propriétés fonctionnelles de l'oreille interne.
Ce projet de recherche s'est mis en place avec la collaboration de Romain David actuellement post-doctorant à l'Institut Max Planck (Leipzig). Sa recherche consiste à mettre en place une méthodologie solide pour observer et caractériser la morphologie du labyrinthe membraneux.

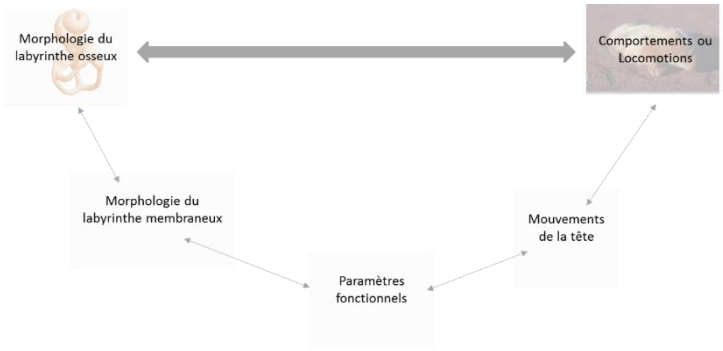

Figure 2 : Ce schéma représente la méthodologie que j'ai mise en place pendant ma thèse pour répondre le plus rigoureusement possible à la question du lien entre la morphologie du labyrinthe osseux et le comportement souterrain (flèche épaisse). Des données inédites et cruciales sur la morphologie du labyrinthe membraneux permettront d'accéder aux paramètres fonctionnels qui sont directement liés aux mouvements de la tête de l'animal, et donc à sa locomotion.

Résultats et Publications

Le mode de vie souterrain impose des mouvements de tête intenses et très fréquents. Ces contraintes mécaniques se retranscrivent dans la morphologie de l'organe gérant l'équilibre et les mouvements de tête. Afin de caractériser cette morphologie particulière de l'oreille interne membraneuse des mammifères fouisseurs, j'ai pu bénéficier d'un financement du Synchrotron européen (ESRF Grenoble), dont la technique permet d'accéder aux tissus mous sans endommager les spécimens. Parmi les spécimens scannés, 13 concernent la présente étude et représentent tous les clades de mammifères fouisseurs (marsupiaux, rongeurs, taupes, tatous). Les modélisations 3D de leur oreille interne sont en cours (Fig. 3).

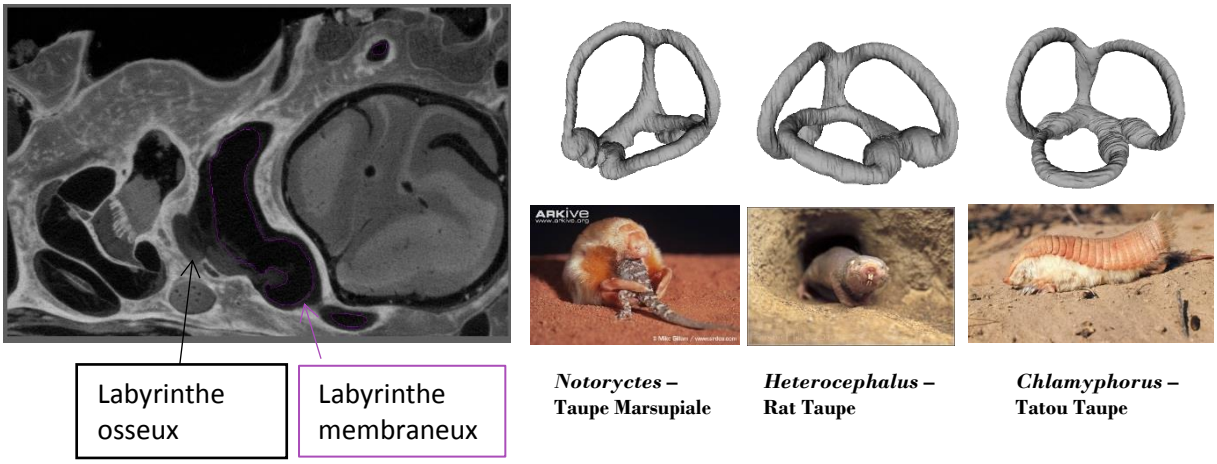

Figure 3 : L'illustration de gauche est une « coupe » issue des images synchrotron. Elle met en avant la présence du labyrinthe membraneux (= structure d'intérêt à modéliser) à l'intérieur du labyrinthe osseux. A droite, on peut observer les modèles 3D des labyrinthes membraneux de trois espèces souterraines phylogénétiquement très éloignées.

Ces premières données anatomiques sont inédites. Bien que la structure générale de l'oreille interne membraneuse semble commune à l'ensemble des mammifères, la morphologie détaillée varie, et ce, même entre des taxons qui sont proches phylogénétiquement. Ceci implique que la forme du labyrinthe comporte des informations fonctionnelles et phylogénétiques. Les résultats attendus seront proposés pour publication dans une revue internationale à fort impact, telle que Nature Ecology and Evolution.

Laboratoire d'accueil avec Justifications et Durée du séjour

La mission se déroulera au Max Planck Institut für evolutionäre Anthropologie à Leipzig (Allemagne) du mercredi 29 mars au jeudi 27 avril 2017 (1 mois).
Les activités prévues seront grandement facilitées par le poste informatique prodiguant l'ensemble des logiciels nécessaires mis à ma disposition par l'institution hôte. L'ensemble du projet nécessite l'expertise du chercheur hôte, Romain David, éminent spécialiste de l'anatomie et la physiologie de l'oreille interne et de l'analyse de données. Aussi, le traitement des données suivra la méthodologie élaborée par lui-même. Dans une perspective plus lointaine, ce séjour me permettrait aussi de consolider des liens pour un projet postdoctoral.
Cette collaboration a été mise en place dès le début de la thèse (voir PV des comités de thèse) et représente une partie considérable de ma thèse. Les précédents séjours dans cette institution m'ont permis de me former sur l'anatomie complexe de cet organe ainsi que sur les différentes méthodes.
Le financement demandé me permettrait de finaliser ce projet clé de mon doctorat et de concrétiser le fruit de la collaboration entre nos deux institutions par l'écriture d'un article scientifique.

Activités prévues et justification de la demande

Le projet ayant débuté au début de ma thèse, il est aujourd'hui presque à sa fin. Les données primaires sont déjà toutes acquises (scans synchrotron). Les données secondaires (modélisation 3D) sont en fin d'acquisition et tous les modèles 3D seront finis pour fin mars 2016. Le projet étant bien avancé, le financement d'un séjour d'un mois est adéquat et pertinent au vue des activités programmées :

- vérification des modèles 3D (quelques jours) : les modèles 3D des labyrinthes membraneux seront finis par mes soins au Muséum (plateau ASIM) avant le départ en mission mais Romain David, le collaborateur, devra vérifier ce travail durant les premiers jours de la mission.
- pose des points repères homologues (landmarks) (1 semaine et demie) : j'utilise les landmarks et les méthodes de morphométrie géométrique afin de caractériser la forme du labyrinthe membraneux.
- intégration des données dans les programmes spécifiques (2 jours) : ces logiciels, créés par Romain David, permettent de caractériser l'anatomie et la physiologie du labyrinthe membraneux.
- analyses (1 jour)
- interprétations (1 semaine)

L'emploi du temps prévisionnel est fiable car il est basé sur l'expérience : j'ai déjà pu mener à bien l'ensemble de ces activités sur les premiers spécimens lors de mes séjours précédents. Les résultats préliminaires sont prometteurs. Grâce à cette mission je pourrai finaliser mon échantillonnage et conclure ce projet. Les résultats nous permettront de caractériser la morphologie de l'oreille interne membraneuse (morphométrie classique et géométrique). Nous obtiendrons également les paramètres fonctionnels de l'oreille telle que la sensibilité.

En conclusion, cette étude va mettre en évidence la corrélation entre l'anatomie de l'oreille interne membraneuse et le mode de vie fouisseur grâce à la méthode développée par le collaborateur Romain David travaillant au Max Planck Institut für evolutionäre Anthropologie à Leipzig. Dans une perspective d'ouverture du projet de recherche, la corrélation établie permettra d'inférer un mode de vie aux fossiles. Replacés dans un contexte évolutif et temporel, ces résultats permettront de préciser l'importance de ce mode de vie dans l'histoire des mammifères, en particulier au passage des grandes crises biologiques.

Budget prévisionnel et co-financement envisagé

Pour 1 mois, du mercredi 29 mars au jeudi 27 avril 2017.
TRAIN : 273 € (Paris -> Leizig le 29/03/17 à 131 € et Leipzig -> Paris le 27/04/17 à 142€)
TRANSPORT en commun sur place : 22 €
LOGEMENT : 725 € (25 € / nuit x 29 nuits). Une chambre est proposée par l'institut.
REPAS : 450 € (soit 15 € / jour)
TOTAL = 1470 €

Mon laboratoire (UMR 7207, CR2P) s'engage à compléter le financement de la mission en cas d'obtention de la bourse de mobilité « Transhumance » (Voir attestation suivante).